Impact du changement climatique dans le système de Humboldt

A. Bel Madani

THÈSE

En vue de l'obtention du

DOCTORAT DE L'UNIVERSITÉ DE TOULOUSE

Délivré par *l'Université Toulouse III - Paul Sabatier*
Discipline ou spécialité : Océanographie Physique

Présentée et soutenue par Ali BEL MADANI
Le 14 décembre 2009

Titre :

Impact du changement climatique dans le Système de Courant de Humboldt simulé par un modèle régional océanique / Impact of climate change in the Humboldt Current System simulated by a regional ocean model

---

JURY

Nicholas Hall (Président)
Eric Guilyardi (Rapporteur)
Sabrina Speich (Rapporteur)
Oscar Pizarro (Examinateur)
Philippe Gaspar (Examinateur)
Francis Codron (Examinateur)
Boris Dewitte (Directeur de thèse)
Vincent Echevin (Co-directeur de thèse)
Abdellatif Orbi (Invité)

Ecole doctorale : *Sciences de l'Univers, de l'Environnement et de l'Espace (SDU2E)*
Unité de recherche : *Laboratoire d'Etudes en Géophysique et Océanographie Spatiales*
Directeurs de Thèse : *Boris Dewitte (directeur de recherche IRD)*
et Vincent Echevin (chargé de recherche IRD)

Remerciements

Je tiens à dédier cette thèse à feu mon grand-père, Sidi Driss Bel Madani, qui avait toujours rêvé de me voir devenir docteur un jour.

Je remercie mon directeur de thèse, Boris Dewitte, pour ses conseils et son aide précieuse tout au long de mes trois années de doctorat. Je le remercie également de m'avoir fait confiance quant à ma capacité de mener à bout mon projet de recherche, ce qui ne fut pas une mince affaire. Enfin, je le remercie pour son soutien sans faille à mon projet professionnel post-doctorat.

Je remercie aussi mon co-directeur de thèse, Vincent Echevin, pour m'avoir accueilli à plusieurs reprises au LOCEAN à Paris, notamment au cours du dernier semestre de ma thèse, qui fut très productif du point de vue scientifique. Je suis également reconnaissant envers Yves du Penhoat, pour son soutien et son intérêt pour le projet, ainsi que pour sa bonne humeur et sa joie de vivre!

Merci également à mes collègues Péruviens du CIMOBP à l'IMARPE (Lima), qui m'ont accueilli à bras ouverts à mon arrivée au Pérou et ont partagé leur quotidien pendant ces deux belles années passées à leur côté. Merci donc à Sara Purca, Jorge Tam, Ricardo Oliveros, Carlos Quispe, Carlos Ruiz, David Correa, Daniel Quispe, Augusto Ingunza, Miguel Saavedra et Jose Pasapera. Plus généralement, je remercie tout le personnel de l'IMARPE pour leur gentillesse et leur bonne humeur. Je ne voudrais pas oublier l'équipe de la représentation de l'IRD au Pérou pour leur assistance au cours de mes démarches diverses et variées, et plus simplement pour leur accueil chaleureux: merci à Pierre Soler, Gérard Hérail, Miriam Soto, Jeannette Gibon, Lourdes Valdivia, Alexandra Roulet, Liliana Lalonde, Alain Corde, Jose Berrospi et Tadeo. Je remercie également les chercheurs, ingénieurs et étudiants de l'IRD expatriés au Pérou ainsi que leurs familles, pour leur amitié et leurs conseils. Arnaud et Sophie Bertrand, Alexis Chaigneau, Raphaële Mis, François et Marcelle Gerlotto, Jérémie Habasque, Abdel Sifeddine, François Colas, Thomas Condom, Hugo et Alexandra Perfettini, Francis et Patricia Bondoux, Mathieu Lengaigne, Céline Valadeau, Yannick et Lizbeth Estevez, Martin Marzloff, Arnaud Gizolme: merci!

La liste ne serait pas complète sans mes collègues français (et étrangers) du LEGOS et du LOCEAN, en particulier ceux qui ont également partagé avec moi l'expérience péruvienne: Julien Boucharel, Lionel Renault, Timothée Brochier, Katerina Goubanova et Sulian Thual. Une pensée particulière pour mes collègues de bureau successifs: Jérôme Bouffard, Fabien Durand, Fernanda Jardon, Anne-Charlotte Peter, Pascal Terray, Myriam Khodri. Un grand merci à l'équipe administrative du LEGOS (Martine Ména, Nadine Lacroux, Catherine Donati, Brigitte Cournou) et du LOCEAN (Dany Thomas, Christiane Willem, Stéphane Ahin), sans qui mes différentes missions entre Toulouse, Paris et Lima (sans oublier toutes les autres!) n'auraient été possibles.

Merci aussi à mes collègues étrangers. Je pense en particulier à David Field ainsi qu'à Soon-Il An. Merci à tous les membres du jury pour avoir accepté de prendre la peine et le temps de se plonger dans mon manuscrit et pour avoir contribué à son amélioration.

Merci à l'IRD, à CLS ainsi qu'au CNRS pour leur soutien financier pendant ces trois années. Merci aussi à l'ANR, à Eur-Oceans ainsi qu'au programme ATUPS de l'UPS pour leur soutien financier aux différents déplacements que j'ai eu à effectuer.

Je remercie les groupes de modélisation, le Program for Climate Model Diagnosis and Intercomparison (PCMDI) et le Working Group on Coupled Modelling (WGCM) du World Climate Research Programme (WCRP) pour leurs rôles dans la mise à disposition de la base de données multi-modèles WCRP Coupled Model Intercomparison Project phase 3 (CMIP3). Le support de cette base de données est fourni par l'Office of Science, U.S. Department of Energy. Les données COADS sont fournies par le NOAA-CIRES Climate Diagnostics Center, Boulder, Colorado, USA, depuis leur site Web à http://www.cdc.noaa.gov/. Je remercie le Centre Européen pour les Prévisions Météorologiques à Moyen-Terme (CEPMMT) pour la mise à disposition des données de la réanalyse ERA-40. Je tiens également à remercier William S. Kessler pour m'avoir aidé à trouver les données ADCP de la NOAA à 95°W (10°N-10°S).

Un grand merci également à toute ma famille ainsi qu'à mes amis pour leur soutien sans faille. Enfin, je tiens à remercier ma femme Dominique qui est à mes côtés depuis plusieurs années et a su y rester pendant ces trois ans parfois difficiles! Domi, je te remercie du fond du cœur.

Acknowledgements

I would like to dedicate this thesis to my late grandfather, Sidi Driss Bel Madani, who always dreamed of seeing me become a doctor some day.

I wish to thank my PhD supervisor, Boris Dewitte, for his guidance and precious help all along the past three years. I am grateful to him for trusting me in regard to my ability to conduct my research project, which was not an easy task. Last but not least, I thank him for his unwavering support to my post-doctoral professional project.

I would also like to thank my PhD co-advisor, Vincent Echevin, for welcoming me several times at LOCEAN in Paris, particularly during the last semester of my thesis, which was very productive from the scientific point of view. I am also grateful to Yves du Penhoat, for his support and his interest in the project, as well as for his good mood and his love of life!

Many thanks also to my Peruvian colleagues of CIMOBP at IMARPE (Lima), who welcomed me with open arms at my arrival in Peru, and who shared their everyday life during these two wonderful years spent together. So thanks to Sara Purca, Jorge Tam, Ricardo Oliveros, Carlos Quispe, Carlos Ruiz, David Correa, Daniel Quispe, Augusto Ingunza, Miguel Saavedra and Jose Pasapera. More generally, I thank all IMARPE staff for their kindness and their good mood. Furthermore, my gratitude goes to the staff of the IRD representation in Peru for their assistance during my various administrative applications and processes, and more simply for their warm welcome: thanks to Pierre Soler, Gérard Hérail, Miriam Soto, Jeannette Gibon, Lourdes Valdivia, Alexandra Roulet, Liliana Lalonde, Alain Corde, Jose Berrospi and Tadeo. I also thank the expatriate scientists, engineers and students of IRD in Peru as well as their families, for their friendship and their advice. Arnaud and Sophie Bertrand, Alexis Chaigneau, Raphaële Mis, François and Marcelle Gerlotto, Jérémie Habasque, Abdel Sifeddine, François Colas, Thomas Condom, Hugo and Alexandra Perfettini, Francis and Patricia Bondoux, Mathieu Lengaigne, Céline Valadeau, Yannick and Lizbeth Estevez, Martin Marzloff, Arnaud Gizolme: thank you!

The list would not be complete without my French (and non-French) colleagues from LEGOS and LOCEAN, especially those who also shared the Peruvian experience with me:

Julien Boucharel, Lionel Renault, Timothée Brochier, Katerina Goubanova and Sulian Thual. A special thought goes to my office mates: Jérôme Bouffard, Fabien Durand, Fernanda Jardon, Anne-Charlotte Peter, Pascal Terray, Myriam Khodri. Many thanks to the administrative staff of LEGOS (Martine Ména, Nadine Lacroux, Catherine Donati, Brigitte Cournou) and LOCEAN (Dany Thomas, Christiane Willem, Stéphane Ahin), without whom my various travels between Toulouse, Paris and Lima (and all the others!) would not have been possible.

Thanks also to my foreign colleagues. In particular, I am thinking of David Field and Soon-Il An. Thanks to all the jury members for accepting to spend the necessary time to read the dissertation and for contributing to improve it.

Thanks to IRD, CLS and CNRS for financial support during these three years. Thanks also to ANR, to Eur-Oceans and to the ATUPS program of UPS for supporting the different trips I made.

I acknowledge the modelling groups, the Program for Climate Model Diagnosis and Intercomparison (PCMDI) and the World Climate Research Programme's (WCRP's) Working Group on Coupled Modelling (WGCM) for their roles in making available the WCRP Coupled Model Intercomparison Project phase 3 (CMIP3) multi-model dataset. Support of this dataset is provided by the Office of Science, U.S. Department of Energy. COADS data is provided by the NOAA-CIRES Climate Diagnostics Center, Boulder, Colorado, USA, from their Web site at http://www.cdc.noaa.gov/. The European Centre for Medium-Range Weather Forecasts (ECMWF) is thanked for making available the ERA-40 reanalysis data. I would also like to thank William S. Kessler for helping me find the NOAA ADCP data at 95°W (10°N-10°S).

Big thanks as well to my family and friends for their encouragement and continuous support. Last but not least, I am deeply grateful to my wife Dominique, who has been at my side for several years and who never failed in her support during the past three years, which were not always easy! Domi, thank you from all my heart.

Table of Contents

Résumé

« Quels sont les pré-requis pour étudier l'influence du changement climatique simulé par les modèles couplés globaux de la génération actuelle sur le système d'upwelling du Pérou-Chili?» constitue la question centrale de cette thèse de doctorat. Grâce à une approche de *downscaling* (descente d'échelle) dynamique réalisé avec le modèle ROMS (*Regional Oceanic Modelling System*) pour une configuration au 1/6° de type *eddy-resolving* (*cad* qui permet de représenter les tourbillons mésoéchelle), nous espérons comprendre les processus qui vont contrôler les changements futurs de la circulation océanique dans cette région influencée par ENSO (El Niño-Oscillation Australe).

Une étude des mécanismes physiques qui contrôlent la variabilité de type ENSO dans les simulations PI (pré-industrielles) réalisées avec les CGCMs (Modèles Couplés de Circulation Générale) de l'ensemble multi-modèle du WCRP-CMIP3 (les « modèles du GIEC ») permet d'identifier les modèles les plus fiables en termes de variabilité équatoriale. Elle est basée sur l'utilisation d'un modèle couplé intermédiaire du Pacifique tropical avec une stratification moyenne et un forçage de vent prescrits, afin de pouvoir dériver explicitement les termes d'advection du bilan de chaleur de la couche de mélange. Cette analyse permet de classifier les modèles en fonction de leur processus ENSO dominant: *zonal advective feedback* ou *thermocline feedback*.

Les modèles au feedback hybride comme dans les observations représentent le mieux les processus couplés qui contrôlent la variabilité de la TSM, ce qui nous conduit à faire l'hypothèse que ce sont ceux qui fournissent les indices de confiance les plus élevés en termes de prédiction de l'évolution d'ENSO avec le réchauffement global. Parmi eux, deux CGCMs (IPSL-CM4 et INGV-ECHAM4) reproduisent le mieux l'état moyen ainsi que la variabilité intrasaisonnière à interannuelle de la température et des courants à la frontière Ouest du domaine du Pérou-Chili (100°W) et sont donc retenus pour des expériences de downscaling sur la région du HCS (Système de Courant de Humboldt).

Les sorties océaniques des simulations PI et $4xCO_2$ (quadruplement de CO_2) réalisées avec ces CGCMs sont utilisées directement comme conditions aux frontières ouvertes du modèle ROMS, tandis qu'un produit de vent haute-résolution (~50km) dérivé des CGCMs au moyen d'une méthode de downscaling statistique ainsi que les flux air-mer issus des CGCMs sont utilisés pour fournir le forçage atmosphérique. Par ailleurs, une simulation régionale de contrôle est réalisée à

l'aide de ROMS avec des conditions aux frontières (réanalyse globale ORCA05 ½°) et un forçage atmosphérique (vents du satellite ERS et flux de la réanalyse atmosphérique globale ERA-40) réalistes sur la période 1992-2000. Cette simulation sert de référence pour les simulations de changement climatique régional.

Elle permet notamment de documenter l'impact des ondes de Kelvin équatoriales intrasaisonnières sur la variabilité près de la côte, et illustrer ainsi l'importance du forçage à distance d'origine équatoriale pour la dynamique régionale du HCS. Nos résultats montrent en particulier que la latitude critique du modèle est située 5 à 15 degrés plus au sud que celle prédite par la théorie linéaire des ondes libres baroclines, surtout pour les oscillations autour de 120 jours. Le modèle régional présente une variabilité du large significative au sud de la latitude critique théorique, ce qui est également le cas dans les données satellite, soulignant ainsi les limites de la théorie linéaire dans le Pacifique Sud Est.

De manière plus générale, ce travail propose une méthodologie pour effectuer des expériences de downscaling du changement climatique, qui constituent le lien nécessaire entre simulations du réchauffement global à l'échelle planétaire et études d'impact sur les écosystèmes, la pêche, l'agriculture et la société à l'échelle locale. Le travail contribue également à améliorer notre compréhension de certains mécanismes d'intérêt pour de telles études du changement climatique à l'échelle régionale.

Abstract

« What do we need to study the influence of climate change simulated by global coupled models of the current generation upon the Peru-Chile upwelling system » is the main question addressed in this PhD thesis. Thanks to a dynamical downscaling approach performed with the ROMS model (Regional Oceanic Modelling System) at an eddy-resolving resolution (1/6°), we aim at understanding the processes that are likely to control possible future changes in the ocean circulation over this region influenced by ENSO (El Niño-Southern Oscillation).

A study of the physical mechanisms that control ENSO-like variability in PI (pre-industrial) simulations performed with CGCMs (Coupled General Circulation Models) of the WCRP-CMIP3 multi-model ensemble (the so-called « IPCC-AR4 models ») allows identifying the most reliable models in terms of equatorial variability. It makes use of an intermediate coupled model of the tropical Pacific with prescribed mean stratification and wind forcing in order to derive explicitly the tendency terms of the mixed layer heat budget. Such analysis allows classifying the models according to the dominant ENSO process: zonal advective feedback or thermocline feedback.

Models with a hybrid feedback like in the observations best represent the coupled processes that control SST variability, which makes us assume that they provide the highest confidence levels in terms of prediction of ENSO evolution under global warming. Among them, two CGCMs (IPSL-CM4 and INGV-ECHAM4) best reproduce mean temperature and currents as well as their intraseasonal-to-interannual variabilities at the western boundary of the Peru-Chile domain (100°W) and are therefore retained for downscaling experiments over the HCS (Humboldt Current System) region.

CGCM outputs from the PI and 4xCO_2 (CO_2 quadrupling) simulations for the oceanic part are used directly as open boundary conditions for ROMS, whereas a high-resolution (~50km) CGCM-derived wind product obtained from a statistical downscaling procedure is used together with raw CGCM air-sea fluxes for the atmospheric forcing. A regional control run using ROMS is performed with realistic boundary conditions (ORCA05 ½° global reanalysis) and atmospheric forcing (ERS satellite winds and ERA-40 global atmospheric reanalysis fluxes) over 1992-2000 in order to provide a benchmark for regional climate change simulations.

This control simulation is also used to document the impact of intraseasonal equatorial Kelvin waves on nearshore variability, and illustrates the importance of the remote forcing of equatorial origin for the regional dynamics of the HCS. In particular, it is found that depending on the vertical baroclinic mode, the critical latitude in the model is about 5 to 15 degrees higher than that predicted by linear free baroclinic wave theory, especially for 120-day oscillations. The regional model features significant offshore variability south of the theoretical critical latitude like in satellite data, underlining the limits of linear theory in the eastern South Pacific.

Overall this work proposes a methodology for climate change downscaling experiments, which are the necessary link between global warming simulations at the global scale and impact studies on ecosystems, fisheries, agriculture and society at the local scale. The work also contributes to improve our understanding of some physical mechanisms of interest for such regional climate change studies.

Introduction

L'océan côtier, défini comme la portion d'océan délimitée d'un côté par la côte et de l'autre par le plateau continental, représente seulement 10 % environ de la surface de l'océan mondial et une partie négligeable de son volume. En revanche, il concentre de nombreuses ressources d'intérêt économique qui sont exploitées intensivement du fait de leur accessibilité, et car plus de la moitié de l'humanité vit à moins de 100 km des côtes. En particulier, la pêche fournit une des principales sources d'approvisionnement en nourriture et occupe un secteur important de l'économie pour de nombreux pays. C'est particulièrement vrai pour les Systèmes d'Upwelling de Bord Est (EBUS), qui concentrent 30% environ des prises de poisson dans le monde sur seulement 0.1 % de la surface couverte par les océans (Durand et al., 1998). Dans ces régions, des vents alizés persistents entraînent la formation d'un intense upwelling côtier, *cad* la remontée/résurgence d'eaux froides et riches en nutriments, qui fournissent des conditions adéquates pour le développement d'une production primaire élevée et d'abondants écosystèmes marins. Il y a quatre EBUS, situés dans les deux hémisphères le long des bords orientaux des deux principaux bassins océaniques (le Pacifique et l'Atlantique): le Courant des Canaries dans l'Atlantique Nord, le Courant du Benguela dans l'Atlantique Sud, le Courant de Californie dans le Pacifique Nord et le Courant de Humboldt dans le Pacifique Sud (figure 0.1).

Dans cette thèse de doctorat, l'accent est mis sur le Système de Courant de Humboldt (HCS) qui caractérise l'océan côtier au large du Pérou et du Chili. Le HCS est le troisième EBUS en termes de productivité primaire par unité de surface, mais de loin le premier en termes de prises de poisson (Chavez et al., 2008): 11 millions de tonnes de poisson sont attrapées chaque année au large du Pérou et du Chili, ce qui représente 12% des prises mondiales, effectuées principalement sur des espèces pélagiques comme la sardine et l'anchois (F.A.O, 2009). Le Pérou en particulier est si productif que plusieurs naufrages de bateaux de pêche sont signalés chaque année à cause du poids excessif de poisson qu'ils transportent. Cette abondance incroyable fait de la pêche une source de revenus importante pour ces pays, d'autant plus qu'une grande partie des prises est exportée. Mise à part la ressource halieutique, une particularité du HCS comparé à d'autres EBUS tient à sa proximité par rapport à l'équateur et à l'orientation de son littoral, qui le rendent très sensible à la variabilité équatoriale, notamment celle liée à ENSO (El Niño-Oscillation Australe), qui est

l'anomalie climatique la plus forte sur la planète aux échelles de temps interannuelles (ex: Neelin et al., 1998; Cane, 2005; McPhaden et al., 2006). Pendant un événement El Niño, la circulation océanique régionale et le climat du HCS subissent des changements spectaculaires: les eaux de surface fraîches (de 15°C à 19°C) qui caractérisent habituellement l'océan côtier du Pérou et du Chili et qui lui ont donné le surnom de "réfrigérateur des tropiques" peuvent monter jusqu'à 8°C au-dessus des normales saisonnières (Blanco et al., 2002; Carr et al., 2002). Ce réchauffement intense de l'océan est accompagné par de fortes précipitations et des inondations sur les côtes habituellement arides du Pérou et du nord du Chili, avec des conséquences dramatiques pour l'agriculture et les activités humaines en général. De plus, le réchauffement de l'océan peut entraîner une réduction significative voire même l'arrêt de l'upwelling côtier, avec des conséquences graves pour l'écosystème marin (Barber et Chavez, 1983). Aux échelles de temps plus longues, les stocks de poissons pélagiques subissent de fortes fluctuations en relation avec la variabilité decadale de l'Océan Pacifique: par exemple, le brusque changement de régime climatique du Pacifique tropical survenu en 1976 a causé l'effondrement des stocks de sardine et la multiplication des anchois (Chavez et al., 2003). Du fait de cette sensibilité du HCS à la variabilité climatique à grande échelle, les changements potentiels à l'échelle régionale liés au réchauffement climatique pourraient être importants et avoir des conséquences biologiques dramatiques. Dans ce contexte, la gestion durable des pêches apparaît comme une question sociale et économique déterminante pour les pays voisins, mais aussi pour le monde entier, à cause de l'importance de la ressource halieutique du HCS à l'échelle globale, en particulier dans un contexte de surpêche et de déclin des stocks de poisson dans de nombreuses parties du monde.

L'IRD (Institut de Recherche pour le Développement), un institut français de recherche publique qui vise à aider les pays en développement dans le développement de leurs capacités de recherche, collabore avec des partenaires de recherche locaux au Pérou et au Chili depuis environ une décennie. De même, il contribue activement à plusieurs projets de recherche dans deux autres EBUS, à savoir le Courant du Benguela et le Courant des Canaries. Récemment, l'institut a commencé à promouvoir des approches pluridisciplinaires pour l'étude des EBUS, partant du principe que des études de l'environnement marin physique ainsi que du climat sont un pré-requis pour des études intégrées des écosystèmes marins associés. Dans ce contexte, l'IRD a pris un rôle déterminant dans la définition du programme PCCC (Peru-Chile Climate Change, P.I. Dr. Boris Dewitte) financé par l'ANR (Agence Nationale de la Recherche), l'agence de financement de la recherche publique française. En effet, la gestion durable des pêches dépend fortement de notre capacité à prévoir les impacts

régionaux du réchauffement climatique. Le programme PCCC propose d'aborder cette question du point de vue océanique avec l'approche de la modélisation à haute résolution. L'objectif de PCCC est double: 1) comprendre les facteurs qui impactent la circulation régionale du Pérou et du Chili avec un intérêt particulier pour les processus de téléconnexion entre la variabilité équatoriale et la circulation côtière; et 2) fournir une évaluation de l'impact du changement climatique sur la circulation régionale du Pérou et du Chili. La présente thèse de doctorat est une contribution majeure à ce programme: elle a permis le développement d'une méthodologie objective d'une part pour analyser les erreurs à grande échelle des modèles couplés susceptibles d'influencer les comportements passés, présents et futurs simulés dans le HCS, et d'autre part pour identifier les modèles les plus appropriés pour étudier le changement climatique dans cette région. De plus, cette thèse a contribué à analyser la dynamique régionale océanique moderne, qui est utilisée comme référence pour comprendre les changements futurs du HCS.

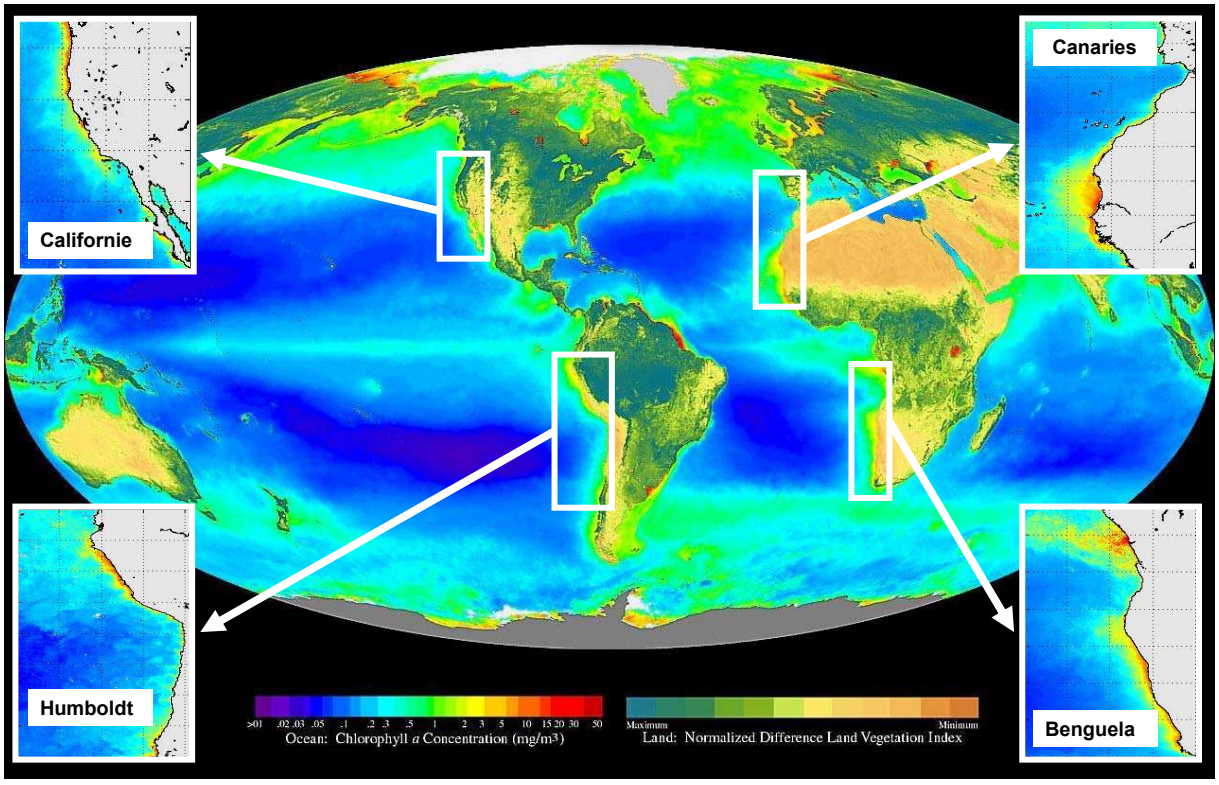

Fig. 0.1: Concentration moyenne de chlorophylle-a en surface (mg/m3) sur la période 09/1997-08/2000 à partir des données satellite SeaWiFS (NASA/Goddard Space Flight Center). Les quatre principaux EBUS sont indiqués: le Courant de Californie, le Courant de Humboldt, le Courant des Canaries et le Courant du Benguela. Les cartes régionales sont mises à disposition par l'IRD/AOOS.

Ce manuscrit présente les principaux résultats obtenus dans le cadre de la thèse. En premier lieu, nous présenterons le fonctionnement physique des EBUS en général et du HCS

en particulier, en liaison avec le contexte actuel de changement climatique et de ses impacts potentiels à l'échelle régionale, en nous basant sur des études antérieures. Dans un second temps, les caractéristiques des modèles climatiques globaux pertinentes pour l'étude de la circulation régionale océanique dans le HCS seront évaluées et utilisées afin d'identifier les modèles les plus appropriés pour des expériences de downscaling (descente d'échelle) sur cette région. Après quoi, l'approche de modélisation sera détaillée et les résultats d'une simulation régionale réalisée sur la période récente et illustrant la variabilité naturelle du HCS ainsi que sa sensibilité au forçage distant d'origine équatoriale sera présentée. Enfin, nous fournirons quelques résultats issus d'expériences de changement climatique régional réalisées dans le contexte de PCCC, dans le but de fournir des indices permettant de prévoir la réponse possible du HCS au changement climatique.

Chapitre 1: Système de Courant de Humboldt et Changement Climatique

Ce chapitre est une synthèse d'études précédentes portant sur la dynamique régionale océanique dans le HCS, suivie par une présentation de l'influence potentielle du réchauffement climatique dans cette région de l'océan mondial. Dans la première section, nous présenterons les principales caractéristiques physiques des EBUS, dans le but de comprendre ce qui les rend si particuliers en termes de physique océanique comme de productivité biologique, avant de nous concentrer sur le HCS et sur ses spécificités comparées à celles des autres EBUS. Dans la deuxième section, nous proposerons une synthèse des travaux antérieurs qui ont tenté de décrire les impacts possibles du changement climatique dans les EBUS en général et dans le HCS en particulier. Ce résumé des connaissances actuelles sur le HCS et sur le changement climatique dans la région sera utilisé comme le point de départ pour le développement de notre approche de modélisation visant à prévoir l'impact du réchauffement climatique futur sur le HCS, qui sera présenté dans les chapitres suivants. A noter: une vue synthétique du réchauffement climatique passé, présent et futur est présentée dans l'annexe A.

1.1. Présentation du Système de Courant de Humboldt

1.1.1. Systèmes d'Upwelling de Bord Est

1.1.1.1. Introduction

Le Système de Courant de Humboldt (HCS), également appelé système d'upwelling du Pérou-Chili, est le Système d'Upwelling de Bord Est (EBUS) de l'Océan Pacifique Sud. Les EBUS sont situés dans les deux hémisphères le long des côtes Ouest des continents bordant les deux principaux bassins océaniques, à savoir l'Océan Pacifique et l'Océan Atlantique. Ils sont visibles depuis l'espace car la production primaire élevée qui caractérise ces systèmes permet d'observer leur variabilités physique et biogéochimique avec la chlorophylle-a, comme l'illustre la figure 0.1. Il est généralement admis qu'il existe quatre EBUS principaux:

- Le **Système de Courant des Canaries**, present le long des côtes de la Guinée-Bissau et du Sénégal jusqu'au nord du Maroc, avec une extension septentrionale le long du Portugal et du nord-ouest de l'Espagne appelé système d'upwelling ibérique occidental;

- Le **Système de Courant du Benguela**, s'étendant de la pointe sud-ouest de l'Afrique du Sud jusqu'en Angola;

- Le **Système de Courant de Californie**, s'écoulant le long de la côte ouest de la Basse-Californie (Mexique) et de la côte ouest des États-Unis (Californie, Oregon, Washington);

- Le **Système de Courant de Humboldt**, qui caractérise presque toute la côte ouest d'Amérique du Sud, du Chili central vers 40°S au nord du Pérou près de l'équateur.

Les emplacements géographiques de ces systèmes d'upwelling sont déterminés par la position des anticyclones des moyennes latitudes, situés dans les bassins Nord et Sud du Pacifique et de l'Atlantique. En effet, ces systèmes de hautes pressions ont des branches orientales caractérisées par des alizés à basse altitude dirigés vers l'équateur. Près de la côte, ces vents ont souvent tendance à avoir une direction parallèle à la côte, induisant un transport d'Ekman des eaux de surface vers l'ouest (Ekman, 1905), qui sont alors remplacées par des eaux plus profondes remontant à la surface. Cet upwelling côtier apporte de l'eau froide et des nutriments vers les couches superficielles, fournissant les conditions adéquates pour le développement d'ichtyo- et de zoo-plancton (Skogen, 2005; Sutor et al., 2005; Vélez et al., 2005), qui sont à la base d'écosystèmes marins très riches et de la pêche la plus productive du

monde (Durand et al., 1998). De plus, les EBUS sont systématiquement associés à un système de courants côtiers, principalement constitués d'un courant de surface dirigé vers l'équateur et par un courant de sub-surface (ou sous-courant) dirigé vers le pôle (Sud). Les instabilités baroclines produites par le cisaillement vertical associé à ces courants peuvent déclencher la formation de méandres et de tourbillons mésoéchelle (Leth et Shaffer, 2001; Leth et Middleton, 2004; Marchesiello et al., 2003, 2004), qui sont communs le long de ces côtes (Chaigneau et al., 2009). On pense que les tourbillons mésoéchelle contribuent de manière significative aux transferts de masse et de chaleur de la zone côtière vers l'océan hauturier. Ils jouent également un rôle important dans la dynamique spatiale des zones de reproduction et de nurserie des petits poissons pélagiques (Logerwell et al., 2001; Lett et al., 2007; Brochier et al., 2008). De plus, la plupart des EBUS comprennent la présence d'ondes libres piégées à la côte d'origine équatoriale (Moore, 1968; Clarke, 1983), qui sont capables de perturber fortement l'hydrographie et les courants locaux. Dans la subsection suivante, les mécanismes physiques de transport et de pompage d'Ekman, la dynamique des courants côtiers, les processus méso- à subméso-échelle et la propagation des ondes piégées à la côte sont brièvement décrits.

1.1.1.2. Dynamique de l'upwelling côtier

Transport et pompage d'Ekman

Selon la théorie d'Ekman (Ekman, 1905), des vents soufflant à basse altitude au-dessus de l'océan forcent une circulation sous la surface, qui est déviée à droite dans l'hémisphère nord et à gauche dans l'hémisphère sud en raison de la force de Coriolis. À la surface, le mouvement résultant est dirigé à 45° par rapport à la direction du vent, dans le sens des aiguilles d'une montre (resp. dans le sens inverse des aiguilles d'une montre) dans l'hémisphère nord (resp. sud). La tension turbulente associée à un tel mouvement force une circulation dans la couche d'eau située juste en-dessous de la couche superficielle, avec un angle qui dépend du coefficient de viscosité verticale turbulente. Le même processus est répété pour chaque couche de la colonne d'eau, avec une décroissance exponentielle des courants associés avec la profondeur. Les déplacements horizontaux associés à la tension de vent superficielle peuvent être décrits sur la colonne d'eau de la surface au fond par la spirale d'Ekman (fig. 1.1). En intégrant les équations associées sur la verticale, on obtient les transports nets zonal T_x et méridional T_y:

$$T_x = \frac{\tau_y}{\rho f}$$

$$T_y = -\frac{\tau_x}{\rho f}$$

où τ_x et τ_y représentent les composantes zonale et méridionale de la tension de vent en surface, ρ représente la densité de l'eau de mer, et f le paramètre de Coriolis:

$$f = 2\Omega \sin\varphi$$

où Ω représente la vitesse de rotation de la terre et φ la latitude.

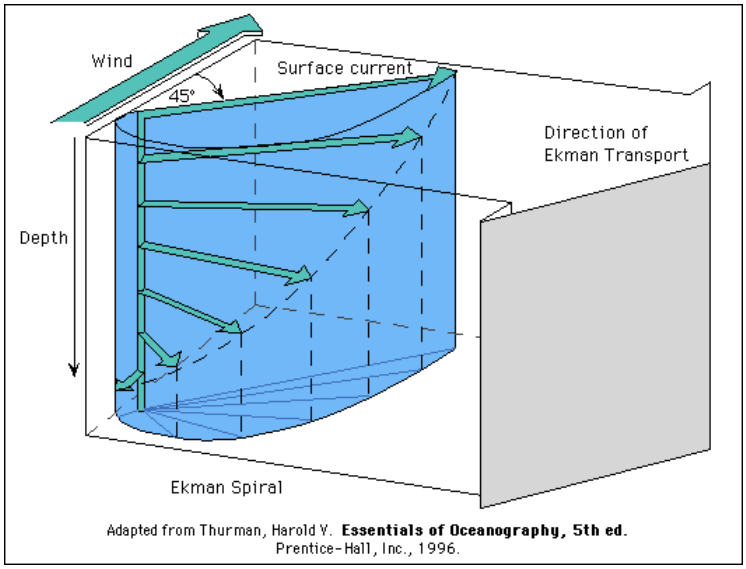

Fig. 1.1: Schéma de la spirale et du transport d'Ekman dans l'hémisphère nord.

Le transport d'eau net, appelé transport d'Ekman, est donc perpendiculaire à la direction du vent et dirigé vers la droite (resp. la gauche) par rapport à la direction du vent dans l'hémisphère nord (resp. sud), comme l'indique la figure 1.1. À cause de la décroissance exponentielle des courants, le transport d'Ekman est principalement restreint dans une couche superficielle appelée couche d'Ekman. En-dessous de la couche d'Ekman, l'influence du vent sur les courants océaniques est faible et peut être aisément négligé.

Dans le cas des EBUS, le transport d'Ekman a une importance fondamentale pour la compréhension de la dynamique océanique. Considérons le cas d'un vent quasi-constant soufflant parallèlement à la côte et dirigé vers l'équateur, comme c'est généralement le cas pour les EBUS. Le transport d'Ekman résultant est dirigé vers l'ouest et les eaux chaudes de la couche d'Ekman s'éloignent alors de la côte en direction du large (fig. 1.2). Pour compenser cette perte de volume, des eaux plus fraîches des couches plus profondes sont advectées vers

le littoral et vers le haut lorsqu'elles atteignent la côte: ce phénomène est appelé upwelling côtier (fig. 1.4).

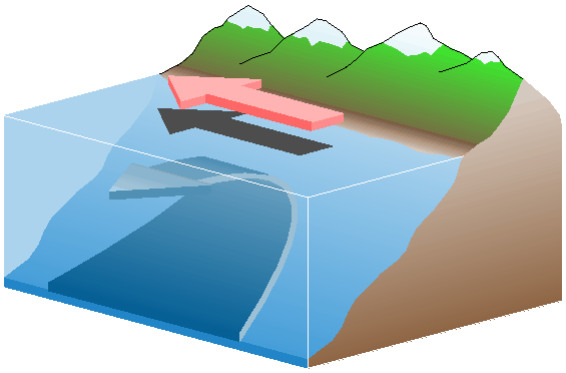

Fig. 1.2: Schéma de l'upwelling côtier dans le HCS. La flèche rose représente les vents côtiers et la flèche bleue représente le transport d'Ekman ainsi que l'upwelling associé.

Il existe un mécanisme secondaire qui contribue également à l'upwelling côtier: le pompage d'Ekman. Le pompage d'Ekman est dû aux variations spatiales des vents de surface et des transports d'Ekman associés, qui induisent des zones de convergence et des zones de divergence des eaux dans la couche d'Ekman. Dans les zones de divergence (resp. de convergence), la conservation du volume d'eau induit des vitesses verticales dirigées vers le haut (resp. vers le bas) à la base de la couche d'Ekman, *cad* un upwelling (resp. un downwelling). Ces vitesses sont appelées pompage d'Ekman (W_{Ek}), lequel peut être écrit:

$$W_{Ek} = \frac{1}{\rho f}\left(\frac{\partial \tau_y}{\partial x} - \frac{\partial \tau_x}{\partial y}\right)$$

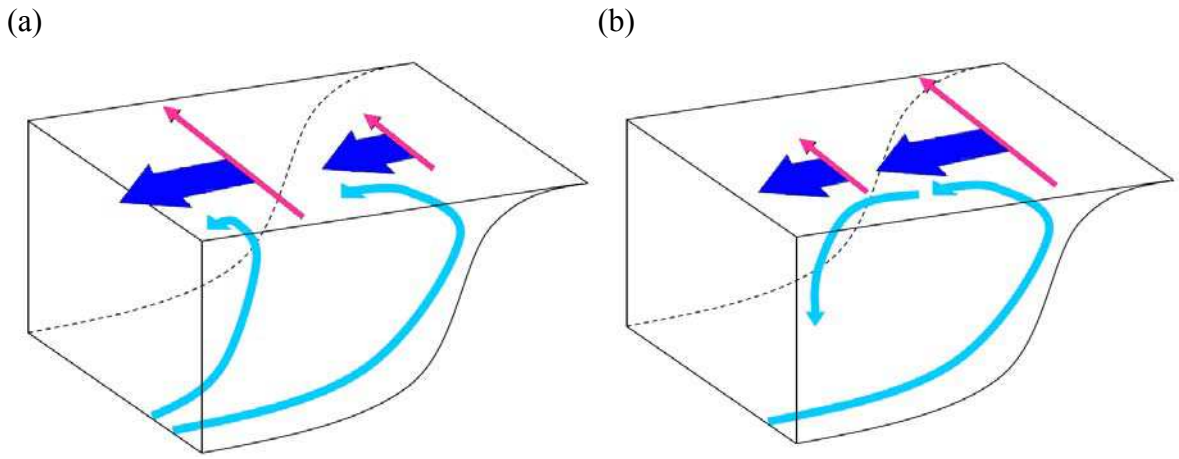

Fig. 1.3: Schéma de l'effet du pompage d'Ekman dans un EBUS de l'hémisphère Sud. Les flèches roses représentent les vents côtiers, les flèches bleu foncé représentent les transports d'Ekman et les flèches bleu clair représentent l'upwelling **(a)** ou le downwelling **(b)** associé.

En présence d'une côte, ce qui est le cas pour les EBUS, les vents côtiers sont plus forts au-dessus de l'océan qu'au-dessus de la terre car la friction à la surface est plus grande sur le continent en raison de la présence d'orographie et de végétation qui ont tendance à réduire l'intensité du vent. Ceci crée un gradient perpendiculaire à la côte des vent parallèles à la côte, d'intensité réduite près du bord dans la zone dite de *drop-off* (diminution brutale du vent). Comme l'ont expliqué Bakun et Nelson (1991), le rotationnel de vent qui en résulte induit un pompage d'Ekman dirigé vers le haut, qui s'ajoute au transport d'Ekman pour former l'upwelling côtier. Ce mécanisme est schématisé sur la figure 1.3 (a). A l'inverse, si le vent était plus fort près de la côte, ceci induirait un transport d'Ekman plus fort près de la côte que plus au large: un secteur de convergence apparaîtrait alors au large et le pompage d'Ekman serait negative, et aurait ainsi un effet de downwelling qui s'opposerait à l'effet d'upwelling dû au transport d'Ekman (fig. 1.3 (b)).

Courants Côtiers

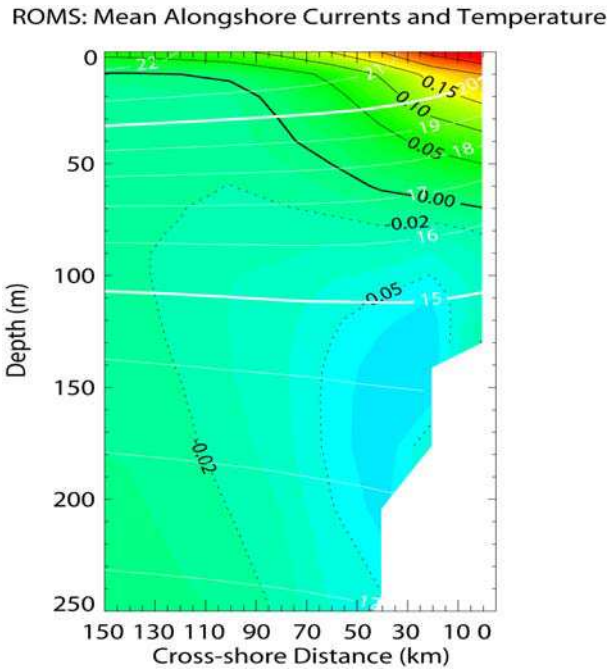

Fig. 1.4: Section verticale perpendiculaire à la côte des courants moyens parallèles à la côte (m/s) et de la température moyenne (°C) simulés par le modèle ROMS (Shchepetkin et McWilliams, 2005) à 10°S près de la côte centrale du Pérou. Les couleurs et les contours noirs représentent les courants. Les lignes continues (resp. pointillées) représentent les valeurs positives (resp. négatives), *cad* les flux dirigés vers l'équateur (resp. vers le pôle). Les contours blancs représentent la température (l'intervalle est de 1°C). L'axe des abscisses (resp. l'axe des ordonnées) représente la distance depuis la côte (resp. la profondeur) et les unités correspondantes sont le km (resp. le mètre).

Une structure similaire de courants côtiers constituée par un courant de surface dirigé vers l'équateur et un courant de sub-surface dirigé vers le pôle (cf. figure 1.4 pour le HCS) est observée pour tous les EBUS. Le mécanisme contrôlant le courant de surface est bien connu: l'upwelling côtier induit une remontée des isothermes et des isopycnes près de la côte en raison de la résurgence des eaux plus fraîches et plus denses (fig. 1.4). Par conséquent, un gradient de densité perpendiculaire à la côte est présent dans la zone littorale, avec des eaux plus denses près de la côte et des eaux moins denses plus au large: ceci induit un flux dirigé vers l'équateur près de la côte en raison de la géostrophie. De plus, le forçage direct par le vent induit également un flux dirigé vers l'équateur dans la couche d'Ekman (fig. 1.1), qui se combine avec le flux géostrophique pour former le courant de surface. En revanche, il n'y a pas de consensus sur l'origine du sous-courant observé le long des EBUS. Une théorie le lie au gradient de pression méridional près de la côte: Les eaux sont de plus en plus chaudes à mesure que l'on se rapporche de l'équateur, ce qui provoque une élévation du niveau de la mer, qui crée à son tour un flux dirigé vers le pôle (Neshyba et al., 1989). Une autre théorie basée sur les résultats d'un modèle d'océan barocline de type "shallow-water" (couches minces) dans le cas idéalisé d'un bord est d'orientation méridionale et d'une tension de vent uniforme et parallèle à la côte relie à la fois le courant de surface et le sous-courant aux différents modes baroclines. Ce modèle est capable de reproduire la profondeur et l'amplitude des courants observés (McCreary, 1981). En particulier, le sous-courant est lié à l'effet de friction de fond sur la pente (au-delà du talus du plateau continental), qui amortit les modes d'ordre élevé et amplifie ainsi le contrôle du sous-courant par les modes d'ordre intermédiaire (McCreary et Chao, 1985).

Processus mésoéchelle et sub-mésoéchelle

L'upwelling côtier induit un important gradient thermique perpendiculaire à la côte dans la zone côtière, avec des eaux plus fraîches upwellées près de la côte et des eaux de surface plus chaudes repoussées vers le large par les effets combinés du transport et du pompage d'Ekman. Par conséquent, un front de température appelé front upwelling est présent à quelques dizaines de kilomètres au large. La position et l'intensité de ce front sont soumis à la variabilité du vent, qui peut être forte aux échelles intrasaisonnières (ex: Garreaud et Muñoz, 2005; Renault et al., 2009). De plus, les vents côtiers favorables à l'upwelling sont également soumis à une variabilité significative le long de la côte en raison des variations d'orographie continentale et de forme du littoral: par exemple, les vents sont généralement

localement plus forts autour des caps parce que le ratio sol-mer d'occupation de la surface de la Terre est plus petit. Inversement, les vents sont généralement plus faibles autour des baies. La combinaison des variabilités spatiales et temporelles du vent engendrent des perturbations de petite échelle le long du front d'upwelling, qui peuvent prendre des formes diverses, comme des méandres, des filaments et des tourbillons. Les méandres sont des portions à méso- et subméso-échelle (longueur typique de quelques dizaines de kilomètres) de grande courbure du front d'upwelling ou des courants côtiers (fig. 1.5). Les filaments sont des intrusions sub-mésoéchelle du front d'upwelling dans la région hauturière (fig. 1.6) et sont caractérisés par une production primaire élevée et une activité biologique intense.

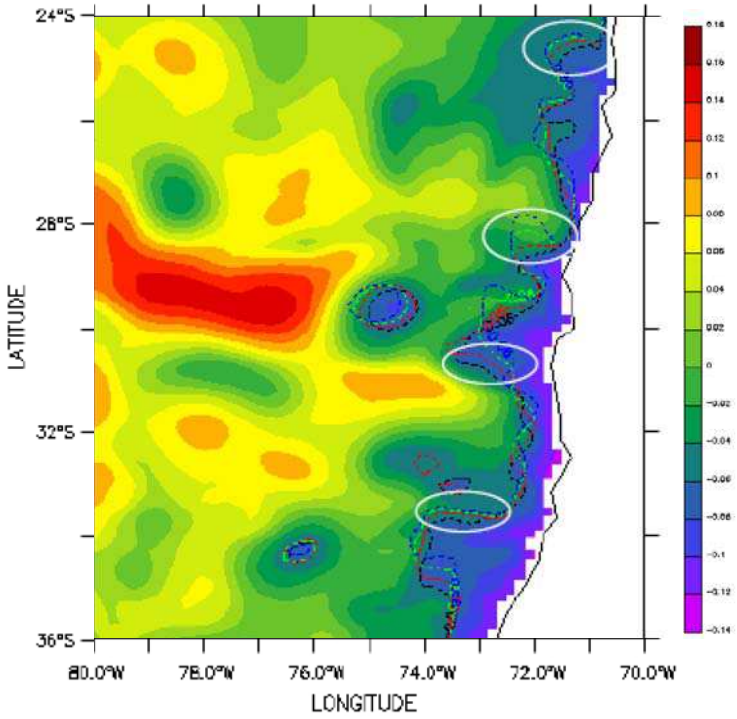

Fig. 1.5: Méandres du front d'upwelling indiqués sur une carte de SLA dans la partie sud du HCS, simulé par le modèle ROMS (résolution 1/6°, conditions aux frontières ouvertes fournies par un modèle océanique global, forçage atmosphérique constitué par des vents satellite observés et des flux air/mer réanalysés) pour le 19 août 1995. L'unité est le mètre. L'intervalle de contour est de 0.02 m. Les lignes en pointillés noirs, rouges, verts et bleus indiquent la position de l'isoligne (-6 cm) le 19 août, le 24 août, le 29 août et le 3 septembre 1995, respectivement. Les ellipses blanches indiquent la position de quelques méandres (V. Echevin, *communication personnelle*).

Les tourbillons, qui peuvent être cycloniques - *courants géostrophiques tournant dans le sens inverse des aiguilles d'une montre (resp. dans le sens des aiguilles d'une montre) dans l'hémisphère nord (resp. sud)* - ou anticyclonique - *courants géostrophiques tournant dans le sens des aiguilles d'une montre (resp. dans le sens inverse des aiguilles d'une montre) dans l'hémisphère nord (resp. sud)* - sont des structures mésoéchelle avec un rayon de l'ordre de

100km (fig. 1.7) et sont communs dans les EBUS (Chaigneau et al., 2009). Les tourbillons cycloniques (resp. anticycloniques) sont également appelés tourbillons au cœur chaud (resp. au cœur froid) parce qu'ils sont associés à une anomalie positive (resp. négative) de niveau de la mer (SLA) et à une anomalie chaude (resp. froide) de température de surface de la mer (TSM), comme l'illustre la figure 1.7. Comme les méandres et les filaments de plus petite échelle, ils peuvent être produits par les variations spacio-temporelles du front d'upwelling, qui sont le résultat d'instabilités baroclines produites par le cisaillement vertical entre le courant de surface et le sous-courant (ex: Leth et Shaffer, 2001; Marchesiello et al., 2003). Les tourbillons mésoéchelle sont produits près de la côte et se propagent vers l'ouest: pour cette raison, ce sont des contributeurs importants aux transferts de propriétés physiques de la région côtière vers l'océan hauturier. Leur variabilité spatiale près de la côte peut aussi déterminer l'emplacement des zones de reproduction des petits poissons pélagiques (Logerwell et al., 2001).

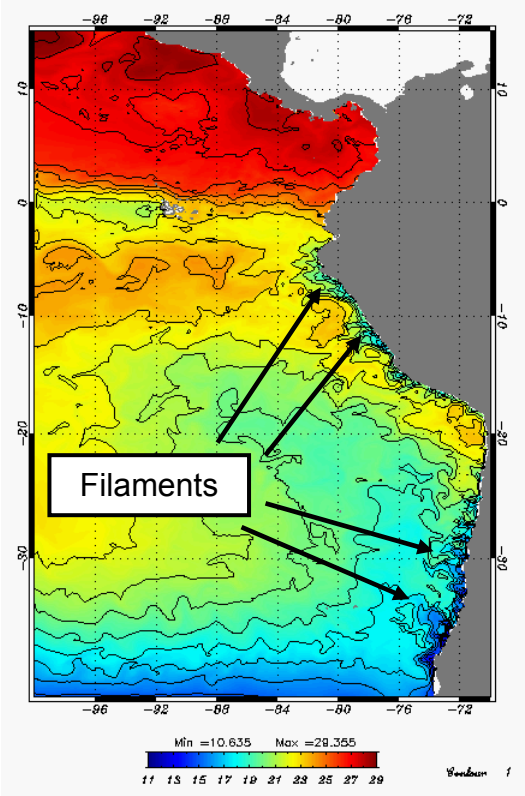

Fig. 1.6: Filaments de sub-mésoéchelle indiqués sur une carte de TSM dans le Pacifique Sud-Est établie à partir de données satellite AVHRR Pathfinder (Vazquez et al., 1995) pour le 1er janvier 1992. L'unité est le °C. L'intervalle de contour est de 1°C.

Ondes piégées à la côte

La présence d'ondes piégées à la côte (CTW) se propageant vers le pôle a été rapportée le long de la côte ouest de l'Amérique du Nord et de l'Amérique du Sud (ex: Brink, 1982; Chapman, 1987) et le long de la côte ouest de l'Afrique (Polo et al., 2008). De telles ondes barocline sont forcées par des ondes de Kelvin équatoriales (EKW) qui se propagent vers l'est le long de l'équateur à travers le Pacifique et l'Atlantique alors que celles-ci atteignent le bord Est bu bassin (Clarke, 1983; Enfield, 1987): d'après la théorie (Clarke, 1983; Grimshaw et Allen, 1988; Clarke et Shi, 1991), pour chaque mode barocline associé à une EKW oscillant à une fréquence donnée, il existe une latitude critique qui sépare la zone de propagation des CTW le long de la frontière océanique (située vers le pôle par rapport à cette latitude) de la zone de réflexion de l'EKW en ondes de Rossby équatoriales (ERW) et en ondes de Rossby extra-tropicales (ETRW) se propageant vers l'ouest (située vers l'équateur par rapport à cette latitude). Les CTW sont associées à des anomalies de niveau de la mer et de vitesse, qui peuvent déstabiliser la thermocline et les courants côtiers (ex: Shaffer et al., 1997; Pizarro et al., 2002). On pense que de telles perturbations ont une influence directe sur le comportement de l'écosystème marin dans les EBUS, comme le proposent Bertrand et al. (2008) pour le HCS.

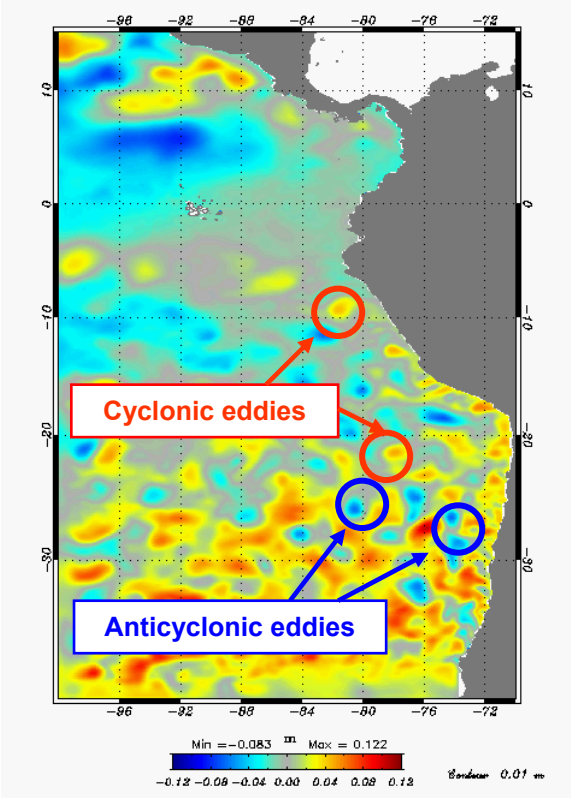

Fig. 1.7: Tourbillons mésoéchelle cycloniques et anticycloniques indiqués sur une carte de SLA dans le Pacifique Sud Est simulé par le modèle ROMS pour le 1er janvier 1992. L'unité est le mètre.

Les quatre EBUS principaux partagent des caractéristiques communes qui ont été brièvement décrites ci-dessus: des vents côtiers favorables à l'upwelling qui induisent une production primaire et une activité biologique intenses via des processus physiques de transport et de pompage d'Ekman; des courants parallèles à la côte dirigés vers l'équateur en surface et vers le pôle en sub-surface; une activité mésoéchelle et sub-mésoéchelle intense; des ondes piégées à la côte se propageant vers le pôle. Cependant, chacun des EBUS possède aussi ses spécificités propres, liées au regime de vent, à l'orientation de la côte, à la bathymétrie, à l'orographie continentale, à la latitude, entre autres facteurs. Quelles sont les particularités du HCS comparé à d'autres EBUS? Qu'est-ce qui le rend potentiellement plus sensible au changement climatique que les autres systèmes? Ceci fait l'objet de la section suivante.

1.1.2. Le Système de Courant de Humboldt: un écosystème productif soumis à des conditions océaniques et atmosphériques très variables

1.1.2.1. Introduction

Le HCS doit son nom à l'explorateur et naturaliste Prussien Alexander von Humboldt (1769-1859) qui voyagea longuement à travers l'Amérique Latine entre 1799 et 1804. Le HCS est le deuxième EBUS le plus étudié après le Système de Courant de Californie, et les premières études qui lui furent consacrées remontent à 1936 (Gunther, 1936a,b). Cet intérêt important de la communauté scientifique s'explique par plusieurs raisons.

Premièrement, le HCS produit plus de poisson par unité de surface que n'importe quelle autre région de l'océan mondial (F.A.O., 2009). Deuxièmement, il est soumis à l'influence directe de la variabilité climatique à grande échelle de l'Océan Pacifique tropical, dont le célèbre phénomène El Niño, qui fut initialement baptisé par des pêcheurs Péruviens et Equatoriens. Troisièmement, la proximité du HCS vis-à-vis de l'équateur et l'orientation de la côte du Pérou permettent de connecter d'une part l'upwelling côtier avec l'upwelling équatorial et la *cold tongue* (langue d'eau froide) de l'Est du Pacifique tropical et d'autre part les courants côtiers avec les courants équatoriaux (Lukas, 1986; Strub et al., 1998; Kessler et al., 2006; Croquette, 2007). Quatrièmement, la cordillère des Andes agit comme un mur naturel qui force les alizés subtropicaux à prendre une direction parallèle à la côte, isole l'océan hauturier de l'influence du climat continental sud-américain et influence le climat du Pacifique Sud-Est de manière significative (Xu et al., 2004; Sepulchre et al., 2009). Cinquièmement, le HCS est caractérisé par la présence d'un *stratocumulus cloud deck* (couverture nuageuse de type stratocumulus) persistant, le plus étendu au monde, qui limite la pénétration solaire dans l'océan (Klein et Hartmann, 1993): avec l'upwelling, il contribue à faire des températures océaniques en face du Pérou les plus fraîches de toute la bande tropicale. Les modèles climatiques globaux de basse résolution rencontrent de nombreux problèmes dans cette région, qui incluent (non exhaustif): une mauvaise représentation de la topographie abrupte des Andes, un forçage de vent trop faible près de la côte, un stratocumulus deck mal représenté et l'absence d'interactions air-mer à petite échelle associées à la variabilité océanique à mésoéchelle (Xu et al., 2004; Large et Danabasoglu, 2006; Seo et al., 2007). Tous ces problèmes introduisent des erreurs significatives à la fois dans le climat régional simulé dans le Pacifique Sud-Est – telles que de forts biais dans les champs moyens de TSM et de flux solaire – et aussi dans le climat à plus grande échelle pour

toute la région du Pacifique –biais chauds en TSM dans la *cold tongue* de l'est du Pacifique et le "problème de la double ITCZ" sont deux exemples bien connus – (Xu et al., 2004; Large et Danabasoglu, 2006), ce qui conduit à de grandes incertitudes dans les prédictions actuelles du changement climatique: par exemple, Bony et Dufresnes (2005) montrent que la principale source d'incertitude parmi les modèles climatiques globaux en termes de rétroaction tropicale nuages-albedo provient d'une sous-estimation de la sensibilité des nuages de couche limite marine aux changements de TSM dans les régions de subsidence (telles que le HCS). Une meilleure compréhension de la dynamique du climat dans cette région est une priorité pour la communauté scientifique travaillant sur le changement climatique et a conduit au développement du projet VOCALS, auquel j'ai participé dans le cadre d'une croisière océanographique effectuée dans la zone de Pisco-San-Juan (autour de 15°S) en octobre 2008. Enfin, le HCS est caractérisé par la présence près de la surface d'une des Zones de Minimum d'Oxygène (OMZs) les plus étendues de l'océan mondial (Anderson et al., 1982; Helly et Levin, 2004), connues pour leur rôle clé dans le cycle global de l'azote.

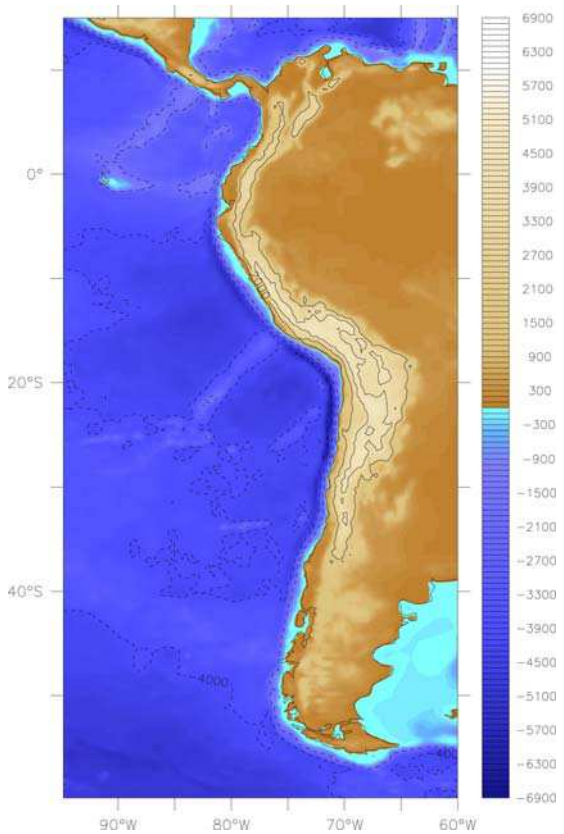

Fig. 1.8: Topographie et bathymétrie de l'Amérique du Sud occidentale établies à partir de données ETOPO1 (Amante et Eakins, 2009), précédemment interpolées sur une grille horizontale 1/3°x1/3°. L'unité est le mètre. Les countours pleins représentent la topographie continentale, tandis que les contours en pointillés représentent la bathymétrie océanique. L'intervalle de contour est de 2000m.

Au cours de cette thèse de doctorat, je me suis principalement concentré sur le deuxième et le troisième point, *cad* sur le forçage distant du HCS par la variabilité du Pacifique équatorial via des connexions océaniques, à savoir les ondes piégées à la côte et les courants océaniques. Cependant, du fait du rôle prédominant de l'atmosphère dans la dynamique du HCS, quelques aspects de la dynamique atmosphérique régionale seront également décrits. Dans la subdivision suivante, les principales caractéristiques du fonctionnement physique du HCS sont brièvement passées en revue.

1.1.2.2. Topographie et bathymétrie: des hautes montagnes aux fosses océaniques profondes

La côte ouest de l'Amérique du Sud s'étend de 7°N à 53°S avec une direction méridionale prédominante (fig. 1.8), et comprend les côtes de Colombie (7°N-1°N), de l'Equateur (1°N-3°S), du Pérou (3°S-18°S) et du Chili (18°S-53°S). C'est une zone de subduction, un type particulier de convergence des plaques tectoniques: la plaque océanique de Nazca, plus dense, est en subduction au-dessous de la plaque continentale Sud-Américaine, qui elle est moins dense. Par conséquent, la bathymétrie est caractérisée par une fosse océanique profonde et étroite atteignant les 6900m de profondeur autour de 20°S, tandis que la topographie comprend une haute chaîne de montagnes avec de nombreux sommets dépassant les 6000m d'altitude, ce qui fait des Andes les montagnes les plus hautes de la zone tropicale. Une distance relativement courte (quelques centaines de kilomètres maximum) sépare la fosse océanique des montagnes: par conséquent, le plateau continental est très réduit voire même inexistant (au nord du Chili par exemple) et une bande côtière étroite excédant rarement les cent kilomètres sépare la côte des Andes. La cordillère des Andes agit comme une barrière naturelle qui force les alizés tropicaux et subtropicaux à prendre une direction parallèle à la côte et isole la région côtière des perturbations atmosphériques produites au-dessus de l'Atlantique ou du continent: par conséquent, les côtes du Pérou et du nord du Chili sont caractérisées par un climat très aride, particulièrement au Chili où l'on trouve le désert le plus sec de la Terre: le désert d'Atacama. Dans le bassin océanique intérieur, la dorsale de Nazca, perpendiculaire à la côte au niveau de la région de Pisco (15°S), remonte jusqu'à la profondeur de 2000 m et sépare le bassin du Pérou au Nord du bassin du Chili au Sud. A l'équateur, la dorsale des Galapagos sépare la Plaque de Nazca au Sud de la Plaque des Cocos au Nord et connecte les Îles Galapagos à l'ouest (90°W) au continent sud-américain situé plus à l'est (~80°W). Le HCS caractérise l'océan côtier de l'ouest de l'Amérique du Sud entre

l'équateur et 40°S environ, région sur laquelle nous nous concentrerons dans le reste de la thèse.

1.1.2.3. Conditions atmosphériques et upwelling côtier

Puisque le forçage atmosphérique n'est pas le point central de ce travail de thèse, nous nous limitons ici à une brève présentation des conditions atmosphériques dans le Pacifique Sud-Est. Les principales composantes de la circulation atmosphérique dans la région sont schématisées sur la figure 1.9:

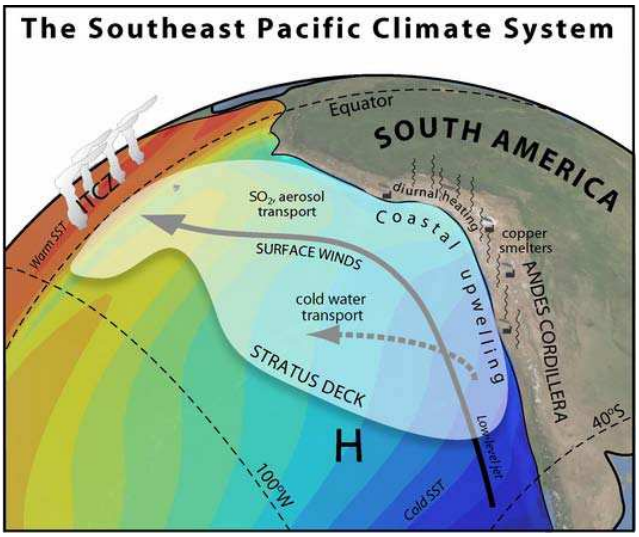

Fig. 1.9: Schéma des principaux systèmes atmosphériques du Pacifique Sud-Est: la Zone de Convergence Inter-tropicale (ITCZ), le *StratoCumulus cloud deck* (*Stratus Deck*), l'anticyclone subtropical (H) et les Jets Côtiers (*low-level jet*). La flèche en trait plein représente les alizés dirigés vers l'equateur et la flèche en pointillés représente le transport d'Ekman associé à l'upwelling côtier. Les couleurs de fond pour l'océan schématisent la TSM moyenne (*figure mise à disposition par Rob Wood, University of Washington*).

- L'Anticyclone Subtropical du Pacifique Sud-Est: c'est le moteur principal de la circulation atmosphérique dans cette région. Comme c'est le cas dans l'Est d'autres bassins océaniques (le Pacifique Nord, Atlantique Nord et Sud), ce système de hautes pressions entraîne des alizés dirigés vers l'équateur en raison de sa rotation anticyclonique (en sens inverse des aiguilles d'une montre dans l'hémisphère sud). La branche orientale de l'anticyclone est bordée à l'Est par la cordillère des Andes qui forcent les alizés à suivre la direction du littoral, produisant ainsi un upwelling côtier persistant au large du Pérou et du Chili. Comme dans d'autre EBUS, des alizés plus forts au large que plus près du bord produisent un pompage d'Ekman important dans les 50-200km près de la côte (Bakun et Nelson, 1991). La force des vents favorables à l'upwelling est modulée par la saisonnalité de

la position de l'anticyclone (fig. 1.10). Pendant l'été austral, le centre du système de hautes pressions est situé vers (95°W, 32°S) et favorise un upwelling côtier entre 40°S et l'équateur; pendant l'hiver austral, il se déplace vers le nord-est jusqu'à environ (85°W, 27°S): par conséquent, les vents du Chili central sont plus faibles voire même favorables au downwelling en hiver, tandis qu'ils sont plus forts au Pérou (Bakun et Nelson, 1991). Ceci explique pourquoi l'upwelling côtier est permanent au large du Pérou, tandis qu'il est saisonnier au large du Chili central. En face de la côte du nord du Chili, entre 18°S et 23°S, les vents sont plus faibles toute l'année, et il en est de même pour l'upwelling: par conséquent, les TSM sont significativement plus chaudes à cet endroit qu'au large du reste des côtes du Pérou et du Chili (fig. 1.11).

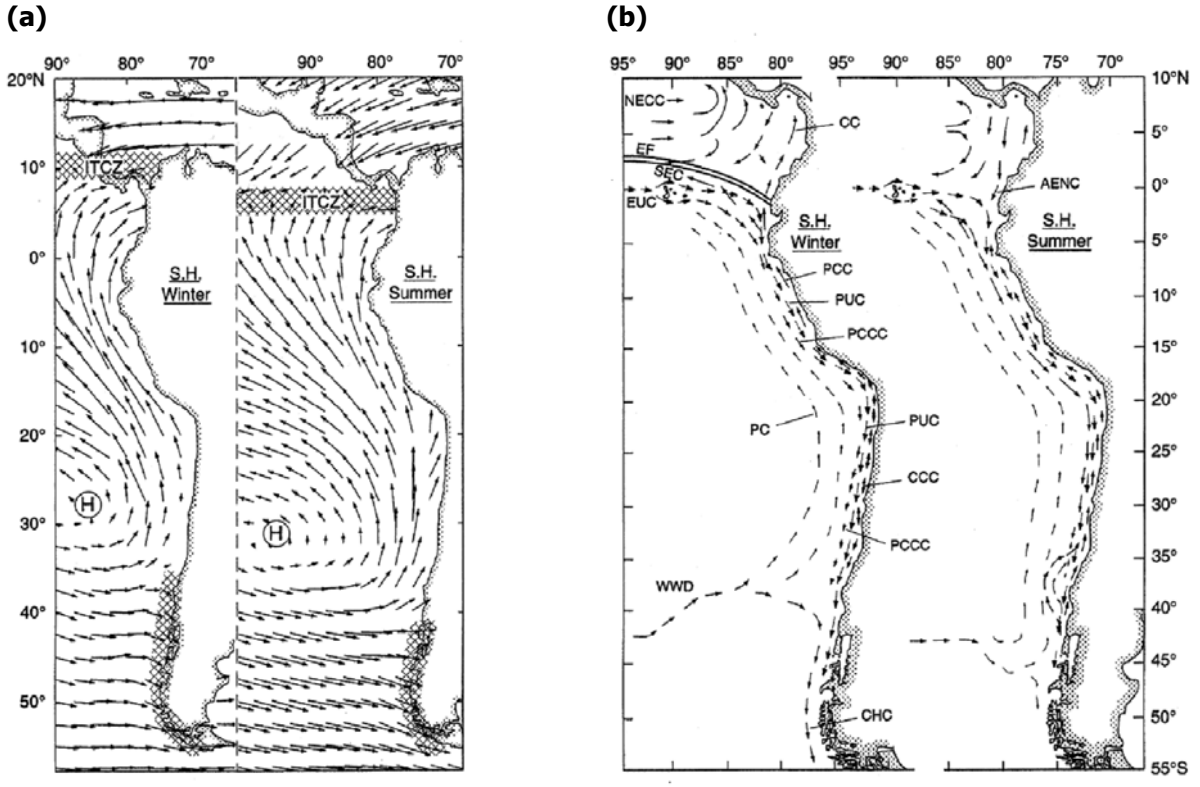

Fig. 1.10: Vents **(a)** et courants **(b)** climatologiques en hiver (août-juin) et en été (février-décembre) dans l'hémisphère sud (S.H). Les vents sont issus de la réanalyse NCEP à 1000 mbar (Kalnay et al., 1996). Les régions de fortes précipitations sont hachurées. Le terme ITCZ indique la position de la Zone de Convergence Inter-Tropicale, et H celle de l'anticyclone du Pacifique Sud-Est. EF représente le Front Équatorial. Les flèches sur le panneau (b) schématisent l'emplacement et l'intensité des principaux courants: la Dérive de Vent D'ouest (WWD), le Sous-Courant Équatorial (EUC), le Courant Sud-Équatorial (SEC), le ContreCourant Nord-Équatorial (NECC), le Courant de Colombie (CC), le Courant Annuel El Niño (AENC), le Courant du Pérou (PC), le ContreCourant du Pérou-Chili (PCCC), le Sous-Courant du Pérou-Chili (PUC), le Courant Côtier du Pérou (PCC), le Courant Côtier du Chili (CCC) et le Courant du Cap Horn (CHC). *Adapté de Strub et al. (1998)*.

- **Jets Côtiers**: ce sont des épisodes de vents parallèles à la côte très intenses (jusqu'à 15 m/s) qui apparaissent au large du Chili central entre 30°S et 35°S au printemps et en été

austral (Garreaud et Muñoz, 2005; Muñoz et Garreaud, 2005; Renault et al., 2009). On en trouve aussi au large du Pérou central dans le secteur de Pisco/San Juan (15°S) et au large du nord du Pérou vers Paita (4°S), avec des vitesses maximales (~7-8 m/s) en automne et en hiver austral (Renault, 2008). Ils ont une influence directe sur l'intensité de l'upwelling côtier en raison du transport et du pompage d'Ekman (Shaffer et al., 1999).

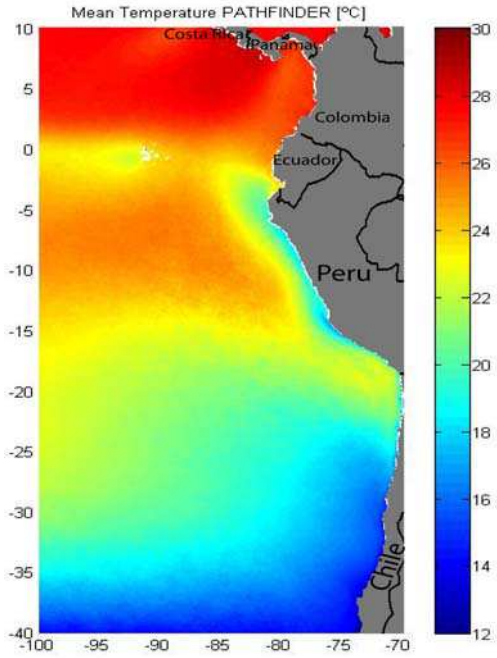

Fig. 1.11: TSM moyennes climatologiques (°C) dans le Pacifique Sud-Est à partir de données satellite AVHRR Pathfinder (Vazquez et al., 1995).

- La **Zone de Convergence Inter-tropicale** (ITCZ), qui borde l'anticyclone du Pacifique Sud Est au nord, est la zone de convergence des alizés de l'hémisphère Sud et de l'hémisphère Nord, et elle est présente tout autour de la planète dans la zone tropicale. Elle est caractérisée par une convection profonde accrue et de fortes pluies. Dans l'Est du Pacifique tropical, elle est située vers 10°N en hiver austral et vers 5°N en été: bien qu'elle ait une forte influence sur le climat régional des pays bordant la Baie du Panama (l'Equateur, la Colombie, certains pays d'Amérique centrale), son influence ne va pas au-delà de 5°S, ce qui fait qu'elle n'est généralement pas considérée pour l'étude de la dynamique du HCS.

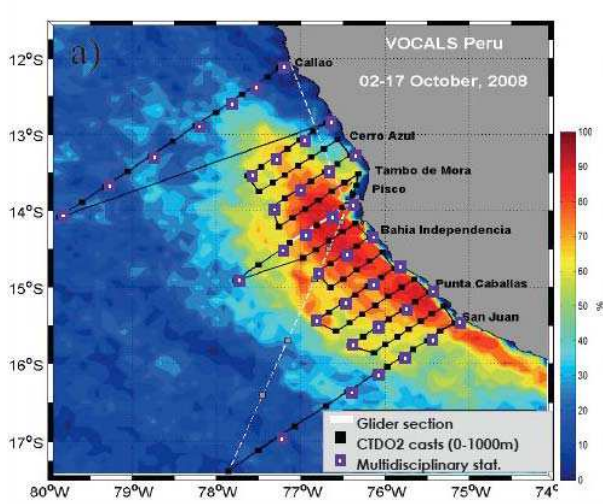

Fig. 1.12: Parcours original et stations de la campagne VOCALS-Rex Pérou conduite à bord du N/O Jose Olaya (IMARPE) du 02/10/08 au 17/10/08 au large de la zone de Pisco-San-Juan au sud du Pérou. L'image en arrière-plan représente le pourcentage climatologique de ciel degagé (%) pour le mois d'octobre, extrait de données SeaWIFS.

- Le *StratoCumulus cloud deck* (*SCu deck*) est la couverture nuageuse persistante de type stratocumulus la plus étendue au monde (Klein et Hartmann, 1993). Sa présence dans le Pacifique Sud-Est limite la pénétration solaire et ainsi le forçage radiatif de l'océan superficiel: avec l'upwelling, il contribute à faire des températures océaniques du Pérou les plus froides de toute la bande tropicale (Yu et Mechoso, 1999). De plus, la contribution du *SCu deck* au bilan de chaleur de l'océan superficiel est significative non seulement à l'échelle régionale (Takahashi, 2005) mais aussi à l'échelle globale. Cependant, les couplages air-mer à fine échelle qui contrôlent sa formation, sa structure et sa variabilité n'ont pas encore été bien documentés. La basse résolution des modèles climatiques globaux est incapable de représenter le *SCu deck*: par conséquent, les températures océaniques simulées sont généralement trop élevées dans la région, ce qui induit des biais importants dans le gradient zonal de TSM à travers le Pacifique tropical et ainsi dans la circulation de Walker, qui est l'un des principaux mécanismes de variabilité climatique tropicale à l'échelle globale. La representation du *SCu deck* par les modèles climatiques constitue une question importante car de tels biais introduisent de grandes incertitudes dans les prédictions du changement climatique futur. L'amélioration de notre compréhension de la dynamique du climat dans cette région est une priorité pour la communauté scientifique travaillant sur le changement climatique, et a conduit au développement du projet VOCALS (www.eol.ucar.edu/projects/vocals/) qui repose sur des mesures de terrain extensives au large du Pérou et du Chili, à la fois océanographiques et atmosphériques, et sur une plate-forme de modélisation. J'ai eu la chance de participer à la campagne océanographique VOCALS-Rex

Pérou conduite à bord du N/O José Olaya (IMARPE, Pérou) au large de la zone de Pisco-San-Juan (autour de 15°S) en octobre 2008 (fig. 1.12). Les mesures de terrain ont permis de caractériser les conditions atmosphériques (lancements de radiosondes), océanographiques (CTD, ADCP, drifters de surface et planeur sous-marin), biogéochimiques (oxygène, fluorescence, chlorophylle-a…) et biologiques (filet Hensen, hydroacoustique) pendant un épisode de *cloud clearing* (ciel dégagé) dû à la présence d'un intense jet côtier. Comprendre les interactions complexes entre l'atmosphère, l'océan et l'écosystème marin constitue un sujet de recherche actuel à l'IRD (Institut de Recherche pour le Développement), l'IMARPE (Institut de recherches Marines Péruvien) et l'IGP (Institut Péruvien de Géophysique).

1.1.2.4. Circulation océanique régionale

Dans ce qui suit, nous passons d'abord en revue les principaux courants présents dans le Pacifique Sud-Est et dans l'Est du Pacifique tropical: le système de courant côtier, appelé HCS, et le système de courant équatorial. Les connexions entre ces deux systèmes sont ensuite présentées, sur la base de travaux précédents.

Le système de courant côtier

Le HCS consiste en un ensemble de courants de surface et de subsurface qui coulent le long des côtes du Pérou et du Chili. Strub et al. (1998) proposent une synthèse sur ce sujet, et les principaux courants sont schématisés sur la figure 1.10b:

- La **Dérive de Vent D'ouest** (WWD) est un courant de surface dirigé vers l'est forcé par la branche Sud de l'anticyclone subtropical entre 40°S et 45°S. En atteignant le continent sud-américain, il se sépare en **Courant du Cap Horn** (CHC) dirigé vers le pôle et en **Courant du Pérou** (PC) dirigé vers l'equateur.

- Le **Courant du Pérou**, parfois appelé Courant Océanique du Pérou, Courant du Chili-Pérou ou même Courant de Humboldt, transporte des eaux froides du Sud vers l'est du Pacifique tropical, où il rejoint finalement la branche sud du **Courant Sud Équatorial** (SEC) dirigé vers l'ouest, et participe avec l'upwelling équatorial à entretenir la *cold tongue* de l'est du Pacifique équatorial (fig. 1.11), présente en hiver austral entre le secteur de Cabo Blanco (4°S) et les Îles Galapagos (Wyrtki, 1967; Strub et al., 1998; Chaigneau et Pizarro, 2005a). Ce courant très large (~500km) est présent entre la surface et 700m de profondeur, et suit la côte à une distance de 500 à 1500km environ (Wyrtki, 1963, 1967). Sa vitesse moyenne se situe

autour de 15-20 cm/s au Sud de 25°S et autour de 5-7 cm/s au Nord de 25°S (Chaigneau et Pizarro, 2005a).

- Le **Courant Côtier du Chili-Pérou** (CPCC), parfois appelé Courant de Humboldt (!), et connu sous le nom de **Courant Côtier du Chili** (CCC) au large du Chili et **Courant Côtier du Pérou** (PCC) au large du Pérou (fig. 1.10b), est un courant de surface dirigé vers l'équateur et situé beaucoup plus près de la côte, dans les 100 premiers kilomètres (Brandhorst, 1971; Bernal et al., 1982; Brink et al., 1983; Huyer et al., 1991). Il s'agit d'un flux géostrophique contrôlé par l'upwelling côtier, conformément à la description proposée à la section 1.1.2 (fig. 1.4). Les vitesses maximales au large du Pérou se situent autour de 10-15 cm/s (Brink et al., 1983; Huyer et al., 1991) en hiver austral, quand les vents parallèles à la côte et l'upwelling sont à leur maximum (Cucalon, 1987; Fiedler, 1994). Au nord du Chili, les vitesses dans le CPCC atteignent leur maximum en automne, en raison de la variation latitudinale du cycle saisonnier des vents parallèles à la côte (Blanco et al., 2001). Comme pour le PC, l'extension septentrionale du CPCC se mêle avec le SEC, et en hiver avec la *cold tongue* (Enfield, 1976; Weare et al., 1976; Fort, 1986) qu'il alimente avec l'eau froide et salée upwellée près de la côte (Strub et al., 1998).

- Le **Contre-Courant du Pérou-Chili** (PCCC) est un courant de surface dirigé vers le pôle et coulant parallèlement à la côte à une distance de 100 à 300km (Wyrtki, 1963; Brandhorst, 1971; Robles, 1979; Bernal et al., 1982; Silva et Fonseca, 1983; Huyer et al., 1991; Strub et al., 1995, 1998) et à des vitesses de l'ordre de 10 cm/s (Huyer et al., 1991). Il transporte des eaux chaudes et salées de la région équatoriale. Cependant, son existence, son origine et ses caractéristiques restent controversées à cause du manque de mesures directes et du peu d'études consacrées jusqu'à present à ce courant. Selon l'étude de modélisation de Penven et al. (2005), le PCCC serait forcé par un rotationnel de vent cyclonique au nord de 15°S en accord avec la relation de Sverdrup (Sverdrup, 1947), et tournerait ensuite vers l'ouest en direction de l'océan hauturier. Bien qu'il ait été observé au large du Pérou, sa présence au large du Chili est sujette à controverse (Fonseca, 1989; Strub et al., 1998; Penven et al., 2005).

- Le **Sous-Courant du Pérou-Chili** (PCUC), également connu sous le nom de Courant de Gunther, d'après E. R. Gunther qui fut le premier à le découvrir (Gunther, 1936a, b), ou simplement comme **Sous-Courant du Pérou** (PUC), est un courant dirigé vers le pôle qui domine le flux littoral en sub-surface en-dessous de 50m de profondeur (Brink et al., 1983). Il est généralement situé dans les 200 premiers kilomètres depuis la côte, au-dessus du plateau continental et de la pente associée (Fonseca, 1989), et s'étend jusqu'à 600-700m de

profondeur (Wyrtki, 1963), avec des vitesses maximales autour de 10-15 cm/s à 100-150m de profondeur au large du Pérou (Huyer, 1980; Huyer et al., 1991) et une profondeur croissante en allant vers le Sud (Gunther, 1936a, b). Le lecteur est invité à se referer à la figure 1.4 (1.1.2) qui représente le PCUC ainsi que le PCCC sur une section perpendiculaire à la côte du Pérou central. Un tel approfondissement du PCUC a été attribué à la conservation de la vorticité potentielle par Penven et al. (2005), et à la décroissance plus rapide des modes baroclines d'ordre inférieur comparés aux modes d'ordre supérieur par McCreary (1981) et par Clarke (1989). Cependant, il se pourrait que le PCUC affleure comme un contre-courant de surface à certains endroits au large du Pérou central et du nord du Chili en raison d'un rotationnel de vent cyclonique (McCreary et Chao, 1985; Penven et al., 2005), ce qui le rend parfois difficile à distinguer du PCCC. Le PCUC s'étend le long de la côte Sud-Américaine jusqu'à 48°S, bien qu'il soit considérablement plus faible au Sud de 38°S (Silva et Neshyba, 1979). Comme le PCCC, il est caractérisé par des eaux chaudes, salées et peu oxygénées (Gunther, 1936a,b; Fonseca, 1989), et a été identifié comme une source majeure des eaux riches en nutriments upwellées près de la côte (Wyrtki, 1963; Brink et al., 1983, Huyer et al., 1987).

Les données de courantomètres places au large du Chili central ont révélé que le PCUC est soumis à des variations significatives d'origine équatoriale à des échelles de temps allant de l'intrasaisonnier (Shaffer et al., 1997) au saisonnier et à l'interannuel (Pizarro et al., 2001, 2002). Il a été montré que la variabilité intrasaisonnière est surtout due à des CTW se propageant le long de la côte en direction du pôle (Shaffer et al., 1997), tandis que la propagation d'ETRW domine la variabilité annuelle du PCUC (Pizarro et al., 2002). En revanche, il a été montré que les vents favorables à l'upwelling ont peu d'effet sur le PCUC (Huyer et al., 1991; Pizarro et al., 2001). Ce dernier représentant une source importante de nutriments pour la production primaire dans le HCS, les fluctuations qu'il subit risquent d'avoir un impact direct sur l'écosystème marin. Un objectif important de la présente thèse de doctorat est d'évaluer l'influence à distance des ondes de Kelvin équatoriales intrasaisonnières (IEKW) sur la variabilité côtière du Pérou et du Chili, et particulièrement sur le CPCC et le PCUC. À cause du manque d'observations de ces courants tant dans le temps que dans l'espace, une approche de modélisation a été favorisée. C'est l'objet du chapitre 3 (section 3.) ainsi que d'un article en préparation (Belmadani et al., in prep.).

Le système de courant équatorial

Une brève vue d'ensemble du système de courant équatorial est présentée ici. Kessler (2006) propose une synthèse des principales études conduites sur la circulation océanique dans l'Est du Pacifique tropical (fig. 1.13), qui constitue l'état de l'art des connaissances sur la structure du système de courant équatorial. À 100°W entre 10°S et 10°N, au moins deux courants de surface ont été observés: le **Contre-Courant Nord Équatorial** (NECC) dirigé vers l'est, et deux branches du **Courant Sud Équatorial** (SEC) dirigées vers l'ouest. De plus, trois courants de sub-surface dirigés vers l'est ont été identifiés: le **Sous-Courant Équatorial** (EUC) et deux Tsuchiya Jets (Tsuchiya, 1975), appelés aussi **Contre-Courants de SubSurface Nord/Sud** (respectivement NSSCC et SSSCC). Quelques précisions sont données ci-dessous pour les principaux courants équatoriaux d'intérêt pour la région du Pérou-Chili, *cad* le SEC, l'EUC et le SSSCC:

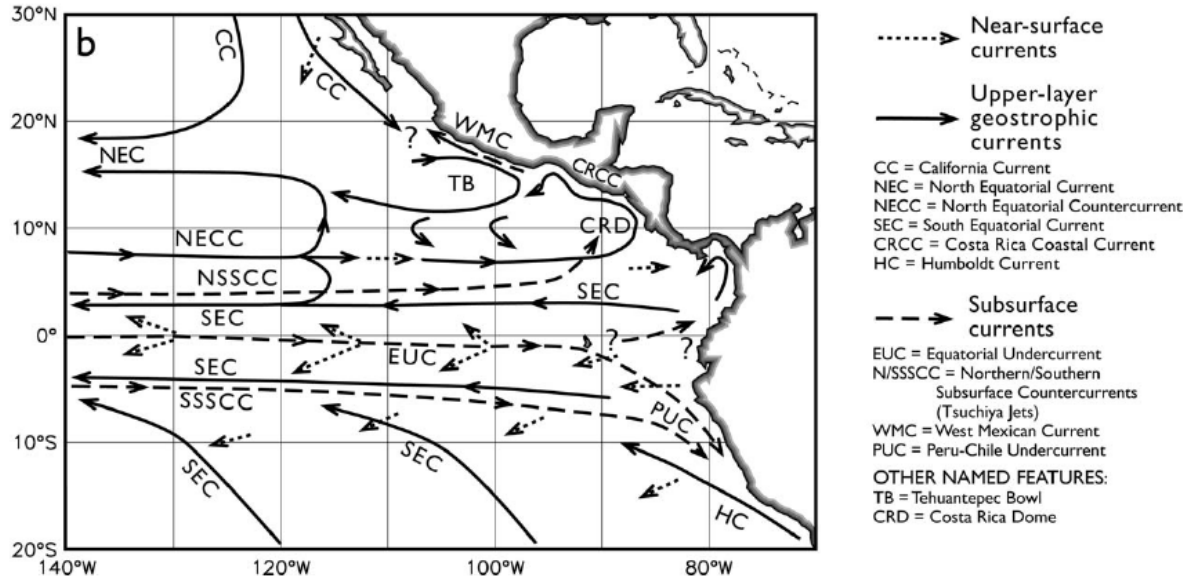

Fig. 1.13: Schéma de la circulation océanique superficielle dans l'Est du Pacifique tropical, d'après Kessler (2006). Les points d'interrogation se réfèrent à des régions où les connexions entre différents courants restent inconnues jusqu'ici.

- Le **SEC** est un courant de surface dirigé vers l'ouest présent le long de l'équateur dans l'Océan Pacifique tropical et forcé par des alizés d'est. Il est alimenté par les eaux froides du HCS qui s'étendent vers l'ouest et forment la *cold tongue*, avant de se diviser près des Galapagos en deux branches séparées par l'EUC (Kessler, 2006). La branche Sud vire vers l'Ouest au Sud-Ouest des Galapagos (Reverdin et al., 1994; Kessler et al., 1998; Johnson et al., 2002). Le SEC est faible à l'Est de 85°W à cause de faibles vents zonaux (Kessler, 2006) et accélère à l'Ouest de 85°W en raison du ralentissement de l'EUC près des Galapagos (Wyrtki, 1966; Reverdin et al., 1994): selon des estimations basées sur des données ADCP

(Johnson et al., 2002), le transport associé au SEC augmente de 12 Sv à 95°W à 35 Sv à 140°W alors qu'il reçoit un apport de 20 Sv de l'EUC près des Galapagos (Wyrtki, 1966; Montes et al., 2009). Le SEC présente aussi deux branches profondes dirigées vers l'ouest, qui pourraient être dues à des spirales cycloniques alimentées par le N/SSSCC (Rowe et al., 2000). Étant surtout forcé par les alizés, le SEC suit leur cycle annuel, avec un minimum de mars à juillet (Kessler, 2006).

- L'**EUC**, également appelé Courant de Cromwell (Cromwell et al., 1954; Knauss, 1960), est un courant de sub-surface dirigé vers l'est, qui lui aussi s'étend à travers le Pacifique tropical et transporte les eaux chaudes de l'Ouest du Pacifique Sud vers l'Est du bassin. Il est contrôlé par le gradient zonal de pression à l'échelle du bassin induit par les alizés dominants. Son transport moyen a été évalué à 39 Sv (Knauss, 1960). Dans la partie orientale du bassin, sa profondeur suit la thermocline qui remonte vers l'est (Wyrtki, 1981; McPhaden et Taft, 1988). Il fait même surface au printemps boreal, ce qui induit alors un flux de surface de 20cm/s dirigé vers l'est à l'ouest des Galapagos (Kessler et al., 1998; Yu et McPhaden, 1999a,b; Johnson et al., 2002), en raison de la faiblesse des alisés. Comme le SEC à l'est des Galapagos, l'EUC se sépare en deux branches à l'ouest des îles (Steger et al., 1998), peut être à cause de l'upwelling local induit par la présence des îles (l'Eden et Timmermann, 2004) qui permet uniquement aux couches plus profondes de s'écouler vers les côtes de l'Equateur et du Pérou (Lukas, 1986; Toggweiler et al., 1991). Cependant, l'étude de modélisation par Karnauskas et al. (2007) suggère que l'EUC est entravé par les îles. Le destin des couches superficielles upwellées de l'EUC est lui aussi controversé, certaines études indiquant une déviation vers le Sud (Blanke et Raynaud, 1997) et d'autres vers le Nord (Sloyan et al., 2003). La branche Sud est la plus forte (Steger et al., 1998), probablement à cause des vents dirigés vers le nord et du rotationnel associé qui advectent le SEC vers le nord et l'EUC vers le sud dans une boucle méridionale (Philander et Delecluse, 1983; Mitchell et Wallace, 1992; Kessler et al., 1998). Bien que l'on trouve de faibles alisés ainsi qu'un gradient zonal de pression inversé à l'est des Îles Galapagos, l'EUC a tout de meme été identifié dans cette région.

- Le **SSSCC**, parfois appelé Contre-Courant Sud Équatorial (SECC), ou Tsuchiya Jet Sud, est un courant de subsurface dirigé vers l'est présent dans l'Est du Pacifique tropical entre 5°S et 10°S (Tsuchiya, 1975). Il est souvent constitué par deux branches distinctes, à 4°S et à 8°S (Rowe et al., 2000; Johnson et al., 2001).

La structure tridimensionnelle complexe des courants est à l'origine du **Front Équatorial** (EF - fig. 1.10b), qui sépare les eaux fraîches de la *cold tongue* au Sud des eaux

plus chaudes de la piscine d'eau chaude (*warm pool*) du Pacifique Est au Nord. Ce front est modulé par le mélange induit par le réchauffement de la *cold tongue* par les ondes tropicales d'instabilité (TIW) qui équilibre l'effet de refroidissement dû à l'upwelling équatorial. De telles ondes sont produites par le cisaillement du SEC dirigé vers l'ouest avec le NECC et l'EUC dirigés vers l'est, et contribuent significativement au bilan de chaleur dans la couche de mélange de l'Est du Pacifique équatorial (Philander, 1978; Yu et al., 1995; Vialard et al., 2001; Chelton et al., 2003; Willett et al., 2006). De juillet à décembre, les vents se renforcent, provoquant une augmentation à la fois de l'upwelling équatorial, du SEC et du NECC, ce qui conduit à une augmentation de l'activité des TIW, qui à son tour s'oppose à l'effet refroidissant dû à l'upwelling (Enfield, 1986; Kessler et al., 1998; Swenson et Hansen, 1999).

Liens entre le HCS et les courants équatoriaux

Le HCS échange des masses d'eau avec l'Est du Pacifique équatorial via ses liens avec les courants équatoriaux. Comme détaillé ci-dessus, le SEC est alimenté par les eaux froides du Courant du Pérou et par celles du CPCC. D'autre part, on suppose que le PCCC provient de la branche sud de l'EUC après la division de celui-ci en deux branches à l'ouest des Îles Galapagos (Lukas, 1986; Reverdin et al., 1994; Hill et al., 1998), ou bien encore du SSSCC (Tsuchiya, 1985). De même, d'après Strub et al. (1998), le PCUC est sensé provenir soit de la branche Nord de l'EUC, qui vire vers le Sud en atteignant la côte de l'Equateur (Lukas, 1986; Hill et al., 1998), soit du SSSCC (Tsuchiya, 1985). Une étude récente par Croquette (2007) basée sur l'utilisation de la modélisation régionale à haute résolution et de particules lagrangiennes a en réalité montré que 68 % des eaux du PCUC à 14°S proviennent de la branche sud du SSSCC (à 8-9°S), 24 % de sa branche nord (à 4°S), et seulement 8 % de l'EUC. À 18°S, l'étude montre que la branche sud du SSSCC fournit la quasi-totalité des eaux du PCUC. Ces résultats ont été confirmés qualitativement par ceux de Montes et al. (2009) qui ont utilisé une approche semblable et ont constaté qu'à 12°S, 20-22 % des eaux du PCUC provenaient de la branche Sud du SSSCC, 15-22 % de sa branche Nord et seulement 4-5 % de l'EUC, les chiffres exacts dependant du forçage considéré aux frontières ouvertes du modèle régional. Cependant, les auteurs ont également constaté que 33-42 % des eaux du PCUC provenaient d'autres courants hauturiers de subsurface dirigés vers l'est et presents au sud de ~10°S, et que les 18-19 % restants provenaient de la recirculation de flux côtiers profonds dirigés vers l'équateur. Ces deux sources n'avaient jamais été considérées auparavant et

illustrent la complexité des connexions entre le HCS et les systèmes de courants équatoriaux et subtropicaux.

Pour résumer cette subsection, les courants côtiers associés au HCS sont semblables à ceux presents dans d'autres EBUS: un flux de surface dominé par un courant dirigé vers l'équateur (le CPCC), et un flux de subsurface dominé par un sous-courant dirigé vers le pôle (le PCUC). Cependant, ce schéma général est complété par un certain nombre d'autres courants de surface, dont le contre-courant de surface dirigé vers le pôle (le PCCC), et dont la structure et la dynamique restent mal comprises. De plus, le HCS est connecté aux courants de l'Est du Pacifique équatorial, qui sont contôlés par des mécanismes distincts. Le CPCC participe avec le PC à alimenter le SEC dans la *cold tongue* avec des eaux fraîches de la zone côtière. Inversement, l'EUC et le SSSCC apportent des eaux chaudes et salées de la region équatoriale à l'océan côtier du Pérou et du Chili, où elles sont advectées vers le pôle par le PCUC et upwellées près de la côte. De manière générale, le HCS est fortement lié à la zone équatoriale par les courants associés à ces deux systèmes et leurs connexions dans les régions de la *cold tongue* et des Galapagos. Le deuxième lien océanique entre le HCS et le Pacifique équatorial est le guide d'onde équatorial et son extension orientale, le guide d'onde côtier de l'Ouest de l'Amérique du Sud: la variabilité de l'upwelling côtier du Pérou et le Chili est sous l'influence d'EKW de grande longueur d'onde à une variété d'échelles temporelles, allant de l'intrasaisonnier à l'interannuel et meme au decadal. D'un intérêt particulier, El Niño-Oscillation Australe (ENSO) est le mode dominant de variabilité interannuelle à l'échelle globale et s'est rendu célèbre pour ses impacts climatiques sur les régions bordant l'Océan Pacifique, et en particulier sur le HCS. Une description plus détaillée des EKW et d'ENSO ainsi que de leurs effets sur le HCS est donnée ci-dessous.

1.1.2.5. Le guide d'ondes équatorial

Ondes de Kelvin équatoriales et ondes piégées à la côte

L'Oscillation de Madden-Julian (MJO; Madden et Julian, 1971, 1972) est un mode de variabilité intrasaisonnière atmosphérique d'échelle planétaire lié à la propagation d'ondes de Kelvin dans l'atmosphère, qui voyagent autour du globe en environ 50 jours (Parker, 1973). La MJO est capable de forcer des Coups de Vent d'Ouest (WWB) au-dessus de zones où les eaux de surface sont chaudes et où la convection profonde est plus intense, comme la *warm*

pool du Pacifique Ouest par exemple (McPhaden, 1993; Kessler et McPhaden, 1995; Kessler et al., 1995). Ces WWB peuvent exciter de longues IEKW de période allant de 50 à 80 jours et voyageant d'Ouest en Est à travers l'Océan Pacifique.

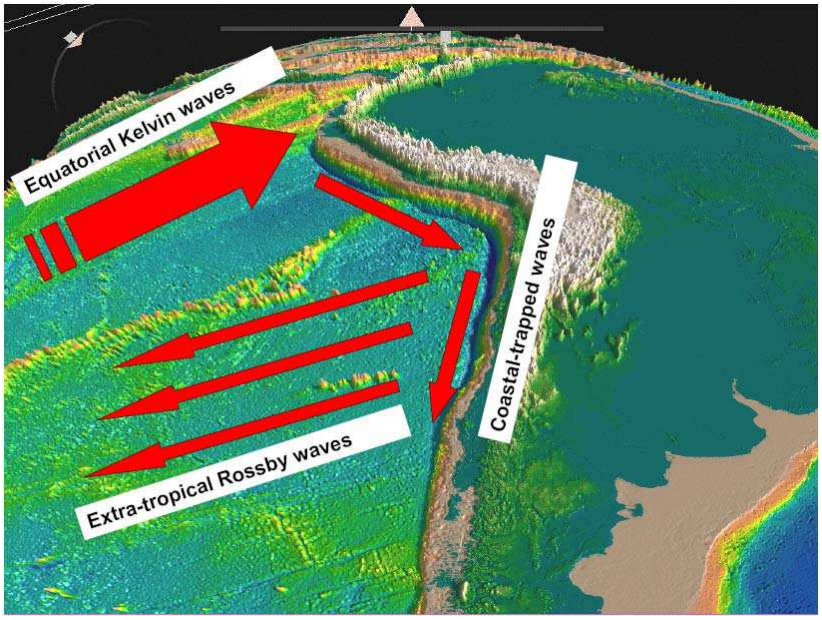

Fig. 1.14: Schéma représentant des ondes de Kelvin équatoriales atteignant la côte de l'Equateur et forçant des ondes piégées à la côte ainsi que des ondes de Rossby extra-tropicales.

Comme nous l'avons mentionné à la section précédente, une partie de l'énergie transmise le long du guide d'onde équatorial est réfléchie à la côte sud-américaine en ondes de Rossby au nord de la latitude critique, tandis que le reste de l'énergie est prise au piège le long du guide d'onde côtier sous la forme de CTW (fig. 1.14) au sud de cette latitude (Clarke, 1983; Grimshaw et Allen, 1988; Clarke et Shi, 1991). Plus la fréquence et/ou le mode barocline est(sont) élevé(e)(s), plus la latitude critique est basse (proche de l'équateur). D'après Clarke et Shi (1991), pour des IEKW de période 50 à 80 jours, la latitude critique se situe à ~7-10°S pour le premier mode vertical. Cela signifie que l'IEKW forcée par les WWB induits par la MJO peut déclencher la propagation vers le sud de CTW le long de la majorité du littoral du Pérou et du Chili, en particulier pour les modes baroclines d'ordre élevé.

La propagation vers le Sud d'anomalies de niveau de la mer (fig. 1.15, fig. 1.16a) et de courants parallèles à la côte a en effet été détectée le long du guide d'onde côtier qui s'étend du nord du Pérou au centre du Chili (ex: Brink, 1982; Shaffer et al., 1997; Blanco et al., 2002; Carr et al., 2002). Il est désormais admis que de telles ondes, en perturbant la thermocline (fig. 1.16b) et les courants côtiers (Shaffer et al., 1997; Hormazabal et al., 2002, 2006), pourraient

avoir une influence directe sur la structure spatiale et sur la dynamique de l'écosystème marin (Bertrand et al., 2008).

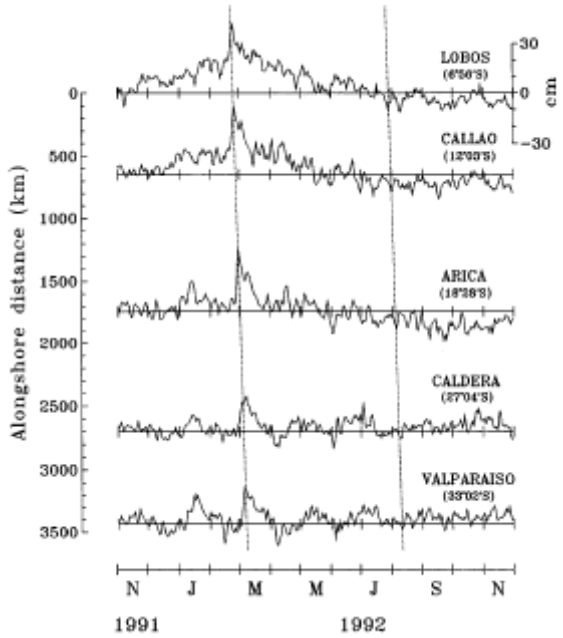

Fig. 1.15: Niveau de la mer enregistré le long de la côte ouest de l'Amérique du Sud à Lobos de Afuera (7°S), Callao (12°S), Arica (18°S), la Caldeira (27°S) et Valparaiso (33°S) entre novembre 1991 et novembre 1992. La pente des lignes en pointillés, qui suit certaines structures choisies du signal de niveau de la mer, est basée sur une vitesse de phase en direction du pôle de 266 km/jours (3.08 m/s). *Source: Shaffer et al., 1997*.

En plus de ces hautes fréquences, d'autres échelles de temps caractérisent la variabilité des EKW. Plusieurs études ont rapporté la présence dans l'est du Pacifique d'oscillations de période allant de 100 à 120 jours associées à des EKW (Cravatte et al., 2003; Dewitte et al., 2008b), qui seraient dues à une dispersion modale liée aux différences existant entre les vitesses de phase des modes baroclines. De plus, des EKW de plus basse fréquence sont également présentes dans le Pacifique équatorial: en effet, les WWB sont plus forts et plus fréquents pendant le printemps et l'été austral et pendant le début d'un événement El Niño, quand la *warm pool* est au plus chaud (Kessler et McPhaden, 1995; Kessler et al., 1995). Par conséquent, la modulation des IEKW aux échelles saisonnière et interannuelle introduit de plus basses fréquences dans le spectre d'énergie des EKW, qui sont alors associées à des latitudes critiques plus hautes à la côte sud-américaine. Ces fréquences déclenchent donc surtout la propagation d'ETRW en direction du large (Dewitte et al., 2008a; Ramos et al., 2008), bien qu'il ait été démontré que des effets non-linéaires dûs à la friction au fond peuvent également introduire des anomalies se propageant vers le pôle aux échelles de temps caractéristiques d'El Niño (Clarke et Van Gorder, 1994; Pizarro et al., 2001). Il a été montré

que de telles ETRW peuvent avoir un impact significatif sur la variabilité du PCUC au large du Chili (Pizarro et al., 2002).

(a)

(b)

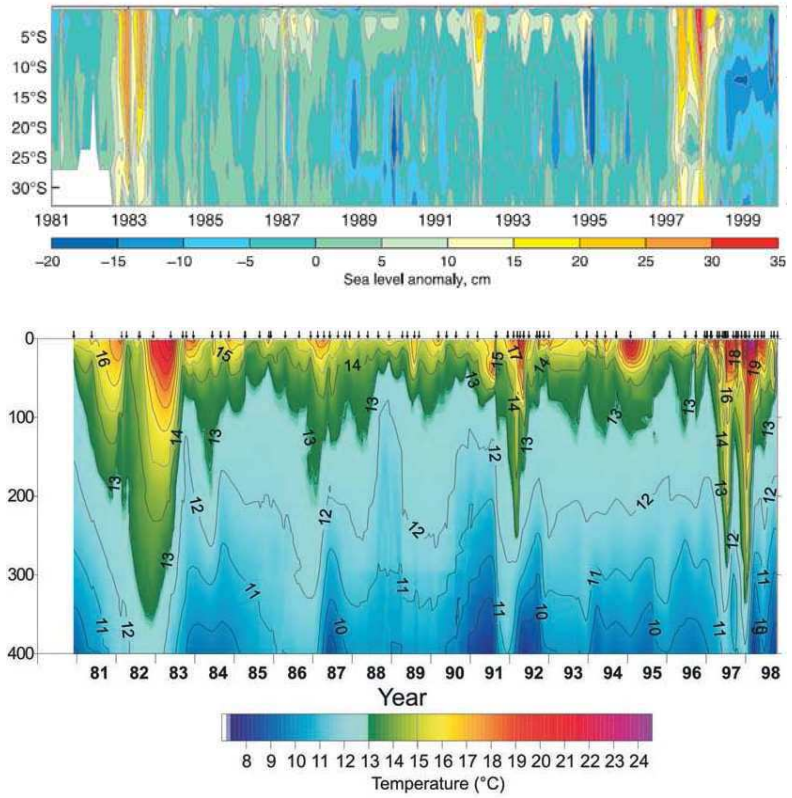

Fig. 1.16: **(a)** Diagramme de hoevmüller (temps vs latitude) des anomalies de niveau de la mer (cm) mesurées par des marégraphes le long de la côte ouest de l'Amérique du Sud entre 1981 et 1999. L'intervalle de contour est 5cm. *Adapté de Carr et al. (2002)*.
(b) Diagramme de hoevmüller (temps vs profondeur) de la température (°C) à 10km au large d'Iquique (20°S) entre 1981 et 1998. L'échantillonnage est indiqué par les flèches. L'intervalle de contour est 1°C. *Adapté de Blanco et al. (2002)*.

ENSO: Variabilité à grande échelle et impacts régionaux

Pendant la phase de développement d'El Niño, des anomalies de vent d'ouest apparaissent au-dessus de la *warm pool*, avec des valeurs maximales situées en-dessous et à l'ouest de la zone de convection profonde, que l'on qualifie de WWB (Kessler et McPhaden, 1995; Kessler et al., 1995). De tels WWB forcent simultanément la propagation vers l'est d'EKW de downwelling (chaud) et la propagation vers l'ouest d'ERW d'upwelling (froid) à travers le bassin. Ces ondes longues baroclines contribuent à propager les anomalies de profondeur de la thermocline le long du guide d'onde équatorial et agissent comme une rétroaction positive à la croissance d'El Niño.

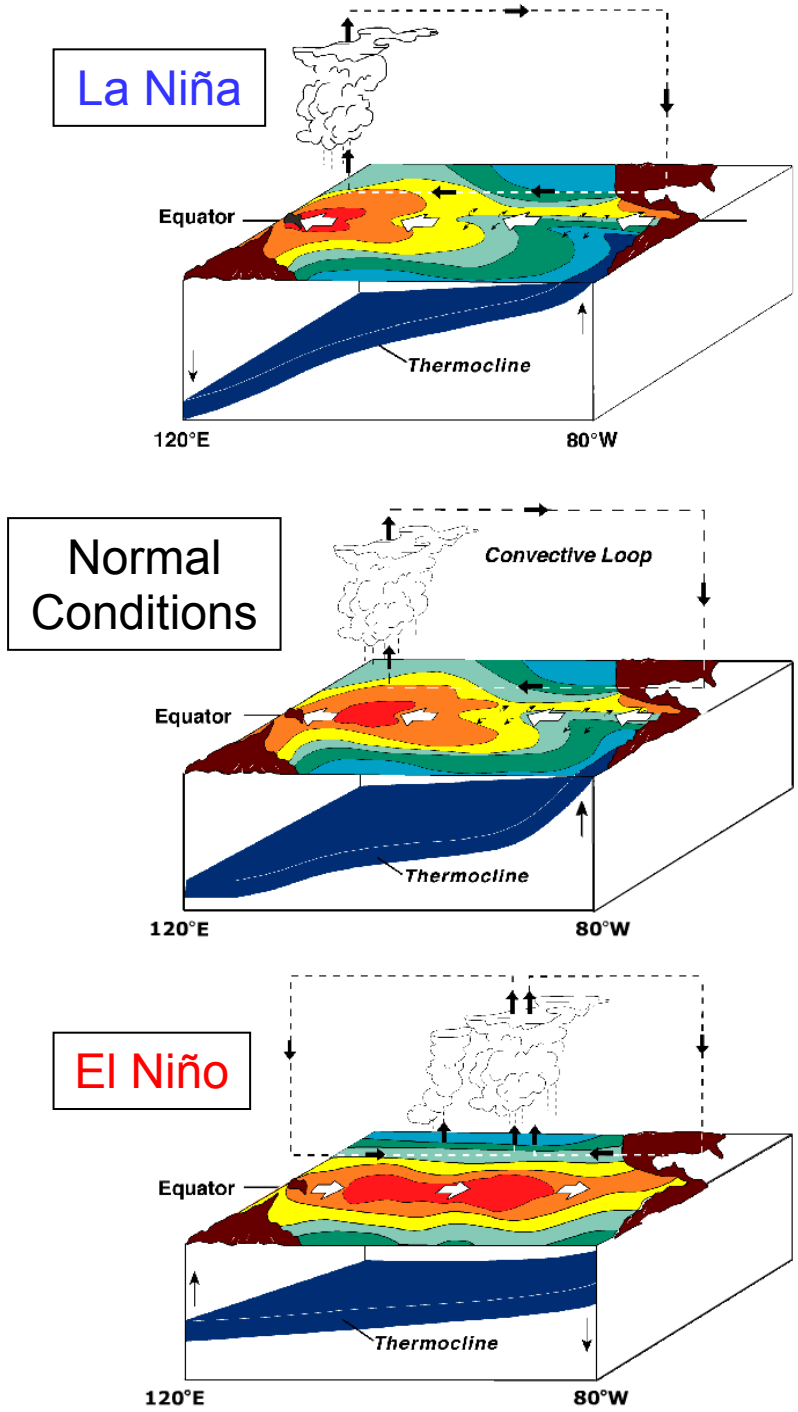

Fig. 1.17: Schéma de la circulation océanique et atmosphérique du Pacifique tropical pendant La Niña (en haut), pendant des conditions ENSO normales (au milieu) et pendant El Niño (en bas). Les traits en pointillés ainsi que les flèches noires en gras représentent la circulation de Walker. Les flèches blanches représentent le flux zonal moyen le long de l'équateur et les flèches noires et fines sur les deux premiers panneaux représentent le transport d'Ekman dirigé vers le pôle et associé à l'upwelling équatorial. Les flèches verticales noires et fines représentent les déplacements verticaux anormaux de la thermocline équatoriale. Les contours colorés symbolisent le champ moyen de TSM et les nuages représentent la convection profonde. *Images fournies par NOAA/PMEL/TAO.*

Le nom "El Niño" (qui signifie "enfant Jésus" en espagnol) fut donné à l'origine par des pêcheurs du Pérou et d'Equateur à un courant de surface dirigé vers le sud aux eaux

anormalement chaudes, affectant la partie Nord du HCS et apparaissant autour de Noël (d'où le nom), connu aujourd'hui sous le nom de Courant Annuel El Niño (AENC, fig. 1.10b - Cucalon, 1987). Tandis qu'un tel courant semble dominé par un cycle annuel et dure seulement quelques semaines, il est soumis à une forte intensification à l'échelle interannuelle et à des températures très élevées qui peuvent durer plusieurs mois, modifiant le climat régional et perturbant fortement l'écosystème marin (Barber et Chavez, 1983). Le courant El Niño ainsi que les épisodes de pluie et d'inondations qui l'accompagnent étaient connus depuis des siècles par d'anciennes civilisations pré-Inca comme les Moche ou les Chimu qui peuplaient les côtes arides du désert du nord du Pérou jusqu'en 1470, lorsqu'ils furent conquis par les Incas issus de la région andine. De nombreuses sources documentaires du nord du Pérou datant des périodes coloniale (1534-1850) et républicaine (1850-aujourd'hui) confirment son existence (Garcia-Herrera et al., 2008). Aujourd'hui, El Niño est plutôt connu comme un réchauffement de l'Océan Pacifique tropical à l'échelle du bassin se produisant tous les 2 à 7 ans et alternant avec une phase froide appelée "La Niña". Grâce aux travaux précurseurs de Bjerknes (1966, 1969), on sait maintenant que de telles variations de TSM dans l'Océan Pacifique sont associées à des changements spectaculaires de la pression atmosphérique à l'échelle du bassin, appelés "Oscillation Australe". Depuis, on interprète ces événements comme le résultat d'un phénomène couplé ocean-atmosphère appelé ENSO. À cause de l'existence de téléconnexions océaniques et atmosphériques à grande échelle entre le Pacifique tropical et de nombreuses autres régions du monde, ENSO est capable d'influencer le climat à l'échelle mondiale, ce qui en fait le mode dominant de variabilité interannuelle sur la Terre.

Pendant la phase neutre d'ENSO (*cad* ni pendant El Niño, ni pendant La Niña), souvent appelée conditions ENSO normales (fig. 1.17), la branche inférieure de la cellule de circulation de Walker force des alizés d'est qui soufflent zonalement à travers le Pacifique tropical. Les vents poussent les couches superficielles chaudes vers la partie occidentale du bassin, où elles se rassemblent et forment la *warm pool* du Pacifique Ouest. Par conséquent, la thermocline y est ~100m plus profonde que dans la partie orientale du bassin caractérisée par la présence de la *cold tongue* du Pacifique Est. Les vents situés juste au Sud de l'équateur induisent un transport d'Ekman vers la gauche, *cad* vers le Sud, tandis qu'au Nord de l'équateur ils induisent un transport d'Ekman vers la droite, *cad* vers le Nord. Cette divergence méridionale de l'eau dans la couche d'Ekman crée un upwelling équatorial, qui remplace les eaux chaudes de surface advectées vers l'ouest et vers le pôle par des eaux plus froides issues

des couches plus profondes. L'upwelling est plus fort à l'est où il entraîne les eaux fraîches à travers la thermocline équatoriale qui est peu profonde. Dans le même temps, des TSMs élevées entretiennent une convection profonde intense et de basses pressions atmosphériques au-dessus de la *warm pool*. Les masses d'air chaud et humide deviennent plus fraîches et plus sêches lorsqu'elles atteignent les couches supérieures, où elles sont prises dans le flux d'ouest de la circulation de Walker. Elles redescendent de nouveau lorsqu'elles atteignent les systèmes de hautes pressions du Pacifique oriental et alimentent finalement les alizés en surface. Le système est proche de l'équilibre, et il est principalement contrôlé par les variations de l'intensité de la circulation de Walker et des alizés associés.

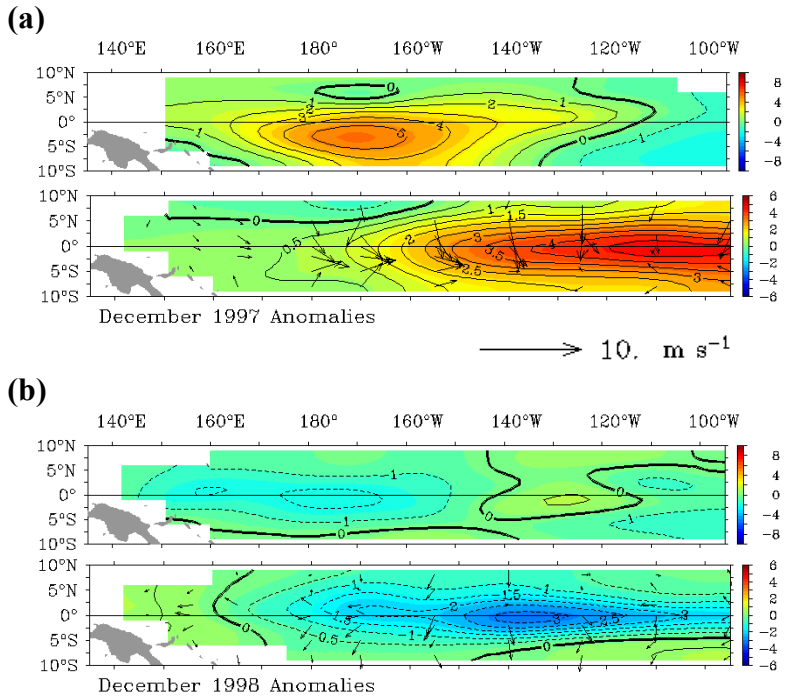

Fig. 1.18: Anomalies de vent zonal (panneau supérieur) et de TSM (panneau inférieur) dans le Pacifique équatorial entre 135°E et 95°W et entre 10°S et 10°N, moyennées sur les mois de décembre 1997 **(a)** et décembre 1998 **(b)**. L'unité est le m/s et le °C pour les anomalies de vent zonal et celles de TSM, respectivement. Les contours en trait plein (resp. en pointillés) sont pour des anomalies positives (resp. négatives), *cad* dirigées vers l'ouest (resp. vers l'est) et chaudes (resp. froides) pour la tension de vent et la TSM, respectivement. Les flèches sur la carte de TSM représentent les anomalies de vent. L'échelle correspondante est indiquée en-dessous de la figure (a). *Images et données fournies par NOAA/PMEL/TAO-TRITON*.

Pendant un événement El Niño, une relaxation des vents d'est dominants est observée au début de l'été austral (figures 1.17 et 1.18a). En réponse, un ajustement de la thermocline se met en place à l'échelle du basin, avec un approfondissement à l'est et une élévation à l'ouest: c'est la rétroaction par la thermocline, ou *thermocline feedback*. Les anomalies de gradient de pression créent aussi un flux de surface dirigé vers l'est qui advecte le bord oriental de la *warm pool* vers l'est. Cette seconde rétroaction positive au cycle d'ENSO

est appelée rétroaction advective zonale, ou *zonal advective feedback*. Les variations verticales de la thermocline et de l'advection horizontale se combinent pour créer des anomalies chaudes de TSM dans le centre et l'Est du Pacifique (fig. 1.18a). En réponse à l'extension zonale de la *warm pool*, les systèmes de basses pressions se déplacent vers le centre du Pacifique équatorial où les vents zonaux convergent, provoquant souvent l'apparition de vents d'ouest au-dessus de la *warm pool*. La cellule de circulation de Walker est modifiée et la convection profonde se produit au niveau du centre et de l'Est du Pacifique. Un événement El Niño dure généralement quelques mois à une année, avant que des rétroactions négatives ne commencent à surmonter les rétroactions positives et permettre au cycle ENSO de se déplacer de la phase chaude (El Niño) à la phase froide (La Niña).

La Niña est semblable aux conditions ENSO normales, à part que celles-ci sont intensifiées: une intensification des alizés d'est (figures 1.17 et 1.18b) est compensée par un approfondissement de la thermocline à l'Ouest et une remontée à l'Est. La convection profonde est déplacée dans l'extrême ouest du Pacifique, tandis que la *warm pool* se contracte vers l'ouest. L'upwelling est plus fort dans la *cold tongue* (fig. 1.18b) et des conditions anormalement froides apparaissent dans le Pacifique Sud-Est, tant dans l'atmosphère que dans l'océan.

Grâce aux recherches théoriques effectuées durant les cinquante dernières années, il est maintenant largement reconnu qu'ENSO résulte de la combinaison de divers processus de rétroactions positives et négatives, qui contribuent à l'intensification ou à l'inhibition des anomalies associées. La principale rétroaction positive est appelée 'feedback de Bjerknes' (Bjerknes, 1969): des anomalies chaudes de la TSM dans la zone de la cold tongue tendent à réduire le gradient est-ouest de TSM, qui en retour entraîne des alizés plus faibles qui induisent des anomalies positives de la thermocline se propageant sous la forme d'EKW de downwelling jusqu'à l'est du bassin, où elles contribuent aux anomalies chaudes via l'upwelling moyen. Inversement, des anomalies froides dans la cold tongue tendent à renforcer le gradient zonal de TSM, qui en retour entraîne des alizés plus intenses qui induisent des anomalies négatives de la thermocline se propageant sous la forme d'EKW d'upwelling jusqu'à l'est du Pacifique tropical, où elles contribuent aux anomalies froides via l'upwelling.

Quatre principales théories ont ensuite été proposées afin de décrire les rétroactions négatives responsables de la transition d'El Niño vers La Niña (et inversement): (i) la théorie de l'oscillateur retardé, impliquant la réflection d'ERW du signe opposé à la frontière ouest en

EKW, qui vont progressivement réduire les anomalies de température causées par les EKW initiales (Suarez et Schopf, 1988; Schopf et Suarez, 1988; Battisti et Hirst, 1989); (ii) la théorie de l'oscillateur du Pacifique ouest, dans laquelle les alizés forcent des EKW du signe opposé, en raison de la circulation anticyclonique hors équateur elle-même due à des anomalies de TSM extra-équatoriales du signe opposé induites par des ondes de Rossby (Weisberg et Wang, 1997); (iii) la théorie de l'oscillateur advectif-réflectif, selon laquelle les déplacements du bord de la warm pool sont contrôlés par les anomalies de l'advection zonale (Picaut et al., 1997); et (iv) la théorie de l'oscillateur rechargé, qui souligne le rôle des processus équatoriaux de recharge/décharge dus au transport de Sverdrup (Jin, 1996; 1997a,b). Ces théories sont complémentaires dans le sens où elles peuvent être combinées de différentes manières pour comprendre la diversité des événements ENSO observés (Jin et An, 1999; Fedorov et Philander, 2000; An et Jin, 2001). Plusieurs études ont été focalisées sur le rôle respectif de deux feedbacks positifs importants - qui contribuent au feedback de Bjerknes - sur ENSO tel que simulé par des modèles couplés simples et intermédiaires du Pacifique tropical: le zonal advective feedback et le thermocline feedback (Hirst, 1986; Jin et An, 1999; An et Jin, 2001; Fedorov et Philander, 2001).

En effet, la tension de vent à la surface influence à la fois l'advection zonale de la TSM moyenne par les anomalies des courants zonaux dans le Pacifique central (le zonal advective feedback), ainsi que l'advection verticale de la température de subsurface par l'upwelling moyen dans le Pacifique oriental (le thermocline feedback). Ces deux feedbacks constituent des termes importants du bilan de chaleur de la couche de mélange dans le Pacifique tropical (Hirst, 1986). En fonction de la position zonale des anomalies de vent, le zonal advective feedback favorise la transition ou la croissance du cycle ENSO et entretient par conséquent des oscillations courtes de 2 à 4 ans ou des oscillations longues de 4 à 6 ans avec une amplitude faible ou forte (An et Wang, 2000; Wang et An, 2001). Par ailleurs, le thermocline feedback est contrôlé par les déplacements verticaux de la thermocline en réponse à l'ajustement à l'échelle du bassin de l'océan aux variations du vent. Il est responsable des cycles ENSO avec de fortes amplitudes et de longues périodes (4 à 6 ans), du fait d'un temps prolongé de recharge/décharge du contenu de chaleur équatorial, conformément au paradigme de l'oscillateur rechargé (Jin, 1996; 1997a,b). En fait, les deux feedbacks coexistent dans la nature, faisant d'ENSO un mode couplé hybride (Fedorov et Philander, 2000). L'équilibre entre les deux est donc un facteur clé dans la détermination de la dynamique et de la structure d'ENSO, incluant la période du cycle. An et Jin (2001) et Fedorov et Philander (2001) ont de plus montré que l'effet combiné de ces deux processus sur

ENSO est sensible à l'état moyen équatorial (en particulier l'intensité des vents d'est, l'upwelling moyen, la profondeur de la thermocline et la différence de température à travers la thermocline), en accord avec les modifications observées dans l'amplitude et la période d'ENSO après le changement de régime climatique de la fin des années 1970 (An et Wang, 2000; Wang et An, 2001).

Une autre caractéristique intéressante d'ENSO réside dans son comportement asymmétrique intrinsèque. Bien que La Niña puisse être considérée dans une large mesure comme l'image miroir d'El Niño, les événements La Niña ont tendance à être plus faibles que les événements El Niño (fig. 1.19). Une telle asymétrie El Niño/La Niña est due à la nature nonlinéaire d'ENSO: en particulier, certaines études ont montré que le chauffage dynamique nonlinéaire (CDN) a permis de renforcer les forts événements El Niño de 1982-83 et 1997-98, tandis qu'il a inhibé les événements La Niña suivants de 1983-85 et 1998-99 (Timmermann et al., 2003; An et Jin, 2004). Le CDN est la somme des termes d'advection nonlinéaire dans la couche de mélange du Pacifique équatorial. Il est contrôlé (i) principalement par les relations de phase spatiales et temporelles entre l'upwelling anormal et la différence entre les anomalies de température en surface et en subsurface du centre à l'Est du Pacifique, et (ii) secondairement par les relations de phase entre les anomalies de courant zonal et le gradient zonal des anomalies de TSM dans l'Est du Pacifique (An et Jin, 2004). Il a été montré que la contribution de l'advection méridionale au CDN est quant à elle nettement plus faible. Ces études ont également permis de mettre en lumière la relation entre les nonlinéarités et la modulation décennale d'ENSO. En particulier, les forts événements El Niño associés à un important CDN ont eu lieu après le changement de régime climatique du Pacifique tropical du milieu des années 1970 (An et Wang, 2000; Wang et An, 2001), une période caractérisée par des anomalies ENSO se propageant vers l'est (Rasmusson et Carpenter, 1982) avec des relations de phase favorables au CDN. A l'inverse, la période précédant le changement de régime était caractérisée par des propagations vers l'ouest et ne permettait pas le développement d'un fort CDN. En conséquence, l'amplitude des événements El Niño et La Niña avait tendance à être plus symétrique à cette époque (fig. 1.19).

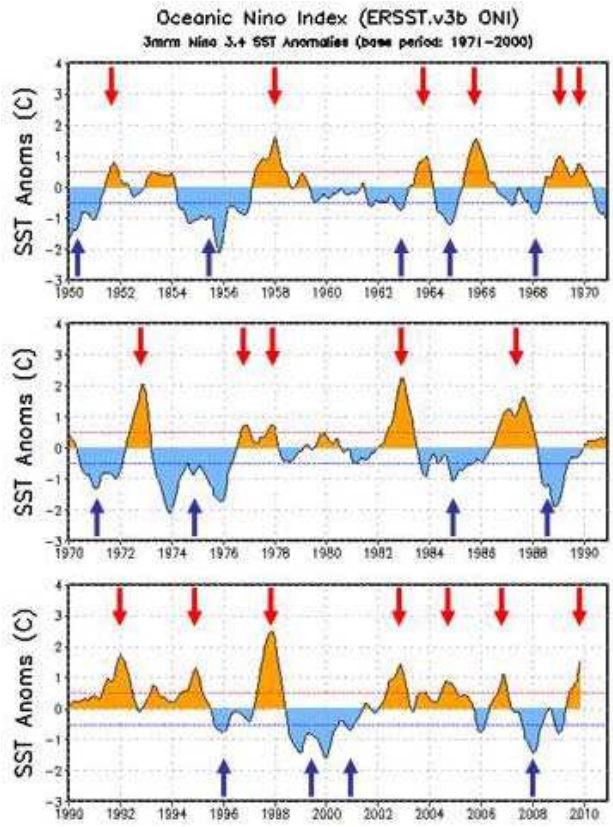

Fig. 1.19: Série temporelle (1950-2010) de l'index Niño océanique (INO), *cad* de la moyenne glissante (3 mois) des anomalies de TSM (°C) moyennées spatialement dans la région Niño3.4 (5°N-5°S, 170°W-120°W), basée sur l'analyse ERSST.v3b (Smith et al., 2008). Les anomalies sont les déviations par rapport aux moyennes hebdomadaires sur la période 1971-2000 (Xue et al., 2003). D'après les standards de la NOAA, un événement El Niño (La Niña) est caracterisé par un INO supérieur ou égal à +0.5°C (inférieur ou égal à -0.5°C) pendant au moins cinq saisons consécutives de 3 mois glissants. Les flêches rouges (bleues) indiquent les événements El Niño (La Niña). Les lignes en pointillés rouges (bleus) indiquent le seuil à +0.5°C (-0.5°C). Les secteurs oranges (bleu clair) correspondent à des anomalies positives (négatives). *Adapté de NOAA/CPC/NCEP.*

El Niño et La Niña affectent en premier lieu le Pacifique tropical et leurs effets se remarquent notamment sur la TSM de certaines zones spécifiques. Un moyen de le mettre en évidence est de moyenner la TSM sur ces zones (fig. 1.20):

- Niño4 (5°S-5°N, 160°E-150°W): la région où les changements de TSM semblent les plus fortement liés aux modifications de la convection dans le Pacifique équatorial;

- Niño3 (5°S-5°N, 90°W-150°W): la région qui présente la plus grande variabilité de TSM aux échelles de temps interannuelles;

- Niño3.4 (5°S-5°N, 120°W-170°W): un compromis entre la forte variabilité de TSM (Niño3) et le changement des précipitations (Niño4) (voir aussi fig. 1.19);

- Niño1+2 (10°S-0°N, 80°W-90°W): la région qui généralement se réchauffe en premier lors du développement d'un événement El Niño.

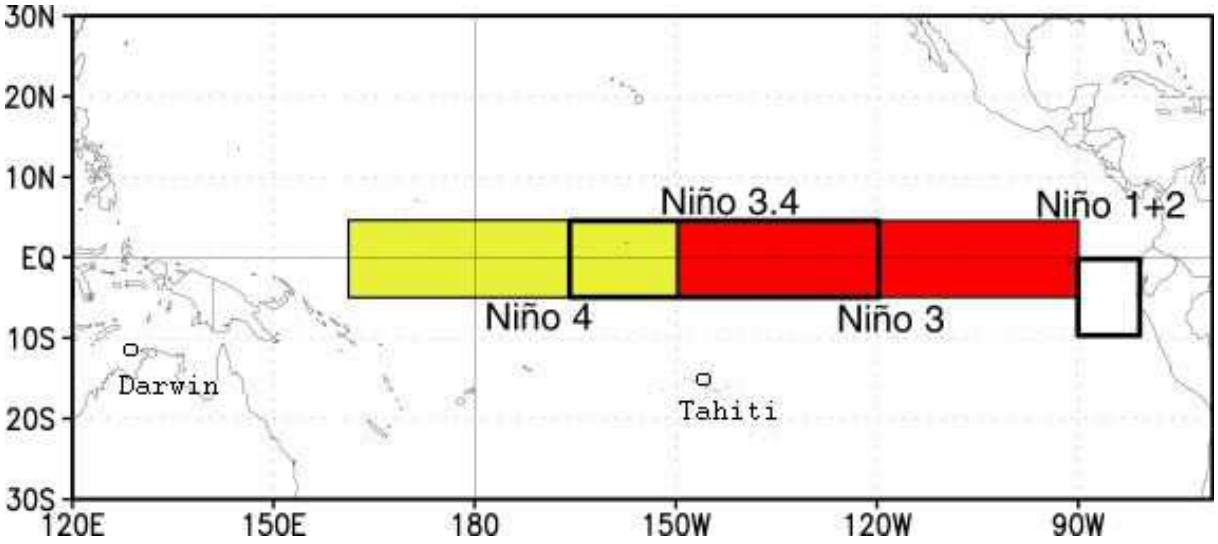

Fig. 1.20: localisation des quatre zones Niño, de Tahiti et de Darwin.

La TSM moyennée sur Niño3 (ou indice Niño3SST) peut également être utilisée pour mettre en évidence la modulation basse-fréquence d'ENSO (échelles de temps décennales à multi-décennales). Un moyen d'y parvenir est: 1) de filtrer l'indice Niño3SST des hautes fréquences; 2) calculer le spectre en ondelettes correspondant; et 3) calculer la série temporelle correspondant à la moyenne de l'ondelette sur la bande 2-7 ans. Cette dernière série (toujours positive) est généralement appelée N3VAR (voir aussi fig. 1.28). Lorsque N3VAR est fort (faible), la période considérée est caractérisée par une forte (faible) amplitude d'ENSO, comme par exemple après (avant) le changement de régime climatique du milieu des années 1970.

L'Oscillation Australe associée au cycle ENSO peut quant à elle être mise en évidence grâce à l'indice SOI (pour *Southern Oscillation Index*), égal à la différence entre les pressions normalisées à Tahiti et à Darwin (fig. 1.20). Cet indice représente la circulation de Walker, son signe est inversé par rapport à l'anomalie de TSM: lorsque l'anomalie de SOI est positive (négative), la circulation de Walker est plus forte (plus faible) et l'anomalie de TSM dans les zones Niño4 à Niño1+2 est négative (positive).

Les pays bordant l'Océan Pacifique sont les plus vulnérables aux changements induits par ENSO: pendant le fort événement El Niño de 1997-98 par exemple (fig. 1.18a et 1.19), le littoral sud-américain occidental, habituellement aride, subissait de fortes précipitations et des inondations importantes, ainsi qu'une chute soudaine des prises d'anchois, tandis que la sécheresse et les incendies de forêt s'étendaient sur les régions habituellement humides de l'Indonésie et du nord de l'Australie. De telles catastrophes naturelles perturbent fortement les écosystèmes marins et terrestres ainsi que les activités humaines dont l'agriculture et la pêche

(Barber et Chavez, 1983). L'impact d'El Niño dans le HCS a été largement décrit dans la littérature, car c'est la partie du monde qui subit les changements les plus spectaculaires pendant El Niño. Ceux-ci incluent:

- Un approfondissement de la thermocline, une réduction de l'upwelling côtier et un fort réchauffement des températures de surface qui peuvent s'étendre 8°C (Blanco et al., 2002; Carr et al., 2002, Colas et al., 2008) (fig. 1.16b). La réduction de l'upwelling côtier conduit à une réduction de la production primaire marine, qui impacte l'écosystème marin tout entier, y compris les niveaux trophiques supérieurs (Barber et Chavez, 1983);

- un renforcement du PCUC, particulièrement au large du Pérou (Smith, 1983; Huyer et al., 1991);

- un déplacement vers le sud de l'ITCZ, provoquant de fortes pluies dans les régions côtières habituellement arides (Huyer et al., 1987, 1991);

- Un affaiblissement de l'anticyclone subtropical et de son influence sur les vents favorables à l'upwelling. Cependant, les vents eux-mêmes ne semblent pas être réduits pendant El Niño, en raison de processus non-linéaires: en effet, comme le propose Enfield (1981), une réduction de la couverture nuageuse près de la côte due à des eaux littorales anormalement chaudes peut augmenter le forçage radiatif et réduire la pression atmosphérique sur le continent, ce qui a pour effet d'entretenir la différence de pression sol-mer, et ainsi les vents parallèles à la côte dirigés vers l'équateur. Selon Bakun et Weeks (2008), des vents parallèles à la côte du Pérou peuvent même être intensifiés pendant El Niño, à cause d'une plus grande concentration en vapeur d'eau dans l'atmosphère conduisant à un effet de serre plus fort ainsi qu'à de plus basses pressions sur la terre. Bakun et Weeks (2008) ont proposé ce mécanisme pour expliquer l'augmentation de l'intensité des vents parallèles à la côte observés au large du Pérou par Bakun (1990) au cours des dernières décennies dans un contexte de réchauffement climatique (voir la section suivante).

Des changements potentiels de la structure et du comportement d'ENSO avec le réchauffement climatique pourraient induire des changements dans le climat régional du Pacifique Sud-Est et dans la circulation régionale du HCS. En particulier, les changements dans l'occurrence et la distribution spatiale d'ENSO survenus au cours des dernières décennies suggèrent une possible co-existence de plusieurs modes couplés dans le Pacifique équatorial. Tandis qu'El Niño est traditionnellement décrit par des anomalies de TSM se développant dans l'est du Pacifique équatorial et qu'on explique plutôt bien avec la théorie de l'oscillateur rechargé (Jin, 1997a,b), des études récentes (Larkin et Harrisson, 2005a; Ashok

et al., 2007; Kao et Yu, 2009; Kug et al., 2009) soulignent l'émergence d'un second type d'El Niño, avec une variabilité de la TSM déplacée vers le Pacifique central (fig. 1.21). Ce second type d'El Niño est connu sous le nom d'El Niño « Modoki » (Ashok et al., 2007), « warm pool » El Niño (Kug et al., 2009) ou « central Pacific » El Niño (Yeh et al., 2009). De façon similaire à l'El Niño conventionnel, El Niño Modoki est la phase chaude d'une oscillation couplée océan-atmosphère. La phase froide est appelée La Niña Modoki. ENSO Modoki met en jeu une physique différente de celle de l'ENSO conventionnel: alors que ce dernier tend à être principalement contrôlé par le thermocline feedback, il a été montré qu'ENSO Modoki est principalement contrôlé par le zonal advective feedback (Kug et al., 2009).

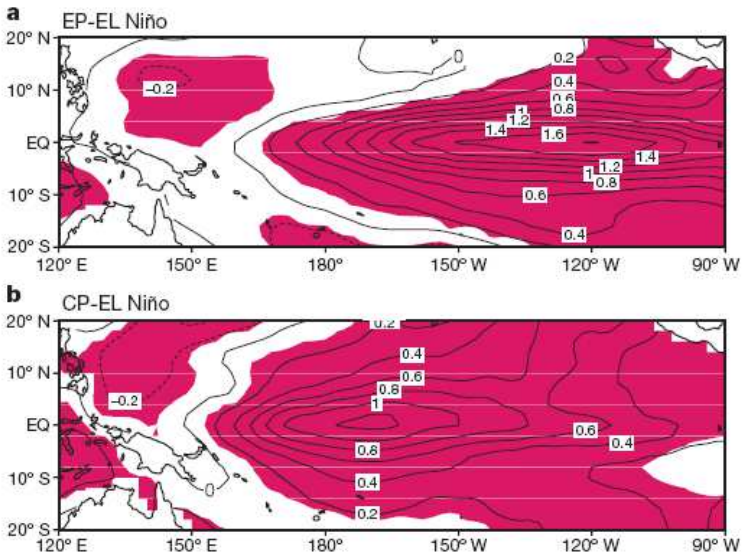

Fig. 1.21: composites des anomalies maximales de TSM dans le Pacifique tropical (relativement à la période 1854-2006) pour **(a)** l'El Niño du Pacifique Est et **(b)** l'El Niño du Pacifique central, d'après Yeh et al. (2009). Les surfaces colorées correspondent à des anomalies de TSM significatives à 95%.

Plusieurs auteurs ont montré qu'El Niño Modoki se produit plus fréquemment depuis les années 1990 (Larkin et Harrisson, 2005a; Ashok et al., 2007; Yeh et al., 2009), indiquant un possible changement d'ENSO avec le réchauffement global. De plus, Yeh et al. (2009) ont montré que 8 des 11 CGCMs qu'ils ont examiné présentent une occurrence plus importante d'El Niño Modoki avec le réchauffement global, contrairement à l'El Niño conventionnel. Ils suggèrent qu'un tel changement est lié à l'aplanissement de la thermocline dans les CGCMs (fig. 1.22). En effet, l'affaiblissement attendu de la circulation de Walker du au réchauffement est associé à un aplanissement de la thermocline dans le Pacifique équatorial (Vecchi et Soden, 2007), qui est susceptible d'amplifier le zonal advective feedback et ainsi l'occurrence

des événements El Niño Modoki par rapport à celle des événements El Niño conventionnels (Ashok et al., 2007; Yeh et al., 2009).

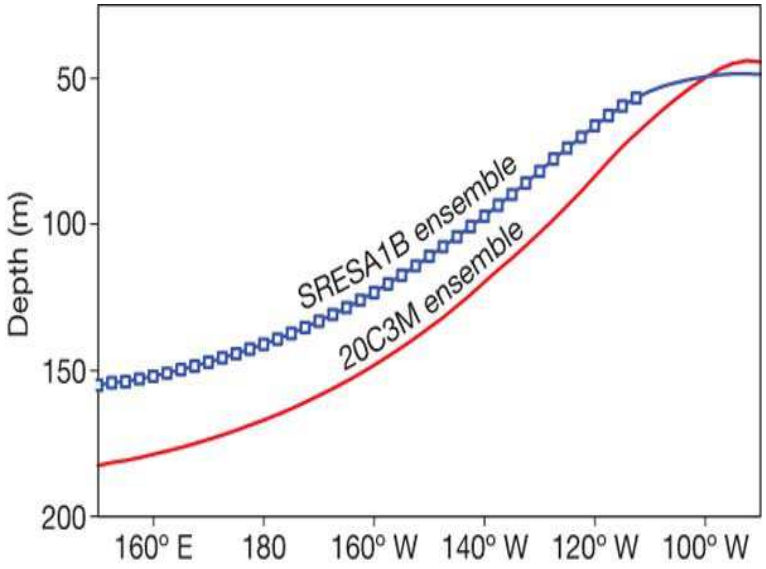

Fig. 1.22: moyenne d'ensemble de la profondeur de la thermocline pour le climat du 20e siècle (en rouge) et celui du 21e siècle (bleu), d'après Yeh et al. (2009). Les carrés bleus indiquent les changements significatifs à 95%.

Enfin, El Niño Modoki est associé à des téléconnexions avec les moyennes latitudes qui sont très différentes de celles de l'El Niño conventionnel (Larkin et Harrisson, 2005b; Weng et al., 2007, 2009; Ashok et al., 2007, 2009a,b; Kao et Yu, 2009; Yeh et al., 2009). Par exemple, plusieurs études récentes soulignent l'impact distinct d'ENSO Modoki sur les pluies en Australie (Wang et Hendon, 2007; Ashok et al., 2009b; Cai et Cowan, 2009; Taschetto et England, 2009). Par ailleurs, l'Ouest de l'Amérique du Nord subit des étés chauds et secs pendant El Niño Modoki, alors que des étés frais et humides prédominent pendant El Niño (Ashok et al., 2007; Weng et al., 2007). Par conséquent, un changement d'ENSO vers une structure de type Modoki en réponse au changement climatique pourrait causer de forts impacts sur le climat global et potentiellement sur le climat régional du HCS.

Une présentation synthétique des impacts possibles du réchauffement climatique dans la région est proposée à la section suivante.

1.2. Le Pacifique Sud-Est: refroidissement régional au sein d'un réchauffement global?

Une présentation générale du réchauffement climatique est disponible en annexe. Certains des sigles utilisés dans la section suivante y sont également définis.

1.2.1. Tendances reconstruites à partir d'enregistrements paléoclimatiques et d'observations historiques

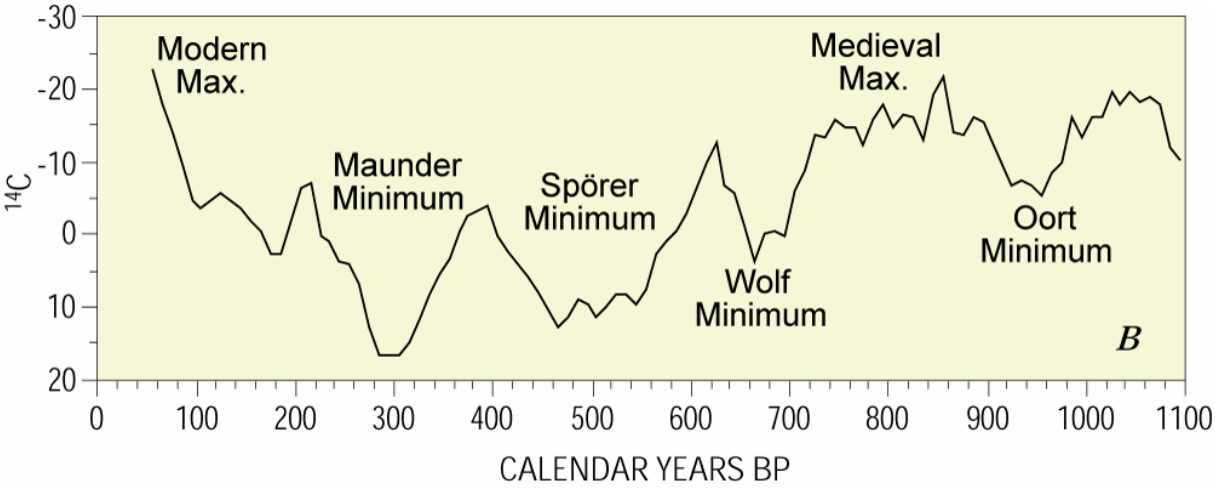

Fig.1.23: Changements de la concentration atmosphérique en ^{14}C (un proxy de l'activité solaire) au cours du dernier millénaire. Notez que les valeurs modernes sont situées du côté gauche de la figure. *Figure mise à disposition par United States Geological Survey (USGS).*

Comme indiqué en annexe A, les changements climatiques du passé ont été parfois contraints par les variations de l'activité solaire (fig. 1.23). Il est aujourd'hui admis que la faible activité solaire du Minimum de Maunder et du Minimum de Spörer figure parmi les principales causes de l'apparition du Petit Age de Glace, une anomalie climatique présente entre 1400 et 1850 environ et caractérisée par une vaste couverture de glace sur l'Amérique du Nord et sur l'Europe (Cronin et al., 2003). De même, des conditions plus chaudes et plus humides sur le Nord de l'Europe pendant la Période Médiévale Chaude (~800-1300 après J.C.) seraient le résultat d'une activité solaire élevée pendant le Maximum Médiéval (Cronin et al., 2003) (fig. 1.23). Ces deux périodes sont des exemples de conditions climatiques globales contrastées, avec une période plus froide que la moyenne (le Petit Age de Glace) et une période plus chaude que la moyenne (la Période Médiévale Chaude). Quelques enregistrements paléoclimatiques datant de ces périodes sont disponibles pour le HCS et

d'autres EBUS et peuvent nous aider à comprendre le comportement spécifique de ces régions sous un climat global plus chaud ou plus froid.

Dans le Système de Courant de Californie, des conditions chaudes et arides prévalaient sur la Terre pendant la Période Médiévale Chaude, tandis que l'océan présentait des TSM fraîches (Graham et al., 2007), suggérant la présence d'un upwelling côtier intense. Dans la partie Nord du HCS (*cad* au Pérou), des conditions très arides ont également été rapportées pour la même période, et pourraient être dues à une migration de l'ITCZ vers le nord (Rein et al., 2004). Les carottes sédimentaires collectées au large de Callao (côte centrale du Pérou) révèlent que la Période Médiévale Chaude fut marquée par des conditions réductrices plus intenses que celles d'aujourd'hui. Des enregistrements paléoclimatiques prélevés dans l'Océan Pacifique tropical révèlent des changements contemporains, indiquant des TSM fraîches dans le centre et dans l'Est du Pacifique tropical durant cette période (Graham et al., 2007). Ce schéma confirmerait l'hypothèse selon laquelle la Période Médiévale Chaude dans la partie Est du Pacifique ressemblait à des conditions La Niña actuelles (Sifeddine et al., *en préparation*). Ces résultats ont tendance à montrer que pendant que la majorité de la planète était exceptionnellement chaude, les EBUS en général et le HCS en particulier étaient caractérisés par un océan côtier plus froid que la normale, et un climat plus sec que la normale sur le continent. Inversement, au cours du Petit Age de Glace, alors que la majorité de la planète connaissait des conditions particulièrement froides, une migration de l'ITCZ vers le sud dans l'Est du Pacifique (Koutavas et Lynch-Stieglitz, 2004) aurait entraîné une augmentation de l'humidité sur le continent ainsi qu'un affaiblissement des vents, de l'upwelling côtier et de la productivité le long des côtes sud-américaines (Sifeddine et al., 2008), conduisant à des TSM anormalement chaudes (Vargas et al., 2007; Sifeddine et al., 2008; Gutierrez et al., 2009). À la fin du Petit Age de Glace, les TSM au large du Pérou et du nord du Chili ont commencé à diminuer de nouveau, peut-être à cause d'un nouveau déplacement de l'ITCZ et de l'anticyclone subtropical du Pacifique Sud-Est vers le nord (Gutierrez et al., 2009), ou d'une augmentation du contraste thermique entre l'océan et le continent (Vargas et al., 2007). Des tendances similaires ont été déduites des TSM reconstruites à partir de carottes sédimentaires prélevées au large des côtes marocaines et remontant à 2500 ans: en accord avec les résultats issus d'autres EBUS, l'upwelling côtier au large du Cap Ghir (31°N) semble être en opposition de phase par rapport à la moyenne globale des anomalies de température, avec une intensification au cours de la Période Médiévale Chaude, une diminution au cours du Petit Age de Glace, et de nouveau une augmentation rapide au 20^{e} siècle (McGregor et al., 2007). Toutefois, ces résultats sont sujets

à controverse, car les observations relevées au cours des dernières décennies indiquent une diminution des vents parallèles à la côte et une augmentation des TSM tout au long de la côte marocaine, à l'exception du Cap Ghir (Barton et Roy, *en preparation*). En effet, il est parfois difficile de déduire des tendances à long terme à partir d'observations *in situ* extraites dans un nombre limité de sites, d'autant que de telles tendances pourraient être sensibles à la période et/ou à la zone géographique choisie(s) (Demarcq, 2009).

Les tendances à long terme de l'activité solaire montrent que la Période Médiévale Chaude est la période la plus récente qui soit similaire à la nôtre en termes de forçage solaire (fig. 1.23). Bien que ce dernier ne se soit avéré que partiellement responsable du changement climatique actuel (Stott et al., 2003), le climat de la Période Médiévale Chaude pourrait être très semblable à celui de la période 1850-1950, qui suivit le Petit Age de Glace et précéda l'époque récente où les effets anthropiques commencèrent à dominer le réchauffement global. Des mesures historiques provenant du HCS et d'autres EBUS fournissent effectivement des preuves d'une tendance à l'augmentation des vents favorables à l'upwelling et au refroidissement de la TSM dans la période récente, en accord avec les proxys paléoclimatiques de l'époque médiévale:

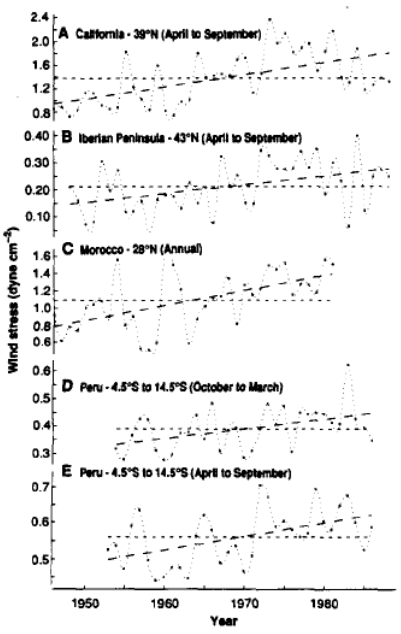

Fig.1.24: Moyennes annuelles des valeurs mensuelles de vent parallèle à la côte (données ICOADS) au large de la Californie **(A)**, de la Péninsule Ibérique **(B)**, du Maroc **(C)** et du Pérou **(D** et **E)**. Pour chacune des séries temporelles, les lignes discontinues représentent la tendance linéaire correspondante, obtenues à partir de la méthode des moindres carrés. *Adapté de Bakun (1990)*.

- les données de vent prises à bord de bateaux marchands montrent une tendance linéaire systématique au cours des dernières décennies à l'augmentation des vents parallèles à

la côte (~ 0,04 dyne.cm^{-2} par décennie pour le centre et le nord du Pérou) au large des côtes de la plupart des EBUS (fig. 1.24) (Bakun, 1990), y compris le nord du HCS (Jahncke et al., 2004). Les mesures de vent prises par le satellite QuickSCAT sur la période 2000-2007 indiquent également des tendances de +0,20 ms^{-1}, +0.24 ms^{-1}, et +0,04 ms^{-1} pour les côtes du Pérou ainsi que du Nord et du centre du Chili (respectivement 18°S-32°S et 32°S-42°S) (Demarcq, 2009);

- une augmentation de la fréquence des tempêtes de sable à échelle synoptique au large de Pisco au sud du Pérou (14°S), et dues au vent parallèle à la côte a été observée depuis 1950 (Escobar, 1993);

- les données des stations côtières de l'IMARPE (l'Institut Péruvien de Recherche en Sciences de la Mer) le long de la côte du Pérou montrent une tendance au refroidissement pour la TSM au Sud de 12°S et une légère tendance au réchauffement au Nord de 12°S au cours des 50 dernières années (S. Purca, *communication personnelle*) ;

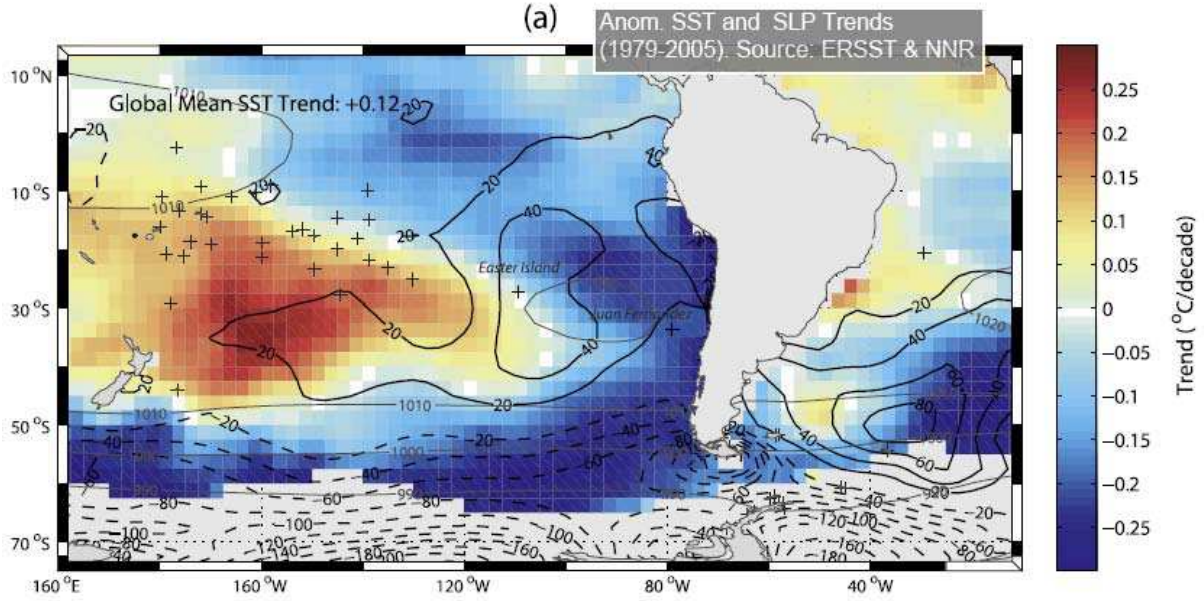

Fig.1.25: Tendances anormales (moyenne mondiale déduite) de TSM (°C/décennie) issues des données analysées ERSST (Smith et Reynolds, 2004) (carrés de couleur). Les lignes épaisses en trait plein (resp. en pointillés) indiquent des tendances positives (resp. négatives) de pression au niveau de la mer (Pa/décennie) provenant de la réanalyse NCEP-NCAR (Kalnay et al., 1996). Les fines lignes grises représentent le champ de pression climatologique moyen. Les croix noires indiquent les stations dans le Pacifique Sud où des données de pression à long terme sont disponibles. *Adapté de Falvey et Garreaud (2009).*

- en accord avec ces résultats, Falvey et Garreaud (2009) ont utilisé des champs globaux de TSM analysée et des données *in situ* sur la période 1979-2005 afin d'établir des tendances significatives au refroidissement sur la côte du Chili et du sud du Pérou (~0,15°C par décennie), mais aucune tendance claire dans la région Nord du Pérou (fig. 1.25). Leurs

résultats montrent également une tendance nette au réchauffement sur le continent, y compris dans la région proche de la côte (non présenté). De telles tendances sont consistentes avec celles simulées par un ensemble de modèles climatiques globaux pour la fin du 20^{e} siècle, ce qui suggère qu'elles sont liées au changement climatique d'origine anthropogénique plutôt qu'à la variabilité décennale: en effet, en supposant que les éventuels modes de variabilité naturelle devraient s'annuler après avoir calculé la moyenne d'ensemble (Cai et Cowan, 2006), les structures de changement climatique communes à la plupart des modèles devraient représenter une réponse au forçage en GES;

- une augmentation nette de la concentration en chlorophylle-a à la surface de l'océan a été observée au large des principaux EBUS (dont le HCS) au cours de la dernière décennie à partir de données satellitaires (fig. 1.26) (Demarcq, 2009), en accord avec des tendances similaires révélées par les mesures *in situ* effectuées au large du Pérou par l'IMARPE au cours des 30 dernières années, qui suggèrent une augmentation possible de l'upwelling côtier.

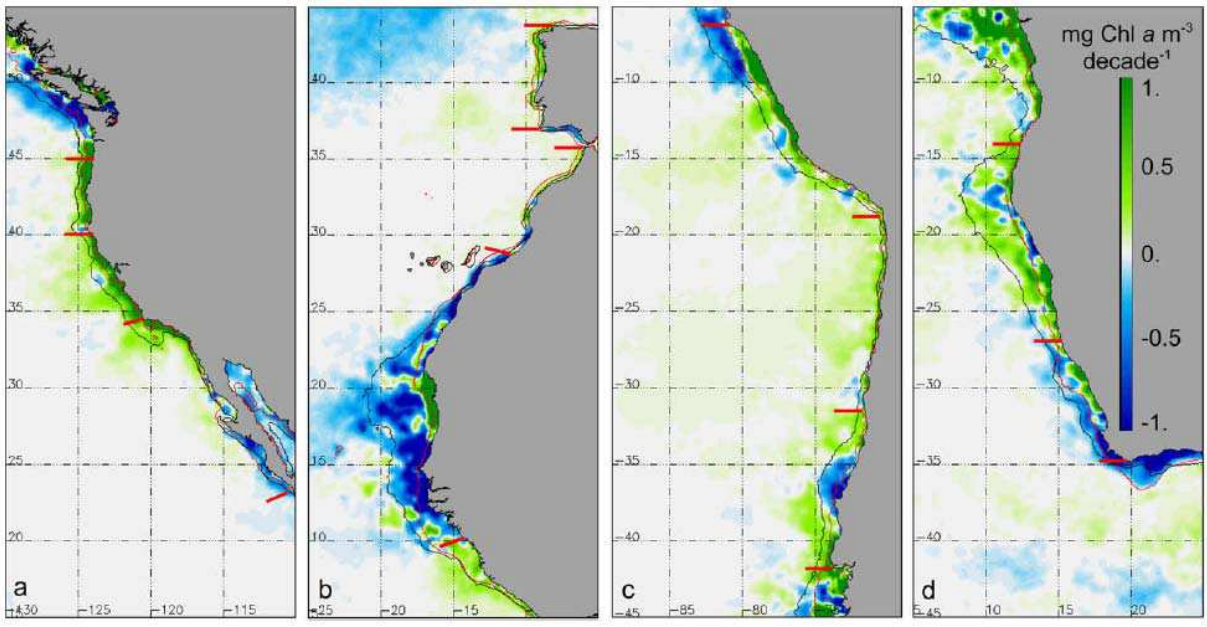

Fig.1.26: Répartition spatiale des tendances en concentration en chlorophylle-a (mg m^{-3} décennie^{-1}) à la surface de l'océan, à partir de données satellite SeaWiFS sur la période 1998-2007 pour les quatre principaux EBUS. Les fines lignes rouges (resp. noires) représentent l'isobathe 200m (resp. la position moyenne de l'isoplète 1 mg.m^{-3}). *Adapté de Demarcq (2009)*.

Sur la base de ces observations, plusieurs théories ont été proposées afin d'expliquer les impacts des changements climatiques passés et du réchauffement global moderne sur les EBUS, et plus particulièrement sur le HCS. D'après l'hypothèse de Bakun (Bakun, 1990), l'intensification observée des vents favorables à l'upwelling ainsi que du refroidissement

conséquent de l'océan côtier dans les EBUS serait due à l'augmentation du contraste thermique terre-mer, consécutive à la réduction du refroidissement nocturne sur le continent avec l'augmentation de l'effet de serre (Sutton et al., 2007), comme le schématise la figure 1.27 pour la côte du Pérou (Bakun et Weeks, 2008). En outre, d'après Sutton et al. (2007), le ratio de réchauffement terre-mer est plus faible à proximité de l'équateur que dans les régions subtropicales car la différence d'humidité entre la terre et la mer (et donc la différence de capacité calorifique) est inférieure plus près de la zone de convergence intertropicale où la pluviométrie est plus élevée. Ceci pourrait expliquer les tendances plus fortes au refroidissement observées au large du Chili par rapport à celles observées au nord du Pérou, au moins partiellement.

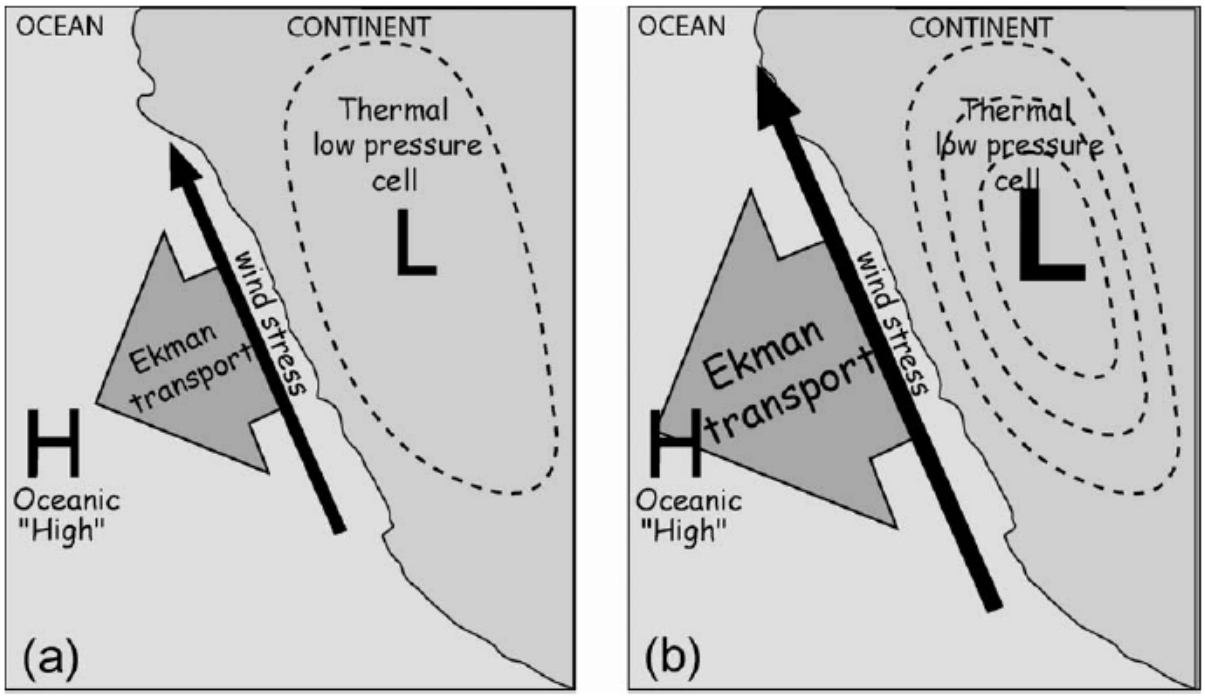

Fig.1.27: Schéma du mécanisme d'intensification de l'upwelling: **(a)** une cellule "thermique" de basses pressions s'accumule sur la masse continentale du littoral, du fait du réchauffement plus rapide de la surface continentale par rapport à l'océan, exerçant ainsi une tension de vent géostrophique dirigée vers l'équateur à la surface de la mer qui, à son tour, provoque un transport d'Ekman des eaux de surface dirigé vers le large, ainsi que la résurgence associée des eaux profondes, nécessaire au remplacement des eaux de surface transportées vers le large; **(b)** l'accumulation des gaz à effet de serre dans l'atmosphère réchauffe le littoral et inhibe son refroidissement nocturne, augmentant alors l'intensité moyenne de la cellule côtière de basses pressions et des vents favorables à l'upwelling, qui en retour provoquent des augmentations quadratiques (ou plus) du transport de surface vers le large et de l'upwelling qui en résulte. *Source: Bakun et Weeks (2008).*

D'autre part, l'affaiblissement observé (Vecchi et al., 2006) et prévu de la circulation de Walker au-dessus du Pacifique tropical et des vents alizés associés (Vecchi et al., 2006; Vecchi et Soden, 2007) devrait provoquer un réchauffement de l'océan Pacifique équatorial, en particulier dans l'Est en raison d'une réduction du gradient zonal de TSM et de la

thermocline (Hansen et al., 2006; Vecchi et al., 2008). Selon cette vision, des eaux tropicales chaudes seraient advectées vers la côte du Pérou (via l'EUC, les Jets Tsuchiya et/ou le CPCC – *cf.* section précédente), où elles pourraient approvisionner le PCUC et enfin l'upwelling côtier: ceci résulterait en une tendance au réchauffement qui s'opposerait à la tendance au refroidissement décrite ci-dessus. En outre, la réduction de la circulation atmosphérique tropicale pourrait avoir une incidence sur la cellule de circulation méridienne dans le Pacifique Sud-Est, bien que la connexion entre les deux systèmes reste mal comprise: par exemple, au cours de certains événements El Niño (mais pas tous), les vents favorables à l'upwelling sont intensifiés (Bakun et Weeks, 2008), alors que les alizés, la circulation de Walker et l'anticyclone subtropical sont plus faibles (voir rubrique 1.2. de ce chapitre).

D'autre part, d'après les séries temporelles analysées par Bakun et Weeks (2008) (leur figure 6), des valeurs positives de corrélation déphasée entre les alizés du Pacifique et les vents au Pérou semblent être présentes toute l'année pendant les années 50 et 60, bien qu'une telle relation apparaisse moins clairement après le changement de régime climatique du Pacifique tropical au milieu des années 70. Enfin, l'effet direct des GES induit par l'augmentation du forçage radiatif pourrait également avoir un effet de réchauffement sur l'océan au large du Pérou et du Chili, même si une telle tendance pourrait être plus faible dans les EBUS qu'ailleurs, parce que la teneur réduite en vapeur d'eau dans l'atmosphère associée à la présence de l'anticyclone subtropical pourrait freiner l'augmentation de l'effet de serre.

Dans l'ensemble, les changements climatiques moderne et futurs dans le HCS semblent être liés à des effets opposés de réchauffement et de refroidissement qui sont susceptibles de moduler la réponse de l'upwelling côtier au réchauffement climatique de manière significative. Ces rétroactions en compétition pourraient être sensibles à la latitude, ce qui pourrait expliquer les différences de tendances observées dans les parties Sud et Nord du HCS.

La modélisation climatique peut être utilisée pour essayer de reproduire les changements observés dans le HCS en relation avec le réchauffement global, et pour en déduire des scénarios futurs à l'échelle régionale. Une telle approche est complémentaire des études basées sur des enregistrements sédimentaires et/ou des observations historiques, en particulier dans la mesure où elle permet de tester la pertinence des théories mentionnées ci-dessus, et éventuellement de quantifier le poids relatif des différents processus de réchauffement et de refroidissement mis en jeu. Une synthèse de la littérature sur les changements climatiques futurs dans le HCS est proposée dans la sous-section suivante.

1.2.2. Tendances actuelles et futures à partir d'études de modélisation

La dynamique de l'upwelling côtier et sa réponse au changement climatique ainsi qu'à la variabilité décennale semblent être guidées par des processus intervenant sur différentes échelles spatiales: 1) à l'échelle mondiale, les émissions de GES induites par le forçage radiatif provoque une tendance au réchauffement partout à la surface de la Terre, y compris dans les EBUS et dans le HCS; 2) à l'échelle d'un bassin océanique, la dynamique du climat équatorial pourrait avoir un impact significatif sur le climat régional; 3) à l'échelle régionale, les changements dans le forçage atmosphérique exercé par les anticyclones subtropicaux peuvent influencer la force et la variabilité des vents favorables à l'upwelling; 4) à l'échelle locale, les interactions terre-air-mer peuvent influencer directement les vents locaux et la dynamique des upwellings côtiers. Tandis que les CGCMs peuvent permettre dans une large mesure d'étudier la réponse des EBUS à des changements s'opérant sur des échelles allant du global au régional, la modélisation océanique à plus haute résolution est nécessaire pour étudier les processus à plus fine échelle tels que ceux liés au contraste thermique terre-mer dans la région côtière, à l'origine de l'hypothèse de Bakun. Dans ce qui suit, nous passons brièvement en revue les principales études de modélisation utilisant les sorties de CGCMs pour en déduire la dynamique et la variabilité à long terme des EBUS et du HCS, avant de présenter quelques résultats issus d'études de modélisation régionale:

- Diffenbaugh (2005) s'est servi des simulations du CMIP3 effectuées par un ensemble multi-modèles de 18 CGCMs pour le climat du 20^{e} siècle et pour les expériences *20th century climate change commitment* et *SRES A2* afin d'étudier la réponse du forçage atmosphérique à grande échelle dans les EBUS au changement climatique mondial. L'auteur trouve des réponses similaires pour les quatre principaux EBUS, incluant une relaxation de la force et de la variabilité du vent dirigé vers l'équateur, au moment de l'année où celui-ci est à son maximum, ce qui est en contradiction avec Bakun (1990). Toutefois, Diffenbaugh (2005) ne propose pas explicitement de mécanisme physique pour expliquer cette diminution du vent. De plus, les modèles qu'il considère sont incapables de reproduire les tendances à long terme et la variabilité interannuelle observées au cours du 20^{e} siècle, ce qui sème le doute sur la fiabilité de ces prévisions d'ensemble. Il convient de noter que presque tous les modèles de la base de données du CMIP3 ont été utilisés dans son étude, sans évaluation préalable des performances individuelles de chaque modèle, ni d'identification de sous-ensembles de modèles plus réalistes.

- D'autre part, Garreaud et Falvey (2008) ont utilisé 9 CGCMs issus du même ensemble de modèles pour étudier les changements dans la variabilité du vent côtier au large du Chili déduits à partir des simulations *Climat du 20^{e} siècle*, *SRES A2* et *B2*. Les auteurs trouvent une réponse cohérente au sein de l'ensemble, avec une augmentation de l'intensité de l'anticyclone subtropical et des vents favorables à l'upwelling. Contrairement à Diffenbaugh (2005), les simulations effectuées sur le climat du 20^{e} siècle montrent des tendances similaires à celles déduites des observations. Afin de mieux documenter l'impact de ces changements sur la région côtière, Garreaud et Falvey (2008) ont forcé un modèle atmosphérique régional avec les sorties des CGCMs: ils montrent que l'intensification à grande échelle des vents dirigés vers l'équateur prévue au large du Chili pour la fin du 21^{e} siècle est associée à 1) une extension vers le sud des vents favorables à l'upwelling jusqu'à environ 41°S, 2) une augmentation de la fréquence et de la durée des événements de jets côtiers, et 3) une intensification des vents du sud en hiver austral, transformant l'upwelling saisonnier au large du Chili à un upwelling quasi-permanent, comme c'est le cas au Pérou.

- Falvey et Garreaud (2009) ont utilisé un ensemble de 21 CGCMs et une vaste compilation d'observations *in-situ* et de produits analysés grillés afin de déduire des tendances récentes et futures pour la température dans la région du HCS, à la fois sur le continent et dans l'océan. En accord avec Bakun (1990) et avec Bakun et Weeks (2008), les auteurs ont constaté une tendance claire au réchauffement sur le continent à la fois dans l'ensemble de modèles et dans les observations, ainsi qu'une tendance au refroidissement dans les observations de TSM au large du Chili. Comme nous l'avons mentionné précédemment, la tendance est moins nette au large du Pérou. D'autre part, bien que les TSM simulées au Pérou ne présentent pas de tendance au refroidissement, une tendance au réchauffement a été observée partout ailleurs dans le monde, sauf dans l'Océan Austral et au large du Chili. Par conséquent, les tendances anormales par rapport à la tendance moyenne globale en TSM (fig. 1.25) sont négatives à la fois au large du Pérou et du Chili, en accord avec l'intensification du système de hautes pressions et des vents parallèle à la côte d'après Garreaud et Falvey (2008). Il convient de noter que ce réchauffement minimum prévu dans le Pacifique Sud-Est ne peut être expliqué par une plus grande efficacité des flux de chaleur latente uniquement, comme c'est le cas dans certaines régions soumises aux alizés telles que l'Atlantique Nord tropical par exemple (Leloup et Clement, 2009), puisque celà nécessiterait un faible changement en vitesse du vent, ce qui n'est pas le cas au large du Pérou et du Chili.

Similairement à Garreaud et Falvey (2008), Snyder et al. (2003) ont utilisé un modèle régional de circulation atmosphérique afin d'étudier les changements dans la tension de vent de surface et dans le rotationnel de la tension de vent dans le Courant de Californie, entre les scénarios PIcntrl et $2xCO_2$. Ils ont également constaté une augmentation des vents favorables à l'upwelling au cours de la saison de l'upwelling. D'autre part, Auad et al. (2006) ont utilisé un modèle océanique régional forcé par des vents de surface « downscalés », des flux de chaleur et des conditions aux frontières ouvertes obtenus à partir d'un scénario de 36% d'augmentation du CO_2. En accord avec Snyder et al. (2003), ils constatent une intensification de l'upwelling côtier en réponse à l'augmentation du vent de surface. Une telle intensification s'est avérée suffisamment forte pour annuler l'augmentation de la stratification de surface due au réchauffement provoqué par le forçage radiatif. En conséquence, un refroidissement modéré a été observé près de la surface, ainsi que des vitesses verticales augmentées durant la saison pic de l'upwelling et une diminution de l'activité mésoéchelle près de la côte.

Pour résumer cette section, les observations historiques et les reconstructions paléoclimatiques à long terme des vents parallèles à la côte et des TSM au large de la côte ouest de l'Amérique du Sud révèlent un comportement distinct pour les parties Nord et Sud du HCS en réponse au changement climatique du 20^{e} siècle: alors que l'on a de plus en plus de preuves de l'intensification des vents favorables à l'upwelling au large du Chili, et du refroidissement conséquent de la surface de l'océan, le schéma est moins clair pour le Pérou. En effet, des observations peu nombreuses et parfois contradictoires relevées au large de la côte Nord et centrale du Pérou ne permettent pas de déduire des tendances clairement positives ou négatives pour le vent et la TSM. Toutefois, les observations suggèrent un comportement similaire pour le Sud du Pérou et pour le Chili, mais la limite nord de la région caractérisée par un upwelling en augmentation semble étroitement liée aux données considérées. Les résultats des études de modélisation du climat et de l'atmosphère confirment les tendances observées le long de la côte du Chili. Cependant, à notre connaissance, jusqu'ici aucune étude similaire n'a été réalisée pour la côte du Pérou, à l'exception des travaux récents de Goubanova et al. (2010) et d'Echevin et al. (2010) menées dans le cadre du programme PCCC (*cf.* chapitre 4). Par ailleurs, les CGCMs de la génération actuelle souffrent de nombreux biais dans le Pacifique Sud-Est, incluant une mauvaise représentation des vents à basse altitude ainsi que des TSM trop élevées. Ces biais sont en partie dus à la faible résolution atmosphérique et océanique des CGCMs, mais aussi à une compréhension incomplète des processus atmosphériques et océaniques couplés dans la région, tels que ceux

à l'origine du *Stratocumulus cloud deck*, ou encore ceux mis en jeu dans la connexion entre l'anticyclone du Pacifique Sud-Est et la circulation de Walker dans le Pacifique tropical, par exemple. En outre, la plupart des études basées sur des simulations de changement climatique dans les EBUS réalisées avec des CGCMs n'évaluent pas la capacité des différents modèles à représenter la dynamique régionale et/ou leur forçage à distance par la dynamique à grande échelle. L'objectif général du programme PCCC consistait à proposer une méthodologie pour étudier l'influence du changement climatique sur le Système de Courant de Humboldt, et qui puisse être appliquée à d'autres EBUS, et dans une certaine mesure, à d'autres régions de l'océan mondial.

1.2.3. Objectifs et méthodologie de la thèse et du programme PCCC

La méthodologie proposée par PCCC traite plusieurs questions qui n'ont été que partiellement résolues par les études antérieures:

1) **l'évaluation des performances des CGCMs du CMIP3**: au lieu de faire des moyennes d'ensemble à partir des jeux de données multi-modèles constitués par des modèles climatiques aux comportements hétérogènes, nous avons choisi dans cette thèse de réaliser une analyse approfondie de ces modèles afin d'identifier les plus pertinents pour l'étude du changement climatique dans le HCS (chapitre deux). En effet, il y a environ 25 modèles dans la base de données du CMIP3, et tous ne pouvaient pas être downscalés, puisque 1) cela nécessiterait des temps de calcul et des ressources humaines énormes, et 2) faire une moyenne d'ensemble des réponses multi-modèles pourrait conduire à des interprétations erronées en raison du nombre de modèles fortement biaisés dans la région. D'après les connaissances actuelles sur les forçages locaux et distants du HCS, trois critères principaux ont été retenus pour effectuer cette sélection: le réalisme de la variabilité ENSO à grande échelle, celui de l'état moyen et de la variabilité de la température et des champs de vitesses dans le Pacifique Sud-Est, et celui du forçage atmosphérique. Appliquée à l'ensemble multi-modèles du CMIP3, une telle méthodologie permet d'identifier un sous-ensemble restreint de modèles qui est alors utilisé pour faire des projections des futurs changements climatiques régionaux avec un meilleur indice de confiance (voir point 3)).

2) **Downscaling du forçage atmosphérique**: comme nous l'avons expliqué en 1.1, l'upwelling côtier est le résultat à la fois du transport d'Ekman et du pompage d'Ekman. Alors qu'une bonne représentation à grande échelle de l'anticyclone subtropical (le cas échéant) devrait permettre de simuler de façon adéquate les vents de surface favorables à l'upwelling et

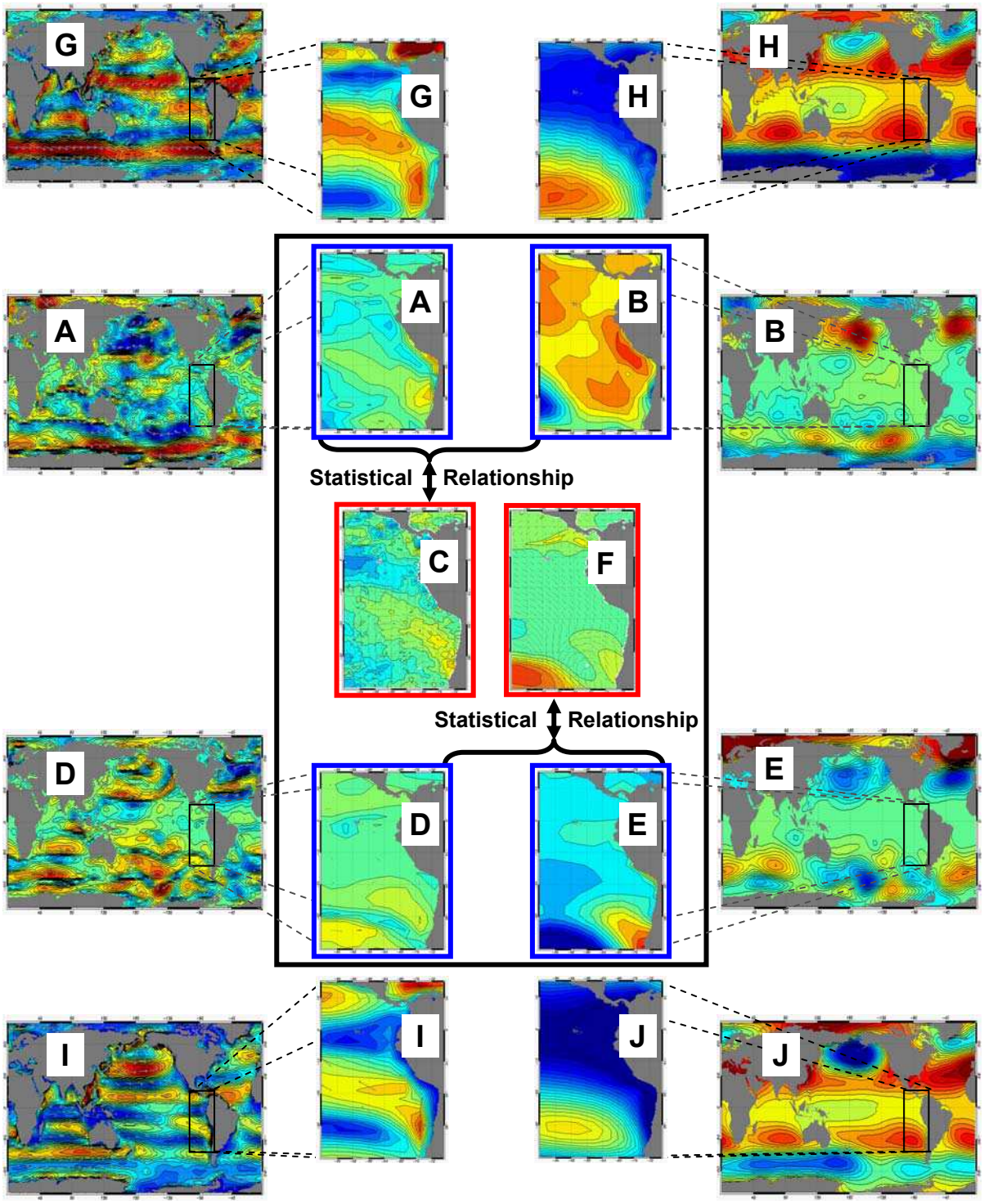

Fig. 1.28: Schéma de la stratégie de downscaling atmosphérique statistique (voir texte): (**A**) anomalies de vent de surface et (**B**) de pression au niveau de la mer issues de NCEP; (**C**) anomalies de vent de surface QuickSCAT; (**D**) anomalies de vent de surface et (**E**) de pression au niveau de la mer issues de IPSL-CM4; (**F**) anomalies de vent de surface downscalées pour IPSL-CM4. (**G**) Vent de surface et (**H**) pression au niveau de la mer climatologiques issus de NCEP; (**I**) Vent de surface et (**J**) pression au niveau de la mer climatologiques issus de IPSL-CM4. Les champs de prédicteurs (prédictants) sont encadrés en bleu (rouge). Noter le changement d'échelle de couleur entre les cartes globales et régionales pour (B), (E), (H) et (J).

ainsi un transport d'Ekman du même ordre de grandeur que les observations, la faible résolution des modèles climatiques globaux ne permet généralement pas de représenter la

zone de *drop-off* du vent près de la côte, ni le rotationnel du vent qui lui est associé, et qui provoque un pompage d'Ekman le long de la côte Ouest d'Amérique du Sud. En outre, la topographie accidentée des Andes n'est pas bien représentée par les CGCMs et introduit des biais à grande échelle dans la circulation atmosphérique du Pacifique Sud-Est, y compris au niveau de l'anticyclone subtropical. Afin de remédier à ce problème, une méthode de downscaling statistique a été développée par Goubanova et al. (2010). Elle consiste à construire une relation statistique (basée sur des régressions linéaires multiples) entre les vents de surface à l'échelle locale à régionale (le prédictant) et les vents de surface ainsi que la pression au niveau de la mer à grande échelle (les prédicteurs) pour le climat actuel observé, puis à appliquer cette relation aux champs correspondants aux prédicteurs simulés par des CGCMs pour un scénario climatique donné. Ceci suppose que cette relation statistique n'est pas sensible au climat moyen, ce qui constitue bien sûr une hypothèse forte. Malheureusement, pour l'instant les vents de surface observés à haute résolution ne peuvent fournir un enregistrement suffisamment long pour nous permettre de tester une telle sensibilité. Il convient cependant de noter que des hypothèses similaires sont faites fréquemment lors de la production de projections du climat futur avec des modèles climatiques globaux, par exemple lorsque des paramétrisations dérivées d'observations modernes sont appliquées à des simulations avec des émissions de GES accrues.

Goubanova et al. (2010) ont ainsi appliqué la relation déduite 1) des anomalies de vent et de pression au niveau de la mer issues de la réanalyse NCEP/NCAR à une résolution de 2.5°x2.5° (Kalnay et al., 1996) (fig. 1.28A et 1.28B) - par rapport à leurs cycles saisonniers respectifs sur la période 2000-2008 (fig. 1.28G et 1.28H) - et 2) des anomalies de vent (par rapport au cycle saisonnier moyen au cours de la même période) du satellite QuickSCAT à une résolution de 0.5°x0.5° (CERSAT, 2002) (fig. 1.28C), aux anomalies de vent et de pression au niveau de la mer extraites des simulations Pré-Industrielle (fig. 1.28D et 1.28E) et 4xCO_2 du modèle IPSL-CM4 à une résolution de 3,75°x2.5° (Marti et al., 2009), par rapport à leurs cycles saisonniers respectifs sur la période 1970-1999 de la simulation *Climat du 20^e siècle*[1] (fig. 1.28I et 1.28J). Le lecteur est invité à se référer à l'annexe A pour une explication détaillée sur le choix des scenarii climatiques Pré-Industriel et 4xCO_2 ainsi qu'à Goubanova et al. (2010) pour plus de détails sur la méthode de downscaling et sa validation. Il convient de noter qu'IPSL-CM4 a été identifié comme faisant partie des "meilleurs" CGCMs dans le Pacifique Sud-Est (chapitre deux).

[1] *Dans ce scénario, les simulations des modèles CMIP3 sont réalisées avec des niveaux historiques de CO2 dans l'atmosphère de 1850 à 2000.*

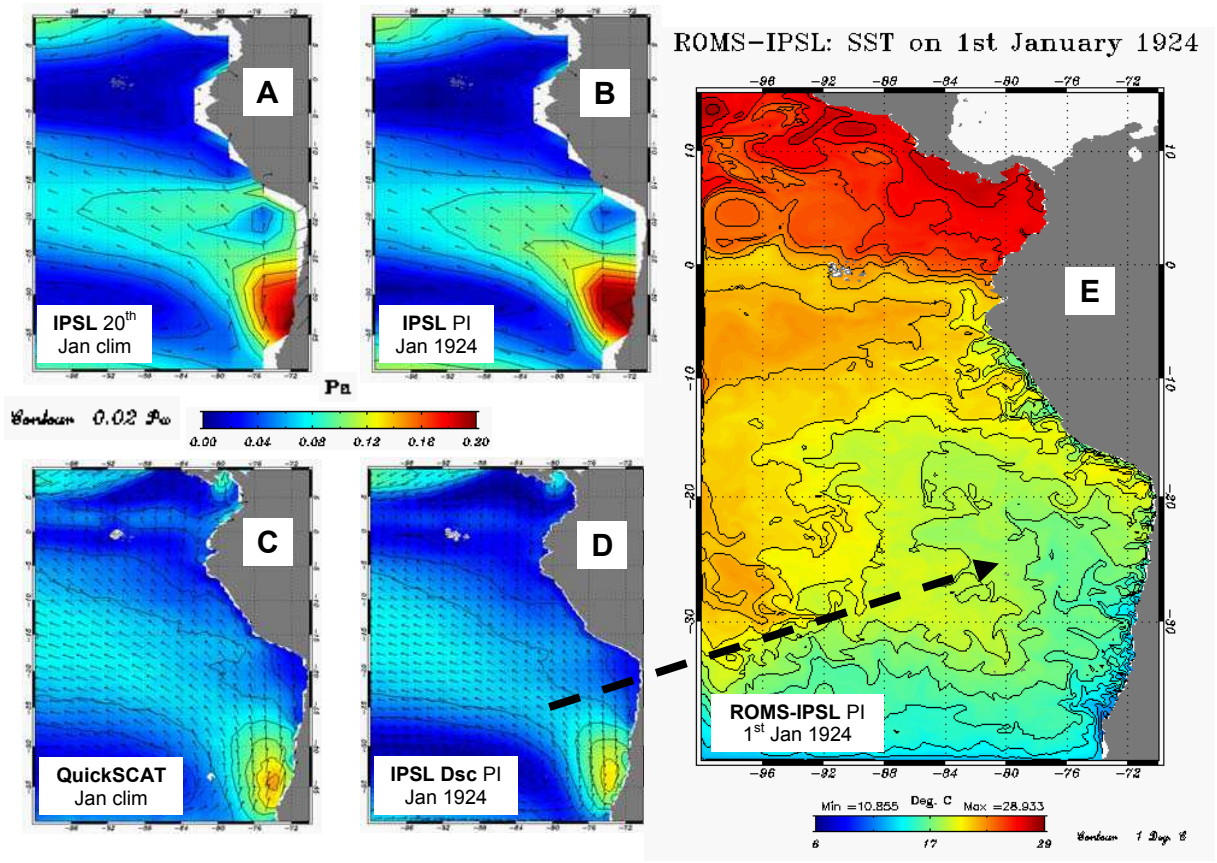

Fig. 1.29: Schéma de la stratégie de forçage atmosphérique de ROMS (voir texte): **(A)** vents de surface climatologiques pour le mois de janvier à partir de la simulation «climat du 20e siècle» du modèle IPSL-CM4, **(B)** vents de surface pour janvier 1924 d'après la simulation dite de «contrôle Pré-industrielle» du modèle IPSL-CM4, **(C)** vents de surface climatologiques pour le mois de janvier à partir de mesures satellitaires QuickSCAT; **(D)** vents de surface downscalés pour janvier 1924 d'après la simulation de «contrôle Pré-industrielle» du modèle IPSL-CM4; **(E)** TSM pour le 1er Janvier 1924 d'après la simulation ROMS forcée par les vents downscalés de la simulation de «contrôle Pré-industrielle» du modèle IPSL-CM4. La flèche noire en pointillés représente le forçage de vent. Les conditions aux frontières ouvertes et les flux atmosphériques sont décrits en figure 1.31. La barre de couleur pour les TSM (°C) est indiquée en dessous du panneau correspondant (IC: 1°C). La barre de couleur pour les vents de surface (Pa) est indiquée sur la partie gauche de la figure (IC: 0,02 Pa). La taille (resp. la direction) des flèches sur (A, B, C, D) représente l'intensité (resp. la direction) du vent en surface.

En particulier, il est caractérisé par un bon équilibre entre le zonal advective feedback et le thermocline feedback et donc par une représentation correcte de la variabilité ENSO (Belmadani et al., 2010), ainsi que par une bonne reproduction de l'anticyclone subtropical (Garreaud et Falvey, 2009). Enfin, les anomalies de vent downscalé pour les simulations Pré-Industrielle (fig. 1.28F) et 4xCO_2 ont été rajoutées au cycle saisonnier de QuickSCAT afin de construire les champs haute résolution (~50km) de vents totaux de surface IPSL-CM4 downscalés (fig. 1.29). Les principaux résultats sont brièvement présentés au chapitre quatre.

3) Downscaling du forçage océanique: similairement à Auad et al. (2006) pour le Courant de Californie, Echevin et al. (2010) ont utilisé un modèle régional océanique du HCS à haute résolution (celui décrit au chapitre trois) forcé par les sorties d'un CGCM. Nous avons forcé le modèle régional avec les vents de surface du modèle IPSL-CM4 downscalés suivant

la procédure de Goubanova et al. (2010), pour deux périodes de 10 ans issues des simulations Pré-Industrielle et 4xCO_2 (fig. 1.29).

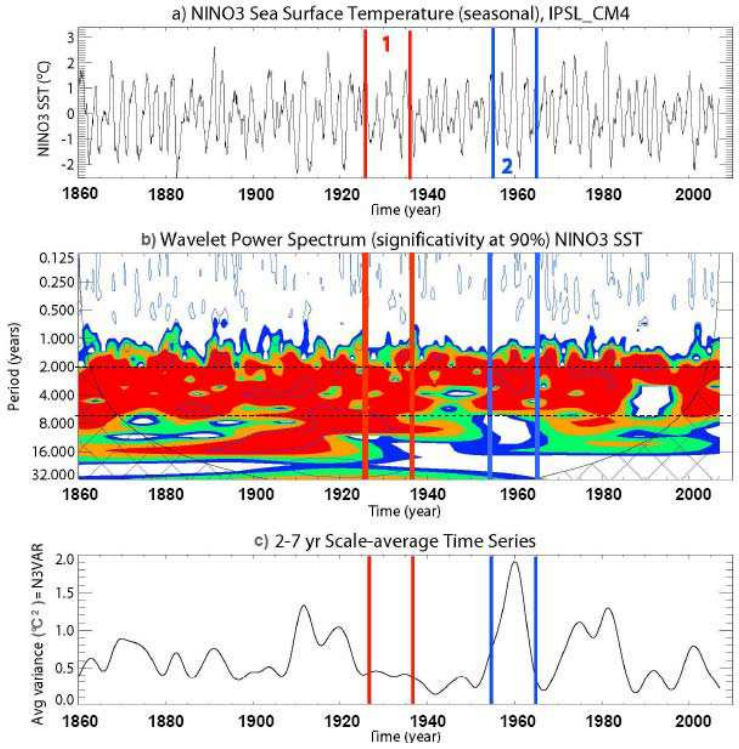

Fig. 1.30: Modulation à basse fréquence d'ENSO sur la période modèle 1860-2007 pour la simulation Pré-Industrielle du modèle IPSL-CM4: **a)** anomalies de TSM filtrées des hautes fréquences (f_c = 1 an^{-1}) et moyennées spatialement dans la région Niño3 (150°W-90°W, 5°S-5°N), **b)** spectre en ondelettes correspondant (seules les valeurs supérieures au niveau de significativité à 90% sont représentées), **c)** série temporelle correspondant à la moyenne de l'ondelette sur la bande 2-7 ans, appelée N3VAR dans ce qui suit. Les unités sont le °C pour a) et le (°C)² pour b) et c). Les lignes verticales rouges (resp. bleues) délimitent la période 1924-1933 (resp. 1955-1964) caractérisée par une faible (resp. forte) amplitude et une faible (resp. forte) modulation d'ENSO. Les lignes horizontales en pointillés noirs sur la figure b) indiquent la bande de fréquence (2-7 ans)$^{-1}$ utilisée pour calculer N3VAR.

La sélection de ces périodes a été réalisée dans le cadre de la présente thèse et se fonde sur l'analyse d'indices de l'activité ENSO dans le Pacifique tropical dérivés des modèles couplés: la modulation à basse fréquence de la variabilité interannuelle de la TSM dans Niño3 (voir 1.2.5) a permis d'identifier des périodes avec une amplitude d'ENSO faible et stable (telles que la période 1 en fig. 1.30), et d'autres avec une amplitude d'ENSO forte et variable (telles que la période 2 en fig. 1.30). Les périodes avec un ENSO faible et stable ont été privilégiées dans cette étude, car dans un premier temps l'accent est mis sur les changements de la variabilité saisonnière et de l'état moyen plutôt que sur les changements de la variabilité interannuelle.

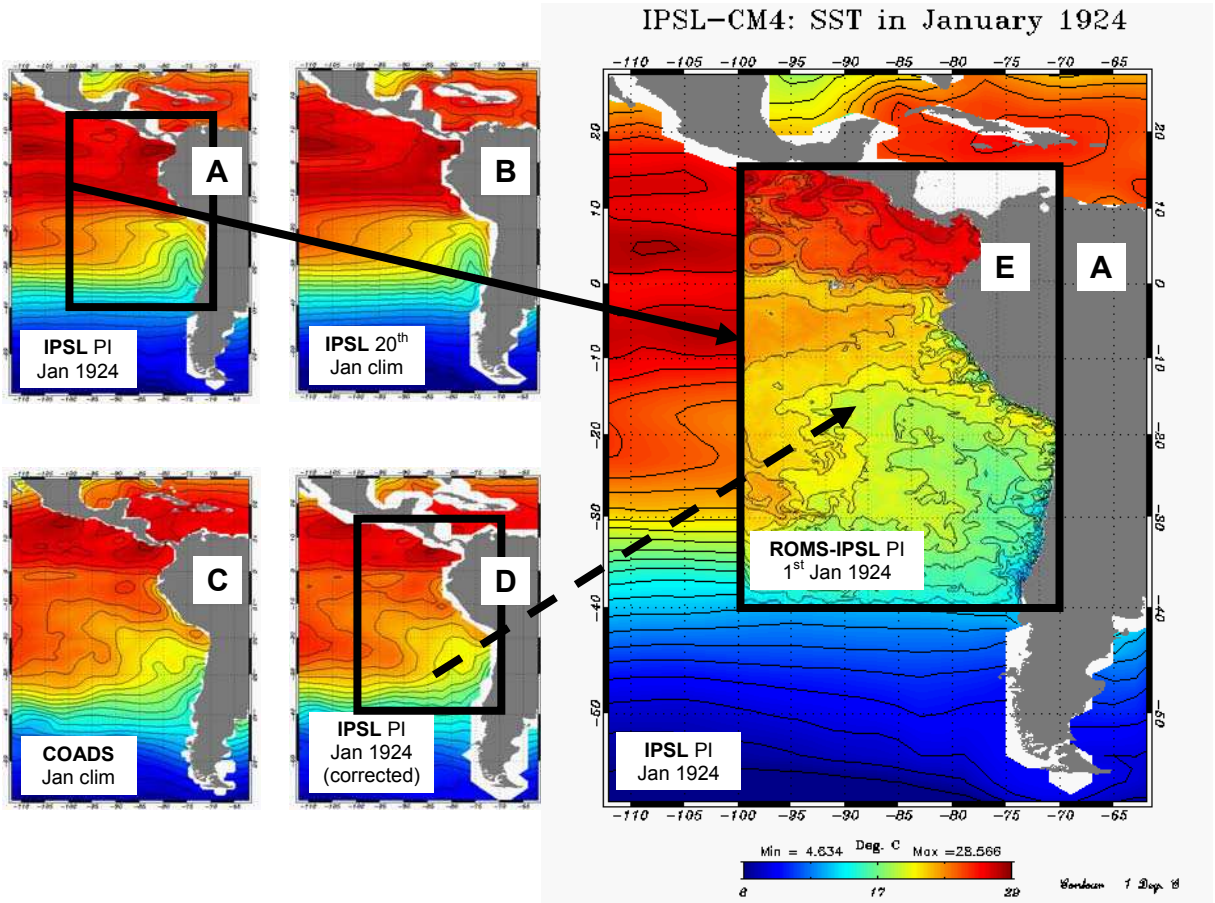

Fig. 1.31: Schéma du downscaling dynamique océanique et de la stratégie de correction des flux (voir texte): **(A)** TSM pour le mois de janvier 1924 d'après la «simulation de contrôle pré-industrielle» du modèle IPSL-CM4; **(B)** TSM climatologiques pour le mois de janvier d'après la simulation «Climat du 20^{e} siècle» du modèle IPSL-CM4; **(C)** TSM climatologiques pour le mois de janvier à partir de données observées COADS; **(D)** TSM corrigée pour le mois de janvier 1924 d'après la «simulation de contrôle pré-industrielle» du modèle IPSL-CM4; **(E)** TSM pour le 1er Janvier 1924 d'après la simulation ROMS forcée aux frontières ouvertes (resp. en surface) par les champs bruts (resp. corrigés) de la «simulation de contrôle pré-industrielle» du modèle IPSL-CM4. Le rectangle noir représente le domaine régional. La flèche noire en trait plein (resp. en pointillés) représente le forçage aux frontières ouvertes (resp. les flux atmosphériques et les termes de relaxation vers les TSM et SSM COADS). Le forçage de vent est décrit en figure 1.29. La barre de couleur (°C) est indiquée dans le coin en bas à droite de la figure (IC: 1°C).

Puisqu'une approche de downscaling statistique ne pouvait être appliquée aux flux air/mer d'IPSL-CM4 en raison de l'absence de données *in situ* à haute résolution dans la région, requises pour construire le modèle statistique, nous avons suivi une stratégie de correction des flux, schématisée en figure 1.31: 1) les cycles saisonniers des flux de chaleur, des flux d'eau douce, ainsi que des termes de relaxation de la TSM et de la SSM (Salinité de Surface de la Mer) ont été calculés sur la période 1960-2000 de la simulation *Climat du 20^{e} siècle* d'IPSL-CM4; et 2) soustraits des champs totaux des simulations Pré-industrielle et 4xCO_2 afin d'en extraire les anomalies par rapport au climat actuel; 3) les données climatologiques COADS à une résolution de 1°x1° (Da Silva et al., 1994) ont finalement été ajoutées aux anomalies de flux afin de produire les flux corrigés utilisés pour forcer le modèle régional. Le lecteur est

invité à se référer à Echevin et al. (2010) pour plus de détails. Les conditions initiales et aux frontières ouvertes pour la température, la salinité, les courants et le niveau de la mer ont été directement extraites des sorties du modèle IPSL-CM4, sans aucune correction préalable (fig. 1.31), car 1) les simulations globales pré-industrielle et $4xCO_2$ ont été initialisées avec les valeurs climatologiques actuelles du World Ocean Atlas 2005 (Locarnini et al., 2006; Antonov et al., 2006), et 2) le modèle régional est capable de générer sa propre dynamique océanique malgré l'influence des frontières ouvertes. Les principaux résultats sont brièvement présentés au chapitre quatre. Une simulation régionale de contrôle réalisée dans le cadre de la thèse avec le modèle régional océanique pour la période récente fournit une référence pour les expériences de changement climatique régional (chapitre trois).

Objectifs de la thèse

« Comment le changement climatique simulé par les modèles couplés globaux de la génération actuelle est-il susceptible d'influencer le système d'upwelling du Pérou-Chili?» constituait la motivation principale lors de la définition de cette thèse de doctorat. Dans cette région de productivité en poissons pélagiques extrêmement élevée et de forte variabilité climatique intrasaisonnière-à-décennale, c'est une question d'une grande importante pour les sociétés des pays voisins dont les économies dépendent fortement de l'exportation de ressources marines vivantes. Cette question centrale a entraîné plusieurs interrogations associées, telles que:

- *« Quels sont les Modèles Couplés de Circulation Générale (CGCMs) les plus fiables dans le Pacifique Sud-Est, et quelles métriques utilisons-nous pour les identifier? »*

-*« A quel point le modèle régional océanique ROMS du Système de Courant de Humboldt (HCS) est-il fiable? Comment prend-il en compte la transmission de la variabilité équatoriale/des ondes équatoriales à la région côtière? Quelle déviation par rapport à la simple théorie linéaire? »*

- *« La modélisation régionale du futur changement climatique confirme-t'elle les tendances et les théories déduites d'observations historiques et de reconstructions paléoclimatiques éparses? »*

Nous avons répondu aux deux premières questions pendant le développement du travail présenté ici, avec comme motivation la nécessité de compléter les différentes étapes requises pour des expériences de downscaling de projections climatiques. Certaines questions

(dont le dernier point mentionné ci-dessus) n'ont cependant pas pu être traitées dans le cadre de la thèse, à cause de la portée très étendue du projet. Ces questions ont été étudiées par d'autres participants au projet PCCC avec qui j'ai collaboré. Dans le cadre de la thèse, une contribution majeure au projet PCCC est située en amont de l'exercice de downscaling lui-même: en plus des développements méthodologiques suivis dans le cadre de PCCC, mon travail a conduit à une meilleure compréhension de certains mécanismes physiques d'intérêt pour PCCC. En particulier, nous avons progressé sur la question spécifique de la compréhension des biais des CGCMs en termes de variabilité ENSO. Dans une seconde partie de la thèse, l'effort était principalement dédié à la compréhension des processus de téléconnexion océanique entre les ondes de Kelvin équatoriales (EKW) et la circulation côtière dans une simulation régionale à haute résolution avec des conditions aux frontières réalistes. J'ai également participé à l'analyse de simulations régionales avec des scénarios de changement climatique idéalisés qui ont été réalisées dans le cadre du projet PCCC, et en particulier à l'évaluation de mécanismes de rétroaction concurrents de réchauffement et de refroidissement en action dans la région du Pérou-Chili.

Dans le chapitre suivant, nous détaillons la méthodologie utilisée pour sélectionner le sous-ensemble de modèles climatiques qui, au final, fournissent le forçage aux frontières du modèle régional océanique. Dans le chapitre trois, la méthode de downscaling océanique est décrite et appliquée à une configuration du HCS avec un forçage réaliste aux frontières sur la période 1992-2000. Cette simulation régionale est utilisée pour documenter les principales caractéristiques de la circulation régionale et de sa variabilité. Une étude spécifique sur l'impact de la variabilité équatoriale à grande échelle sur la variabilité côtière dans la région est également présentée dans le même chapitre, dans le but de mieux comprendre le lien entre la variabilité et les changements climatiques à l'échelle du bassin et à l'échelle régionale. La simulation est également destinée à être utilisée comme référence pour évaluer le réalisme des simulations régionales obtenues à l'aide du forçage aux frontières fourni par les CGCMs. Dans le quatrième et dernier chapitre, les résultats obtenus à partir d'expériences de changement climatique régional sont présentés et discutés, avant de conclure la présente thèse de doctorat et proposer quelques perspectives futures.

Introduction

The coastal ocean, defined as the portion of the ocean limited by the coast on one side and by the continental shelf on the other side, represents only about 10% of the surface of the world ocean, and a negligible part of its volume. However, it concentrates many resources of economical interest which are intensively exploited because of their accessibility and because more than one half of humanity lives less than 100 km away from the ocean. Of particular interest, fisheries provide one of the main sources of food supply and constitute an important sector of the economy in many countries. This is particularly true for Eastern Boundary Upwelling Systems (EBUS'es), which concentrate about 30% of fish catches over 0.1% of the surface covered by the oceans (Durand et al., 1998). In these regions, persistent alongshore trade winds drive strong coastal upwelling of cold, nutrient-rich waters that provide the conditions for high primary production and intense marine ecosystems. There are four EBUS'es which are found in both hemispheres along the eastern boundary of the two main ocean basins (the Pacific and the Atlantic): the Canary Current in the North Atlantic, the Benguela Current in the South Atlantic, the California Current in the North Pacific, and the Humboldt Current in the South Pacific (fig. 0.1).

In this PhD thesis, the focus is on the Humboldt Current System (HCS) that is embedded in the coastal ocean off Peru and Chile. The HCS is the third EBUS in terms of density of primary productivity, but by far the first in terms of fish catch (Chavez et al., 2008): 11 million tons of fish are caught every year off Peru and Chile, which represents 12% of global fish catch, mainly on pelagic species like sardine and anchovy (F.A.O, 2009). Peru in particular is so productive that several drownings of fishing boats are reported every year because of the excessive weight of fish they carry. This incredible abundance makes fishing an important source of income for these countries, especially because a large fraction of their pelagic fish is exported. Apart from fish catch, a particularity of the HCS compared to other EBUS'es is its proximity to the equator and the orientation of its coastline, which makes it very sensitive to equatorial variability, including ENSO (El Niño-Southern Oscillation), the strongest climate anomaly on the planet at interannual time scales (*e.g.* Neelin et al., 1998; Cane, 2005; McPhaden et al., 2006). During the occurrence of an El Niño event, the regional ocean circulation and climate of the HCS undergo dramatic changes: the cool surface waters (about 15°C to 19°C) that normally characterize Peru and Chile's coastal ocean and gave it

the nickname of « refrigerator of the tropics » can rise up to 8°C above normal temperature (Blanco et al., 2002; Carr et al., 2002). This strong warming of the ocean is accompanied by high rainfall and floodings over the usually arid coasts of Peru and northern Chile, which has severe consequences on the agriculture and on human activities in general. In addition, the warming of the ocean can cause coastal upwelling to reduce significantly or even to shut down, which has serious impacts on the marine ecosystem (Barber and Chavez, 1983). At longer timescales, stocks of pelagic fish exhibit strong variations in relation to decadal variability in the Pacific Ocean: for instance, the climate shift of the tropical Pacific that occurred in 1976 lead the collapse of sardine stocks and the multiplication of anchovies (Chavez et al., 2003). Because of the sensitivity of the HCS to large scale climate variability, potential changes at the regional scale in relation to global warming could be important and have spectacular biological consequences. In this context, the sustainable management of fisheries appears as a key societal and economical issue for the neighbouring countries, but also for the whole world because of the importance of the fish resource of the HCS at global scale, especially in the context of overfishing and decline of fish stocks in many parts of the world.

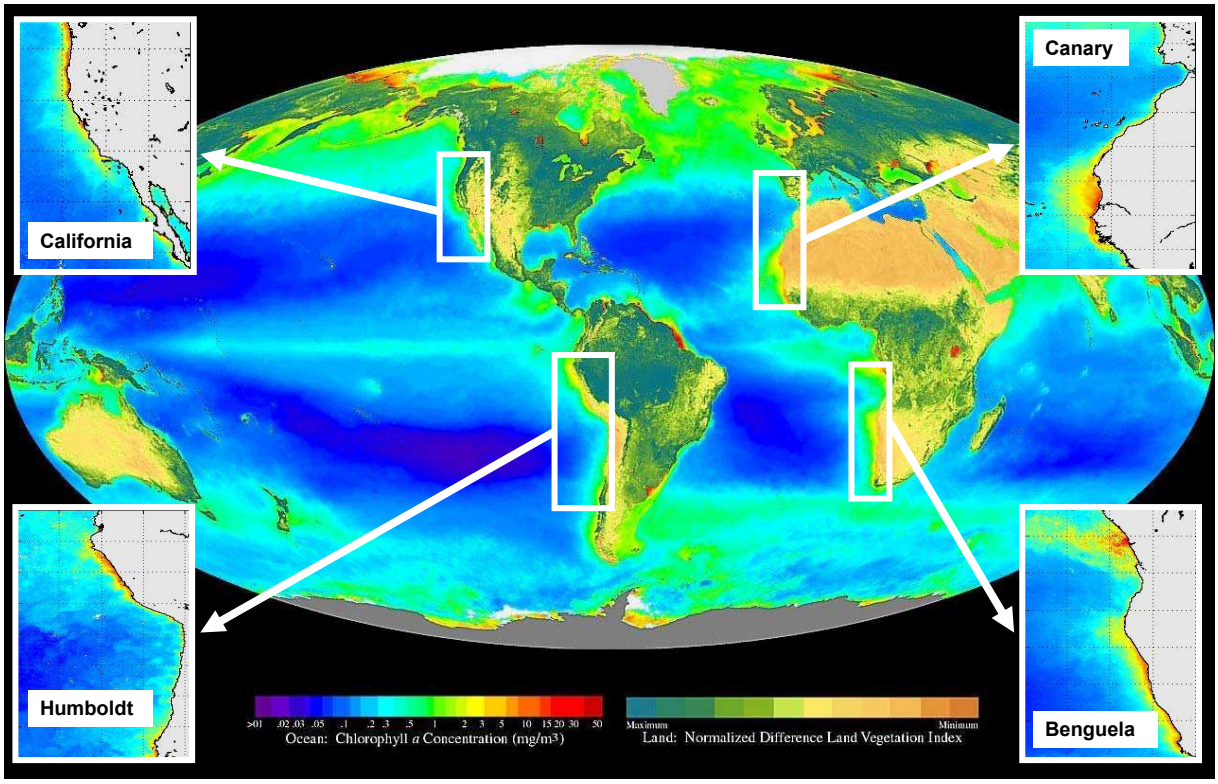

Fig. 0.1: Mean surface chlorophyll-a concentration (mg/m^3) over the period 09/1997-08/2000 from SeaWiFS satellite data (NASA/Goddard Space Flight Center). The four main EBUS'es are indicated: the California Current, the Humboldt Current, the Canary Current and the Benguela Current. Regional maps courtesy of IRD/AOOS.

IRD (Institut de Recherche pour le Développement), a French institute of public research that aims at assisting developing countries in the improvement of their research capacities, has been collaborating with local research partners from Peru and Chile for about a decade. Likewise, it also actively contributes to research projects in two other EBUS'es, namely the Benguela Current and the Canary Current. Recently, the institute has started to promote integrated multidisciplinary approaches for the study of EBUS'es, stating that in-depth studies of the physical marine environment and climate are a pre-requisite for comprehensive studies of the associated marine ecosystems. In this context, IRD has taken a leading role in the definition of the PCCC (Peru-Chile Climate Change) program (P.I. Dr Boris Dewitte) funded by ANR (Agence Nationale de la Recherche), the French research funding agency. Indeed, the sustainable management of fisheries highly depends on our ability to predict regional impacts of global warming. The PCCC program proposes to address this issue from the oceanic point of view with the approach of high resolution ocean modelling. The objective of PCCC is twofolds: 1) to understand the factors that impact the regional circulation off Peru and Chile with a focus on the processes of teleconnexion between equatorial variability and coastal circulation, and 2) to provide an estimate of the impact of climate change on the regional circulation off Peru and Chile. The present PhD thesis is a major contribution to this program: it allowed building an objective methodology to analyze large-scale biases of coupled models likely to influence the simulated past, present and future behaviour in the HCS, and to identify the most relevant models for the study of climate change in this region. In addition, it contributed to analyze modern regional ocean dynamics, which are used as a baseline to understand future changes in the HCS.

The present dissertation reports the main results that were obtained in the framework of the thesis. First, a presentation of the physical functioning of EBUS'es in general and of the HCS in particular will be proposed based on earlier works, and related to the context of climate change and its possible impacts on the regional scale. Then, characteristics from state-of-the-art global climate models of relevance to the study of regional ocean circulation in the HCS will be assessed and used to identify the most appropriate models to be used for downscaling experiments over this region. Next, the modelling approach will be detailed, and results from a regional simulation performed over the recent period that illustrate the natural variability of the HCS and its sensitivity to remote equatorial forcing will be presented. Last, some results from regional climate change experiments performed in the context of PCCC will be provided in order to give clues to anticipate the possible response of the HCS to climate change.

Chapter 1: Humboldt Current System and Climate Change

This chapter is a synthesis of previous studies on the regional ocean dynamics in the HCS, followed by a presentation of the possible influence of global warming in this region of the world ocean. In the first section, the main physical characteristics of EBUS'es will be presented, in order to understand what makes them so peculiar in terms of both ocean physics and biological productivity, before we focus on the HCS and on its specificities compared to other EBUS'es. In the second section, a review of past works that attempted to describe the possible impacts of climate change in EBUS'es in general and in the HCS in particular will be proposed. This summary of present knowledge on the HCS and on climate change in the region will be used as the basis for the development of our modelling approach aimed at predicting the possible impact of future global warming on the HCS, which will be presented in the next chapters. Note that a synthetic view of past, present and future global warming is presented in appendix A.

1.1. Presentation of the Humboldt Current System

1.1.1. Eastern Boundary Upwelling Systems

1.1.1.1. Introduction

The Humboldt Current System (HCS), also called the Peru-Chile upwelling system, is the Eastern Boundary Upwelling System (EBUS) of the South Pacific Ocean. EBUS'es are found in both hemispheres along the west coasts of continents bordering the two main ocean basins, namely the Pacific Ocean and the Atlantic Ocean. They can be easily distinguished from space because the high primary production that characterizes these systems makes possible to monitor their physical and biogeochemical variability with chlorophyll-a, as illustrated in figure 0.1. It is generally admitted that there are four main EBUS'es:

- The **Canary Current System**, covering the coasts of Guinea-Bissau and Senegal up to northern Morocco, with a northern extension off Portugal and northwestern Spain called the western Iberian upwelling system;

- The **Benguela Current System**, extending from the southwestern tip of South Africa up to Angola;

- The **California Current System**, flowing along the west coast of Baja California in Mexico and the whole west coast of the United States of America (California, Oregon, Washington);

- The **Humboldt Current System**, which characterizes almost the whole western coast of South America, from central Chile near 40°S to northern Peru near the equator.

The geographical locations of these upwelling systems are determined by the positions of mid-latitude anticyclones, found in the North and South Pacific and Atlantic basins. Indeed, these high-pressure systems have eastern branches with low-level trade winds directed equatorward. Near the coast, these winds often tend to have an alongshore direction, which induces westward Ekman transport of surface waters (Ekman, 1905) replaced by deeper waters which upwell at the surface. This coastal upwelling brings cold water and nutriments to the surface layers, providing the right conditions for the development of ichtyo- and zoo-plankton (Skogen, 2005; Sutor et al., 2005; Vélez et al., 2005), which sustain very rich marine ecosystems and the world's most productive fisheries (Durand et al., 1998). In addition, EBUS'es are systematically associated to a system of coastal currents, mainly constituted by an equatorward surface current and by a poleward under-current. Baroclinic instabilities

generated by vertical shear stresses associated to these currents can trigger the growth of mesoscale meanders and eddies (Leth and Shaffer, 2001; Leth and Middleton, 2004; Marchesiello et al., 2003, 2004), which are common along these coasts (Chaigneau et al., 2009). Mesoscale eddies are believed to have a significant contribution to mass and heat transfer from the nearshore area to the open ocean. They also play an important role in the dynamics of pelagic fish reproduction patterns and early life stages (Logerwell et al., 2001; Lett et al., 2007; Brochier et al., 2008). In addition, most EBUS'es feature the presence of free coastal-trapped waves of equatorial origin (Moore, 1968; Clarke, 1983), which are capable of strongly perturbating the local hydrography and currents. In the next subsection, the physical mechanisms of Ekman transport and pumping, coastal current dynamics, mesoscale to sub-mesoscale processes and coastal-trapped wave propagation are briefly described.

1.1.1.2. Coastal upwelling dynamics

Ekman transport and pumping

According to Ekman's theory (Ekman, 1905), low-level winds blowing above the ocean surface force a circulation below the surface, which is deviated to the right in the northern hemisphere and to the left in the southern hemisphere due to the Coriolis force. At the surface, the resultant water motion is at 45° from wind direction, clockwise (resp. counter-clockwise) in the northern (resp. southern) hemisphere. The turbulent tension associated to such motion forces a circulation in the water layer just below the surface layer, with an angle that depends on the coefficient of vertical eddy viscosity. The same process is repeated for each layer of the water column, with an exponential decay of the associated currents. Horizontal motion associated to surface wind forcing can be described over the water column from the surface to the bottom by the Ekman spiral (fig. 1.1). By integrating the associated equations over the vertical, one obtains the net zonal and meridional transports T_x and T_y:

$$T_x = \frac{\tau_y}{\rho f}$$

$$T_y = -\frac{\tau_x}{\rho f}$$

where τ_x and τ_y are for the zonal and meridional components of the surface wind stress, ρ is for seawater density and f is for the Coriolis parameter:

$$f = 2\Omega \sin\varphi$$

where Ω is for the earth's rotation rate and φ is for latitude.

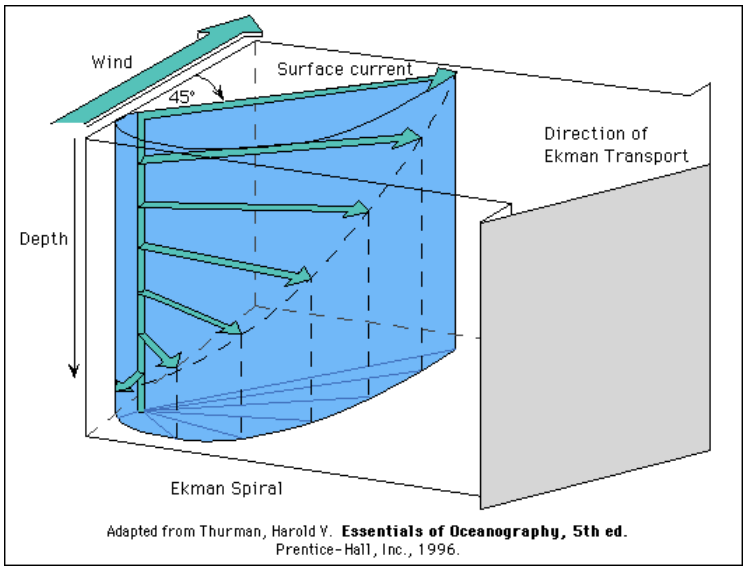

Fig. 1.1: Schematic of the Ekman spiral and transport in the northern hemisphere.

Hence the net transport of water called the Ekman transport is at right angles with the wind direction, and is directed to the right (resp. to the left) of wind direction in the northern (resp. southern) hemisphere, as indicated on figure 1.1. Because of the exponential decay of water motion, the Ekman transport is mainly confined in a top layer called the Ekman layer. Below the Ekman layer, the effect of the wind forcing on the ocean currents is weak and can be easily neglected.

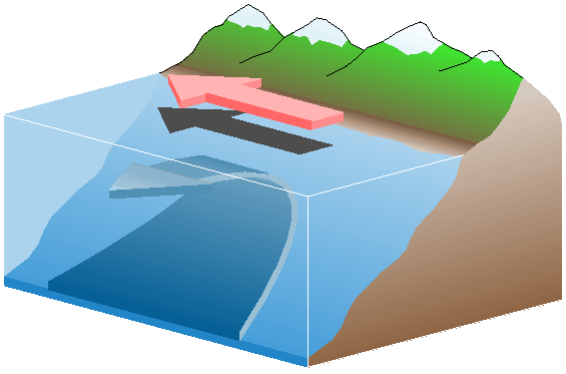

Fig. 1.2: Schematic of coastal upwelling in the HCS. The pink arrow is for the alongshore winds, and the blue arrow is for the offshore Ekman transport and the associated upwelling.

In the case of EBUS'es, the Ekman transport is of fundamental importance for the understanding of ocean dynamics. Consider the case of a quasi-constant wind blowing parallel to the coast with an equatorward direction, as it is generally the case for EBUS'es. The resulting Ekman transport will thus have a westward direction and warm waters of the Ekman layer move away from the boundary in the offshore direction (fig. 1.2). To compensate this

loss of volume, cooler waters from deeper layers are advected shoreward and upward when they reach the boundary: this phenomenon is called coastal upwelling (fig. 1.4).

There is a secondary mechanism that also contributes to coastal upwelling: Ekman pumping. Ekman pumping is due to spatial variations of the surface winds and of the associated Ekman transports, that induce areas of convergence and areas of divergence of the waters in the Ekman layer. In areas of divergence (resp. convergence), the conservation of water volume drives upward (resp. downward) vertical velocities at the base of the Ekman layer, *ie* upwelling (resp. downwelling). These velocities are called the Ekman pumping (W_{Ek}), which can be written:

$$W_{Ek} = \frac{1}{\rho f}\left(\frac{\partial \tau_y}{\partial x} - \frac{\partial \tau_x}{\partial y}\right)$$

(a) (b)

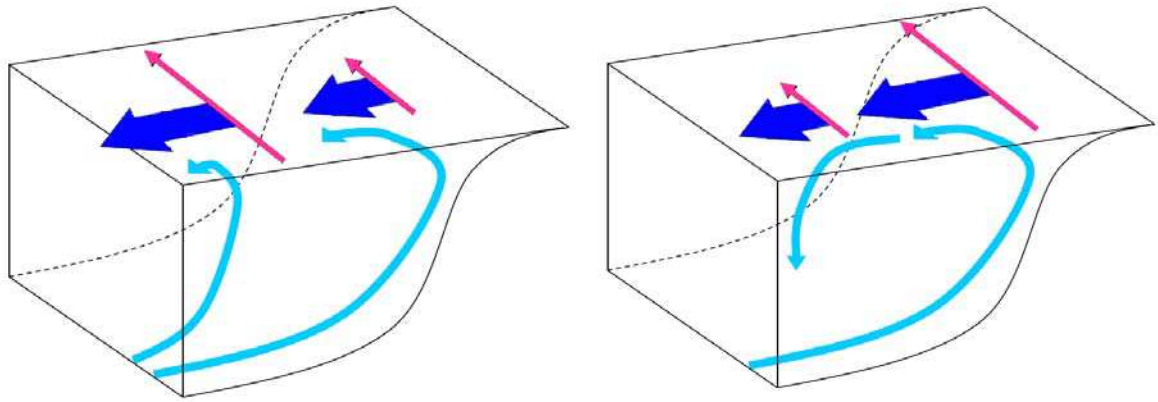

Fig. 1.3: Schematic of the effect of Ekman Pumping on a southern hemisphere EBUS. The pink arrows are for the alongshore winds, the dark blue arrows are for the offshore Ekman transports and the light blue arrows are for the associated upwelling (a) or downwelling (b).

In the presence of a coastline, which is the case for EBUS'es, the alongshore winds are stronger over the ocean than over the land because the friction at the surface is increased over the continent due to the presence of orography and vegetation which tend to reduce the wind intensity. This creates a cross-shore gradient of alongshore wind intensity, which is reduced near the coast in the so-called wind drop-off zone. As explained by Bakun and Nelson (1991), the resultant wind stress curl drives upward Ekman pumping which contributes to the coastal upwelling, together with Ekman transport. This mechanism is schematized on figure 1.3 (a). Likewise, if the wind were stronger near the coast, it would induce stronger Ekman transport near the coast than farther offshore: an area of convergence would appear off the coast and the

Ekman pumping would be negative and have a downwelling effect that counteracts the upwelling effect of Ekman transport (fig. 1.3 b).

Coastal Currents

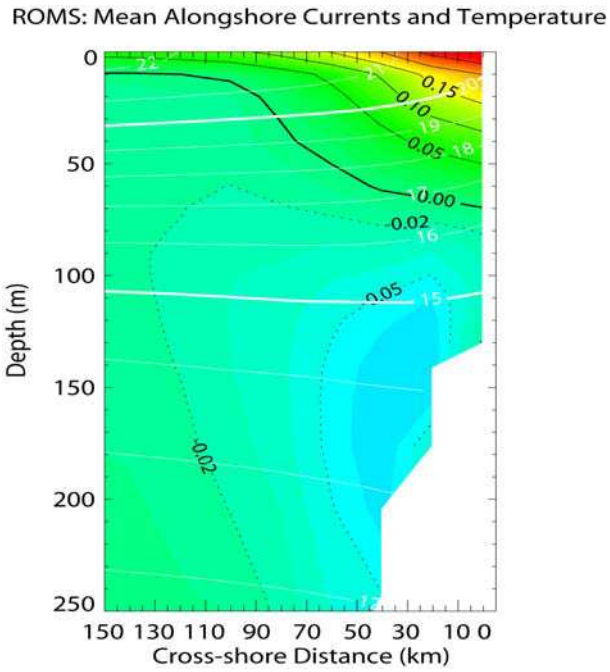

Fig. 1.4: Vertical section in the cross-shore direction of the mean alongshore currents (m/s) and the mean temperature (°C) simulated by the ROMS model (Shchepetkin and McWilliams, 2005) at 10°S near the central Peru coast. Colours and black contours are for currents. Full (resp. dashed) lines are for positive (resp. negative) values, *ie* for equatorward (resp. poleward) flow. White contours are for temperature (interval is 1°C). The x-axis (resp. y-axis) is for cross-shore distance (resp. depth) and the corresponding units are km (resp. metres).

A similar structure of coastal currents constituted by an equatorward surface current and a poleward subsurface current (cf. figure 1.4 for the HCS) is observed for all EBUS'es. The mechanism controlling the equatorward surface current is well-known: coastal upwelling causes a rise of the isotherms and isopycns near the coast due to the cooler and denser waters upwelled at the surface (fig. 1.4). Hence, a cross-shore density gradient is present in the coastal zone, with denser waters near the coast and less dense waters offshore: this induces an equatorward flow close to the coast due to geostrophy. In addition, direct wind forcing in the Ekman layer also drives an equatorward flow (fig. 1.1), which combines with the geostrophic flow to form the surface current. On the other hand, so far there is no consensus on the origin of the poleward undercurrent observed along EBUS'es. One theory relates it to the alongshore meridional pressure gradient: waters are increasingly warmer towards the equator, causing the sea level to be higher which creates a poleward flow (Neshyba et al., 1989). Another theory based on the results of a shallow-water baroclinic ocean model in the idealized case of a

meridional eastern boundary and spatially-uniform alongshore wind forcing relates both the equatorward surface current and the poleward undercurrent to the different baroclinic modes and succeeds in reproducing the depth and magnitude of the observed currents (McCreary, 1981). The poleward undercurrent in particular is related to the effect of bottom friction over the continental slope, which damps the higher order modes and thereby enhances the control of the undercurrent by the intermediate order modes (McCreary and Chao, 1985).

Mesoscale and sub-mesoscale processes

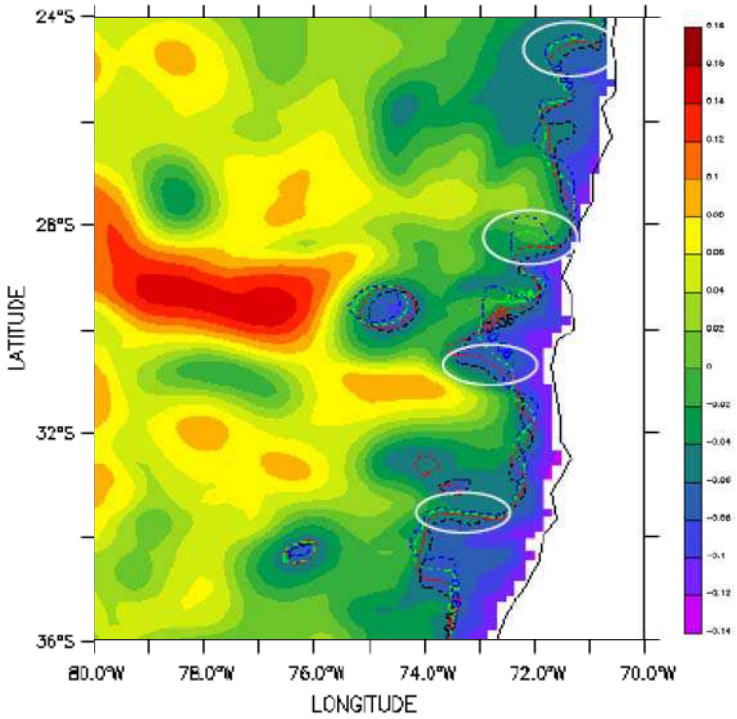

Fig. 1.5: Meanders of the upwelling front indicated on a map of SLA in the southern HCS simulated by the ROMS model (1/6° resolution, open boundary conditions from a global ocean model, atmospheric forcing from observed satellite winds and reanalyzed air/sea fluxes) for 19th August 1995. Unit is meter. Contour interval is 0.02 m. The black, red, green and blue dashed lines indicate the position of the (-6 cm)-isoline on 19th August, 24th August, 29th August, and 3rd September 1995, respectively. White ellipses indicate the position of a few meanders (*V. Echevin, personal communication*).

Coastal upwelling induces a strong cross-shore thermal gradient in the nearshore area, with cooler waters upwelled near the coast and warmer surface waters pushed away from the coast by the combined effects of Ekman transport and Ekman pumping. As a consequence, a sharp temperature front called the upwelling front is present a few dozens of kilometres offshore. The position and intensity of this front is subject to wind variability, which can be rather strong on intraseasonal time scales (*e.g.* Garreaud and Muñoz, 2005; Renault et al., 2009). In addition, upwelling-favorable alongshore winds are also subject to significant

alongshore variability due to the varying continental orography and the shape of the coastline: for instance, winds are generally locally stronger around capes because the land-sea surface occupation ratio is smaller, and weaker around bay areas. The combined spatial and temporal wind variabilities create small scale perturbations along the upwelling front, which can take various forms, namely meanders, filaments (also called plumes) and eddies. Meanders are mesoscale and sub-mesoscale (typical length is a few dozen kilometres) large-curvature portions of either the upwelling front or the coastal currents (fig. 1.5). Filaments are sub-mesoscale intrusions of the upwelling front into the offshore region (fig. 1.6), and are characterized by high primary production and biological activity.

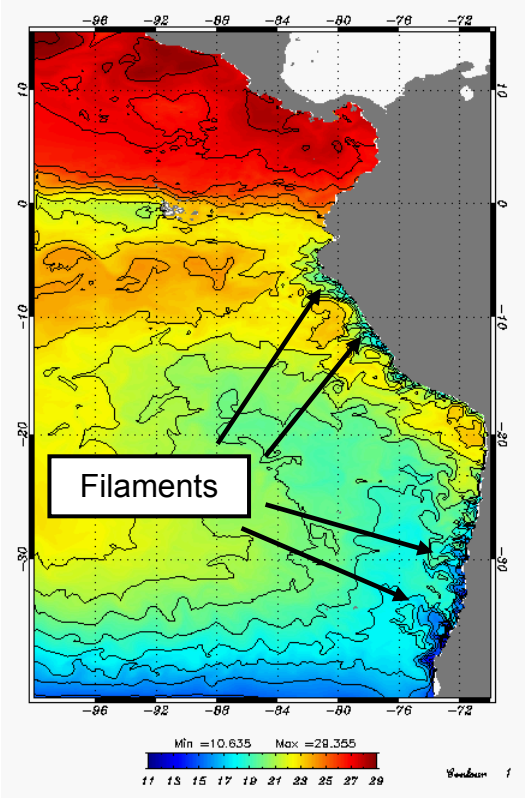

Fig. 1.6: Sub-mesoscale filaments indicated on a map of SST in the eastern South Pacific from AVHRR Pathfinder satellite data (Vazquez et al., 1995) for 1st January 1992. Unit is °C. Contour interval is 1°C.

Eddies, which can be cyclonic – *counter-clockwise (resp. clockwise) geostrophic currents in the northern (resp. southern) hemisphere* – or anticyclonic – *clockwise (resp. counter-clockwise) geostrophic currents in the northern (resp. southern) hemisphere* – are mesoscale features with a radius of the order of 100km (fig. 1.7) and are common in EBUS'es (Chaigneau et al., 2009). Cyclonic (resp. anticyclonic) eddies are also called warm-core (resp. cold-core) eddies because they are associated to a positive (resp. negative) sea level anomaly (SLA) and a warm (resp. cold) sea surface temperature (SST) anomaly, as illustrated on figure

1.7. Like the smaller scale meanders and filaments, they can be generated by spatio-temporal variations of the upwelling front, which are the result of baroclinic instabilities generated by vertical shear between the equatorward surface current and the poleward undercurrent (*e.g.* Leth and Shaffer, 2001; Marchesiello et al., 2003). Mesoscale eddies are generated near the coast and propagate westwards: for this reason, they are important contributors for the transfer of physical properties from the coastal region to the open ocean. Their nearshore spatial variability can also determine the location of spawning areas for small pelagic fish species (Logerwell et al., 2001).

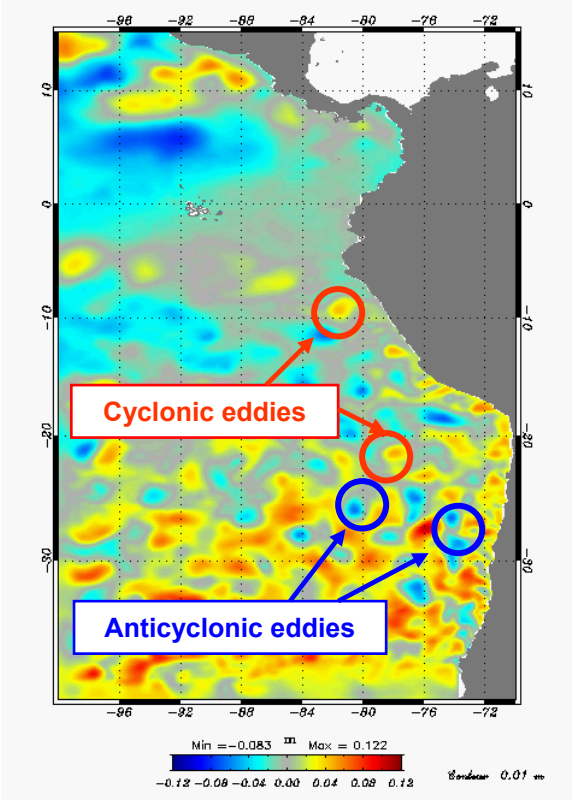

Fig. 1.7: Cyclonic and anticyclonic mesoscale eddies indicated on a map of SLA in the eastern South Pacific simulated by the ROMS model for 1st January 1992. Unit is meter.

Coastal-trapped waves

The presence of poleward-propagating coastal-trapped waves (CTW) has been reported along the west coast of North and South America (*e.g.* Brink, 1982; Chapman, 1987) and along the west coast of Africa (Polo et al., 2008). Such baroclinic waves are forced by equatorial Kelvin waves (EKW) travelling eastward across the equatorial Pacific and Atlantic as they impinge on the eastern boundary (Clarke, 1983; Enfield, 1987): according to theory

(Clarke, 1983; Grimshaw and Allen, 1988; Clarke and Shi, 1991), for each baroclinic mode associated to an EKW of any given frequency, a critical latitude can be found that separates the zone of CTW propagation along the ocean boundary (poleward of that latitude) from the zone of reflection of the EKW as westward-propagating equatorial Rossby waves (ERW) and extra-tropical Rossby waves (ETRW) (equatorward of that latitude). CTW are associated to anomalies of sea level and velocity, which can destabilize the thermocline and the coastal currents (*e.g.* Shaffer et al., 1997; Pizarro et al., 2002). Such perturbations are thought to have a direct impact on the behaviour of the marine ecosystem in EBUS'es, as proposed by Bertrand et al. (2008) for the HCS.

The four main EBUS'es share common characteristics that were briefly described above: upwelling-favorable alongshore winds that drive intense primary production and biological activity through physical processes of Ekman transport and pumping; alongshore coastal currents with equatorward flow at sea surface and poleward flow below the surface; intense mesoscale and sub-mesoscale activity; poleward-propagating coastal-trapped waves. However, each EBUS also has its own specificities, related to wind regime, coastline orientation, bottom topography, continental orography, latitude, among other factors. What are the peculiarities of the HCS compared to other EBUS'es ? What makes it potentially more sensitive to climate change than the other systems? This is the object of the next section.

1.1.2. The Humboldt Current System: a highly productive ecosystem under strongly variable oceanic and atmospheric conditions

1.1.2.1. Introduction

The HCS was named after the Prussian naturalist and explorer Alexander von Humboldt (1769-1859) who travelled extensively across Latin America between 1799 and 1804. The HCS is the second most studied EBUS after the California Current System, with the first studies conducted as early as 1936 (Gunther, 1936a,b). This important interest of the scientific community has several reasons.

First, the HCS produces more fish per unit area than any other region of the world ocean (F.A.O., 2009). Second, it bears the direct influence of large scale climate variability of the tropical Pacific Ocean, including the famous El Niño phenomenon, which was originally named by Peruvian and Ecuadorian fishermen. Third, its proximity to the equator and the orientation of the Peru coast connects coastal upwelling with equatorial upwelling and with the eastern tropical Pacific cold tongue on the one hand, and the coastal currents with currents of the eastern equatorial Pacific on the other hand (Lukas, 1986; Strub et al., 1998; Kessler et al., 2006; Croquette, 2007). Fourth, the Andes mountain range acts as a natural wall which forces the subtropical trade winds to have an alongshore direction, prevents the offshore region from the influence of continental South American climate and has a significant impact on eastern South Pacific climate (Xu et al., 2004; Sepulchre et al., 2009). Fifth, it features a persistent stratocumulus cloud deck, the widest in the world, which limits solar penetration into the upper ocean (Klein and Hartmann, 1993): combined with upwelling, it makes ocean temperatures off Peru the coldest in the tropical band. Coarse-resolution global climate models experience many problems in this region, which include (but are not limited to): a bad representation of the steep topography of the Andes, weak nearshore wind forcing, a poorly represented stratocumulus deck and absent small-scale air-sea interactions associated to mesoscale oceanic variability (Xu et al., 2004; Large and Danabasoglu, 2006; Seo et al., 2007). All these issues introduce significant errors not only in the simulated regional climate of the eastern South Pacific – such as strong biases in the mean SST and solar heat flux fields – but also in the simulated larger-scale climate of the Pacific region – warm SST biases in the eastern Pacific cold tongue region and the "double ITCZ problem" being two well-known examples – (Xu et al., 2004; Large and Danabasoglu, 2006), which leads to large uncertainties in climate change predictions: for instance, Bony and Dufresnes (2005) show that the main

source of uncertainty in tropical cloud-albedo feedback among global climate models comes from an underestimated sensitivity of marine boundary layer clouds to SST changes in subsidence regions (such as the HCS). Improving our understanding of climate dynamics in this region is a priority for the scientific community working on climate change and has led to the development of the VOCALS project to which I participated through an oceanographic cruise conducted in the Pisco-San Juan area (around 15°S) in October 2008. Last, the HCS is characterized by the presence near the surface of one of the most extended Oxygen Minimum Zones (OMZs) of the world ocean (Anderson et al., 1982; Helly and Levin, 2004), which are known for their key role in the global nitrogen cycle.

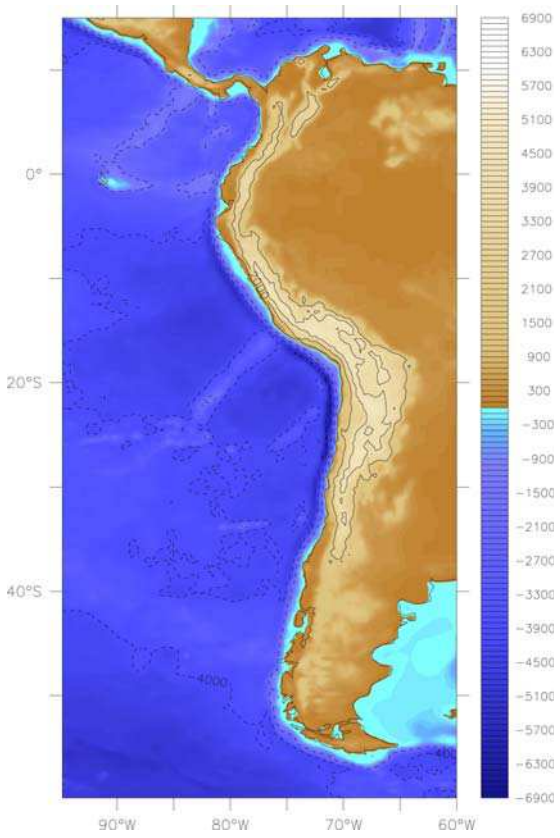

Fig. 1.8: Topography and bathymetry of western South America from ETOPO1 data (Amante and Eakins, 2009), previously interpolated onto a 1/3°x1/3° horizontal grid. Unit is metre. Plain countours are for continental topography, whereas dashed contours are for ocean bathymetry. Contour interval is 2000m.

In this PhD thesis, I mainly focused on the second and third point, *ie* on the remote forcing of the HCS by equatorial Pacific variability through oceanic pathways, namely coastal-trapped waves and ocean currents. However, because of the predominant role of the atmosphere in the dynamics of the HCS, some aspects of regional atmospheric dynamics will also be described. In the next subsection, the main characteristics of the physical functionning of the HCS are briefly reviewed.

1.1.2.2. Topography and bathymetry: from high mountains to deep trenches

The west coast of South America extends from 7°N to 53°S with a dominant meridional direction (fig. 1.8), and covers the coasts of Colombia (7°N-1°N), Ecuador (1°N-3°S), Peru (3°S-18°S) and Chile (18°S-53°S). It is a subduction zone, a particular type of converging tectonic plates: the denser oceanic Nazca Plate subducts underneath the less-dense continental South American Plate. As a result, the bathymetry is characterized by a deep and narrow oceanic trench reaching 6900m depth around 20°S, whereas the topography features a high mountain range with many summits exceeding 6000m high, which makes the Andes the highest mountains in the tropical zone. A relatively short distance (a few hundred kilometres to the most) separates the trench and the mountains: as a consequence, the continental shelf is very reduced or even absent (in northern Chile for instance), and a narrow coastal band rarely exceeding a hundred kilometres separates the coast from the Andes. The Andes act as a natural barrier which forces tropical and subtropical trade winds to have an alongshore direction, and isolates the coastal region from atmospheric perturbations generated over the Atlantic or the continent: as a consequence, the coasts of Peru and northern Chile are characterized by a very arid climate, especially in Chile where the dryest desert on Earth is found: the Atacama desert. In the inner oceanic basin, the Nazca ridge running perpendicular to the coast from the Pisco region (15°S) seawards rises up to 2000 m depth and separates the Peru basin to the North from the Chile basin to the South. At the equator, the Galapagos rise separates the Nazca Plate from the Cocos Plate and connects the Galapagos Islands (90°W) to the South American continent (~80°W). The HCS characterizes the coastal ocean off western South America roughly from the equator to 40°S, which is the region we will focus on in the rest of the thesis.

1.1.2.3. Atmospheric conditions and coastal upwelling

Since we do not focus on the atmospheric forcing in this PhD work, only a brief presentation of the atmospheric conditions of the eastern South Pacific is made here. The main components of the atmospheric circulation in the eastern South Pacific region are schematized on figure 1.9:

- the **Subtropical High**, also called South Pacific High or south-eastern Pacific Subtropical Anticyclone: it is the main driver of atmospheric circulation in this region. As for

other eastern oceanic basins (North Pacific, North and South Atlantic), this high-pressure system drives equatorward trade winds due to its anticyclonic rotation (counter-clockwise in the southern hemisphere). The eastern branch of the anticyclone is limited to the East by the Andes mountains which force the trade winds to follow the coastline direction, generating persistent coastal upwelling off Peru and Chile. As in other EBUS'es, stronger trade winds offshore generate significant Ekman pumping in the 50-200km next to the coast (Bakun and Nelson, 1991). The strength of the upwelling-favorable winds is modulated by the seasonality in the position of the anticyclone (fig. 1.10).

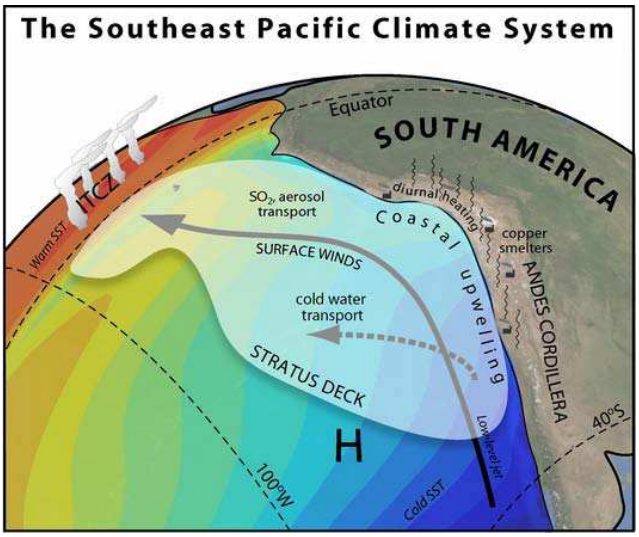

Fig. 1.9: Schematic of the main atmospheric systems in the eastern South Pacific: the Inter-Tropical Convergence Zone (ITCZ), the StratoCumulus cloud deck (Stratus Deck), the Subtropical High (H), and Coastal Jets (low-level jet). The full-line arrow represents equatorward trade winds, and the dashed-line arrow represents the Ekman transport associated to coastal upwelling. The background colors for the ocean schematize annual mean SST (*image courtesy Rob Wood, University of Washington*).

During the austral summer, the center of the high-pressure system is located near (95°W, 32°S) and favours coastal upwelling from 40°S to the equator; during the austral winter, it moves northeastward to about (85°W, 27°S): as a consequence, winds off central Chile are weaker or even downwelling-favorable in winter, whereas they are stronger off Peru (Bakun and Nelson, 1991). For this reason, coastal upwelling is permanent off Peru but seasonal off central Chile. Off the northern Chile coast between 18°S and 23°S, winds are weaker all year long, and so is upwelling: as a result, SSTs are significantly warmer there than off the rest of Peru and Chile (fig. 1.11).

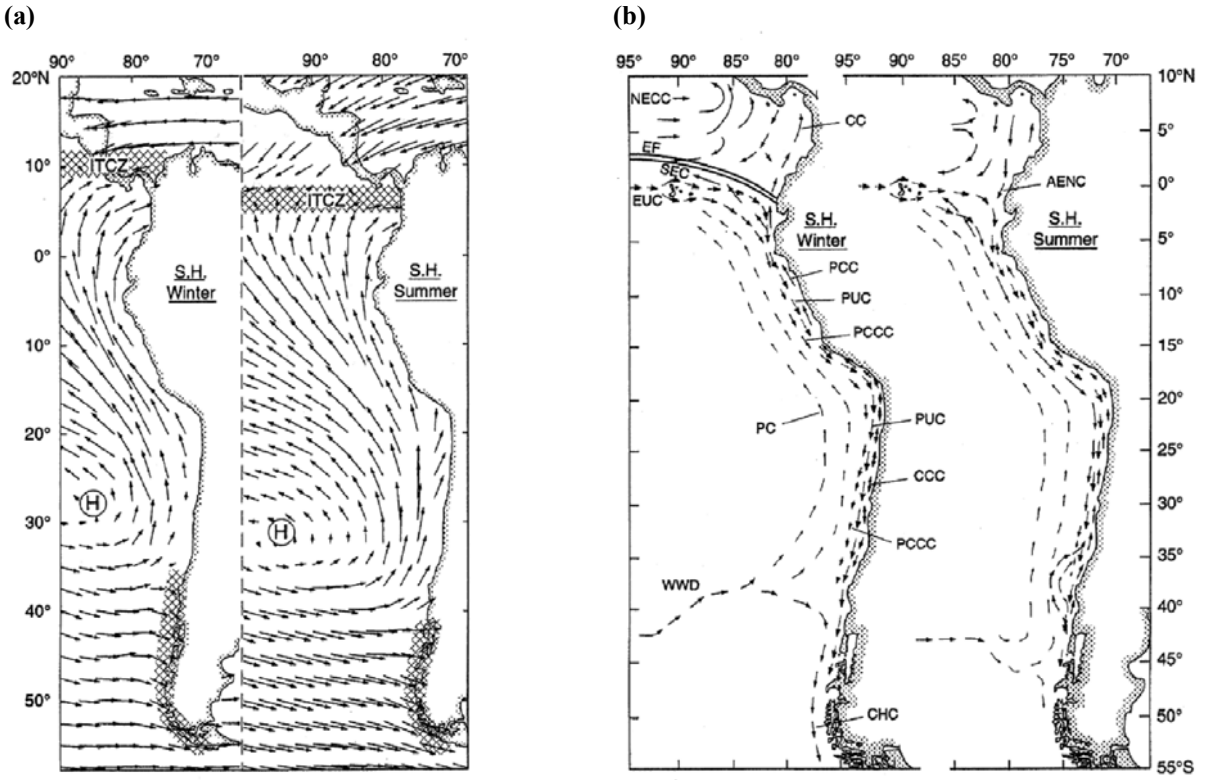

Fig. 1.10: Climatological winds (a) and currents (b) during southern hemisphere (S.H.) winter (June-August) and summer (December-February). Winds are from the NCEP reanalysis at 1000 mb (Kalnay et al., 1996). Regions of heavy precipitation are hatched. ITCZ is for Inter-Tropical Convergence Zone. H is for Subtropical High. EF is for Equatorial Front. Schematic vectors (b) indicate the location and relative strengths of the main currents: the West Wind Drift (WWD), the Equatorial Undercurrent (EUC), the South Equatorial Current (SEC), the North Equatorial Countercurrent (NECC), the Colombia Current (CC), the Annual El Niño Current (AENC), the Peru Current (PC), the Peru-Chile Countercurrent (PCCC), the Poleward Undercurrent (PUC), the Peru Coastal Current (PCC), the Chile Coastal Current (CCC) and the Cape Horn Current (CHC). *Adapted from Strub et al. (1998)*.

- **Coastal Jets**: these are episodes of very strong alongshore winds (up to 15 m/s) blowing off central Chile between 30°S and 35°S in austral spring and summer (Garreaud and Muñoz, 2005; Muñoz and Garreaud, 2005; Renault et al., 2009). Some are also found off central Peru in the Pisco/San Juan area (15°S) and northern Peru near Paita (4°S), with maximum velocities (~7-8 m/s) in austral fall and winter (Renault, 2008). They have direct consequences on the strength of coastal upwelling due to Ekman transport and pumping (Shaffer et al., 1999).

- the **Inter-Tropical Convergence Zone** (ITCZ), which limits the eastern South Pacific High at its northern edge, is the zone of convergence of northern and southern hemisphere trade winds, and is present around the planet in the tropical zone. It is characterized by enhanced deep convection and heavy rainfall. In the eastern tropical Pacific, it is located near 10°N in the austral winter and near 5°N in summer: although it has a strong impact on the regional climate of the countries surrounding the Panama Bight (Ecuador,

Colombia, Central American countries), its influence does not go southwards beyond 5°S, so it is generally not considered when studying the dynamics of the HCS.

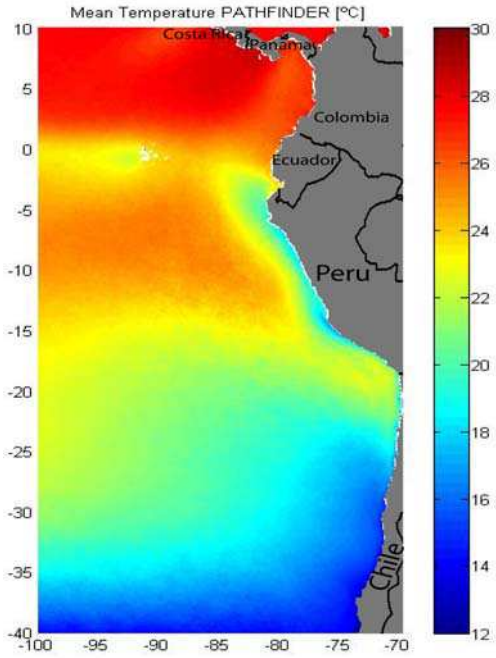

Fig. 1.11: Climatological mean SST (°C) in the eastern South Pacific from AVHRR Pathfinder satellite data (Vazquez et al., 1995).

- the **StratoCumulus cloud deck** (SCu deck) is the widest persistent stratocumulus cloud cover in the world (Klein and Hartmann, 1993). Its presence in the eastern South Pacific limits solar penetration and thus radiative forcing of the upper ocean: combined with upwelling, it makes ocean temperatures off Peru the coldest in the tropical band (Yu and Mechoso, 1999). Moreover, its contribution to the heat budget of the upper ocean is significant not only at the regional scale (Takahashi, 2005) but also at the global scale. However, the fine-scale air-sea couplings that drive its formation, structure and variability have not been very well documented so far. Coarse-resolution global climate models are not able to reproduce the SCu deck: as a result, the simulated ocean temperatures are too warm in the region, inducing important biases in the zonal gradient of SST in the tropical Pacific and thus in the Walker circulation, which is one of the main mechanisms of tropical climate variability at the global scale. This is an important issue because such biases introduce large uncertainties in climate change predictions. Improving our understanding of climate dynamics in this region is a priority for the scientific community working on climate change and has led to the development of the VOCALS project (http://www.eol.ucar.edu/projects/vocals/) which comprises both extensive oceanographic and atmospheric field measurements off Peru and

Chile and a modelling framework. I have had the chance to participate to the VOCALS-Rex Peru oceanographic survey conducted aboard the R/V Jose Olaya (IMARPE, Peru) off the Pisco-San Juan area (around 15°S) in October 2008 (fig. 1.12). Field measurements allowed characterizing the atmospherical (radiosonde launchings), oceanographical (CTD, ADCP, surface drifters and a glider), biogeochemical (oxygen, fluorescence, chlorophyll-a…) and biological conditions (Hensen net, hydroacoustics) during an episode of cloud clearing due to the presence of a strong coastal jet. Understanding the complex interactions between the atmosphere, the ocean and the marine ecosystem is the topic of current research conducted at IRD (Institut de Recherche pour le Développement), IMARPE (the Peruvian Marine Research Institute) and IGP (the Peruvian Institute of Geophysics).

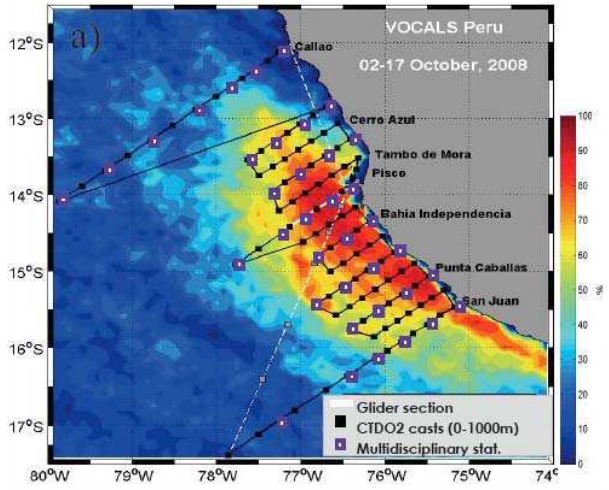

Fig. 1.12: Original track and stations of the VOCALS-Rex Peru cruise conducted aboard the R/V Jose Olaya (IMARPE) from 10/02/08 to 10/17/08 off the Pisco-San Juan area in southern Peru. The background image is for climatological cloud clearing rate (%) for October derived from SeaWIFS data.

1.1.2.4. Regional ocean circulation

Here we first review the main currents present in the eastern South and tropical Pacific Ocean: the coastal current system, known as the HCS, and the equatorial current system. The connections between both systems is then presented, based on earlier works.

The coastal current system

The HCS consists of an ensemble of surface and subsurface currents that flow along the coasts of Peru and Chile. A review on this topic was proposed by Strub et al. (1998) and the main currents are schematized on figure 1.10b:

- the **West Wind Drift** (WWD) is an eastward surface current forced by the southern branch of the subtropical anticyclone between 40°S and 45°S. Upon reaching the South American continent, it splits into the poleward **Cape Horn Current** (CHC) and the equatorward **Peru Current** (PC).

- the **Peru Current**, sometimes called the Oceanic Peru Current, the Chile-Peru Current or even the Humboldt Current, transports cold Southern Ocean waters towards the eastern tropical Pacific, where it eventually joins the southern branch of the westward **South Equatorial Current** (SEC) and participates together with equatorial upwelling to maintain the eastern equatorial Pacific cold tongue (fig. 1.11) present in austral winter between the Cabo Blanco area (4°S) and the Galapagos Islands (Wyrtki, 1967; Strub et al., 1998; Chaigneau and Pizarro, 2005a). This broad current (~500km) is present between the surface and about 700m depth, and follows the coast about 500 to 1500km offshore (Wyrtki, 1963, 1967). Its mean speed is around 15-20 cm/s South from 25°S and 5-7 cm/s North from 25°S (Chaigneau and Pizarro, 2005a).

- the **Chile-Peru Coastal Current** (CPCC), sometimes called the Humboldt Current (!) or the Inshore Peru Current, and called **Chile Coastal Current** (CCC) off Chile and **Peru Coastal Current** (PCC) off Peru (fig. 1.10b), is an equatorward surface current located much closer to the coast, within the first 100km (Brandhorst, 1971; Bernal et al., 1982; Brink et al., 1983; Huyer et al., 1991). It is a geostrophic flow driven by coastal upwelling, such as that depicted in 1.1.2 (fig. 1.4). Its maximum velocities off Peru are around 10-15 cm/s (Brink et al., 1983; Huyer et al., 1991) in austral winter when both the alongshore winds and upwelling are strongest (Cucalon, 1987; Fiedler, 1994). In northern Chile, velocities in the CPCC are highest in autumn, due to the latitudinal variation of the seasonal cycle of the alongshore winds (Blanco et al., 2001). Like the PC, its northern extent merges with the SEC, and in winter time with the cold tongue (Enfield, 1976; Weare et al., 1976; Strong, 1986) that it feeds with the cold and salty water upwelled near the coast (Strub et al., 1998).

- the **Peru-Chile Counter-Current** (PCCC) is a poleward surface current flowing parallel to the coast at a distance between 100km and 300km (Wyrtki, 1963; Brandhorst, 1971; Robles, 1979; Bernal et al., 1982; Silva and Fonseca, 1983; Huyer et al., 1991; Strub et al., 1995, 1998) and speeds around 10 cm/s (Huyer et al., 1991). It carries warm and salty waters from the equatorial region. However, its existence, origin and characteristics are still debated because of the lack of direct measurements and the few studies dedicated to this current. According to the modelling study by Penven et al. (2005), the PCCC is forced by cyclonic wind stress curl north of 15°S in agreement with the Sverdrup relation (Sverdrup,

1947), and then turns west towards the open ocean. Although it has been observed off Peru, its presence off Chile is controversial (Fonseca, 1989; Strub et al., 1998), consistently with the results from Penven et al. (2005).

- The **Peru-Chile Under-Current** (PCUC), also known as the Gunther Current after E. R. Gunther who was the first to discover it (Gunther, 1936a,b), or simply as the **Peru Under-Current** (PUC), is a poleward current that dominates nearshore subsurface flow below 50m depth (Brink et al., 1983). It is generally located in the first 200km from the coast over the continental shelf and slope (Fonseca, 1989) and down to 600-700m depth (Wyrtki, 1963), with maximum velocities around 10-15 cm/s at 100-150m depth off Peru (Huyer, 1980; Huyer et al., 1991) and increasing depth towards the South (Gunther, 1936a,b). See figure 1.4. (1.1.2.) for a cross-shore section off central Peru. Such deepening of the PCUC was attributed to the conservation of potential vorticity by Penven et al. (2005), and to the faster decay of the lower order baroclinic modes compared to the higher order modes by McCreary (1981) and by Clarke (1989). However, it might outcrop as a surface counter current at some locations off central Peru and northern Chile due to cyclonic wind stress curl (McCreary and Chao, 1985; Penven et al., 2005), which sometimes makes it difficult to separate from the PCCC. The PCUC extends over the South American coast down to 48°S, though it is considerably weaker South of 38°S (Silva and Neshyba, 1979). Like the PCCC, it is characterized by poorly-oxygenated warm and salty waters (Gunther, 1936a,b; Fonseca, 1989), and was identified as a major source for the nutrient-rich waters upwelled near the coast (Wyrtki, 1963; Brink et al., 1983, Huyer et al., 1987).

Current meter data off central Chile revealed that it is subject to significant variations of equatorial origin at time scales ranging from intraseasonal (Shaffer et al., 1997) to seasonal and interannual (Pizarro et al., 2001, 2002). Intraseasonal variability was shown to be mostly due to CTW propagating poleward along the coast (Shaffer et al., 1997), whereas ETRW propagation dominates the annual variability of the PCUC (Pizarro et al., 2002). Conversely, upwelling-favorable winds were shown to have little effect on the PCUC (Huyer et al., 1991; Pizarro et al., 2001). Being an important nutrient supply for primary production in the HCS, its fluctuations are likely to have a direct impact on the marine ecosystem. A main focus of the present PhD thesis is to assess the remote influence of intreaseasonal equatorial Kelvin waves (IEKW) on coastal variability off the coasts of Peru and Chile, and especially on the CPCC and the PCUC. Because of the scarcity of the observations of these currents in both time and space, a modelling approach was privileged. This is the subject of chapter 3. (section 3.) and of an article in preparation (Belmadani et al., in prep).

The equatorial current system

A brief overview of the equatorial current system is presented here. Kessler (2006) proposes a review of the main studies conducted on the oceanic circulation in the eastern tropical Pacific (fig.1.13) that constitute state-of-the-art knowledge on the structure of the equatorial current system. At 100°W between 10°S and 10°N, at least two surface currents have been observed: the eastward **North Equatorial Counter Current** (NECC) and two westward branches of the **South Equatorial Current** (SEC). In addition, three eastward subsurface currents were identified: the **Equatorial Under-Current** (EUC), and two Tsuchiya Jets (Tsuchiya, 1975), the **Northern / Southern Subsurface Counter Currents** (respectively NSSCC and SSSCC). A few precisions are given below for the main equatorial currents of interest for the Peru-Chile region, the SEC, the EUC and the SSSCC:

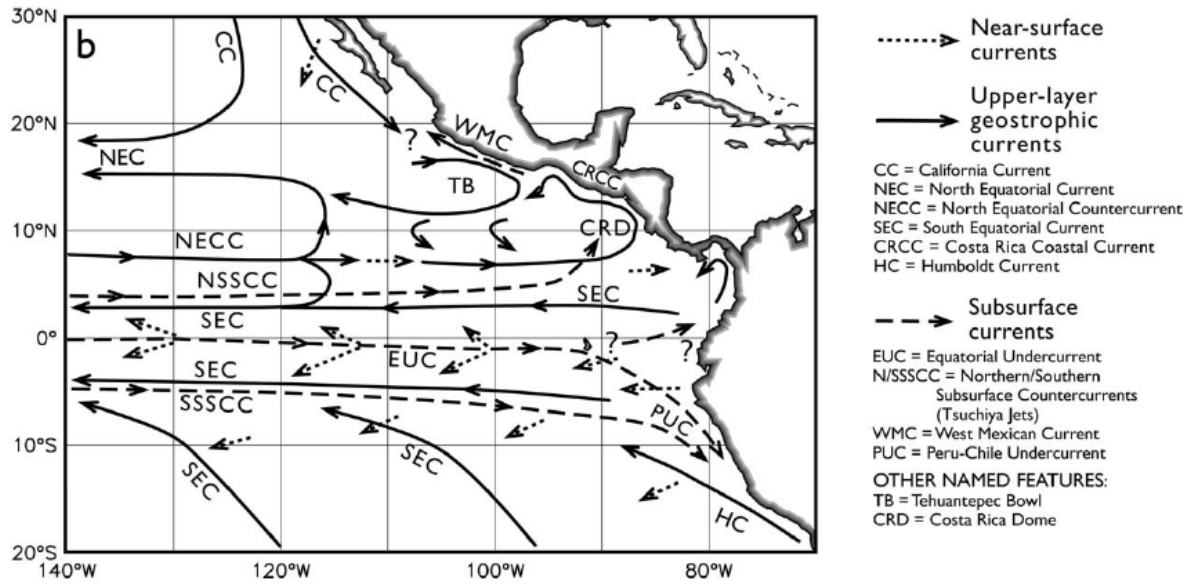

Fig. 1.13: Schematic of the upper ocean circulation in the eastern tropical Pacific, after Kessler (2006). Question marks refer to regions where connections between currents remain undocumented so far.

- The **SEC** is a westward surface current present along the equator in the tropical Pacific Ocean and is driven by easterly trade winds. It is fed by cold waters from the HCS which extend westward and form the eastern Pacific cold tongue, before splitting near the Galapagos in two branches separated by the EUC (Kessler, 2006). The southern branch veers southwestward West from the Galapagos (Reverdin et al., 1994; Kessler et al., 1998; Johnson et al., 2002). The SEC is weak East of 85°W because of the weak zonal winds (Kessler, 2006)

and accelerates West of 85°W due to the deceleration of the EUC near the Galapagos (Wyrtki, 1966; Reverdin et al., 1994): according to estimates based on ADCP data (Johnson et al., 2002), the transport associated to the SEC increases from 12 Sv at 95°W to 35 Sv at 140°W as it receives an input of 20 Sv from the EUC near the Galapagos (Wyrtki, 1966; Montes et al., 2009). The SEC also presents two deep westward branches, possibly due to cyclonic gyres fed by the N/SSSCC (Rowe et al., 2000). Being dominantly forced by the trade winds, the SEC follows their annual cycle, with a minimum from March to July (Kessler, 2006).

- The **EUC**, also called the Cromwell Current (Cromwell et al., 1954; Knauss, 1960), is an eastward subsurface current, which also extends across the tropical Pacific and carries warm waters from the western South Pacific. Is is driven by the basin-scale zonal pressure gradient induced by the dominant easterlies. Its mean transport was estimated at 39 Sv (Knauss, 1960). In the eastern part of the basin, its depth follows the thermocline that rises towards the east (Wyrtki, 1981; McPhaden and Taft, 1988). It even surfaces in boreal spring and induces a 20cm/s eastward flow west from the Galapagos (Kessler et al., 1998; Yu and McPhaden, 1999a,b; Johnson et al., 2002), due to the weak easterlies. Like the SEC east of the Galapagos, it splits in two branches west of the islands (Steger et al., 1998), possibly because of local upwelling induced by the presence of the islands (Eden and Timmermann, 2004) that allows only the deeper layers to flow towards the coasts of Ecuador and Peru (Lukas, 1986; Toggweiler et al., 1991). However, the modelling study by Karnauskas et al. (2007) suggests that the EUC is obstructed by the islands. The fate of the upwelled surface layers of the EUC also remains controversial, some studies pointing out a deviation to the South (Blanke and Raynaud, 1997) and others to the North (Sloyan et al., 2003). The southern branch is stronger (Steger et al., 1998), possibly because of the northward meridional winds and the associated wind stress curl that advect westward wind-induced momentum (the SEC) to the north and eastward EUC momentum to the south in a meridional-cell pattern (Philander and Delecluse, 1983; Mitchell and Wallace, 1992; Kessler et al., 1998). Whereas weak easterlies and reverted zonal pressure gradient are found east from the Galapagos islands, the EUC has been identified in this region.

- The **SSSCC**, sometimes refered to as South Equatorial Counter-Current (SECC) or Southern Tsuchiya Jet, is an eastward subsurface current present in the eastern tropical Pacific between 5°S and 10°S (Tsuchiya, 1975). It is often constituted by two distinct branches at 4°S and 8°S (Rowe et al., 2000; Johnson et al., 2001).

The complex tridimensional structure of the currents is at the origin of the **Equatorial Front** (EF – fig.1.10b) which separes the cold tongue waters to the South from the warm

waters of the eastern Pacific warm pool to the north. This front is modulated by mixing, induced by the warming effect of tropical instability waves (TIW) on the cold tongue that balances the cooling effect due to equatorial upwelling. Such waves are produced by the shear between the westward SEC and the eastward NECC and EUC and contribute significantly to the heat budget in the mixed layer of the eastern equatorial Pacific (Philander, 1978; Yu et al., 1995; Vialard et al., 2001; Chelton et al., 2003; Willett et al., 2006). From July to December, winds strengthen, causing equatorial upwelling as well as the SEC and the NECC to increase, which results in increased TIW activity, that in turn balances the effect of upwelling (Enfield, 1986; Kessler et al., 1998; Swenson and Hansen, 1999).

Links between the HCS and the equatorial currents

The HCS exchanges water masses with the eastern equatorial Pacific via its connections with the equatorial currents. As detailed above, the SEC is fed by the cold waters from both the Peru Current and the CPCC. On the other hand, the PCCC is supposed to originate from the southern branch of the EUC after its splitting west from the Galapagos Islands (Lukas, 1986; Reverdin et al., 1994; Hill et al., 1998), or from the SSSCC (Tsuchiya, 1985). Similarly, the PCUC is thought to originate from the northern branch of the EUC, which veers South upon reaching the coast of Ecuador (Lukas, 1986; Hill et al., 1998), or from the SSSCC (Tsuchiya, 1985). A recent study by Croquette (2007) using high resolution regional modelling and lagrangian particles actually showed that 68% of the PCUC waters at 14°S were brought by the southern branch of the SSSCC (at 8-9°S), 24% by its northern branch (at 4°S), and only 8% by the EUC. At 18°S, the southern branch of the SSSCC was shown to provide almost the totality of the PCUC waters. These results were qualitatively confirmed by those of Montes et al. (2009) who used a similar approach and found that at 12°S, 20-22% of the PCUC waters came from the southern branch of the SSSCC, 15-22% from the northern branch, and 4-5% from the EUC, depending on the considered open boundary forcing. However, the authors also found that 33-42% of the PCUC waters originated from other offshore eastward subsurface currents south of ~10°S, and that the remaining 18-19% came from the recirculation of deep nearshore equatorward flow. These two sources had never been considered before and illustrate the complexity of the connections between the HCS and the equatorial and sub-tropical current systems.

To summarize this section, coastal currents associated to the HCS are similar to other EBUS'es, with surface flow dominated by an equatorward surface current (the CPCC) and

poleward flow dominated by a poleward undercurrent (the PCUC). However, this general picture is completed by a number of other surface currents, including a poleward counter-current (the PCCC), which structure and dynamics remain poorly understood. In addition, the HCS is connected to the currents of the eastern equatorial Pacific, which are governed by distinct mechanisms. The CPCC, together with the PC, participate to feed the SEC in the cold tongue with cold waters from the coastal zone. On the other hand, the EUC and the SSSCC bring warm and salty waters to the coastal ocean off Peru and Chile where they are advected polewards by the PCUC and upwelled near the coast. Overall, the HCS appears to be strongly connected to the equatorial zone through their respective currents and their connections in the cold tongue and Galapagos regions. The second oceanic pathway between the HCS and the equatorial Pacific is the equatorial wave guide and its eastern extension, the coastal wave guide of western South America: the variability of coastal upwelling off Peru and Chile is strongly influenced by long EKW at a variety of time scales, from intraseasonal to interannual and decadal. Of particular interest, the El Niño-Southern Oscillation (ENSO) is the dominant mode of interannual variability at the global scale and is known for its large impacts on the HCS. A more detailed description of EKW and ENSO and of their effect on the HCS is given below.

1.1.2.5. The equatorial wave guide

Equatorial Kelvin waves and coastal-trapped waves

The Madden-Julian Oscillation (MJO; Madden and Julian, 1971, 1972) is a planetary-scale mode of atmospheric intraseasonal variability related to the propagation of Kelvin waves in the atmosphere, which travel around the globe in about 50 days (Parker, 1973). The MJO is able to force Westerly Wind Bursts (WWB) over areas of warm surface waters where deep convection is enhanced, such as the western Pacific warm pool (McPhaden, 1993; Kessler and McPhaden, 1995; Kessler et al., 1995). These WWB can excite 50- to 80-day long IEKW travelling from West to East across the Pacific Ocean.

As mentioned in the previous section, a fraction of the wave energy transmitted along the equatorial wave guide is reflected at the South American coast as planetary waves north from the critical latitude, whereas the rest is trapped along the coastal wave guide in the form of CTW (fig.1.14) south from that latitude (Clarke, 1983; Grimshaw and Allen, 1988; Clarke and Shi, 1991). The higher the frequency and/or the baroclinic mode, the lower the critical

latitude. According to Clarke and Shi (1991), for 50- to 80-day IEKW, the critical latitude is found at ~7-10°S for the first vertical mode. This means that the IEKW forced by MJO-induced WWB are likely to trigger southward propagating CTW along most of Peru and Chile's coastline, especially for the higher order baroclinic modes.

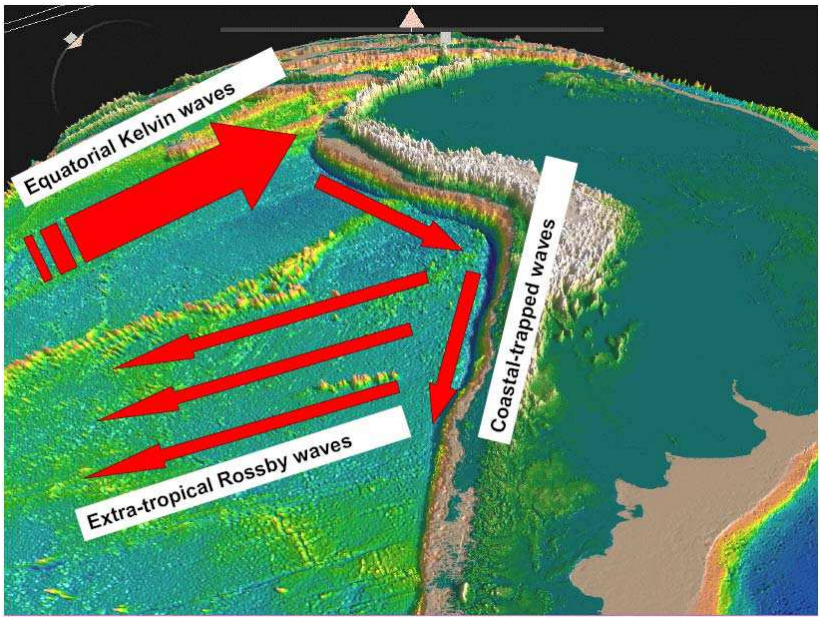

Fig. 1.14: Schematic of equatorial Kelvin waves impinging on the coast of Ecuador and forcing coastal-trapped waves as well as extra-tropical Rossby waves.

Poleward propagating anomalies of sea level (fig.1.15, fig.1.16a) and alongshore velocities have indeed been detected along the coastal wave guide extending from northern Peru down to central Chile (*e.g.* Brink, 1982; Shaffer et al., 1997; Blanco et al., 2002; Carr et al., 2002). It is now admitted that such waves, by perturbing the thermocline (fig.1.16b) and the coastal currents (Shaffer et al., 1997; Hormazabal et al., 2002, 2006), could have a direct influence on the spatial structure and dynamics of the marine ecosystem (Bertrand et al., 2008).

In addition to these high frequencies, other time scales characterize the variability of EKW. Several studies have reported the presence of 100- to 120-day oscillations in the spectrum of eastern Pacific EKW (Cravatte et al., 2003; Dewitte et al., 2008b), which are thought to be the result of modal dispersion due to the differences in phase speeds of the baroclinic modes.

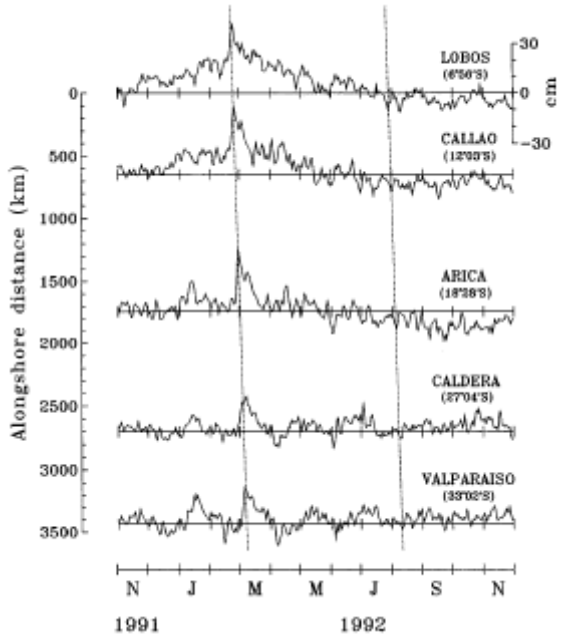

Fig. 1.15: Sea level records along the west coast of South America from Lobos de Afuera (7°S), Callao (12°S), Arica (18°S), Caldera (27°S), and Valparaiso (33°S) between November 1991 and November 1992. The slope of the dotted lines following selected sea level features is based on a poleward phase speed of 266 km/day (3.08 m/s). *Source: Shaffer et al., 1997*.

Besides, lower-frequency EKW are also present in the equatorial Pacific: indeed, WWB are stronger and more frequent during austral spring and summer and during the onset of an El Niño event, when the warm pool is warmest (Kessler and McPhaden, 1995; Kessler et al., 1995). As a consequence, the modulation of IEKW at seasonal and interannual time scales introduces lower frequencies in the energy spectrum of the EKW, which are associated to higher critical latitudes at the South American coast. These frequencies mostly trigger the offshore propagation of ETRW (Dewitte et al., 2008a; Ramos et al., 2008), though nonlinear effects due to bottom friction have been shown to introduce poleward-propagating anomalies on El Niño time scales (Clarke and Van Gorder, 1994; Pizarro et al., 2001). Such ETRW have been shown to have a significant impact on the variability of the PCUC off Chile (Pizarro et al., 2002).

ENSO: large-scale variability and regional impacts

During the developing phase of El Niño, westerly wind anomalies emerge over the warm pool, with maximum values below and to the west of the deep convection area, refered to as WWB (Kessler and McPhaden, 1995; Kessler et al., 1995). Such WWB force the simultaneous eastward propagation of downwelling (warm) EKW and westward propagation

of upwelling (cold) ERW across the basin. These long baroclinic waves contribute to propagate thermocline depth anomalies along the equatorial wave guide and act as a positive feedback to the growth of El Niño.

(a)

(b)

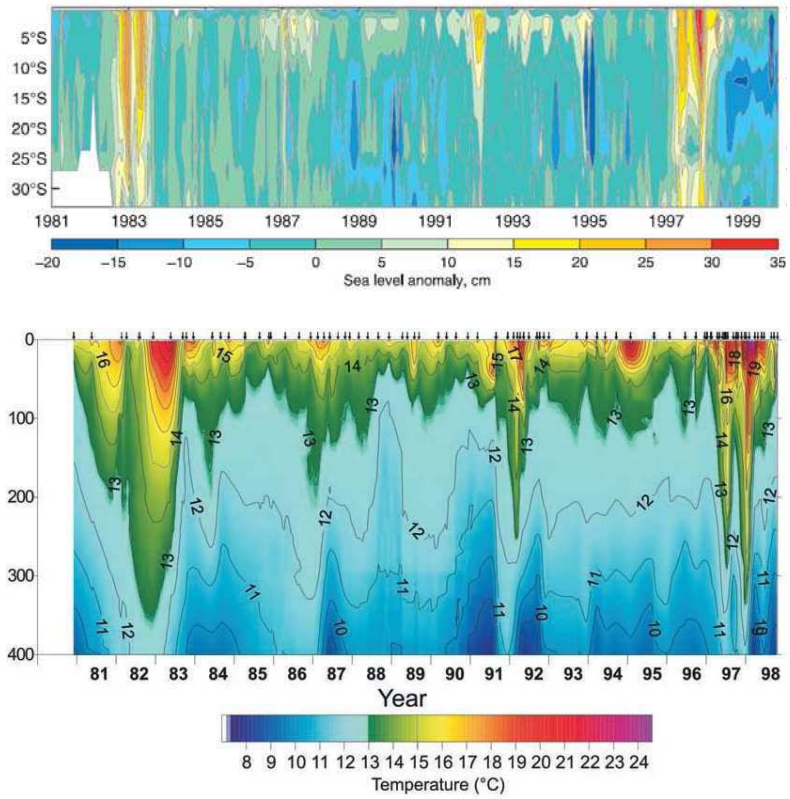

Fig. 1.16: **(a)** Time-latitude plot of sea level anomalies (cm) measured by tide gauges along the west coast of South America between 1981 and 1999. Contour interval is 5cm. *Adapted from Carr et al. (2002)*.
(b) Time-depth plot of temperatures (°C) 10km offshore of Iquique (20°S) between 1981 and 1998. Sampling is indicated by arrows. Contour interval is 1°C. *Adapted from Blanco et al. (2002)*.

The name "El Niño" (which means child Jesus in spanish) was originally given by fishermen from Peru and Ecuador to a southward current of anomalously warm surface waters affecting the northern part of the HCS and appearing around Christmas (hence the name), the Annual El Niño Current (AENC, fig.1.10b – Cucalon, 1987). Whereas such current appears to be dominated by an annual cycle and lasts only a few weeks, it is subject to strong intensification at the interannual scale and very warm temperatures that can last several months, modifying the regional climate and strongly perturbating the marine ecosystem (Barber and Chavez, 1983). The El Niño current and the associated rainfall and flooding episodes have been known for centuries by early pre-Inca civilizations such as Moche or Chimu who lived on the shores of the arid northern Peru desert until 1470, when they were conquered by the Incas who came from the Andinean region. Many documentary sources of

northern Peru from the colonial period (1534-1850) and from the republican period (1850-present) confirm its existence (Garcia-Herrera et al., 2008). Today, El Niño is rather known as a basin-scale warming of the tropical Pacific Ocean occurring every 2 to 7 years and alternating with a cold phase called "La Niña". Thanks to the early observational and theoretical works by Bjerknes (1966, 1969), it is also known that such variations of SST in the Pacific Ocean are associated to spectacular basin-wide changes in sea level pressure, called "the Southern Oscillation". Since then, these events have been understood as a coupled ocean-atmosphere phenomenon called ENSO. Because of the existence of large-scale oceanic and atmospheric teleconnections between the tropical Pacific and many other regions of the world, ENSO is able to affect climate at the global scale, making it the dominant mode of interannual variability on Earth.

During the neutral phase of ENSO (*ie* neither El Niño nor La Niña), usually refered to as normal ENSO conditions (fig.1.17), the lower branch of the Walker circulation cell forces easterly trade winds that blow zonally across the tropical Pacific. The winds push the warm surface layers towards the western part of the basin, where they gather and form the western Pacific warm pool. As a result, the thermocline is about 100m deeper there than in the eastern part of the basin characterized by the presence of the eastern Pacific cold tongue. Winds just South from the equator induce an Ekman transport to the left, *ie* to the South, whereas North from the equator they induce an Ekman transport to the right, *ie* to the North. This meridional divergence of water in the Ekman layer creates equatorial upwelling, which replaces the warm surface waters advected westward and poleward by colder waters from the deeper layers. Upwelling is stronger in the east where it drags cool waters across the shallow equatorial thermocline. In the same time, warm SSTs sustain intense deep convection and low atmospheric pressure over the warm pool region. The warm and humid air masses get cooler and drier as they reach higher layers, where they are caught in the eastward flow of the Walker circulation. They go down again as they reach the high pressure systems of the eastern Pacific, and eventually feed the low-level trade winds. The whole system is close to stability and is mainly controlled by variations in the strength of the Walker circulation and of the associated trade winds.

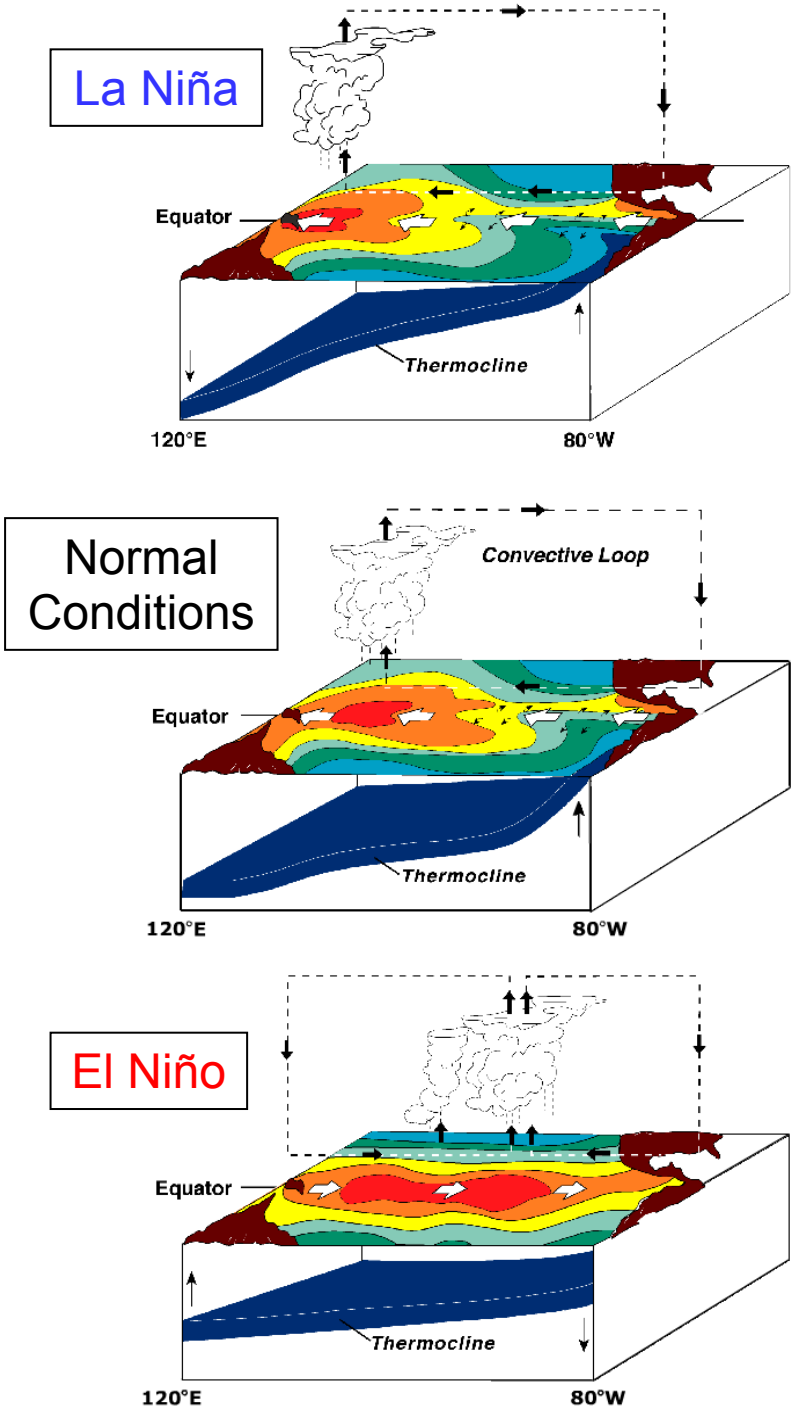

Fig. 1.17: Schematic of the circulation in the upper ocean and lower atmosphere of the tropical Pacific during La Niña (top), normal ENSO conditions (middle) and El Niño (bottom). Dashed lines and bold black arrows are for the Walker circulation. White arrows are for the mean zonal flow along the equator, and thin black arrows on the top two panels are for the poleward Ekman transport associated to equatorial upwelling. Thin black vertical arrows are for anomalous vertical displacements of the equatorial thermocline. Coloured contours symbolize the mean SST field, and clouds represent deep convection. Image courtesy of NOAA/PMEL/TAO.

During an El Niño event, a relaxation of the dominant easterlies is observed at the beginning of austral summer (figs. 1.17 and 1.18a). As a response, there is a basin-wide adjustment of the thermocline which deepens in the east and shoals in the west, called the

thermocline feedback. Pressure gradient anomalies also create an eastward surface flow that advects the eastern edge of the warm pool eastwards. This second positive feedback to the ENSO cycle is called the zonal advective feedback. Vertical variations of the thermocline and horizontal advection combine to create warm SST anomalies in the central and eastern Pacific (fig. 1.18a). In response to the zonal extension of the warm pool, low pressure systems move towards the central equatorial Pacific where the zonal winds converge, often provoking the emergence of westerly winds over the warm pool. The Walker circulation cell is modified and deep convection occurs over the central to eastern Pacific. An El Niño event generally lasts for a few months up to a year, before negative feedbacks start to overcome the positive feedbacks and allow the ENSO cycle to move from the warm phase (El Niño) to the cold phase (La Niña).

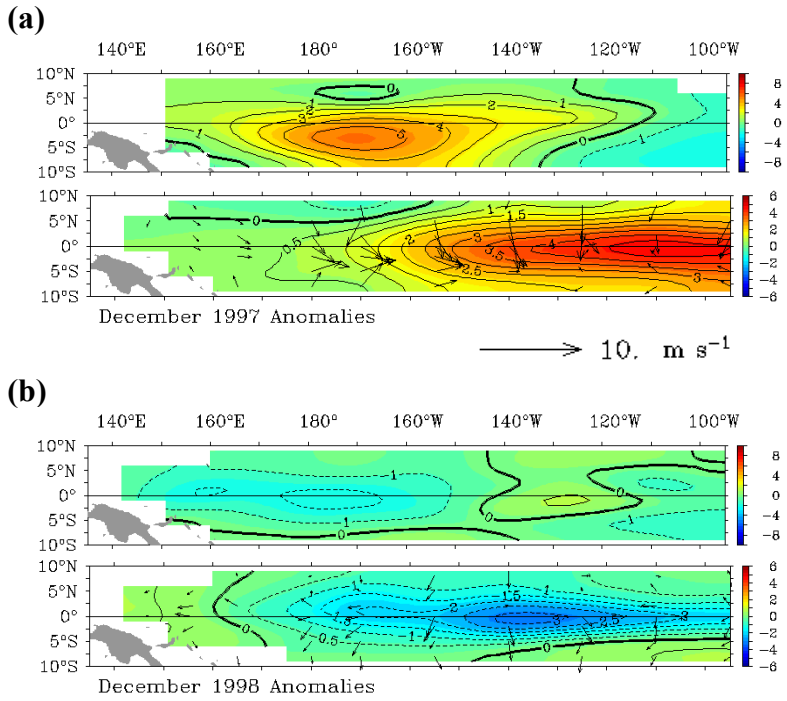

Fig. 1.18: Anomalies of zonal wind (top panel) and SST (bottom panel) in the equatorial Pacific between 135°E and 95°W and between 10°S and 10°N, averaged over (a) December 1997 and (b) December 1998. Unit is m/s and °C for zonal wind anomalies and SST anomalies, respectively. Plain (resp. dashed) contours are for positive (resp. negative) anomalies, *ie* westerly (resp. easterly) and warm (resp. cold) for wind stress and SST, respectively. Arrows on the SST plot are for wind anomalies. Corresponding scaling is indicated below the figure. Image and data courtesy of NOAA/PMEL/TAO-TRITON.

La Niña is similar to normal ENSO conditions, except they are intensified: an intensification of the easterly trade winds (figs. 1.17 and 1.18b) is balanced by a deepening of the thermocline in the west and a shoaling in the east. Deep convection is displaced in the far western Pacific, as the warm pool is contracted towards the west. Upwelling is stronger over

the cold tongue (fig. 1.18b) and anomalous cold conditions emerge over the eastern South Pacific, both in the atmosphere and in the ocean.

Thanks to extensive theoretical research conducted for the last fifty years or so, it is now widely recognized that ENSO results from the combination of various positive and negative feedback processes that contribute to the enhancement or damping of associated anomalies. The major positive feedback is the so-called 'Bjerknes feedback' (Bjerknes, 1969): warm SST anomalies in the cold tongue tend to reduce the east-west SST gradient, which in turn leads to weaker easterly winds that induce positive thermocline anomalies propagating eastward as downwelling EKW towards the eastern tropical Pacific, where they contribute to the warm anomalies via upwelling. Conversely, cold SST anomalies in the cold tongue tend to increase the zonal SST gradient, which in turn leads to stronger easterlies that induce negative thermocline anomalies propagating as upwelling EKW towards the east, where they contribute to the cold anomalies via upwelling.

Four major theories for ENSO have then been proposed to describe the negative feedbacks responsible for the transition from El Niño to La Niña and back: (i) the delayed oscillator theory, involving the reflection of ERW of the opposite sign at the western boundary as EKW, which progressively reduce the temperature anomalies caused by the initial EKW (Suarez and Schopf, 1988; Schopf and Suarez, 1988; Battisti and Hirst, 1989); (ii) the western Pacific oscillator theory, in which the easterly trade winds force EKW of the opposite sign, as a result of anticyclonic circulation off the equator due to off-equatorial SST anomalies of the opposite sign induced by Rossby waves (Weisberg and Wang, 1997); (iii) the advective-reflective oscillator theory, whereby displacements of the edge of the warm pool are driven by anomalous zonal advection (Picaut et al., 1997); and (iv) the recharge oscillator theory, which highlights the role of equatorial recharge/discharge processes due to Sverdrup transport (Jin, 1996; 1997a,b). These theories are complementary in the sense that they may be combined in various ways to understand the observed diversity of ENSO events (Jin and An, 1999; Fedorov and Philander, 2000; An and Jin, 2001). Several studies have focused on the respective role of two important positive feedbacks - that contribute to the Bjerknes feedback - on ENSO as simulated by simple and intermediate coupled models of the tropical Pacific: the zonal advective feedback and the thermocline feedback (Hirst, 1986; Jin and An, 1999; An and Jin, 2001; Fedorov and Philander, 2001).

Indeed, surface wind stress influences both zonal advection of mean SST by anomalous zonal currents in the central Pacific (the zonal advective feedback), and the

vertical advection of subsurface temperature by the mean upwelling in the eastern Pacific (the thermocline feedback). Both feedbacks are important terms of the heat budget of the mixed layer in the tropical Pacific (Hirst, 1986). Depending on the zonal location of wind anomalies, the zonal advective feedback favors the transition or the growth of the ENSO cycle and consequently sustains short 2-4 years or long 4-6 years oscillations with low or high amplitude (An and Wang, 2000; Wang and An, 2001). On the other hand, the thermocline feedback is driven by vertical displacements of the thermocline as a result of the basin-wide adjustment of the ocean to wind variations. It is responsible for high amplitudes and long ENSO cycles (4-6 years) because of a longer time of recharge/discharge of the equatorial heat content, accordingly to the recharge oscillator paradigm (Jin, 1996; 1997a,b). In fact, the two feedbacks coexist in nature, making ENSO a hybrid coupled mode (Fedorov and Philander, 2000). The balance between the two is thus a key factor in the determination of the dynamics and structure of ENSO, including the ENSO time scale. An and Jin (2001) and Fedorov and Philander (2001) further showed that the combined effect of both processes on ENSO is sensitive to the mean equatorial state (especially the intensity of the easterly winds, the mean upwelling, the thermocline depth, and the temperature difference across the thermocline), consistently with the observed change in ENSO amplitude and period after the late 1970s climate shift (An and Wang, 2000; Wang and An, 2001).

Another interesting feature of ENSO is its intrinsic asymmetric behaviour. Although La Niña may be seen to a large extent as the mirror image of El Niño, La Niña events tend to be weaker than El Niño events (fig. 1.19). Such El Niño/La Niña asymmetry is due to the nonlinear nature of ENSO: in particular, some studies have shown that nonlinear dynamical heating (NDH) strengthened the strong 1982-83 and 1997-98 El Niño events, whereas it weakened the following 1983-85 and 1998-99 La Niña events (Timmermann et al., 2003; An and Jin, 2004). NDH is the sum of nonlinear advection terms in the mixed layer of the equatorial Pacific. It is controled (i) mainly by the spatial and temporal phase relationships between anomalous upwelling and the difference between surface and subsurface temperature anomalies in the central to eastern Pacific, and (ii) secondarily by the phase relationships between anomalous zonal currents and the zonal gradient of SST anomalies in the eastern Pacific (An and Jin, 2004). The contribution of meridional advection to NDH has been shown to be much weaker. These studies have also highlighted the relationship between ENSO nonlinearities and the decadal modulation of ENSO. In particular, strong El Niño events associated to high NDH occurred after the mid 1970's climate shift of the tropical Pacific (An

and Wang, 2000; Wang and An, 2001), a period characterized by eastward-propagating ENSO anomalies (Rasmusson and Carpenter, 1982) with phase relationships favorable to NDH. Conversely, the period before the shift was characterized by westward propagations and did not allow the development of strong NDH. As a result, the magnitude of El Niño and La Niña events tended to be more symmetric (fig. 1.19).

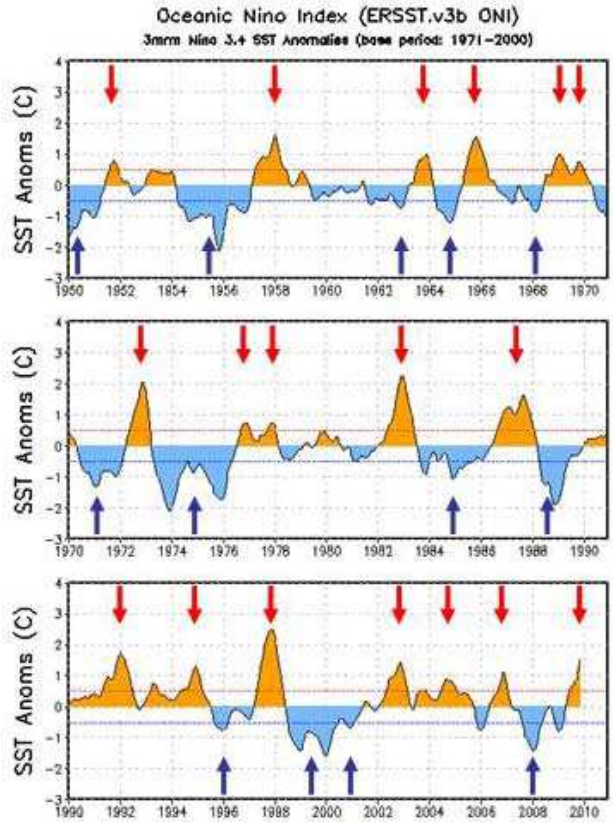

Fig. 1.19: Time series (1950-2010) of oceanic Niño index (ONI), *i.e.* area-averaged 3-month running-mean SST anomalies (°C) in the Niño3.4 region (5°N-5°S, 170°W-120°W), based on Extended Reconstructed SST analysis (ERSST.v3b – Smith et al., 2008). Anomalies are departures from the 1971-2000 base period weekly means (Xue et al., 2003). According to NOAA standards, an El Niño (La Niña) event is characterized by an ONI greater than or equal to +0.5°C (lower than or equal to -0.5°C) for at least five consecutive overlapping 3-month seasons. Red (blue) arrows indicate El Niño (La Niña) events. Red (blue) dotted lines indicate the +0.5°C (-0.5°C) threshold. Orange (light blue) sectors are for positive (negative) anomalies. *Adapted from NOAA/CPC/NCEP.*

El Niño and La Niña first impact the tropical Pacific and their effects may be seen in the SST over specific areas. A way to characterize it is to average SST over these areas (fig. 1.20):

- Niño4 (5°S-5°N, 160°E-150°W): the region where SST changes seem to be most strongly connected to convection changes in the equatorial Pacific;

- Niño3 (5°S-5°N, 90°W-150°W): the region that presents the largest SST variability on interannual time scales;

- Niño3.4 (5°S-5°N, 120°W-170°W): a compromise between strong SST variability (Niño3) and precipitation changes (Niño4) (see also fig. 1.19);

- Niño1+2 (10°S-0°N, 80°W-90°W): the region that generally warms first during the development of an El Niño event.

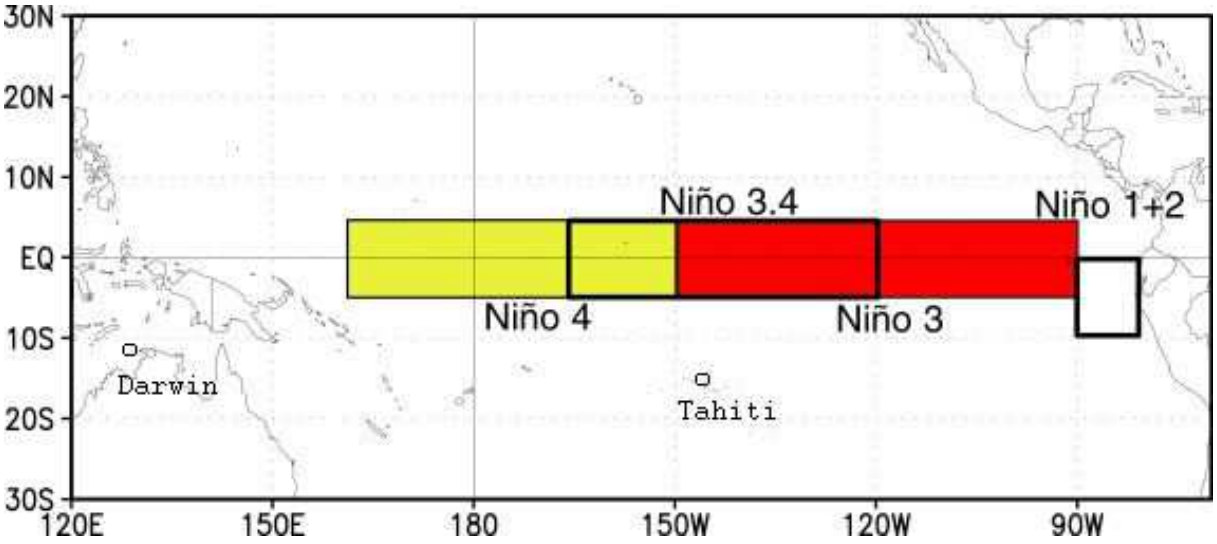

Fig. 1.20: localization of the four Niño regions, Tahiti and Darwin.

SST averaged over Niño3 (also called Niño3SST index) may also be used to characterize low-frequency modulation of ENSO (decadal to multi-decadal time scales). A way to do it is: 1) to filter the Niño3SST index from the high frequencies; 2) compute the corresponding wavelet power spectrum; and 3) compute the corresponding scale-average time series over the 2-7 years frequency band. This latter series (always positive) is generally called N3VAR (see also fig. 1.28). When N3VAR is strong (weak), the considered time period is characterized by a strong (weak) ENSO amplitude, *e.g.* after (before) the mid-1970s climate shift.

The Southern Oscillation associated to the ENSO cycle can be characterized with the SOI (*Southern Oscillation Index*), equal to the difference between normalized pressure at Tahiti and Darwin (fig. 1.20). Such index represents the Walker circulation, its sign is opposite to that of SST anomalies: when SOI anomaly is positive (negative), the Walker circulation is stronger (weaker) and the SST anomalies in the Niño4 to Niño1+2 regions are negative (positive).

Surrounding countries of the Pacific Ocean are the most vulnerable to changes induced by ENSO: during the strong 1997-98 El Niño event for instance (fig. 1.18a and 1.19), the usually arid western South American coastline was experiencing heavy rainfall and

dramatic floodings, as well as a sudden drop of anchovy catches, whereas drought and forest fires were spreading over the normally humid regions of Indonesia and northern Australia. Such natural catastrophes strongly perturb marine and terrestrial ecosystems as well as human activities including agriculture and fisheries (Barber and Chavez, 1983). The impact of El Niño in the HCS has been extensively described in the literature, because it is the part of the world that suffers the most spectacular changes during El Niño. These include:

- a deepening of the thermocline, a reduction of coastal upwelling and a strong warming of surface temperatures that can reach 8°C (Blanco et al., 2002; Carr et al., 2002, Colas et al., 2008) (fig.1.16b). The reduction of coastal upwelling drives a reduction of marine primary production, which impacts the whole marine ecosystem including the higher trophic levels (Barber and Chavez, 1983);

- a strengthening of the PCUC, especially off Peru (Smith, 1983; Huyer et al., 1991);

- a southward shift of the ITCZ, causing heavy rainfall in the normally arid regions of the coastal zone (Huyer et al., 1987, 1991);

- a weakening of the subtropical high and its influence on the upwelling-favorable winds. However, upwelling-favorable winds themselves do not appear to be reduced during El Niño, due to nonlinear effects: indeed, as discussed by Enfield (1981), a reduction of the cloud cover next to the coast due to warmer coastal water may enhance radiative forcing and reduce atmospheric pressure over the continent, sustaining the land-sea pressure difference and thereby equatorward coastal winds. According to Bakun and Weeks (2008), coastal winds off Peru may even be enhanced during El Niño, due to increased water vapour content in the atmosphere leading to increased greenhouse effect and thereby to lower pressures over land. This mechanism was proposed by Bakun and Weeks (2008) to explain the increase in the strength of alongshore winds observed off Peru by Bakun (1990) over the last decades in the context of global warming (see next section).

Possible changes in the structure and behaviour of ENSO under global warming are thus likely to induce changes in the regional climate of the eastern South Pacific, and in the regional circulation of the HCS. In particular, changes in the occurrence and spatial distribution of ENSO during recent decades suggest the possible co-existence of various coupled modes in the equatorial Pacific. Whereas El Niño in the traditional view is depicted as SST anomalies developing in the eastern equatorial Pacific and is described quite well by the recharge oscillator theory (Jin, 1997a,b), recent studies (Larkin and Harrisson, 2005a; Ashok et al., 2007; Kao and Yu, 2009; Kug et al., 2009) have highlighted the emergence of a

second type of El Niño, with SST variability displaced towards the central Pacific (fig. 1.21). This second type of El Niño is known as El Niño « Modoki » (Ashok et al., 2007), « warm pool » El Niño (Kug et al., 2009) or « central Pacific » El Niño (Yeh et al., 2009). Similarly to the conventional El Niño, El Niño Modoki is the warm phase of a coupled ocean-atmosphere oscillation. The cold phase is called La Niña Modoki. ENSO Modoki involves different physics to the conventional ENSO: whereas the conventional ENSO tends to be controlled mostly by the thermocline feedback, ENSO Modoki has been shown to be mainly controlled by the zonal advective feedback (Kug et al., 2009).

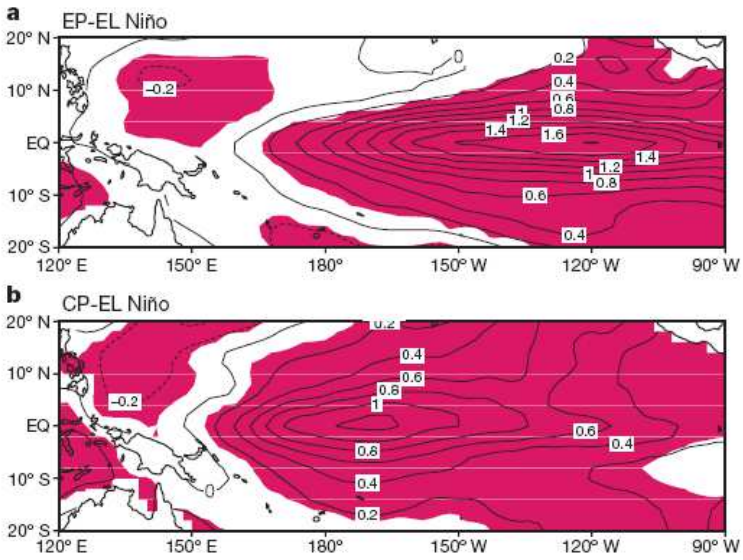

Fig. 1.21: composites of peak-season SST anomalies (relatively to 1854-2006) for **(a)** the Eastern Pacific El Niño and **(b)** the Central Pacific El Niño, after Yeh et al. (2009). Shaded areas are for SST anomalies significant at the 95% confidence level.

Several authors have shown that El Niño Modoki occurs more frequently since the 1990s (Larkin and Harrisson, 2005a; Ashok et al., 2007; Yeh et al., 2009), indicating a possible change of ENSO induced by global warming. Furthermore, Yeh et al. (2009) showed that 8 out of the 11 CGCMs they examined were having a higher occurrence of El Niño Modoki relatively to conventional El Niño under global warming. They suggested that such change was related to the flattening of the thermocline in the CGCMs (fig. 1.22). Indeed, the predicted weakening of the Walker circulation due to global warming is associated to a flattening of the thermocline in the equatorial Pacific (Vecchi and Soden, 2007), which is likely to enhance the zonal advective feedback and hence the occurrence of El Niño Modoki vs conventional El Niño events (Ashok et al., 2007; Yeh et al., 2009).

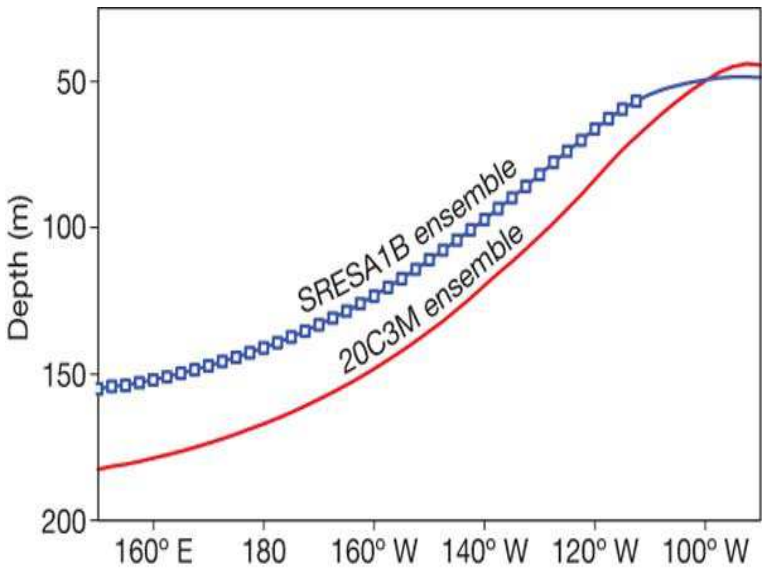

Fig. 1.22: the ensemble mean thermocline depth for 20th century (red) and 21th century climate (blue), after Yeh et al. (2009). Blue squares are for changes significant at the 95% confidence level.

Last but not least, El Niño Modoki is associated to very different teleconnections with mid-latitudes compared to those of the conventional El Niño (Larkin and Harrisson, 2005b; Weng et al., 2007, 2009; Ashok et al., 2007, 2009a,b; Kao and Yu, 2009; Yeh et al., 2009). For instance, several recent studies have pointed out the distinct impact of ENSO Modoki on australian rainfall (Wang and Hendon, 2007; Ashok et al., 2009b; Cai and Cowan, 2009; Taschetto and England, 2009). On the other hand, western North America experiences dry and warm summers during El Niño Modoki, whereas wet and cool summers prevail during El Niño (Ashok et al., 2007; Weng et al., 2007). Hence, a shift towards a Modoki-type of ENSO in response to climate change could cause large impacts on global climate and possibly on the regional climate of the HCS.

A synthetic presentation of the possible impacts of global warming in the region is proposed in the next section.

1.2. The eastern South Pacific: regional cooling in a warming climate ?

Please note that a general presentation of global warming can be found in appendix A. Some of the acronyms used in the following section are also defined in appendix A.

1.2.1. Reconstructed trends from paleoclimate records and historical observations

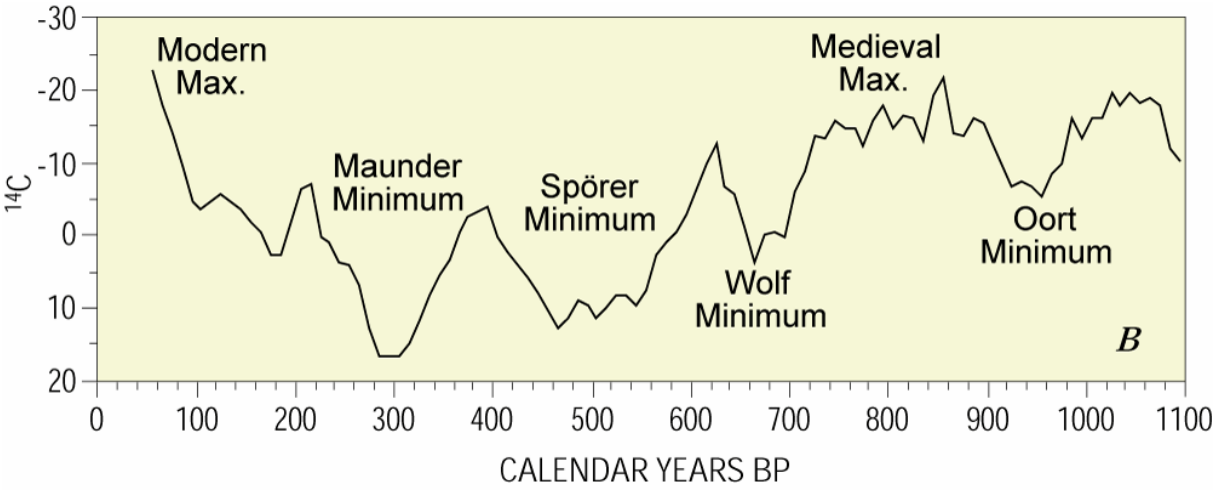

Fig.1.23: Changes in ^{14}C atmospheric concentration (a proxy of solar activity) during the past millenium. Note that the present day is on the left hand side of the figure. *Image courtesy of the United States Geological Survey (USGS).*

As underlined in appendix A., past climate change was sometimes constrained by variations in solar activity (fig. 1.23). It is widely recognized that low solar activity during the Maunder and Spörer Minima may be among the principal causes of the Little Ice Age, a climate anomaly which occurred between about 1400 and 1850 AD and was characterized by expanded ice cover over North America and Europe (Cronin et al., 2003). Likewise, warmer and wetter conditions over northern Europe during the Medieval Warm Period (~800-1300 AD) are thought to be the result of high solar activity during the Medieval Maximum (Cronin et al., 2003) (fig.1.23). These two periods are examples of contrasted global climate states, with a cooler than average era (the Little Ice Age) and a warmer than average era (the Medieval Warm Period). A few paleoclimate records from these periods are available in the HCS and other EBUS'es, and can help understanding the specific behaviour of these regions under a warmer or a cooler global climate.

In the California Current System, dry and warm conditions were prevailing on land during the Medieval Warm Period, whereas the ocean was characterized by cool SSTs

(Graham et al., 2007), suggesting strong coastal upwelling. In the northern part of the HCS (*ie* Peru), very arid conditions were also reported for the same period, which might be due to a northward shift of the ITCZ (Rein et al., 2004). Sediment cores collected off Callao in central Peru reveal that the Medieval Warm Period was marked by stronger reducing conditions than today. Proxy records from the tropical Pacific Ocean show contemporaneous changes indicating cool central and eastern tropical Pacific SSTs during this period (Graham et al., 2007). This pattern is consistent with the hypothesis that the dry Medieval Warm Period in the Eastern Pacific region resembled modern La Niña conditions (Sifeddine et al., *in prep.*). These results tend to show that whereas most of the planet was unusually warm, EBUS'es in general and the HCS in particular were characterized by a cooler than average coastal ocean, and a drier than average weather over land. Conversely, during the Little Ice Age, whereas most of the globe was experiencing unusually cold conditions, a southward displacement of the ITCZ in the eastern Pacific region (Koutavas and Lynch-Stieglitz, 2004) caused increased humidity on land along the South American coast (Sifeddine et al., 2008) and weaker alongshore winds, coastal upwelling and marine productivity leading to anomalously warm SSTs (Vargas et al., 2007; Sifeddine et al., 2008; Gutierrez et al., 2009). At the end of the Little Ice Age, SSTs off Peru and northern Chile started to decrease again, possibly because of a northward shift of the ITCZ and of the eastern Pacific subtropical anticyclone (Gutierrez et al., 2009) or increased land-sea thermal contrast (Vargas et al., 2007). Similar trends were inferred from SST reconstructed from sediment cores collected off the Moroccan coast and extending back to 2500 years ago: consistently with findings from other EBUS'es, coastal upwelling off Cap Ghir (31°N) appeared to be out of phase relatively to global average long-term temperature anomalies, with an intensification during the Medieval Warm Period, a reduction during the Little Ice Age, and a rapid increase in the 20th century (McGregor et al., 2007). However, these results are subject to controversy, as observations from recent decades show a decrease in alongshore winds all along the Moroccan coast except off Cap Ghir and an increase of coastal SSTs (Barton and Roy, *in prep.*). Indeed, long-term trends are sometimes difficult to infer from *in-situ* observations at a limited number of sites, as they may be sensitive to the chosen time period and/or geographic area (Demarcq, 2009).

Long-term trends in solar activity show that the Medieval Warm Period is the most recent period similar to present day in terms of solar forcing (fig. 1.23). Though the latter was shown to be only partly responsible for modern climate change (Stott et al., 2003), the period 1850-1950 after the Little Ice Age and before anthropogenic effects start to dominate global warming could feature a very similar climate state to the Medieval Warm Period. Historical

measurements from the HCS and other EBUS'es do actually show evidence for increasing upwelling-favorable winds and cooling SST trends in the recent period, consistently with paleo-proxies from medieval times:

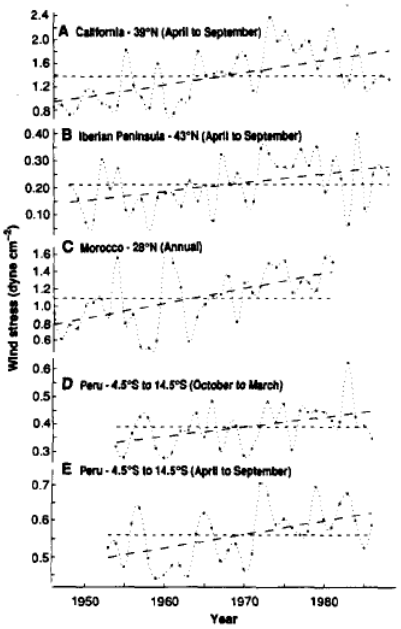

Fig.1.24: Within-year averages of monthly estimates of alongshore wind stress off California (**A**), Iberian peninsula (**B**), Morocco (**C**), and Peru (**D** and **E**). The dotted lines are for the long-term mean of the corresponding time series. The dashed lines are for the linear trend fitted by the least-squares method. *Adapted from Bakun (1990)*.

- shipboard wind data show a systematic linear trend during recent decades for increasing alongshore winds (~0.04 dyne.cm^{-2} per decade for central and northern Peru) off the coasts of most EBUS'es (fig. 1.24) (Bakun, 1990), including the northern HCS (Jahncke et al., 2004). QuickSCAT satellite wind measurements over 2000-2007 also indicate trends of 0.20 m.s^{-1}, 0.24 m.s^{-1}, and 0.04 m.s^{-1} for the coasts of Peru, northern Chile (18°S-32°S) and central Chile (32°S-42°S), respectively (Demarcq, 2009);

- an increasing occurrence of synoptic-scale alongshore wind-driven dust storms off Pisco in southern Peru (14°S) has been observed since 1950 (Escobar, 1993);

- coastal station data along the Peru coast from IMARPE (the Peruvian Marine Research Institute) show a cooling trend for SST South from 12°S and a slight warming trend North from 12°S during the last 50 years (S. Purca, *personal communication*);

- consistently with these results, Falvey and Garreaud (2009) used global analyzed SST fields and *in situ* data over 1979-2005 to derive significant cooling trends over the coast of Chile and southern Peru (~0.15°C per decade), but no clear trend in the northern Peru region (fig. 1.25). Their results also show a clear warming trend over the continent, including

the near-shore region (not shown). Such trends were found to be consistent with those simulated by an ensemble of global climate models for the late 20th century, which suggests that they are related to anthropogenic climate change rather than decadal variability: indeed, assuming that modes of natural variability (if present) should cancel out after computing the ensemble mean (Cai and Cowan, 2006), climate change patterns common to most models should represent a response to GHG forcing;

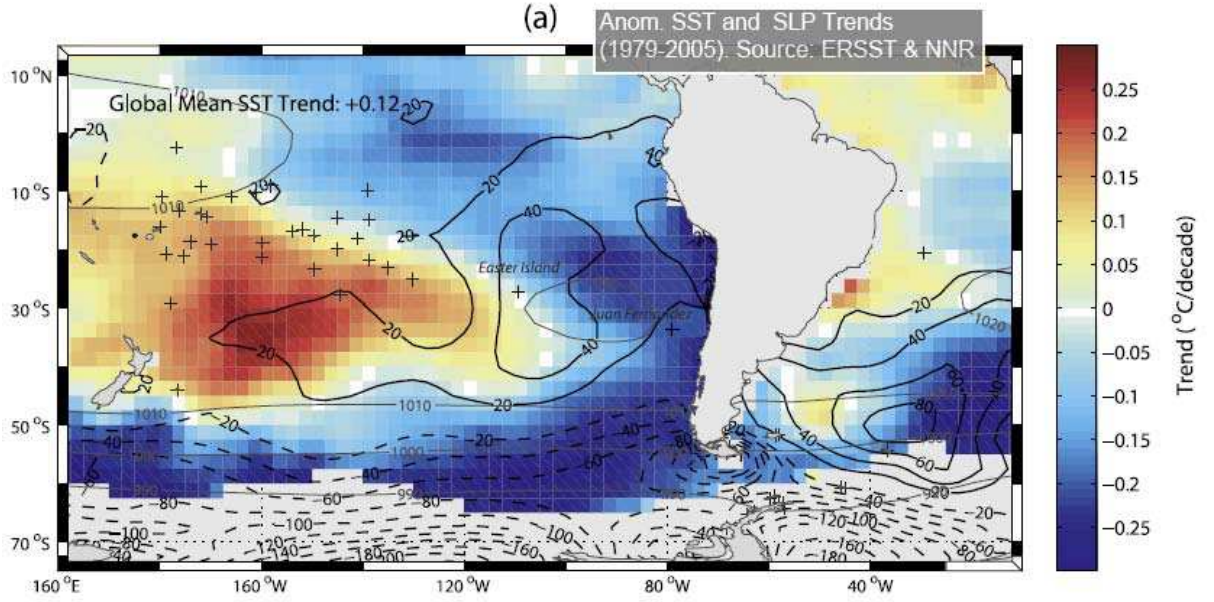

Fig.1.25: Anomalous (*i.e.* global mean subtracted) SST trends (°C/decade) derived from ERSST (Smith and Reynolds, 2004) analyzed data (colored squares). Thick solid (resp. dashed) lines indicate positive (resp. negative) Sea Level Pressure (SLP) trends (Pa/decade) derived from NCEP-NCAR Reanalysis (Kalnay et al., 1996). Thin gray lines show the climatological mean pressure field. Black crosses indicate stations in the South Pacific where long-term pressure records are available. *Adapted from Falvey and Garreaud (2009)*.

- a clear increase in surface chlorophyll-a was observed from satellite data off major EBUS'es (including the HCS) during the last decade (fig. 1.26) (Demarcq, 2009), consistently with similar trends revealed by in-situ measurements undertaken off Peru by IMARPE over the last 30 years, suggesting a possible increase in coastal upwelling.

Based on these observations, several theories have emerged to explain past climate change and modern global warming impacts on EBUS'es and specifically on the HCS. According to Bakun's hypothesis (Bakun, 1990), the observed intensification of upwelling-favorable winds and consequent cooling of the coastal ocean in EBUS'es is due to the increasing land-sea thermal contrast consequent to reduced night-time continental cooling with the increasing greenhouse effect (Sutton et al., 2007), as schematized in figure 1.27 for

the coast of Peru (Bakun and Weeks, 2008). In addition, according to Sutton et al. (2007), the land-sea warming ratio is weaker near the equator than in the subtropics because land-sea humidity difference (and hence difference in heat capacities) is lower closer to the ITCZ where rainfall is higher, which might explain the stronger cooling tendencies observed off Chile compared to northern Peru, at least partially.

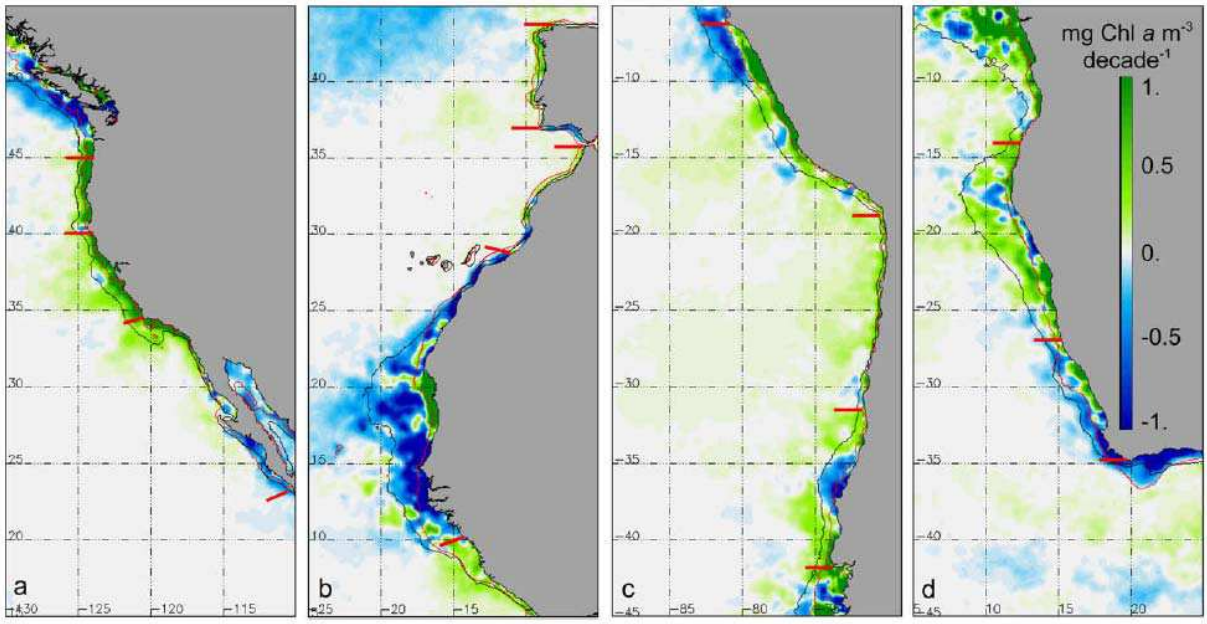

Fig.1.26: Spatial trends in chlorophyll-a concentration (mg m^{-3} $decade^{-1}$) from SeaWiFS satellite data over 1998–2007 for the four major EBUS'es. Thin red (resp. black) lines are for the 200m isobath (resp. mean position of the 1mg m^{-3} isopleth). *Adapted from Demarcq (2009)*.

On the other hand, the observed (Vecchi et al., 2006) and expected weakening of the Walker circulation over the tropical Pacific and of the associated easterly trade winds (Vecchi et al., 2006; Vecchi and Soden, 2007) should induce a warming of the equatorial Pacific Ocean, especially in the east because of a reduced zonal SST and thermocline gradient (Hansen et al., 2006; Vecchi et al., 2008). According to this vision, warmer tropical waters will be advected towards the coast of Peru (through the EUC, the Tsuchiya Jets, and/or the PCCC – see previous section) where they may feed the PCUC and eventually, coastal upwelling, resulting in a warming tendency that opposes the cooling tendency depicted above. In addition, the reduced tropical atmospheric circulation might have an impact on the meridional circulation cell of the eastern South Pacific, though the connection between both systems remains poorly understood: for instance, during some (but not all) El Niño events, upwelling-favorable winds are enhanced (Bakun and Weeks, 2008), though both the Walker circulation and the subtropical high are weaker (see section 1.2. of this chapter). On the other

hand, according to the time series analyzed by Bakun and Weeks (2008) (their figure 6), some sort of positive lagged-correlation seems to be present all year round between Pacific trade winds and Peru winds during the 50s and 60s, though the relationship is less clear after the mid 70s climate shift of the tropical Pacific.

Finally, the direct effect of GHG-induced increasing radiative forcing could also have a warming effect on the ocean off Peru and Chile, though such tendency might be weaker in EBUS'es than elsewhere because reduced water vapor in the atmosphere associated to the presence of subtropical highs might reduce the increase in greenhouse effect. Overall, modern and future climate change in the HCS seem to be driven by competing warming and cooling effects that can significantly modulate the response of coastal upwelling to global warming. Such competing feedbacks might be sensitive to latitude, which could explain the observed differences in trends between southern and northern parts of the HCS.

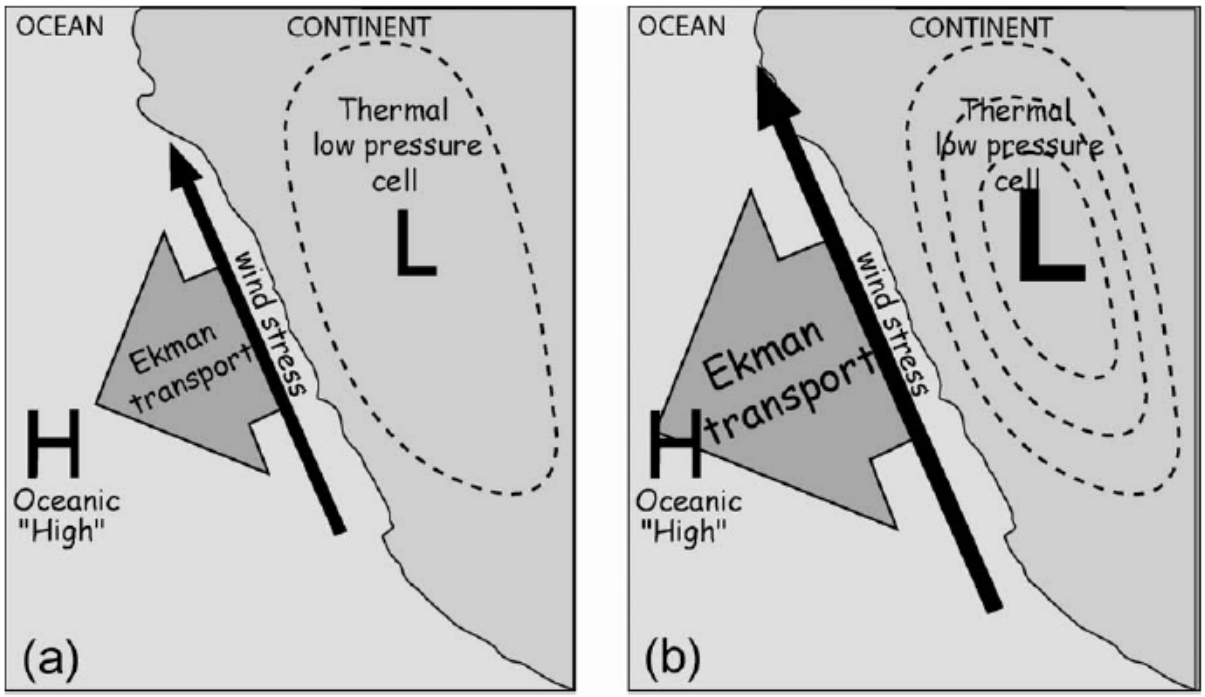

Fig.1.27: Diagram of upwelling intensification mechanism: (**a**) a ''thermal" low-pressure cell builds up over the coastal landmass due to heating of the continental surface relative to the more slowly heating ocean, exerting equatorward geostrophic wind stress on the sea surface that, in turn, drives offshore-directed Ekman transport of ocean surface water and corresponding upwelling of deeper waters required to replace the surface waters transported offshore; (**b**) buildup of greenhouse gases in the atmosphere inhibits night-time cooling of the heated coastlands, increasing average intensity of the coastal low-pressure cell and associated upwelling-favorable wind, which in terms drives quadratic (or greater) increases in offshore surface transport and resulting upwelling. *Source: Bakun and Weeks (2008)*.

Climate modelling can be used to try to reproduce the observed global warming-related climate changes in the HCS and infer future scenarios at the regional scale. Such

approach is complementary to observational studies based on sediment records and/or historical measurements, especially in that it allows testing the relevance of the afore-mentioned theories and possibly quantifying the relative strength of the different warming and cooling processes at stake. In the next sub-section, a review of the literature on future climate change in the HCS is proposed.

1.2.2. Simulated present and future trends from modelling studies

Coastal upwelling dynamics and their response to climate change as well as decadal variability appear to be driven by processes of different spatial scales: at the global scale, GHG-induced radiative forcing induces a warming trend everywhere on the Earth's surface, including EBUS'es and the HCS; at ocean basin-scale, equatorial climate dynamics might have a significant impact on the regional climate; at the regional scale, changes in the atmospheric forcing exerted by subtropical highs can influence upwelling-favorable wind strength and variability; at the local scale, land-air-sea interactions can directly influence the local winds and coastal upwelling dynamics. Whereas CGCMs can allow studying to a large extent the response of EBUS'es to changes at scales from global to regional, higher-resolution ocean modelling is needed to study finer-scale processes such as those related to land-sea thermal contrast in the coastal area, at the origin of Bakun's hypothesis. In the following, we briefly review the main modelling studies using CGCM outputs to infer long-term dynamics and variability of EBUS'es and the HCS, before we present a few results from regional modelling studies:

- Diffenbaugh (2005) used CMIP3 simulations performed by a multi-model ensemble of 18 CGCMs for the 20th century climate, 20th century climate change commitment and SRES A2 experiments to study the response of the large scale atmospheric forcing in EBUS'es to global climate change. He found similar responses for the four main EBUS'es, including a relaxation of the strength and variability of peak-season equatorward wind forcing, in contradiction to Bakun (1990). However, he did not explicitly propose any physical mechanism to explain the weaker winds. Moreover, the models were not able to reproduce the long-term trends and interannual variabilities observed during the 20th century, which raises doubt on the reliability of such ensemble predictions. Noteworthy, nearly all models from the CMIP3 multi-model database were used in his study, without any assessment of individual model skill or identification of a subset of more realistic models.

- On the other hand, Garreaud and Falvey (2009) used 9 CGCMs from the same model ensemble to study changes in coastal wind variability off Chile as inferred from 20th century, SRES A2 and SRES B2 simulations. They found a consistent response among the ensemble, featuring an increase in subtropical high intensity and in upwelling-favorable winds. Conversely to Diffenbaugh (2005), the simulations performed over 20th century climate exhibited similar trends to those inferred from the observations. In order to better document the impact of such changes in the coastal region, they forced a regional atmospheric model with outputs from the CGCMs: they showed that the projected large-scale intensification of equatorward winds off Chile for the late 21st century was associated to 1) a southward extension of upwelling-favorable winds until around 41°S, 2) an increase in the occurrence and duration of coastal jet events, and 3) an intensification of southerly winds in austral winter, shifting the seasonal upwelling off Chile to a quasi-permanent state, just like in Peru.

- Falvey and Garreaud (2009) used both a 21-CGCM ensemble and an extensive collection of *in-situ* observations and analyzed gridded products to infer recent and future temperature trends in the HCS region, both on land and in the ocean. Consistently with Bakun (1990) and Bakun and Weeks (2008), they found clear warming trends over the continent in both the model ensemble and the observations, and a cooling trend in SST observations off Chile. As mentioned earlier, the tendency was less clear off Peru. On the other hand, though the simulated SSTs did not exhibit any cooling trend, warming trends were observed everywhere else around the globe except in the Southern Ocean and off Chile. Hence, anomalous trends relative to global mean SST trend (fig. 1.25) are negative off both Peru and Chile, consistently with intensified high pressure system and alongshore winds from Garreaud and Falvey (2009). Note that this projected minimum warming in the eastern South Pacific cannot be explained by a larger efficiency of latent heat flux only as it is the case in some trade wind regions like the tropical North Atlantic for instance (Leloup and Clement, 2009), since this would require the change in wind speed to be small, which is not the case off Peru and Chile.

Similarly to Garreaud and Falvey (2009), Snyder et al. (2003) used a regional atmospheric circulation model to study the changes in surface wind stress and wind stress curl in the California Current between PIcntrl and 2xCO_2 scenarios. They also found an increase in upwelling-favorable winds during the upwelling season. On the other hand, Auad et al. (2006) used a regional ocean model forced by downscaled surface winds, heat fluxes and ocean

boundary conditions from a 36% CO_2 increase scenario in the same region. Consistently with Snyder et al. (2003), they found an intensification of coastal upwelling in relation to a surface wind increase. Such intensification was shown to be strong enough to overcome the rise in surface stratification due to the warming induced by radiative forcing. As a result, a moderate cooling was observed near the surface, together with increased vertical velocities during the peak upwelling season and a decrease in nearshore eddy activity.

To summarize this section, historical observations and paleoclimate reconstructions of long-term alongshore winds and SST off the west coast of South America reveal distinct behaviour for the northern and southern parts of the HCS in response to 20th century climate change: whereas growing evidence is found for an intensification of upwelling-favorable winds off Chile and consequent cooling of the surface ocean, the picture is less clear for Peru. Indeed, scarce and sometimes contradictory records off the coast of central and northern Peru do not allow inferring clear positive or negative wind and SST trends. However, the observations suggest a similar behaviour for southern Peru and Chile, but the northern limit of the region characterized by increasing upwelling seems highly dependent on the considered data. Results from climate and atmospheric modelling studies confirm the observed trends for the Chile coast. However, to our knowledge so far no similar study has been carried out for the coast of Peru, except the recent works by Goubanova et al. (2010) and Echevin et al. (2010) conducted in the framework of the PCCC program (see chapter 4). On the other hand, state-of-the-art CGCMs currently suffer from numerous biases in the eastern South Pacific, including a bad representation of low-level winds and too warm SSTs. Such biases are partly due to their coarse atmospheric and oceanic resolutions, and also to an incomplete understanding of coupled atmospheric and oceanic processes in the region, such as the origin of the Stratocumulus Cloud Deck, or the connection between the eastern South Pacific anticyclone and the Walker circulation over the tropical Pacific, for instance. In addition, most studies based on CGCM simulations of climate change in EBUS'es do not assess the skill of individual models in reproducing regional dynamics and/or their remote forcing by large-scale dynamics. The general objective of the PCCC program is to provide a methodology to study the influence of climate change on the Humboldt Current System, which can be applied to other EBUS'es, and to some extent, to other regions of the world ocean.

1.2.3. Objectives and methodology of the thesis and of the PCCC program

The methodology proposed by PCCC addresses several issues that were only partly resolved by previous studies:

1) Skill assessment of CMIP3 CGCMs: instead of ensemble-averaging multi-model datasets constituted by climate models with heterogeneous behaviour, we chose in this thesis to perform extensive analyzes of these models in order to identify the most relevant ones for the study of climate change in the HCS (chapter two). Indeed, there are about 25 models in the CMIP3 database, and all of them could not be downscaled, since 1) it would require enormous computational costs and human resources, and 2) ensemble-averaging multi-model responses could lead to erroneous interpretations because of the number of strongly biased models in the region. Based on current knowledge on remote and local forcing mechanisms of the HCS, three main criteria were retained to make this selection: the fidelity of large-scale ENSO variability; that of the mean state and variability of the temperature and velocity fields in the eastern South Pacific; and that of the atmospheric forcing. Applied to the CMIP3 multi-model ensemble, such methodology allows identifying a reduced subset of models, which is used to make future predictions of regional climate change with a better confidence level (see point 3)).

2) Downscaling of the atmospheric forcing: as explained in 1.1, coastal upwelling is the result of both Ekman transport and Ekman pumping. Whereas a correct large-scale representation of the subtropical high (if achieved) should allow simulating adequately the equatorward upwelling-favorable surface winds and thereby an Ekman transport of the observed order of magnitude, the coarse resolution of global climate models generally does not allow representing the wind drop off zone near the coast and the associated wind stress curl, which drives Ekman pumping along the western South American coast. In addition, the steep topography of the Andes is not well resolved by CGCMs and results in large scale biases in the atmospheric circulation of the eastern South Pacific including the subtropical high. To address this issue, a statistical downscaling method was developed by Goubanova et al. (2010). It consists in building a statistical relationship (based on multiple linear regression) between regional- to local-scale surface winds (the predictand) and large-scale surface winds and sea level pressure (the predictors) for observed present-day climate, and applying this relationship to the corresponding predictor fields simulated by CGCMs for a given climate scenario. This assumes that the afore-mentioned statistical relationship is not sensitive to the background climate, which is of course a strong hypothesis. Unfortunately, so far observed high-resolution surface winds cannot provide a record long enough for us to be able to test

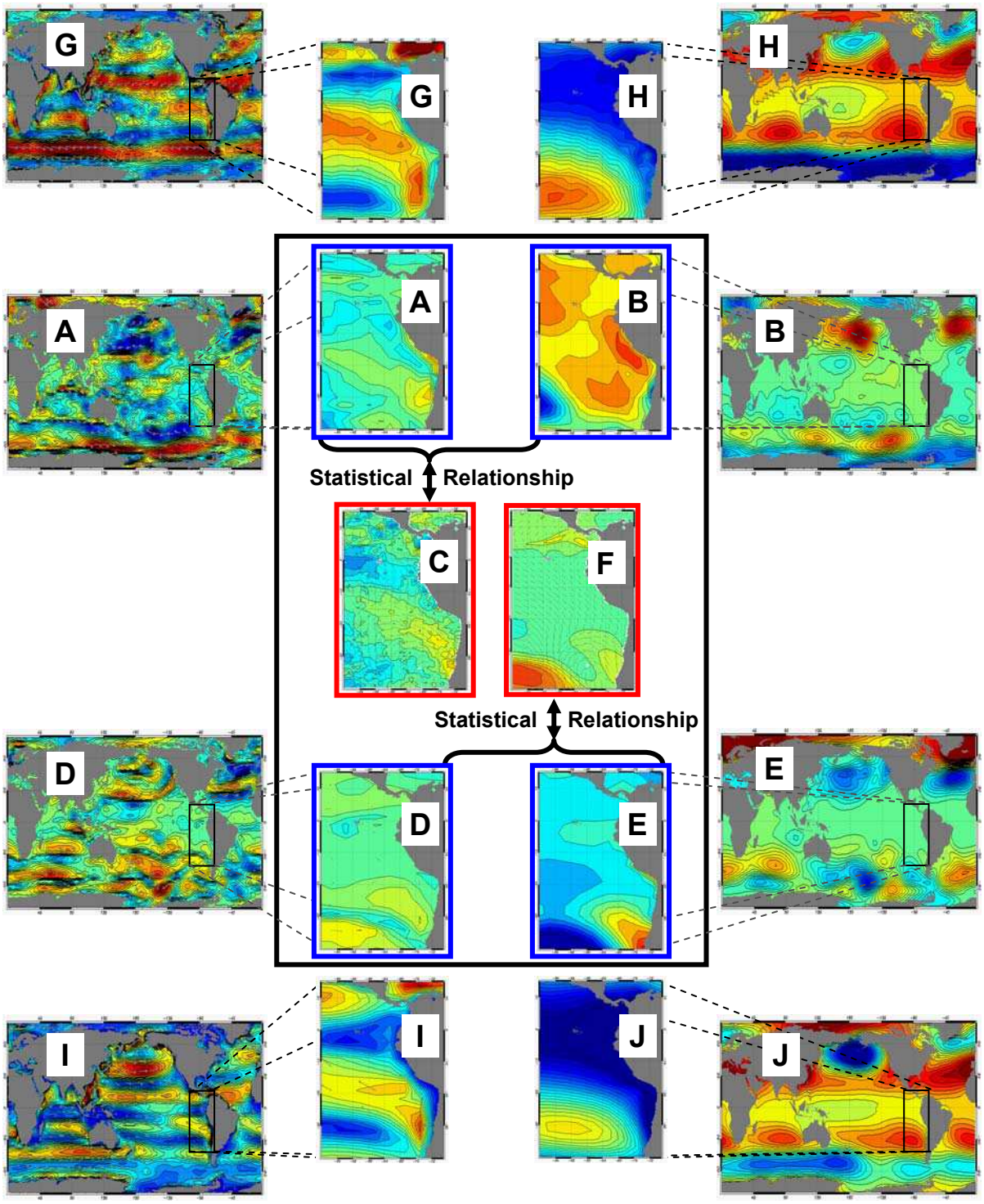

Fig. 1.28: Schematic of the statistical atmospheric downscaling strategy (see text): (**A**) NCEP surface wind anomalies and (**B**) sea level pressure anomalies; (**C**) QuickSCAT surface wind anomalies; (**D**) IPSL-CM4 surface wind anomalies and (**E**) sea level pressure anomalies; (**F**) downscaled IPSL-CM4 surface wind anomalies. (**G**) NCEP climatological surface winds and (**H**) sea level pressure; (**I**) IPSL-CM4 climatological surface winds and (**J**) sea level pressure. Predictor (predictand) fields are framed in blue (red). Note the change in color scale between global and regional maps for (B), (E), (H) and (J).

such sensitivity. Note however that similar assumptions are frequently made when producing future climate projections with global climate models, for instance when applying

parameterizations derived from modern observations to simulations with increased GHG emissions.

Goubanova et al. (2010) applied the relationship inferred from 2.5°x2.5° NCEP/NCAR reanalysis (Kalnay et al., 1996) wind and sea level pressure anomalies (fig. 1.28A and 1.28B) - relative to their respective seasonal cycles over 2000-2008 (fig. 1.28G and 1.28H) - and 0.5°x0.5° QuickSCAT satellite (CERSAT, 2002) wind anomalies (fig. 1.28C) (relative to the seasonal cycle over the same period) to 3.75°x2.5° wind and sea level pressure anomalies from the IPSL-CM4 (Marti et al., 2009) Pre-Industrial (fig. 1.28D and 1.28E) and 4xCO_2 simulations, relative to their respective seasonal cycles over the 1970-1999 period from the *« Climate of the 20th century »* simulation[1] (fig. 1.28I and 1.28J).

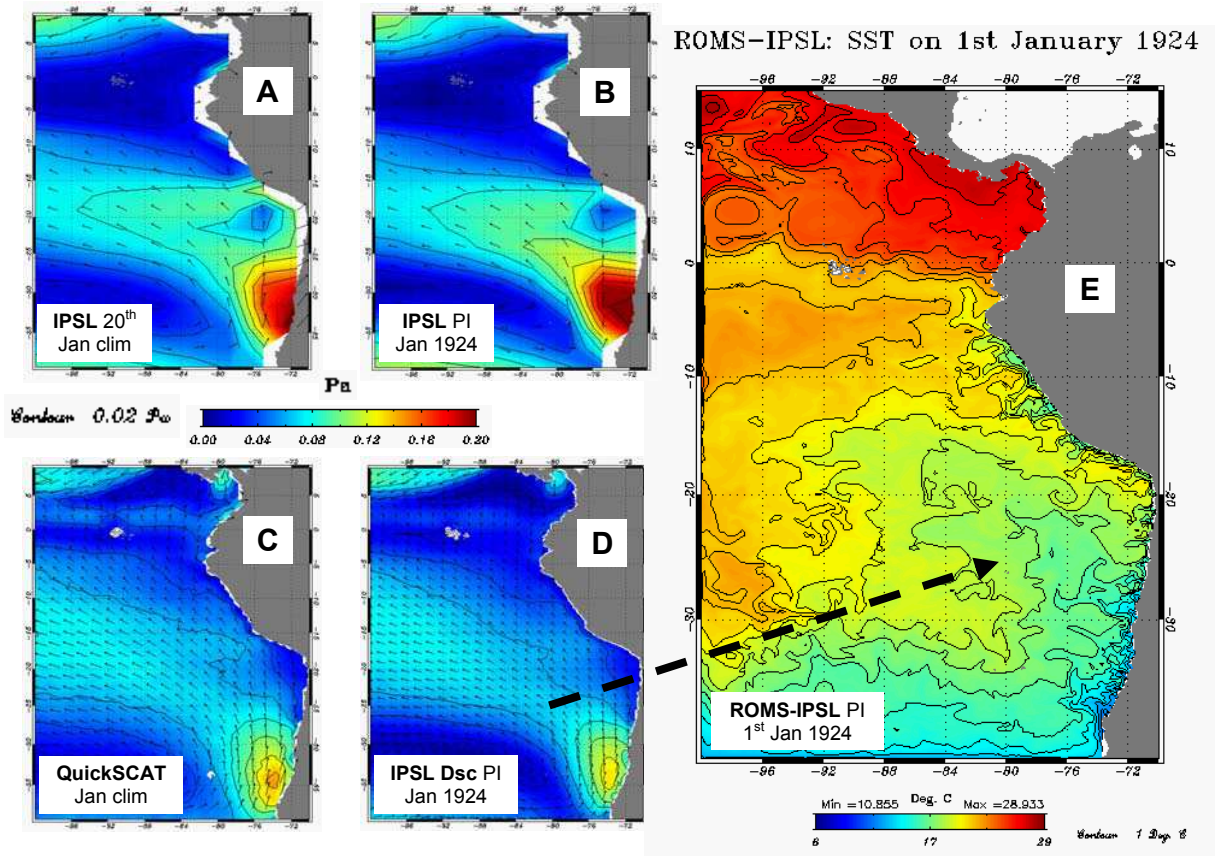

Fig. 1.29: Schematic of the ROMS wind forcing strategy (see text): (**A**) climatological surface winds for January from the IPSL-CM4 *« Climate of the 20th Century »* simulation; (**B**) surface winds for January 1924 from the IPSL-CM4 *« Pre-Industrial Control »* simulation; (**C**) climatological surface winds for January from QuickSCAT satellite measurements; (**D**) downscaled surface winds for January 1924 from the IPSL-CM4 *« Pre-Industrial Control »* simulation; (**E**) SST for 1st January 1924 from the ROMS simulation forced by downscaled winds from the IPSL-CM4 *« Pre-Industrial Control »* simulation. The black dashed arrow represents the wind forcing. The open boundary and atmospheric flux forcings are described in figure 1.31. The colour bar for SST (°C) is indicated below the corresponding panel (CI: 1°C). The colour bar for surface winds (Pa) is indicated on the left part of the figure (CI: 0.02 Pa). The size (resp. direction) of the arrows on (A, B, C, D) is for the magnitude (resp. direction) of surface wind.

[1] *In this scenario, CMIP3 model simulations are performed with historical levels of atmospheric CO_2 from 1850 to 2000.*

The reader is invited to refer to appendix A for a detailed explanation on the choice of the Pre-Industrial and 4xCO_2 climate scenarios and to Goubanova et al. (2010) for more details on the downscaling method and its validation. Note that IPSL-CM4 was identified as among the "best" CGCMs in the eastern South Pacific (chapter two). In particular, it features a good balance between zonal advective and thermocline feedbacks and hence a correct representation of ENSO variability (Belmadani et al., 2010), as well as a good reproduction of the subtropical anticyclone (Garreaud and Falvey, 2009).

Finally, the downscaled Pre-Industrial (fig. 1.28F) and 4xCO_2 wind anomalies were added to the QuickSCAT seasonal cycle in order to derive the total high-resolution (~50km) downscaled IPSL-CM4 surface wind fields (fig. 1.29). The main results are briefly presented in chapter four.

3) Downscaling of the oceanic forcing: similarly to Auad et al. (2006) for the California Current, Echevin et al. (2010) used a high-resolution regional oceanic model of the HCS (the same as the one described in chapter three) forced by CGCM outputs.

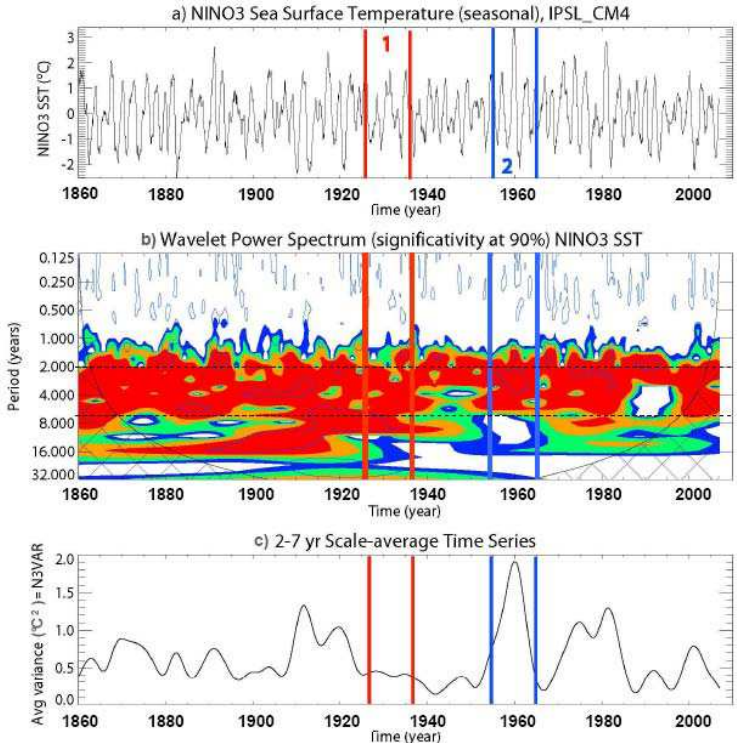

Fig. 1.30: Low-frequency modulation of ENSO over model years 1860-2007 for IPSL-CM4 Pre-Industrial simulation: **a)** Lowpass-filtered SST anomalies (f_c=1 year^{-1}) spatially averaged over the Niño3 region (150°W-90°W, 5°S-5°N); **b)** Corresponding wavelet power spectrum (only values above the 90% significance level are plotted); **c)** Corresponding 2-7 year scale-average time series, hereafter called N3VAR. Units are °C for a) and (°C)² for b) and c). The red (resp. blue) vertical lines limit the 1924-1933 (resp. 1955-1964) period characterized by weak (resp. strong) ENSO amplitude and modulation. The dotted black horizontal lines in b) indicate the (2-7 year)$^{-1}$ frequency band used to compute N3VAR.

They forced the regional model with the IPSL-CM4 surface winds downscaled as in Goubanova et al. (2010), for two selected 10-year periods of the Pre-Industrial and 4xCO_2 simulations (fig. 1.29). The selection of these time periods was performed in the framework of the present thesis and was based on indices of coupled-model derived ENSO activity in the tropical Pacific: the low-frequency modulation of niño3 SST interannual variability (see 1.2.5) allowed identifying periods with weak and stable ENSO amplitude (such as period 1 on fig. 1.30) and others with strong and varying ENSO amplitude (such as period 2 on fig. 1.30). Periods with a weak and stable ENSO were privileged in their study because the focus is on changes in the mean state and seasonal variability rather than interannual variability.

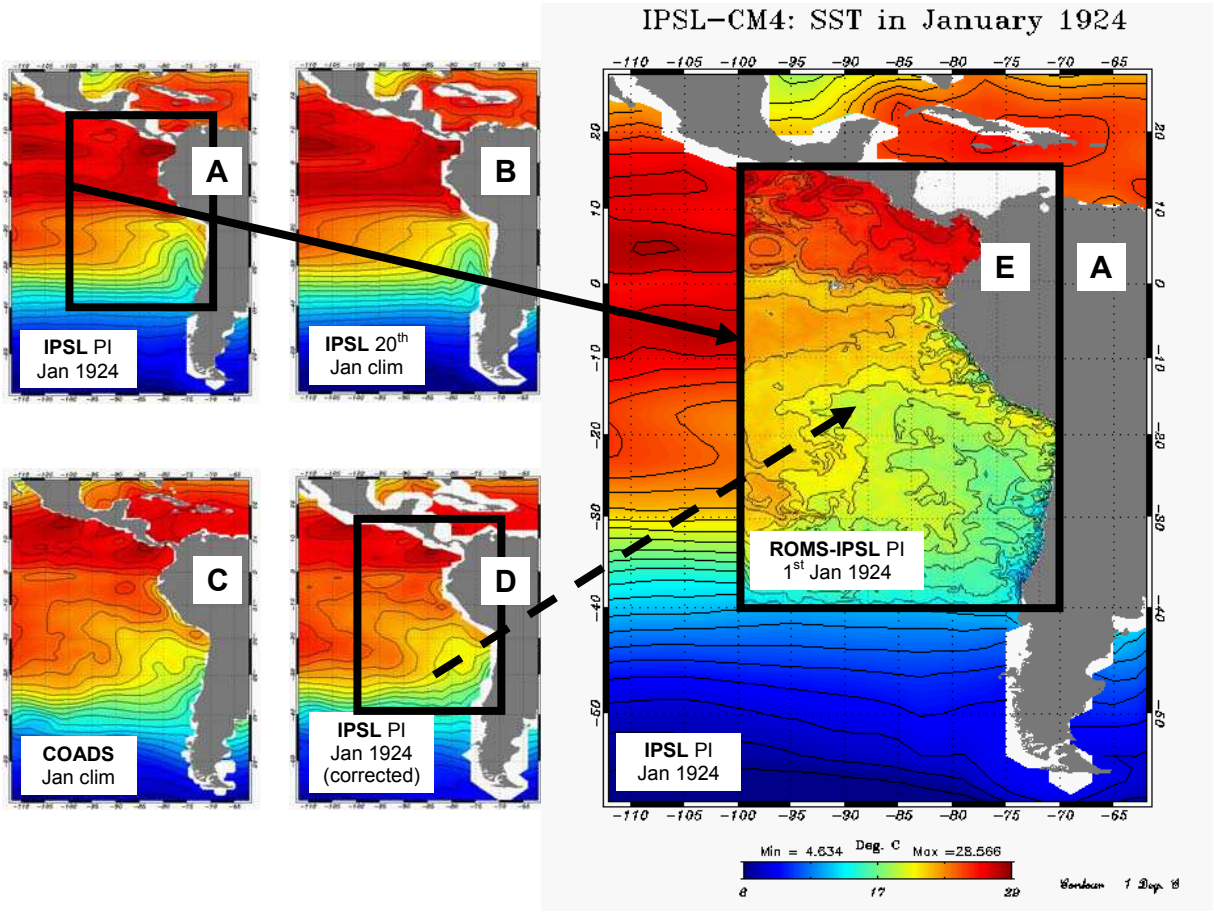

Fig. 1.31: Schematic of the dynamical oceanic downscaling and flux correction strategy (see text): (**A**) SST for January 1924 from the IPSL-CM4 *« Pre-Industrial Control »* simulation; (**B**) climatological SST for January from the IPSL-CM4 *« Climate of the 20th Century »* simulation; (**C**) climatological SST for January from COADS observed data; (**D**) corrected SST for January 1924 from the IPSL-CM4 *« Pre-Industrial Control »* simulation; (**E**) SST for 1st January 1924 from the ROMS simulation forced at the open boundaries (resp. at the free surface) by raw (resp. corrected) fields from the IPSL-CM4 *« Pre-Industrial Control »* simulation. The black rectangle is for the regional domain. The black plain (resp. dashed) arrow represents the open boundary forcing (resp. atmospheric flux forcing and restoring to COADS SST and SSS). The wind forcing is described in figure 1.29. The colour bar (°C) is indicated in the bottom right corner of the figure (CI: 1°C).

As a statistical downscaling approach could not be applied to IPSL-CM4 air/sea fluxes because of the lack of high-resolution *in-situ* data in the region needed to build the statistical model, the authors followed a flux correction strategy which is summarized on figure 1.31: 1) the seasonal cycles of heat fluxes, freshwater fluxes, SST and SSS restoring terms were computed over the 1960-2000 period from the IPSL-CM4 *« Climate of the 20th century »* simulation; and 2) substracted from the total fields from the Pre-Industrial and 4xCO_2 simulations in order to derive anomalies relative to present-day climate; 3) climatological 1°x1° COADS data (Da Silva et al., 1994) were finally added to the flux anomalies in order to produce the corrected fluxes used to force the regional model. The reader is invited to refer to Echevin et al. (2010) for more details. Open boundary and initial conditions for temperature, salinity, currents and sea level were directly extracted from IPSL-CM4 model outputs without any correction (fig. 1.31), as 1) the Pre-Industrial and 4xCO_2 global model simulations were initialized with present day climatological values from the World Ocean Atlas 2005 (Locarnini et al., 2006; Antonov et al., 2006), and 2) the regional model is able to generate its own ocean dynamics in spite of the influence of the open boundaries. The main results are briefly presented in chapter four. A regional control run performed in the framework of the thesis with the regional oceanic model over the recent period provides a benchmark for these regional climate change experiments (chapter three).

Objectives of the thesis

« How is climate change simulated by global coupled models of the current generation likely to influence the Peru-Chile upwelling system?» has been the main motivation for the definition of this PhD thesis. In this region of extremely high pelagic fish productivity and strong intraseasonal-to-decadal climate variability, such question is of great importance for societies of the surrounding countries whose economies heavily rely on the exportation of living marine resources. This central issue has lead to several related interrogations, such as:

- *« Which are the most reliable Coupled General Circulation Models (CGCMs) in the eastern South Pacific, and which metrics do we use to identify them? »*

-*« How reliable is the ROMS regional ocean model for the Humboldt Current System (HCS)? How does it account for the transmission of equatorial variability/equatorial waves to the coastal region? What is the deviation from simple linear theory? »*

- *« Does regional modeling of future climate change confirm trends and theories inferred from scarce historical observations and paleoclimate reconstructions? »*

We have addressed the first two questions during the development of the work presented here, with, as a background motivation, the need to complete the various steps required for downscaling experiments of climate projections. Some questions (including the last point mentioned above) could not be answered in the framework of the thesis, due to the extended scope of the project. These questions were addressed by others that participated to the PCCC project and with whom I collaborated. As mentioned in the introduction, the present PhD thesis is a key component of PCCC. Within the thesis, a major contribution to the PCCC project is located up-stream of the downscaling exercice itself: in addition to methodological developments undergone in the framework of PCCC, my work led to improved understanding of some physical mechanisms of interest to PCCC. In particular, progress has been accomplished concerning the specific question of the understanding of the biases of the CGCMs in terms of ENSO variability. In a second stage of the thesis, the main effort was dedicated to the understanding of the processes of oceanic teleconnection between equatorial Kelvin waves and coastal circulation in a regional high-resolution simulation with realistic boundary conditions. I also partipated to the analysis of the regional simulations with idealized climate change scenarios that were carried out within the PCCC project, and in particular to the assessment of competing warming and cooling feedback mechanisms at stake in the Peru-Chile region.

In the next chapter, we detail the methodology we used to select the subset of climate models which eventually provide the boundary forcing for the regional oceanic model. In chapter 3, the oceanic downscaling method is described, and applied to a configuration of the HCS with a realistic boundary forcing over the period 1992-2000. This regional simulation is used to document the main features of regional circulation and variability. A specific study on the impact of large scale equatorial variability on nearshore variability in the region is also presented in the same chapter, in order to better understand the link between climate variability and change at basin and regional scales. The simulation is also meant to be used as a reference run to assess the realism of the regional simulations obtained using the boundary forcing from the CGCMs. In the fourth and last chapter, preliminary results from regional climate change experiments are presented and discussed, before we conclude on the present PhD thesis and propose some future perspectives.

Chapter 2: Global Climate Models: ENSO and the Eastern South Pacific

This chapter is dedicated to the analysis of large scale climate as simulated by the IPCC models relevant to the study of the impact of global warming on the Humboldt Current System. Indeed, as detailed in the next two chapters, our modelling approach requires to downscale low resolution fields provided by the IPCC models to a regional oceanic model of the Peru-Chile upwelling system. Due to the heterogeneous behaviours of the climate models over many parts of the world including the Pacific Ocean, the most 'realistic' models under past/present climate have to be identified first in order to provide regional climate projection scenarios with the best possible confidence. For this purpose, we need to define criteria that correspond to key climate features that a model has to represent as accurately as possible. From the introduction, we have identified two main criteria: the reliability of **ENSO-like variability** over the tropical Pacific Ocean, and the simulated **mean oceanic state and variability** in the Eastern South Pacific. The representation of the atmospheric forcing in the eastern South Pacific, namely the subtropical anticyclone and the associated equatorward winds, is also assessed. However, it was not retained as a selection criterion, since: 1) few models are shown to qualify for the first two criteria (see below), and 2) the statistical downscaling procedure of the atmospheric forcing allows correcting a large fraction of the large-scale biases exhibited by the coupled models (see chapter four). Nevertheless, a brief description of these features is given in this chapter.

The choice of the two retained criteria was motivated by the observed behaviour of the Humboldt Current System. It is known for instance that the coasts of Peru and Chile undergo dramatic changes during an El Niño event (see previous chapter), which include changes in regional climate (Strub et al., 1998; Bakun and Weeks, 2008; Goubanova et al., 2010) and ocean dynamics (Huyer et al., 1987; Blanco et al., 2002; Carr et al., 2002; Colas et al., 2008), as well as in marine ecosystems and fisheries (Barber and Chavez, 1983). The name El Niño itself was given by fishermen from the coasts of northern Peru and Ecuador. An accurate representation of ENSO is thus of primary importance for the purpose of simulating regional ocean circulation on interannual time scales. Likewise, the future of the HCS depends to a large extent on the future evolution of ENSO under global warming. The CMIP3 multi-model

ensemble gathers the latest generation of CGCMs (Meehl et al., 2007), which have been improving significantly in the representation of ENSO during recent years (AchutaRao and Sperber, 2002; 2006; Joseph and Nigam, 2006). Most CMIP3 models exhibit ENSO-like variability (*e.g.* van Oldenborgh et al., 2005; Capotondi et al., 2006; Guilyardi, 2006), with periods within the observed 2-7 years range and a fair representation of SST anomalies over the eastern tropical Pacific (AchutaRao and Sperber, 2006). Yet, they still feature many errors in both the simulated ENSO variability (amplitude, period, asymmetry, regularity, spatial pattern) and the simulated background climate (see Guilyardi et al., 2009 for a review on these issues). As mentioned in the introductory chapter, ENSO involves competing feedback processes - and a near-annual coupled mode of tropical Pacific variability (see below) - which participate to shape the structure and dynamics of ENSO variability. Hence, assessing these feedbacks in CMIP3 models is of primary importance for the identification of the most reliable models in regard to ENSO and its future evolution.

On the other hand, dynamics of the Peru-Chile upwelling are influenced by the water masses and the large-scale circulation present in the Eastern South and tropical Pacific regions (see previous chapter): in particular, a part of the waters upwelled along the coast are of equatorial origin. They are transmitted from the equatorial Pacific to the coastal region off western South America via the equatorial current system and then via the poleward Peru-Chile undercurrent (Lukas, 1986; Huyer et al., 1987; Croquette, 2007; Montes et al., 2009). It therefore appears necessary to assess the properties of the water masses that are imposed at the limits of the regional oceanic model because these properties will directly impact coastal upwelling dynamics. The atmospheric forcing is also very important in eastern boundary systems such as the HCS because the variability of coastal upwelling is governed to a large extent by Ekman dynamics (see previous chapter).

The analysis is divided into three parts. First, physical mechanisms of ENSO-like variability are assessed in the IPCC multi-model ensemble, and implications on the structure of the dominant ENSO mode are discussed. The conducted work is the subject of an article entitled « ENSO feedbacks and associated time scales of variability in a multi-model ensemble » by A. Belmadani, B. Dewitte and S.-I. An, which was recently accepted by the *Journal of Climate* (in January 2010). Section 1. is a transcription of this article. Second, results from this study are complemented in section 2. by the description of the role of the near-annual mode on ENSO dynamics. In the same section, models identified in section 1. as the most reliable in regard to ENSO-related processes are further assessed in terms of spatial and

temporal properties of ENSO, which allows reducing the subset of models to be used for the regional downscaling. Finally, in section 3., the mean state and variability at the open boundaries of the regional domain are assessed for the remaining models, allowing us to reduce even more the subset of relevant models for our regional climate change study. In the same section, main characteristics of the wind forcing are given for the same models.

2.1. ENSO feedbacks and associated time scales of variability in a multi-model ensemble

Ali Belmadani[1,2], Boris Dewitte[1,2] and Soon-Il An[3]

[1] Université de Toulouse; UPS (OMP-PCA); LEGOS, 14 Av. Edouard Belin, F-31400 Toulouse, France

[2] IRD; LEGOS, F-31400 Toulouse, France

[3] Department of Atmospheric Sciences/Global Environment Laboratory, Yonseï University, Seoul, South Korea

Submitted to *J. Climate*

3rd of September, 2008

Revised version #1

25th of May, 2009

Revised version #2

17th of November, 2009

Revised version #3 (accepted)

28th of January, 2010

Corresponding Author: Ali Belmadani, Université de Toulouse; UPS (OMP-PCA); LEGOS, 14 Av. Edouard Belin, F-31400 Toulouse, France. E-mail: ali.belmadani@ird.fr

Résumé

L'état moyen du Pacifique équatorial détermine la prévalence d'un ENSO 'lent' de type oscillateur rechargé sur un ENSO 'rapide' de surface quasi-biennal, le premier étant contrôlé dans une large mesure par le *thermocline feedback*, et le second étant relié à un *zonal advective feedback* amplifié. Dans cette etude, nous utilisons des diagnostiques dynamiques pour étudier l'importance relative de ces deux *feedbacks* (rétroactions) dans le *Coupled Model Intercomparison Project*, ainsi que sa relation avec les différences de variabilité de type ENSO observées parmi les modèles. La contribution des termes d'advection (verticale contre zonale) au taux de variation de la TSM est estimée à l'aide d'un modèle océanique du Pacifique tropical de type intermédiaire, 'paramétrisé' à partir des sorties des CGCMs, ce qui permet de classifier ces derniers en 3 groupes qui prennent en compte les processus de rétroaction dominants du cycle ENSO: l'advection zonale, située principalement dans le Pacifique Ouest, l'advection verticale, située principalement dans le Pacifique Est, et la combinaison de ces deux mécanismes. Un nouveau résultat apporté par cette étude est le fait que les biais des termes d'advection sont liés dans une large mesure aux biais de la circulation de surface moyenne, lesquels sont utilisés pour déterminer le feedback ENSO dominant pour chaque CGCM. En se basant sur cette classification, l'analyse révèle aussi que les modèles présentent des comportements distincts en ce qui concerne les caractéristiques d'ENSO: pour la plupart des modèles, une contribution amplifiée (resp. diminuée) du zonal advective feedback est associée à un ENSO plus rapide (resp. plus lent) et à une tendance vers un état moyen plus froid (resp. plus chaud) dans le Pacifique Ouest et central. Ces résultats supportent l'interprétation selon laquelle les biais de l'état moyen sont entretenus par le mode de variabilité privilégié associé au mécanisme de rétroaction dominant dans les modèles. En particulier, les modèles avec un zonal advective feedback dominant présentent une asymétrie 'froide' de TSM (ou *skewness* négative) dans l'Ouest du Pacifique équatorial.

Abstract

The background state of the equatorial Pacific determines the prevalence of a 'slow' recharge oscillator-type ENSO over a 'fast' quasi-biennial surface-driven ENSO. The first is controlled to a large extent by the thermocline feedback, whereas the latter is related to enhanced zonal advective feedback. In this study, we use dynamical diagnostics to investigate the relative importance of these two feedbacks in the Coupled Model Intercomparison Project and its relation with the differences in ENSO-like variability among the models. The focus is on the role of the mean oceanic surface circulation in controlling the relative weight of the two feedbacks.

By the means of an intermediate-type ocean model of the tropical Pacific 'tuned' from the CGCM outputs, the contribution of the advection terms (vertical versus zonal) to the rate of SST change is estimated. A new finding is that biases in the advection terms are to a large extent related to the biases in the mean surface circulation. The latter are used to infer the dominant ENSO feedback for each CGCM. This allows classifying the CGCMs in 3 groups that account for the dominant feedback process of the ENSO cycle: horizontal advection (mainly in the western Pacific), vertical advection (mainly in the eastern Pacific), and the combination of both mechanisms.

Based on such classification, the analysis also reveals that the models exhibit distinctive behaviour with respect to the characteristics of ENSO: for most models, an enhanced (resp. diminished) contribution of the zonal advective feedback is associated to faster (resp. slower) ENSO and a tendency towards a cooler (resp. warmer) mean state in the western-to-central Pacific Ocean. The results support the interpretation that biases in the mean state are sustained/maintained by the privileged mode of variability associated to the dominant feedback mechanism in the models. In particular, the models having a dominant zonal advective feedback exhibit significant cold SST asymmetry (or negative skewness) in the western equatorial Pacific.

2.1.1. Introduction

The reliability of climate projections for the next century depends on the accuracy of Coupled General Circulation Models (CGCMs) in representing the effect of the increasing concentration of greenhouse gases on the climate system at global and regional scales. It also depends on their ability to simulate realistic past and present climate variability and coupled ocean-atmosphere processes at different time scales. Of particular interest, the El Niño-Southern Oscillation (ENSO) is the dominant source of interannual variability in the tropical climate system. It has been well-known for its impacts on weather, ecosystems and societies in the surrounding countries of the Pacific Ocean and even worldwide. Yet, a wide range of other coupled ocean-atmosphere modes of variability coexist at different time scales within the frequency spectrum of interannual variability: they range from near-annual (Jin et al., 2003; Kang et al., 2004) and quasi-biennial (Meehl, 1987; Ropelewski et al., 1992) to decadal (Tourre et al., 1999; Zhang et al., 1999) time scales.

However, most CGCMs fail to reproduce such a rich spectrum (AchutaRao and Sperber, 2002; 2006). This includes those from the CMIP3 multi-model dataset, collected for the needs of the Intergovernmental Panel on Climate Change Fourth Assessment Report (IPCC-AR4). In particular, many of them tend to produce a faster ENSO than observed, confined to the quasi-biennial time scale (Guilyardi et al., 2004). The tendency of a model to privilege one time scale of variability over the others has to be related to the basic dynamics of the coupled tropical Pacific system.

In this respect, some studies (An and Wang, 2000; Wang and An, 2001) have shown that the frequency of ENSO is dependent on the spatial structure of zonal wind stress anomalies, especially the longitudinal position of the westerly anomalies. An and Wang (2000) argue that the delayed oscillator theory (Suarez and Schopf, 1988; Schopf and Suarez, 1988; Battisti and Hirst, 1989) only qualitatively describes the effect of the zonal location of the wind anomalies on the ENSO frequency: according to the authors, the time scales related to the negative feedback induced by equatorial wave dynamics (involving the propagation and reflection of Kelvin and Rossby waves) fail to reproduce the observed and modelled ENSO frequencies. Instead, the zonal position of the zonal wind stress anomalies directly influences the zonal currents in the central equatorial Pacific. As a result, the zonal advection of mean SST by the anomalous zonal currents, called the ‘zonal advective feedback’, is involved. According to An and Wang (2000), the zonal advective feedback favors the transition of the ENSO cycle rather than the growth and consequently a shorter oscillation of 2-4 years with a lower amplitude when the zonal wind stress is shifted westwards. Conversely, when the zonal wind stress is shifted eastwards, the zonal advective feedback favors the growth of the ENSO cycle rather than the

transition and consequently a longer oscillation of 4-6 years with a higher amplitude (An et al., 1999; An and Wang, 2000).

Easterly wind anomalies can also influence the feedbacks of the ENSO cycle: for instance, the observed post-1970s central Pacific surface warming induced anomalous easterlies in the eastern Pacific as a result of the strengthening of the trade winds. This caused the mean upwelling to increase. As a result, the vertical advection of subsurface temperature by the mean upwelling, called the 'thermocline feedback', was enhanced (Wang and An, 2001). Consequently, the eastward migration of both SST anomalies associated with ENSO and anomalous surface zonal wind stress caused a prolongation of the ENSO period: indeed, such migration was associated to an increased oceanic adjustment time of recharge/discharge (An and Wang, 2000), accordingly to the recharge oscillator paradigm (Jin, 1997a,b).

These results support the interpretation that the balance between the zonal advective feedback and the thermocline feedback - which are important contributors to the heat budget of the upper ocean in the Pacific basin (Hirst, 1986) - is a key parameter in the determination of the structure and dynamics of the coupled ENSO mode and the frequency of the ENSO cycle. The two feedback mechanisms destabilize different leading coupled modes: whereas the thermocline feedback favours the 'recharge oscillator mode' (Jin, 1997a,b) characterized by a strong ENSO with a longer 4-6 years oscillation, the zonal advective feedback involves the 'gravest ocean basin mode' (Jin and Neelin, 1993) characterized by a weak ENSO with a shorter 2-4 years oscillation (An and Jin, 2001).

On the other hand, Jin and An (1999) proposed an extension of the recharge oscillator model (Jin, 1997a,b) - which initially focused on the thermocline feedback alone and the slow dynamics of ENSO - by including the zonal advective feedback in the SST equation. They show that both feedbacks are dynamically connected through the geostrophic balance between the upper ocean zonal currents and the meridional gradient of the thermocline depth. They also show that the two feedbacks contribute in a similar way to the transition and growth of ENSO (see also An and Jin (2001), Kang et al. (2001)). In fact, both feedbacks have to be taken into account in order to explain the main properties of ENSO (*e.g.* the simultaneous development of SST anomalies throughout the central to eastern Pacific), conversely to earlier theoretical studies which considered the zonal advective feedback alone (Picaut et al., 1997) or the thermocline feedback alone (Suarez and Schopf, 1988; Jin, 1997a,b).

An and Jin (2001) used the conceptual model of Jin and An (1999) to further explore the sensitivity of ENSO growth rate and frequency to the basic state parameters that control the strength of the zonal advective feedback and the thermocline feedback. They showed that whereas the thermocline feedback (zonal advective feedback) considered alone leads to eigenmodes in the low-

frequency (high-frequency) regime under 0.3 $year^{-1}$ (above 1 $year^{-1}$), the combined effect of both feedbacks on the frequency regime is sensitive to the mean state. This result is consistent with the observed change in ENSO frequency and amplitude after the late 1970s climate shift (An and Wang, 2000; Wang and An, 2001).

A similar approach making use of a simplified version of the Cane-Zebiak (CZ) coupled model (Zebiak and Cane, 1987) was adopted by Fedorov and Philander (2001): they performed a stability analysis, *i.e.* they studied the tendency of the model to favour one coupled mode of oscillation over the other in response to changes in basic parameters of the mean state: intensity of the trade winds, thermocline depth, and temperature difference across the thermocline. Their analysis revealed the existence of 2 types of unstable modes: the 'delayed oscillator' mode with long oscillations (~ 5 years), driven by vertical movements of the thermocline as a result of the basin-wide adjustment of the ocean to wind changes, and the 'SST' mode with a shorter time scale (~2 years), controlled by advection and by entrainment across the thermocline. In spite of a slightly different formalism (including a focus on the importance of the mean thermocline rather than the mean upwelling), these results resemble those obtained by An and Jin (2001). They confirm the importance of the mean state and the associated balance between thermocline and zonal advective feedbacks upon ENSO frequency. In fact, both feedbacks coexist in the real world, which makes ENSO a hybrid coupled mode (Fedorov and Philander, 2000).

Long term CGCM simulations from an extensive multi-model dataset offer the opportunity to document the role of the balance between ENSO feedbacks in setting the time scale of ENSO variability and the characteristics of the mean state. Some recent studies have been dedicated to the understanding of the numerous biases in the mean state exhibited by CGCMs of the current generation (AchutaRao and Sperber, 2006), which contribute to limit their current skill for climate change projections. The assessment of the stability of the models is particularly interesting as it provides material for the understanding of the models' biases and the characteristics of the simulated ENSO variability (Battisti and Hirst, 1989; Jin and Neelin, 1993; Fedorov and Philander, 2001). For this purpose, most studies have been relying on statistical analyses from the model outputs in order to estimate the strength of the thermocline feedback versus the zonal advective feedback.

For instance, van Oldenborgh et al. (2005) – hereafter refered to as 'VPC05' - show that among the CMIP3 simulations, the ones that present the higher-frequency ENSO cycle are the ones that have a weak east Pacific upwelling feedback loop (and consequently enhanced zonal advective cooling). In their formalism, the zonal advective feedback (resp. thermocline feedback) is quantified from the linear regression between the rate of Sea Surface Temperature (SST) change and the zonal

wind stress (resp. thermocline depth) anomalies in the equatorial band (Burgers and van Oldenborgh, 2003).

On the other hand, Guilyardi (2006) – hereafter refered to as 'G06' - proposes the concept of S-mode (SST mode) and T-mode (thermocline mode) described by several authors (Hirst, 1986; Neelin et al., 1998; Fedorov and Philander, 2001) to classify the IPCC models in groups according to their privileged ENSO regime (S-mode regime or hybrid mode regime). His diagnostic, based on lag-correlation analyses between ENSO indices (Trenberth and Stepaniak, 2001), allows separating westward and eastward propagations of SST anomalies. Indeed, the S-mode which is related to the zonal advective feedback presents low amplitude, high frequency ENSO cycles with westward propagating anomalies. On the other hand, the thermocline feedback-related T-mode features high amplitude, low frequency ENSO cycles and eastward propagations. The dominant direction of propagation is determined by the effect of ocean-atmosphere coupling on equatorial Kelvin and Rossby wave dynamics, as underlined by Hirst (1986): the zonal advective feedback (resp. thermocline feedback) tends to destabilize the first baroclinic mode Rossby wave (resp. the Kelvin wave) and to damp the Kelvin wave (resp. the first baroclinic mode Rossby wave), thus favouring westward (resp. eastward) propagating features.

These statistical approaches provide meaningful pieces of information to understand the model biases and assess their realism. However, by construction, they do not explicitly resolve the underlying mechanisms responsible for the tendency of a model to favour one regime over the other. In addition, they do not consider non-linearities which participate to the feedback processes and can drastically imprint characteristics of the ENSO variability (Timmermann and Jin, 2002).

In the present study, a different approach is proposed. It is based on the use of a simple dynamical ocean model tuned from the CGCMs to infer the feedback processes most responsible for the model biases. As a complement to the studies by VPC05 and G06, the focus is on the dominance of the zonal advective feedback over the thermocline feedback in the CGGMs. Our objectives are two folds: 1) investigate the relevance of dynamical regimes for classifying the IPCC models; 2) target the key physical processes responsible for the prevalence of one regime over the other in the CGCMs. Overall, we aim at providing a physical interpretation of the model simulations and indices to understand the models' responses to increased CO_2 (and assess their relevance for the study of the impact of climate change on ENSO variability).

Similar diagnostics to the ones used by Dewitte et al. (2007a) to study ENSO variability are applied here to the CGCMs of the CMIP3 archive, extending their approach to a more comprehensive data set. It is verified that in most cases, the too high (resp. too low) ENSO frequency and the cold

(resp. warm) bias of the mean temperature state can be related to the over-estimation (resp. under-estimation) of particular coupled feedback processes. This allows classifying the models in three relevant groups for the understanding of ENSO dynamics and the interpretation of biases: zonal advective feedback, thermocline feedback and hybrid feedback-dominated models.

The paper is organised as follows. Section 2 is devoted to the presentation of the multi-model dataset and the reanalysis products used in this study. The methodology will also be detailed in this section. Section 3 describes some characteristics of the ENSO mode in the multi-model ensemble, as well as the mean biases related to both zonal advective and thermocline feedbacks. Section 4 is a discussion, followed by concluding remarks in section 5.

2.1.2. Datasets and methodology

2.1.2.1. Datasets

Model Number	Model Name	Modelling Group	Atmosphere Resolution	Ocean Resolution	Length of Simulation (yrs)
1	BCCR-BCM2.0	BCCR/NERSC/GFI (Norway)	1°x1°L31	1°x1°L33	155
2	CCCMA-CGCM3.1	CCCMA (Canada)	3.75°x3.71°L31	1.88°x1.86°L29	155
3	CCCMA-CGCM3.1-t63	CCCMA (Canada)	2.81°x2.79°L31	1.41°x0.93°L29	155
4	CNRM-CM3	Météo France/CNRM (France)	2.81°x2.79°L45	2°x1°L33	150
5	CSIRO-MK3.0 (run1)	CSIRO (Australia)	1.88°x1.86°L18	1.88°x0.93°L31	134
6	CSIRO-MK3.5	CSIRO (Australia)	1.88°x1.86°L18	1.88°x0.93°L31	134
7	GFDL-CM2.0	NOAA GFDL (USA)	2.5°x2°L24	1°x0.33°L50	129 (U) 150 (T,S,SST,τ)
8	GFDL-CM2.1	NOAA GFDL (USA)	2.5°x2.02°L24	1°x0.33°L50	150
9a	GISS-AOM (run1)	NASA/GISS (USA)	4°x3°L12	4°x3°L31	155
9b	GISS-AOM (run2)	NASA/GISS (USA)	4°x3°L12	4°x3°L31	155
10	GISS-MODEL-E-H	NASA/GISS (USA)	5°x4°L20	1°x1°L33	125
11	GISS-MODEL-E-R	NASA/GISS (USA)	5°x4°L20	5°x4°L33	104
12	IAP-FGOALS1.0-g (run1)	LASG/IAP (China)	2.81°x2.79°L26	1°x1°L33	155
13	INGV-ECHAM4	INGV (Italy)	1.125°x1.12°L19	1°x1°L33	100
14	INM-CM3.0	INM (Russia)	5°x4°L21	2.5°x2°L33	134
15	IPSL-CM4	IPSL (France)	3.75°x2.54°L19	2°x1°L31	147
16	MIROC3.2-HIRES	CCSR/NIES/FRCGC (Japan)	1.125°x1.12°L56	1.125°x0.56°L33	100
17	MIROC3.2-MEDRES	CCSR/NIES/FRCGC (Japan)	2.81°x2.79°L20	1.41°x0.56°L33	150
18	MIUB-ECHO-G	MIUB (Germany)	3.75°x3.71°L19	2.81°x0.5°L20	147
19	MPI-ECHAM5	MPI (Germany)	1.88°x1.87°L32	1°x1°L40	123
20	MRI-CGCM2.3.2A	MRI (Japan)	2.81°x2.79°L30	2.5°x0.5°L23	154
21	NCAR-CCSM3.0 (run2)	NCAR (USA)	1.41°x1.40°L26	1.125°x0.27°L40	150
22	UKMO-HadCM3 (run1)	Met Office (UK)	3.75°x2.5°L19	1.25°x1.25°L20	148
23	UKMO-HadGEM1	Met Office (UK)	1.875°x1.25°L38	1°x0.34°L40	78 (U,T,S) 147 (SST,τ)

Table 1. Description of the coupled models considered in this study. The run number is specified if there is more than one ensemble member (different initial conditions). Resolutions are given along the equator. Due to gaps in the data some models show variables with different time spans.

The multi-model ensemble used in this study is presented in table 1. It consists of the CGCMs of the CMIP3 dataset that have provided enough data on 25 July 2007 through the IPCC data center at PCMDI, or for some of them (BCCR-BCM2.0, MPI-ECHAM5 and NCAR-CCSM3.0) directly from the modelling groups (for a part of the data at least).

The pre-industrial control experiment (picntrl) - for which the concentration of greenhouse gases is fixed to estimates from 1850 - was chosen in order to evaluate the performance of the models under past/present climate conditions for three main reasons: 1) this experiment is the one that provides the longest time series and thus the best statistical confidence; 2) the fixed external forcings for long time series make these simulations appropriate for the study of the physical mechanisms of natural climate variability; and 3) make the analyses at interannual to decadal scales much easier to conduct (no need to remove the trend as in the « 20c3m » climate of the 20th century experiment for instance). Monthly outputs were used since we focus on low frequency mechanisms.

CMIP3 model outputs were compared to those provided by the SODA reanalysis project, an ongoing effort to reconstruct historical ocean climate variability on space and time scales similar to those captured by the atmospheric reanalysis projects. In this paper, we used the monthly outputs of SODA 1.4.2 version. SODA uses an Ocean General Circulation Model (OGCM) based on the Parallel Ocean Program numerics (Smith et al., 1992), with a 0.25°x0.4° horizontal resolution at the equator and 40 vertical levels with 10m spacing near the surface. The constraint algorithm is based on optimal interpolation data assimilation. Assimilated data includes temperature and salinity profiles from the World Ocean Database 2001 (MBT, XBT, CTD, and station data), as well as additional hydrography, SST, and altimeter sea level. The model was forced by daily surface winds provided by the European Center for Medium Range Weather Forecasts (ECMWF) ERA-40 reanalysis (Uppala et al., 2005) for the 44-year period from January 1, 1958 to December 31, 2001. Surface freshwater flux for the period 1979 to present were provided by the Global Precipitation Climatology Project monthly satellite-gauge merged product (Adler et al., 2003), combined with evaporation obtained from the same bulk formula used to calculate latent heat loss. The reader is invited to refer to Carton et al. (2000) and Carton and Giese (2008) for a more detailed description of the SODA system.

In order to assess the realism of the chosen reference, CMIP3 model outputs were also compared to those from NCEP Global Ocean Data Assimilation System (Hereafter GODAS) (Behringer and Xue, 2004). Like SODA, GODAS is a global ocean reanalysis, but it covers a shorter period, from 1980 to 2007. It is based on the GFDL Modular Ocean Model version 3 (Pacanowski and Griffies, 2000), with a 1° zonal x 1/3° meridional resolution at the equator and 40 vertical levels with 10m spacing near the surface. The three-dimensional variational data assimilation scheme

originally designed by Derber and Rosati (1989) was modified to include salinity profiles (derived from temperature profiles using a local T-S climatology based on the World Ocean Database 1998). Assimilated data also includes temperature profiles from XBT, TAO, TRITON and PIRATA moorings and from Argo profiling floats. Momentum, heat and freshwater fluxes are from the NCEP atmospheric Reanalysis 2 (Kanamitsu et al., 2002).

The NOAA Extended Reconstructed Sea Surface Temperature (ERSST) version 3 monthly data, available on a 2° global grid (Smith et al., 2008), was used to provide a third independent estimate for the length of the ENSO cycle. This data set covers the 129-year 1880-2008 period.

2.1.2.2. Method

Diagnosing the ENSO mode:

The ENSO mode was diagnosed from the results of the Singular Value Decomposition (SVD; e.g. Bretherton et al., 1992) between the SST and wind stress anomalies in the tropical Pacific Ocean (11°S-11°N) over the whole available time period (table 1). The term anomalies used in this paper refers to the monthly model outputs from which monthly climatology has been removed.

The period of the ENSO cycle is defined here as the period associated to the dominant significant peak in the 1 to 10-year frequency range of the Fast Fourrier Transform (FFT) power spectrum of the time serie associated to the first SVD mode for SST anomalies. The statistical significance of such peak was assessed against red noise level with the same lag-1 autocorrelation (Torrence and Compo, 1998). The spectrum was computed by ensemble-averaging the spectra obtained from a 20-year running window (15 years for the reanalysis products that span a shorter period) with a 50% overlapping factor and hann filtering, in order to increase the number of degrees of freedom and thus gain statistical confidence in the detected peaks.

The only drawback of this method is that the frequency axis of the resulting smoothed spectrum has a low resolution in the interannual band: this implies wide error bars for the obtained estimates of the ENSO period. In order to reduce significantly such uncertainty, the running window used to compute the spectra would need to be, say, five times wider. This would require 500-year simulations from the multi-model ensemble, whereas only 100-150 years of data were available for most CGCMs. Another issue related to the relatively short length of the simulations is that centennial-scale ENSO modulation is ignored. Yet, it has been recently shown to have a significant influence on the spectral properties of ENSO in a 2000-year simulation of the GFDL-CM2.1 model (Wittenberg, 2009). Caution is therefore needed for the interpretation of the results from the FFT analysis

performed here, as discussed in section 3.3. The values for the ENSO period are expected to be slightly larger than the ones obtained from the Niño3-SST index (G06): indeed, the geographical domain used for this study has a wider meridional extension and thus the SVD analysis tends to capture some 'slower' variability modes.

Model Name	*ENSO Period (yrs)*
SODA 1.4.2	3.7
GODAS	5.0
BCCR-BCM2.0	4.0
CCCMA-CGCM3.1	---
CCCMA-CGCM3.1-t63	---
CNRM-CM3	3.3
CSIRO-MK3.0 (run1)	2.0
CSIRO-MK3.5	5.0
GFDL-CM2.0	3.3
GFDL-CM2.1	5.0/2.5
GISS-AOM (run1)	---
GISS-AOM (run2)	---
GISS-MODEL-E-H	---
GISS-MODEL-E-R	---
IAP-FGOALS1.0-g	3.3
INGV-ECHAM4	4.0
INM-CM3.0	3.3
IPSL-CM4	2.5
MIROC3.2-HIRES	---
MIROC3.2-MEDRES	---
MIUB-ECHO-G	2.0
MPI-ECHAM5	4.0
MRI-CGCM2.3.2A	2.0
NCAR-CCSM3.0 (run2)	2.2
UKMO-HadCM3 (run1)	2.9
UKMO-HadGEM1	4.0

Table 2. ENSO Periods of the models.

Results of the SVD are presented for the multi-model ensemble in figure 1, and the estimated ENSO periods are listed in table 2. Consistently with previous analyses (VPC05; Capotondi et al., 2006; G06), though most CGCMs are able to capture ENSO-like interannual variability, they show a great diversity of spatial patterns for both wind stress and SST anomalies, together with a wide range of dominant ENSO frequencies: from 2.0 years (CSIRO-MK3.0, MIUB-ECHO-G and MRI-CGCM2.3.2A) to 5.0 years (CSIRO-MK3.5 and GFDL-CM2.1), SODA showing a typical ENSO period of 3.7 years.

In order to check the validity of the ENSO period estimate provided by the SVD analysis computed with SODA, the spectrum of Niño3 SST anomalies was computed from the ERSST data set (not shown). With a 15-year running window, the ENSO periods over both the 44-year SODA period (1958-2001) and the 129-year ERSST period (1880-2008) are equal to the value obtained from the SVD performed with SODA: 3.7 years. Note however that with a 20-year window (like for the CGCMs) over the entire period covered by ERSST, ENSO is characterized by a 3.3 years period. These results validate to a large extent the SVD approach and the choice of SODA to estimate the observed length of the ENSO cycle. However, they raise the issue of the width of the moving window and hence the issue of the limited time periods spanned by the reanalyses. Caution is thus needed here for interpreting the modelled ENSO time scales in case of small differences with SODA (~0.3-0.4 years). Note that GODAS, which considers the period after the 1976 climate shift known to be characterized with lower ENSO frequency (Moon et al., 2004), exhibits a longer time scale.

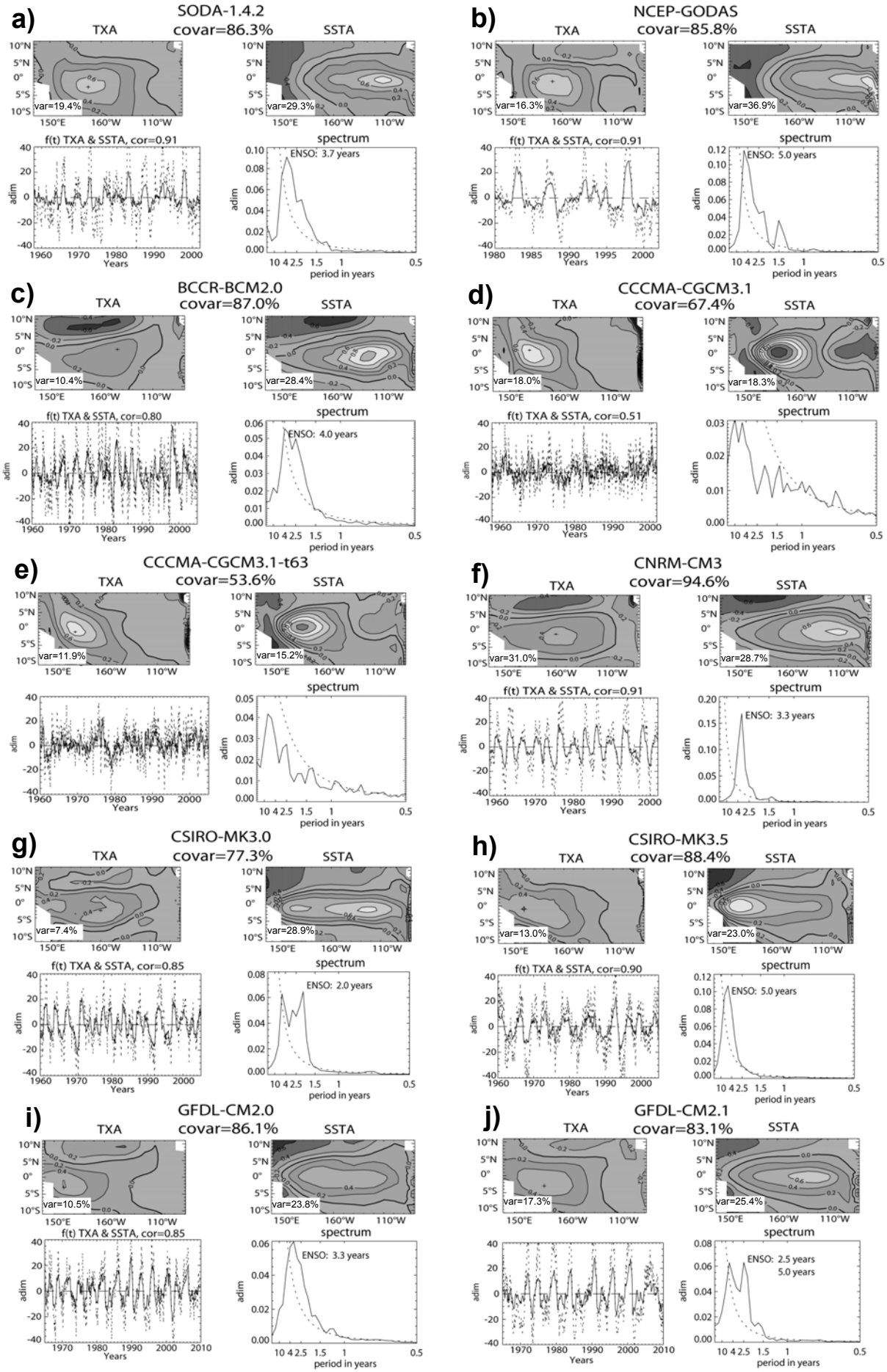
a)
SODA-1.4.2
covar=86.3%
TXA
SSTA
var=19.4%
var=29.3%
f(t) TXA & SSTA, cor=0.91
spectrum
ENSO: 3.7 years
b)
NCEP-GODAS
covar=85.8%
var=16.3%
var=36.9%
f(t) TXA & SSTA, cor=0.91
ENSO: 5.0 years
c)
BCCR-BCM2.0
covar=87.0%
var=10.4%
var=28.4%
f(t) TXA & SSTA, cor=0.80
ENSO: 4.0 years
d)
CCCMA-CGCM3.1
covar=67.4%
var=18.0%
var=18.3%
f(t) TXA & SSTA, cor=0.51
ENSO: 3.3 years
e)
CCCMA-CGCM3.1-t63
covar=53.6%
var=11.9%
var=15.2%
f)
CNRM-CM3
covar=94.6%
var=31.0%
var=28.7%
f(t) TXA & SSTA, cor=0.91
ENSO: 3.3 years
g)
CSIRO-MK3.0
covar=77.3%
var=7.4%
var=28.9%
f(t) TXA & SSTA, cor=0.85
ENSO: 2.0 years
h)
CSIRO-MK3.5
covar=88.4%
var=13.0%
var=23.0%
f(t) TXA & SSTA, cor=0.90
ENSO: 5.0 years
i)
GFDL-CM2.0
covar=86.1%
var=10.5%
var=23.8%
f(t) TXA & SSTA, cor=0.85
ENSO: 3.3 years
j)
GFDL-CM2.1
covar=83.1%
var=17.3%
var=25.4%
ENSO: 2.5 years
5.0 years
Years
adim
period in years

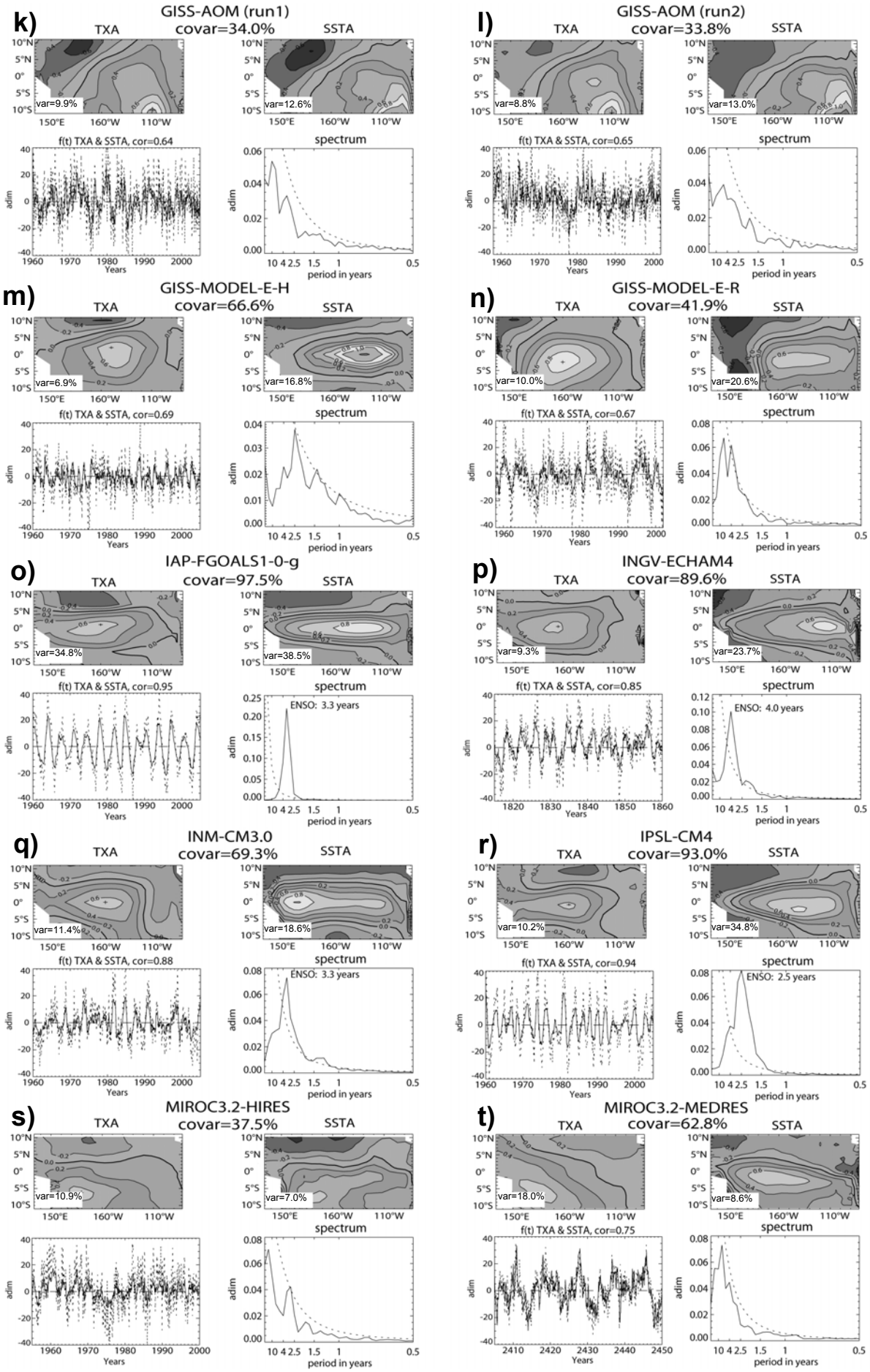
k)
GISS-AOM (run1)
covar=34.0%
TXA
SSTA
var=9.9%
var=12.6%
f(t) TXA & SSTA, cor=0.64
spectrum
l)
GISS-AOM (run2)
covar=33.8%
var=8.8%
var=13.0%
f(t) TXA & SSTA, cor=0.65
m)
GISS-MODEL-E-H
covar=66.6%
var=6.9%
var=16.8%
f(t) TXA & SSTA, cor=0.69
n)
GISS-MODEL-E-R
covar=41.9%
var=10.0%
var=20.6%
f(t) TXA & SSTA, cor=0.67
o)
IAP-FGOALS1-0-g
covar=97.5%
var=34.8%
var=38.5%
f(t) TXA & SSTA, cor=0.95
ENSO: 3.3 years
p)
INGV-ECHAM4
covar=89.6%
var=9.3%
var=23.7%
f(t) TXA & SSTA, cor=0.85
ENSO: 4.0 years
q)
INM-CM3.0
covar=69.3%
var=11.4%
var=18.6%
f(t) TXA & SSTA, cor=0.88
ENSO: 3.3 years
r)
IPSL-CM4
covar=93.0%
var=10.2%
var=34.8%
f(t) TXA & SSTA, cor=0.94
ENSO: 2.5 years
s)
MIROC3.2-HIRES
covar=37.5%
var=10.9%
var=7.0%
t)
MIROC3.2-MEDRES
covar=62.8%
var=18.0%
var=8.6%
f(t) TXA & SSTA, cor=0.75
Years
period in years
adim

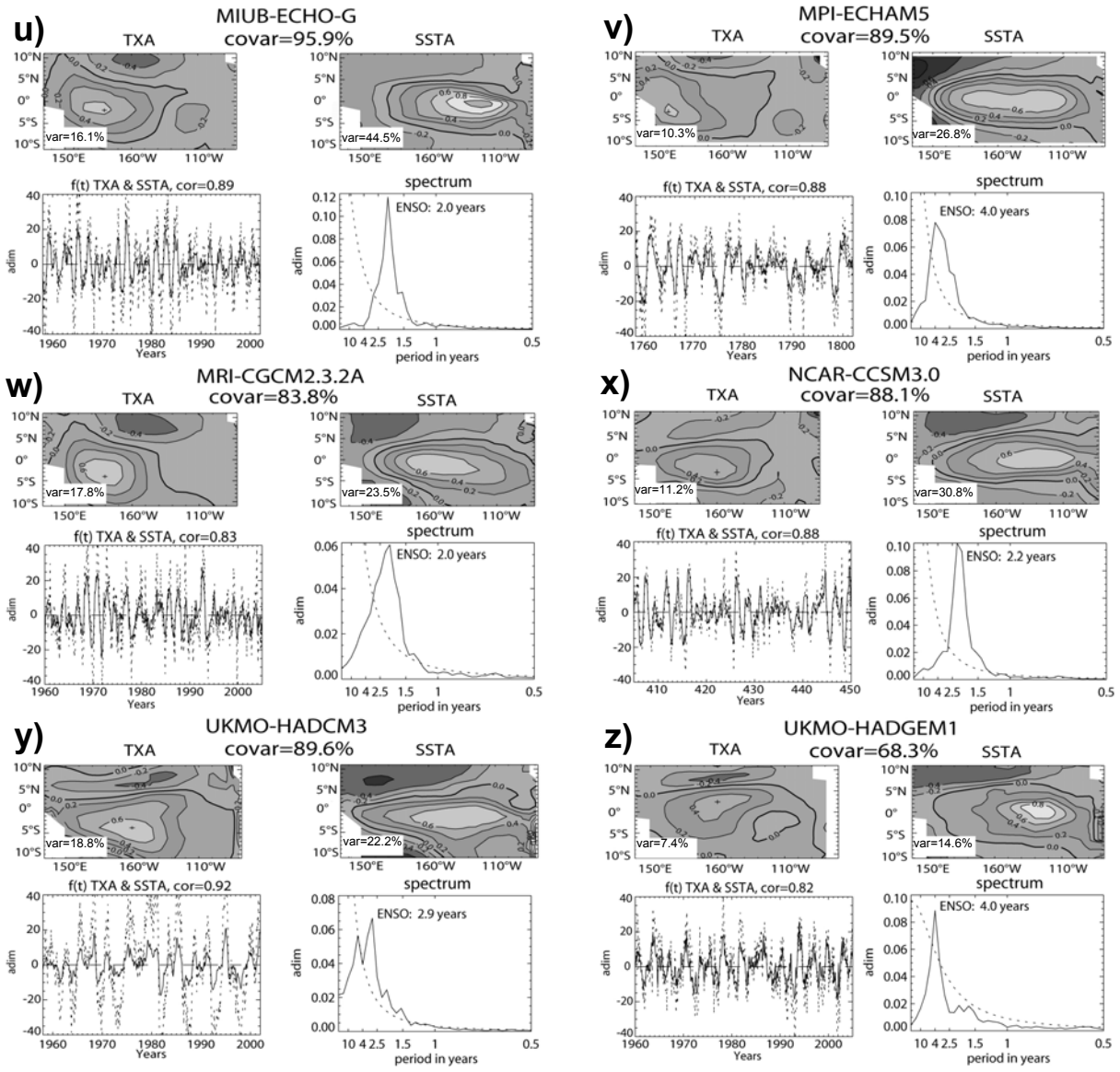

Fig. 1. First SVD mode between wind stress and SST anomalies (11°S-11°N, 134°E-81°W):
(a) SODA 1.4.2, **(b)** NCEP-GODAS, **(c)** BCCR-BCM2.0, **(d)** CCCMA-CGCM3.1 (T47), **(e)** CCCMA-CGCM3.1 (T63), **(f)** CNRM-CM3, **(g)** CSIRO-MK3.0, **(h)** CSIRO-MK3.5, **(i)** GFDL-CM2.0, **(j)** GFDL-CM2.1, **(k)** GISS-AOM (run1), **(l)** GISS-AOM (run2), **(m)** GISS-MODEL-E-H, **(n)** GISS-MODEL-E-R, **(o)** IAP-FGOALS1.0g, **(p)** INGV-ECHAM4, **(q)** INM-CM3.0, **(r)** IPSL-CM4, **(s)** MIROC3.2-HIRES, **(t)** MIROC3.2-MEDRES, **(u)** MIUB-ECHO-G, **(v)** MPI-ECHAM5, **(w)** MRI-CGCM2.3.2A, **(x)** NCAR-CCSM3.0, **(y)** UKMO-HadCM3, **(z)** UKMO-HadGEM1.
For each model, from left to right and top to bottom: spatial patterns for zonal wind stress and SST anomalies, associated adimensionalized time series (full line for SST, dashed line for wind stress anomalies), and the corresponding frequency spectra adimensionalized by the energy integrated over the whole frequency domain (full line for SST, dashed line for red noise).
CI = 0.2 units. Spatial patterns are adimensionalized by their respective variance over the domain and multiplied by 10. The location of maximum variance in wind stress anomalies is indicated by a cross on the map of the associated SVD mode. Percentage of explained variance for SST and zonal wind stress are indicated on the corresponding panels. Percentage of explained covariance is also provided. Correlation value between time series is indicated above the corresponding panel and the dominant ENSO period is mentioned on the spectrum plot. Time series are shown over a 45-year period for the CGCMs and over the available time span for the reanalyses.

Spectrums exhibit a variety of shapes, from a narrow band centered around the main peak of interannual variability (*e.g.* CNRM-CM3, MIUB-ECHO-G) to a wide spectrum with several peaks (*e.g.* CSIRO-MK3.0, UKMO-HadCM3). Note that two dominant peaks of similar magnitude were

found for GFDL-CM2.1 at 2.5 and 5.0 years (table 2), whatever the chosen length for the running window. We chose to retain the lower frequency peak for the estimate of the ENSO period, in order to extract a longer ENSO cycle than for GFDL-CM2.0 (3.3 years), consistently with the spectral analysis of the Niño3 index performed by Wittenberg et al. (2006).

Seven models do not exhibit any significant peak in the interannual frequency band: CCCMA-CGCM3.1 (T47), CCCMA-CGCM3.1 (T63), GISS-AOM (run 1 & 2), GISS-MODEL-E-H, GISS-MODEL-E-R, MIROC3.2-HIRES, MIROC3.2-MEDRES. Among them, five models (CCCMA-CGCM3.1-T63, GISS-AOM, GISS-MODEL-E-R, MIROC3.2-HIRES and -MEDRES) simulate unrealistic characteristics of the dominant mode of tropical variability: in particular, the covariances explained by the first SVD mode are considerably lower (respectively 54%, 34%, 34%, 42%, 38% and 63% for CCCMA-CGCM3.1-T63, GISS-AOM run 1, run 2, E-R, MIROC3.2-HIRES and -MEDRES models) than that for SODA (86%) and GODAS (83%). In addition, the associated SST anomaly patterns exhibit displaced and under/over-estimated maxima for these models in comparison with SODA (fig.1). Consequently these seven CGCMs will not be taken into account in the rest of the study. Note that most of these models are not considered either in the analyses of the studies by VPC05 and G06 due to the absent (GISS-AOM, GISS-MODEL-E-R) or weak (CCCMA-CGCM3.1-T47, GISS-MODEL-E-H, MIROC3.2-HIRES, -MEDRES) ENSO variability. In the following, for clarity, only the 16 CGCMs listed in bold character in table 2 will be considered in the rest of the paper.

Diagnosing the privileged dynamical regime:

Rather than using a statistical approach to determine the privileged ENSO regime for the CGCMs, we make use of a simple dynamical model of the tropical Pacific with prescribed wind forcing and a linearization of the ocean dynamics around a mean oceanic state derived from the CGCMs. Such procedure has two main advantages: 1) despite the simplified formulation of the embedded mixed-layer model (see below), it allows deriving explicitly the actual contribution of the tendency terms of the SST equation (including non-linear advection), which would require the manipulation of large datasets (tridimensional temperature and velocity fields) if based solely on the direct CGCM outputs; 2) it makes possible to get a direct estimation of upwelling from the CGCMs (which remains difficult to obtain from the direct model outputs), which can be compared to an estimate from a different wind product.

The linear model is the oceanic component of an Intermediate Coupled Model (ICM) named LODCA (Linear Ocean Dynamically Coupled to Atmosphere) and described by Dewitte (2000). For

clarity we will simply refer to the linear model as 'LODCA'. It can be viewed as an extension of the oceanic component of the CZ model in the context of several baroclinic modes instead of one. The model solves an infinite number of horizontal modes for each baroclinic mode. The circulation is driven by adiabatic, linear shallow-water wave dynamics. It includes three baroclinic modes with characteristics of phase speed c_n, wind projection coefficient (Lighthill 1969)

$$P_n = \frac{H_{th}}{\int_{-H_{mix}}^{0} F_n^2(z)dz},$$

friction r_n, and « thermocline coefficient »

$$scl_n(z) = \frac{g}{N^2(z)}\frac{dF_n}{dz}(z),$$

where N^2 is the Brünt-Väisälä frequency, F_n are the solutions of the eigenvalue problem with the appropriate boundary conditions (Fjelstad, 1933), H_{mix} = 50 m and H_{th} = 150 m are the zonally-uniform constant mixed-layer depth and an adimensionalizing coefficient (corresponding roughly to the observed mean thermocline depth in the central Pacific), respectively. The P_n quantify the amount of momentum flux that projects on a particular baroclinic mode. In that sense they characterize the thermocline structure and bring information on how the ocean has to respond (in the linear sense) to wind stress forcing. The geostrophic currents are computed from the contributions of the three baroclinic modes, and upwelling is inferred from the divergence of the mixed layer currents. The scl_n weight the different sea level baroclinic contributions to thermocline displacements - see Dewitte (2000) for details.

Values for these parameters are prescribed to those obtained from the results of a vertical mode decomposition of the mean equatorial stratification performed for each of the IPCC models. The density profile used for the decomposition is taken at the location (along the equator) of the maximum variability of the zonal wind stress anomaly pattern associated to the first SVD mode between SST and wind stress anomalies (see above). This choice was motivated by the fact that this is where the impact of the wind forcing on the ocean dynamics is the strongest at interannual time scales. The procedure allows fitting the mean stratification and vertical structure of LODCA to that of each of the CGCMs.

Like in Zebiak and Cane (1987), SST anomalies are computed from a fully non-linear surface mixed layer temperature equation that considers mostly large scale zonal and vertical advections (Dewitte, 2000):

$$\frac{\partial T'}{\partial t} = -u'(\overline{T}+T')_x - \overline{u}(T')_x - v'(\overline{T}+T')_y - \overline{v}(T')_y - \gamma.\{M(\overline{w}+w') - M(\overline{w})\}\overline{T}_z$$
$$- \gamma.M(\overline{w}+w')\frac{T'-T'_{sub}(h',\overline{h})}{H_{mix}} - \alpha T'$$

(M(x) is a step function: M(x)=x if x≥ 0 ; M(x)=0 if x<0).

T', (*u'*, *v'*, *w'*) and *h'* stand for the anomalies for SST, surface velocity field (vertical velocities are at the base of the mixed layer) and thermocline displacements, respectively. Barred quantities represent climatological fields and the prime marks represent anomalies relative to the seasonal cycle. T_{sub} represents subsurface temperature at the base of the mixed layer and is parameterized as in Dewitte and Périgaud (1996). *x*, *y* and *z* indices stand for the partial derivatives according to the respective spatial coordinates. γ is the efficiency factor relating entrainment to upwelling. It varies from west to east between the values of 0.5 and 1.0, in order to take the effect of a zonally varying mixed-layer depth into account (see Dewitte, 2000). α is a damping coefficient equal to $(115 \text{ days})^{-1}$.

$-u'(\overline{T}+T')_x$ is for zonal advection of temperature by the zonal current anomalies. It comprises both anomalous advection of mean temperature $-u'(\overline{T})_x$ and non-linear zonal advection $-u'(T')_x$ terms. $-\overline{u}(T')_x$ is for zonal advection of temperature anomalies by the mean zonal currents. $-v'(\overline{T}+T')_y$ and $-\overline{v}(T')_y$ are for the meridional counterparts. $-\gamma.\{M(\overline{w}+w') - M(\overline{w})\}\overline{T}_z$ is for vertical entrainment of mean temperature across the thermocline by the vertical current anomalies and is only for upwelling. $-\gamma.M(\overline{w}+w')\frac{T'-T'_{sub}(h',\overline{h})}{H_{mix}}$ is for vertical entrainment of temperature anomalies across the thermocline by the total upwelling. It comprises both vertical advection of temperature anomalies by the mean currents $-\gamma.\overline{w}\frac{T'-T'_{sub}(h',\overline{h})}{H_{mix}}$ and non-linear vertical advection $-\gamma.w'\frac{T'-T'_{sub}(h',\overline{h})}{H_{mix}}$ terms. For simplicity, $-\gamma.\{M(\overline{w}+w') - M(\overline{w})\}\overline{T}_z$ and $-\gamma.M(\overline{w}+w')\frac{T'-T'_{sub}(h',\overline{h})}{H_{mix}}$ will be respectively refered to as $-w'.(\overline{T})_z$ and $-w.(T')_z$ in the rest of the paper. $-\alpha T'$ is a Newtonian damping term and includes the contribution of surface heat flux anomalies.

LODCA is similar to the CZ model, except it takes the vertical structure explicitly into account with three baroclinic modes, and uses a different parameterization of subsurface temperature (Dewitte and Périgaud, 1996; Dewitte, 2000). The main advantage in comparison to a model using only one baroclinic mode – *e.g.* the CZ model - is that sea level and zonal current anomalies are more realistic

with more than one vertical mode (Dewitte et al., 1999; 2002). This is because wave dissipation is not solely taken into account through a Rayleigh-type friction, but also through vertical propagation of energy (Dewitte and Reverdin, 2000). Hence we expect to better represent with LODCA the contribution of the tendency terms of the SST equation and derive a more robust estimate of the dominant feedbacks in the CGCMs than with a model using one baroclinic mode.

More generally, the other interesting aspects of the approach with LODCA are: 1) to provide a method for comparing models having different characteristics (resolution and mixing scheme among others); 2) to evaluate for each CGCM to which degree its tropical variability can be considered a 'linear' response to the wind forcing.

The linear model is forced with wind stress as derived from the IPCC models, in order to fit its dynamics to those of the CGCMs with a focus on the equatorial waveguide. A preliminary step consists in deriving the climatological velocity and SST fields from the CGCMs in order to prescribe them in LODCA. This allows achieving a complete fit of the mean state to that of the CGCMs. For the velocity field, this is achieved by forcing LODCA with the climatological wind stress from the CGCMs. The climatology for SST is directly inferred from the CGCMs' outputs. In a second step, LODCA - in which these climatologies are prescribed - is forced with the wind stress anomalies so as to derive SST anomalies and the tendency terms of the SST equation. Similar methodology was used in Dewitte et al. (2007a,b).

Model Name	Niño3-SST (LODCA & CGCM)	
	Correlation	RMS difference (°C)
SODA 1.4.2	0.85	0.76
GODAS	0.78	0.64
BCCR-BCM2.0	0.89	0.57
CNRM-CM3	0.96	0.84
CSIRO-MK3.0 (run1)	0.86	0.57
CSIRO-MK3.5	0.89	0.40
GFDL-CM2.0	0.87	0.44
GFDL-CM2.1	0.85	0.78
IAP-FGOALS1.0-g (run1)	0.96	0.57
INGV-ECHAM4	0.94	0.34
INM-CM3.0	0.90	0.51
IPSL-CM4	0.94	0.41
MIUB-ECHO-G	0.89	0.62
MPI-ECHAM5	0.77	0.78
MRI-CGCM2.3.2A	0.82	0.48
NCAR-CCSM3.0 (run2)	0.90	0.40
UKMO-HadCM3 (run1)	0.93	0.58
UKMO-HadGEM1	0.86	0.42

Table 3. Comparison between CGCM and LODCA outputs.

The simulated SST anomalies from LODCA are compared to the direct CGCM outputs. The results of the comparison are provided in table 3 for the Niño3-SST index, which shows a good agreement between LODCA and the CGCMs: the correlation is above 75% for all the models. The

discrepancies between the LODCA SSTs and the CGCM SSTs may be due to a number of processes: these include the non-linearities present in the CGCMs but not in LODCA (the latter only accounts for non-linear advection associated to long wavelength equatorial waves), the reflections of the equatorial waves (LODCA having an idealized coastline with no through-flow), the dispersion and dissipation processes associated to thermocline variability (LODCA having a steady homogeneous thermocline for the baroclinic component), or the surface heat fluxes (which are very simply parameterized in LODCA). Nonetheless, results of table 3 indicate that the variability of most models can be accounted for to a large extent by linear dynamics.

A simple theoretical framework is then used to provide a diagnostic of the privileged dynamical regime in the IPCC models, based on the estimation of the tendency terms of the SST equation. The inspection of the variability of these various tendency terms provides pieces of information on the relative importance of the thermocline (vertical advection) and zonal advective (zonal advection) feedbacks. Note that in the conceptual model of Jin and An (1999), only anomalous zonal advection of mean temperature ($-u'.(\overline{T})_x$) and mean vertical advection of anomalous temperature ($-\overline{w}.(T')_z$) are considered to analyse the relative importance of the thermocline and zonal advective feedbacks. In theory, all terms should be taken into account. Here, all the advection terms are considered in the analysis: it reveals that the deviations (from the real world) in the balance between the two feedbacks are best accounted for by the mean vertical advection of anomalous temperature ($-\overline{w}.(T')_z$) and the mean zonal advection of anomalous temperature ($-\overline{u}.(T')_x$), as will be seen below. Note that this does not mean that $-u'.(\overline{T})_x$ is not a significant contributor to the SST changes. However this term does not account for the main differences between models (see below).

In the following section, results based on the LODCA simulations are used to classify the models in groups relevant for their main ENSO dynamical regime.

2.1.3. ENSO regime and mean state

2.1.3.1. SST tendency terms: variability and biases

In the rest of the study, it is assumed that for most CGCMs, biases in ENSO variability can be accounted for by the over- or under-estimation of the zonal advective feedback and/or the thermocline feedback. This means that the role of the wind response to SST anomalies, the damping and the atmospheric noise properties are not investigated here, in spite of their importance for the ENSO cycle (*e.g.* VPC05, Philip and van Oldenborgh, 2009a,b). Note however that according to the same

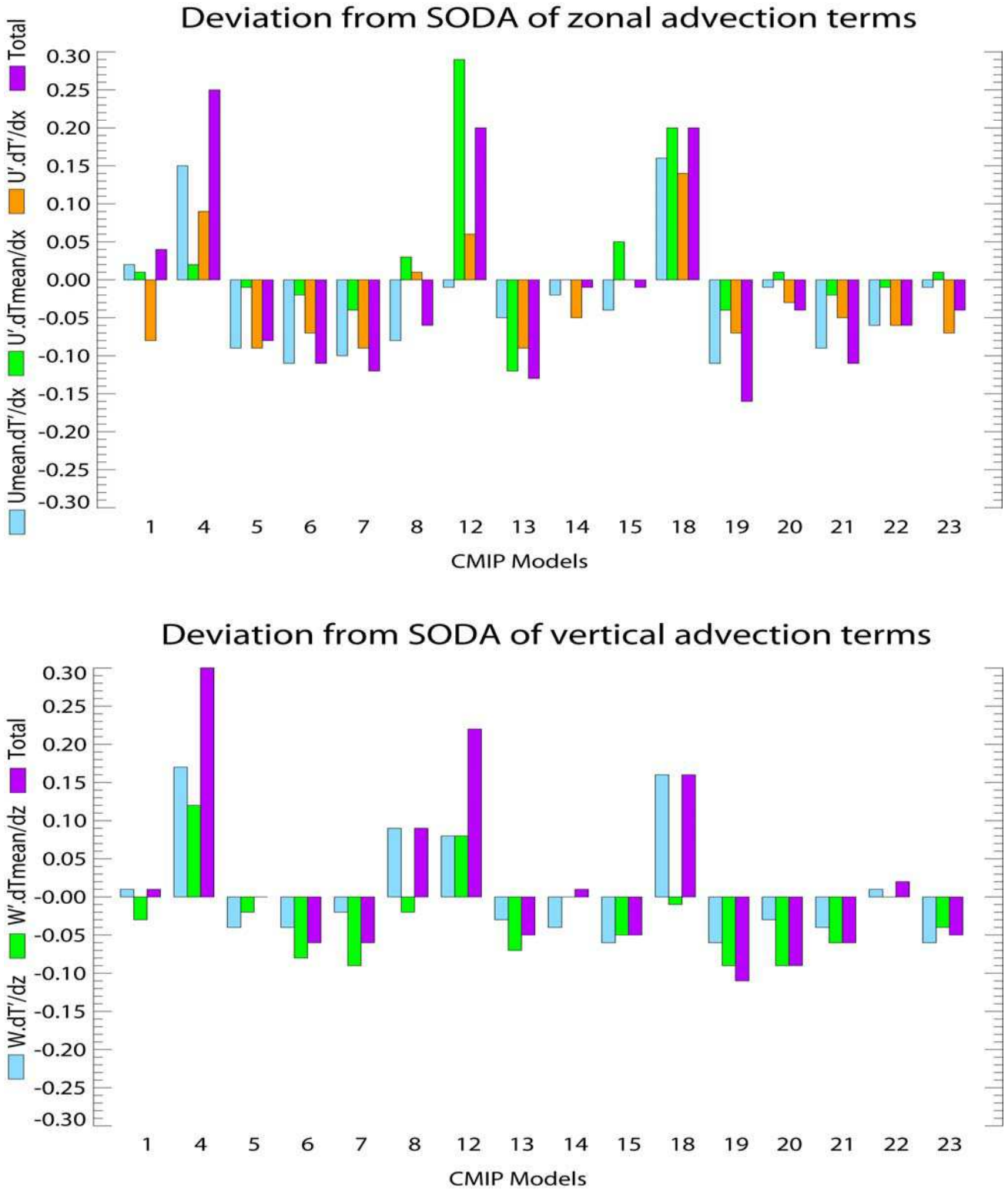

Fig. 2. Histogram of the deviation in the variability of the advection terms (referenced to SODA) for the CMIP3 models: (top panel) zonal advection terms averaged in the Niño4eq region and (bottom panel) vertical advection terms averaged in the Niño3eq region. Model names are referenced in table 1. Units are °C/month.

studies, the dominant contributors to the SST changes associated to ENSO are the zonal advective and thermocline feedbacks: although the present study does not explicitly consider the dominant role of

the atmospheric component in the simulated ENSO, its effect on SST is implicitly taken into account in the heat budget analysis performed with the linear model.

The variability of the tendency terms (as derived from the LODCA simulations performed with each CGCM) are assumed to provide estimates of the strength of zonal/vertical advection processes. Deviations from the results obtained with LODCA fitted to the SODA reanalysis are thus expected to reflect the tendency of the CGCMs towards one feedback regime or the other. A classification of the CGCMs in terms of the dominant feedback process is therefore proposed. It is based on the departures in the variability of the zonal and vertical advection terms respectively in the western/central Pacific and the eastern Pacific, as detailed in the following.

Figure 2 presents the deviation of the variability (rms) of the zonal and vertical advection terms relatively to SODA, obtained from the 16 studied CGCMs. For simplicity, we will refer as "departure" the deviation from SODA hereafter, unless specified. A detailed examination of figure 2 allows quantifying which tendency terms account the most for the departures in total zonal/vertical advection. For instance, the top panel of figure 2 indicates that mean zonal advection of anomalous temperature ($-\bar{u}.(T')_x$ - light blue bars) can be significantly larger or smaller in the IPCC models than in SODA, with a tendency to have a deviation from SODA comparable to that of total zonal advection (purple bars). Similarly, the bottom panel of figure 2 reveals that the departure in mean vertical advection of anomalous temperature is comparable to the departure in total vertical advection, except for two models (namely CSIRO-MK3.0 and INM-CM3.0).

Departures in	have the :	Same sign as departure for total zonal/vertical advection			Same order of magnitude as departure for total zonal/vertical		
tendency terms	relatively to :	SODA	GODAS	Ensemble Mean	SODA	GODAS	Ensemble Mean
$-\bar{u}.(T')_x$		15	12	13	10	6	11
$-u'.(\bar{T})_x$		11	14	12	3	7	8
$-u'.(T')_x$		13	10	13	7	5	5
$-w.(T')_z$		14	7	15	11	6	10
$-w'.(\bar{T})_z$		10	12	14	9	3	6

Table 4. Number of CGCMs with departures in tendency terms representative of the departure for total zonal/vertical advection.

In order to quantify such observations, table 4 presents for each tendency term the number of models that have a departure (relatively to different references) of the same sign/order of magnitude ($^{+}$/- 50 % of the value) as that of the sum of the zonal/vertical advection terms. It reveals that whatever the reference, zonal/vertical advection by the mean currents are the most representative terms to account for the departures in total zonal/vertical advection. These terms can thus be considered "proxies" of the departures of the CGCMs with respect to the strength of the zonal

advective/thermocline feedback. Results relatively to GODAS are a bit less conclusive. This may be due to the shorter period spanned by GODAS as will be discussed later on.

2.1.3.2. Model classification

In order to assess the relative importance of the zonal advective feedback and the thermocline feedback in the CGCMs, the variability of $-w.(T')_z$ - averaged in the Niño3eq region (150°W-90°W, Eq.) - as a function of the variability of $-\overline{u}.(T')_x$ - averaged in the Niño4eq region (160°E-150°W, Eq.) - is presented in figure 3. Interestingly, figure 3 indicates that there is no clear linear relationship between the two advection terms among all the models. This illustrates the diversity in behaviours of the CGCMs of the IPCC in terms of the privileged dynamical regime. The CGCMs are gathered around GODAS and the ensemble mean, with models having a tendency to overestimate mean zonal advection (blue group) and others mean vertical advection (red group). In between, there is a group (green) of models that exhibit a balance between advection terms comparable to both GODAS and the ensemble mean. SODA also belongs to this category, though having larger zonal advection than the other references.

In order to assess to which extent the ratio between $-w.(T')_z$ and $-\overline{u}.(T')_x$ is controlled by the mean state (and more specifically by the mean circulation characteristics), we first suppose a linear behaviour of vertical currents around the mean upwelling. By doing this, we assume that perturbations in the eastern Pacific are weak in comparison to the mean vertical flow, so that $w.(T')_z \approx \overline{w}.(T')_z$. The vertical gradient of temperature anomalies $(T')_z$ in the eastern Pacific depends on the SST anomalies, but also on the anomalies of subsurface temperature T'_{sub}, itself depending on the displacements of the thermocline. As a first approximation, this quantity varies linearly with anomalous thermocline displacements, so we infer that $w.(T')_z \approx \overline{w}.\frac{T' - ah'}{H_{mix}}$, where $a = \frac{\partial T_{sub}}{\partial h}$ is a constant quantity. Here T' is for SST anomalies in the Niño3 region (150°W-90°W, 5°S-5°N). The Niño3.4 region (170°W-120°W, 5°S-5°N) may also be used here to some extent (see below).

On the other hand, when averaged over the central/western Pacific, the zonal gradient of temperature anomalies $(T')_x$ is mainly controlled by SST anomalies east of the date line: indeed, the anomalies are generally much weaker over the warm pool, and their typical zonal scale L does not vary much among the models which tend to have an overestimated westward extension (fig. 1). Hence

$\bar{u}.(T')_x \propto \bar{u}.\frac{T'}{L}$ in most cases. Here T' is for SST anomalies in the central Pacific, roughly in the Niño3.4 region.

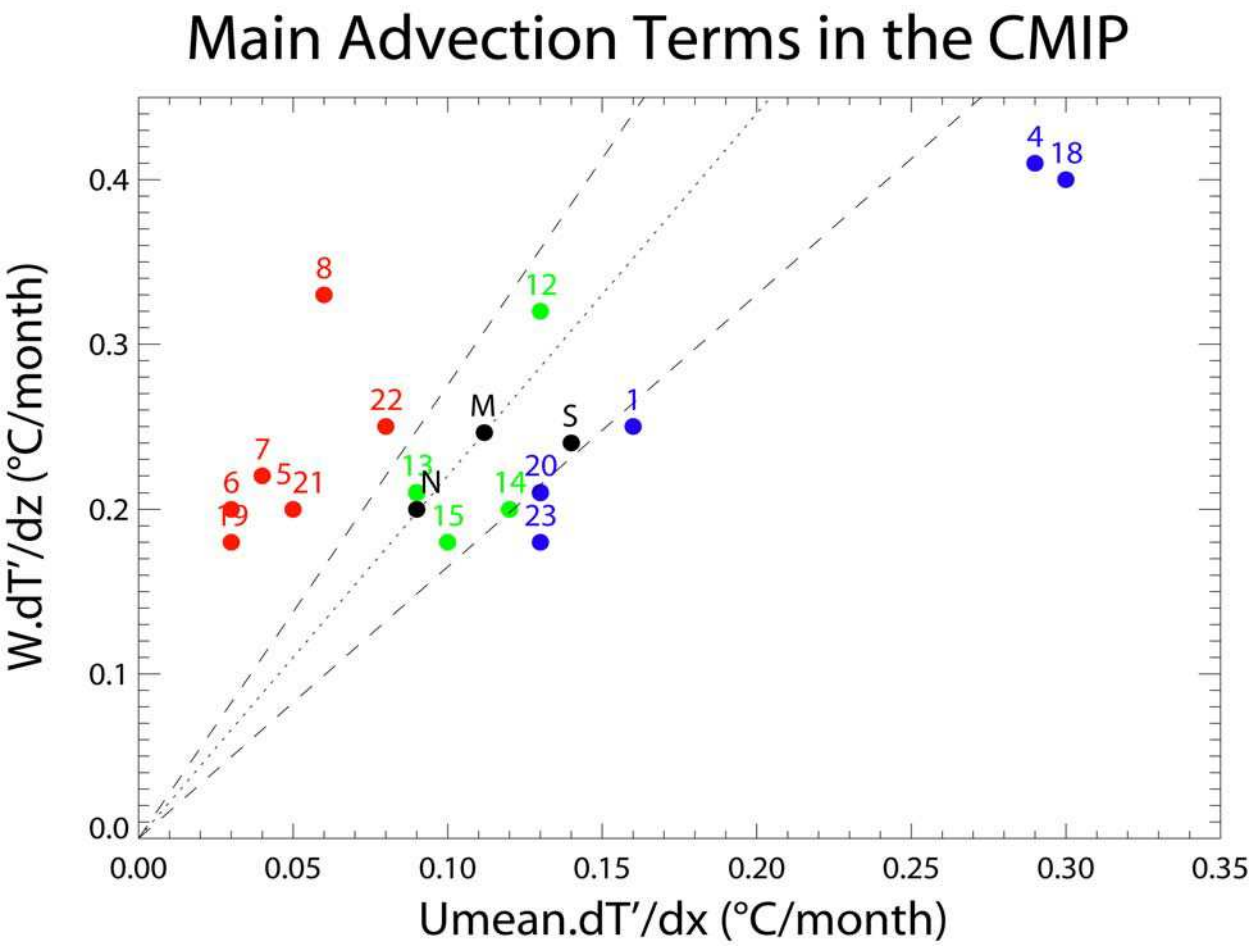

Fig. 3. Scatterplot of the RMS of vertical advection of anomalous temperature by the total equatorial vertical currents $-w.(T')_z$ vs. the RMS of zonal advection of anomalous temperature by the equatorial mean zonal currents $-\bar{u}.(T')_x$ for the CMIP3 models.
$-w.(T')_z$ ($-\bar{u}.(T')_x$) is averaged in the Niño3eq (Niño4eq) region. The dotted line represents the straight line having a slope corresponding to the multi-model ensemble mean (i.e. mean value of $w.(T')_z / \bar{u}.(T')_x$), and the dashed lines have slopes corresponding to 125% and 75% of the slope of the dotted line. Colours of the model dots and labels correspond to their positions relative to the dashed lines: green between them, blue on their right hand side and red on their left hand side. Black colour is for the references: S stands for SODA, N stands for GODAS, and M stands for the multi-model ensemble mean. Model names are referenced in table 1. Note that CSIRO-MK3.0 and NCAR-CCSM3.0 have the same position. Units are °C/month.

Consequently, a simplified SST equation that accounts for the biases of the zonal/vertical advection terms can be written as follows:

$$\frac{\partial T'}{\partial t} = -\left[\left(\frac{\bar{u}}{L} + \frac{\bar{w}}{H_{mix}}\right).T' - \frac{a\bar{w}}{H_{mix}}h'\right]$$

where T' (resp. h') is for SST (resp. thermocline) anomalies in the Niño3.4 region.

The differences among the models are significantly higher for $\overline{u}$ than for $\overline{w}$ as will be seen below (fig.4), so we can consider as a first approximation that $\frac{\overline{u}}{L} + \frac{\overline{w}}{H_{mix}} \approx b\overline{u} + c$ (where b and c do not vary much among the models). The ratio between the variabilities of $-w.(T')_z$ and $-\overline{u}.(T')_x$, which quantifies the biases in the relative strength of the ENSO feedbacks can then be estimated through the ratio between the variabilities of $\frac{a\overline{w}}{H_{mix}}h'$ and $\frac{\overline{u}}{L}T'$. The latter is proportional to $\frac{\overline{w}}{\overline{u}}$ times the ratio between the variability of h' over that of T' in the central to eastern Pacific. The inverse quantity of the latter ratio is comparable to the α parameter quantifying what VPC05 call the "upwelling feedback" *i.e.* upwelling and mixing of thermocline temperature anomalies. According to VPC05 (their figure 6), α shows little variation among the CGCMs for the Niño3.4 region, except for GFDL-CM2.1 and MRI-CGCM2.3.2A. Note that for the Niño3 region, most CGCMs (except the latter two and INM-CM3.0) exhibit an α of the same order as that of TAO data (or overestimate it by a factor less than two), which suggests that the use of Niño3.4 to estimate T' and h' in $\overline{w}.\frac{T' - ah'}{H_{mix}}$ is valid to a large extent.

Under these assumptions, we argue that the balance between the zonal advective feedback and the thermocline feedback is mainly controlled by the mean tridimensional velocity field within the mixed layer (itself determined by the background state of the coupled system). In order to support this statement, we present a similar figure to figure 3, considering only the mean zonal and vertical currents (figure 4).

Consistently with the simplifications proposed above, figure 4 exhibits a distribution of the balance between zonal and vertical motion among the models similar to that in figure 3, but emphasizes the differences between models. Again three groups of models can be distinguished: the models located on the left of the flattest dashed line have strong mean equatorial zonal currents relatively to mean equatorial upwelling, in comparison to the ratio from SODA. Thus these CGCMs can be considered as dominated by the zonal advective feedback (group 1). Similarly, the models located on the right of the steepest dashed line can be considered as dominated by the thermocline feedback (group 3). The models located between the dashed lines have a fairly reasonable balance between zonal advective and thermocline feedbacks (group 2), with a $\overline{w}/\overline{u}$ ratio comprised in the arbitrarily chosen range of the multi-model mean $\overline{w}/\overline{u}$ ratio +/- 33%.

Only four models are classified differently by figure 3 and figure 4: IAP-FGOALS1.0-g, UKMO-HadGEM1, UKMO-HadCM3 and CSIRO-MK3.0. In addition, the latter two exhibit in figure

4 a stronger relative importance of vertical movements than the other models from the hybrid group (and the reference), which is consistent with their behaviour in figure 3. It was checked that considering SODA as the reference instead of the multi-model mean leads to the same classification for all models, as it exhibits a dynamical regime very similar to that of the ensemble mean.

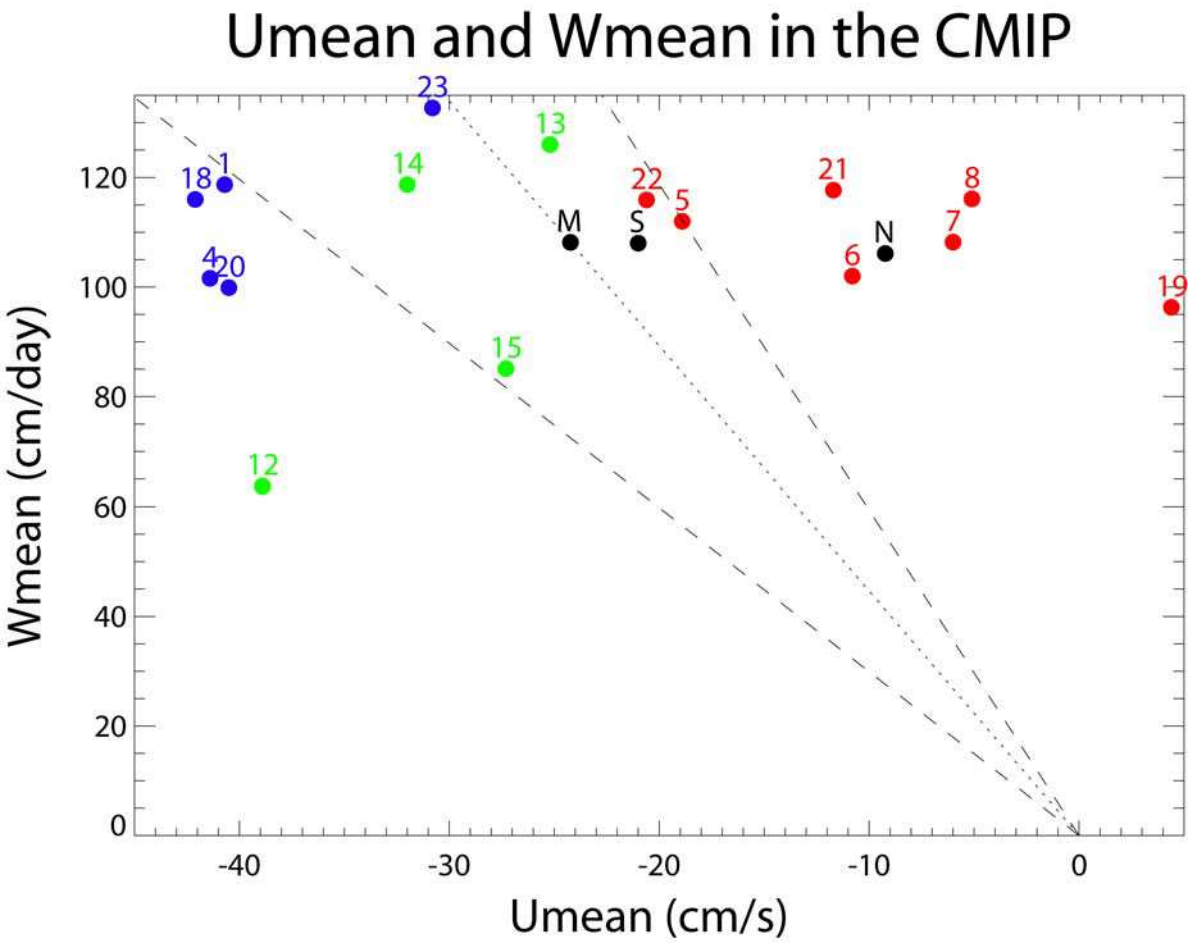

Fig. 4. Scatterplot of the mean vertical velocities $\overline{w}$ (averaged over Niño3eq) vs. the mean surface zonal velocities $\overline{u}$ (averaged over Niño4eq) for the CMIP3 models.
The dotted line has a slope corresponding to the multi-model ensemble mean and the dashed lines have slopes corresponding to 67% and 133% of the slope of the dotted line. Colours are from fig. 3. Black colour is for the references: S stands for SODA, N stands for GODAS, and M stands for the multi-model ensemble mean. Model names are referenced in table 1. Units for zonal (vertical) currents are $cm.s^{-1}$ ($cm.day^{-1}$).

On the other hand, according to this classification, the GODAS reanalysis belongs to the thermocline feedback regime category. This is partly due to the fact that GODAS spans the period characterized by enhanced ENSO activity and a warmer mean state that favors the thermocline feedback and slower time scales of interannual variability (An, 2004; Moon et al., 2004). Noteworthy, the SVD analysis (see section 2.2) performed for SODA and GODAS over 1980-2001 reveals identical ENSO periods for both reanalyses (5.0 years - not shown). In addition, the SODA heat budget performed over 1980-2001 leads to an increased relative contribution of the thermocline feedback compared to the budget over 1958-2001. Still, SODA in that case remains in the previously

defined green group (hybrid feeback). This suggests that the differences between SODA and GODAS have to be related to either differences in forcings and/or model physics/parameterizations. It is known for instance that assimilation of temperature and salinity into an ocean model can make the currents less realistic (Burgers et al., 2002). Thus, reanalysis products based on different models and assimilation schemes like SODA and GODAS are likely to generate different velocity fields. Note however that SODA compares well with TAO ADCP data for the period from 1990 onwards (Carton and Giese, 2008). For this reason, and since SODA spans a longer period than GODAS (and since it is consistent with the CGCMs ensemble mean), it is retained as the 'reference' in the rest of the paper. It is worth mentioning here that the choice of the reference only determines the limits between the different groups of models. It does not affect the differences among the CGCMs in regard to the relative importance of zonal and vertical advection terms in the heat budget, and their biases diagnosed later in the paper.

To summarize, we have identified from the heat budget of each CGCM that biases in the simulated mean surface circulation ($\overline{u},\overline{w}$) can be used to classify the CGCMs in groups relevant to their dominant ENSO regime. In the following, ENSO properties and model biases are interpreted in the light of this classification.

2.1.3.3. Impact on the ENSO period

In the following, we investigate to which extent characteristics of the ENSO mode can be related to the biases in the mean state identified above: as detailed in the introduction, it is expected that models with a dominant zonal advective feedback have a short ENSO period, because of local surface wind-SST interactions due to 'fast' advection in the mixed-layer (*e.g.* Wang and An, 2001; Fedorov and Philander, 2001). On the other hand, models exhibiting a dominant thermocline feeback should have increased ENSO variability in the low frequency range, because of the 'slow' basin-wide adjustment and an increased recharge/discharge time of equatorial upper ocean heat content, accordingly to the recharge oscillator paradigm of ENSO (Jin, 1996, 1997a,b).

Figure 5 presents the ENSO periods (table 2) as a function of the $\overline{u}/\overline{w}$ ratio, *i.e.* the relative strength of the zonal advective feedback vs. the thermocline feedback. Although the models exhibit significant scattering, a tendency for increasing (resp. decreasing) frequencies with a higher (resp. lower) $\overline{u}/\overline{w}$ ratio is observed: consistently with earlier studies (Fedorov and Philander, 2001; VPC05; G06), models dominated by the zonal advective feedback tend to simulate a higher ENSO frequency on average (2.9 years, with 95% confidence in the 1.8-4.0 interval) than those dominated by the thermocline feedback (3.9 years, with 95% confidence in the 2.4-5.4 interval). Assuming that multi-

model behaviour follows a gaussian distribution within each group, the confidence intervals were derived from the standard error on the mean ENSO period for each group. The probability that the true mean period for group 3 is lower than that for group 1 is less than 20%. In other words, the probability that the tendency mentioned above is significant is over 80%.

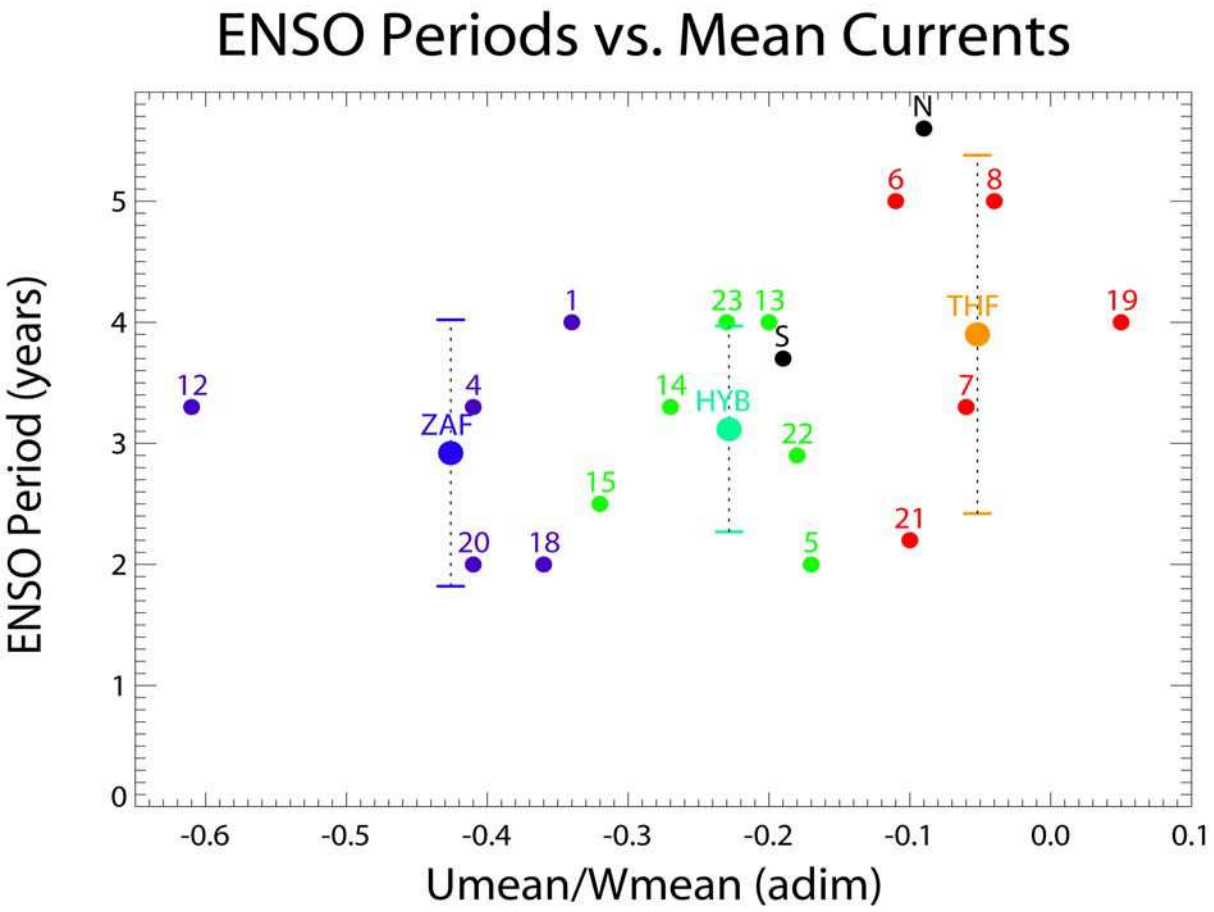

Fig. 5. Scatterplot of the ENSO period vs. the $\overline{u}/\overline{w}$ ratio (see fig. 4) for the CMIP3 models.
Model names are referenced in table 1. The colour code is derived from figure 4 (see text). Black colour is for the references: S (resp. N) stands for SODA (resp. GODAS). For each group (ZAF for zonal advective feedback, HYB for hybrid feedback, THF for thermocline feedback), the larger dot represents the mean ENSO period. Error bars correspond to the 95% confidence interval associated to the mean period. Units for ENSO period are years. Units for $\overline{u}/\overline{w}$ are day/s, *i.e.* the values have to be multiplied by 86400 for the ratio to be nondimensional.

On the other hand, the mean ENSO period for group 2 lies in between group 1 and group 3 (3.1 years, with 95% confidence in the 2.3-4.0 interval), but is closer to the value for group 1. In fact, the probability that the true mean period for group 2 is lower than that for group 1 is of the order of 35%. This makes the distinction between groups 1 and 2 likely to be spurious (though it is more likely not to be so). Nevertheless, the arbitrary definition of the limits between groups (see previous section) might be able to explain this proximity between ENSO time scales from the zonal advective feedback and hybrid groups. Obviously, a more extended multi-model data set comprising a larger number of members (ensemble simulations for each CGCM for instance) is required here in order to increase our

confidence level in the ENSO period estimate. In addition, as underlined before the relatively short length of the simulations does not allow taking into account the possible low-frequency modulation of ENSO: since it might impact the structure of the ENSO mode as suggested by Wittenberg (2009), this cautions against over-interpreting the afore-mentioned tendencies. However, the fact that the hybrid group follows the general tendency relating a shorter ENSO period with a higher relative strength of the zonal advective feedback tends to confirm our results. Note that similar tendencies were obtained when plotting the ENSO period against the ratio of the variability of $\overline{u}.(T')_x$ over the variability of $w.(T')_z$, as defined on figure 3 (not shown).

One may note that the dominant ENSO period derived from SODA and ERSST (3.7 years) is higher than that of group 2, but smaller than that of group 3. The ENSO period from ERSST over 1880-2009 is shorter with a 20-year running window than with a 15-year window (3.3 years vs. 3.7 years). Hence, the difference in the width of the windows used for the CGCMs and for the references might explain - together with the bias of hybrid models towards the higher frequencies - why the ENSO time scale for SODA is 'biased' towards the lower frequencies. Despite these discrepancies, the results suggest that a realistic representation of coupled ENSO feedbacks leads to realistic time scales of ENSO variability.

Note also that other biases might contribute to the heterogeneous ENSO periods found within each model category. For instance, Yu et al. (2008) showed that the biennial ENSO in the NCAR-CCSM3.0 model is partly due to biases in the mean SST field of the Indian Ocean and in the Indian and Australian monsoon variability.

2.1.4. Discussion

2.1.4.1. On the origin of mean circulation biases

The previous section allowed relating biases in the mean surface circulation to both the dynamics of the ENSO mode (surface or thermocline-driven) and the dominant time scale of ENSO in the IPCC models. However, the reason why a CGCM tends towards favouring the zonal advective feedback or the thermocline feedback remains unclear. In the light of the previous results, some clues are provided in order to understand the origin of these biases. As a first step, one can focus on the biases of $\overline{u}$ which exhibit the largest variability among the ensemble compared to $\overline{w}$ (fig. 4). A similar reasoning can also be applied to $\overline{u}.(T')_x$ (fig. 3). This tends to confirm that biases in the

representation of ENSO feedbacks are mainly controlled by biases in mean zonal currents in the central/western Pacific.

Biases in zonal surface circulation may imprint SST and subsurface temperature fields. As underlined by previous studies, a common bias of the CGCMs is their tendency to have an overestimated westward extension of the cold tongue. This is the result of the larger trade winds than observed for most models (G06, Guilyardi et al., 2009) and of the consequent overestimated mean zonal currents over the western Pacific. As a result of the westward displacement of the western edge of the cold tongue (and thus of the eastern edge of the warm pool), there is a tendency of the IPCC models to have a cooler warm pool than observed (Lin, 2007).

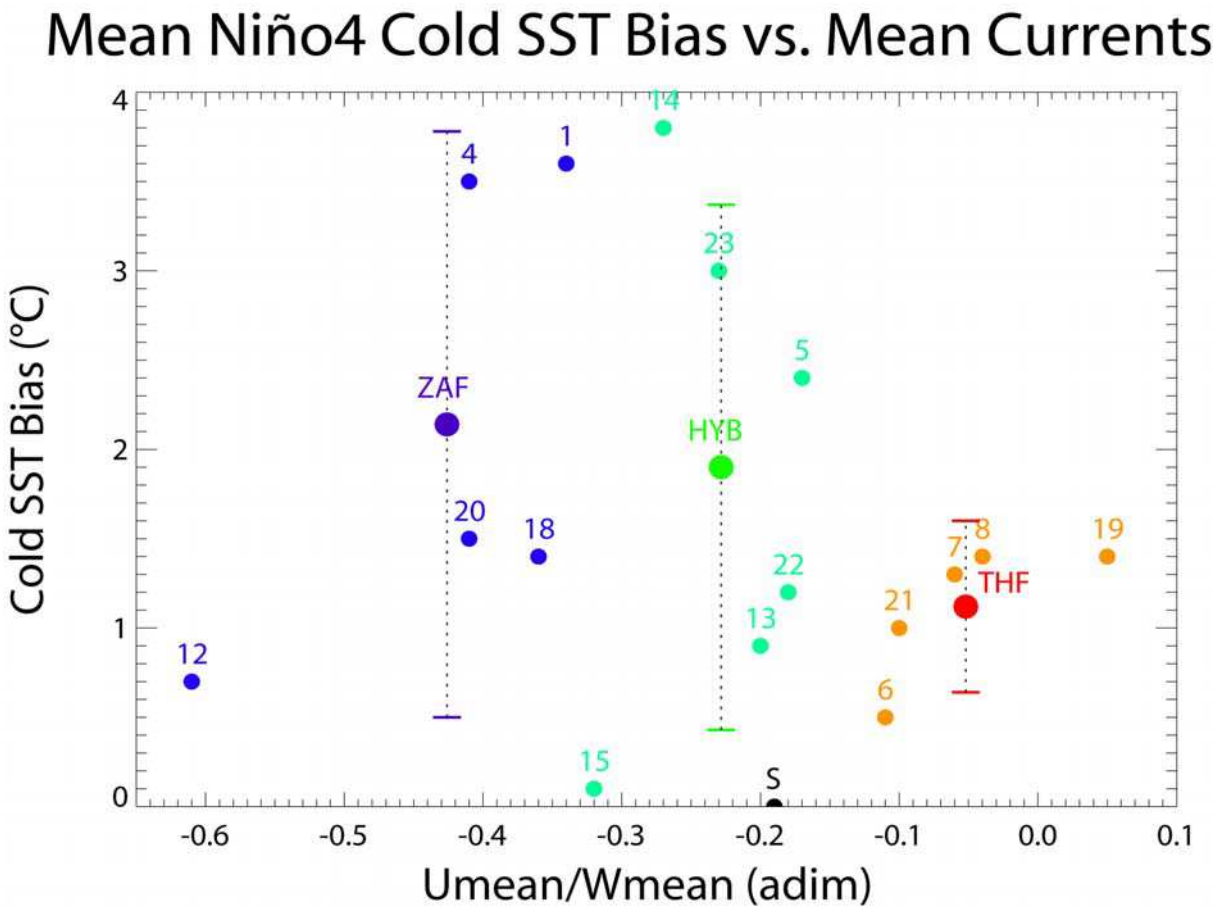

Fig. 6. Same as figure 5 but for the mean SST bias in the western equatorial Pacific. SST was averaged over the Niño4 region. Positive values correspond to a cold bias. Units for SST bias are °C.

In order to diagnose the mean temperature bias around the edge of the warm pool – located near the date line in the observations - in the models, the mean SST bias pattern was spatially averaged for all models in the Niño4 box, and examined against the $\overline{u}/\overline{w}$ ratio in the light of the classification presented above (figure 6). In spite of the rather heterogeneous behaviours of the models within each group, a tendency towards increased (resp. damped) cooling associated to the increased dominance of

the zonal advective (resp. thermocline) feedback can be distinguished. On average, the models of group 1 exhibit a 2.1°C cold SST bias (with 95% confidence in the 0.5-3.8°C interval), the models of group 2 a 1.9°C cold SST bias (with 95% confidence in the 0.4-3.4°C interval), and the models of group 3 a 1.1°C cold SST bias (with 95% confidence in the 0.6-1.6°C interval). Similarly to figure 5, the probability that the true mean of group 1 is lower than that of group 3 (resp. group 2) is of the order of 20% (resp. 35%). This is consistent with the tendencies and confidence levels inferred from figure 5 and adds some degree of confidence to our results. Again, similar tendencies were obtained when plotting the SST bias against the ratio of the variability of $\bar{u}.(T')_x$ over the variability of $w.(T')_z$ (not shown).

One can note that all the models have a colder mean Niño4 SST than SODA. It is suggested that this bias could result from a cooling due to the overestimated mean wind stress, and a warming/cooling associated to the non-linear advection of the equatorial waves, as will be seen below. The systematic cold bias due to the wind forcing is thought to vary from one model to another and may explain the important variance of the total SST bias observed within each group. It is however striking that our classification in dynamical regime is consistent with the magnitude of the cold bias in the models.

As a consistency check, the mean bias of the 20°C isotherm depth in the Niño4eq region was also examined, and a similar tendency is observed (not shown): on average, the thermocline is shallower in group 1 (resp. 2) than in group 2 (resp. 3), which implies that the biases in zonal advection are likely to impact the temperature not only at the surface, but also below the surface.

Non-linear advection in the models is then diagnosed from the heat budget of the linear model simulations (section 2.2). Indeed, Dewitte et al. (2007a) suggest that both climatological and anomalous westward advection of temperature anomalies have the tendency to cool the western-central equatorial Pacific. As a first step, the asymmetry of SST anomalies

$$asymmetry = \frac{m_3}{m_2}$$

was computed for all models in order to diagnose the El Niño-La Niña asymmetry: a positive asymmetry means stronger warm events than cold events. Likewise, a negative asymmetry means stronger cold events than warm events.

$m_k = \sum_{i=1}^{N} \frac{\left(x_i - \overline{X}\right)^k}{N}$ is the k-th moment where (x_i) are the N observations of mean value $\overline{X}$.

An and Jin (2004) showed that SST skewness can be considered a proxy of ENSO non-linearities in the eastern equatorial Pacific. Consistently with previous studies that analyzed the previous (An et al., 2005) and current generation of CGCMs (VPC05), we found that the models

show a wide range of behaviours: some like CNRM-CM3 or MIUB-ECHO-G are negatively skewed over most parts of the basin, while others like UKMO-HadCM3 present a pattern that is closer to the observations, with positive values in the east and negative ones in the west (not shown). We find that most models tend to have a higher negative asymmetry than SODA on average over the tropical Pacific. In particular, SST in the western equatorial Pacific is generally more negatively skewed in the models than in SODA. This has to be related to the non-linear zonal advection as shown below.

An et al. (2005) found that SST asymmetry increases linearly with the non-linear dynamical heating (hereafter NDH= $-u'.(T')_x - v'.(T')_y - w'.(T')_z$) in the eastern equatorial Pacific. A similar result is found for our model ensemble, with a coefficient of determination R^2=86.5% - which is the proportion of variability in the model data set that is accounted for by the linear statistical model (Steel and Torrie, 1960) - indicating that most of the variability among the models can be explained by a linear fit (not shown). We also checked that NDH is dominated by non-linear vertical advection in the eastern equatorial Pacific (An and Jin, 2004), which leads to a linear relationship between SST asymmetry and non-linear vertical advection in the Niño3 region (R^2=82.7% - not shown). Conversely, in the western equatorial Pacific where the thermocline is much deeper than in the east, non-linear vertical advection is weaker at the surface and non-linear zonal advection dominates NDH.

Figure 7 presents the scatterplot of non-linear zonal advection versus SST asymmetry in the Niño4eq region. Interestingly, a linear relationship is observed among the CGCMs, negative asymmetry increasing with non-linear zonal advection. Two models do not fit with the linear trend (BCCR-BCM2.0 and INM-CM3.0), which is due to the large asymmetry simulated by these models. Their large negative/positive asymmetry may be due to other non-linear processes in the tropical ocean-atmosphere coupled system than the advection processes considered here: vertical mixing in the ocean mixed layer (An and Jin, 2004), the asymmetric response of the atmosphere to warm and cold SST anomalies (Kang and Kug, 2002), the contribution of atmospheric non-linearities (Kessler and Kleeman, 1999; Perez et al., 2005; Philip and van Oldenborgh, 2009a,b) or the thermodynamic control on deep convection (Hoerling et al., 1997). Note also that the Niño4 box may not be appropriate for quantifying asymmetry in the West for all the models. For instance, INM-CM3.0 has a peak of variability in the far western Pacific (fig. 1q).

Considering the proposed classification in ENSO regime, we find that models dominated by the zonal advective feedback exhibit large negative asymmetry along with high non-linear zonal advection, except BCCR-BCM2.0 and MRI-CGCM2.3.2A. For the latter, the prevalence of the zonal advective feedback relatively to the thermocline feedback is due to a stronger negative departure of vertical advection than that of zonal advection (figure 2), which explains why non-linear zonal advection is lower and SST anomalies are positively skewed. Models dominated by the thermocline feedback

show higher asymmetry and lower non-linear zonal advection than SODA, except GFDL-CM2.1 which has closer values, and GFDL-CM2.0 which has slightly higher negative asymmetry. Surprisingly, all models having a hybrid feedback (except IPSL-CM4) also show higher asymmetry and lower non-linear advection than SODA: in most cases it is because the hybrid feedback is due to low mean vertical advection balancing the low zonal advection (CSIRO-MK3.0, INM-CM3.0, UKMO-HadCM3 – see figure 2). For UKMO-HadGEM1, it is due to a non-linear term of the opposite sign to the other zonal advection terms (figure 2). Interestingly, the ocean reanalysis almost lies on the regression line, supporting the interpretation presented above.

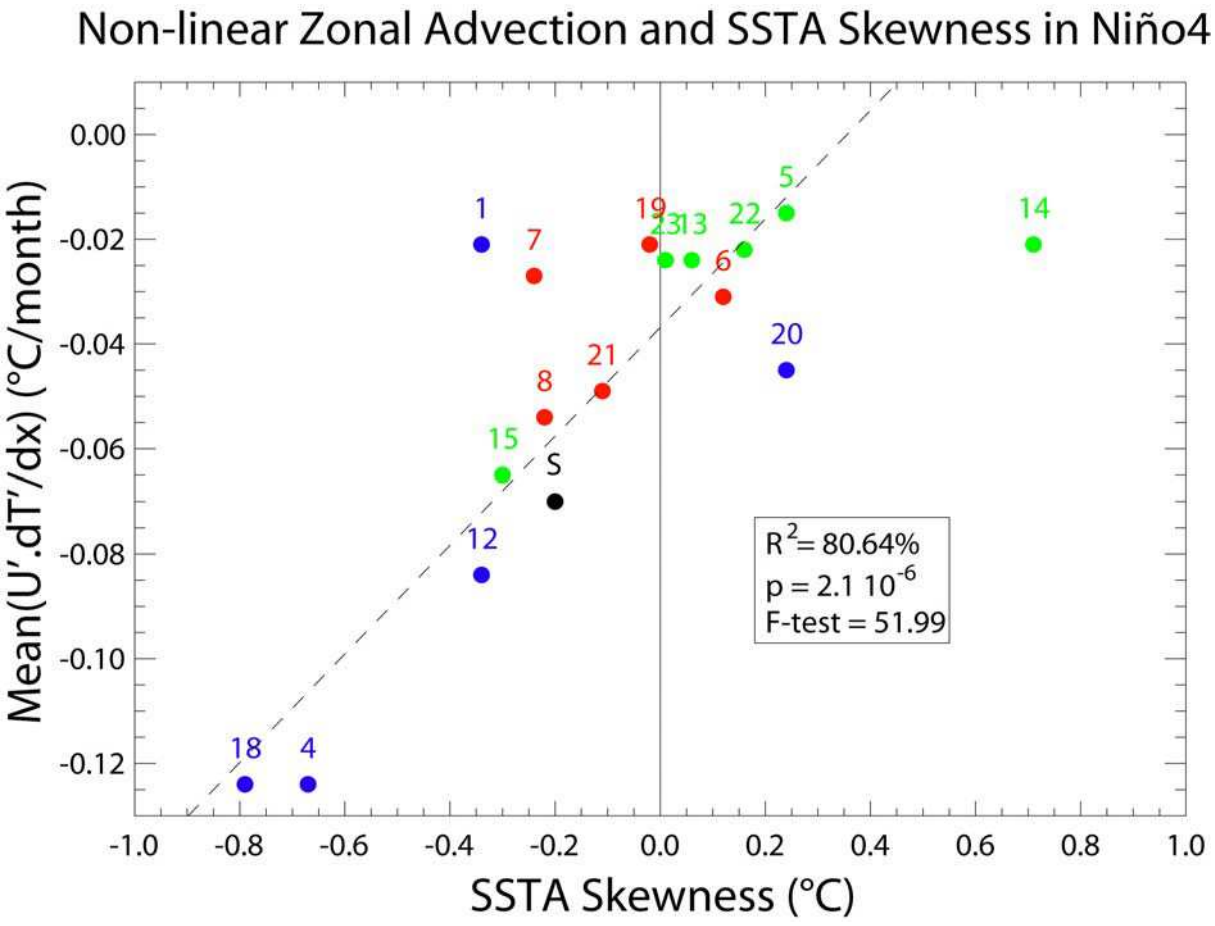

Fig. 7. Scatterplot of mean non-linear zonal advection (averaged over Niño4eq) vs. asymmetry of SST anomalies (averaged over Niño4) for the CMIP3 models.
Model names are referenced in table 1. The colour code is that of figure 6. The dotted line represents the result of the linear regression calculated for all models except BCCR-BCM2.0 and INM-CM3.0, with corresponding statistics marked on the plot. Units for non-linear advection (asymmetry) are °C/month (°C).

To summarize, it is proposed here that the mean cold bias around the edge of the western Pacific warm pool observed for all the models (fig. 6) is induced by a combination of mean and non-linear zonal advection terms, which are determined for most models by the privileged dynamical regime. It is then interesting to note that the biases in both the mean temperature field and the strength of non-linear advection are consistent with the biases in mean zonal circulation. These results suggest

the existence of a tropical rectification mechanism of ENSO dynamics by the privileged dynamical regime: the western equatorial Pacific cooling caused by zonal advection might lead to a strengthening of the mean trade winds through the linear response of the atmosphere to SST anomalies. Changes in the mean circulation may then feedback on the ENSO variability: in particular, the cooling tendency is associated to a shallower thermocline. This may result in enhanced anomalous transport in the upper layer and consequently increased anomalous zonal current anomalies that favour non-linear zonal advection. In addition, according to Philip and van Oldenborgh (2009a), the variability in non-linear zonal advection in the Niño4 region may originate from the non-linear atmospheric response to SST anomalies in the eastern Pacific. On the other hand, some studies point out the possible role of the mean trade winds in the off-equatorial region in the overestimation of zonal wind stress in the tropical Pacific (An and Wang, 2000; Wang and An, 2001). Further study is still needed in order to clearly document the respective roles of the tropics and the extra-tropics in the overestimation of the western Pacific zonal wind stress in the IPCC models.

2.1.4.2. Differences with earlier attempts to identify ENSO feedbacks in CGCMs

As mentioned in the introduction, this study is aimed at complementing those of VPC05 and G06 in regard to the determination of the privileged dynamical regime in the CMIP3 models.

VPC05 did not explicitly classify the models according to the ENSO regime. Instead, they provided a more qualitative interpretation of model behaviour. Since no clear classification was provided, no relation can be inferred from their study between dynamical regimes and ENSO time scale. However, they did mention a group of models which is more wind driven, mainly via zonal advection, and stated that these models tend to have a short ENSO cycle. Among them, three models are analyzed by both VPC05 and the present study (CSIRO-MK3.0, INM-CM3.0, NCAR-CCSM3.0): none of them are classified by the present paper as zonal advective feedback-dominated. In fact, the feedback loops characterized by VPC05 do not account for the same processes as the ones identified here, as discussed below.

The main difference between the two studies comes from the formulation of the SST equation: while the dynamical model used here explicitly resolves the contributions of the tendency terms, the analysis proposed by VPC05 relies on the results of a linear model, which regresses the rate of SST change on zonal wind stress and thermocline depth anomalies (Burgers and van Oldenborgh, 2003). Wind stress actually induces both horizontal advection in the mixed layer and upwelling across the thermocline, in addition to evaporation. Upwelling is then able to influence thermocline depth anomalies, which makes the separation between the respective effects of wind stress and thermocline

anomalies on SST subject to debate. Hence an enhanced SST response to wind anomalies for instance does not necessarily lead to a short or to a long ENSO cycle, since it involves both zonal advection and thermocline feedbacks.

In addition, their study requires the linear assumption formulated in the SST equation. By doing so, they neglect the contribution of non-linear advection, though it is known to be responsible for El Niño-La Niña asymmetry, extreme El Niño events, and mean state changes at decadal time scales (Timmermann and Jin, 2002; An and Jin, 2004).

Lastly, we described the dependence of the balance between the ENSO feedbacks ($\frac{\overline{w}.(T')_z}{\overline{u}.(T')_x}$) on both the mean circulation ($\frac{\overline{w}}{\overline{u}}$) and the 'upwelling feedback' α assessed by VPC05: their study does not take the former into account, despite its major role in the stability of ENSO in the CGCMs. Conversely, our study does not find any clear relationship between the ENSO regime – and thus the ENSO period - and the 'wind feedback' as defined by VPC05. In the case of the three wind-driven short-ENSO models mentioned previously: 1) INM-CM3.0 is characterized here by a quite realistic period (3.3 years) and a hybrid ENSO regime, but comes with a very broad frequency band in VPC05 (1.5-9 years), which implies much uncertainty on their estimate of the cycle length; 2) the short ENSO cycle exhibited by NCAR-CCSM3.0 might be due to teleconnections with dynamics from outside the Pacific (Yu et al., 2008), rather than the ENSO regime which is diagnosed here as thermocline driven (section 3.3); 3) the present paper does not specificly explain the short ENSO cycle for CSIRO-MK3.0 in spite of its realistic mean circulation (fig.4). However, it is one of the few CGCMs with an ENSO time scale which is way outside the usual range found within each category (fig. 5).

On the other hand, seven out of twelve CGCMs that both G06 and the present study analyze have coherent dynamical regimes, assuming that the separation between S- and T-modes based on the direction of propagation of SST anomalies can provide an estimate of the dominant feedback process. Among these models, four present a hybrid mode: INM-CM3.0, IPSL-CM4, UKMO-HadCM3 and UKMO-HadGEM1. Interestingly, they are among the most realistic models in terms of spatial and temporal structure of the ENSO mode, except INM-CM3.0 which features an unrealistic maximum of SST anomalies over the warm pool (fig.1q). However, no clear relationship is found between ENSO frequency and El Niño mode by G06, and only a slight tendency towards lower ENSO frequency by models exhibiting a T-mode is observed.

The main differences with the present study are that no subsurface data is considered in G06, and that the dominant feedback is diagnosed in G06 from the direction of propagation of SST

anomalies. Most models exhibit an S-mode or a hybrid mode. Even the observed data from after the 1976 climate shift feature a moderate T-mode, consistently with the observed tendency towards westward propagation of SST anomalies before the shift and mixed eastward propagation and standing oscillations after the shift (An and Jin, 2000; Wang and An, 2001). This implies that the diagnostic proposed in order to separate models with an S-mode and models with a T-mode does not allow very marked categories, conversely to the present study (fig.4). In particular, few models exhibit a T-mode, as a dominant thermocline feedback may still be associated to mixed eastward and westward propagation if the zonal advective feedback is also present.

Nevertheless, an inverse relation is observed by G06 for a subset of models between ENSO frequency and 'interannual coupling strength' - *i.e.* the sensitivity of western Pacific wind anomalies to eastern Pacific SST anomalies -, consistently with results from simple coupled models (Zebiak and Cane, 1987; An and Jin, 2000; Fedorov and Philander, 2000). In fact, the coupling strength controls both the growth rate and the frequency of ENSO, as long as the relative contribution of the zonal advective feedback and the thermocline feedback is kept constant (An and Jin, 2001). The relation found by G06 is therefore not necessarily contradictory with results from the present study, but it is not sufficient to explain the range of ENSO frequencies exhibited by the whole ensemble of CGCMs. For instance, MRI-CGCM2.3.2A features a high frequency ENSO cycle together with high coupling, possibly because of the dominant zonal advective feedback in this model.

2.1.5. Conclusions

In this study, 16 CGCMs of the CMIP3 multi-model ensemble were analyzed under pre-industrial climate conditions in order to investigate the impact of the mean oceanic state over time scales of ENSO variability. Results of the SVD between wind stress anomalies and SST anomalies allow characterizing ENSO-like variabilities. A large diversity of characteristics is found between the models in terms of amplitude, pattern and frequencies, consistently with previous studies (VPC05; G06; Capotondi et al., 2006).

A simple linear model of the tropical Pacific Ocean forced by winds from the CGCMs is used to estimate the zonal and vertical advection contributions to the rate of SST change in all the models. It reveals that the main source of error in the ensemble with regards to the dominant feedbacks (thermocline versus zonal advective feedbacks) can be inferred from the mean advection of anomalous temperature. A simple diagnostic based on the mean velocity fields in the surface layer is therefore proposed to classify the models according to their privileged ENSO regime. It leads to three groups of models characterized by their tendency to enhance one feedback over the other. The group

of models presenting a balance between zonal and vertical advection comparable to SODA corresponds to the so-called 'hybrid feedback' group and gathers the most realistic models in terms of the ENSO mode ocean dynamics.

ENSO frequencies are then analyzed according to the classification by the dominant feedback. Consistently with previous results from theory, observed data and modelling studies (Fedorov and Philander, 2001; VPC05; G06), it is shown that models dominated by the zonal advective (resp. thermocline) feedback have a short (resp. long) ENSO cycle. Indeed, whereas an overly dominant thermocline feedback favours the slow time scale of variability, the dominance of the zonal advective feedback is associated to faster horizontal advection of SST anomalies, which rectifies ENSO-like variability towards more energy in the high frequency band. Climate models from the hybrid group (CSIRO-MK3.0, INGV-ECHAM4, INM-CM3.0, IPSL-CM4, UKMO-HadCM3 and UKMO-HadGem1) have ENSO periods closer to the observations on average, and are considered the most reliable for climate projections under increasing concentrations of greenhouse gases. Note however that this might be less true for CSIRO-MK3.0 and INM-CM3.0: in these two models, the SST variability associated to ENSO is displaced towards the western equatorial Pacific (fig. 1). This may be the result of other mechanisms which were not explicitly taken into account in the present study, such as those contributing to the damping term of the SST equation for instance (*e.g.* the cloud feedback in the western Pacific).

The rectification of ENSO variability by the dominant feedback process through the impact of the mean ocean state – particularly in the western Pacific - on the equatorial dynamics is further investigated in the CGCMs: mean temperature biases and asymmetry of SST anomalies - mainly driven by non-linear zonal advection in the western equatorial Pacific - are assessed. Consistently with the results of Dewitte et al. (2007a), models dominated by the zonal advective (resp. thermocline) feedback have a higher (resp. lower) cold bias on average (though showing large variance from a model to another), and generally an increased negative (resp. a damped negative or even a positive) asymmetry. The models with a hybrid feedback mostly exhibit a moderate cold bias and a slightly positive asymmetry of SST anomalies, caused for most of them by relatively low zonal advection (compensated by low vertical advection). It is suggested that the mean cold (warm) bias of the western equatorial Pacific associated to strong (weak) westward climatological zonal currents is caused by non-linear advection.

Overall, this study provides a detailed methodology based on the use of a simplified tropical Pacific ocean model for diagnosing the dominant mode of variability in the tropical Pacific. Strikingly, despite the numerous differences in model physics and parameterizations, a coherent classification of the models can be established based on the coupled instability theory: biases of the

models can indeed be interpreted within these groups. It confirms the need of improving the mean climatological state simulated by state-of-the-art climate models, so as to improve the characteristics of simulated interannual variability under past/present climate conditions, and therefore our level of confidence in the climate projections for the next century.

This should provide useful information for the interpretation of the simulations with these same models considering an increase in CO_2 concentration, in the context of assessment studies of the impact of climate change on ENSO variability. In particular, warming conditions are generally associated to a flattening thermocline, *i.e.* to a smaller zonal contrast of the thermocline between the warm pool and the cold tongue, and to a larger vertical gradient of temperature in the eastern Pacific mixed layer (An et al., 2008). Such changes may modify the prevalence of one feedback over the other. The latter tendency would tend to increase the strength of the thermocline feedback in the eastern Pacific. However, the decrease in the slope of the thermocline is accompanied for some models by a shallower thermocline and for others by a deeper thermocline in the eastern equatorial Pacific (Philip and van Oldenborgh, 2006). Depending on the amplitude of ENSO variability, a deeper (resp. shallower) thermocline in the east generally goes along with a reduction (resp. increase) of the thermocline feedback in the eastern equatorial Pacific, because vertical displacement of the thermocline tends to have less (resp. more) impact on the temperature of water which upwells into the surface mixed layer.

The combination of these different effects makes it difficult to speculate about the future evolution of the balance between the zonal advective feedback and the thermocline feedback under global warming. In addition, the simultaneous impact of the wind forcing on both feedback processes does not allow formulating a clear hypothesis to be associated to the observed reduction of the walker circulation in the IPCC models considering the increase in CO_2 concentration (Vecchi and Soden, 2007). Indeed, the present study focuses on the biases in the oceanic component of the system. Yet, ENSO is a coupled ocean-atmosphere mode of climate variability, and the differences in atmospheric behaviour between models can often be larger than those in oceanic responses. A limitation to this work is that the atmospheric response to SST anomalies and its effect on the zonal advective feedback and the thermocline feedback were not explicitly documented. Nevertheless, the former are driven to a large extent by the atmospheric part of the cycle, which implies that the atmospheric responses of the models were still implicitly taken into account by the methodology presented here. The possible changes of ENSO feedbacks under global warming and their relation with changes in both the mean surface winds and thermocline characteristics are topics for future research.

Acknowledgements

We are grateful to D. Battisti, J. Boucharel, M. Lengaigne and Y. duPenhoat for fruitful discussions, to S. Bertrand and A. Chaigneau for their help with statistical computation, and to E. Guilyardi, S.Y. Philip, G.J. van Oldenborgh and an anonymous reviewer for their help in the improvement of the original manuscript. We acknowledge the modelling groups, the Program for Climate Model Diagnosis and Intercomparison (PCMDI) and the World Climate Research Programme's (WCRP's) Working Group on Coupled Modelling (WGCM) for their roles in making available the WCRP Coupled Model Intercomparison Project phase 3 (CMIP3) multi-model dataset. Support of this dataset is provided by the Office of Science, U.S. Department of Energy. GODAS data was provided by the NOAA/OAR/ESRL PSD, Boulder, Colorado, USA, from their web site at http://www.esrl.noaa.gov/psd/. ERSST data was also provided by the NOAA Earth System Research Laboratory (ESRL). We would like to thank the Peru-Chile Climate Change (PCCC) program of Agence Nationale de la Recherche (ANR) for financial support. S.-I. An was supported by "National Comprehensive Measures against Climate Change" Program by Ministry of Environment, Korea (Grant No. 1600-1637-301-210-13).

References

AchutaRao, K., and K. Sperber, 2002: Simulation of the El Niño-Southern Oscillation: Results from the Coupled Model Intercomparison Project (CMIP). *Climate Dyn.*, **19**, 191-209.

---, and ---, 2006: ENSO simulation in coupled ocean-atmosphere models: are the current models better ? *Climate Dyn.*, **27**, 1-15.

Adler, R. F., G. J. Huffman, A. Chang, R. Ferraro, P.-P. Xie, J. Janowiak, B. Rudolf, U. Schneider, S. Curtis, D. Bolvin, A. Gruber, J. Susskind, P. Arkin, and E. Nelkin, 2003: The Version-2 Global Precipitation Climatology Project (GPCP) Monthly Precipitation analysis (1979-present). *J. Hydrometeorol.*, **4**, 1147-1167.

An, S.-I., 2004: Interdecadal changes in the El Niño-La Niña asymmetry. *Geophys. Res. Lett.*, **31**, L23210, doi:10.1029/2004GL021699.

---, and F.-F. Jin, 2000: An eigen analysis of the interdecadal changes in the structure and frequency of ENSO Mode. *Geophys. Res. Lett.*, **27**, 1573-2576.

---, and B. Wang, 2000: Interdecadal change of the structure of the ENSO mode and its impact on the ENSO frequency. *J. Climate*, **13**, 2044-2055.

---, and F.-F. Jin, 2001: Collective role of thermocline and zonal advective feedbacks in the ENSO mode. *J. Climate*, **14**, 3421-3432.

---, and ---, 2004: Nonlinearity and asymmetry of ENSO. *J. Climate*, **17**, 2399-2412.

---, F.-F. Jin, and I.-S. Kang, 1999: The role of zonal advection feedback in phase transition and growth of ENSO in the Cane-Zebiak model. *J. Meteor. Soc. Japan*, **77**, 1151-1160.

---, Y.-G. Ham, J.-S. Kug, F.-F. Jin, and I.-S. Kang, 2005: El Niño-La Niña asymmetry in the Coupled Model Intercomparison Project simulations. *J. Climate*, **18**, 2617-2627.

---, J.-S. Kug, Y.-G. Ham, and I.-S. Kang, 2008: Successive modulation of ENSO to the future greenhouse warming. *J. Climate*, **21**, 3-21.

Battisti, D. S., and A. C. Hirst, 1989: Interannual variability in the tropical atmosphere/ocean system: Influence of the basic state and ocean geometry. *J. Atmos. Sci.*, **46**, 1687-1712.

Behringer, D.W., and Y. Xue, 2004: Evaluation of the global ocean data assimilation system at NCEP: The Pacific Ocean. *Eighth Symposium on Integrated Observing and Assimilation Systems for Atmosphere, Oceans, and Land Surface*, AMS 84th Annual Meeting, Washington State Convention and Trade Center, Seattle, Washington, 11-15.

Bretherton, C. S., C. Smith, and J. M. Wallace, 1992: An intercomparison of methods for finding coupled patterns in climate data. *J. Climate*, **5**, 541-560.

Burgers, G., and G. J. van Oldenborgh, 2003: On the impact of local feedbacks in the central Pacific on the ENSO cycle. *J. Climate*, **16**, 2396-2407.

---, M. A. Balmaseda, F. C. Vossepoel, G. J. van Oldenborgh, and P. J. van Leeuwen, 2002: Balanced ocean-data assimilation near the equator. *J. Phys. Oceanogr.*, **32**, 2509-2529.

Capotondi, A., A. Wittenberg, and S. Masina, 2006: Spatial and temporal structure of tropical Pacific interannual variability in 20th century coupled simulations. *Ocean Mod.*, **15**, 274-298.

Carton, J. A., and B. S. Giese, 2008: SODA: A reanalysis of ocean climate. *Mon. Wea. Rev., in press.*

---, G. A. Chepurin, X. Cao, and B. S. Giese, 2000: A Simple Ocean Data Assimilation analysis of the global upper ocean 1950-1995, Part 1: methodology. *J. Phys. Oceanogr.*, **30**, 294-309.

Cibot, C., E. Maisonnave, L. Terray, and B. Dewitte, 2005: Mechanisms of tropical Pacific interannual-to-decadal variability in the ARPEGE/ORCA global coupled model. *Climate Dyn.*, **24**, 823-842.

Derber, J. C., and A. Rosati, 1989: A global oceanic data assimilation system. *J. Phys. Oceanogr.*, **19**, 1333-1347.

Dewitte, B., 2000: Sensitivity of an intermediate coupled ocean-atmosphere model of the tropical Pacific to its oceanic vertical structure. *J. Climate*, **13**, 2363-2388.

---, and C. Périgaud, 1996: El Niño-La Niña events simulated with Cane and Zebiak's model and observed with satellite or in situ data. Part II: model forced with observations. *J. Climate*, **9**, 1188-1207.

---, and G. Reverdin, 2000: Vertically propagating annual and interannual variability in an OGCM simulation of the tropical Pacific in 1985-1994. *J. Phys. Oceanogr.*, **30**, 1562-1581.

---, ---, and C. Maes, 1999: Vertical structure of an OGCM forced simulation of the tropical Pacific in 1985–1994. *J. Phys. Oceanogr.,* **29,** 1542–1570.

---, D. Gushchina, Y. duPenhoat, and S. Lakeev, 2002: On the importance of subsurface variability for ENSO simulation and prediction with intermediate coupled models of the Tropical Pacific: A case study for the 1997-98 El Niño. *Geophys. Res. Lett.,* **29** (14)**,** doi:10.1029/2001GL014452.

---, C. Cibot, C. Périgaud, S.-I. An, and L. Terray, 2007a: Interaction between Near-Annual and ENSO modes in a CGCM simulation: Role of the equatorial background mean state. *J. Climate*, **20**, 1035-1052.

---, S.-W. Yeh, B.-K. Moon, C. Cibot, and L. Terray, 2007b: Rectification of the ENSO variability by interdecadal changes in the equatorial background mean state in a CGCM simulation. *J. Climate,* **20**, 2002-2021.

Fedorov, A. V., and S. G. Philander, 2000: Is El Niño changing ? *Science,* **288**, 1997. doi:10.1126/science.288.5473.1997

---, and ---, 2001: A stability analysis of tropical ocean-atmosphere interactions: bridging measurements and theory for El Niño. *J. Climate,* **14**, 3086-3101.

Fjelstad, J. E., 1933: Interne wellen. *Geofys. Publi.,* **10**, 35pp.

Guilyardi, E., 2006: El Niño-mean state-seasonal cycle interactions in a multi-model ensemble. *Climate Dyn.*, **26**, 329-348.
---, S. Gualdi, J. M. Slingo, A. Navarra, P. Delecluse, J. Cole, G. Madec, M. Roberts, M. Latif, and L. Terray, 2004: Representing El Niño in coupled ocean-atmosphere GCMs: The dominant role of the atmospheric component. *J. Climate*, **17**, 4623-4629.
---, A. Wittenberg, A. Fedorov, M. Collins, C. Wang, A. Capotondi, G. J. van Oldenborgh, and T. Stockdale, 2009: Understanding El Niño in ocean-atmosphere general circulation models: Progress and challenges. *Bull. Amer. Meteor. Soc.*, doi:10.1175/2008BAMS2387.1, 325-340.
Hirst, A. C., 1986: Unstable and damped equatorial modes in simple coupled ocean-atmosphere models. *J. Atmos. Sci.*, **43**, 606-630.
Hoerling, M. P., A. Kumar, and M. Zhong, 1997: El Niño, La Niña, and the nonlinearity of their teleconnections. *J. Climate*, **10**, 1769-1786.
Jin, F.-F., 1996: Tropical ocean-atmosphere interaction, the Pacific cold tongue, and the El Niño-Southern Oscillation. *Science*, **274**, 76-78.
---, 1997a: An equatorial ocean recharge paradigm for ENSO. Part I: Conceptual model. *J. Atmos. Sci.*, **54**, 811-829.
---, 1997b: An equatorial ocean recharge paradigm for ENSO. Part II: A stripped-down coupled model. *J. Atmos. Sci.*, **54**, 811-829.
---, and J. D. Neelin, 1993: Modes of interannual tropical ocean-atmosphere interaction – A unified view. Part I: Numerical results. *J. Atmos. Sci.*, **50**, 3477-3503.
---, and S.-I. An, 1999: Thermocline and zonal advective feedbacks within the equatorial ocean recharge oscillator model for ENSO. *Geophys. Res. Lett.*, **26** (19), 2989-2992.
---, J.-S. Kug, S.-I. An, and I.-S. Kang, 2003: A near-annual coupled ocean-atmosphere mode in the equatorial Pacific Ocean. *Geophys. Res. Lett.*, **30**, 1080, doi:10.1029/2002GL015983.
Kanamitsu, M., W. Ebisuzaki, J. Woollen, S.-K. Yang, J. J. Hnilo, M. Fiorino, and G. L. Potter, 2002: NCEP-DOE AMIP-II Reanalysis (R-2), *Bull. Amer. Meteor. Soc.*, **83**, 1631-1643.
Kang, I.-S., and J.-S. Kug, 2002: El Niño and La Niña sea surface temperature anomalies: Asymmetric characteristics associated with their wind stress anomalies. *J. Geophys. Res.*, **107** (D19), 4372-4381.
---, S.-I. An, and F.-F. Jin, 2001: A symmetric approximation of the SST anomaly equation for ENSO. *J. Meteor. Soc. Japan*, **79**, 1-10.
---, J.-S. Kug, S.-I. An, and F.-F. Jin, 2004: A near-annual Pacific Ocean basin mode. *J. Climate*, **17**, 2478-2488.
Kessler, W., and R. Kleeman, 1999: Rectification of the Madden-Julian oscillation into the ENSO cycle. *J. Climate*, **13**, 3560-3575.
Lighthill, M. J., 1969: Dynamical response of the Indian Ocean to the onset of the southwest monsoon. *Philos. Trans. Roy.Soc. London, Ser. A*, **265**, 45-92.
Lin, J. L., 2007: The double-ITCZ problem in IPCC AR4 coupled GCMs: Ocean–atmosphere feedback analysis. *J. Climate*, **20**, 4497–4525.
Meehl, G. A., 1987: The annual cycle and interannual variability in the tropical Indian and Pacific Ocean regions. *Mon. Wea. Rev.*, **115**, 27-50.
Moon, B.-K., S.-W. Yeh, B. Dewitte, J.-G. Jhun, I.-S. Kang, and B. P. Kirtman, 2004: Vertical structure variability in the equatorial Pacific before and after the Pacific climate shift of the 1970s. *Geophys. Res. Lett.*, **31**, L03203, doi:10.1029/2003GL018829.
Neelin, J. D., D. S. Battisti, A. C. Hirst, F.-F. Jin, Y. Wakata, T. Yamagata, and S. E. Zebiak, 1998: ENSO theory. *J. Geophys. Res.*, 1**03**, 14261-1290.
Pacanowski, R. C., and S. M. Griffies, 2000: MOM 3.0 Manual. *GFDL technical note*, 31 January 2000. Available on the GFDL web site.
Perez, C. L., A. M. Moore, J. Zavala-Garay, and R. Kleeman, 2005: A comparison of the influence of additive and multiplicative stochastic forcing on a coupled model of ENSO. *J. Climate*, **18**, 5066-5085.
Philip, S. Y., and G. J. van Oldenborgh, 2006: Shifts in ENSO coupling processes under global warming. *Geophys. Res. Lett.*, **33**, L11704.
---, and ---, 2009a: Significant atmospheric nonlinearities in the ENSO cycle. *J. Climate*, **22**, 4014-4028.
---, and ---, 2009b: Atmospheric properties and the ENSO cycle: models versus observations. *Clim. Dyn.*, doi:10.1007/s00382-009-0579-7.
Picaut, J., F. Masia, and Y. du Penhoat, 1997: An advective-reflective conceptual model for the oscillatory nature of the ENSO. *Science*, **277**, 663-666.
Ropelewski, C. F., M. S. Halpert, and X. Wang, 1992: Observed tropospheric biennial variability and its relationship to the Southern Oscillation. *J. Climate,* **5,** 594–614.
Schopf, P. S., and M. J. Suarez, 1988: Vacillations in a coupled ocean-atmosphere model. *J. Atmos. Sci.*, **45**, 549-566.
Smith, R. D., J. K. Dukowicz, and R. C. Malone, 1992: Parallel ocean general circulation modeling. *Physica D.*, **60**, 38-61.
Smith, T. M., R. W. Reynolds, T. C. Peterson, and J. Lawrimore, 2008: Improvements to NOAA's Historical Merged Land-Ocean Surface Temperature Analysis (1880-2006). *J. Clim.*, **21**, 2283-2296.
Steel, R. G. D., and J. H. Torrie, 1960: *Principles and procedures of statistics*, New York: MacGraw-Hill, 187-287.

Suarez, M. J., and P. S. Schopf, 1988: A delayed oscillator for ENSO. *J. Atmos. Sci.*, **45**, 3283-3287.
Timmermann, A., and F.-F. Jin, 2002: A nonlinear mechanism for decadal El Niño amplitude changes. *Geophys. Res. Lett.*, **29**, doi:10.1029/2001GL013369.
Torrence, C., and G. P. Compo, 1998: A practical guide to wavelet analysis. *Bull. Amer. Meteor. Soc.*, **79**, 1, 61-78.
Tourre, Y. M., Y. Kushnir, and W. B. White, 1999: Evolution of interdecadal variability in sea level pressure, sea surface temperature, and upper ocean temperature over the Pacific Ocean. *J. Phys. Oceanogr.,* **29,** 1528–1541.
Trenberth, K. E., and D. P. Stepaniak, 2001: Indices of El Niño evolution. *J. Climate*, **14**, 1697–1701.
Uppala, S. M., P. W. Kalberg, A. J. Simmons, U. Andrae, V. da Costa Bechtold, M. Fiorino, J. K. Gibson, J. Haseler, A. Hernandez, G. Kelly, X. Li, K. Onogi, S. Saarinen, N. Sokka, R. P. Allan, E. Anderson, K. Arpe, M. A. Balmaseda, A. C. M. Beljaars, L. van den Berg, J. Bidlot, N. Borman, S. Caires, A. Dethof, M. Dragosavac, M. Fisher, M. Fuentes, S. Hagemann, E. Holm, B. J. Hoskins, L. Isaksen, P. A. E. M. Janssen, R. Jenne, A. McNally, J.-F. Mahfouf, J.-J. Mocrette, N. A. Rayner, R. W. Saunders, P. Simon, A. Sterl, K. E. Trenberth, A. Untch, D. Vasiljevic, P. Viterbo, and J. Woollen, 2005: The ERA-40 re-analysis, *Quart. J. Roy.Meteor. Soc.*, **131**, 2961-3012.
van Oldenborgh, G. J., S. Y. Philip, and M. Collins, 2005: El Niño in a changing climate : a multi-model study. *Ocean Science*, **1**, 81-95.
Vecchi, G. A., and B. J. Soden, 2007: Global warming and the weakening of the tropical circulation. *J. Climate,* **20,** 4316–4340.
Wang, B., and S.-I. An, 2001: Why the properties of El Niño changed during the late 1970s. *Geophys. Res. Lett.,* **28,** 3709–3712.
Wittenberg, A. T., 2009: Are historical records sufficient to constrain ENSO simulations? *Geophys. Res. Lett.,* **36,** L12702, doi:10.1029/2009GL038710.
---, A. Rosati, N.-C. Lau, and J. J. Ploshay, 2006: GFDL's CM2 global coupled climate models. Part III: Tropical Pacific climate and ENSO. *J. Climate,* **19,** 698–722.
Yu, J.-Y., F. Sun and H.-Y. Kao, 2008: Contributions of Indian Ocean and monsoon biases to the excessive biennial ENSO in CCSM3. *J. Climate,* submitted.
Zebiak, S. E., and M. A. Cane, 1987: A model El Niño-Southern Oscillation. *Mon. Wea. Rev.,* **115,** 2262–2278.
Zhang, R.-H., L. M. Rothstein, and A. J. Busalacchi, 1999: Interannual and decadal variability of the subsurface thermal structure in the Pacific Ocean. *Climate Dyn.,* **15,** 703–717.

2.2. Properties of ENSO and the near-annual mode in climate models

2.2.1. Role of the near-annual mode in the ENSO cycle

In the previous section, emphasis was put on the role of the balance between the main oceanic feedbacks on the characteristics of ENSO variability. In particular, a dominant zonal advective feedback tends to favour a fast quasi-biennial horizontally-driven ENSO, whereas a dominant thermocline feedback tends to produce a slow recharge oscillator-like ENSO. Here we complement the study by Belmadani et al. (2009) with a focus on the specific role of the 'near-annual mode' (hereafter NAM).

According to earlier works based on both observations from the recent decades and conceptual modelling, tropical climate variability is dominated by two unstable modes that are independent from each other: ENSO and the NAM, also known as the 'mobile mode' or the 'fast coupled mode' of the tropical Pacific (Jin et al., 2003 – hereafter J03; Kang et al., 2004 – hereafter K04). Whereas the former was shown to be mainly related to the thermocline feedback and only moderately due to the zonal advective feedback (Jin, 1997a,b; Jin and An, 1999), the latter was described as a 'Pacific Ocean Basin mode' (hereafter POB) or 'gravest ocean mode' (Cane and Moore, 1981; Mantua and Battisti, 1995) modified by the zonal advective feedback (J03; K04). Indeed, POB is a free solution of the linear reduced-gravity model of the tropical upper-ocean dynamics under equatorial β-plane approximations, related to the basin-wide eastward propagation of equatorial Kelvin waves and the associated slower westward propagation of first baroclinic off-equatorial Rossby waves. The near-annual periodicity of POB is set by the time taken by Kelvin waves to cross the basin (around 2 months with a phase speed of the order of 2.5 $m.s^{-1}$ for the first baroclinic mode) plus the time taken by Rossby waves to cross the basin (around 6 months with a phase speed of the order of 1 $m.s^{-1}$ for the first baroclinic mode). The analytical study by Neelin and Jin (1993) and the more recent works by J03 and K04 showed that the zonal advective feedback is effective in destabilizing POB through ocean-atmosphere coupling. The latter study made use of the two-strip simple coupled model of An and Jin (2001) to show the sensitivity of both ENSO and the NAM to the background state of tropical Pacific climate: for the 1980-2001 period, the slow ENSO mode was found to be the most unstable coupled mode, and the fast NAM to be the secondary unstable mode, whereas for the 1999-2001 period characterized by weaker mean upwelling and thus a larger relative contribution of the zonal advective feedback, the dominant unstable mode turned out to be the NAM, and the secondary mode to be ENSO. Note that observational evidence of the NAM was presented by J03 and K04 using observed and reanalysis datasets, which also revealed the

existence of a stronger NAM for the post-1998 years (after the major 1997-98 El Niño event) than during the 1980s and 1990s when the thermocline feedback was most active and ENSO variability dominated by Jin (1997)'s recharge oscillator paradigm (Jin, 1997a,b), supporting the afore-mentioned modelling results.

The co-existence of these two coupled modes in the real world has several important implications. One is that they are responsible to a large extent to the richness of the spectrum of tropical climate variability, which extends from near-annual and quasi-biennial (Meehl, 1987; Ropelewski et al., 1992) to decadal (Tourre et al., 1999; Zhang et al., 1999) time scales and beyond. Their inverse dependencies to the mean state suggest a strong interaction between both coupled modes: in particular, minor nearly-annual El Niño events of the warm early 1990s and La Niña events of the cold early 2000s may be due to the NAM (J03; K04). This means that the NAM is likely to modify ENSO and its periodicity. However, the superimposition of both coupled modes associated to the relatively short observational records make the NAM and its interaction with ENSO difficult to observe in the real world (Mantua and Battisti, 1995; J03). Long term CGCM simulations in which the NAM can develop and be identified offer the opportunity to document its role on the ENSO variability and mean state. In this respect, Dewitte et al. (2007 –hereafter D07) demonstrated from a previous version of the CNRM-CM3 model (member of the CMIP3 dataset), that the ENSO mode and the NAM could interact to produce a quasi-biennial ENSO (Cibot et al., 2005). Such interaction takes place through non-linearities associated with the zonal advective feedback: D07 showed that the cold bias of the coupled model over the western Pacific warm pool was due to the asymmetry of both ENSO and the NAM. The latter is the result of advection of anomalous temperature by the mean zonal currents ($-\bar{u}.(T')_x$) and non-linear zonal advection ($-u'.(T')_x$), the main contributors to the zonal advective feedback in this model. As mentioned in the previous section, we suggest that biases in the mean temperature field are likely to feedback on the dynamical regime of ENSO, and thereby on the time scale of ENSO variability: cold biases tend to enhance the zonal advective feedback and the NAM, whereas warm biases tend to favour the thermocline feedback and damp the NAM. In the following, we extend the approach of D07 to a more comprehensive data set: the CGCMs of the CMIP3 archive. It is verified that in most cases, the over-estimation (resp. under-estimation) of the zonal advective feedback can be related to the high (resp. low) energy level of near-annual activity. Note that only the 16 CGCMs with a statistically significant ENSO (see previous section) are considered here.

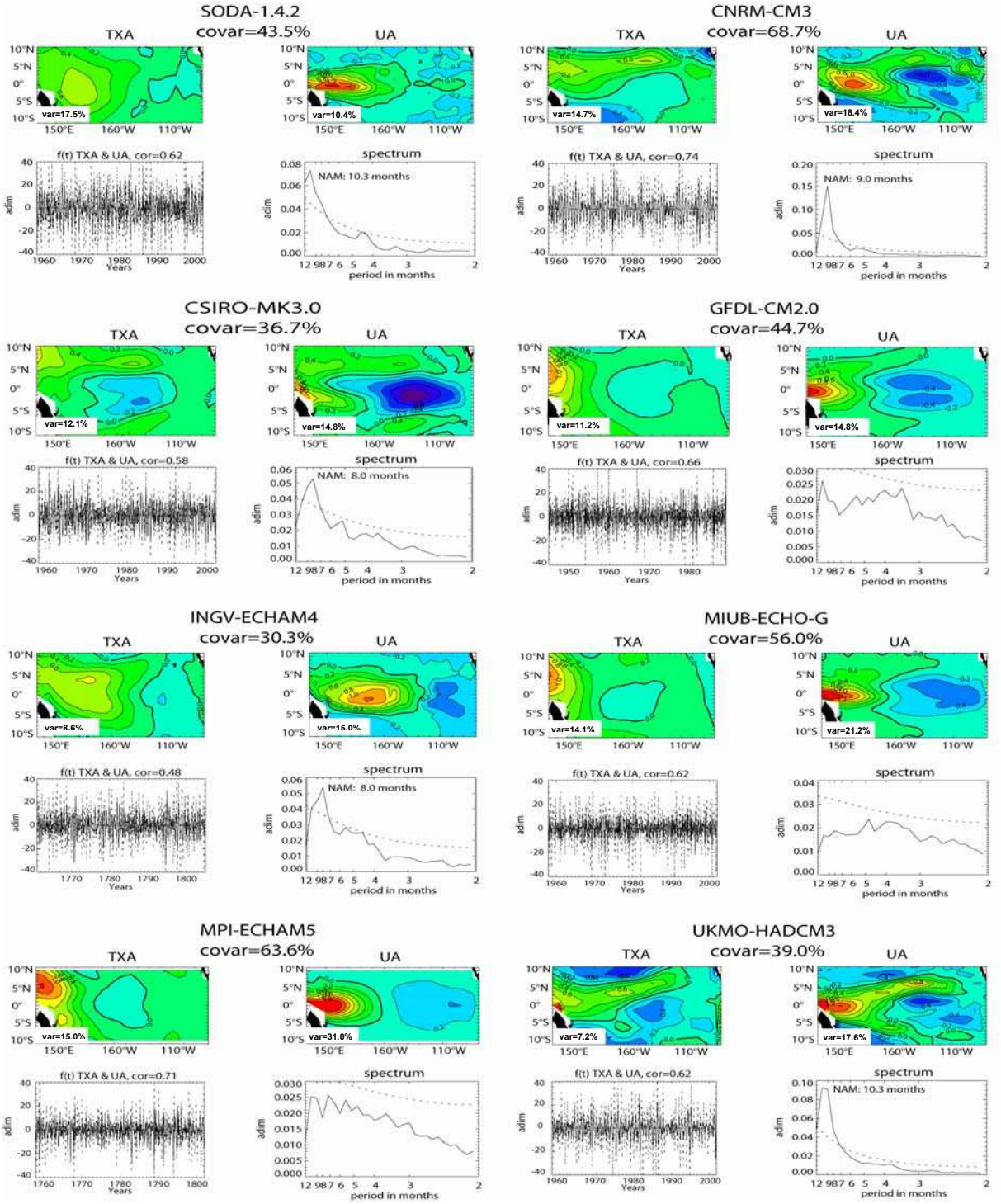

Fig. 2.1. First SVD mode between the 12-month high-pass-filtered wind stress and surface zonal current anomalies (11°S-11°N, 134°E-81°W): **(a)** SODA 1.4.2, **(b)** CNRM-CM3, **(c)** CSIRO-MK3.0, **(d)** GFDL-CM2.0, **(e)** INGV-ECHAM4, **(f)** MIUB-ECHO-G, **(g)** MPI-ECHAM5, **(h)** UKMO-HadCM3. For each model, from left to right and top to bottom: spatial patterns for zonal wind stress and current anomalies, associated adimensionalized time series (full line for currents, dashed line for wind stress anomalies), and the corresponding frequency spectra adimensionalized by the energy integrated over the whole frequency domain (full line for currents, dashed line for red noise). CI = 0.2 units. Spatial patterns are adimensionalized by their respective variance over the domain and multiplied by 10. Percentage of explained variance for zonal currents and wind stress are indicated on the corresponding panels. Percentage of explained covariance is also provided. Correlation value between time series is indicated above the corresponding panel and the dominant NAM period is mentioned on the spectrum plot if significant.

Following D07, the NAM in the models was diagnosed from the results of the SVD between the 12-month high-pass-filtered surface zonal current and wind stress anomalies in the tropical Pacific Ocean area (defined as 11°S-11°N, 120°E-70°W) for the whole available time periods of simulation (table 1 from previous section). Surface zonal currents are estimated here as the average of the top four model levels, since these correspond to the first thirty or fourty meters depth for most CGCMs. Anomalies, frequency spectra and NAM periods are computed in a similar way to that of the ENSO mode (see previous section). Results are presented in figure 2.1 for the same models as in figure 1 from the previous section. Most models, including SODA, show similar spatial patterns: a relatively strong maximum variability in the western equatorial Pacific for zonal currents, with a symmetric horseshoe pattern for several models (CNRM-CM3, CSIRO-MK3.0, GFDL-CM2.0, MIUB-ECHO-G, UKMO-HadCM3), typical of Rossby waves and consistently with D07. The associated wind stress patterns also show a maximum variability in the western equatorial Pacific. The coupled nature of this fast mode of variability is confirmed by the rather strong correlation values between time series associated to currents and wind stress (table 2.1).

Table 2.1. Near-Annual Characteristics of the models.

Model Name	Model Number	NAM Period (months)	Correlation between time series	Near-Annual Activity Index ($x10^{-3}$ $(m/s)^2$)
SODA 1.4.2	----	10.3	0.62	11.58
BCCR-BCM2.0	1	----	0.59	2.35
CNRM-CM3	4	9.0	0.74	9.25
CSIRO-MK3.0 (run1)	5	8.0	0.58	1.11
CSIRO-MK3.5	6	10.3	0.61	1.24
GFDL-CM2.0	7	----	0.66	2.41
GFDL-CM2.1	8	8.0	0.68	5.41
IAP-FGOALS1.0-g (run1)	12	9.0	0.76	3.05
INGV-ECHAM4	13	8.0	0.48	2.59
INM-CM3.0	14	9.0	0.68	2.98
IPSL-CM4	15	9.0	0.58	3.78
MIUB-ECHO-G	18	----	0.62	6.88
MPI-ECHAM5	19	----	0.71	2.66
MRI-CGCM2.3.2A	20	7.2	0.87	5.51
NCAR-CCSM3.0 (run2)	21	8.0	0.68	2.50
UKMO-HadCM3 (run1)	22	10.3	0.62	3.33
UKMO-HadGEM1	23	10.3	0.61	3.02

Concerning temporal characteristics, results are more contrasted. A NAM seems to be detectable for most models in the [7.5 - 10.5] $month^{-1}$ frequency band (table 2.1), although it is not statistically significant for some of them, like GFDL-CM2.0, MIUB-ECHO-G or MPI-ECHAM5 for example. This is believed to be due to the fact that NAM activity characteristics (in particular its period) are sensitive to changes in the mean state, which the SVD analysis cannot grasp. However, the similar structure of the mode captured by the SVD analysis among the models suggests the

existence of such mode for most CGCMs. For this reason, and because we do not focus here on the time scale of the NAM, this lack of statistical significance for some models will not be considered in the rest of the study. Conversely, some models have a very marked peak, CNRM-CM3 or even UKMO-HadCM3 being good examples. SODA also features a clear peak at 10.3 months associated to the NAM. The period of the NAM is quite heterogenous (table 2.1), going from 7.2 months for MRI-CGCM2.3.2A to 10.3 months for CSIRO-MK3.5 and the UKMO models.

In order to infer an index of NAM activity, zonal current anomalies are first averaged over the Niño-4 box (5°S-5°N, 160°E-150°W), the region over which the NAM exhibits a peak in variance (figure 2.1). The scale-average time series of the corresponding wavelet energy spectrum in the [6 – 18] month^{-1} frequency band is then derived and the mean value over the whole time period provides an index of NAM activity. The near-annual activity index presents a wide range of values (table 2.1). Note that SODA exhibits a rather strong value compared to the models which has to be related to the shorter time period of the record and the fact that SODA has a richer spectrum of variability than the CGCMs. Other indices of NAM activity were tested, based on the results of the SVDs. They lead to comparable results. We chose to retain the NAM activity index based on the full zonal current anomalies for simplicity. An index based on SST anomalies was also tested. Such index exhibits similar tendency than the one based on zonal current anomalies although with a much reduced standard deviation between models. This is due to the fact that the NAM has a weaker signature in SST than in surface zonal current (Wu and Kirtman, 2005; D07). The index of NAM activity can then be used to assess the dependence of the NAM on the dominant ENSO feedback mechanism.

In the following, we investigate to which extent characteristics of the NAM can be related to the biases in the mean state identified in the previous section: according to previous studies (J03; K04; D07), it is expected that models with a dominant zonal advective feedback favor the enhancement of the NAM, leading to a 'fast' ENSO period (see previous section). On the other hand, models exhibiting a dominant thermocline feedback and thereby a 'slow' ENSO period (see previous section) should have a damped NAM.

Figure 2.2 presents the near-annual activity index for the 16 models, classified into the 3 groups: models dominated by the zonal advective feedback, models dominated by the thermocline feedback, and those with the combination of both mechanisms. Interestingly, models from the thermocline feedback group (group 3) have lower levels of near-annual activity. Models from the zonal advective feedback group (group 1) have a high near-annual activity index on average, though large discrepancies are found within the members of this group, while models from the hybrid feedback group (group 2) exhibit intermediate values that are more homogeneous. Most models from

group 1 (see corresponding error bars) have higher NAM index values or at least of the same order of magnitude than all models from group 2, and similarly, most models from group 2 have higher values or of the same order of magnitude than all models from group 3 (except GFDL-CM2.1). This confirms the fact that an enhanced (resp. diminished) zonal advective feedback is associated to a relatively larger (resp. smaller) NAM variability, itself leading to faster (resp. slower) interannual variabilities through time scale interactions (D07). Models with a hybrid dynamical regime are generally associated to intermediate energy levels of the NAM index. A similar tendency is observed when adimensionalizing the NAM index by the Niño3-SST index variability (not shown), even if the models with a dominant zonal advective feedback have on average a larger ENSO variability than the models of the other groups.

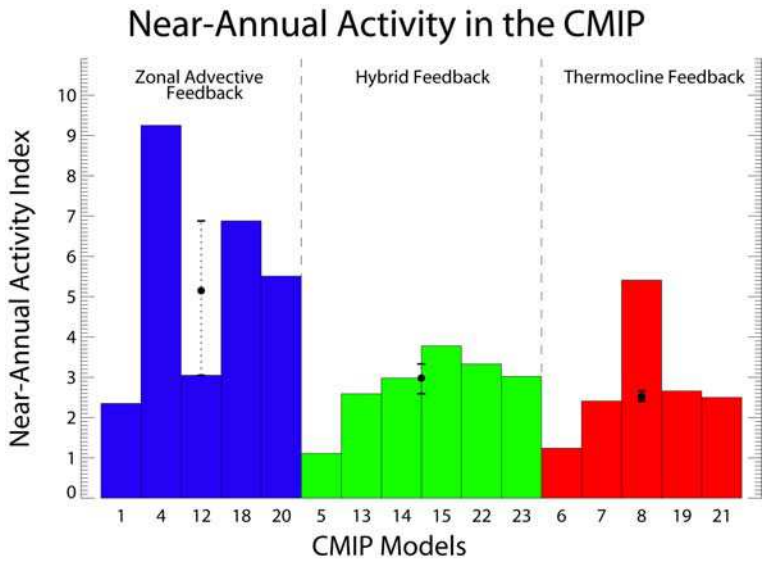

Fig. 2.2. Histogram of the Near-Annual Activity Index of the CMIP3 models. Model names are referenced in table 1 from previous section. The colour code is that of figure 6 from previous section. The black dot represents the mean value for each group. The mean was calculated excluding the models deviating from the mean by more than the standard deviation of the considered group. Error bars are provided, that correspond to the highest and lowest values of the models retained for the calculation of the mean value.

To summarize, it is shown here that consistent with theory, the NAM in IPCC climate models is enhanced when the mean state is colder over the western Pacific warm pool than observed, leading to favour the zonal advective feedback and a fast advective-reflective-type ENSO (Picaut et al., 1997), and damped when the mean state is warmer over the warm pool, setting the conditions for a dominant thermocline feedback together with a slow recharge-oscillator-type ENSO (Jin, 1997a,b).

a)

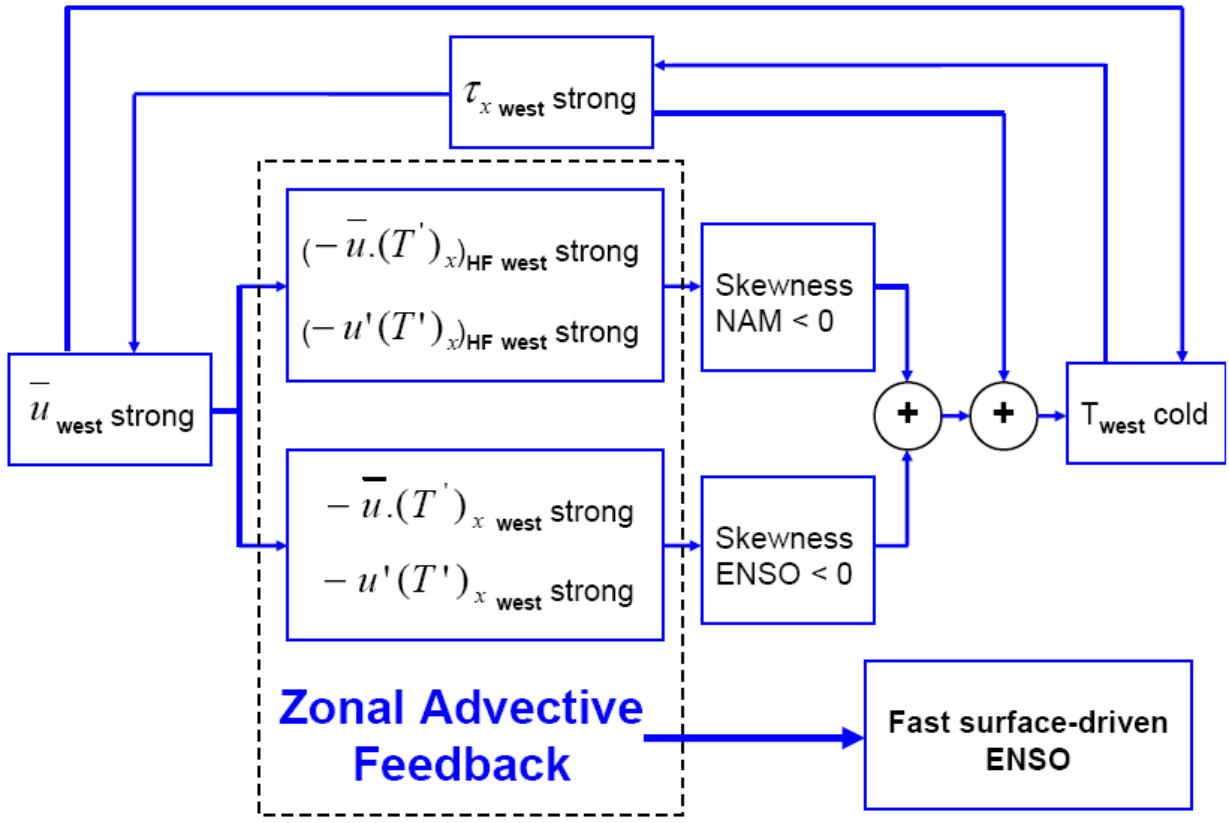
$\tau_{x\ \text{west}}$ strong
$(-\bar{u}.(T')_x)_{\text{HF west}}$ strong
$(-u'(T')_x)_{\text{HF west}}$ strong
$\bar{u}_{\text{west}}$ strong
$-\bar{u}.(T')_{x\ \text{west}}$ strong
$-u'(T')_{x\ \text{west}}$ strong
Skewness NAM < 0
Skewness ENSO < 0
T_{west} cold
Zonal Advective Feedback
Fast surface-driven ENSO

b)

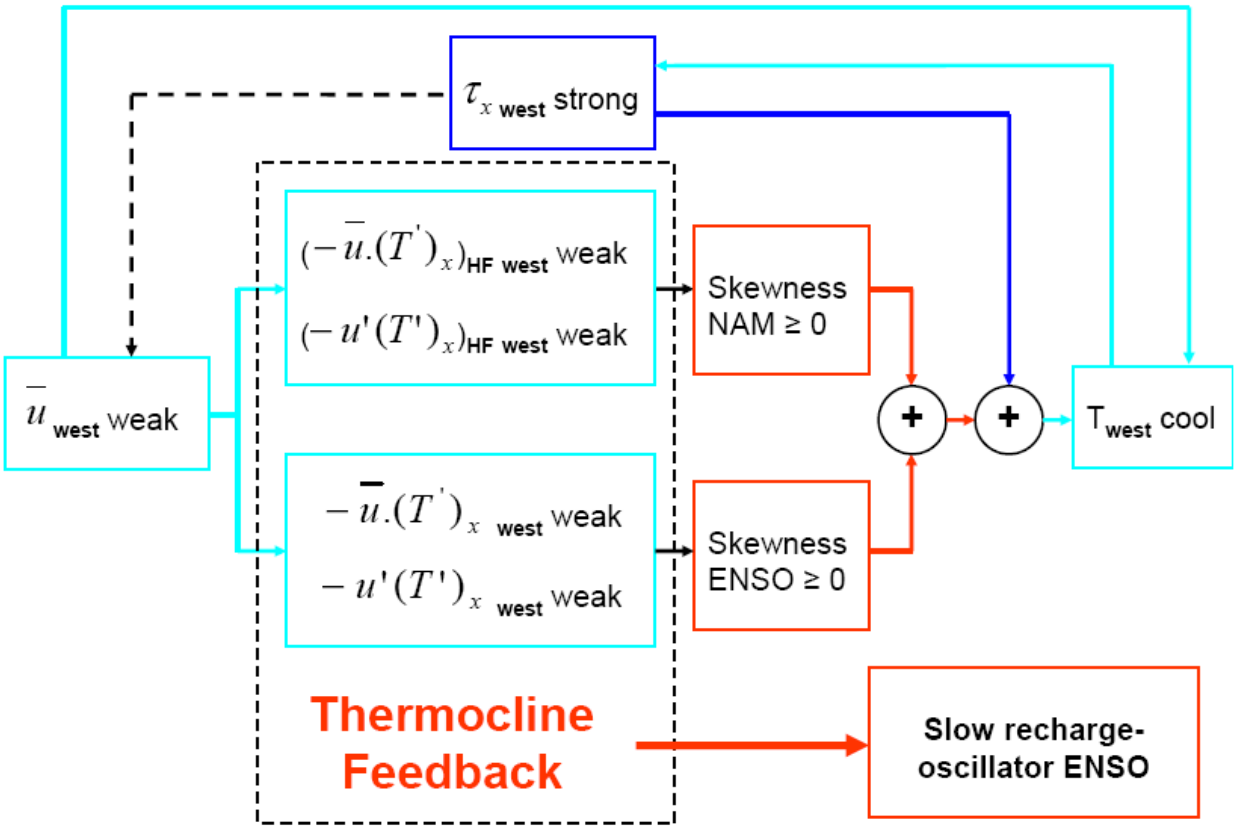
$\tau_{x\ \text{west}}$ strong
$(-\bar{u}.(T')_x)_{\text{HF west}}$ weak
$(-u'(T')_x)_{\text{HF west}}$ weak
$\bar{u}_{\text{west}}$ weak
$-\bar{u}.(T')_{x\ \text{west}}$ weak
$-u'(T')_{x\ \text{west}}$ weak
Skewness NAM ≥ 0
Skewness ENSO ≥ 0
T_{west} cool
Thermocline Feedback
Slow recharge-oscillator ENSO

Fig. 2.3. Schematic of the mechanisms involved in the interaction between ENSO, NAM and the mean state for **a)** a dominant zonal advective feedback and **b)** a dominant thermocline feedback. The colour code is for the temperature bias associated to the different processes: blue is for a colder state than observed, red is for a warmer state, and light blue is for a slightly colder state. In **a)**, strong easterlies over the warm pool ($\boldsymbol{\tau_{x}}_{west}$) tend to have a cooling effect on the surface ocean ($\mathbf{T}_{west}$) through mixing and entrainment, and through the forcing of strong westward surface flow ($\bar{u}_{west}$) that advects colder waters from the east towards the western Pacific. $\bar{u}_{west}$ is an index of the zonal advective feedback, involving overestimated advection of the temperature anomalies by the mean zonal currents ($-\bar{u}(T')_x$) and overestimated non-linear zonal advection *ie* the advection of temperature anomalies by the zonal current anomalies ($-u'(T')_x$). Such biases in the variability of non-linear advection at interannual (ENSO) and near-annual (NAM) time scales tend to produce cold SST asymmetry over the warm pool, which contributes to the cold bias in the mean temperature state. The latter feedbacks on the wind regime and sustains overestimated easterlies over the western equatorial Pacific, which contribute to enhance the zonal advective feedback. As a consequence, ENSO dynamics are controlled by zonal advection, and are associated to short time scales. In **b)**, warm pool easterlies are also overestimated - it is a common bias in coupled models (Guilyardi, 2006; Guilyardi et al., 2009) - and have a cooling effect on the surface ocean. However, a dominant thermocline feedback associated to enhanced eastern Pacific upwelling (see section 1.) tends to reduce the influence of the zonal advective feedback on ENSO, leading to weaker mean zonal currents and zonal advection terms. The weaker variability of non-linear advection and the weaker mean currents create a build-up of anomalous heat over the warm pool, which opposes the cold bias due to the wind forcing. As a result, the cold bias is reduced in the models with a dominant thermocline feedback, but still contributes to maintain the local winds. In this case, ENSO dynamics are controlled by vertical advection, and are associated to longer time scales. The dashed black arrow indicates that despite the overestimated wind stress, the mean westward currents tend to be weaker than observed.

Based on previous studies and results from the previous section, it is suggested that the NAM has a specific role in the modulation of ENSO by changes in the mean state and in the related feedback mechanisms (figure 2.3): the asymmetry of SST over the warm pool due to ENSO- and NAM-related non-linearities (see previous section) produces a non-zero residual which sign and amplitude depend on the dominant ENSO feedback mechanism. Thus models having a dominant zonal advective feedback will favour a cooling tendendy of the mean state over the warm pool region, producing a positive feedback on the NAM (cooler mean state will enhance NAM activity), whereas models having a dominant thermocline feedback through ENSO nonlinearity will tend to reduce the impact of the NAM on the mean state leading to a negative feedback. Such hypothesis will need to be investigated further in the light of the results of the analyses of the non-linear advection terms at both interannual and near-annual frequencies.

2.2.2. ENSO spatial and temporal properties in hybrid CGCMs

In section 1., we identified a group of six hybrid CGCMs in terms of ENSO feedbacks. Following Guilyardi et al. (2009), such a process-oriented study focusing on the physical mechanisms of the ENSO cycle can be used to identify a subset of more reliable models for the study of the impact of global warming on ENSO. Because of the strong influence of ENSO on the Humboldt Current System (Barber and Chavez, 1983), these climate models should also be more appropriate for the study of regional climate change off the western coast of South America. However, the fact that these models reproduce rather well the coupled instabilities that drive the ENSO mode does not guarantee the fidelity of spatial and temporal properties of ENSO, in particular those related to the fields at the ocean-atmosphere interface: surface winds and SST. CGCMs are much more complex models than simple or even intermediate coupled models of the tropical Pacific such as the Zebiak and Cane model (Zebiak and Cane, 1987) or LODCA (Dewitte, 2000): they rely on many parameterizations that can introduce significant differences with purely linear equatorial wave dynamics. Yet, surface fields are important for the initialization and forcing of a regional ocean model of the Peru-Chile coast. For this reason, we decided to investigate spatial and temporal characteristics of ENSO in the hybrid CGCMs, so as to further select the most relevant models for our regional study.

SVD analyzes between anomalies of wind stress and SST such as those performed by Belmadani et al. (2010) can be used to characterize the spatial and temporal behaviour of ENSO in the models (fig. 2.4 and table 2.2). As underlined by Belmadani et al. (2010), ENSO is characterized by the simultaneous development of zonal wind stress anomalies in the western and central tropical Pacific and SST anomalies in the eastern tropical Pacific (fig. 2.4). A notable exception is INM-CM3.0, for which maximum SST variability is located in the far western Pacific. CSIRO-MK3.0 also features a local peak over the warm pool region, although variability is higher in the eastern part of the basin. The coupled nature of the ENSO mode can be characterized here by the high correlation between time series associated to the first SVD mode: values vary among the CGCM ensemble between 82% and 94%, which are of the order of the observed value (91% for SODA). Since wind variability associated to ENSO is weak over the eastern Pacific, we focus here on the SST pattern.

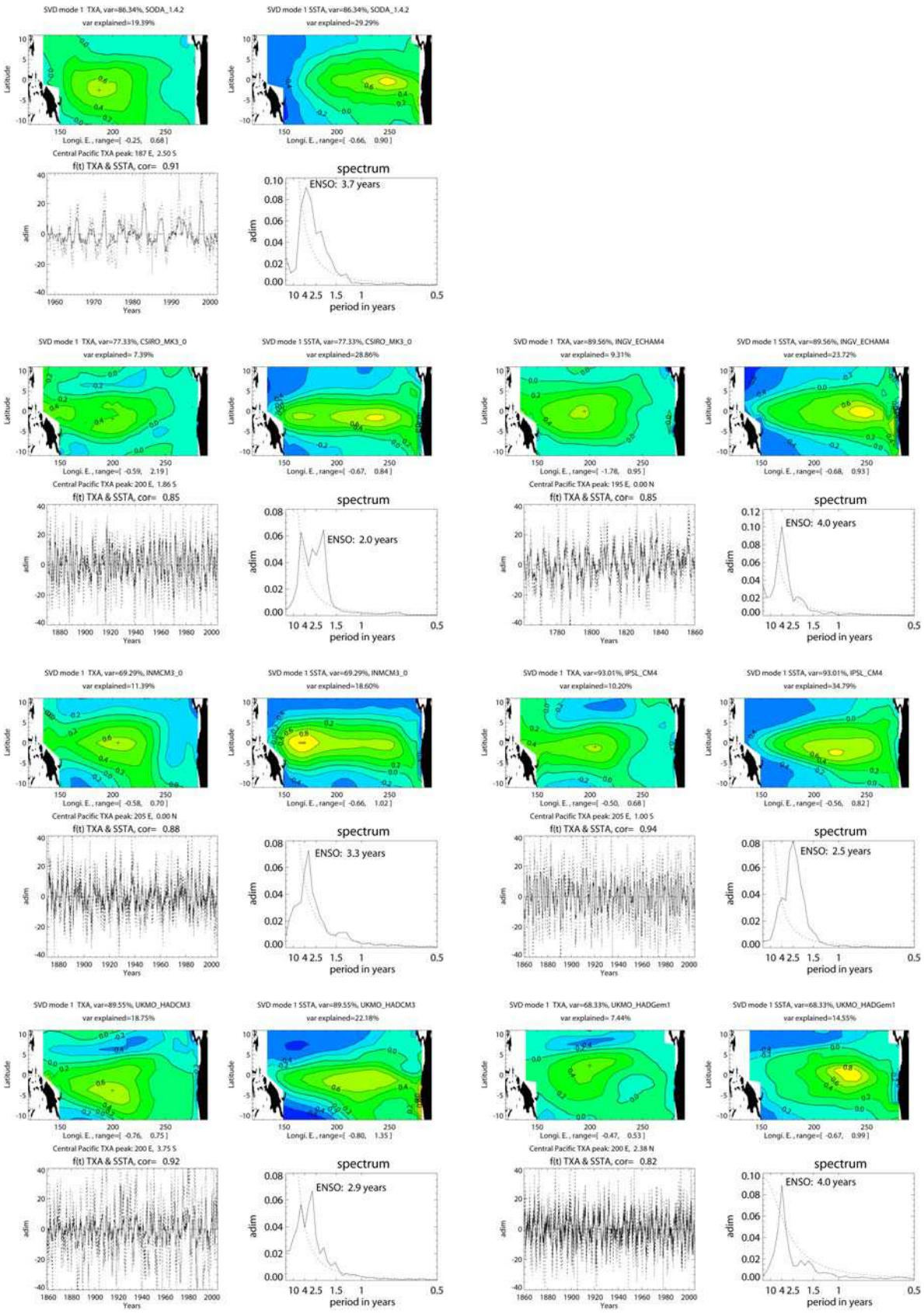

Fig. 2.4. Same as fig.1 from Belmadani et al. (2010), but for the hybrid models. From left to right and top to bottom: SODA 1.4.2, CSIRO-MK3.0, INGV-ECHAM4, INM-CM3.0, IPSL-CM4, UKMO-HadCM3, UKMO-HadGEM1.

All the CGCMs tend to have a wider zonal extent and a narrower meridional extent (except maybe UKMO-HadGEM1) than SODA. However, like SODA they all exhibit a meridionally asymmetric pattern for SST anomalies associated to ENSO, with stronger variability in the Southern tropical Pacific than in the Northern tropical Pacific, highlighting the influence of large-scale ENSO anomalies on nearshore variability off Peru. In terms of amplitude of SST variability, most models fall within the observed range. Computing the spatial correlation coefficient between patterns of first SVD mode SST anomalies from the CGCMs and from SODA allows quantifying the differences in spatial distribution of ENSO-related anomalies (table 2.2): whereas INGV-ECHAM4, IPSL-CM4, UKMO-HadCM3 and UKMO-HadGEM1 are well correlated to SODA, CSIRO-MK3.0 and especially INM-CM3.0 exhibit weaker values, which has to be related to the misplaced variability peaks in these models. The latter CGCM tends to produce a central Pacific El Niño (Larkin and Harrisson, 2005; Ashok et al., 2007, Kao and Yu, 2009), which is known to have very little influence on the South American coast (Kug et al., 2009), thereby limiting the interest of such model for the study of Peru-Chile climate change.

Model	Explained covariance (%)	Explained SST variance (%)	Explained τ_x variance (%)	PC time series correlation (%)	SST amplitude (adim.)	ENSO period (years)	Spatial correlation* with SODA (%)
CSIRO-MK3.0	77.3	28.9	7.4	85	0.84	2.0	72.4
INGV-ECHAM4	89.6	23.7	9.3	85	0.93	4.0	88.6
INM-CM3.0	69.3	18.6	11.4	88	1.02	3.3	49.3
IPSL-CM4	93.0	34.8	10.2	94	0.82	2.5	88.2
UKMO-HadCM3	89.6	22.2	18.8	92	0.79	2.9	82.2
UKMO-HadGEM1	68.3	14.6	7.4	82	0.99	4.0	87.0
SODA-1.4.2	86.3	29.3	19.4	91	0.90	3.7	100.0

Table 2.2. Spatial and temporal characteristics of the first SVD mode between anomalies of wind stress and SST in the tropical Pacific (fig. 2.4) for the CGCMs and SODA. * The domain used for the spatial correlation is (11°S-11°N, 135°E-80°W)

In the "real world" characterized here by SODA, more than 85% of the covariance between anomalies of surface wind stress and SST can be explained by ENSO (table 2.2). In the model world, this rate varies between about 70% to more than 90%. In particular, CSIRO-MK3.0, INM-CM3.0 and UKMO-HadGEM1 exhibit weaker explained covariance than SODA. In terms of SST variance, about 30% is explained by ENSO in the case of SODA, whereas most CGCMs show weaker values, especially INM-CM3.0 and the two UK Met Office models (HadCM3 and HadGEM1). In terms of wind variability, a significantly weaker part is explained by ENSO in the climate models compared to SODA, with the exception of UKMO-HadCM3.

The period of the ENSO cycle is heterogeneous among the hybrid models, ranging from biennial (CSIRO-MK3.0) to quadriannual (INGV-ECHAM4, UKMO-HadGEM1), versus 3.7 years for the reanalysis. This reflects the fact that even if hybrid CGCMs have a closer ENSO

time scale on average to that of SODA than CGCMs with a dominant zonal advective feedback or a dominant thermocline feedback (Belmadani et al., 2010), other processes such as the spatial distribution of the wind patch for instance are also likely to affect the ENSO time scale (Guilyardi et al., 2004; Zelle et al., 2005; Capotondi et al., 2006; Merryfield, 2006): a peak of wind variability displaced to the west (resp. east) tends to favour shorter (resp. longer) time scales (An and Wang, 2000), due to a shorter (resp. longer) time taken by upwelling equatorial Rossby waves to reach the western boundary where they are reflected as Kelvin waves and eventually act as a negative feedback to the growth of El Niño, according to the delayed oscillator paradigm (Suarez and Schopf, 1988). In addition, the meridional gradient of the wind stress can also have an effect on the ENSO time scale, as the phase velocity of the excited Rossby waves decreases poleward (Kirtman, 1997). In this respect, INGV-ECHAM4, INM-CM3.0 and UKMO-HadGEM1 exhibit the most realistic time scales among the ensemble.

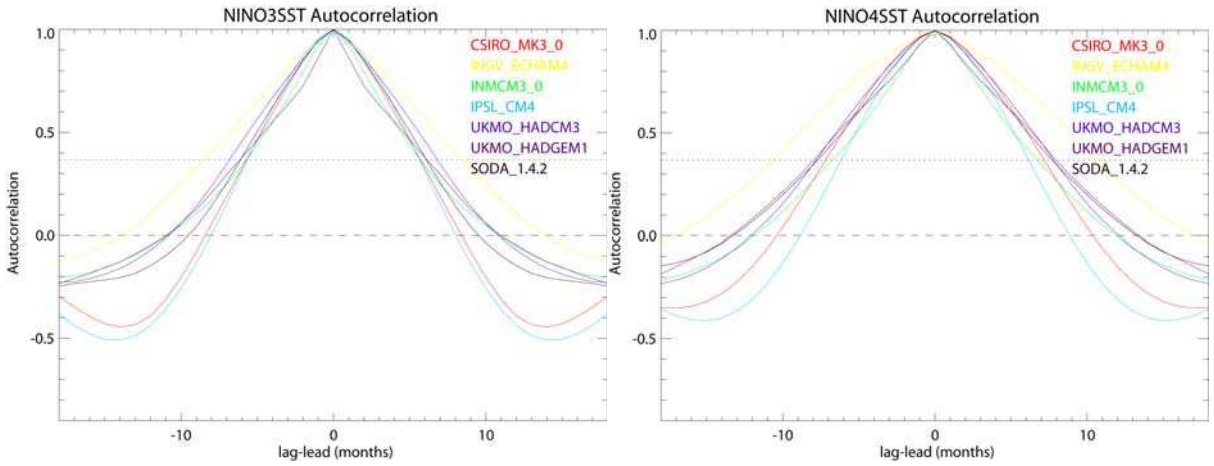

Fig. 2.5. Autocorrelation of (left) Niño3 SST and (right) Niño4 SST indices over an 18-month lead–lag period for the CGCMs and for SODA. The horizontal dotted line indicates a value of e^{-1}=0.368.

Another measure of the ENSO time scale is provided by the autocorrelation functions of ENSO indices such as Niño3 SST and Niño4 SST anomalies (fig. 2.5): the width at decorrelation values (e^{-1}) provides an estimate of El Niño or La Niña event duration. A first order approximation for the ENSO period can thus be obtained by doubling such value. INGV-ECHAM4 exhibits a significantly longer cycle (~34 months *i.e.* 2.8 years for Niño3 and ~42 months *i.e.* 3.5 years for Niño4) than the other models and SODA, which is qualitatively consistent with the estimate derived from the SVD analysis (table 2.2). On the other hand, CSIRO-MK3.0, INM-CM3.0 and IPSL-CM4 tend to have the shortest periods among the hybrid models: ~1.9 years for Niño3 and between 2.0 and 2.3 years for Niño4,

which is also consistent with the SVD analysis, except maybe for INM-CM3.0. The UK Met Office models exhibit the best agreement with SODA: ~2.2-2.3 years for Niño3, 2.7 years for Niño4. In the SVD analysis, the HadGEM1 model exhibits a quadriannual ENSO, which is also the case for SODA (3.7 years); HadCM3 exhibits a shorter time scale (2.9 years), though with a secondary peak beyond 4 years. Overall, these results are qualitatively consistent with the SVD analysis for most models. As the autocorrelation function only provides an estimate of event duration and not of cycle length, quantitative differences with the ENSO period estimates derived from the SVD analysis should not be over-interpreted. Note that the same diagnosis was used by Joseph and Nigam (2006) for a subset of the CMIP3 models, including UKMO-HadCM3 for which results were found to be consistent with the ones presented here.
Following Joseph and Nigam (2006), the decorrelation threshold in the opposite phase ($-e^{-1}$) is used to assess the ability of the models to shift from El Niño to La Niña and back (fig. 2.5). Only CSIRO-MK3.0 and IPSL-CM4 are able to cross this threshold, opposite to the other models and SODA, which means that these two models tend to have a too regular cycle. In the real world, a La Niña event does not always follow an El Niño event (and vice-versa): in some cases neutral conditions can prevail for several years, such in 1978-1982 or in 1959-1962; in other cases several consecutive El Niño or La Niña events can occur, such as in 1999-2001 or in 2002-2005 (fig. 1.19). None of the hybrid models stays in the same phase over the considered 36-month time interval unlike the MIROC3.2-HIRES model for instance (see Joseph and Nigam, 2006 – their figure 2), confirming the oscillatory behaviour of ENSO in these models. Note that whereas CSIRO-MK3.0 and IPSL-CM4 reach their minima in the considered interval, it is not the case for the other models, which reflects the fact that the latter tend to have ENSO periods exceeding 36 months. This might provide an explanation for the quantitative differences with estimates from the SVD analysis.

Model	Niño3 SSTA: RMS (°C)	Niño3 SSTA: skewness (°C)	Correlation (%): Niño3 SSTA, Niño4 TXA	Niño4 SSTA: RMS (°C)	Niño4 SSTA: skewness (°C)	Correlation (%): Niño4 SSTA, Niño4 TXA
CSIRO-MK3.0	0.91	-0.17	61.5	0.82	+0.20	57.8
INGV-ECHAM4	0.79	-0.02	65.9	0.60	+0.05	73.3
INM-CM3.0	0.90	+0.23	54.1	1.02	+0.50	55.6
IPSL-CM4	1.00	+0.11	70.5	0.70	-0.30	67.8
UKMO-HadCM3	0.88	+0.32	67.5	0.81	+0.16	74.5
UKMO-HadGEM1	0.69	+0.03	49.2	0.56	+0.09	57.6
SODA-1.4.2	0.96	+0.91	71.5	0.64	-0.32	78.2

Table 2.3. Statistics of Niño3 and Niño4 SST indices for the CGCMs and for SODA.

Niño3 and Niño4 indices are frequently used in the literature to assess simple ENSO statistics, such as ENSO amplitude (RMS of the time series), skewness (defined as in Belmadani et al., 2010) or Gill-type linearity (assessed with the correlation coefficient between western Pacific

wind anomalies and eastern Pacific SST anomalies). Table 2.3 presents these statistics computed for our model ensemble.

Most CGCMs feature an amplitude of eastern Pacific ENSO in relatively good agreement with that of SODA, except INGV-ECHAM4 and UKMO-HadGEM1 which underestimate ENSO amplitude by ~18% and ~28%, respectively. This is qualitatively consistent with the results of van Oldenborgh et al. (2005), and more importantly, quantitatively consistent with Guilyardi (2006) who used the same diagnostic as the one presented here. A notable exception is UKMO-HadCM3 for which we find an amplitude of 0.88°C versus 0.77°C for Guilyardi (2006). Note however that Guilyardi (2006) indicates an error bar of +/-0.09°C, *i.e.* an amplitude ranging from 0.68°C to 0.86°C. He also uses a longer time span than the one considered here: 341 years versus 148 years, respectively. Hence, the differences between the two studies for this model might be related to decadal and multi-decadal ENSO modulation - which are significant for this model (see below) -, an issue which has been illustrated by Wittenberg (2009) with a 2000-year simulation performed with the GFDL-CM2.1 model. On the other hand, most CGCMs tend to overestimate western Pacific ENSO amplitude, except INGV-ECHAM4, IPSL-CM4 and UKMO-HadGEM1 which exhibit a rather good agreement with SODA. Such behaviour may be related to the overestimated westward extension of the ENSO SST anomaly pattern for most CMIP3 models (fig.2.4), itself related to the overestimated westward extension of the cold tongue due to stronger zonal winds than observed (see Belmadani et al., 2010). Note that the former statement is less true for UKMO-HadGEM1 and to a smaller extent for INGV-ECHAM4 (fig.2.4), which tends to confirm this hypothesis.

It is known that SST anomalies are positively skewed in the eastern tropical Pacific and negatively skewed in the western tropical Pacific, a see-saw pattern which is captured by the SODA reanalysis (table 2.3). Consistently with results from Belmadani et al. (2010), IPSL-CM4 is the only hybrid model with a negative skewness in Niño4 (not only is the sign correct but also the magnitude). Belmadani et al. (2010) proposed to attribute such behaviour to the rather low nonlinear zonal advection for all the hybrid models except IPSL-CM4 which presents a value close to that of SODA (see their figure 6). INGV-ECHAM4 and UKMO-HadGEM1 have the smallest positive values, which is likely related to the smaller SST variability. ENSO skewness presents marked biases also in the eastern Pacific: all the models underestimate it by at least a factor three (for UKMO-HadCM3) and two of them even show negative values (CSIRO-MK3.0 and INGV-ECHAM4).

In terms of linearity, most models have Niño3SSTA/Niño4TXA correlation values of the order of SODA (71.5%), except INM-CM3.0 and UKMO-HadGEM1 which have a lower degree of linearity (respectively 54.1% and 49.2%). This is consistent with the results of Guilyardi (2006) (his figure 8) who find larger scatter between Niño3SSTA and Niño4TXA for these two models than for the other hybrid models. In the western Pacific, three models have significantly lower correlation values between SST anomalies and local wind anomalies: CSIRO-MK3.0, INM-CM3.0 and UKMO-HadGEM1 (table 3).

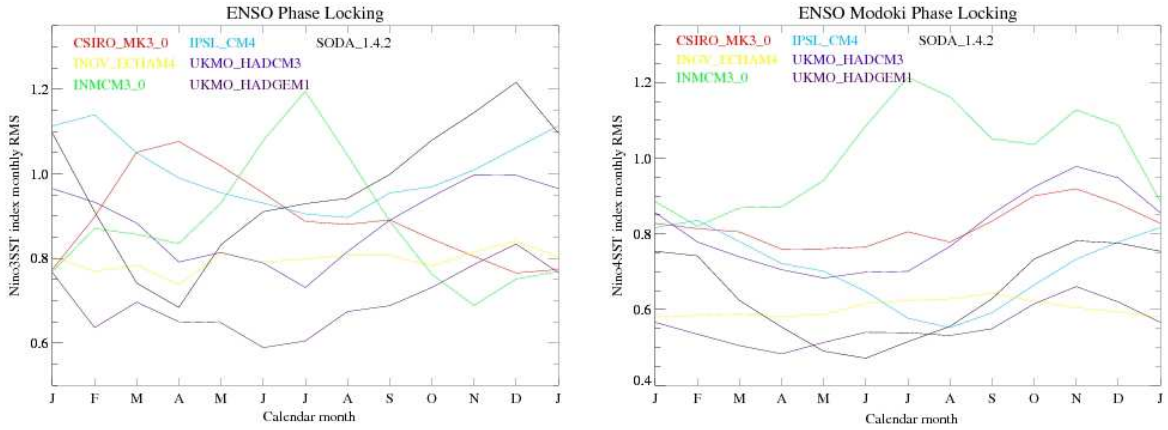

Fig. 2.6. Seasonal phase-locking of ENSO: standard deviation of (left) Niño3 SST and (right) Niño4 SST indices for each calendar month, for the CGCMs and for SODA.

Another important feature of ENSO is its seasonal phase locking. Indeed, as noted in the introductory chapter, El Niño tends to peak in the central to eastern tropical Pacific during the boreal winter season (*e.g.* Rasmusson and Carpenter, 1982). El Niño Modoki also tends to be synchronized with the seasonal cycle, with a peak season in the central to western tropical Pacific ranging from boreal summer to winter (*e.g.* Ashok et al., 2007). Following Joseph and Nigam (2006), we use the standard deviation of ENSO indices (Niño3 for the conventional ENSO and Niño4 for ENSO Modoki) for each calendar month to assess phase locking in the CGCMs (fig. 2.6). Models exhibit widespread behaviour in terms of ENSO peak season in both the eastern and the western Pacific. In the eastern Pacific, IPSL-CM4, UKMO-HadGEM1 and UKMO-HadCM3 have their ENSO peaking in boreal winter (consistently with Joseph and Nigam (2006) for the latter model), just like SODA. On the other hand, CSIRO-MK3.0 and INM-CM3.0 peak in boreal spring and summer, respectively. INGV-ECHAM4 does not exhibit any clear seasonal preference. In the central/western Pacific, CSIRO-MK3.0, UKMO-HadCM3 and UKMO-HadGEM1 have their peak season in boreal fall, like for SODA. IPSL-CM4 tends to peak in winter, whereas INM-CM3.0 peaks in

summer, though with a marked semi-annual cycle and a secondary maximum in fall. Again, INGV-ECHAM4 is not seasonally-discriminating.

As explained in the introductory chapter and in the first section of the present chapter (Belmadani et al., 2010), ENSO is subject to low-frequency modulation, which can impact significantly its structure and dynamics. Here we use wavelet analysis together with the N3VAR and N4VAR (equivalent to N3VAR for the Niño4 region) indices to document such decadal modulation in the CGCMs (figures 2.7 and 2.8). As expected, SODA exhibits significant low-frequency modulation of ENSO amplitude, with clear shifts in the mid- to late 70s and in the early 90s in both Niño3 and Niño4 regions. A change from bi-annual to quadri-annual cycles in the mid-70s is also evident in the corresponding wavelet spectra. Most CGCMs tend to underestimate decadal modulation of ENSO amplitude in the eastern Pacific, which is particularly obvious for UKMO-HadGEM1, INGV-ECHAM4 and to a smaller extent for INM-CM3.0. UKMO-HadCM3 and CSIRO-MK3.0 exhibit the best agreement with SODA, whereas IPSL-CM4 tends to slightly overestimate decadal modulation. Changes in the frequency of ENSO can be detected for most models except UKMO-HadGEM1 which tends to maintain a quadri-annual ENSO during the considered 150-year study period. Note that these results are not always consistent with those of Lin (2007), who finds for instance significant interdecadal variability of ENSO amplitude and frequency for UKMO-HadGEM1 and little variability of the amplitude for IPSL-CM4. However, his study is based on a different climate scenario, in which GHG forcing slowly increases at the observed rate (20C3M), which may provide an explanation for such differences. In addition, his findings are based on a qualitative assessment of Niño3 SST wavelet spectra, rather than on a quantitative assessment such as the one performed here on ENSO amplitude with N3VAR.

Opposite to the eastern Pacific, most CGCMs tend to strongly overestimate decadal modulation in the western Pacific, except INGV-ECHAM4 and UKMO-HadGEM1 which exhibit a rather good agreement with SODA in terms of N4VAR mean value and standard deviation. Such behaviour may be related to the overestimated SST variability in this region. Opposite to eastern Pacific ENSO, changes in the frequency of central/western Pacific ENSO are detected for all the hybrid models.

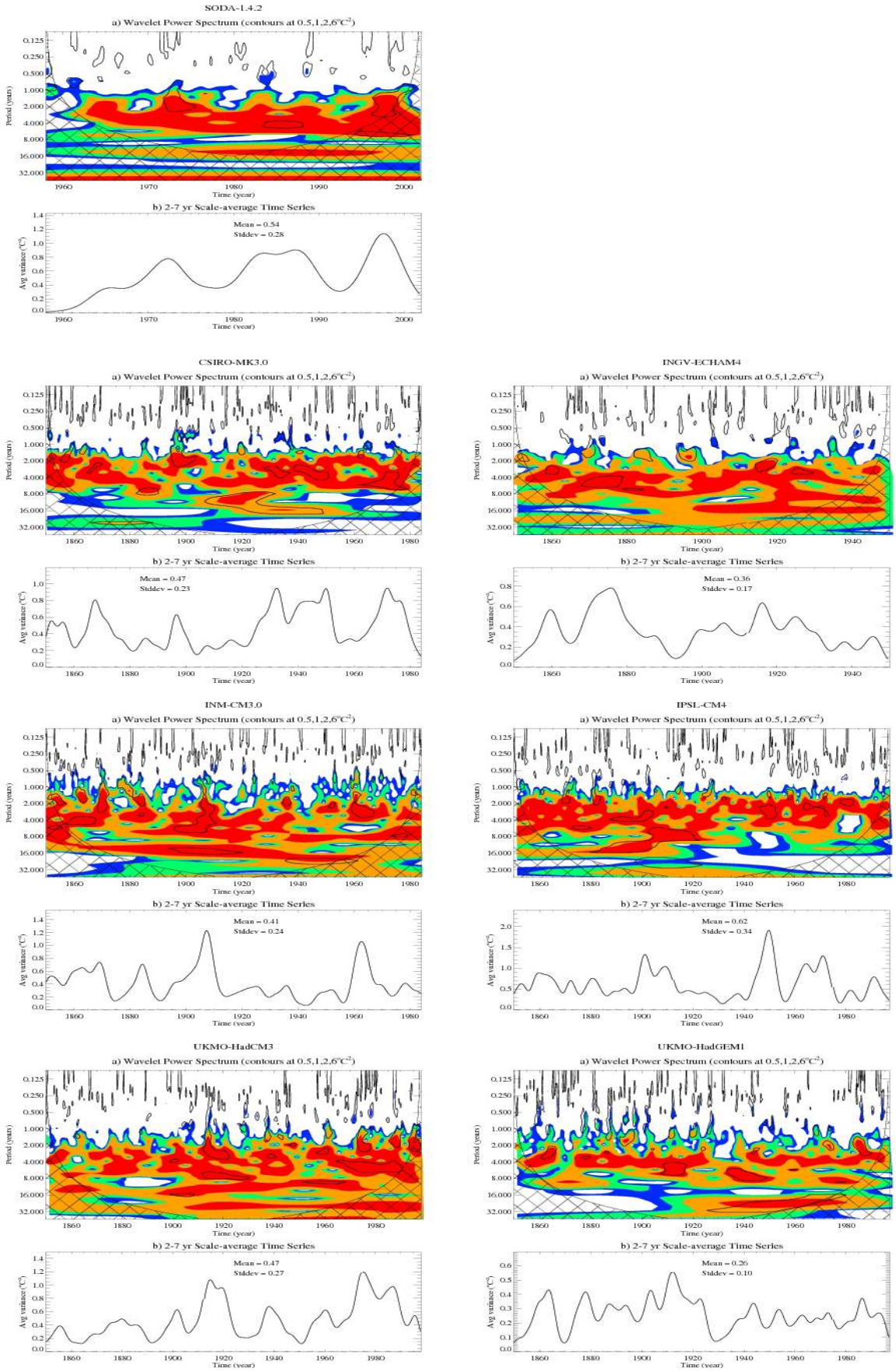

Fig. 2.7: Low-frequency modulation of ENSO for the CGCMs and for SODA. For each model: **a)** Wavelet power spectrum of Niño3 SST anomalies (only values above the 90% significance level are plotted); **b)** Corresponding 2-7 year scale-average time series (N3VAR). Units are (°C)².

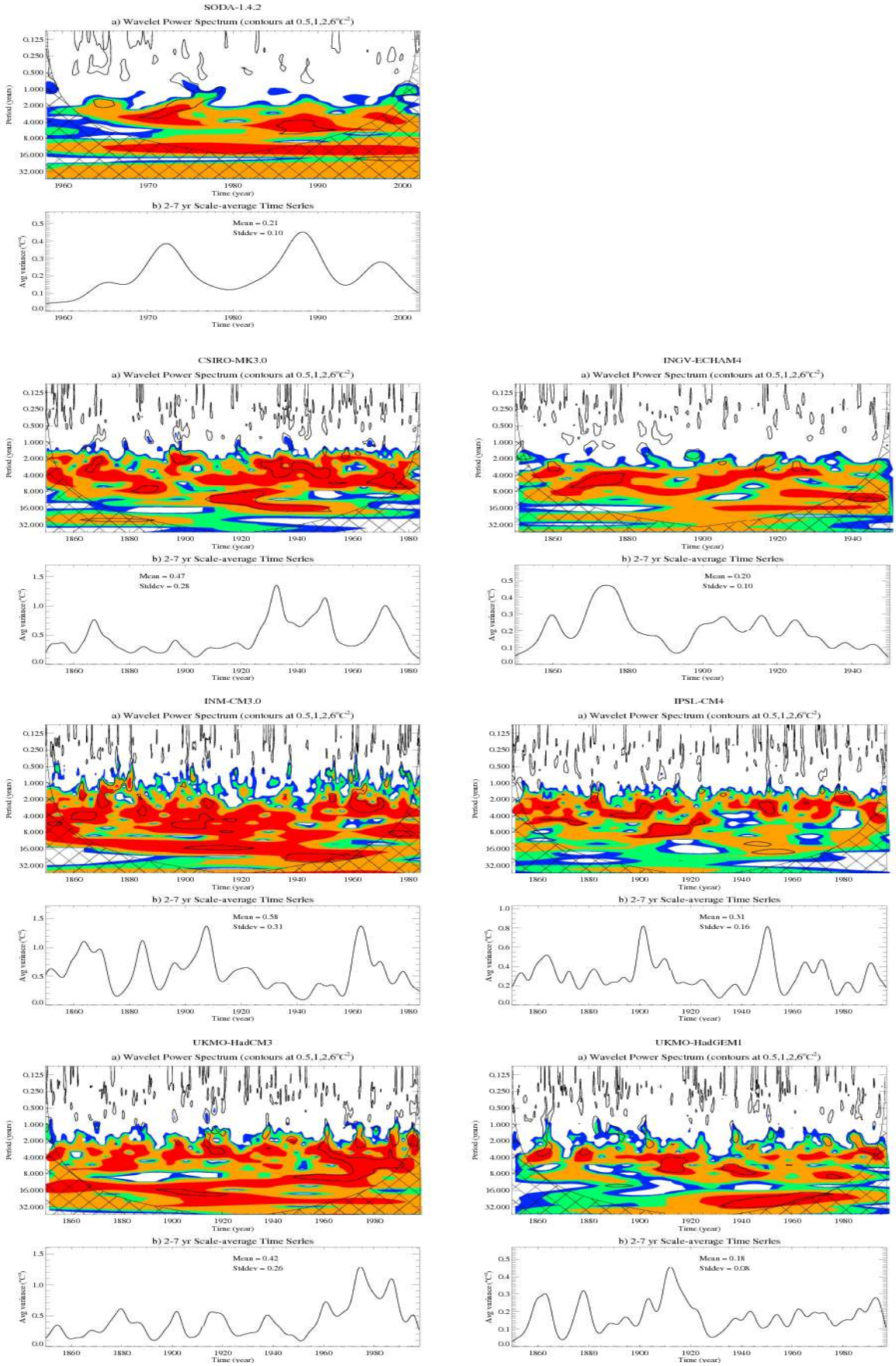

Fig. 2.8. Same as fig. 2.7, except for Niño4.

Overall, INGV-ECHAM4, IPSL-CM4 and UKMO-HadCM3 exhibit the 'best' agreement with SODA in terms of spatial and temporal properties of ENSO, whereas INM-CM3.0 is the most unrealistic among the hybrid models. CSIRO-MK3.0 does a good job with respect to ENSO amplitude and decadal modulation, whereas UKMO-HadGEM1 performs well in terms of ENSO pattern, period, phase shift and phase locking. We decided here to select the latter model rather than the former, because the afore-mentioned three "best" models do not perform very well in terms of ENSO period (except INGV-ECHAM4), and because at least one of them does not perform very well in terms of ENSO phase shift and phase locking. In contrast, all these three models have good skills in terms of ENSO amplitude and decadal modulation of ENSO period, and only one of them (INGV-ECHAM4) features a significantly underestimated decadal modulation of ENSO amplitude. In addition, as mentioned at the end of the introductory chapter, climate change downscaling experiments are performed over 10-year periods, which are too short for the assessment of decadal modulation at the regional scale. For the rest of the analysis, we thus decided not to consider the CSIRO-MK3.0 and INM-CM3.0 models, and focus the analysis of the behaviour of the IPCC models in the eastern South Pacific on the four 'best' models in terms of large scale tropical variability: INGV-ECHAM4, IPSL-CM4, UKMO-HadCM3 and UKMO-HadGEM1.

At this point, it is important to note that although we have tried to take into account as many aspects of ENSO as possible for the skill assessment of CMIP3 CGCMs, this analysis does not pretend to be exhaustive by any means. ENSO is a complex multiform phenomenon resulting from interactions between the ocean and the atmosphere on a range of time scales, from intraseasonal to multi-decadal. Even though our understanding of ENSO has remarkably increased since the early works of Bjerknes in the 1960s, there are still numerous issues regarding its structure, dynamics and teleconnections that are yet to be understood. Here we tried to combine a dynamical approach, allowing to diagnose biases of the models in the representation of complex coupled feedbacks, with a more conventional statistical approach, based on commonly used ENSO metrics, in order to identify the most relevant CGCMs for the study of the impact of global warming on the Humboldt Current System, at least in terms of large-scale equatorial forcing. Other metrics and/or diagnostics might provide a different group of candidates for such a regional downscaling project. However, we have shown in the first section of the present chapter that our results are consistent to a large extent with those of Guilyardi (2006), who used different diagnostics to identify the different feedbacks (or ENSO modes) in the CMIP3 CGCMs. In addition, we have checked that the results presented in the present section are consistent to a large extent with other studies using similar simple ENSO

statistics to assess model performance. This mixed dynamical/statistical approach and the consistency of our results with those from previous studies gives us confidence in the choice we have made. Last, downscaling experiments are meant to be performed with forcings from several CGCMs, in order to be able to provide error estimates for projected changes at the regional scale. It is an *a posteriori* way to check the relevance of our choice of CGCMs.

It is also important to mention that we have chosen to assess ENSO behaviour in the models before analyzing their characteristics at the boundaries of the regional domain – instead of the opposite, or instead of performing both analyses for all the models – mainly for a practical reason. Indeed, most CGCM fields that were required for the analysis of ENSO variability presented here are either surface fields (SST, zonal wind stress) or vertical equatorial sections (temperature, salinity), which represent a relatively reasonable – though significant – amount of data over the CMIP3 multi-model ensemble. Conversely, the diagnostics performed at the regional scale require several bidimensional fields at the three open boundaries of the regional domain (zonal and meridional currents, temperature, salinity) as well as surface atmospheric fields such as zonal and meridional wind stress (see next section). Such a higher number of bidimensional fields requires much more disk space and processing, hence the relevance of limiting the number of models to be considered in the regional analysis, which is presented in the next section.

2.3. Eastern South Pacific mean state and variability in hybrid CGCMs

As underlined before, ENSO is obviously an important feature that a coupled model has to represent with the best possible acuracy (see previous section for the chosen criteria) in the perspective of regional climate change studies over the ocean off Peru and Chile. However, another aspect that needs special care when selecting the most relevant climate models for our downscaling experiments is the simulated mean state and variability at the open boundaries of the regional ocean model. Indeed, we chose in this thesis to study the impact of an idealized global warming scenario ($4xCO_2$) in the stabilized regime. Under such scenario, different models are likely to exhibit different changes in the mean state and variability at the regional scale, relatively to their preindustrial behaviours. These simulated mean states and variabilities in the eastern South Pacific under preindustrial climate have first to be assessed and compared to observed or reanalyzed data, in order to identify the ones that 'best' simulate the ocean along the northern, southern and western boundaries of the regional model. As detailed in the previous section, four climate models of the hybrid group exhibit spatial and temporal ENSO characteristics (amplitude, spatial distribution, period, phase locking, modulation…) closer to the observed: INGV-ECHAM4 (Roeckner et al., 1996; Madec et al., 1998), IPSL-CM4 (Marti et al., 2009), UKMO-HadCM3 (Gordon et al., 2000; Pope et al., 2000; Johns et al., 2003) and UKMO-HadGem1 (Johns et al., 2006; Martin et al., 2006; Ringer et al ., 2006). These four coupled models are therefore analyzed at the limits of the regional model: 100°W-70°W, 15°N-40°S (fig. 2.9).

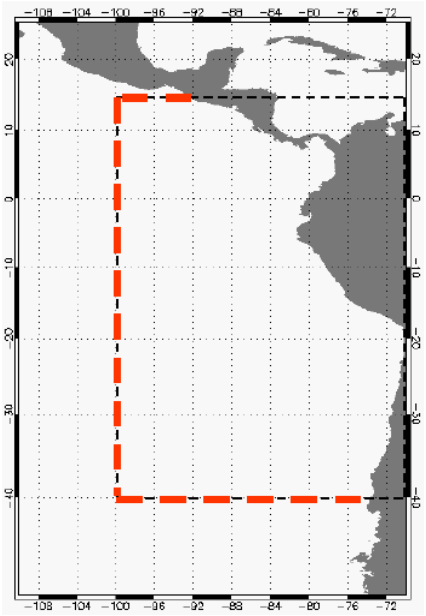

Fig. 2.9. Regional domain (dashed black lines) within the eastern South Pacific, with open boundaries (dashed red lines) at 100°W, 15°N and 40°S. Grey colour is for land.

The analysis is conducted on the mean state and on the seasonal, interannual and intraseasonal variations of the main oceanic variables (particularly currents and temperature – salinity variations are weak over this region) at the northern, southern and especially western boundaries of the domain. Indeed, the latter crosses the equatorial waveguide and the associated current system and thereby concentrates most variability of both the thermocline and the large scale currents that is transmitted to the Peru-Chile coast (Strub et al., 1998; Kessler, 2006). To our knowledge, so far no study has been dedicated to the sensitivity of the regional ocean circulation to the eastern equatorial Pacific mean state and variability: for this reason, the modelled temperature and velocity fields are compared to those from observed data (when available), from the SODA 1.4.2 reanalysis (1958-2001) (Carton and Giese, 2008) and from the ORCA05 model (1992-2000) (Madec et al., 1998), which is used as the boundary forcing for the regional control run (see chapter three). The comparison is performed for different frequency bands (seasonal, intraseasonal and interannual) and is used to conduct the selection process. In addition, we have chosen to repeat these analyses for a model with a strongly biased ENSO cycle, dominated by the zonal advective feedback (CNRM-CM3 - Déqué et al., 1994; Madec et al., 1998; Royer et al., 2002), in order to compare the differences found between models from the same group (hybrid) with the differences found between models from two different groups. Indeed, the CNRM-CM3 model has strong mean zonal currents in the western equatorial Pacific and a dominant contribution of zonal advection to equatorial SST changes, similarly to other models dominated by the zonal advective feedback - like IAP-FGOALS or MIUB-ECHO-G (see section 1 of the present chapter). It also features a large cold bias in the warm pool, strong near-annual activity (see section 2 of the present chapter) and although its ENSO time scale is close to the observed (3.3 years vs. 3.7 years), it is interesting to note that previous versions of this model exhibit a biennial ENSO (*e.g.* Dewitte et al., 2007a), all of which are typical of a dominant zonal advective feedback. The time periods for each model considered in this analysis are indicated in table 2.4.

CGCM/Reanalysis	**INGV-ECHAM4**	**IPSL-CM4**	**UKMO-HadCM3**	**UKMO-HadGEM1**	**CNRM-CM3**	ORCA05	SODA-1.4.2
Time span for computation (years)	1761-1860	1860-2009	1859-1949	1859-1938	1930-2079	1992-2000	1958-2001
Length of simulation (years)	100	150	91	80	150	9	44

Table 2.4. Time spans considered here for five CGCMs (INGV-ECHAM4, IPSL-CM4, UKMO-HadCM3, UKMO-HadGEM1, CNRM-CM3), an OGCM (ORCA05) and an ocean reanalysis (SODA-1.4.2).

Yet, before analyzing the oceanic forcing at the open boundaries of the regional domain, characteristics of the wind structure (seasonal cycle, variability) simulated by the four hybrid CGCMs over the eastern South Pacific are presented. Indeed, such analysis can be helpful to understand biases of the coupled models in the ocean, since the ocean circulation and dynamics in

the eastern South Pacific are dependent on the atmospheric forcing to a large extent, and particularly on the wind structure (see chapter one). In addition, although the fidelity of the wind forcing was not chosen as a selection criterion (see the introduction of the present chapter), it is also used to illustrate the interest of the statistical downscaling procedure (see also chapter four).

2.3.1. The wind structure over the ESP

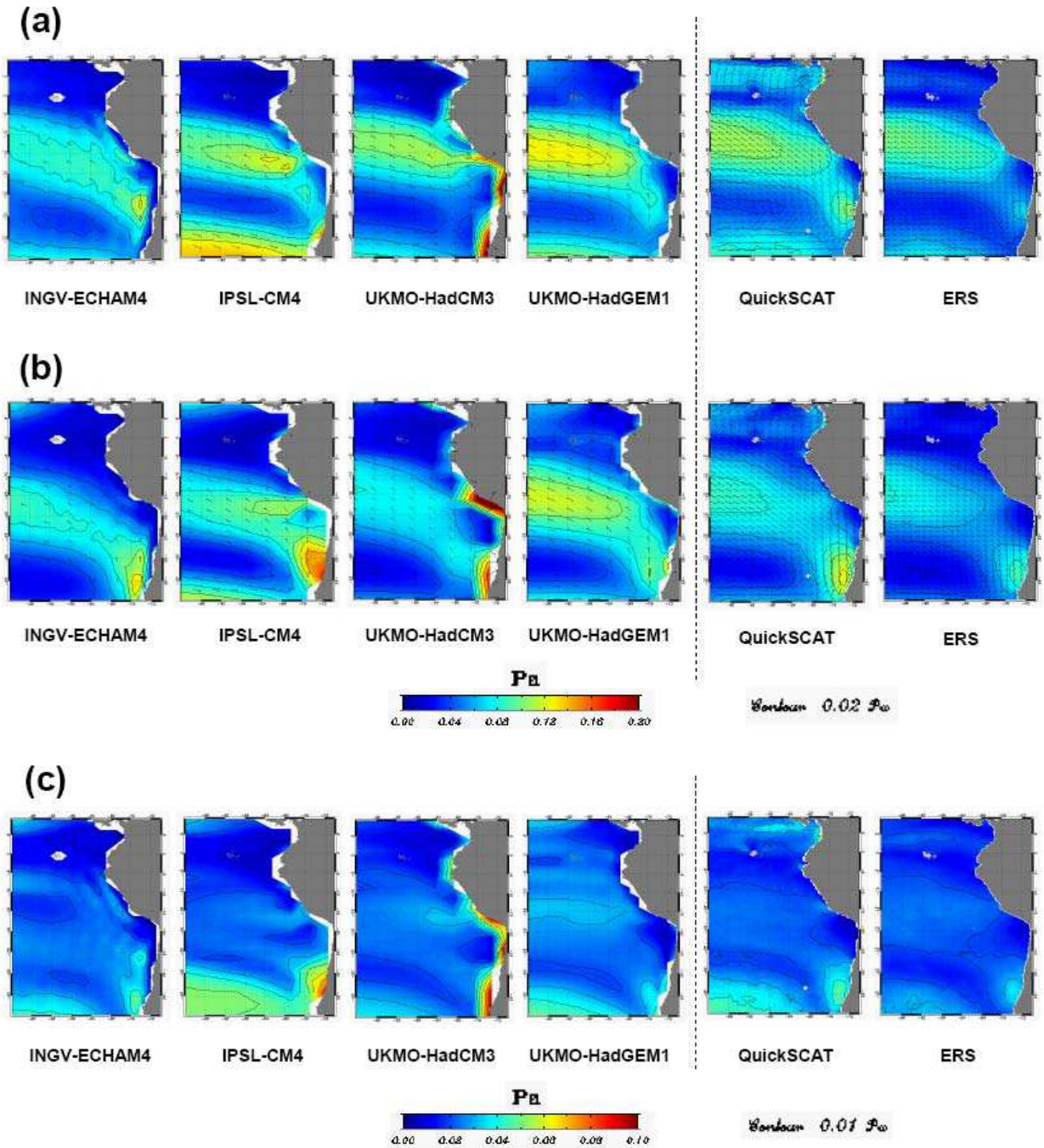

Fig. 2.10. Surface wind stress (Pa) over the ESP from the CGCMs (INGV-ECHAM4, IPSL-CM4, UKMO-HadCM3 and UKMO-HadGEM1) and from satellite observations (QuickSCAT and ERS): climatological mean surface wind stress in **(a)** austral winter (April to September) and **(b)** austral summer (October to March). **(c)** Surface wind stress variability (RMS). The colour bar and contour interval for mean wind stress (resp. wind stress variability) is indicated below (b) (resp. (c)). The size (resp. direction) of the arrows on (a) and (b) is for the magnitude (resp. direction) of the wind stress.

Main characteristics of the surface winds simulated by the CGCMs are presented on figure 2.10, and compared to those from QuickSCAT (CERSAT, 2002) and ERS (Bentamy et al., 1996) satellite data. Note that there are some differences between the two observed datasets in the region, as previously noted by Croquette et al. (2007): despite similar structures, the magnitude of the winds measured by ERS is lower than that measured by QuickSCAT, which was shown to have a better agreement with *in-situ* data from coastal stations along the Peru coast (Croquette et al., 2007). In addition, ERS misses a large fraction of the variability north of the equator, which is mainly related to the ITCZ. Both data sources however reproduce the structure and seasonality of the ESP anticyclone and of the associated winds (fig. 2.10 a and b), already described in the previous chapter: during the southern hemisphere winter (fig. 2.10a), the anticyclone is in its northernmost position, driving strong alongshore winds along the coasts of central Chile and central Peru. In summer (fig. 2.10b), the anticyclone tends to relax and moves about five degrees southwards. As a consequence, coastal winds are weaker off Peru but stronger off central Chile between about 30°S and 35°S, a region characterized by the presence of coastal jets. Maps of wind stress variability reflect the zone of influence of the subtropical high, with maximum variabilities offshore in the southwestern corner of the regional domain, and off central Chile in the coastal jet area. A local maximum off the Pisco-San Juan area (14-16°S) is also visible in both datasets.

The four CGCMs also feature the presence of the SEP anticyclone, as well as its relaxation and poleward migration in austral summer. However, they exhibit significant differences with the observed wind patterns. UKMO-HadCM3 and INGV-ECHAM4 are able to reproduce the magnitude of the observed winds, particularly in the northwestward branch: 0.08-0.10 Pa and 0.06-0.08 Pa in winter, 0.06 Pa and 0.06-0.08 Pa in summer, for respectively UKMO-HadCM3 and INGV-ECHAM4; versus 0.08-0.10 Pa and 0.08 Pa in winter, 0.06-0.08 Pa and 0.04-0.06 Pa in summer for QuickSCAT and ERS, respectively (fig. 2.10a,b). However, both CGCMs have biases in the first two degrees or so from the coast (one or two grid points), where UKMO-HadCM3 greatly overestimates the alongshore winds and INGV-ECHAM4 greatly underestimates them (it is also evident in maps of wind stress variability – see fig. 2.10c). As discussed in the previous chapter, this is mostly due to the coarse resolution of the simulated atmospheric fields (see table 1 from section 1) and to the poor representation of low-level winds over the andinean region characterized by steep orography. Nevertheless, the INGV model features the presence of small-scale local maxima of the wind stress in the central Chile and central Peru coastal jet areas just like in the observations (fig. 2.10a,b,c), with the right seasonality (greatest in winter off Peru and in summer off Chile) and amplitude (0.08 Pa in winter off Peru, 0.10-0.12 Pa in summer off Chile).

On the other hand, IPSL-CM4 and UKMO-HadGEM1 overestimate the strength (fig. 2.10a, b) and variability (fig. 2.10c) of surface winds in the offshore region, particularly those associated with the northern and southern branches of the subtropical high during the winter season: 0.10-0.12 Pa and 0.12 Pa for the northern branch, 0.12 Pa and 0.06-0.08 Pa for the southern branch, for respectively IPSL-CM4 and UKMO-HadGEM1; versus 0.08-0.10 Pa and 0.08 Pa for the northern branch, 0.06-0.08 Pa and 0.04-0.06 Pa for the southern branch for QuickSCAT and ERS, respectively. Winds are also overestimated in the two coastal jet areas for the IPSL-CM4 model (0.08-0.10 Pa in winter off Peru, 0.12-0.14 Pa in summer off Chile), whereas the magnitude of alongshore coastal winds is better represented by UKMO-HadGEM1 (fig. 2.10a,b,c), except for the central Chile coastal jet (in summer) which is slightly weaker (0.08-0.10 Pa) than in QuickSCAT data (0.10-0.12 Pa), but stronger than in ERS data (0.06-0.08 Pa). Both models are however able to represent the seasonality of the Peru and Chile coastal jets, in relation with the seasonality of the anticyclone (fig. 2.10a,b).

2.3.2. Exchanges between the ESP and the Pacific Ocean basin: importance of the equatorial region

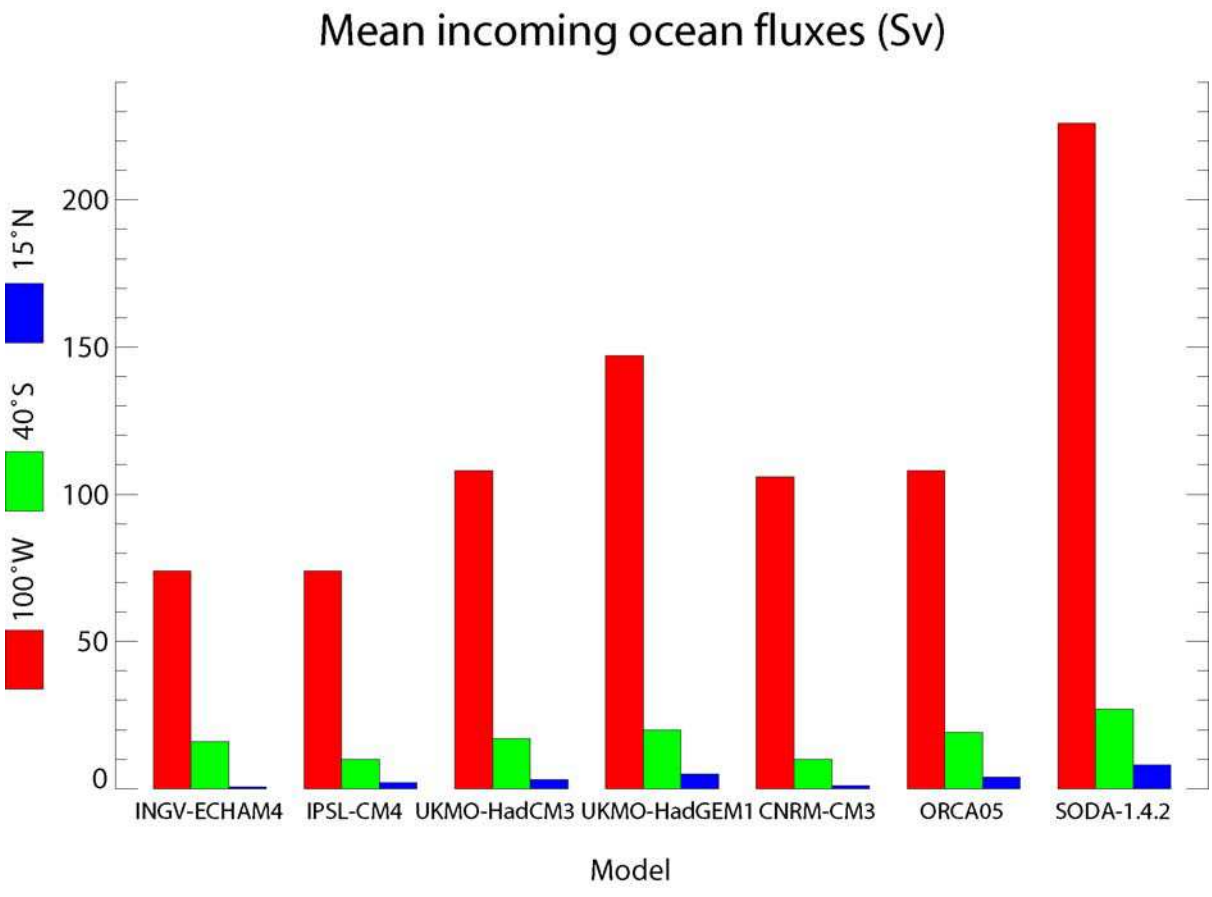

Fig. 2.11. Mean incoming fluxes (Sv) at the three open boundaries for five CGCMs (INGV-ECHAM4, IPSL-CM4, UKMO-HadCM3, UKMO-HadGEM1, CNRM-CM3), an OGCM (ORCA05) and an ocean reanalysis (SODA-1.4.2).

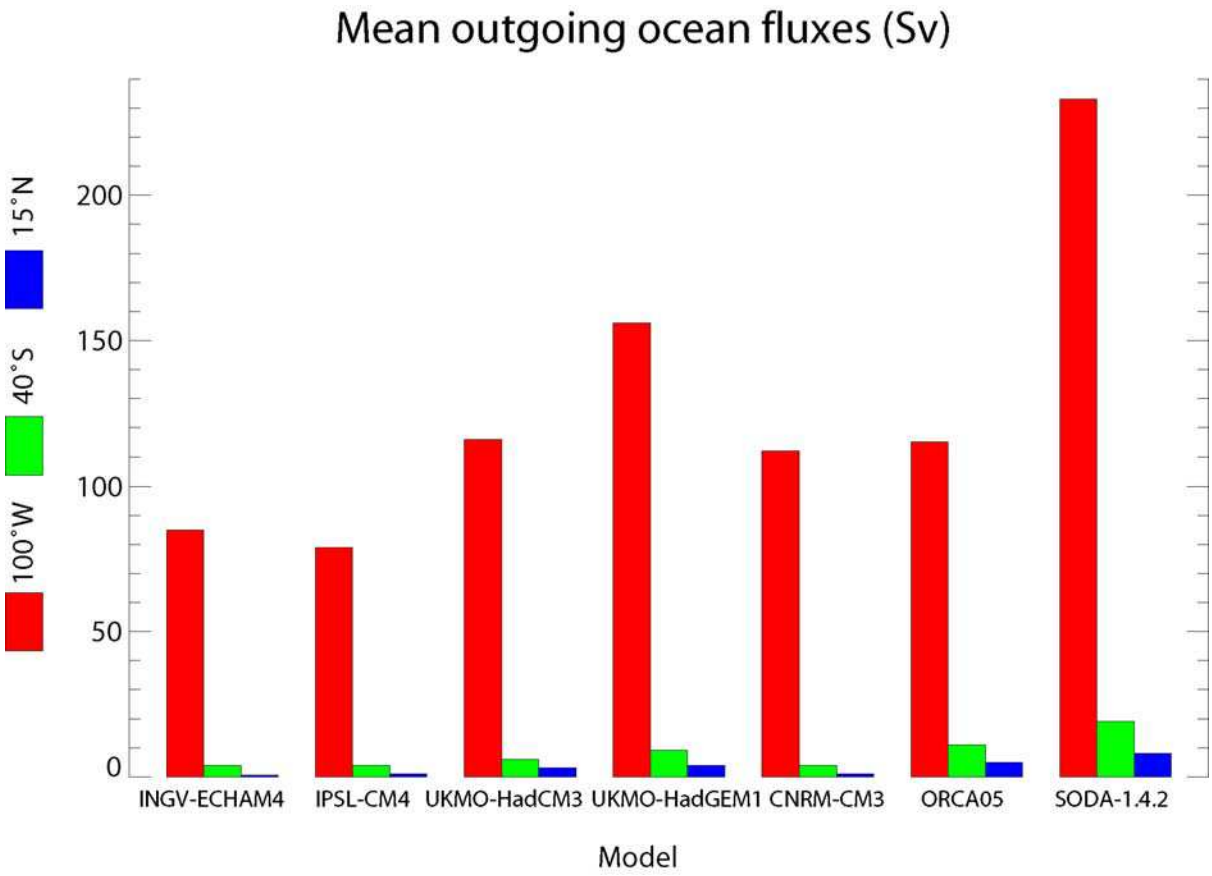

Fig. 2.12. Same as fig. 2.11, except for outgoing fluxes.

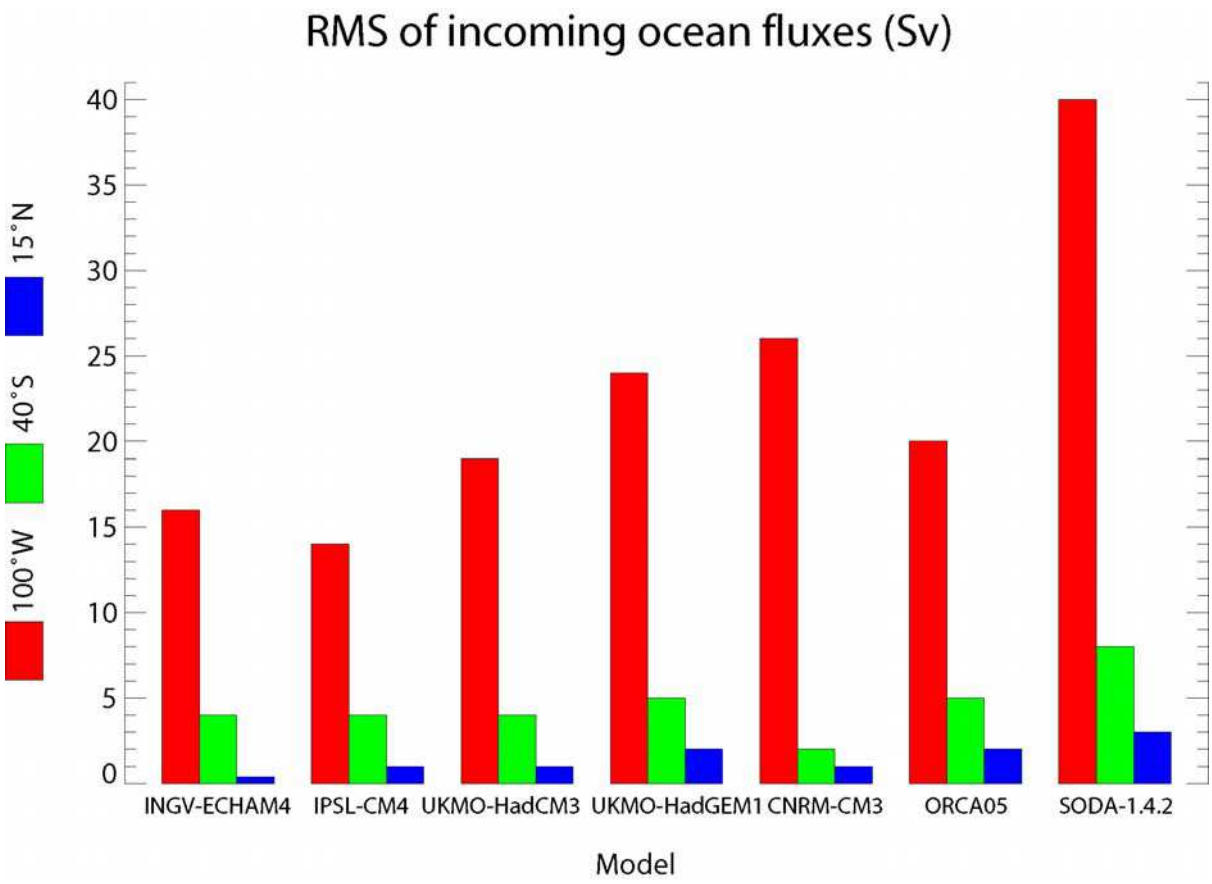

Fig. 2.13. Same as fig. 2.11, except for the variability (RMS) of incoming fluxes (Sv).

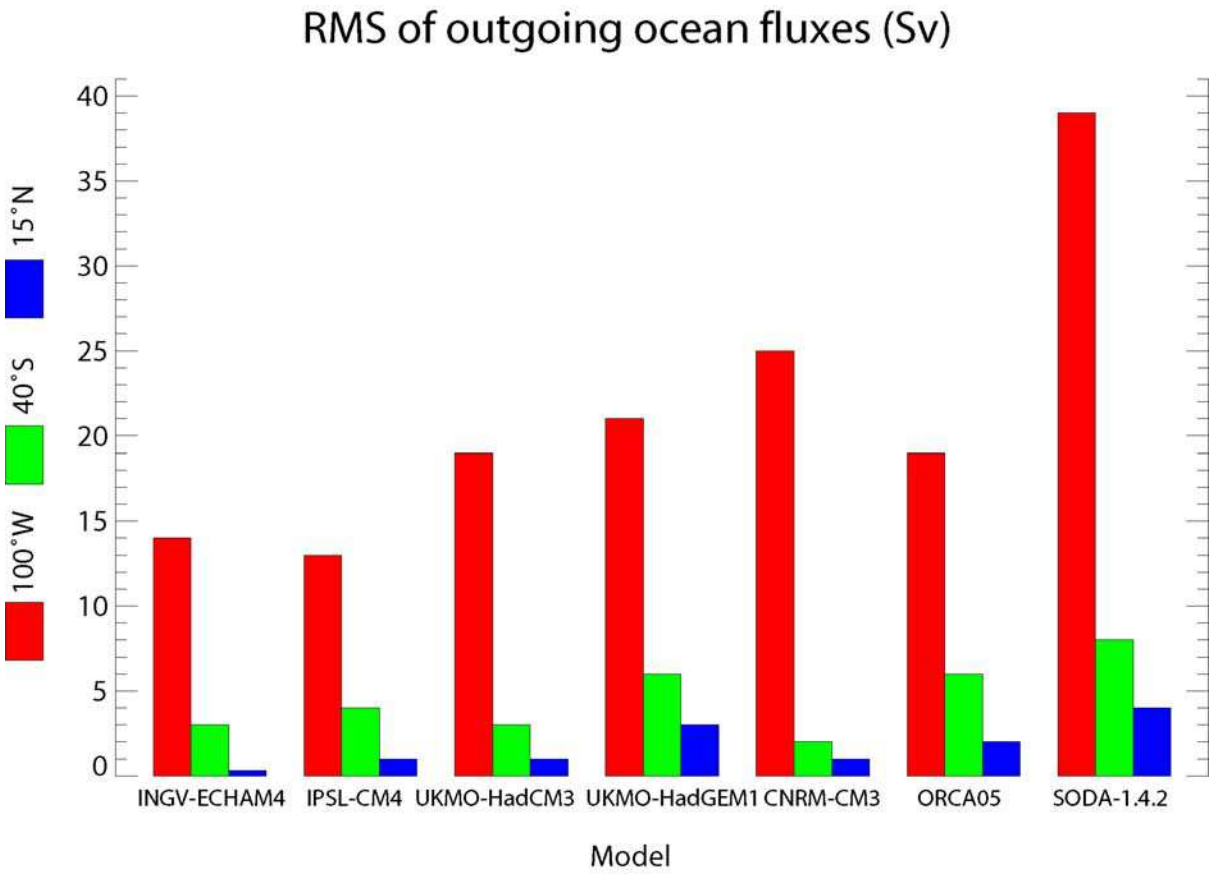

Fig. 2.14. Same as fig. 2.13, except for outgoing fluxes.

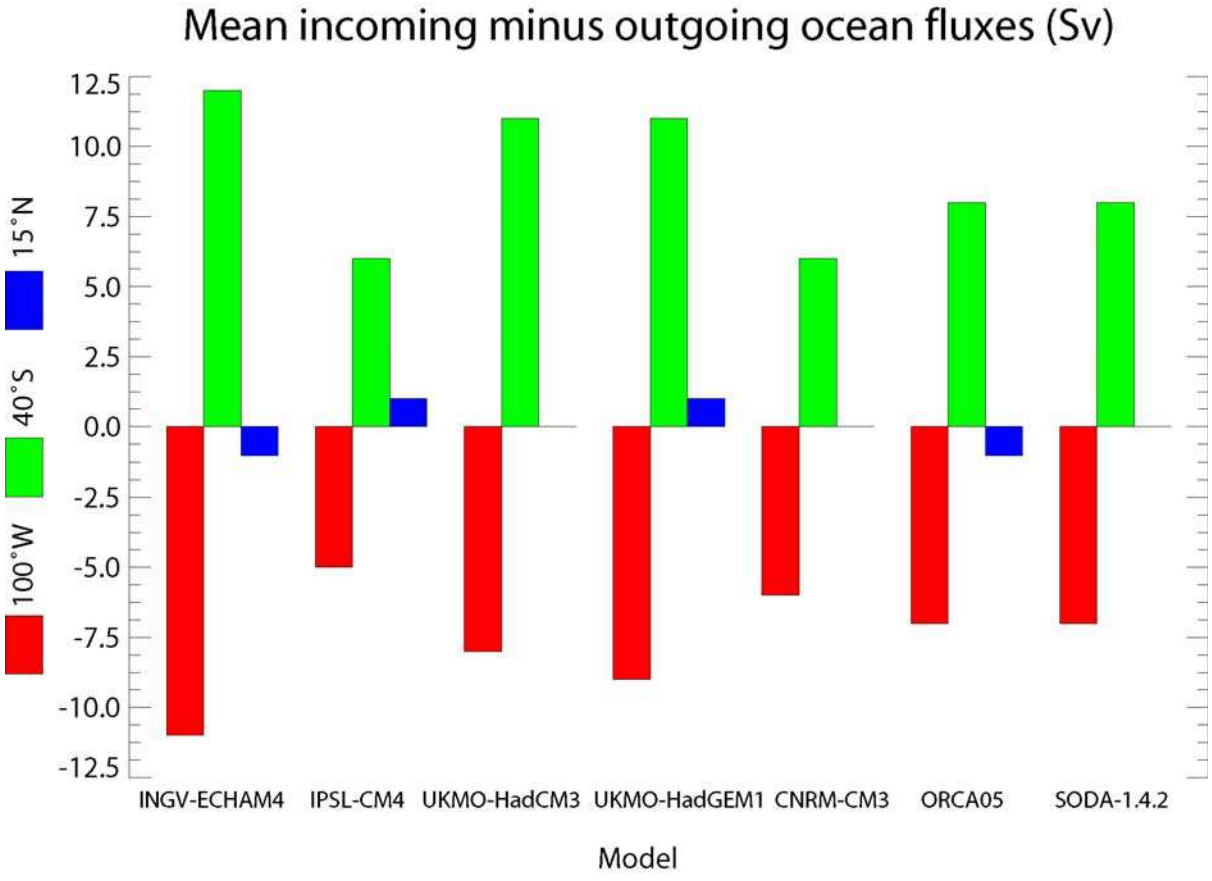

Fig. 2.15. Same as fig.2.11, except for the difference between mean incoming fluxes and mean outgoing fluxes (Sv).

In order to confirm that the western boundary is the main oceanic pathway from the open ocean to the coastal region off western South America and back, variations of the incoming and outgoing ocean transports are integrated from the sea surface to the ocean floor over each of the three open boundaries for each model of the studied ensemble (figures 2.11 to 2.15, and fig. 2.16 for the example of INGV-ECHAM4). It appears clearly that for all the models, the western limit of the domain concentrates the majority of the total exchanges with the wider Pacific Ocean: around 80-90 % of total incoming fluxes and 90-95 % of total outgoing fluxes, depending on the considered models and/or reanalyses (figures 2.11 and 2.12). In addition, the variability of incoming (resp. outgoing) fluxes is 12 to 40 (resp. 7 to 47) times higher there than at the northern boundary and 3.5 to 13 (resp. 3.2 to 12.5) times higher than at the southern boundary (figures 2.13 and 2.14). Furthermore, the majority of fluxes transiting through the western boundary is concentrated in the equatorial band (10°S to 10°N) (not shown): this allows reducing the analysis to the vertical section at 100°W between 10°S and 10°N, which is used in the following as a metric for CGCM validation. Note that the computation was also performed in the first thousand meters depth and yielded similar results (not shown).

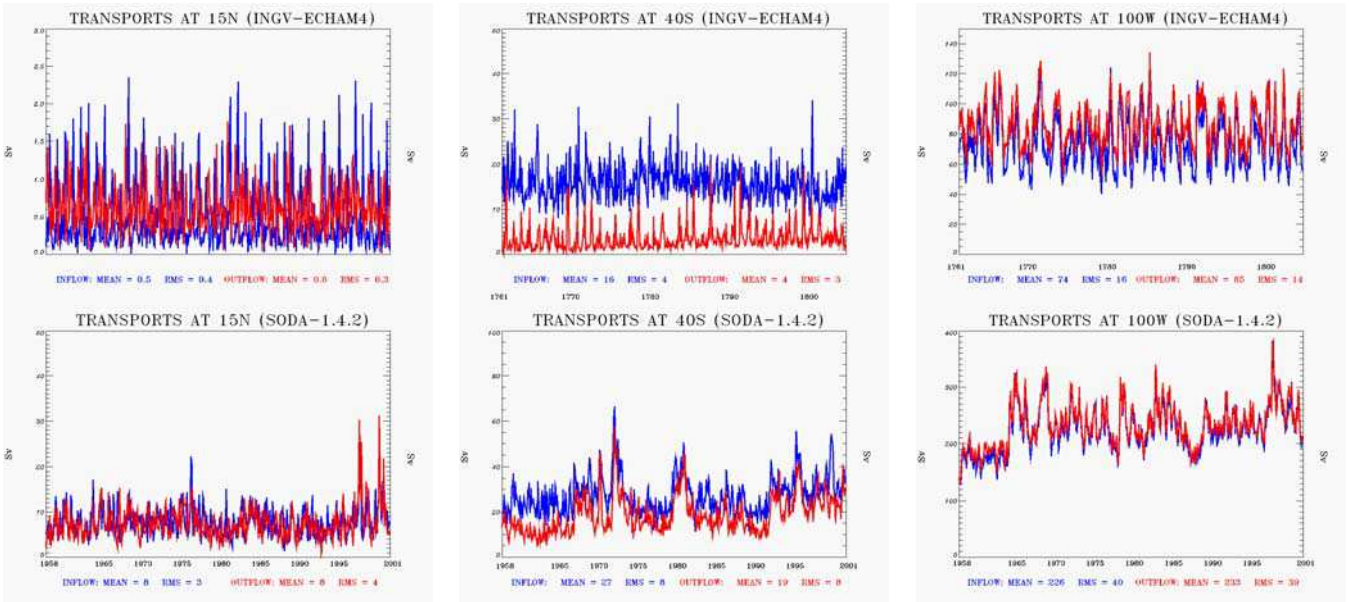

Fig. 2.16. Incoming (blue) and outgoing (red) transports (Sv) at the northern, southern and western boundaries (resp. from left to right) as a function of time for INGV-ECHAM4 (1761-1804) and SODA-1.4.2 (1958-2001) (resp. from top to bottom). Note the differences in vertical scale among the subplots.

The analysis reveals several interesting features. First, one may note that SODA simulates much stronger fluxes than that of the CGCMs and ORCA in terms of mean value (1.5-3 times higher for the total fluxes) and variability (1.3-4 times higher depending on the considered boundary) for the three open boundaries (figures 2.11 to 2.14, fig. 2.16). It is difficult to figure out

whether it is SODA that over-estimates fluxes or the CGCMs (and ORCA) that under-estimate them. Noteworthy, SODA being constrained by assimilated data, it is likely to exhibit important biases particularly under the surface and/or off the equator where the density of observations is lower, and still converge towards a 'realistic' solution in the regions where the density of observations is higher and/or where ocean dynamics are well known (in the equatorial Pacific for instance): it is well-known that assimilation of temperature and salinity into an ocean model can introduce biases in the currents compared to the real world (Burgers et al., 2002). Note however that SODA compares well with TAO ADCP data at (0°N, 140°W) for the period from 1990 onwards (Carton and Giese, *personal communication*). In addition, we have checked that its mean equatorial currents at 100°W are in good agreement with observed values (see below). On the other hand, the order of magnitude of the fluxes simulated by ORCA (an OGCM forced by observed/reanalyzed atmospheric fluxes but without data assimilation) are in better agreement with those from the CGCMs (figures 2.11 to 2.14). This may be partially explained by the fact that it is based on the same oceanic model (OPA 8 - Madec et al., 1998) as some some of them (CNRM-CM3, IPSL-CM4 and INGV-ECHAM4), except with a higher resolution: 0.5°x0.5° for ORCA vs. 2°x0.5° for CNRM-CM3 and 2°x1° for IPSL-CM4 and INGV-ECHAM4. Characteristics of the CGCMs at the limits of the regional domain are thus systematically compared to those from both ORCA and SODA, and caution is required in the interpretation of the results in case of marked differences. The availability of some observed data from shipboard ADCP measurements allows assessing some characteristics of the equatorial currents simulated by SODA and ORCA, as detailed in the next sub-section. Another remarkable feature that appears in the results obtained with SODA is a signature of the 1997-98 El Niño event, characterized by a clearly identified, large though temporary positive transport anomaly at the northern and western boundaries, which are the most influenced by equatorial dynamics (fig. 2.16).

Regional simulations forced by CGCMs are compared to a regional control run forced by ORCA05 (and by observed atmospheric fluxes), as detailed in the next chapter. This choice was motivated by practical reasons of data availability, and also because the equatorial currents at 90°W were shown to be in better agreement with geostrophic currents derived from TAO CTD data (Kessler, 2006) for ORCA than for SODA (Echevin et al., *in prep.*): around 10 cm/s in the core of the EUC northern branch (see chapter one for a description of the equatorial current system) for ORCA and TAO data vs. over 20 cm/s for SODA. Velocities in the core of the EUC southern branch (resp. SEC) are around 10 cm/s (resp. 20 cm/s) for both models as well as for TAO data. In addition, the seasonal cycle of both branches of the EUC are in better agreement with TAO ADCP data at 110°W (McPhaden et al., 1998; Izumo, 2005) for ORCA than for SODA:

whereas the former model is able to reproduce the two observed maxima in April and in October, the latter model features a maximum of the northern (resp. southern) branch in April (resp. October) and a secondary maximum in December (resp. June) with a weak semi-annual cycle. As a result, correlation coefficients of seasonal model velocities in both branches at 90°W with TAO EUC velocities at 110°W are significantly higher for ORCA than for SODA: 0.64 (resp. 0.75) for ORCA vs. 0.41 (resp. 0.24) for SODA for the northern (resp. southern) branch.

Note that fluxes transiting through the northern boundary are much weaker than those transiting through the western boundary and even through the southern boundary (figures 2.11 and 2.12). This is likely due to the reduced zonal length of the vertical section at 15°N between 100°W and the Central American coast (about 7 degrees). It is particularly true for the CGCMs because their coarse horizontal resolutions allow only a few gridpoints to be taken into account in the calculation of the fluxes. Depending on the model, the incoming flux can be greater or lower than the outgoing flux at the northern boundary, conversely to the southern boundary where the incoming flux is always the most important, and the western boundary where the outgoing flux is stronger (fig. 2.15).

2.3.3. Equatorial mean state: zonal currents and temperature

2.3.3.1. Zonal currents

The spatial structure of the mean equatorial currents at the western boundary (see previous chapter) is studied in detail in the CGCMs.

First, it is checked that SODA provides a rather 'realistic' picture of the mean currents compared to observed data (fig. 2.17). For this purpose, shipboard ADCP measurements from 22 cruises conducted on NOAA ships *Ka'imimoana* and *Ronald H. Brown* (e.g. McTaggart and Johnson, 1999) between October 1996 and January 2009 along the equatorial section at 95°W between 10°S and 10°N (tables 2.5 and 2.6) were computed in order to infer an observed climatology of the equatorial currents near 100°W. The climatology was derived by ensemble-averaging ADCP data over the available 12-year period for each calendar month (table 2.6). As no data is available for March, July and December, a linear interpolation was performed with the neighbouring climatological months in order to fill these gaps. The climatology was then used to compute time-mean sections of equatorial currents (fig. 2.17), as well as their seasonal variability

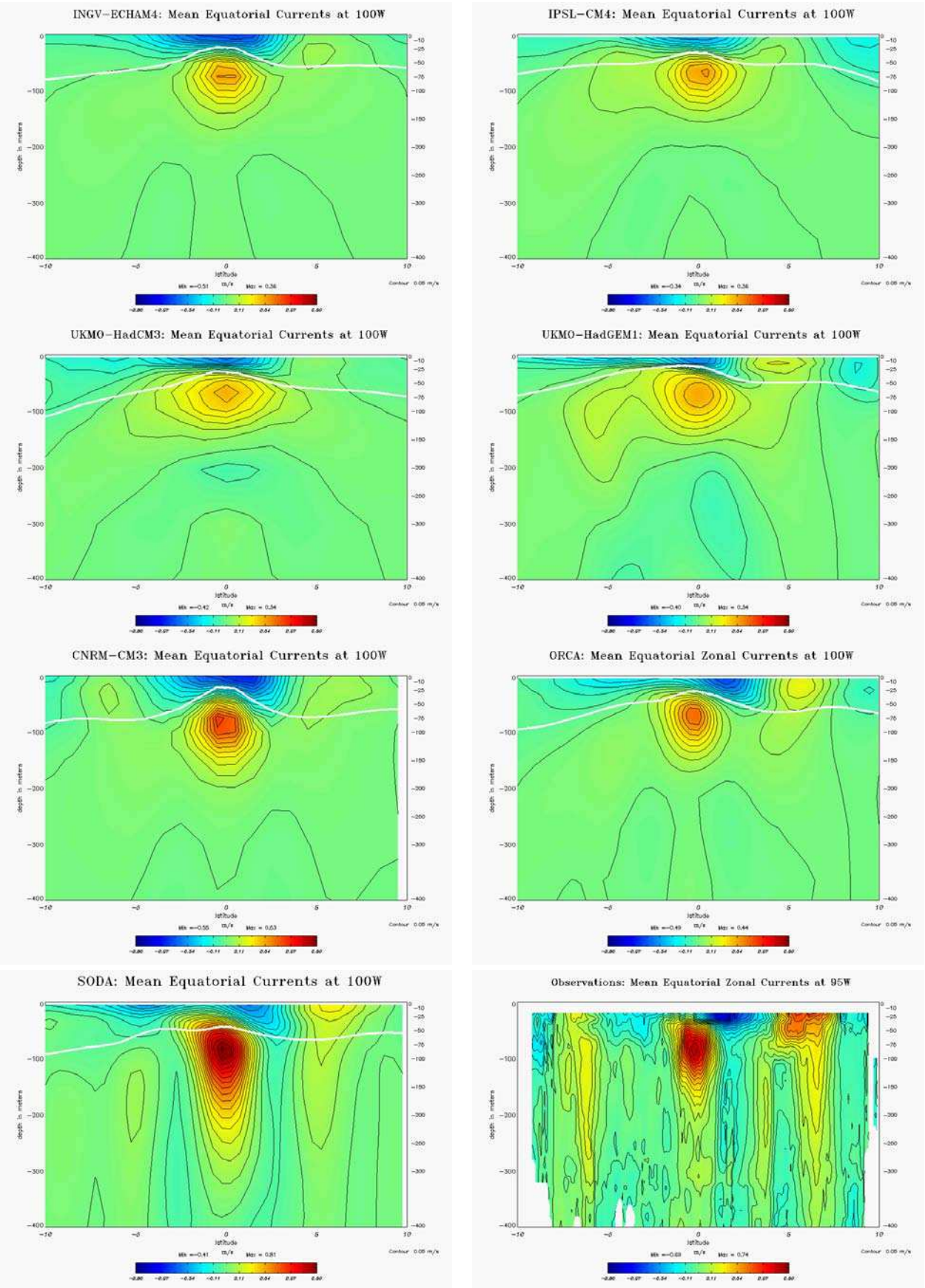

Fig. 2.17. Vertical sections of the mean zonal currents (m/s) for (from left to right and top to bottom): INGV-ECHAM4, IPSL-CM4, UKMO-HadCM3, UKMO-HadGEM1, CNRM-CM3, ORCA05, SODA-1.4.2 at 100°W and ADCP data at 95°W (see text). Mean 20°C isotherm depth is also indicated on the model plots (bold white line). Contour interval is 5 cm/s. Colour scale is blue-red: -80cm/s – 80cm/s.

(fig. 2.29). The results are directly comparable to those from Johnson et al. (2002) – their figure 2. – who used similar data on the period 1991-2001. Sections of total variability of the equatorial currents were also computed using the data over the whole period and ignoring the gaps between each cruise (fig. 2.28).

Year	1996	1997	1998	1999	2000	2001	2002	2003	2004	2005	2006	2007	2008	2009
Number of cruises	1	2	2	2	1	4	2	2	2	1	2	2	2	1

Table 2.5. Number of NOAA cruises along the 95°W section (see text) per year over the period October 1996 to January 2009.

Month	Jan.	Feb.	Mar.	Apr.	May	Jun.	Jul.	Aug.	Sep.	Oct.	Nov.	Dec.
Number of cruises	1	3	0	4	1	1	0	1	1	3	5	0

Table 2.6. Number of NOAA cruises along the 95°W section (see text) per calendar month over the period October 1996 to January 2009.

Compared to the observations, SODA is able to represent accurately most features of the equatorial current system at 100°W (fig. 2.17):

- the EUC, between 50m and 100m depth at the equator just below the thermocline - estimated with the 20°C isotherm - (note that although the EUC extends too deep in the water column, its core is located at the right position) with maximum velocities around 0.5 to 1 m/s;
- the SEC, mainly in the first 50 metres of the water column, separated in two branches at 2°N and 5°S with slightly underestimated maximum velocities between 20 and 50 cm/s ;
- the NECC, around 5°N with a maximum at sea surface around 20 cm/s (around 50 cm/s in ADCP data);
- the SSSCC, between 100 and 200m depth around 5°S, with maximum velocities around 10 cm/s.

On the other hand, ORCA exhibits a too weak EUC (fig. 2.17), possibly because of the weak equatorial zonal winds – at least east of 100°W – in the ERS data (see 2.3.1), which provide the wind forcing for this simulation (see chapter three): weaker easterly trade winds are likely to induce a weaker zonal pressure gradient across the tropical Pacific and hence a weaker EUC. In addition, the EUC does not extend deep enough, probably due to the too shallow thermocline (see 2.3.3.2), which determines its depth (see chapter one). The SSSCC is absent, and westward velocities are absent beyond a hundred metres depth: the latter bias may be due to the shallow thermocline (and mixed layer, its base being close to the thermocline in this region), or to the absence of the SSSCC (see chapter one), or both. Nevertheless, the NECC is well represented (except its too weak intensity), and so is the surface westward flux at 10°N, absent from SODA

though observed with ADCP data. The two branches of the SEC are more realistic than in SODA, with a northern branch that is stronger than the southern branch.

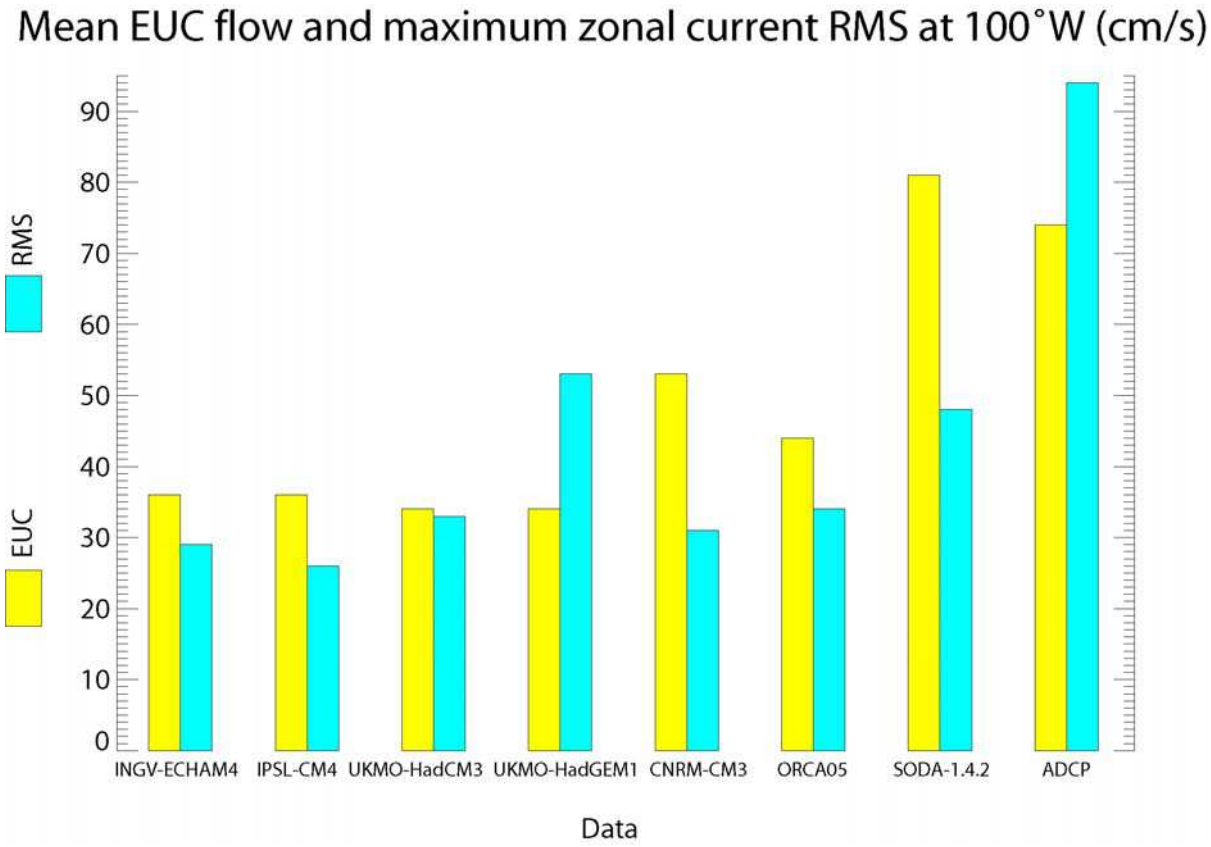

Fig. 2.18. Mean velocities (cm/s) in the core of the EUC and maximum zonal current variability (cm/s) at 100°W (between 10°S and 10°N and between 0m and 400m depth) for the GCMs, for SODA-1.4.2 and for ADCP measurements.

CGCMs exhibit an EUC that is systematically too weak, that does not extend deep enough, and does not feature any Tsuchiya jet at 5°S, except for UKMO-HadGEM1 (see figures 2.17 and 2.18). As for ORCA, such biases are likely due to the systematically underestimated zonal winds in the equatorial band (see 2.3.1) and thermocline depths (see 2.3.3.2). The SEC exhibits a unique branch – except in the case of UKMO-HadGEM1 –, possibly because of the coarse oceanic resolution of these models and the associated topography in the Galapagos Islands area, since the splitting of the SEC in two branches is due to the presence of the islands (see chapter one). Associated velocities are too low for all the CGCMs, which is again likely a consequence of the weak equatorial easterlies (see chapter one). UKMO-HadGEM1 simulates the westward surface flux around 10°N, which is present in ADCP measurements and in ORCA, as well as in IPSL-CM4 whose oceanic component is built on the same code as that of ORCA (OPA 8). Last, UKMO-HadGEM1 is the only CGCM featuring a significant mean NECC, although INGV-ECHAM4 and UKMO-HadCM3 exhibit a weaker surface current as detailed hereafter (fig. 2.28). Note that the significantly higher oceanic resolution of the HadGEM1 model (see table 1 from section 1)

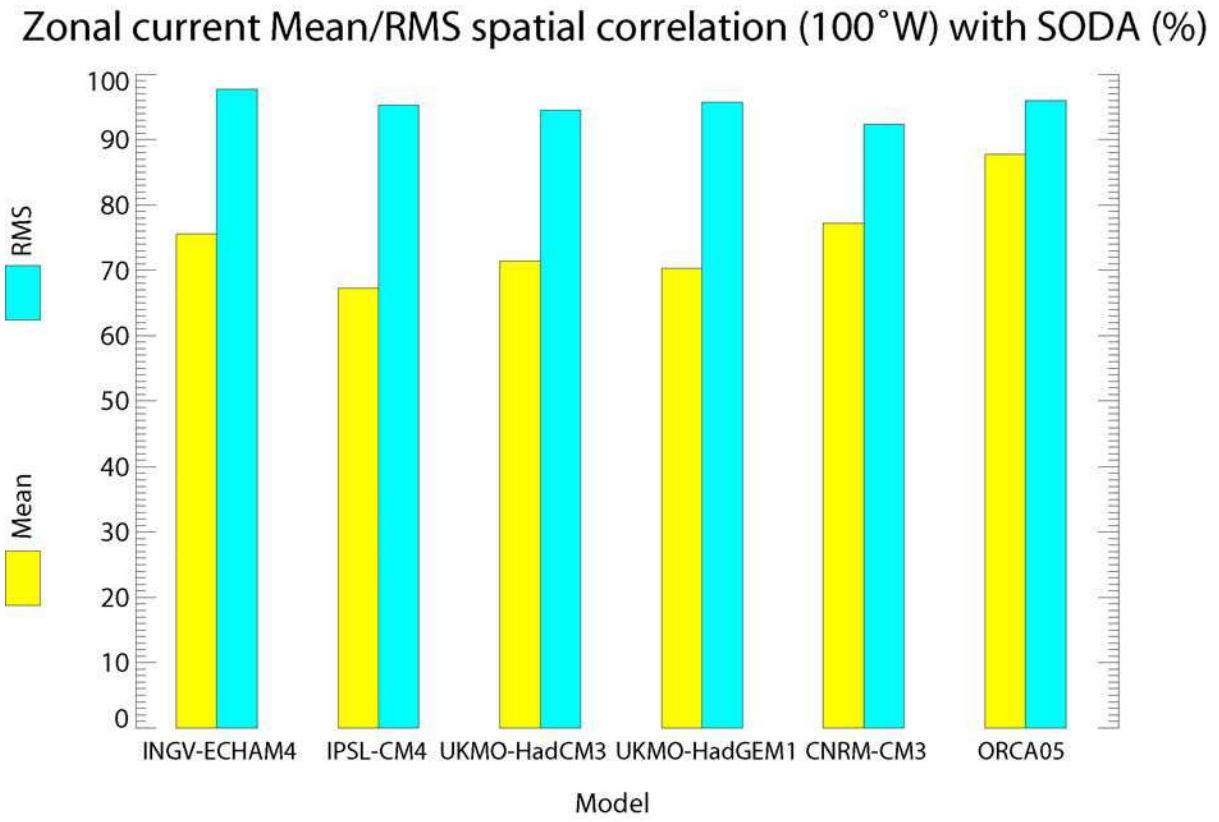

Fig. 2.19. Spatial correlations (%) computed at 100°W (between 10°S et 10°N and between 0m and 400m depth) for mean zonal currents and zonal current variabilities (RMS) from the different GCMs relatively to SODA-1.4.2.

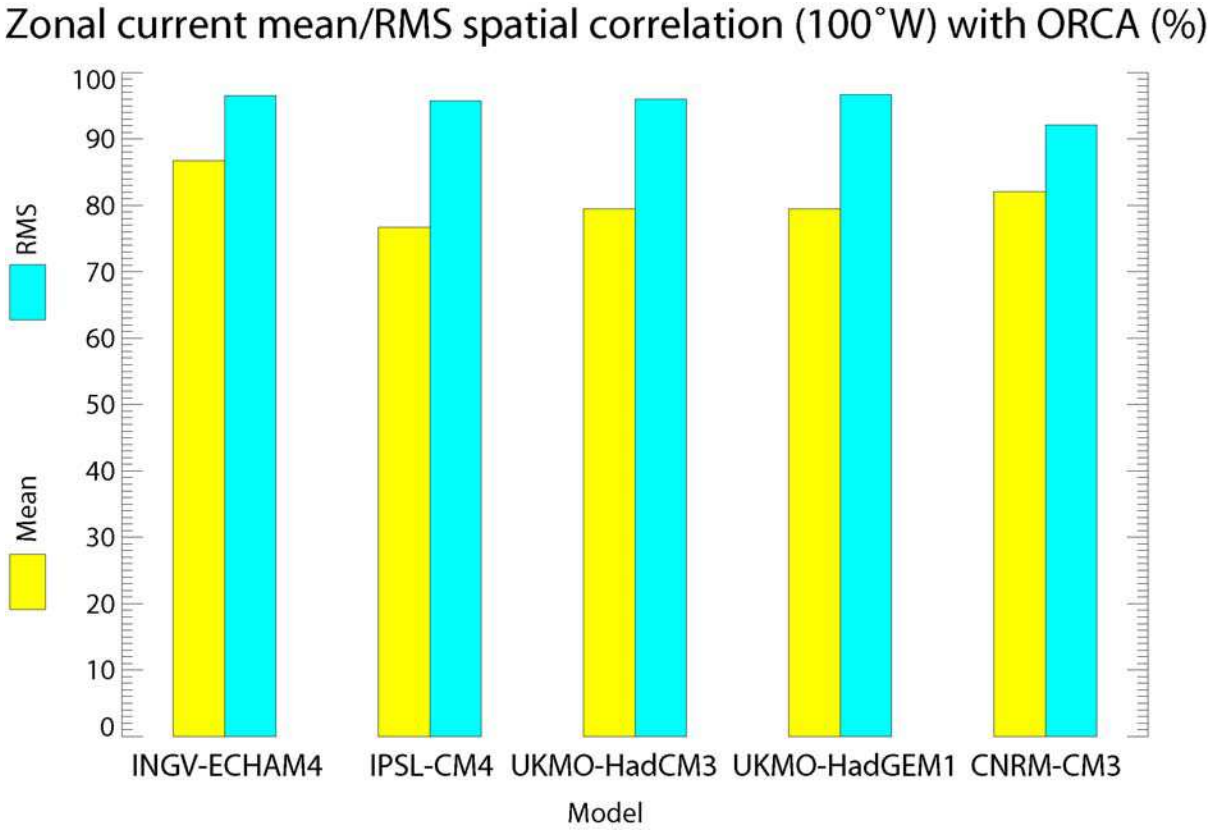

Fig. 2.20. Same as fig.2.19, except relatively to ORCA05.

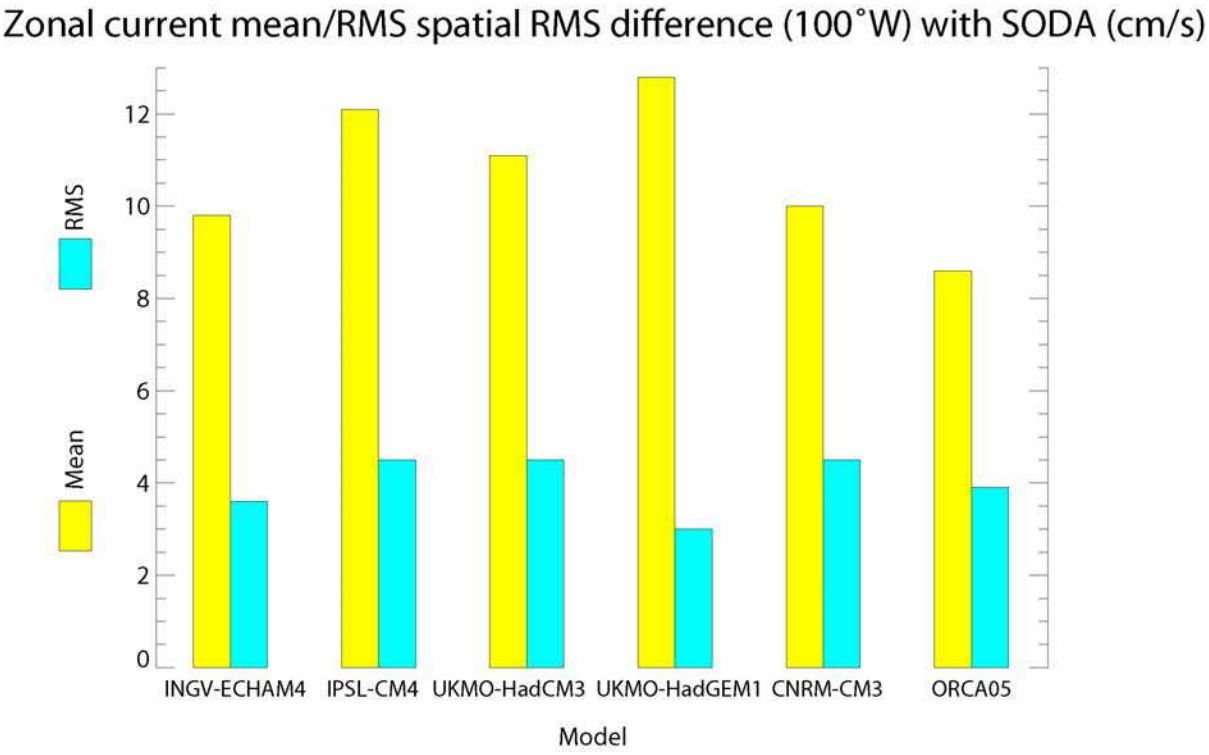

Fig. 2.21. Same as fig.2.19, except for spatial RMS difference (cm/s).

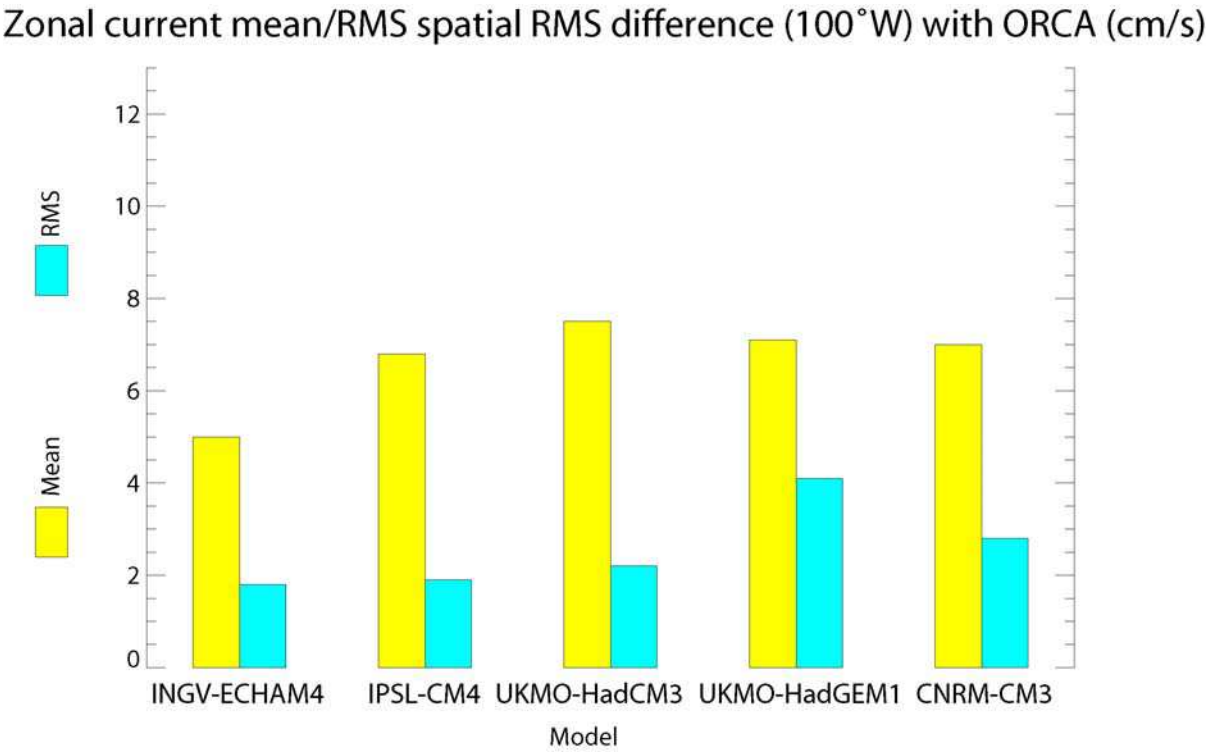

Fig. 2.22. Same as fig.2.21., except relatively to ORCA05.

probably provides a good explanation for its better representation of the equatorial currents compared to the other CGCMs.

In order to quantify the agreement between the mean currents (and their variability for different frequency bands) simulated by the CGCMs and those simulated by SODA and by ORCA, the

corresponding spatial correlation coefficients (figures 2.19 and 2.20) and RMS difference (figures 2.21 and 2.22) were calculated. These figures provide similar results: for instance, the mean currents from INGV-ECHAM4, CNRM-CM3 and ORCA05 are those with the highest correlations and smallest RMS differences. Differences are small among the CGCMs, especially for the spatial correlation, since all of them do simulate an EUC and a SEC located at the equator at depths close to the observed.

These differences do not necessarily reflect the skill of the models in reproducing the equatorial currents, since all points of the section considered for the calculation have an equal weight, which implies for example that the presence or the absence of the NECC is not a critical criterion for the calculation of these indices. On the other hand, trying to weight the equatorial currents for this computation is a tricky exercice since it is necessarily subjective. Nevertheless, spatial correlations can constitute a more relevant metric for the evaluation of temperature variability (figures 2.26 and 2.27) for instance as detailed further on.

2.3.3.2. Temperature

SODA is able to reproduce most features of the mean temperature field derived from XBT data over 1979-1992 (Kessler, 2006), which is also the case for ORCA (fig. 2.23):

- Temperatures comprised between 28°C at the surface and 13°C at 150 m;
- A deeper yet more diffuse thermocline associated to cooler surface waters to the South than to the North of the equator, due to the mean position of the ITCZ (in the northern hemisphere at this longitude – not shown) and to the presence of the eastern Pacific cold tongue (and of the equatorial front);
- A tilt of the isotherms at the equator near the surface associated to equatorial upwelling;
- A deepening of the isotherms at the equator below 100m depth associated to the presence of warm waters advected by the EUC.

Note however that SODA – as well as XBT data – exhibits an equatorial thermocline significantly deeper than those of the CGCMs and of ORCA (see also fig.2.24), despite a mean temperature structure very similar to that of the latter (see also figures 2.25 to 2.27). Although the models are forced by weaker winds in the equatorial band, several of them actually feature stronger off-equatorial winds associated to the ESP subtropical high (see 2.3.1). As detailed in the introductory chapter, these winds force a northwestward flow (in the form of both the CPCC and the PC) which feeds the cold tongue region with cooler waters from the Humboldt Current region.

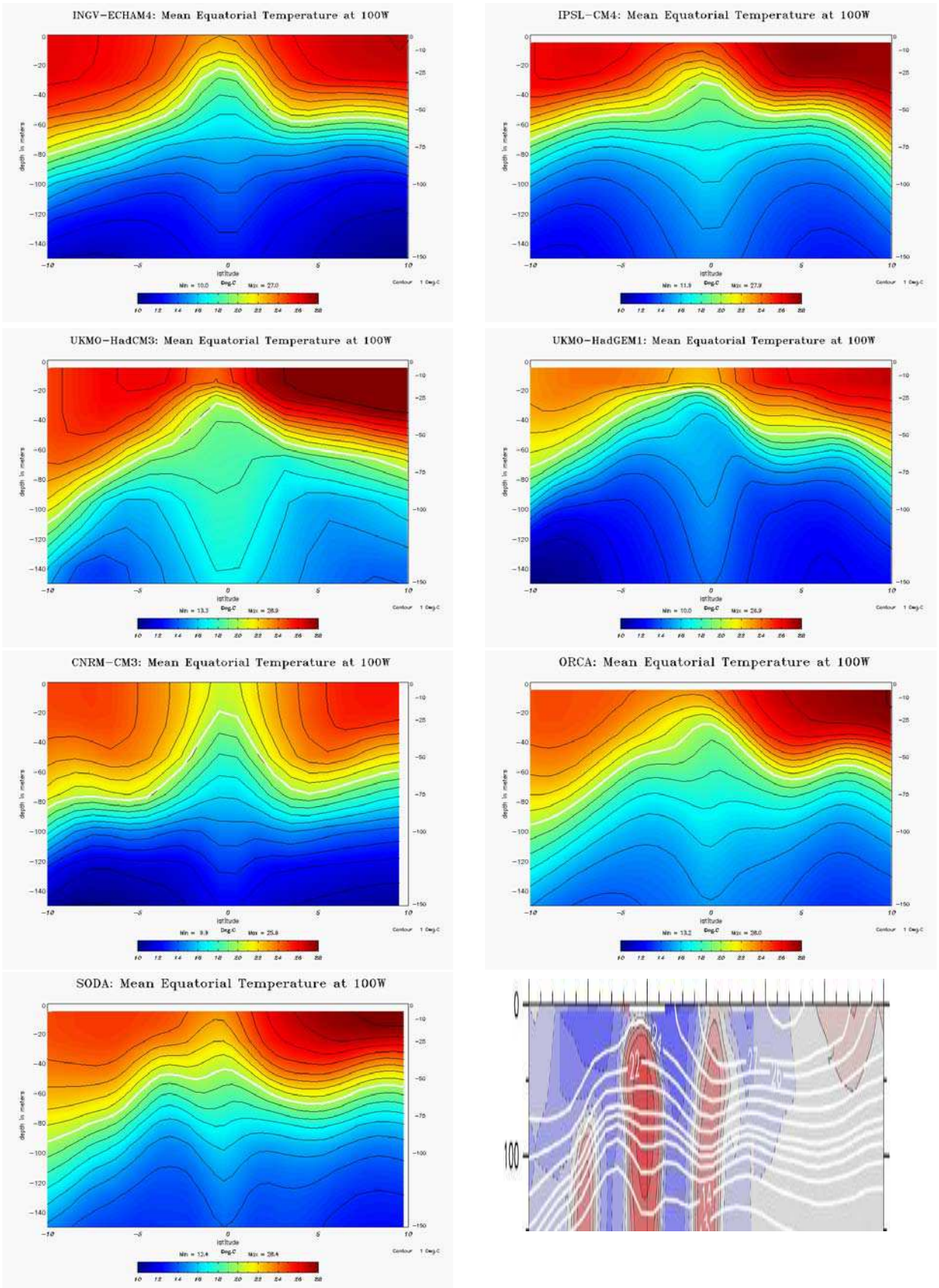

Fig. 2.23. Same as fig.2.17 but for mean temperature (°C). Contour interval is 1°C. Colour scale is blue-red: 10°C – 28°C. The bold white line on the model plots is for the 20°C isotherm depth. The bottom right panel (white lines) is reproduced from Kessler (2006) (his figure 6) and is for XBT measurements (see text).

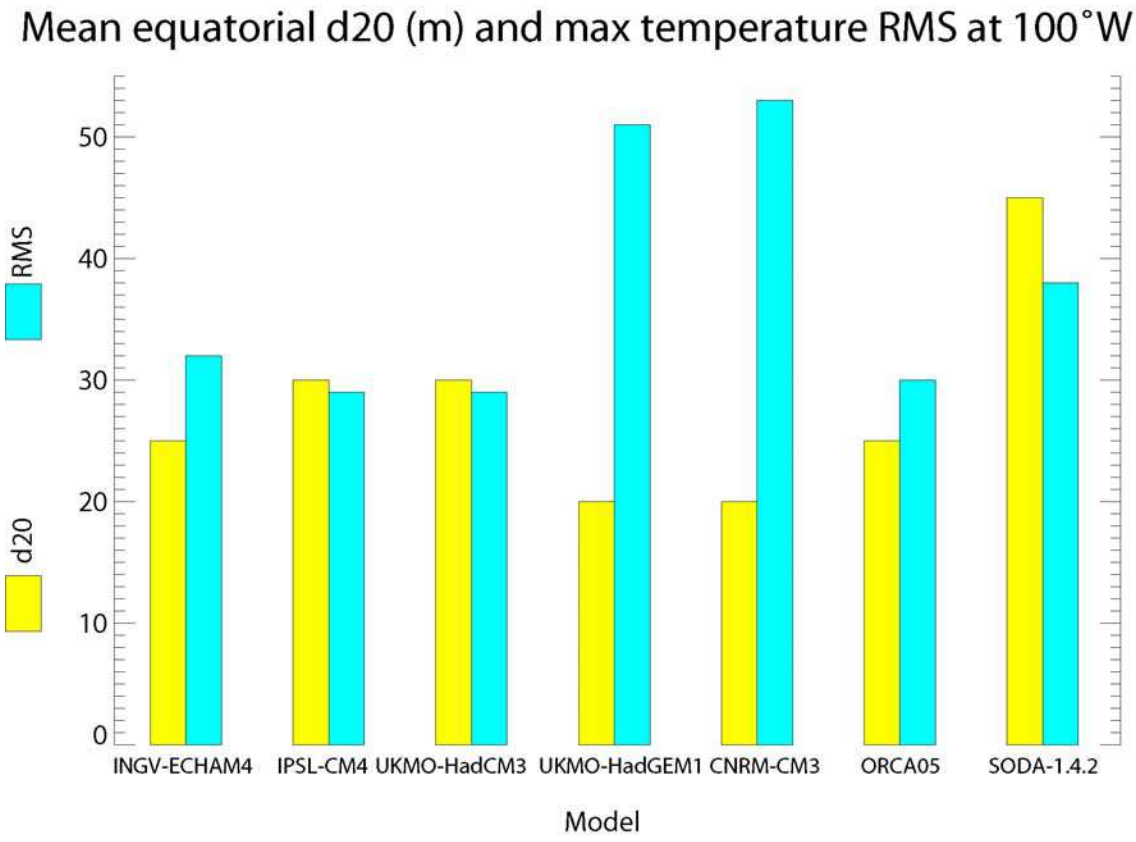

Fig. 2.24. Mean 20°C isotherm depth (m) at the equator and maximum temperature variability (°C) at 100°W (between 10°S and 10°N and between 0m and 400m depth) for the GCMs and for SODA-1.4.2.

Indeed, even if some models probably do not resolve coastal upwelling because of biases in the surface winds especially near the coast, Humboldt Current waters of subtropical origin are still likely colder than equatorial waters. As a consequence, equatorial temperatures are cooler than observed and the thermocline is shallower. Note that the models that exhibit the strongest cold biases at 100°W (IPSL-CM4 and UKMO-HadGEM1 – see fig. 2.25) are also the ones that most strongly overestimate surface winds associated to the northwestward branch of the anticyclone (see 2.3.1), supporting the present interpretation.

Plots of the mean temperature difference between CGCMs and SODA help assessing the differences between the former and the latter (fig.2.25). For INGV-ECHAM4 and IPSL-CM4, temperatures in the surface layer are close to the observed, whereas they are too high for UKMO-HadCM3 and too low for UKMO-HadGEM1 and for CNRM-CM3. Yet, below the thermocline, UKMO-HadCM3 presents the weakest mean temperature biases among the CGCMs (though it is too warm at the equator), the others being cooler, particularly INGV-ECHAM4, CNRM-CM3 and especially UKMO-HadGEM1. IPSL-CM4 exhibits the smallest temperature differences with

SODA in the EUC, whereas UKMO-HadCM3 exhibits a warm bias and the other CGCMs some cold biases (particularly UKMO-HadGEM1 and CNRM-CM3).

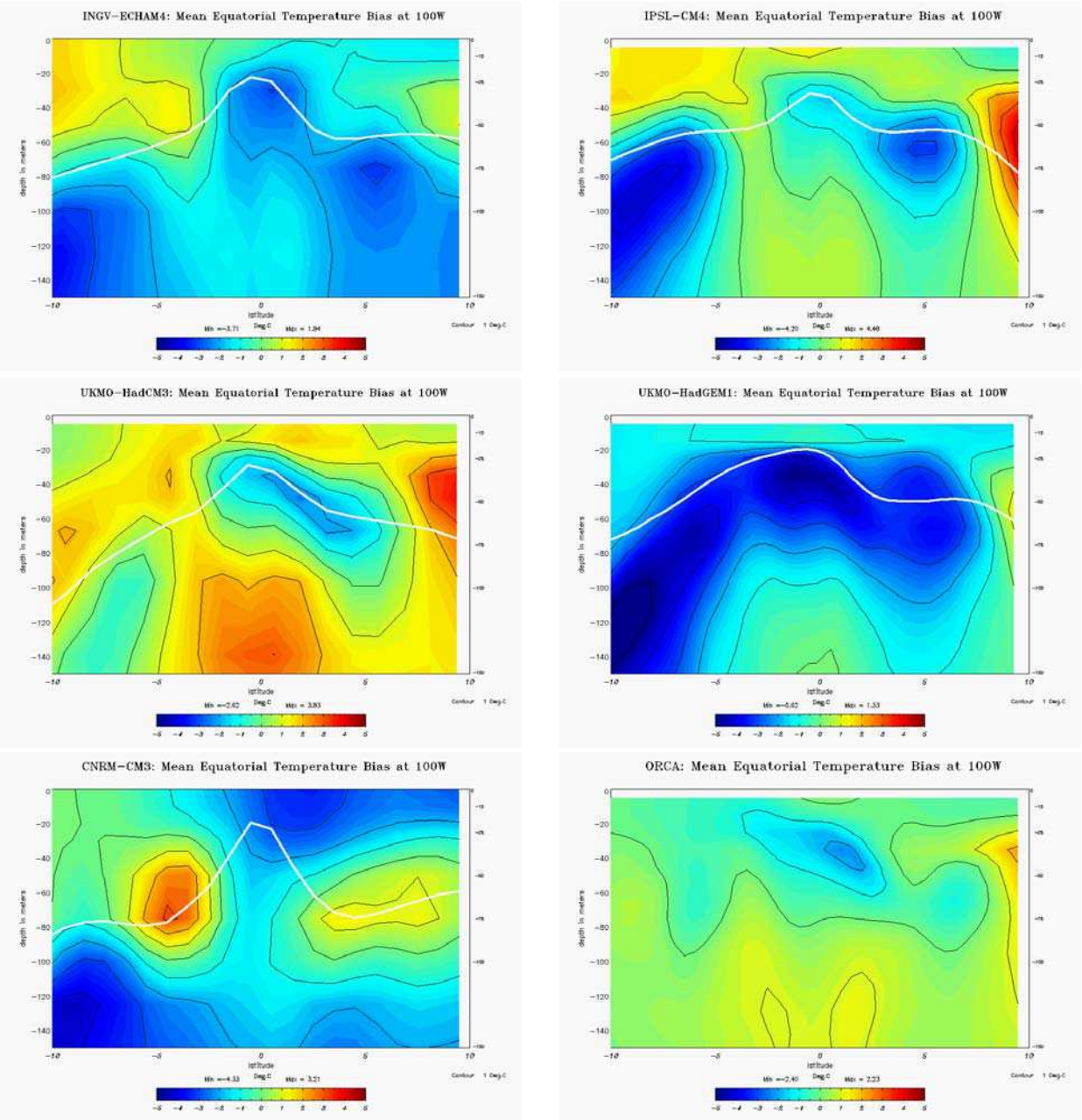

Fig. 2.25. Same as fig.2.23 but for mean temperature difference with SODA-1.4.2 (°C). Colour scale is blue-red: -5°C – 5°C. The white line indicates the mean 20°C isotherm for each CGCM.

Assessing these biases is very important for the downscaling exercice since they will be transmitted to the regional model via the surface (NECC) and especially the subsurface eastward currents (EUC, SSSCC) and ultimately influence the regional model solution. In this respect, IPSL-CM4 provides the least biased boundary conditions compared to available XBT and reanalyzed data.

In regard to the North/South asymmetry, it is present at the surface for the four hybrid CGCMs (to a smaller extent for INGV-ECHAM4), but not for CNRM-CM3 (fig.2.23). On the other hand, INGV-ECHAM4 is the most realistic model in terms of subsurface asymmetry, IPSL-CM4, UKMO-HadCM3 and CNRM-CM3 being too symmetric and UKMO-HadGEM1 showing an almost reversed asymmetry. All the CGCMs share the same bias: a too marked thermocline to the South, which is likely due to the weaker equatorial easterlies (fig. 2.10). Indeed, in SODA, the thermocline South from the equator is more diffuse though deeper than in the CGCMs: compared to most hybrid CGCMs, even if temperatures are warmer in the reanalysis (and in XBT data) because weaker off-equatorial winds advect less cold water, the local wind forcing is stronger and produces more vertical mixing across the thermocline, making it more diffuse. Equatorial upwelling – actually its signature in surface layer temperature and stratification – is the most 'realistic' for INGV-ECHAM4 and for IPSL-CM4, whereas UKMO-HadCM3 and particularly UKMO-HadGEM1 feature too high equatorial stratification and CNRM-CM3 greatly over-estimates upwelling (fig. 2.23).

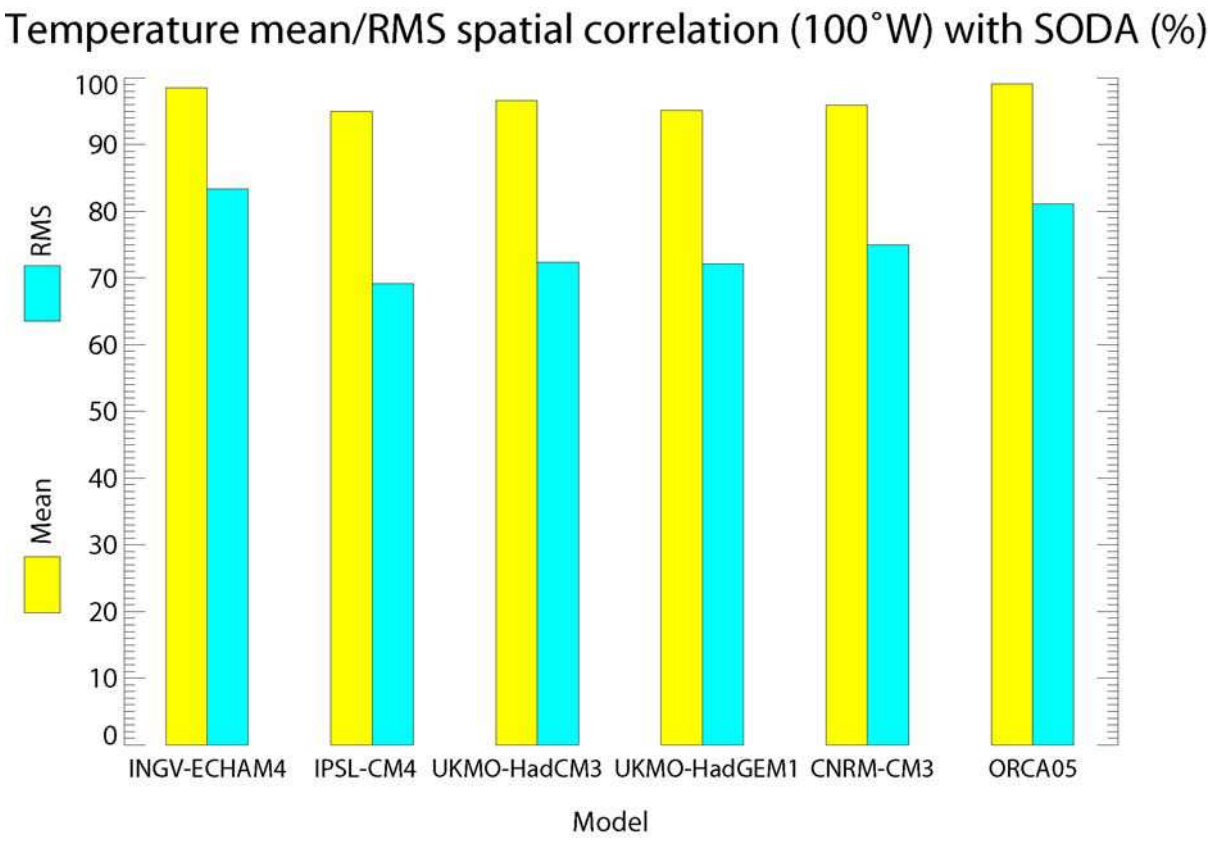

Fig. 2.26. Spatial correlations (%) computed at 100°W (between 10°S et 10°N and between 0m and 400m depth) for mean temperature and temperature variabilities (RMS) from the different GCMs relatively to SODA-1.4.2.

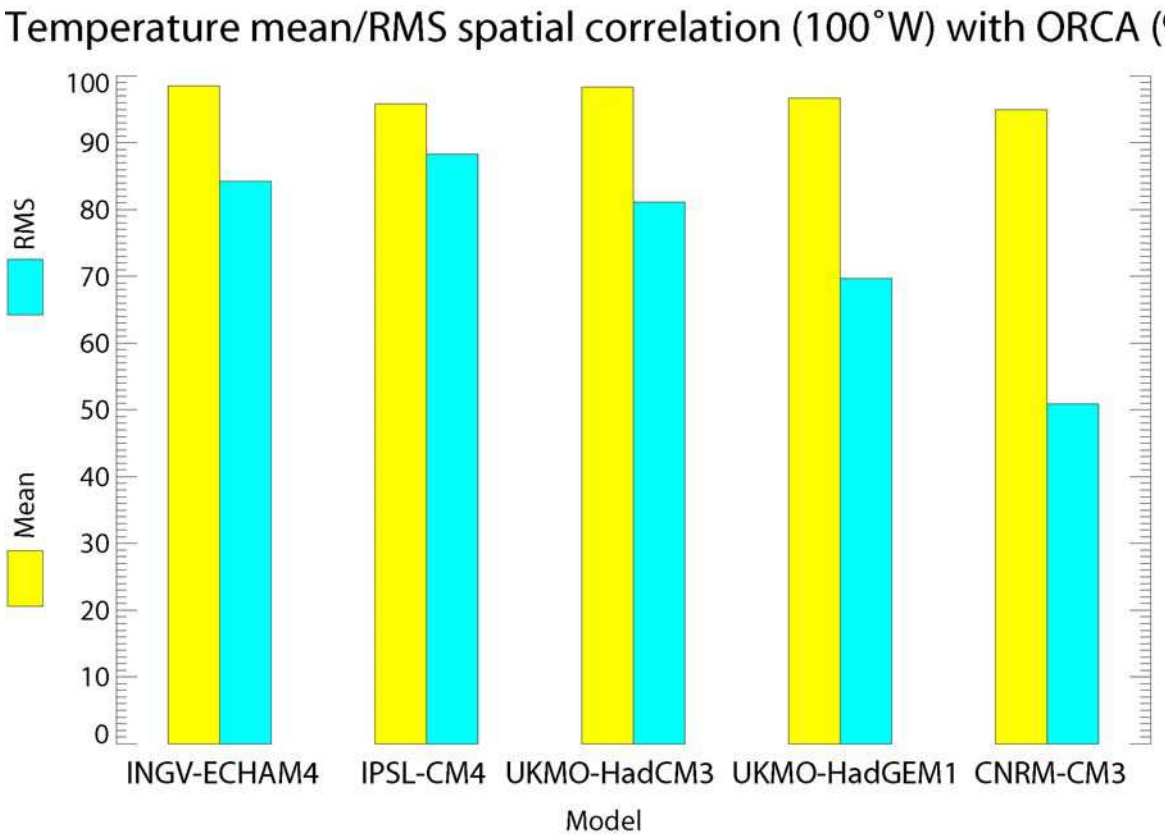

Fig. 2.27. Same as fig.2.26, except relatively to ORCA05.

2.3.4. Equatorial intraseasonal-to-interannual variability: zonal currents and temperature

first of all, let us remind the reader that the analysis is based on monthly data, since higher sampling is not available from PCMDI. As a consequence, some high frequency phenomena (*e.g.* equatorial waves, tropical instability waves) cannot be assessed with such data, as discussed below in the sub-section dedicated to intraseasonal variability.

2.3.4.1. Zonal currents

Total Variability

In regard to current variability at 100°W, it is strongest for all the models at the equator in the surface layer, and extends over a few hundred metres down the water column (fig.2.28). More precisely, the variability peak is located in the vicinity of the thermocline in the zone of maximum shear between the SEC and the EUC for UKMO-HadGEM1 (like for SODA and ADCP data), and

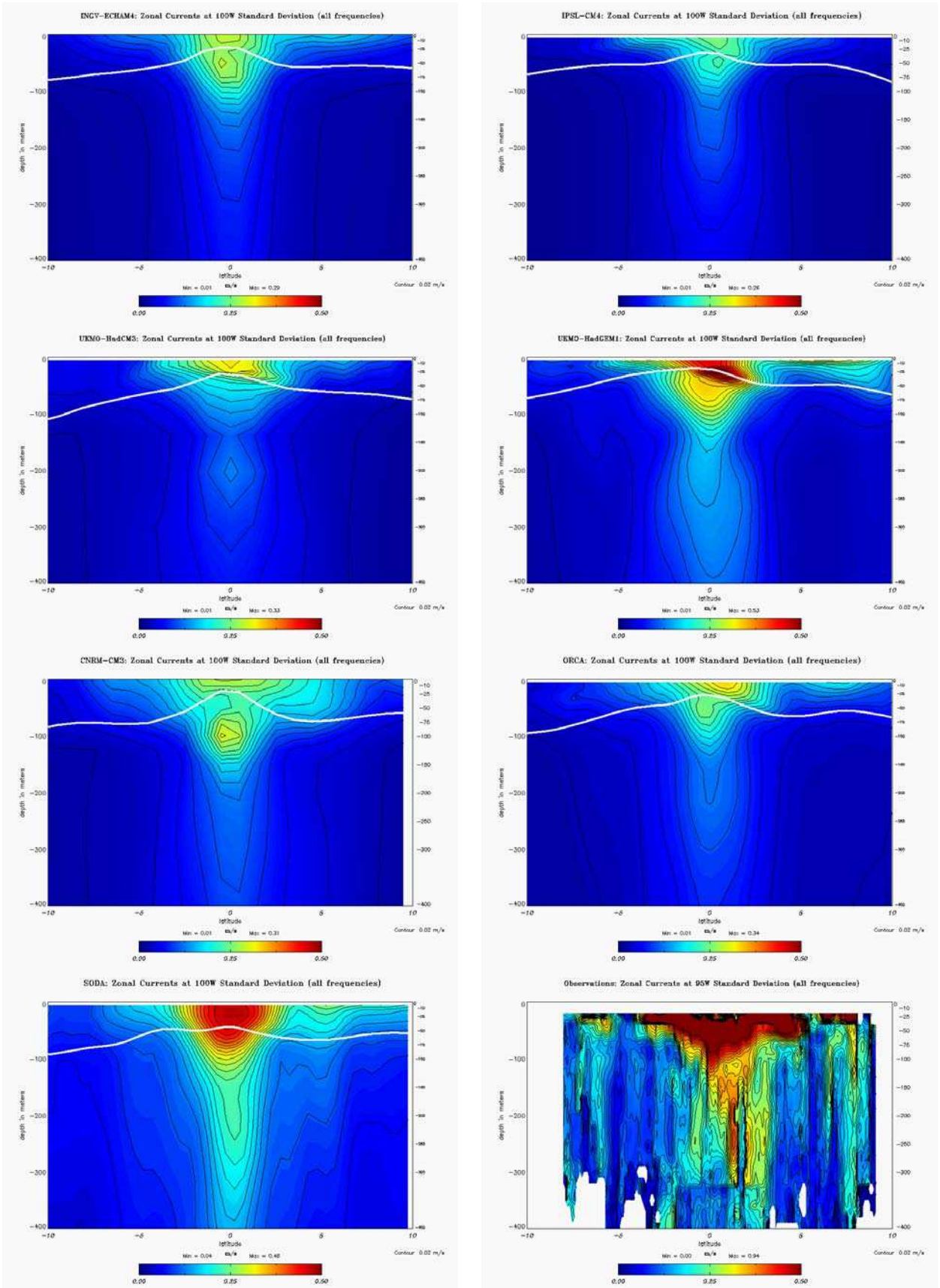

Fig. 2.28. Total zonal current variability (RMS, m/s) for (from left to right and top to bottom): INGV-ECHAM4, IPSL-CM4, UKMO-HadCM3, UKMO-HadGEM1, CNRM-CM3, ORCA05 and SODA-1.4.2 at 100°W and ADCP data at 95°W (see text). Mean 20°C isotherm depth is also indicated on the model plots (white bold line). Contour interval is 2cm/s. Colour scale is blue-red: 0 cm/s –50 cm/s.

around the SEC for the other hybrid CGCMs (like for ORCA). Note that this zone of maximum shear appears clearly on this figure for all the CGCMs except INGV-ECHAM4 and CNRM-CM3 (the latter features a peak in the EUC). UKMO-HadGEM1 is the only CGCM whose peak of variability is of the same order of magnitude as that from SODA (fig.2.18) - though current variability is under-estimated in the deeper layers, particularly in the off-equatorial region -, whereas for UKMO-HadCM3 (and CNRM-CM3), it is of the same order as that from ORCA (*i.e.* 30% weaker). Variability is weaker for INGV-ECHAM4 and IPSL-CM4. However, relatively to the mean currents, UKMO-HadGEM1 has a very strong maximum variability (around 125%), whereas the other CGCMs present more realistic levels: around 60% for INGV-ECHAM4 and CNRM-CM3 (like for SODA), around 70% for IPSL-CM4 and UKMO-HadCM3 (like for ORCA).

All the models exhibit a local maximum of weak intensity in the EUC (and the SEC for UKMO-HadGEM1 and CNRM-CM3), except UKMO-HadCM3. It is also the case in the NECC (except for IPSL-CM4 and CNRM-CM3 that do not seem to represent it), including for INGV-ECHAM4 and UKMO-HadCM3 for which such current, though weak, is present. UKMO-HadGEM1 is the only model that presents a local maximum at 100m, 5°S (fig. 2.28), which corresponds to the southern Tsuchiya jet (SSSCC).

In order to quantitatively assess spatial scales of variability for all the models, maps from figure 2.28 – vertical equatorial sections of zonal current variability – were vertically (resp. meridionally) averaged, and fitted to a gaussian curve over the meridional (resp. vertical) axis. The corresponding full width at half maximum (FWHM) provides an estimate of the meridional (resp. vertical) scale (table 2.7). Note that for the vertical scale, since the maximum variability is close to the surface, the meridionally averaged variability maps were fitted to the negative part of a gaussian curve, and only half of the FWHM of the corresponding full gaussian curve was used.

Model	Vertical scale (m)	Meridional scale (°)
INGV-ECHAM4	53	3.6
IPSL-CM4	45	3.9
UKMO-HadCM3	50	5.2
UKMO-HadGEM1	59	4.2
CNRM-CM3	80	3.9
ORCA05 (monthly outputs)	52	3.8
SODA-1.4.2	63	3.4

Table 2.7. Vertical scale (m) and meridional scale (°) of zonal current variability for the GCMs and for SODA-1.4.2.

Results show that most models including ORCA tend to slightly underestimate vertical scales of variability compared to SODA (by 15-30%), except UKMO-HadGEM1 which exhibits the

smallest difference with SODA (~6%) and CNRM-CM3 which significantly overestimates vertical scales (~27%). On the other hand, meridional scales are slightly overestimated by most models (by 5-25%) except UKMO-HadCM3, which strongly overestimates the latitudinal extension around the equator (~53%). Interestingly, the four models that use OPA for the ocean dynamics (INGV-ECHAM4, IPSL-CM4, CNRM-CM3, ORCA05) have meridional scales of zonal current variability that are very close to each other (and the closest to SODA among the ensemble), suggesting a dominant role of the ocean and possibly of equatorial wave dynamics.

Note finally that observed variability from shipboard ADCP data is about twice that of SODA. Because of the scarcity of the observed data, a maximum 22 values could be used at a given location to compute current variability, which corresponds to the total number of oceanographic cruises. At some locations, only two values were available (because of technical issues like instrumental failure for instance), and in some regions only one measurement was available (hence the gaps between 300m and 400m depth and around 10°S and 10°N): for this reason, caution is required in the interpretation of the differences between variability from SODA and from observations. Nevertheless, they show an overall good qualitative agreement, which increases our confidence in the results from SODA.

Annual cycle, interannual and intraseasonal variability

In order to better understand the origin of equatorial current variability in the models, the seasonal cycle is separated, and a filtering of the corresponding anomalies is performed for different frequency bands: [1-5] months for intraseasonal variability, [7-18] months for near-annual variability (the [5-7] month band is not taken into account here in order to eliminate possible semi-annual harmonics that may be already present in the seasonal cycle), and [18-+∞[months for interannual variability, the latter being computed for the CGCMs over a period of the same duration as that of the SODA period (44 years) so as to obtain comparable metrics. Note that we have checked that considering the whole available time span for each CGCM (see table 1 from Belmadani et al., 2010) in the computation of interannual variability yielded similar results (not shown). For the four hybrid CGCMs, anomalies relatively to the mean seasonal cycle still contain a significant fraction of the variability with periodicity around one year (not shown). Indeed, spatial distributions of seasonal and near-annual variabilities are very similar, except for their intensity (the ratio is around 2 to 3 depending on the models – not shown). This suggests a significant interannual-to-decadal modulation of the seasonal cycle of the equatorial currents at 100°W for these models. In the following, the seasonal cycle refers to the sum of the mean

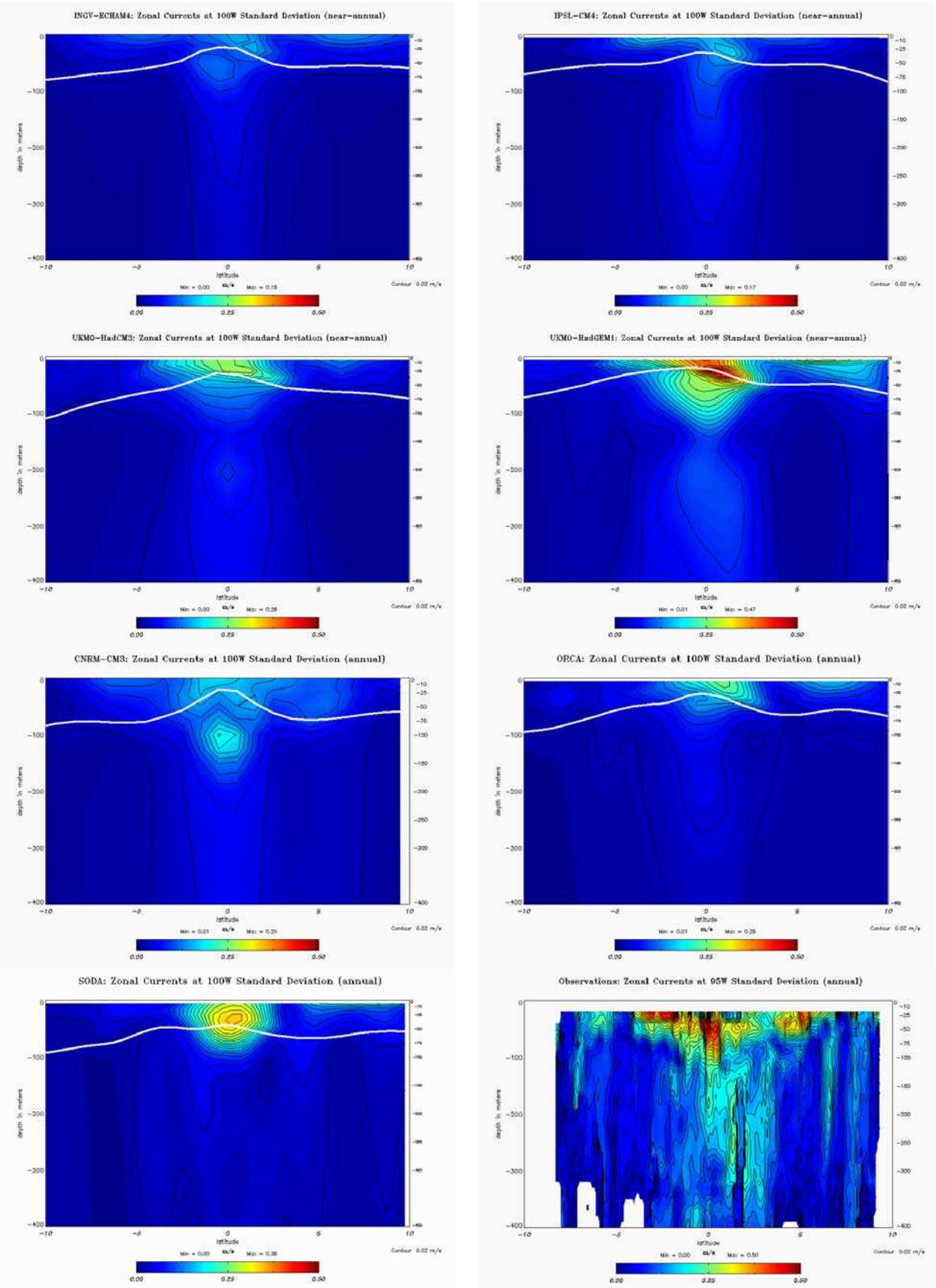

Fig. 2.29. Seasonal variability of zonal currents (m/s) at 100°W for (from left to right and top to bottom) INGV-ECHAM4, IPSL-CM4, UKMO-HadCM3, UKMO-HadGEM1, CNRM-CM3, ORCA05 and SODA-1.4.2 at 100°W and ADCP data at 95°W (see text). 20°C isotherm depth is also indicated on the model plots (bold white line). Contour interval and colour scale are as in fig.2.28.

seasonal cycle and the associated anomalies previously filtered in the near-annual band.

For all the CGCMs, the seasonal cycle dominates the spectrum of variability similarly to SODA (and ORCA), with a maximum at the equator in the surface layer in the zone of maximum shear between the EUC and the SEC (between 30m and 75m depending on the model – fig. 2.29) and a secondary peak around 5°N, *i.e.* in the NECC if present, which is the case for all the models except IPSL-CM4 and CNRM-CM3. The amplitude of the seasonal cycle (fig.2.29) is under-estimated for INGV-ECHAM4 and IPSL-CM4 by respectively 57% and 51%, whereas it is over-estimated for UKMO-HadGEM1 by 34% (fig.2.30) compared to SODA. UKMO-HadCM3 exhibits an amplitude of seasonal variability 'only' 20% weaker than SODA. On the other hand, the amplitude of seasonal variability in CNRM-CM3 is only ~57% of the SODA value.

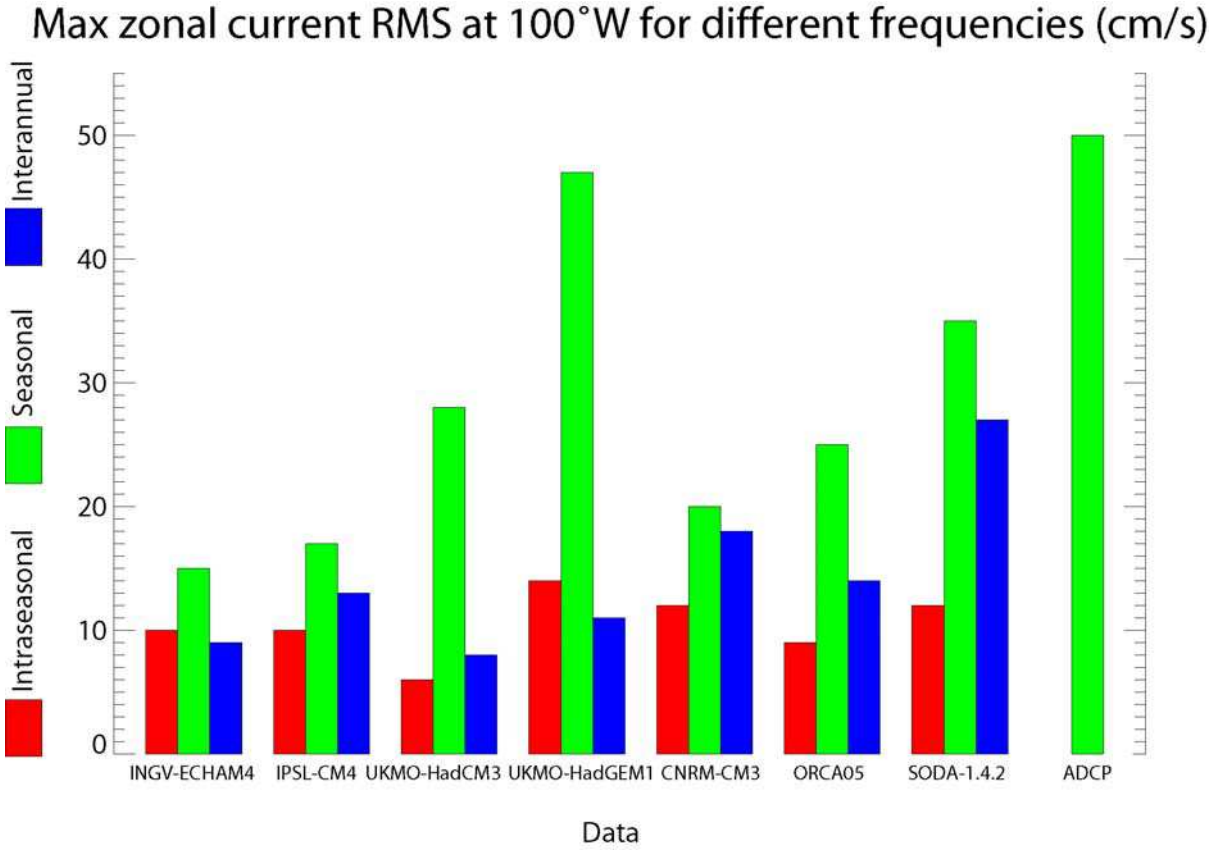

Fig. 2.30. Maxima of seasonal, interannual and intraseasonal zonal current variability (cm/s) at 100°W (between 10°S and 10°N and between 0m and 400m depth) for the GCMs, for SODA-1.4.2 and for ADCP measurements. Note that due to the scarcity of the ADCP data, observed interannual and intraseasonal variabilities could not be assessed.

Next, we assess interannual zonal current variability in the models (fig.2.31), which is weak for CGCMs (especially for the hybrid) and for ORCA (for the latter, this may be due to the short length of the available record) compared to SODA. Like for SODA, it is strongest for the CGCMs at the equator near the surface and below the thermocline (between 50m and 75m depending on the model). UKMO-HadGEM1 is the only CGCM for which the interannual signal is marked in the

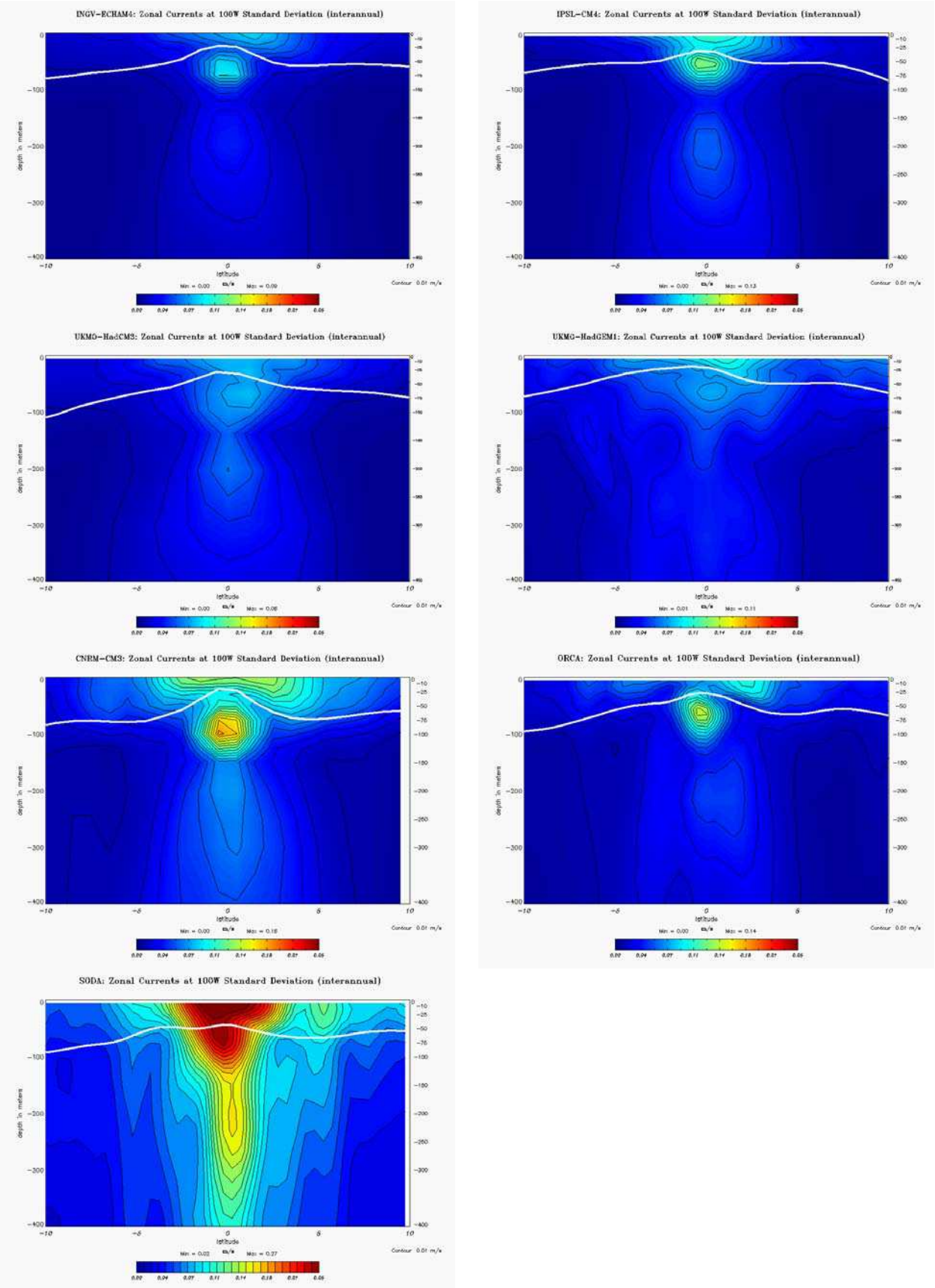

Fig. 2.31. Same as fig.2.29 but for interannual zonal current variability (m/s). Note the change in colour scale: contour interval is 1cm/s. Colour scale is blue-red: 0 cm/s –25 cm/s.

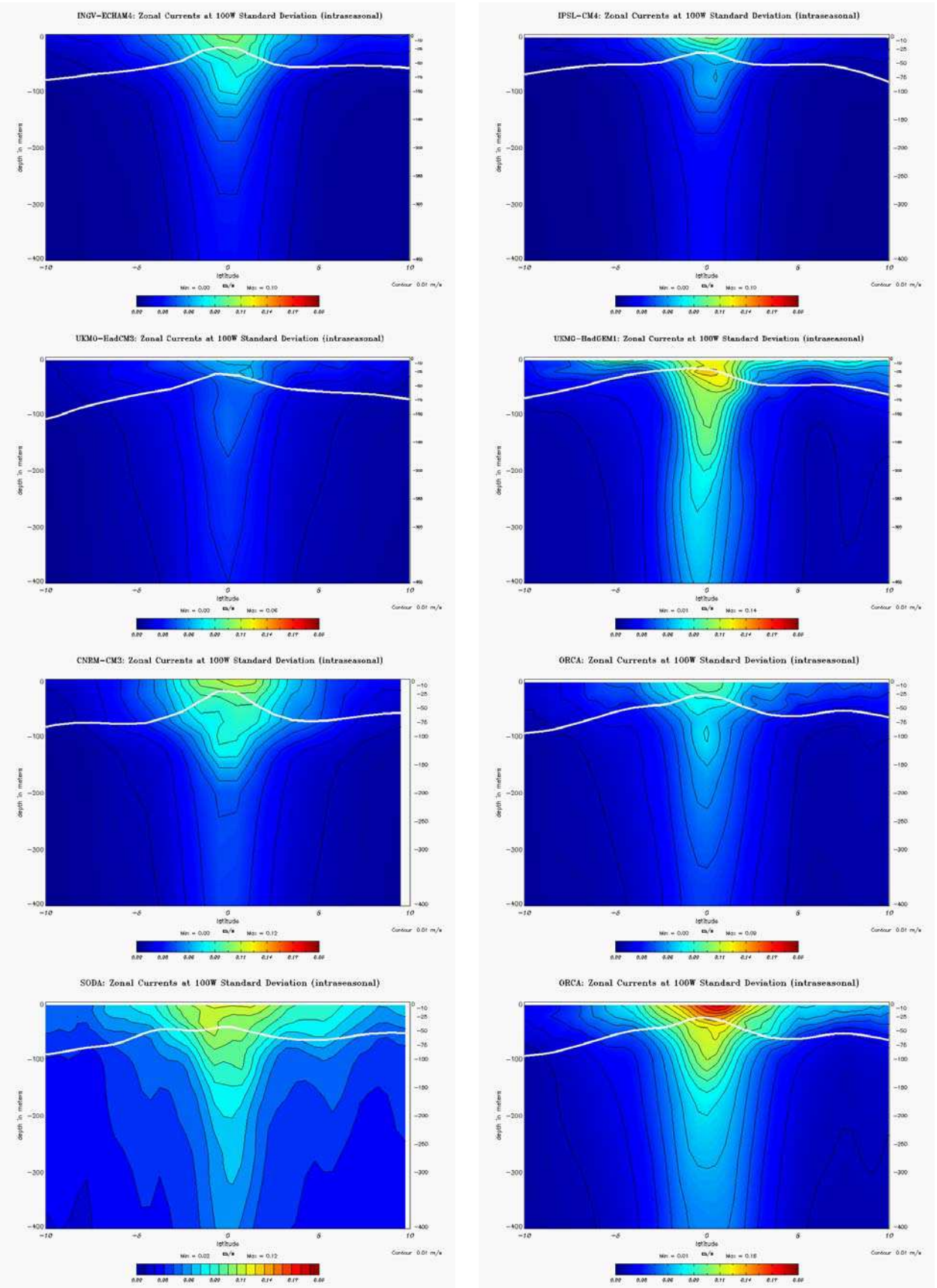

Fig. 2.32. Same as fig.2.29 but for intraseasonal zonal current variability (m/s). The bottom right panel represents the results obtained with 5-daily ORCA outputs. Note the change in colour scale: contour interval is 1cm/s. Colour scale is blue-red: 0 cm/s –20 cm/s.

NECC, like for SODA. CNRM-CM3 is the model that least underestimates levels of interannual variability (by ~33% compared to SODA). However, its maximum is confined in the EUC. In addition, it is the only model that exhibits peak interannual variability of the same order (~90%) as peak seasonal variability, the other models exhibiting a ratio between maximum interannual variability and seasonal cycle amplitude between ~23% (UKMO-HadGEM1) and ~76% (IPSL-CM4), with SODA exhibiting a ratio of ~77% (values derived from fig.2.30).

Last, the distribution and amplitude of intraseasonal variability as represented by SODA is reproduced by the models (except UKMO-HadCM3 that presents levels around the half of those obtained for the other CGCMs), *i.e.* it has a weak intensity compared to other frequency bands and it is concentrated at the equator with a maximum near the surface (fig. 2.32).

Not surprisingly, for ORCA for which 5-daily averages are available, intraseasonal zonal current variability is twice larger than that obtained from the monthly means, a statement which holds for temperature (fig.2.36). This indicates that monthly means from the CGCMs are not very indicated for the study of intraseasonal variability, as expected. The unavailability of oceanic outputs from the CGCMs at a higher sampling frequency might constitute a limitation for the study of regional climate change impacts (see chapter four). Indeed, intraseasonal equatorial variability is dominated by intraseasonal equatorial Kelvin waves (IEKW), which can force coastal-trapped waves (CTW) that can significantly influence the variability of coastal upwelling and nearshore eddy activity (chapter one). This statement motivated us to conduct a specific study on the role of intraseasonal variability of equatorial origin on the regional ocean dynamics (see chapter three).

To summarize, based on different metrics proposed to assess both the mean state and the variability of zonal currents at the western boundary of the regional domain, UKMO-HadGEM1 'best' reproduces the oceanic conditions simulated by SODA among the hybrid CGCMs, both qualitatively (*e.g.* presence of the Tsuchiya Jet at 5°S, of the NECC) and quantitatively (*e.g.* amplitude of zonal current variability).

2.3.4.2. Temperature

Total variability

In regard to temperature variability, it is largest for all the models in the subsurface in the vicinity of the thermocline (fig. 2.33), where the vertical temperature gradient is strongest.

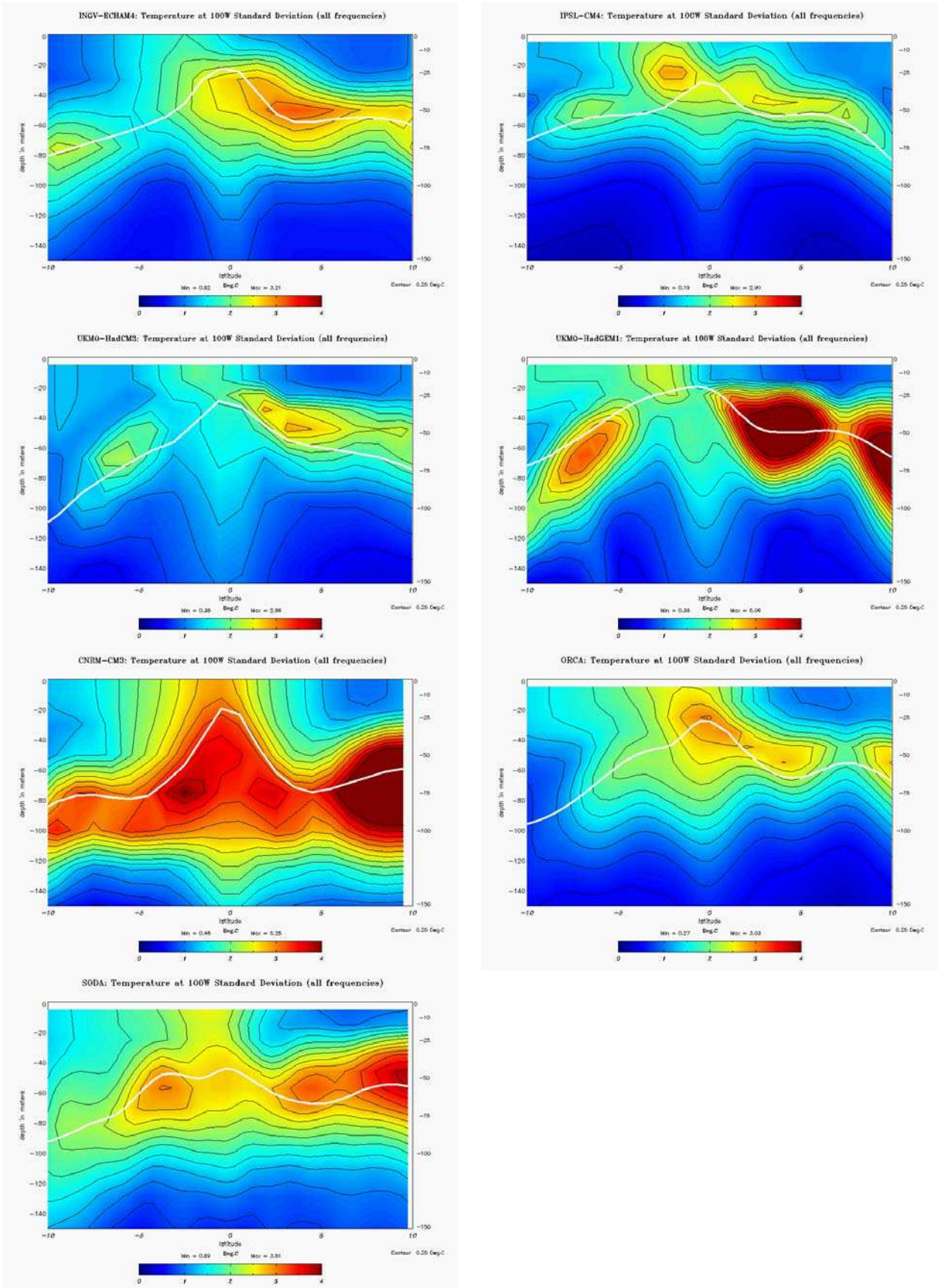

Fig. 2.33. Same as fig.2.28 but for total temperature variability (RMS, °C). Contour interval is 0.25°C. Colour scale is blue-red: 0°C – 4°C.

More precisely, peaks of variability are located where the equatorial thermocline is the most stratified (fig. 2.23), *i.e.* at 10°N around 50-60m depth for UKMO-HadGEM1, CNRM-CM3 and SODA, at 3-4°N around 50-60m depth for all the models (except maybe for CNRM-CM3), and at the equator around 30m for IPSL-CM4 and ORCA. Hybrid CGCMs feature a variability of the same order as that of ORCA and SODA, except UKMO-HadGEM1 that over-estimates variability in the thermocline, just like CNRM-CM3 (fig.2.24).

All the models also exhibit one or several local maxima to the South of the equator, at 5°S around 50-60m for IPSL-CM4, UKMO-HadGEM1, ORCA and SODA, around 70-80m at 10°S for INGV-ECHAM4 and CNRM-CM3, and around 5°S for UKMO-HadCM3 as well as for CNRM-CM3. In addition, one may note that for all the models, the zone of maximum variability covers the surface layer between 0°N and 5°S, close to the SEC (fig. 2.17), equatorial current variability (fig. 2.28) inducing a variability of the temperature near the surface. Note that in the real world, a significant fraction of such variability is due to tropical instability waves (TIW) produced by shears between the SEC, the EUC and the NECC (see chapter one). It is unlikely that the same processes account for eastern equatorial pacific surface temperature variability in the models: indeed, TIWs are associated to periodicities around one month (*e.g.* Vialard et al., 2001), which cannot be assessed with the monthly means.

The spatial correlation coefficient previously introduced for currents allows quantifying the differences between variabilities of model temperature fields (figures 2.26 and 2.27). Such index is quite appropriate because the differences between models are larger than for currents. Particularly, INGV-ECHAM4 presents a distribution of total variability that is well correlated to SODA and to ORCA, whereas UKMO-HadGEM1 and CNRM-CM3 have weaker values (especially when ORCA is taken as a reference).

Annual cycle, interannual and intraseasonal variability

Similarly to the analysis performed on currents, the structure of seasonal, intraseasonal and interannual temperature variations are studied in detail for the model ensemble. For hybrid CGCMs, the signature of large low-frequency modulation of the seasonal cycle is diagnosed, with a rather weak mean cycle (except for UKMO-HadGEM1) and excessive near-annual variability (except for IPSL-CM4), particularly for the UKMO-HadGEM1 model (fig.2.34). It is interesting to note that peaks of seasonal variability correspond to a large extent to those of total variability for these models, which implies that seasonal cycle is the main contributor to temperature variability at the surface and below in the eastern tropical Pacific. The seasonal cycle thereby dominates the

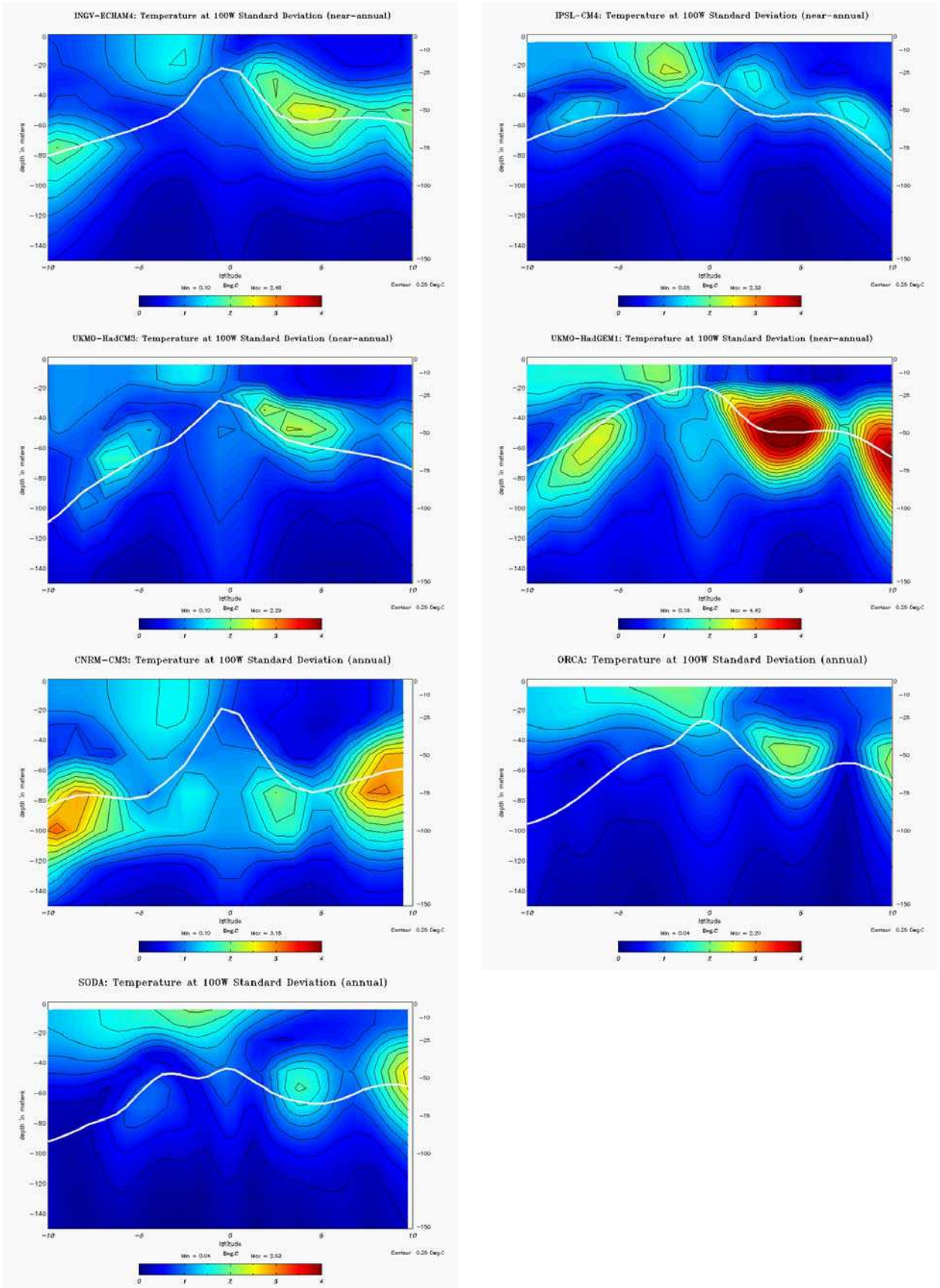

Fig. 2.34. Same as fig.2.33 but for seasonal temperature variability (°C).

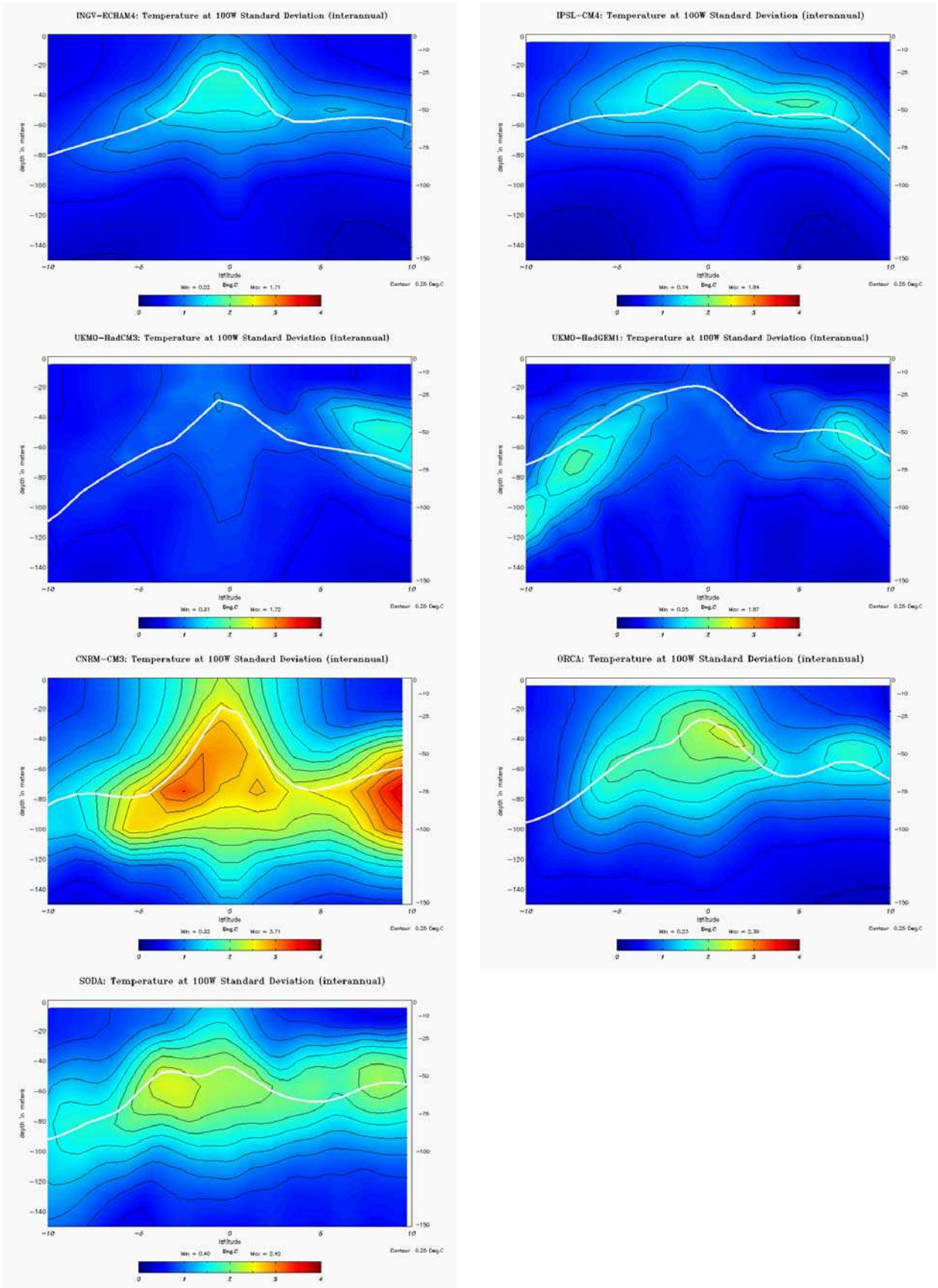

Fig. 2.35. Same as fig.2.34 but for interannual temperature variability (°C).

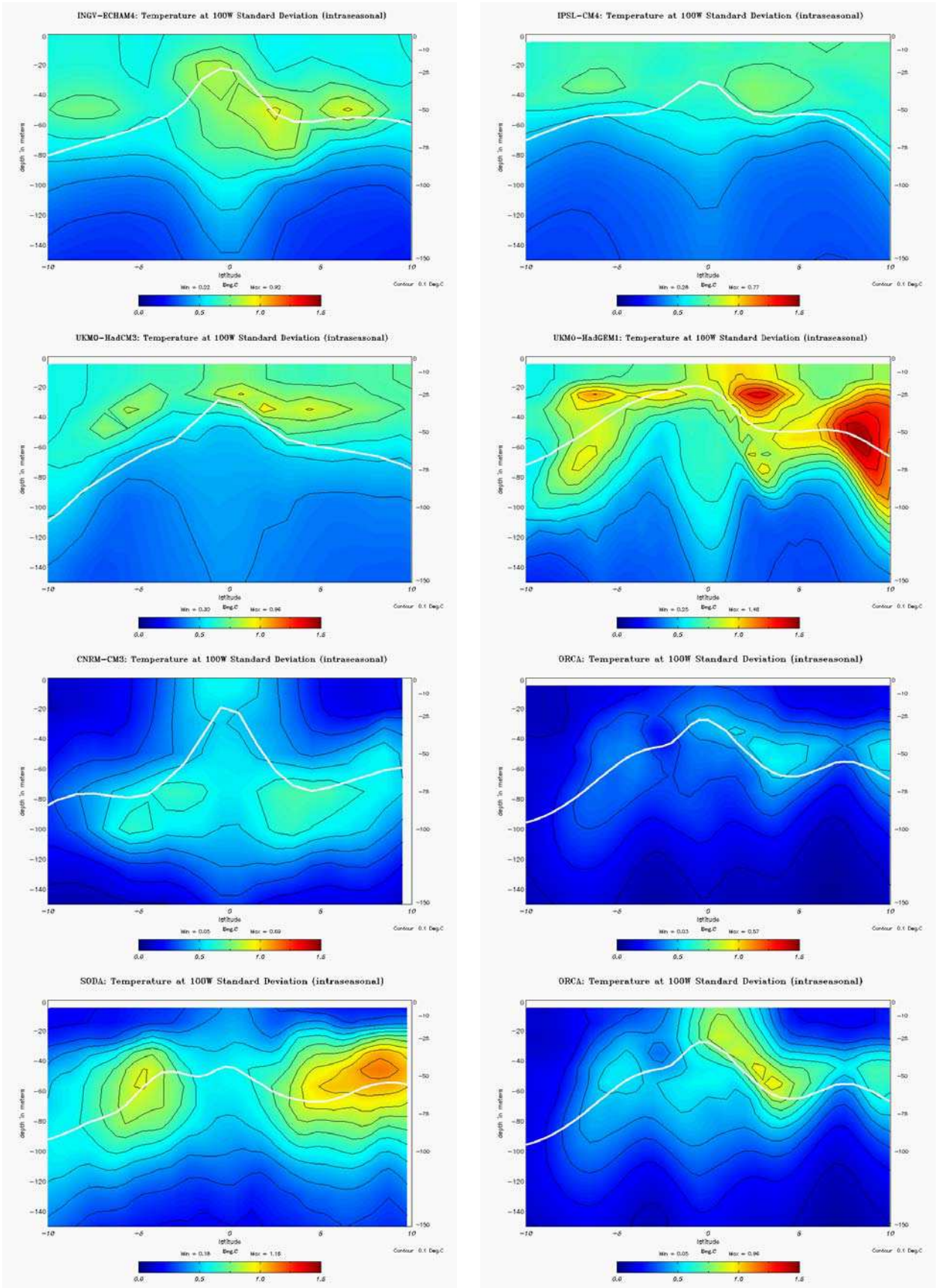

Fig. 2.36. Same as fig.2.32 but for intraseasonal temperature variability (°C). Note the change in colour scale: contour interval is 0.1°C. Colour scale is blue-red: 0°C – 1.5°C.

other modes of variability for these CGCMs, but it is neither the case for the references (SODA and ORCA) nor for CNRM-CM3, which are dominated by interannual variability (figures 2.35 and 2.37). Yet, hybrid CGCMs reproduce almost all the peaks of the annual cycle simulated by SODA and ORCA: near the surface at the equator (with a southward extension), and around the thermocline at 5°N, 10°N and between 5°S and 10°S. For CNRM-CM3, the variability is over-estimated at all frequencies except intraseasonal (fig.2.37) and is too deep, which implies weak spatial correlations with SODA and ORCA (figures 2.38 and 2.39).

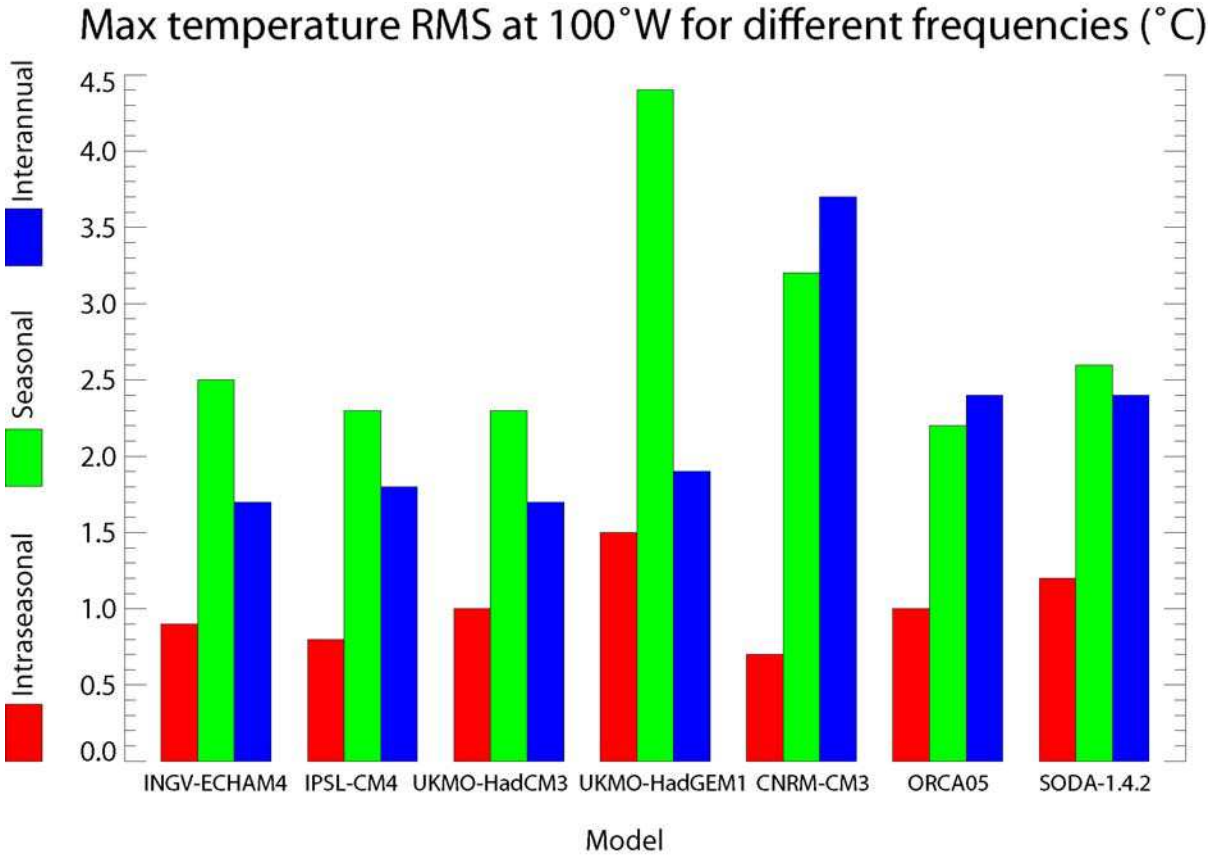

Fig. 2.37. Maxima of seasonal, interannual and intraseasonal temperature variability (°C) at 100°W (between 10°S and 10°N and between 0m and 400m depth) for the GCMs and for SODA-1.4.2.

Similarly to the velocity field, interannual variability of temperature is weak for hybrid CGCMs (figures 2.35 and 2.37). It is largest around 40m depth at the equator with a secondary peak between 5°N and 10°N for INGV-ECHAM4 and IPSL-CM4 as well as for ORCA and SODA, whereas it is absent from the equator for models of the UK Met-Office, though with a lobe around 10°N for UKMO-HadCM3 and an additional lobe for UKMO-HadGEM1 around 5°S-10°S. From the quantitative side, INGV-ECHAM4 is the best correlated CGCM to the chosen references, and UKMO-HadGEM1 is the one that presents the smallest agreement (figures 2.38 and 2.39).

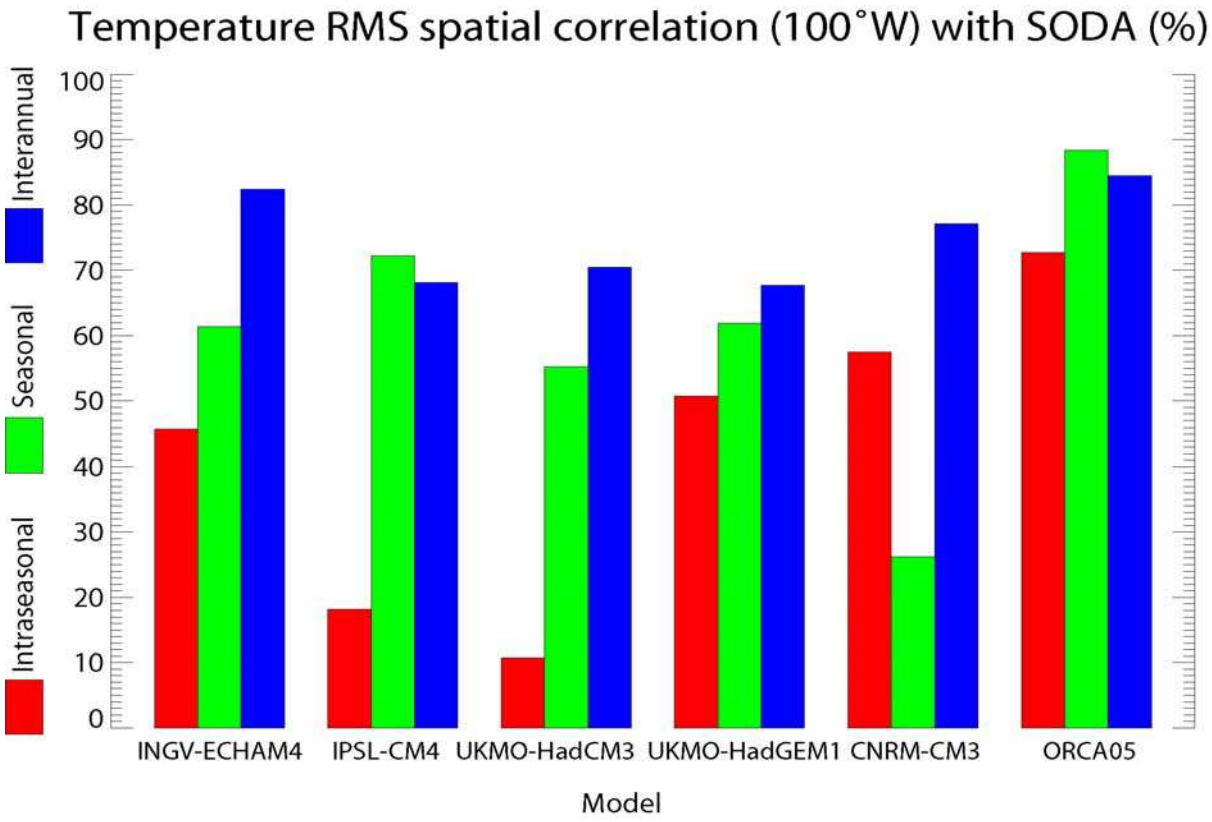

Fig. 2.38. Spatial correlations (%) computed at 100°W (between 10°S et 10°N and between 0m and 400m depth) for seasonal, interannual and intraseasonal temperature variabilities from the different GCMs relatively to SODA-1.4.2.

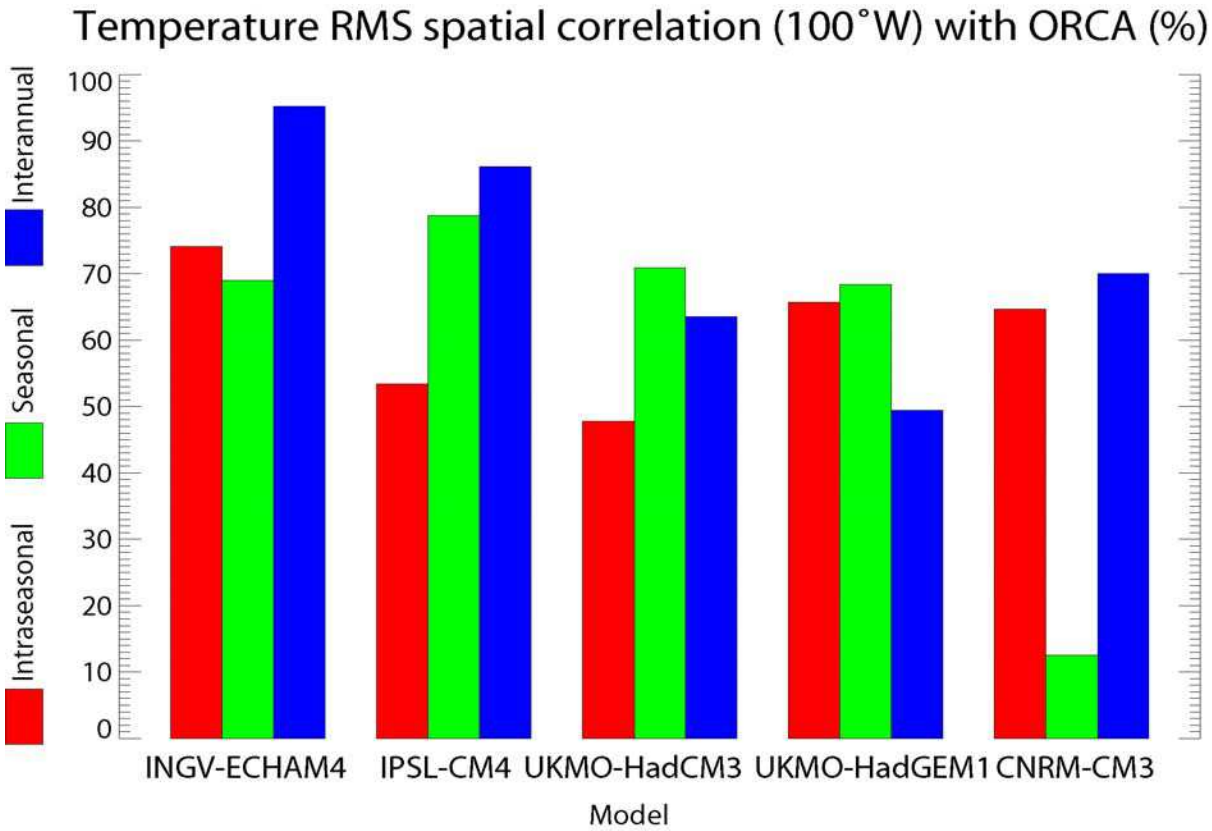

Fig. 2.39. Same as fig.2.38., except relatively to ORCA05 (5-daily outputs).

Last, intraseasonal variability exhibits large differences among the models (fig.2.36). SODA and 5-daily outputs from ORCA are taken as references - here again the impact of the sampling frequency of ORCA outputs on intraseasonal variability is large: 5-daily outputs amplify intraseasonal temperature variability by ~60-70%. Despite large differences between SODA and ORCA, note that the orders of magnitude are similar and maxima are located around the thermocline. Among the CGCMs, INGV-ECHAM4 and UKMO-HadCM3 present the smallest differences with the references in terms of structures and orders of magnitude: both feature an RMS around 1°C near the thermocline, and a strongly damped variability in the deeper layers, especially below the EUC. Intraseasonal variability is weak for IPSL-CM4 and for CNRM-CM3 (and too deep for the latter *i.e.* below the thermocline), whereas it is over-estimated for UKMO-HadGEM1. Because of the differences found between SODA and ORCA, values of spatial correlation are sensitive to the chosen reference. However, IPSL-CM4 and UKMO-HadCM3 show the largest differences with both SODA and ORCA.

To summarize, IPSL-CM4 'best' represents both the mean state and the variability of the temperature field at the western boundary of the regional domain simulated by SODA among the hybrid CGCMs, both qualitatively (*e.g.* presence of equatorial upwelling) and quantitatively (*e.g.* mean temperature in the EUC). INGV-ECHAM4 and UKMO-HadCM3 present slightly larger biases, though their respective patterns and magnitudes of intraseasonal temperature variability are closer to the obervations.

2.3.5. Conclusions

A set of diagnostics was set up in order to evaluate biases of five coupled models of the IPCC-AR4 (INGV-ECHAM4, IPSL-CM4, UKMO-HadCM3, UKMO-HadGEM1 and CNRM-CM3) in terms of mean state and variability at the limits of the regional Peru-Chile domain, with the purpose of selecting the two to three models used to perform regional downscaling of global warming experiments. Such diagnostics mainly focus on the temperature and zonal velocity fields

at the western boundary of the domain (100°W) in the equatorial band (10°S to 10°N), as it is there that the majority of the "oceanic information" provided by global climate models is transmitted to the Peru-Chile area.

In spite of similar characteristics in terms of ENSO processes (Belmadani et al., 2010), results indicate rather heterogeneous behaviour among the models at the western boundary of the regional domain, as might be expected from complex climate models with different physics, parameterizations and resolutions: warm or cold biases, over- or under-estimated seasonal cycles, presence or absence of some equatorial currents (the two branches of the SEC, the SSSCC, the NECC). Some biases are however shared by the whole model ensemble: too weak EUC and SEC, the absence of currents below 150 to 200m depth, an equatorial thermocline about 20 meters too shallow, an excessive stratification in the cold tongue region, an excessive low-frequency modulation of the seasonal cycle (near-annual variability is twice to three times larger than mean seasonal variability), and under-estimated interannual zonal current variability (30-50% of the observed) - with the exception of CNRM-CM3 for the last two statements.

Nevertheless, the analysis allows identifying the models that present the weakest differences with SODA data: UKMO-HadGEM1 is the only CGCM that is able to reproduce most observed features of the equatorial current system, whereas IPSL-CM4 and INGV-ECHAM4 have the weakest biases in terms of temperature (see table 2.8 for a summary). The latter two also simulate currents with some degree of fidelity, whereas UKMO-HadGEM1 exhibits strong biases in the representation of the temperature field. Temperature biases in the EUC and in the SSSCC such as those simulated by UKMO-HadGEM1 may have a strong influence on the regional circulation in the Eastern South Pacific and induce large biases in the regional domain: indeed, colder equatorial temperature than observed is likely to be advected towards the coast and feed the PCUC, as suggested by Croquette (2007) and Montes et al. (2009). PCUC water being a major source for coastal upwelling, temperature biases are likely to be transmitted to the coastal area and then to the offshore region through Ekman transport, thereby influencing the whole temperature structure – and hence the ocean circulation and dynamics – of the eastern South Pacific. On the other hand, a temperature state in the Eastern tropical Pacific such as that simulated by IPSL-CM4 or INGV-ECHAM4 should provide more appropriate boundary conditions, even with a weaker EUC and the absence of secondary pathways for the advection of equatorial waters to the coastal region (such as the Tsuchiya Jets), since the presence of the EUC may still ensure that the equatorial waters will be advected towards the coast. Such hypothesis will have to be tested with different downscaling experiences. For instance, a comparison of regional simulations forced by ORCA and by SODA should document the influence of the mean equatorial currents on the regional circulation off Peru

and Chile. In addition, UKMO-HadGEM1 presents a main drawback in comparison to the other CGCMs: 3D variables (T, S, U, V) are not available on the PCMDI data portal – that distributes IPCC model outputs – for the $4xCO_2$ scenario, and only the transient regime of the $2xCO_2$ scenario is available, whereas our approach requires studying a stabilized regime easily comparable to the preindustrial scenario. For these reasons, we select the IPSL-CM4 and INGV-ECHAM4 models. Being built on the same oceanic model (Madec et al., 1998) but different atmospheric models (respectively LMDZ-4 - Hourdin et al., 2006; and ECHAM4 - Roeckner et al., 1996), the comparison of regional simulations forced by these two models also allows estimating the impact of the atmospheric forcing on the Humboldt Current System, which constitutes an important issue taking into account the fact that coastal upwelling (and equatorial upwelling) dynamics are determined to a large extent by the wind forcing and by the associated Ekman transports and pumpings.

UKMO-HadGEM1 might however be retained as a third CGCM for the downscaling, as UKMO-HadCM3 does not seem to present any particular advantage relatively to the other CGCMs. The CNRM-CM3 model, a typical zonal advective feedback-dominated model with strong biases in the tropical Pacific (Belmadani et al., 2010), also exhibits strong biases in the eastern South Pacific, most of which are absent from hybrid CGCMs. This would tend to confirm the relevance of the categories identified by Belmadani et al. (2010), particularly for our downscaling approach.

A brief assessment of the wind forcing provided by the CGCMs reveals contrasted behaviour over the ESP, and allows explaining part of their oceanic biases. Overall, INGV-ECHAM4 and UKMO-HadGEM1 that feature a higher atmospheric resolution (see table 1 from section 1) tend to simulate more 'realistic' wind forcing over the region than the coarser-resolution IPSL-CM4 and UKMO-HadCM3. However, results from the statistical downscaling of the atmospheric forcing simulated by IPSL-CM4 show that large-scale biases in the mean state can be efficiently corrected, which increases our confidence in the projections inferred from this model (see chapter four). Nevertheless, such procedure does not allow correcting biases in the wind variability, which has been shown to be significant for this model, especially near the coast (up to ~+50% compared to QuickSCAT – see fig.2.10c). In this respect, comparisons with regional simulations performed with INGV-ECHAM4 forcing should provide an estimate of errors in projections of the impact of future global warming on the Humboldt Current system.

Model	T_{mean}	$D20_{eq}$	RMS(T)	U_{mean}	RMS(U)
INGV-ECHAM4	+ surface + subsurface asymmetry - subsurface	+ equatorial upwelling	+ total variability + interannual variability (eq.) - at 10°S	+ spatial agreement	+ meridional scale - seasonal variability
IPSL-CM4	+ surface + EUC temperature	+ $D20_{eq}$ + equatorial upwelling	+ seasonal variability + interannual variability (eq.) - intraseasonal variability	+ westward flow at 10°N	+ meridional scale - no NECC variability - vertical scale - seasonal variability
UKMO-HadCM3	- surface	+ $D20_{eq}$	- intraseasonal variability - seasonal variability		+ seasonal variability - weak EUC variability - meridional scale - intraseasonal variability
UKMO-HadGEM1	- subsurface - EUC temperature - subsurface asymmetry	- equatorial upwelling	+ at 10°N - total variability - seasonal variability (high) - intraseasonal variability (high) - interannual variability	+ SSSCC + SEC: 2 branches + westward flow at 10°N + NECC	+ variability peak + SSSCC + vertical scale + Interannual NECC variability - RMS_{max}/U_{mean} ratio - seasonal variability
CNRM-CM3	- surface - subsurface - EUC temperature - no surface asymmetry	- equatorial upwelling	+ at 10°N + dominant interannual variability - total variability - seasonal variability - intraseasonal variability (deep) - interannual variability (high)	+ EUC speed + spatial agreement	+ meridional scale + interannual variability - displaced maximum - no NECC variability - vertical scale - seasonal variability

Table 2.8. Summary of the simulated circulation characteristics and "skill" in the CGCM. Plus marks (+) indicate features from SODA and/or ORCA that are well reproduced, minus marks (-) indicate significant biases relative to these references.

Chapter 3: Regional dynamics and large scale forcing of the Humboldt Current System

In the previous chapter, we detailed the different steps that were followed for the purpose of selecting the « best » global climate models for the study of climate change in the HCS. Based on CGCM skill in reproducing dynamical processes and spatio-temporal characteristics of basin-scale ENSO variability, temperature and current mean state and variability in the eastern tropical Pacific, and to some extent, dynamics of the atmospheric forcing in the eastern South Pacific, two models were identified: IPSL-CM4 and INGV-ECHAM4. The next step consists in using these models under preindustrial climate and CO_2 quadrupling as boundary conditions for a high-resolution regional ocean model configuration of the HCS. Such method allows taking into account the large-scale variability and atmospheric forcing simulated by CGCMs for a warmer climate, and describing accurately regional ocean dynamics including mesoscale features, both at the same time. Indeed, CGCMs are currently the most reliable tools for the prediction and study of future climate change, but their spatial resolution is too coarse to provide any information readily usable for the assessment of future impacts on the HCS. On the other hand, regional modelling is an efficient tool for the study of ocean dynamics at the regional scale, but it needs an accurate/appropriate boundary forcing in order to provide a reliable/realistic description of regional ocean circulation. The downscaling approach provides the regional model with boundary conditions that take large-scale changes induced by global warming into account, in order to infer smaller-scale changes in the HCS.

The comparison of two simulations performed with the outputs of a given CGCM as boundaries conditions for the regional model, but with different GHG atmospheric concentrations (*ie* preindustrial and $4xCO_2$) provides a picture of regional-scale climate change as predicted from that CGCM. However, and as discussed earlier, even the « best » CGCMs still feature a number of biases in their representation of present and past oceanic and atmospheric dynamics. Thus repeating regional climate change experiments with boundary forcings derived from several of these « best » CGCMs is a way to measure the uncertainty related to regional climate projections in the HCS. Nevertheless, the regional model needs to provide realistic simulations under preindustrial climate. A regional control run performed

with realistic open boundary conditions (OBCs) and surface forcing over the recent period is used as a reference for present-day regional ocean circulation in the HCS, so as to estimate our confidence in the projected regional climate changes derived from the different CGCM forcings.

The present chapter is organized as follows: first, a presentation of the regional ocean model is given, together with a brief synthesis of previous modelling efforts for the HCS region. Second, the regional control simulation is used to investigate the link between coastal and equatorial intraseasonal sea level and current variability, through the propagation of equatorial Kelvin waves, extra-tropical Rossby waves and coastal-trapped waves. Such study is to be submitted before the end of 2009 to the *Journal of Geophysical Research*, after a few additional diagnostics are carried out (see chapter 4)..A transcription of this article in preparation is provided in this chapter. Note that it includes a section on the validation of the simulation performed with ROMS. Note also that the results from regional climate change experiments are presented in the next and last chapter.

3.1. Regional ocean modelling of the Humboldt Current System

Most studies focusing on the regional dynamics of the Humboldt Current System have relied on satellite and/or in situ observations (see chapter 1, section 1.2), sometimes combined with the use of simple linear wave models (*e.g.* Shaffer et al., 1997; Pizarro et al., 2001). However, only a few authors have privileged the approach of tridimensional modelling of the eastern South Pacific. Medium-resolution OGCMs have been used recently to study Kelvin wave and planetary wave propagation (Dewitte et al., 2008; Ramos et al., 2008). Though these approaches have proven to be successful for simulating several aspects of the circulation and variability in the region, the model spatial resolution (about 1/3° to 1/4°) is too low to allow representing correctly mesoscale and submesoscale features. In addition, these models are generally based on vertical z-coordinates (constant-depth vertical levels), which are known to produce unrealistic velocity fields near the slopes and over shelves: it is obviously a problem in EBUS'es as most processes related to coastal upwelling and subsurface poleward flow are located near the continental shelf and slope. In the recent years, higher-resolution regional models such as the ROMS (Regional Ocean Modelling System) model (Shchepetkin and McWilliams, 2005) have started to be extensively used over many regions of the world ocean, including EBUS regions (*e.g.* Di Lorenzo et al., 2005; Penven et al., 2001). One of the main advantages of ROMS is the use of sigma-coordinates on the vertical (see below). A regional configuration in the HCS region was first developed by Penven et al. (2005) for the Peru region (90°W-70°W, 20°S-3°N) at 1/9° resolution to study the mean circulation, seasonal cycle, and mesoscale dynamics. It is a reference for regional ocean modelling in the region of interest here. This configuration and slightly modified versions have been used to study the connection between equatorial currents and coastal currents (Montes et al., 2009), and to force biogeochemical and individual-based-models focusing on the northern HCS (Echevin et al., 2008; Lett et al., 2007; Brochier et al., 2008). A few studies including the present thesis have then proposed meridionally extended configurations that include the ocean off Chile (Croquette, 2007; Colas et al., 2008; Combes et al., 2009). On the other hand, regional coupled ocean-atmosphere models have recently started to emerge. In the framework of the VOCALS project (see chapter 1, section 1.2), Xie et al. (2007) have developed a regional configuration of the eastern tropical Pacific, which extends from 30°N to 30°S and has been successful to reproduce some aspects of the regional climate system, including the structure and variability of the ITCZ and the presence of the stratocumulus cloud deck.

However, they use a ½° ocean resolution, which is too low to resolve the mesoscale ocean circulation.

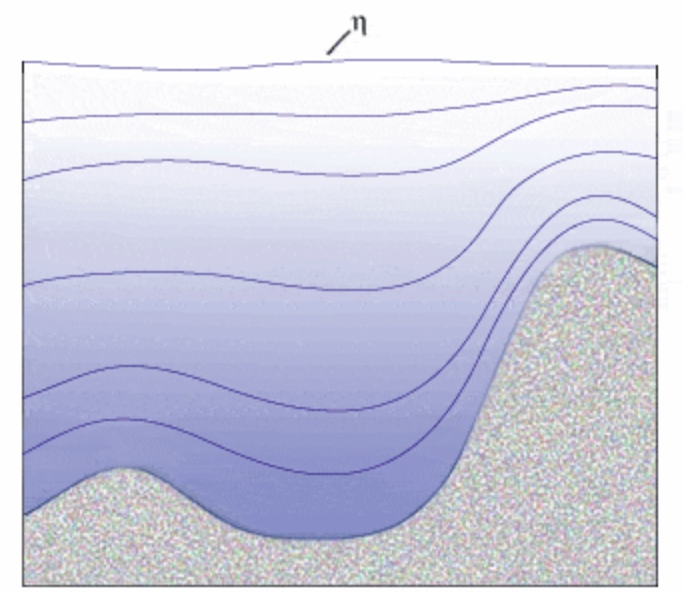

Fig. 3.1: Schematic of terrain-following sigma vertical coordinates. η is for the free surface elevation. The number of sigma-levels is fixed over the domain. The vertical resolution is higher near the surface and near the bottom.

The regional ocean circulation model used here is ROMS. ROMS solves the hydrostatic primitive equations with a free-surface explicit scheme. Baroclinic and barotropic components are computed separately, with a shorter time step for the former. The equations are discretized over a tridimensional Arakawa-C grid with curvilinear horizontal coordinates and stretched, terrain-following sigma coordinates (fig. 3.1) on 32 vertical levels. The main advantage of sigma coordinates compared to, say, z-coordinates, is the increased vertical resolution in shallow water areas such as the continental shelf and the coastal zone, which is of great interest for the modelling of coastal upwelling processes. However, their main drawback is the emergence of spurious flow in areas of sharp changes in topography due to errors in the pressure gradient induced by the terrain-following coordinates. In order to reduce such errors, bottom topography from ETOPO2 (Smith and Sandwell, 1997) has been smoothed as in Penven et al. (2005) after being interpolated onto the model grid. A third order upstream biased advection scheme allows considering diffusion implicitly and limiting dispersion (Shchepetkin and McWilliams, 1998). Subgrid-scale vertical mixing is parameterized using the KPP boundary layer scheme (Large et al., 1994).

ROMS is used here at an eddy-resolving resolution (1/6° at the equator) over the eastern South Pacific in a domain covering 15°N to 40°S, and 70°W to 100°W, with lateral open boundaries on its northern, western and southern edges (fig. 3.2). Compared to

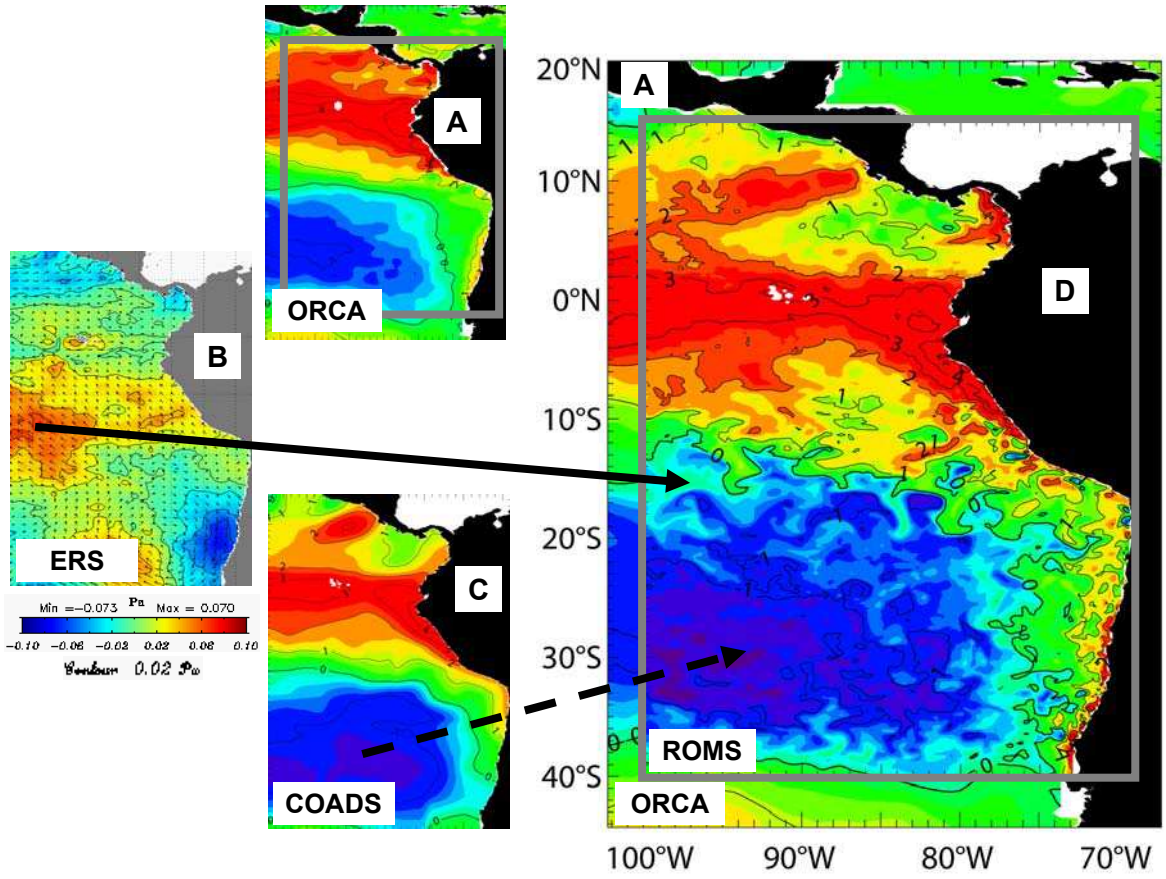

Fig. 3.2: Schematic of the downscaling and forcing strategy: (**A**) OBCs from the ORCA global model; (**B**) surface wind forcing from ERS1-2 satellite data; (**C**) atmospheric fluxes from ERA-40 reanalysis and COADS observed data; (**D**) ROMS simulation. The grey rectangle is for the regional domain. The black plain (resp. dashed) arrow represents the wind forcing (resp. atmospheric forcing and restoring to COADS SST and SSS). Maps are for SST (A, C, D) and surface wind (B) anomalies during the peak phase of El Niño (15th February 1998). Contour values for SST anomalies (°C) are indicated on the corresponding maps (CI: 1°C). The colour bar for wind anomalies (Pa) is indicated below the corresponding panel (CI: 0.02 Pa). The size (resp. direction) of the arrows on (B) is for the magnitude (resp. direction) of the wind anomalies.

Penven et al. (2005), the resolution is lower, but the domain is also wider: the choice of model resolution is a compromise between the representation of fine scale structures and extensive computational costs. Bottom topography has been modified near the open boundaries (figure 1 from the next section) to match with that from the lower-resolution 1/2° ORCA05 model (Madec et al., 1998). Oceanic outputs from the latter provide the OBCs and initial conditions for temperature, salinity, horizontal velocities and sea level every 5 days over 1992-2000 (fig. 3.2). Despite the relatively short length of simulation (9 years), this time period presents the advantage of spanning contrasted basin-scale climate conditions, including the strong 1997-98 El Niño event and the 1998-99 La Niña event. In addition, a large choice of satellite and in-situ data are available for this period, such as AVISO merged satellite altimetric data (Le Traon et al., 1998) and TAO array observations (*e.g.* McPhaden et al., 1998) for instance, which can be used to validate some aspects of the regional model and the boundary forcing.

OBCs were processed with a combination of an Orlanski scheme for temperature, salinity and baroclinic velocities and a Flather scheme for sea surface elevation and barotropic velocities (Marchesiello et al., 2001). To force the model at the free surface, wind stress from the ERS1-2 satellite scatterometer measurements (50km resolution – Bentamy et al., 1996) and fluxes (heat, freshwater, solar shortwave radiation) from the European Center for Medium Range Forecasts (ECMWF) ERA-40 global atmospheric reanalysis (1.25° resolution - Uppala et al., 2005) were averaged on a 5-daily basis (fig. 3.2). Heat and water fluxes include a restoring term to COADS 0.5° monthly climatological SST and SSS fields (Da Silva et al., 2004) (fig. 3.2). Bottom topography, atmospheric forcing, initial and boundary conditions were linearly interpolated onto the model grid using the ROMSTOOLS software (Penven et al., 2008). A 2-year spin-up was performed with climatological values derived from the forcing and from the boundary conditions, after which model outputs were saved every 5 days from 1st January 1992 onwards. The simulation was conducted on a cluster of PCs (over 2 nodes with 8 processors each) at CIMOBP, the numerical modelling center of IMARPE in Callao, Peru.

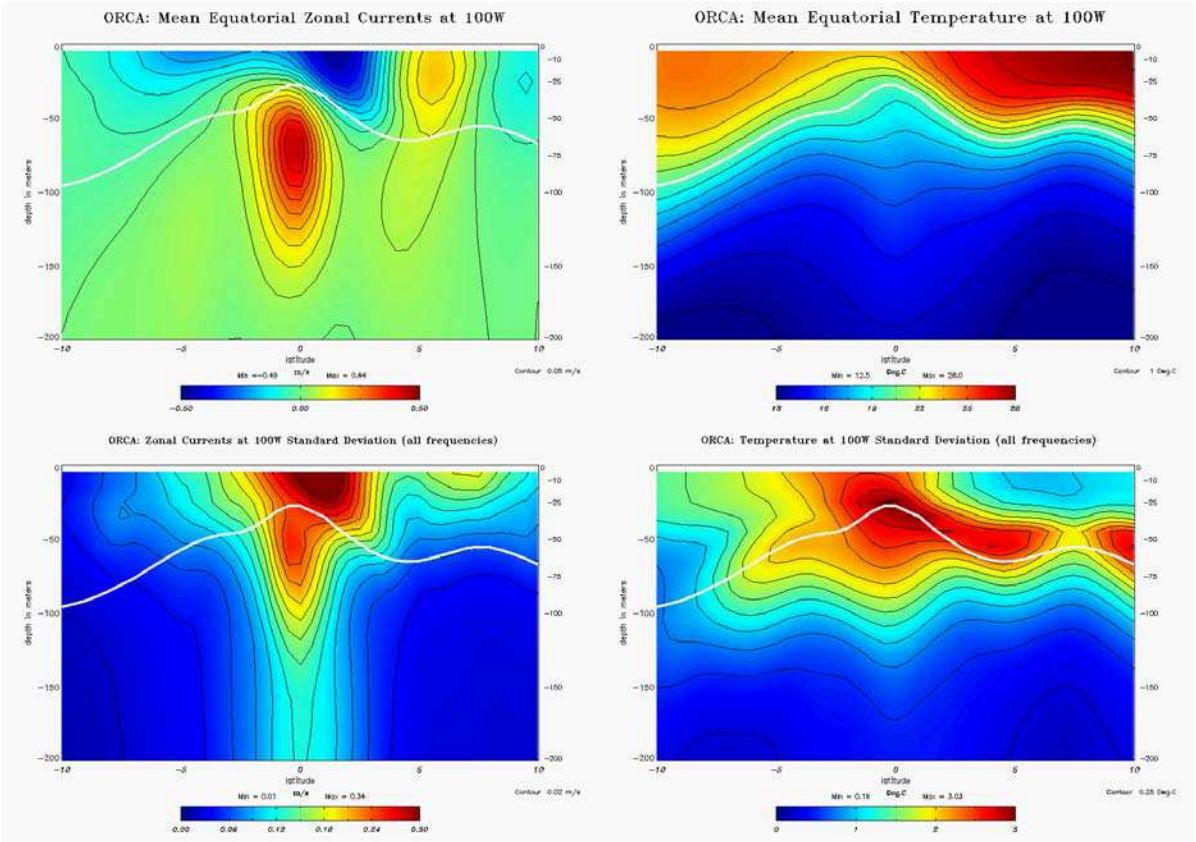

Fig. 3.3: Vertical sections at 100°W (10°N-10°S, 0-200m) of (from left to right and top to bottom) the mean zonal currents (m/s), the mean temperature (°C), zonal current variability (RMS) and temperature variability (RMS) for ORCA05. Mean 20°C isotherm depth is also indicated (bold white line). Contour intervals are 5 cm/s, 1°C, 2 cm/s, and 0.25°C, respectively. Colour scales (blue-red) are (-50cm/s – 50cm/s), (13°C – 28°C), (0cm/s – 30cm/s), and (0°C – 3°C), respectively.

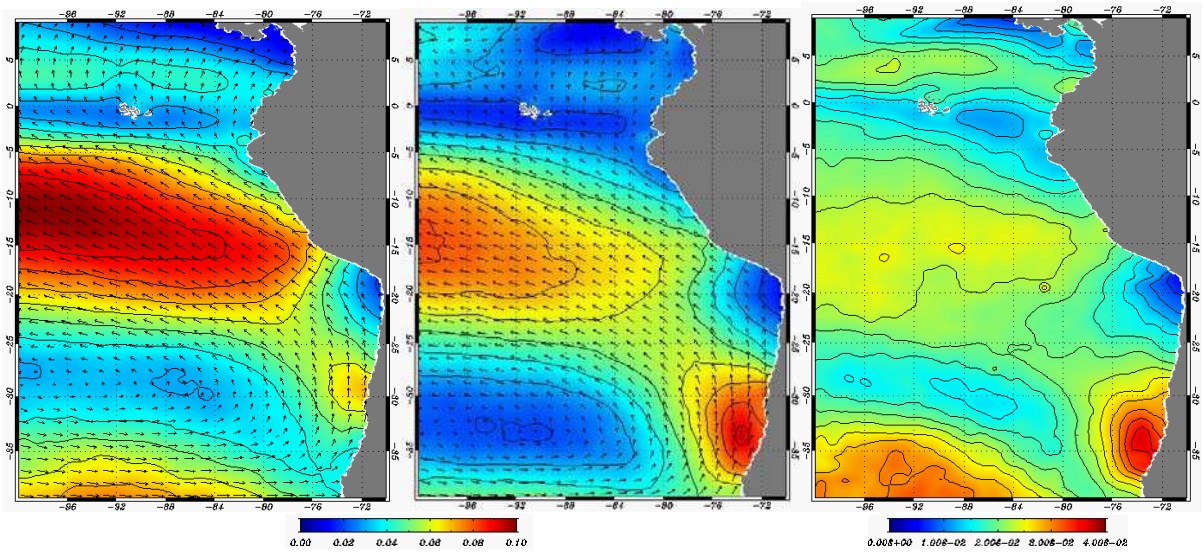

Fig. 3.4: Surface wind stress (Pa) over the ESP from ERS satellite observations: climatological mean surface wind stress in **(**left**)** austral winter (April to September) and **(**middle**)** austral summer (October to March); **(**right**)** surface wind stress variability (RMS). The colour bar for mean wind stress (resp. wind stress variability) is indicated on the left (resp. right). The size (resp. direction) of the arrows (left and middle panels) is for the magnitude (resp. direction) of the wind stress.

As seen in chapter two, open boundary conditions near the equator and surface atmospheric forcing are the main sources of large-scale variability that is transmitted to the regional model:

- warm equatorial waters from ORCA are advected from the western boundary by the EUC under the surface and by the NECC in the surface layer, which exhibit significant variability (fig. 3.3);

- equatorial temperature variability simulated by ORCA is highest in the vicinity of the thermocline and South of the equatorial front, which separes warm waters of the eastern equatorial Pacific warm pool to the North from cooler waters of the eastern equatorial Pacific cold tongue to the South (fig. 3.3);

- the latter are associated to both equatorial upwelling and the westward advection of cold waters by the SEC (fig. 3.3);

- surface winds from ERS data exhibit significant seasonal variability associated with the southward (resp. northward) migration of the subtropical high in summer (resp. winter) (fig. 3.4);

- coastal jet areas are associated to local maxima of wind variability near the coast of central Chile (~35°S) and of central Peru (~15°S) to a smaller extent (fig. 3.4).

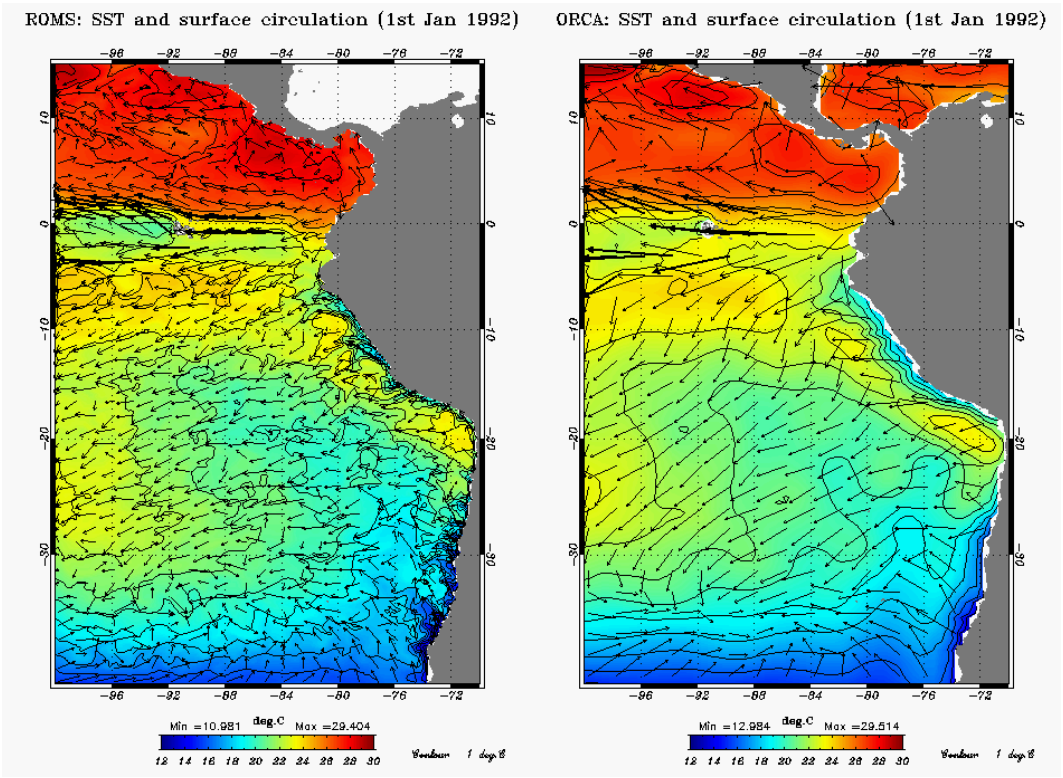

Fig. 3.5: SST (°C) and surface circulation (m/s) over the ESP for 1st January 1992 as simulated by ROMS (left) and ORCA (right). Contour interval is 1°C. The size (resp. direction) of the arrows (left and middle panels) is for the magnitude (resp. direction) of the surface currents.

The simulation performed with ROMS allows reproducing most aspects of the circulation and temperature state simulated by the parent ORCA model in the ESP. As an illustration, SST and surface currents from ROMS and ORCA are compared for 1st January 1992 (fig. 3.5): both models provide a similar description of the regional circulation, including for instance the wind-driven anticlockwise circulation in the offshore region, offshore Ekman transport near the coast associated to coastal upwelling, the westward SEC and its splitting near the Galapagos, and the presence of the equatorial front. However, the higher resolution in the ROMS model allows accounting for smaller-scale processes, which can be seen in the more complex surface circulation pattern and in the fine scale features of the SST field. In particular, ROMS is able to represent more accurately the upwelling front near the coast, characterized by the presence of meanders and filaments. Upwelling is also stronger in the ROMS simulation, which tends to cool the SST at the regional scale. The resolution of mesoscale circulation and of the associated variability in ROMS induces a stronger amplitude of SST variability over the region compared to ORCA, despite a similar spatial distribution (fig. 3.6).

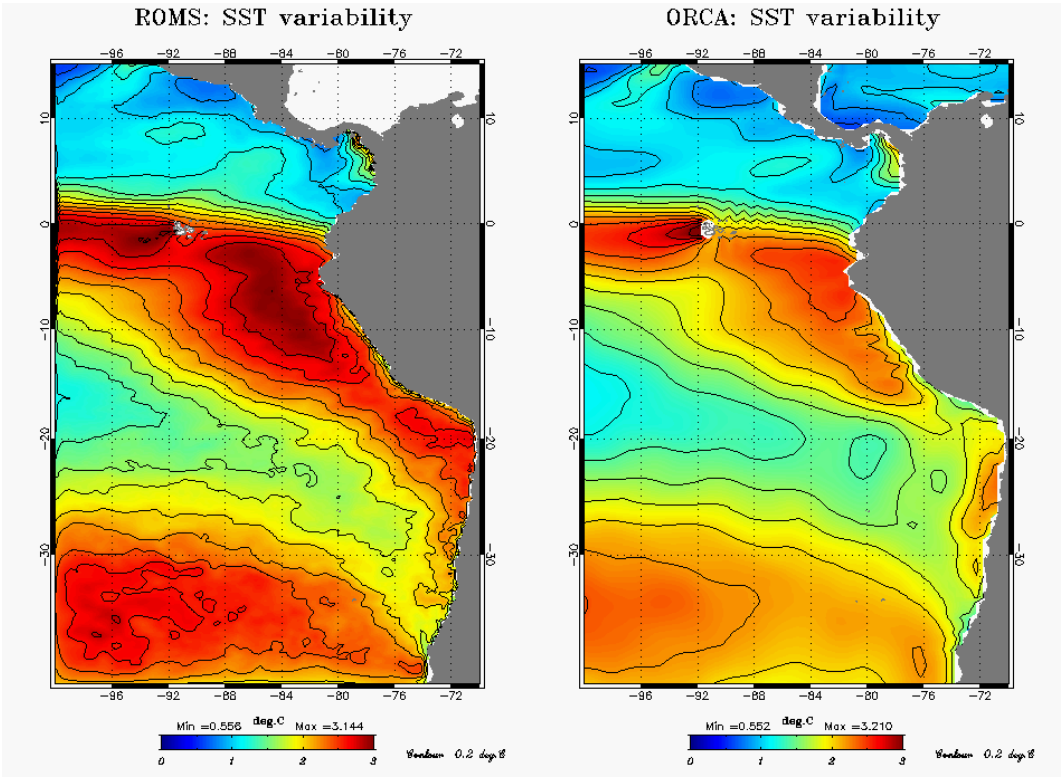

Fig. 3.6: SST (°C) variability (RMS) over the ESP simulated by ROMS (left) and ORCA (right). Contour interval is 0.2°C.

3.2. The intraseasonal coastal-trapped and Rossby waves in the Humboldt system: where does the critical latitude stand?

3.2.1 Introduction and Background

3.2.1.1. Introduction

The Humboldt Current System (HCS), also known as the Peru-Chile coastal upwelling, is the Eastern Boundary Upwelling System (EBUS) of the South Pacific Ocean. Persistent alongshore trade winds blowing off the west coast of South America drive strong coastal upwelling of cold, nutrient-rich waters (Strub et al., 1998) that sustain high biological productivity (Chavez, 1995) together with the most productive marine ecosystem in the world ocean (Chavez et al., 2008; F.A.O., 2009).

A singularity of the HCS compared to other EBUS's is its proximity to the equator. The connection between equatorial currents and the HCS (McCreary, 1981; Lukas, 1986; Kessler, 2006; Montes et al., 2009) and the coastline that behaves as an extension of the equatorial wave guide make the HCS very sensitive to equatorial variability, at time scales ranging from intraseasonal (Brink, 1982; Enfield, 1987; Spillane et al., 1987; Shaffer et al., 1997; Hormazabal et al., 2002; Camayo and Campos, 2006) and seasonal (Pizarro et al., 2002; Dewitte et al., 2008a) to interannual (Pizarro et al., 2001, 2002; Vega et al., 2003; Ramos et al., 2008) and decadal (Montecinos et al., 2007).

Under such a highly variable environment, the marine ecosystem undergoes drastic changes, especially during the occurrence of an El Niño event (Barber and Chavez, 1983). At decadal time scales, stocks of pelagic fish such as sardines and anchovies display strong fluctuations in relation to the low-frequency modulation of ENSO: for instance, the mid-1970s climate shift of the tropical Pacific caused the sardine stocks to collapse, which were replaced by anchovies (Chavez et al., 2003). In this context, a clear picture of how equatorial Pacific variability is transmitted to the coastal regions off Peru and Chile appears to be a key issue for the sustainable management of fisheries (Bertrand et al., 2008), which is of primary importance because of its social and economical consequences.

Here the focus is on intraseasonal oscillations: as demonstrated by Clarke and Shi (1991) (hereafter CS91), frequencies around 50 to 80 days are the most efficiently trapped along the South American coast. These frequencies are typical of Intraseasonal Equatorial Kelvin Waves (IEKW) travelling from West to East across the Pacific Ocean and forced by Westerly Wind Bursts (WWB) blowing over the western Pacific warm pool (McPhaden,

1993; Kessler and McPhaden, 1995; Kessler et al., 1995; Dewitte et al., 2008b). Such WWB have been shown to originate mainly from the global scale Madden-Julian Oscillation (MJO; Madden and Julian, 1971, 1972), though pairs of cross-equatorial cyclones are thought to play a role as well (Keen, 1982). The MJO, which is associated to frequencies ranging from 30 to 90 days, is able to trigger WWB over areas of warm surface waters where deep convection is enhanced, such as the far western Pacific.

At all frequencies, a part of the wave energy transmitted along the equator by Equatorial Kelvin Waves (EKW) is reflected at the eastern boundary of the basin as Equatorial Rossby Waves (ERW) and Extra-Tropical Rossby Waves (ETRW), whereas the rest is trapped at the coast in the form of Coastal-Trapped Waves (CTW). For a Kelvin wave oscillating at a given frequency, there exists a critical latitude for each baroclinic mode that determines whether free wave motion is trapped or reflected: reflection occurs equatorward of that latitude, whereas unforced motion is trapped poleward of it (Clarke, 1983; Grimshaw and Allen, 1988; CS91). The higher the frequency and/or the higher the vertical mode, the lower the critical latitude.

According to CS91, for 50- to 80-day IEKW, the critical latitude ranges from 7 to 10°S for the first baroclinic mode. This implies that IEKW at such frequencies are likely to trigger first baroclinic mode CTW propagating along most of the South American coast from northern Peru (around 7-10°S) down to central Chile. The journey is even longer for the higher order vertical mode CTW, as the corresponding critical latitudes are closer to the equator than for the gravest ocean mode.

Such waves are capable of perturbing significantly local and regional hydrography and currents (Shaffer et al., 1997; Hormazabal et al., 2002, 2006). For instance, Shaffer et al. (1997) used observed sea level, CTD and current meter data as well as a simple CTW model (Brink, 1982; Brink and Chapman, 1987) to investigate the influence of remotely forced intraseasonal CTW on the poleward Peru-Chile Under-Current (PCUC – Strub et al., 1998) at 30°S off Chile. Their results show that 50-day fluctuations of velocities in the core of the PCUC were poorly correlated to both the local winds and currents observed 140 km farther offshore but strongly related to WWB blowing thousands of kilometres away in the western tropical Pacific and to sea level variations along the South American coast. The PCUC constitutes a main source for waters upwelled near the coast (Strub et al., 1998): intraseasonal downwelling and upwelling CTW are therefore likely to modulate temperature and nutrient content of the upwelled waters and thereby have a strong influence on marine primary production and the pelagic ecosystem.

In addition, by perturbating the poleward flow, the 50-day CTW might be capable of strongly modifying vertical shears between the PCUC and the equatorward surface jet, the Chile-Peru Coastal Current (CPCC – Strub et al., 1998). These modifications are likely to enhance baroclinic instabilities and thereby the generation of mesoscale eddies (Pedlosky, 1987) which are common along these coasts (Penven et al., 2005; Chaigneau et al., 2008). A possible modulation of the mesoscale activity by CTW could have important physical and biological consequences: eddies are known to participate to the transfer of mass and heat from the coastal region to the open ocean, and they also play a key role in the dynamics of fish early life stages and reproduction patterns (Logerwell et al., 2001; Lett et al., 2007; Brochier et al., 2008).

50-day EKW excited by the WWB being more frequent and energetic during austral spring and summer and during the onset of an El Niño event (Kessler et al., 1995), a significant fraction of the seasonal variations and interannual modulation of coastal upwelling and mesoscale activity might be related to the planetary scale MJO and to other sources of intraseasonal atmospheric variability over the western tropical Pacific. In addition, the MJO is modulated at decadal time scales and is more active since the 1970s climate shift due to increased warming of the Indo-Pacific region (Slingo et al., 1999), which may be related to global warming (Fedorov et al., 2006; Hansen et al., 2006; Vecchi et al., 2006, 2008). Such low-frequency modulation has also been diagnosed in IEKW activity (Dewitte et al., 2008b): a detailed study of the impact of IEKW on coastal upwelling and mesoscale eddy activity might therefore provide some clues to anticipate the possible response of the HCS to global warming.

3.2.1.2. Limits of the linear theory

As underlined by CS91, the critical latitude is higher for low frequencies because Kelvin waves propagating poleward along a meridional or nonmeridional boundary with constant phase speeds are associated to greater alongshore water particle displacements:

$v = -i\omega\Delta s(t)$ (1), with $\Delta y(t) = \Delta s(t)\sin\theta$

where v is for alongshore velocity, ω is for the frequency of wave motion, $\Delta s(t)$ (resp. $\Delta y(t)$) is for alongshore (resp. northward) particle displacement as a function of time, and θ is for the coastline angle relatively to the East direction.

This induces greater planetary vorticity $\beta\Delta y(t)$, which controls the phase speed of Rossby waves (Pedlosky, 1987) and is normally negligible for Kelvin-like motions. Planetary

vorticity is linked to relative vorticity $\frac{\partial v}{\partial n}$ and to vortex stretching $-\frac{f}{c_n^{\,2}} p$ through the vorticity equation:

$$\frac{\partial v}{\partial n} + \beta \Delta y - \frac{f}{c_n^{\,2}} p = 0 \qquad (2), \qquad \text{with } n \sin\theta = x$$

$$\beta = \frac{2\Omega \cos(\phi)}{R}$$

$$\text{and } f = 2\Omega \sin(\phi)$$

where n is for cross-shore distance landward from the coast, x is for longitude (positive eastward), c_n is for phase speed of the n^{th} baroclinic mode, p is for pressure divided by the mean water density, Ω is for earth rotation rate, R is for earth radius, and Φ is for latitude.

At a given latitude, planetary vorticity becomes high enough for frequencies low enough to overcome relative vorticity, provoking the radiation of Rossby waves. Planetary vorticity being proportional to β, it becomes increasingly lower with higher latitudes for a given frequency: when the critical latitude is reached, it starts to be overcome by relative vorticity and wave motion is trapped near the coast. The vertical structure of Kelvin waves is also crucial in that higher order baroclinic modes travelling along the coast at lower speeds are trapped at lower latitudes because the generation of relative vorticity by vortex stretching being inversely proportional to c_n^2, relative vorticity is greater compared to planetary vorticity: for a given latitude, the frequency threshold necessary for planetary vorticity to take over is lower. Likewise, for a given frequency, the latitude threshold is higher.

However, CS91 make a strong assumption in their theory: they suppose that the bottom is flat near the ocean boundary. Although this is relatively true a few degrees offshore along most of Peru and Chile's coastline where high depths are reached, the cross-shore gradient of bottom topography is large inside the Rossby radii of deformation (figures 3.7, 3.8 and 3.22), which limits significantly the validity of such assumption. As a result, the varying topography is likely to have a direct effect on stratification and thus on baroclinic modes and their phase speeds (Killworth and Blundell, 1999). Irregularities of the bottom can also result in scattering of the baroclinic modes *i.e.* the transfer of energy between the different modes (Johnson, 1991). In addition, bottom friction over the continental shelf and slope may reduce alongshore velocities associated to the CTW, especially for the higher-order modes. This means that alongshore particle displacements are likely to be affected, which should have a direct effect on the relative strength of the terms of the vorticity equation, and consequently on the critical latitude.

In fact, linear theory describes the behaviour of idealized coastal Kelvin waves (CKW) rather than CTW that characterize coastlines in the real world, in particular that of Peru and Chile. One can then wonder to which extent can linear theory formalised by CS91 be applied in this region so as to understand the propagating variability associated to intraseasonal frequencies? Are there any non-linear processes likely to affect CTW propagation, and if so, what are their potential effects on the critical latitude?

In addition, to our knowledge, so far no study has been conducted on the impact of CTW on coastal currents of the HCS at other locations than at 30°S. In spite of the important findings that were brought to the scientific community thanks to the current meters off Chile (Shaffer et al., 1997; Hormazabal et al., 2002, 2006), there still lacks a clear picture of the influence of intraseasonal CTW propagation along the coasts of Peru and Chile on the nearshore currents.

High-resolution numerical modelling can offer the opportunity to document such issues. Here we use a regional model configuration of the eastern South Pacific forced by an Ocean General Circulation Model (OGCM) to explore the behaviour of intraseasonal CTW propagating over a varying topography, assess possible differences with results predicted from linear theory, and study the influence of CTW on nearshore currents of the HCS all along the coast from the equator to 40°S. Space-time spectral analysis (Hayashi, 1979, 1982) is used to derive IEKW, CTW and ERW propagation characteristics, namely direction, wavelength and frequency. A vertical mode decomposition of the model variability is used in order to interprete the simulated variability within the linear formalism and compare our results with those predicted from theory as proposed by CS91. An analysis based on EOFs of alongshore currents is conducted so as to characterize the cross-shore structure of CTW. Finally, a nondimensional parameter which measures the relative importance of stratification vs. bottom depth on CTW propagation is compared for the regional (ROMS) and global (ORCA) models and helps assessing differences in propagating characteristics exhibited by these two models.

In section 2, the regional model and the global model are presented, together with the observed data used for model validation. The methods mentioned above are also described in this section. Modelling results from the regional model are presented in section 3. Differences between CTW and CKW propagations are discussed in section 4 by comparing results from the regional model to those from the lower resolution OGCM. Section 5 is a discussion followed by concluding remarks.

3.2.2. Models, observations and methods

3.2.2.1. Numerical models

ROMS

The ROMS (Regional Ocean Modelling System) regional ocean circulation model (Shchepetkin and McWilliams, 2005) is used at an eddy-resolving resolution (1/6° at the equator) in a study region extending from 15°N to 40°S, and from the coast to 100°W, with lateral open boundaries on its northern, western and southern sides. ROMS solves the hydrostatic primitive equations with a free-surface explicit scheme, and stretched, terrain-following sigma coordinates on 32 vertical levels. Subgrid-scale vertical mixing is parameterized using the KPP boundary layer scheme (Large et al., 1994). Bottom topography from ETOPO2 (Smith and Sandwell, 1997) has been interpolated onto the model grid, smoothed as in Penven et al. (2005) in order to reduce pressure gradient errors and modified at the open boundaries (fig. 3.7) to match with bottom topography from the ORCA05 model (1/2° resolution - Madec et al., 1998; Barnier et al., 2006).

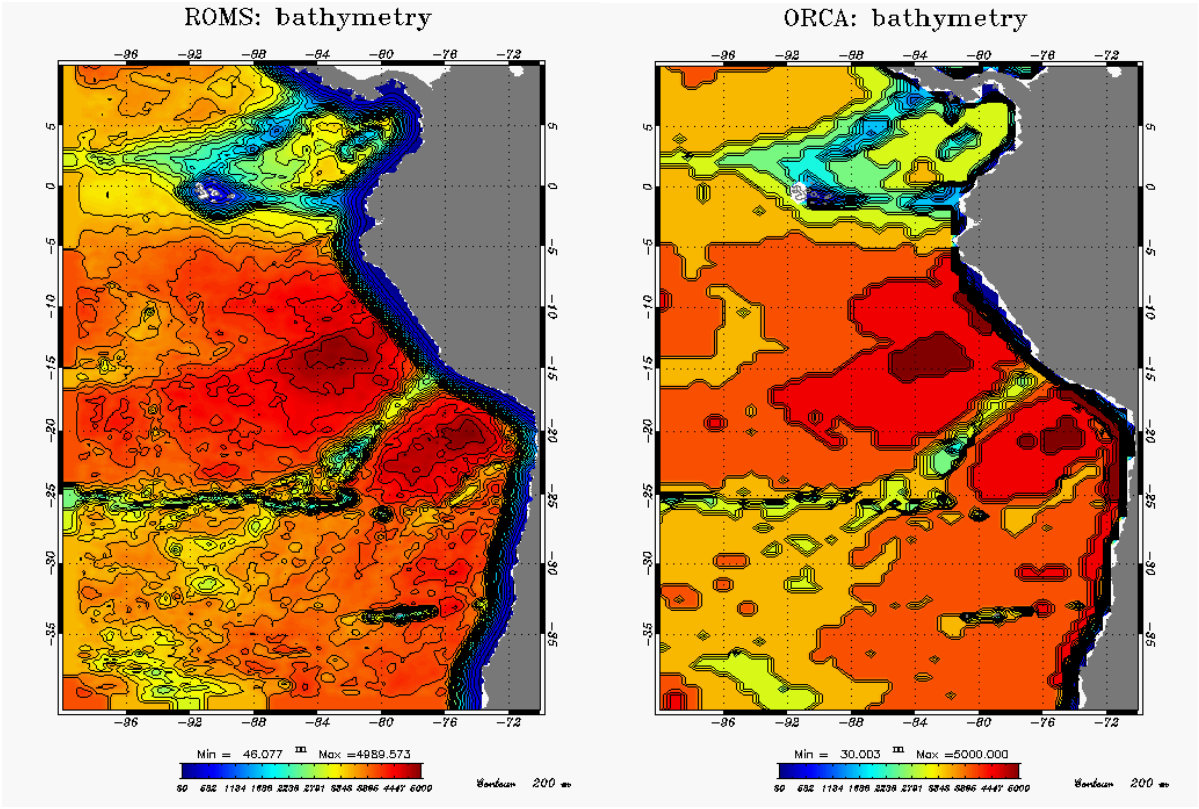

Fig. 3.7. Bottom topography (m) for the ROMS (left) and ORCA (right) models. Contour interval is 200m.

5-daily oceanic outputs from the former provide the open boundary conditions for temperature, salinity, velocity and sea level over the period 1992-2000. They were treated using a combination of an Orlanski scheme for the tracers and for baroclinic velocities and a

Flather scheme for the barotropic mode (Marchesiello et al., 2001). Initial conditions are from climatological values from the World Ocean Atlas 2005 (Locarnini et al., 2006; Antonov et al., 2006). To force the model at the air/sea interface, 5-daily wind stress from the ERS1-2 satellite scatterometer measurements (50km resolution – Bentamy et al., 1996) and fluxes (heat, freshwater, solar shortwave radiation) from the European Center for Medium Range Forecasts (ECMWF) ERA-40 global atmospheric reanalysis (1.25° resolution - Uppala et al., 2005) were used. Heat fluxes include a restoring term to COADS 0.5° monthly climatological SST and SSS fields (Da Silva et al., 2004).

The model grid, atmospheric forcing, initial and boundary conditions were linearly interpolated onto the ROMS grid using the ROMSTOOLS software (Penven et al., 2008). A 2-year spin-up was performed with climatological values derived from the forcing and the boundary conditions, after which model outputs were saved every 5 days from 1st January 1992 onwards.

ORCA

The primitive equation ORCA model (Madec et al., 1998; Barnier et al., 2006) is an OGCM run with a global 1/2° resolution for the 1992-2000 period. It has 31 z-levels in the vertical with 10 m intervals between 0 and 100 m, and 500 m at 4750 m depth. The model has a rigid lid and the sea surface height is computed diagnostically. The horizontal diffusion on the tracers and velocity is bilaplacian with a constant coefficient of 1.4×10^{11} m^4/s. The OGCM is forced by ERS1-2 winds, NCEP heat fluxes (Kalnay et al., 1996) and CMAP freshwater fluxes (Xie and Arkin, 1996) as in Lengaigne et al. (2002). The model resolution is not sufficient to allow eddies to be resolved explicitly.

3.2.2.2. Observed sea level data

The sea levels simulated by ROMS and by ORCA are compared to AVISO satellite altimetric data (http://www.aviso.oceanobs.com/) available from October 1992 to December 2000. Weekly data available on a 1/3° gridded field result from optimal interpolation of combined altimetric data from Topex/Poseidon and ERS1-2 satellites (Le Traon et al., 1998).

3.2.2.3. Methodology

The propagating nature and spatio-temporal characteristics of IEKW, ERW and CTW are diagnosed using a wavelength-frequency decomposition (Hayashi, 1979, 1982). This bi-variate space-time analysis consists in the projection of an unidimensional dataset varying

over time onto a selected number of wavelengths (four travelling wave numbers and stationary waves in this case) for both possible directions of propagation (East/West for IEKW and ERW, North/South for CTW), followed by a direct Fourier transform of the resulting time series associated to each wavelength. Applied to high-pass filtered sea level and alongshore current anomalies, it allows separating standing and propagating oscillations and identifying their direction of propagation (if any), dominant frequencies and associated wavelengths.

Unless specified, the term anomalies used in this paper refers to the total 5-daily signal from which a monthly climatology interpolated (using a spline function) onto a 5-daily temporal grid was removed. Anomalies are thus considered as departures from climatological values that only contain low frequency components of the signal such as the annual and semi-annual harmonics, which would not be the case if a mean climatology computed directly from the 5-daily outputs was used. In the following, intraseasonal anomalies refer to the high-pass filtered anomalies with a 150-day cut-off frequency, since we focus on time scales of periodicity lower than 120 days: indeed, the preferential intraseasonal frequency band along the equator features long-wavelength Kelvin waves at ~50, 70, and 100 $days^{-1}$ (Dewitte et al., 2008b).

A vertical mode decomposition of the model stratification from ROMS and from ORCA is performed at each time step in order to derive baroclinic mode contributions to pressure and current anomalies, which can help understanding the dynamical response of the model ocean to the large scale equatorial forcing. The decomposition was applied to equatorial, coastal and regularly-spaced zonal sections inside the regional domain so as to describe the vertical structure of the anomalies related to IEKW, CTW and ETRW, respectively. The coastal sections selected to diagnose CTW activity were extracted from a coastal band (first twelve grid points *i.e.* two degrees) between the Galapagos islands (1.4°S) and the southern boundary. Vertical modes form an orthogonal basis and can describe any perturbation of the density field.

Two simplifying assumptions were made. First, we assumed that linearization was appropriate. This requires interface deviations to be small compared to mean layer thickness, which should be true on intraseasonal time scales: for instance, the typical amplitude of 70- and 120-day IEKW-induced 20°C isotherm depth variations derived from TAO measurements (McPhaden et al., 1998) at 95°W over the period 1992-1999 is about 5m (Cravatte et al., 2003 – their figure 4a), whereas the mean depth is around 50m. The same order of magnitude was

found for 30-90 day bandpass-filtered 20°C isotherm depth variations over 2000-2004 (Jiang et al., 2009 – their figure 4a).

Second, we assumed that the Wentzel–Kramers–Brillouin (WKB) approximation was appropriate, allowing the analysis to be done independently at each grid point. This requires that the background state of the ocean changes over a length scale that is large relatively to the wavelength of the perturbations. Yet, the model density structure can exhibit sharp changes over short distances in this region, particularly near the coast where isotherms rise due to coastal upwelling and bottom topography, and near the equator where the equatorial front separates the cold tongue waters to the south from the eastern Pacific warm pool waters to the north. Moreover, in addition to IEKW, the eastern equatorial Pacific is characterized by the presence of tropical instability waves, with zonal scales around 1000 km and frequencies around (15-45 day)$^{-1}$ (*e.g.* Vialard et al., 2001). Nevertheless, the method is justified *a posteriori* by the model results, especially offshore in the off-equatorial region where the density change length scale is much larger than the local first Rossby radius of deformation (fig. 3.8).

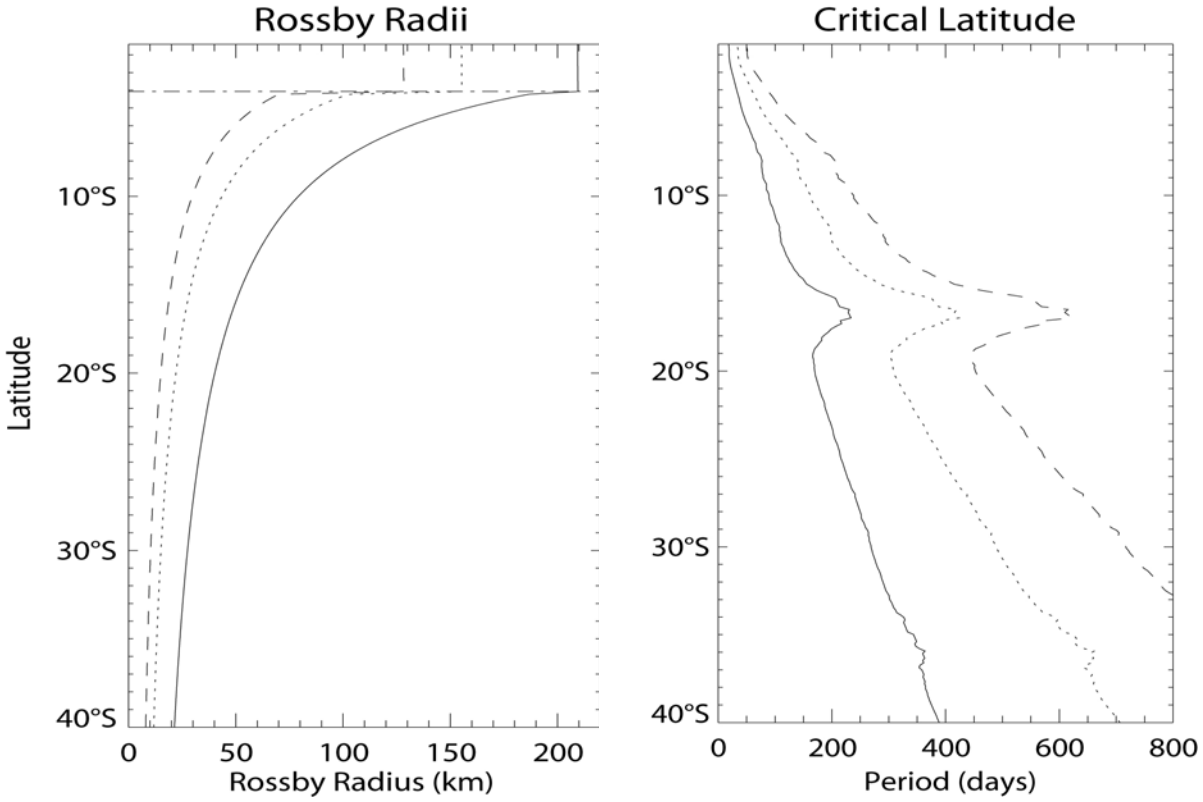

Fig. 3.8. Left: first, second, and third baroclinic mode Rossby radii of deformation (km) as a function of latitude (full, dotted, and dashed lines, respectively) for the ROMS simulation. The dashed-dotted line indicates the latitude used to separate the computation for the equatorial region and for the extra-tropics. Right: critical latitude (°) as a function of frequency (days) for the first, second, and third baroclinic modes (full, dotted, and dashed lines, respectively) for the ROMS simulation. Phase speeds were averaged along the 3000m isobath from 5°S to 40°S.

Similar methodology was used successfully in previous studies for the equatorial Pacific (Dewitte et al., 2008b; Belmadani et al., 2010) and the eastern South Pacific (Dewitte et al., 2008a). Note that the WKB approximation was used by Killworth and Blundell (1999), who argue that variations of bottom topography have a significant influence on baroclinic modes and their phase speeds near the coast but a weak impact on the propagation of the long ETRW in the inner basin. Caution is therefore required in the interpretation of the results obtained from the coastal area. It is especially true for ROMS, since horizontal resolution and smoothing of bottom topography tend to widen the continental shelf and slope in the model grid, conversely to ORCA which features a lower resolution that leads to a narrower shelf and sharper slopes (fig. 3.7).

Due to the computational cost of the method, the zonal sections were separated by 1° intervals from the equator to 20°S, and by 5° intervals from 20°S to 35°S. The sections have a fixed length and are limited to the east by the coastline. The length was chosen to be equal to that of the section between the western boundary and the westernmost grid point on land south of the equator (located around 81.5°W, 5°S). The southern boundary was excluded from the analysis because of the side effects associated to the sponge layer used at the open boundaries.

The higher meridional sampling North of 20°S is motivated by the CS91 estimates of critical latitudes for intraseasonal time scales: according to their study, the critical latitudes for the first baroclinic mode range from 7-10°S for 50- to 80-day IEKW to 14°S for 120-day IEKW. These values were derived using the following formulation for a smooth nonmeridional boundary:

$$T_{C_n} = -\frac{4\pi R \tan(\phi)}{c_n \sin(\theta)} \quad (3)$$

where Tc_n is for the critical period of the wave for the nth baroclinic mode and Φ is for the critical latitude. See CS91 for details.

In order to complement results from the baroclinic mode decomposition performed near the coast, Empirical Orthogonal Functions (EOFs) are computed over cross-shore vertical sections of the alongshore current anomalies every 5 degrees of latitude from 5°S to 35°S. A band-pass filter was previously applied to the anomalies in order to extract different frequencies of interest within the [50-120 day] intraseasonal frequency band, which were identified from space-time analysis. Note that cut-off frequencies used for band-pass filtering throughout the paper are equal to the frequency of interest +/- 10 days. Cross-shore direction

was determined at each latitude for both ROMS and ORCA models from the estimated coastline angle θ (see 3.2).

For the ROMS model, the EOF calculation is performed over the grid points located inside the first baroclinic mode Rossby radius of deformation. The objective is to capture the signal associated to CTW propagation and separate it from offshore variability which is likely to be influenced by ETRW propagation. Following Chelton et al. (1998), the Rossby radii of deformation λ_n were computed for each vertical mode n using the baroclinic mode phase speeds c_n derived from the vertical mode decomposition of the mean stratification near the coast. In the equatorial band (from the equator to ~5°S), λ_n is defined as

$$\lambda_n = \sqrt{\frac{c_n}{2\beta}} \qquad (4)$$

Outside of the equatorial band in the southern hemisphere, λ_n is defined as

$$\lambda_n = -\frac{c_n}{f} \qquad (5)$$

For the ORCA model, the coarse 0.5° grid does not allow the EOF analysis to be performed inside the first Rossby radius with a sufficient number of grid points to represent accurately the cross-shore structure of the Principal Components (PCs). Instead, the analysis was performed on a 2° cross-shore extension for each latitude. Once the EOFs are performed, spatial patterns and frequency spectra of the time series associated to the PCs are analyzed for both models in order to identify coastally-trapped structures oscillating at the frequency of interest. Time series associated to such structures are then lag-correlated in order to track coherent poleward propagation along the coast.

The parameter of stratification S is used to quantify the relative influence of stratification and topography on CTW propagation. Following Jordi et al. (2005), it is defined as:

$$S = \frac{NH}{fL} \qquad (6)$$

where N, H and L are typical values for buoyancy frequency, depth and cross-shelf horizontal scale, respectively. For each latitude, cross-shore topography was used to derive H and L, which were chosen to correspond to the location of maximum slope seaward from the shelf break. N was also determined at the same location, using mean temperature and salinity profiles from the model (ROMS and ORCA) to compute profiles of density accordingly to the UNESCO (1981) formulas for the equation of state, and then profiles of buoyancy frequency with a centered first differences numerical scheme - see Chelton et al. (1998) for details. The

sensitivity of S to the value chosen for N was tested by using the mean value over the water column instead of the bottom value and appeared to be weak along the coasts of Peru and Chile (not shown). For $S >> 1$, stratification dominates and waves tend to have a baroclinic structure, whereas for $S << 1$, bottom topography dominates and waves tend to have a barotropic structure.

3.2.3 Regional model results

3.2.3.1 Regional downscaling and model validation

In order to assess the ability of the regional model to reproduce the remotely forced variability simulated by the global model and transmitted to the regional domain along the equatorial wave guide, equatorial Sea Level Anomalies (SLAs) simulated by both models are compared (fig. 3.9). Note that SLA refers to the sea level signal from which time-mean average was removed. The simulated equatorial variabilities are assessed against satellite altimetry. Both model simulations qualitatively with the observed data, featuring a succession of positive and negative SLAs that are transmitted along the equator from the western boundary. The signature of the 1997-98 El Niño event is clear in both simulations, and is associated to two positive peaks of SLA - previously described by several authors (Blanco et al., 2002; Strub and James, 2002; Colas et al., 2008a) - of successively around 20 cm and 30 cm, values which are however about 30% weaker than observed.

As in the modelling study by Colas et al. (2008a) who use a very similar configuration of the ROMS model except with a higher resolution, the two peaks of El Niño appear again very clearly along the coast in both simulations, though also about 30% weaker than in the observations (fig. 3.10).

Again, the amplitude is slightly higher for the second peak (~25 cm, vs. ~20 cm for the first peak), just as observed (see also Blanco et al., 2002; Strub and James, 2002). Note however that altimetric data is noisy near the coast, which is due to the rather coarse resolution (1/3°) of the AVISO product, so caution is needed in the interpretation of model-data mismatch. The simulated SLAs extend from the equator to at least central Chile (40°S) with relatively small energy loss, even during neutral ENSO years. Opposite to ORCA, ROMS exhibits some smaller scale features especially South of 10°S, which are related to the mesoscale activity not resolved by ORCA (see also fig.3.12).

(a)

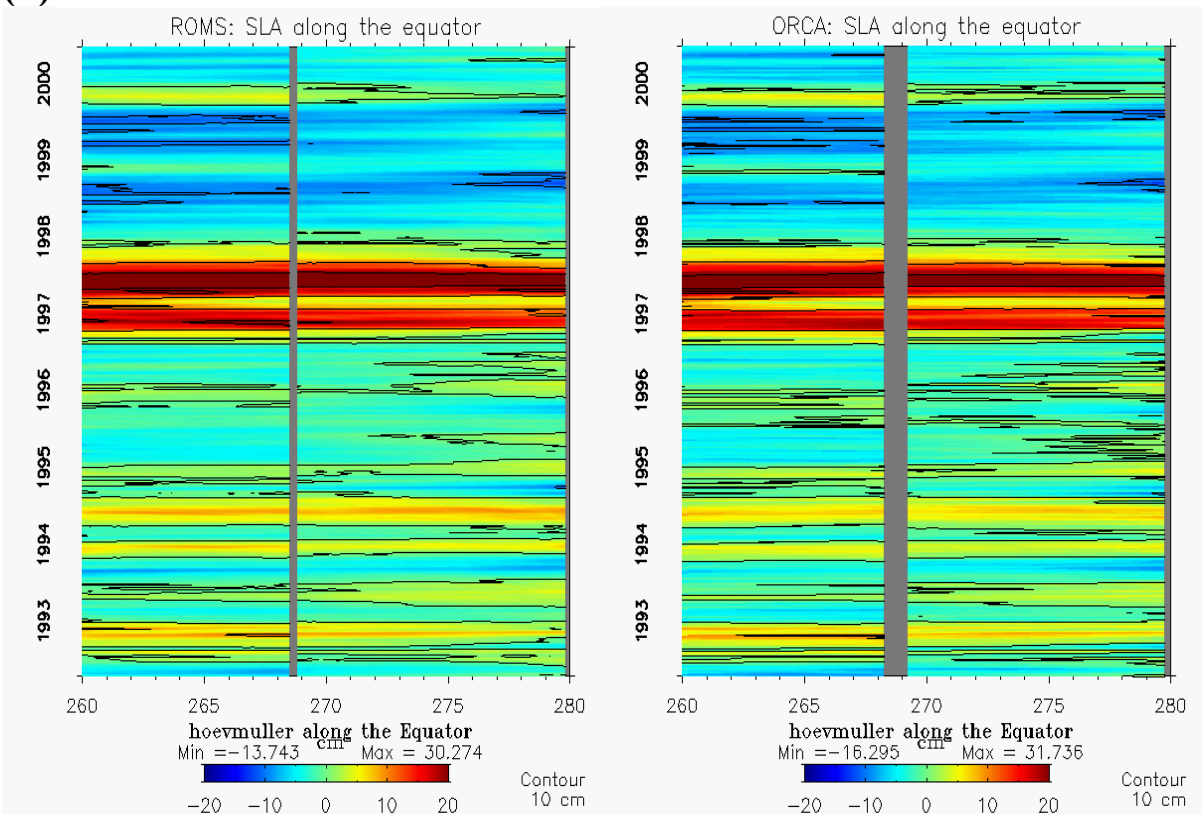

(b)

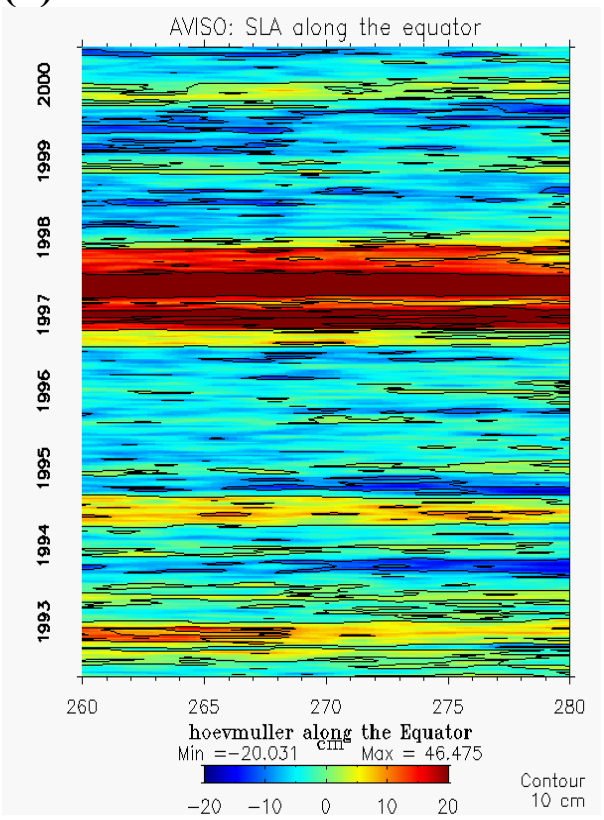

Fig. 3.9. SLA (cm) **(a)** simulated by ROMS (left panel), by ORCA (right panel) and **(b)** from AVISO altimetric data along the equator from 100°W to 80°W. Contour interval is 10cm.

(a)

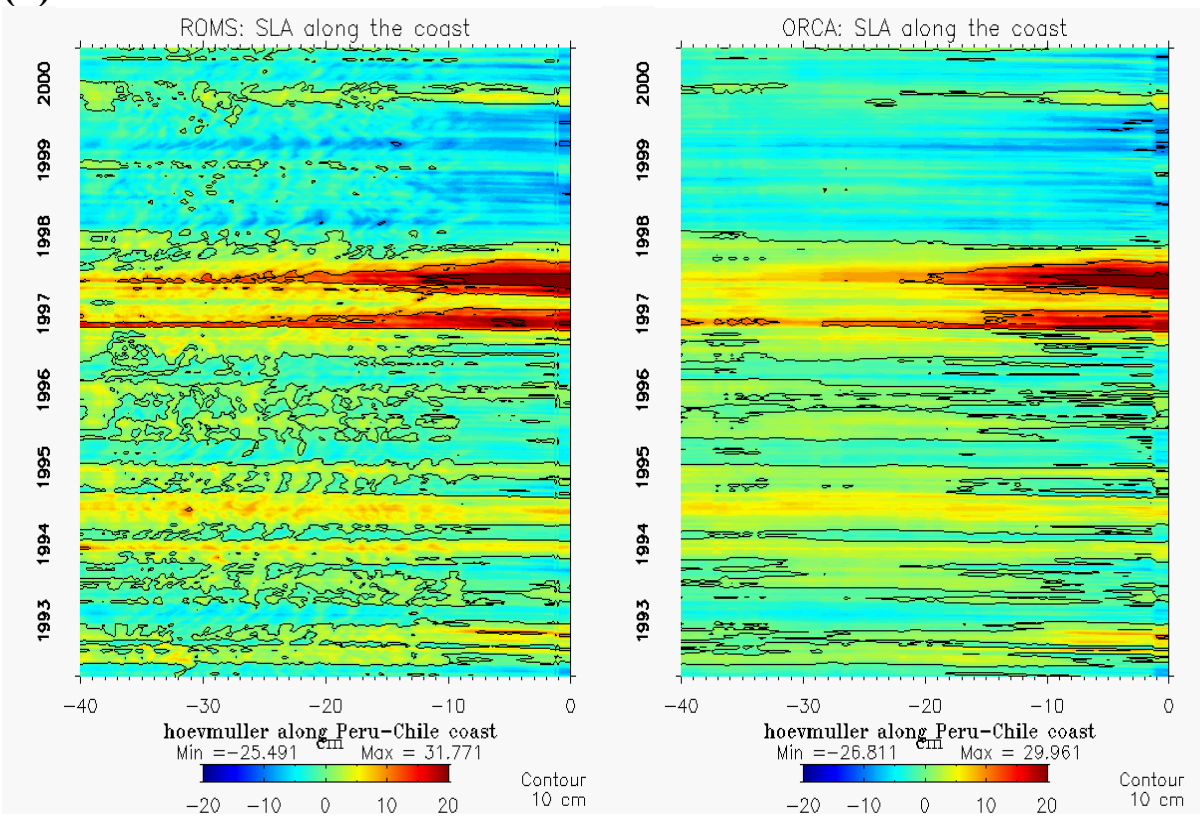

(b)

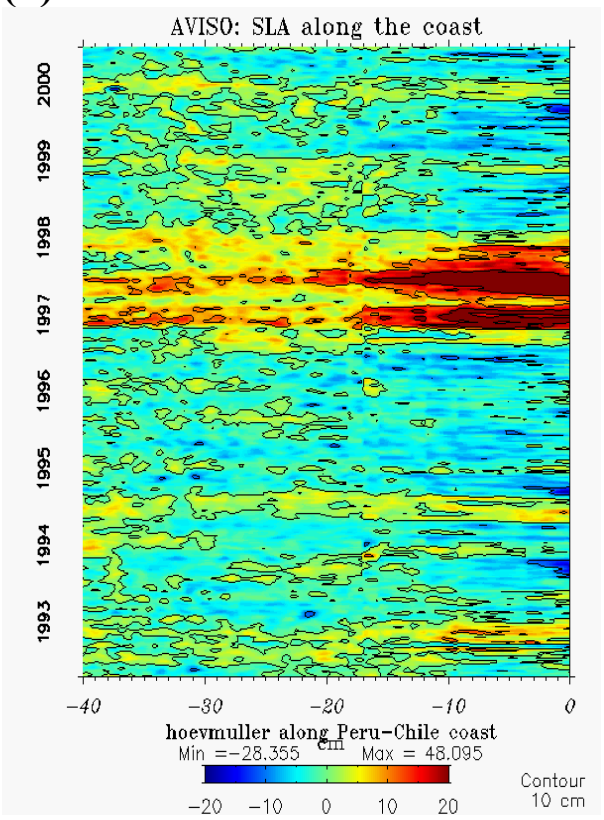

Fig. 3.10. SLA (cm) **(a)** simulated by ROMS (left panel), by ORCA (right panel) and **(b)** from AVISO altimetric data along the coast from 0°N to 40°S. Contour interval is 10cm.

Such hovmuller diagrams help identifying the different time scales associated to the simulated variabilities and thereby allow assessing the dynamical processes at stake in the two models. In particular, at the equator, both signals contain significant intraseasonal, seasonal and interannual variability (fig.3.9). In addition to the two El Niño peaks, the seasonal cycle is clearly distinguishable with an amplitude around 5 to 10 cm, and so is intraseasonal variability, with an amplitude of the order of a few centimetres.

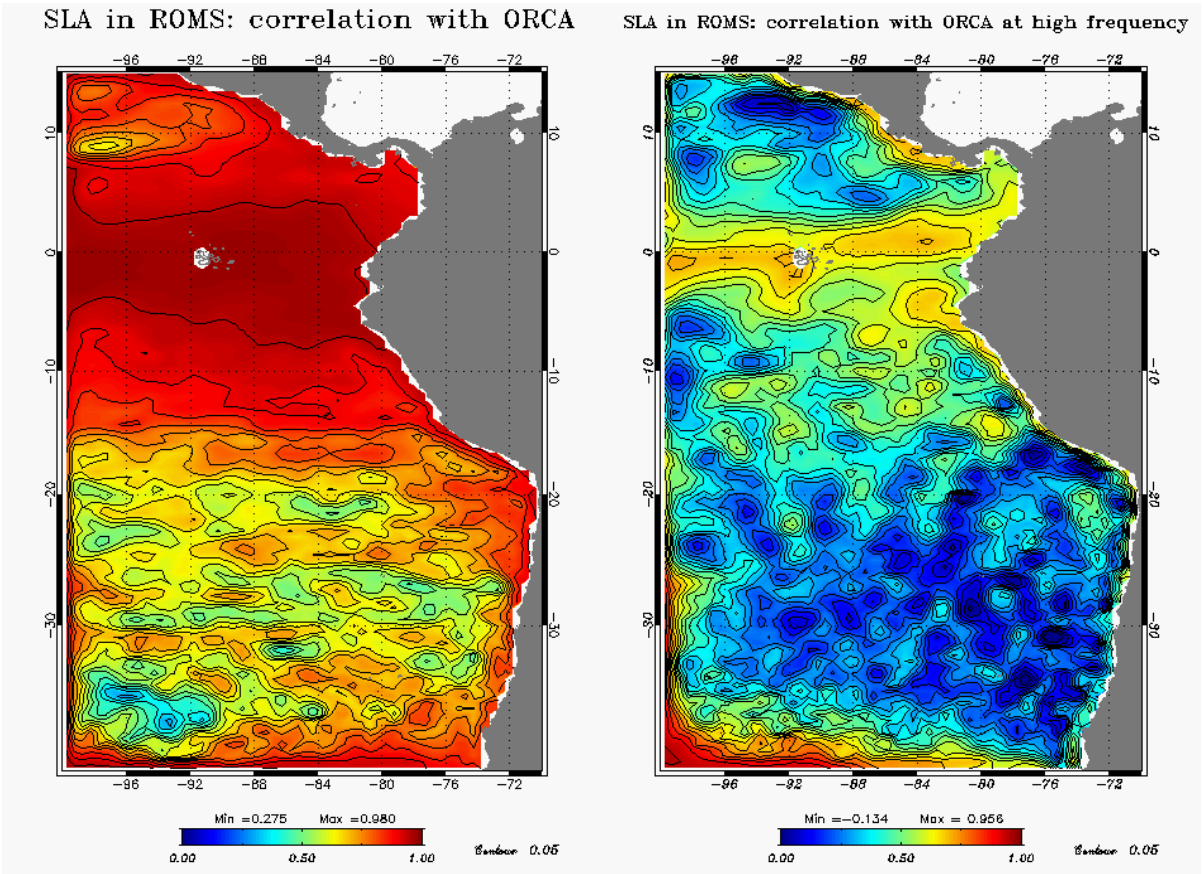

Fig. 3.11. Correlation maps between SLA simulated by ROMS and by ORCA. Left panel (resp. right panel) is for total (resp. high-pass filtered) SLA. Cut-off frequency is f_c = 150 days. Contour interval is 0.05.

On the whole, sea levels from ROMS and ORCA are in relatively good agreement over the study region, with correlations over 70% in mosts parts of the domain and particularly inside the equatorial band (10°N-10°S) and along the coast, except offshore between 20°S and 35-40°S (fig. 3.11, left panel), a region where sea level variability is dominated by mesoscale processes (Chaigneau and Pizarro, 2005a,b).

For intraseasonal frequencies, the picture is somewhat similar (fig. 3.11, right panel): correlations are highest along the open boundaries, near the equator and close to the coast, whereas they are weakest in the southern half of the inner basin. However, correlation values are significantly lower than for the total signals: for instance, they are around 70% along the

equator, against over 90% for the total signal. Nevertheless, intraseasonal equatorial variability in ROMS is mainly controlled by that of ORCA in a narrow band between 2°N and 4°S, which splits into two branches East from the Galapagos islands. Upon reaching the coast, this intraseasonal variability is trapped North and South of the equator. In the southern hemisphere, coastal-trapped intraseasonal variabilities from ROMS and ORCA agree rather well until about 25°S to 30°S. Note that both models are in good agreement in the offshore region between 5°S and 15°S, suggesting the presence of intraseasonal ETRW in both simulations north of the critical latitude (CS91).

Maps of modelled and observed intraseasonal sea level variabilities tend to confirm these statements (fig. 3.12). In particular, whereas intraseasonal variability is present in the ORCA simulation in the equatorial region and nearshore, it is very weak offshore South of 10°S to 15°S, except in the south-western corner of the domain in the region of high sea level variability controlled by large scale ocean processes (Webb and de Cuevas, 2003). In contrast, the ROMS simulation displays significant variability over this region, with small scale structures that seem to be connected to nearshore variability particularly off the regions of Pisco-San Juan (15°S to 18°S) and central Chile (25°S to 35°S) where strong coastal jets (Fuenzalida et al., 2008; Renault et al., 2009) associated to local maxima of eddy activity (Chaigneau et al., 2008) were observed. These patterns are qualitatively consistent with data from altimeter records, though with amplitudes about 40% weaker, just like in the rest of the domain and particularly in the equatorial region. Both models are however able to simulate significant variability near the coast along the whole shoreline, with smaller cross-shore scales for ORCA that seem to be related to the narrower continental shelf and/or to the coarser resolution in this model (fig.3.7).

The regional model is also able to reproduce the cross-shore and alongshore structures of the main coastal currents of the HCS, namely the poleward PCUC and the equatorward CPCC: the mean coastal currents simulated by ROMS at 10°S (fig. 3.13) compare rather well with the geostrophic currents measured by Huyer et al. (1991) or with the velocity field simulated by a coarser-resolution regional model (Dewitte et al., 2008a) in the same area. The variation of mean PCUC speed over latitude was found to be consistent with the results from Dewitte et al. (2008a), and reveals that mean velocities never exceed about 10 to 15 cm/s (not shown).

(a)

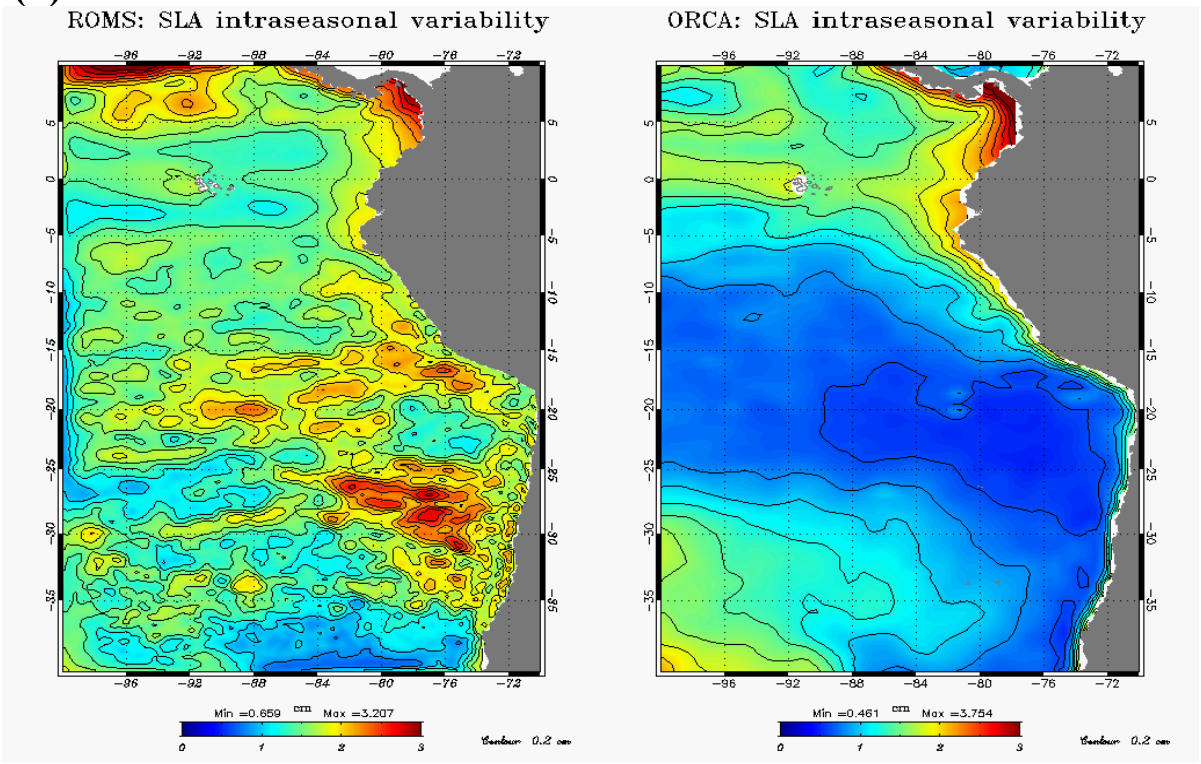

(b)

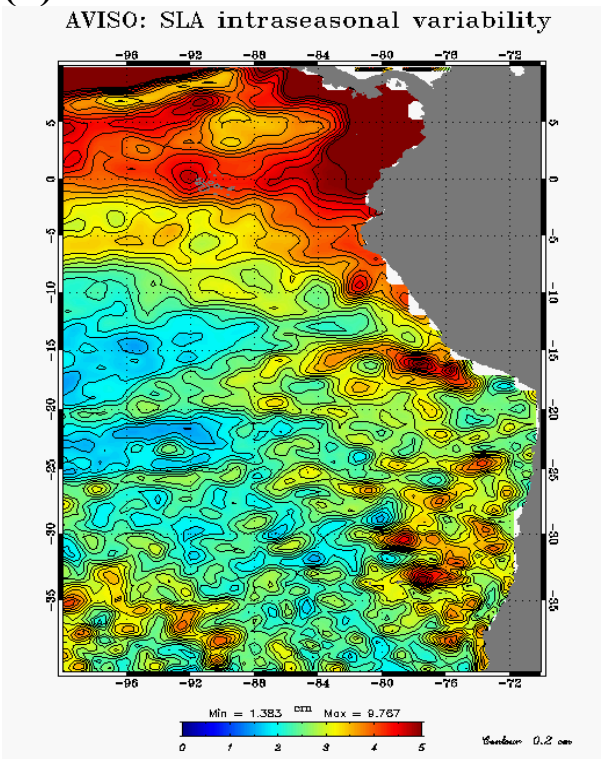

Fig. 3.12. High-pass filtered (f_c = 150 days) SLA variability (RMS) **(a)** simulated by ROMS (left panel), by ORCA (right panel) and **(b)** from AVISO data. Note that the colour scale is different for the latter. Unit is cm. Contour interval is 0.2 cm.

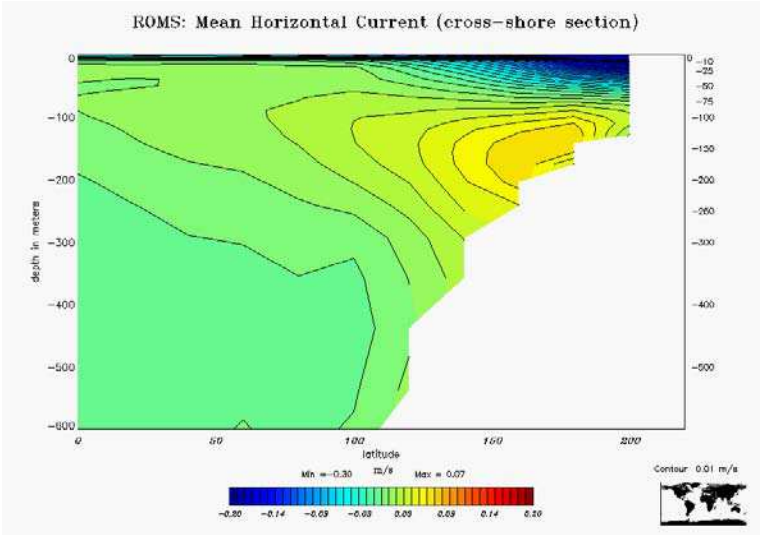

Fig. 3.13. Cross-shore section of the mean alongshore currents (m/s) simulated by ROMS at 10°S near the coast. Positive values are for poleward flow. Contour interval is 0.01 m/s.

Overall, the primitive-equation eddy-resolving ROMS model appears as a valuable tool for the study of remotely forced intraseasonal variability in the eastern South Pacific. In the following, results from regional modelling are used to describe the fate of IEKW when they reach the eastern boundary of the tropical Pacific Ocean.

3.2.3.2 The propagation, reflection and coastal-trapping of IEKW

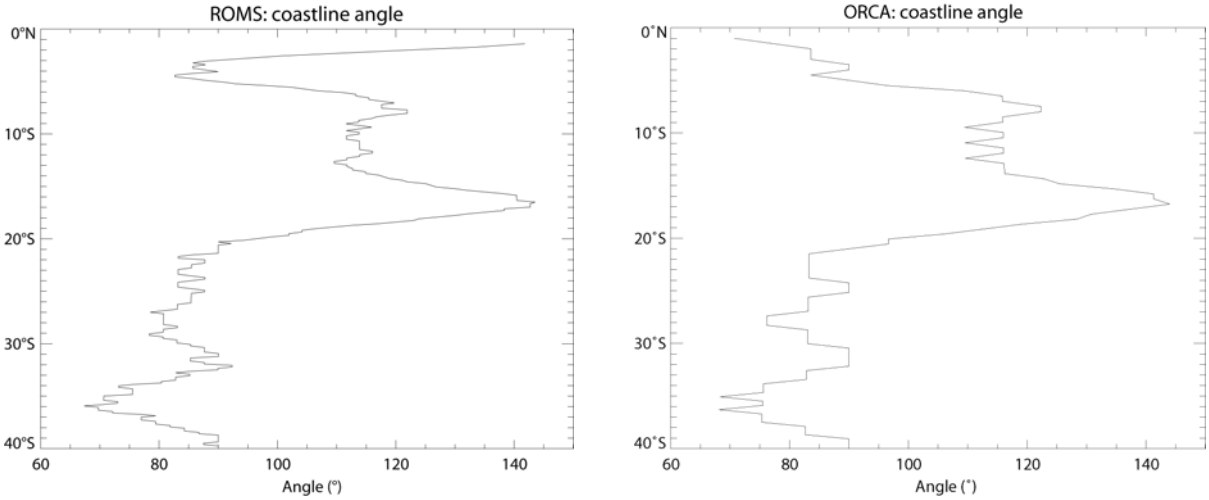

Fig. 3.14. Coastline angle relatively to the East direction between 1°S and 40°S for the ROMS (left) and ORCA (right) models.

First, let us assume that the flat-bottom approximation is valid along the coasts of Peru and Chile, and hence that coastally-trapped wave motion can be described by linear theory. According to CS91, at intraseasonal frequencies higher than 120 days, first (resp.

second) baroclinic mode Kelvin waves are all trapped along the South American coast South of 14°S (resp. 8°S). Such values were derived from estimates of phase velocities based on the buoyancy frequency provided by data from S. Levitus. It is supposed here that mention is made to a dataset similar to the 1°x1° gridded product by Levitus et al. (1994) and Levitus and Boyer (1994): such a coarse resolution is of the same order as the Rossby radii of deformation (fig. 3.8), so the uncertainty in the estimates of critical latitudes is large and unquantified.

In order to check the relevance of the CS91 critical latitudes for our model configurations, we applied the formulation (3) to estimates of coastline angle and baroclinic mode phase speeds from the ROMS and ORCA models. The former was estimated at each latitude for both models from the position of the coastline defined by the land-sea mask: the resulting angle was smoothed in order to reduce noise originating from model resolution and from the contour of the land-sea mask (fig. 3.14). Except between 1°S and 3°S, coastline angles from both models are very similar.

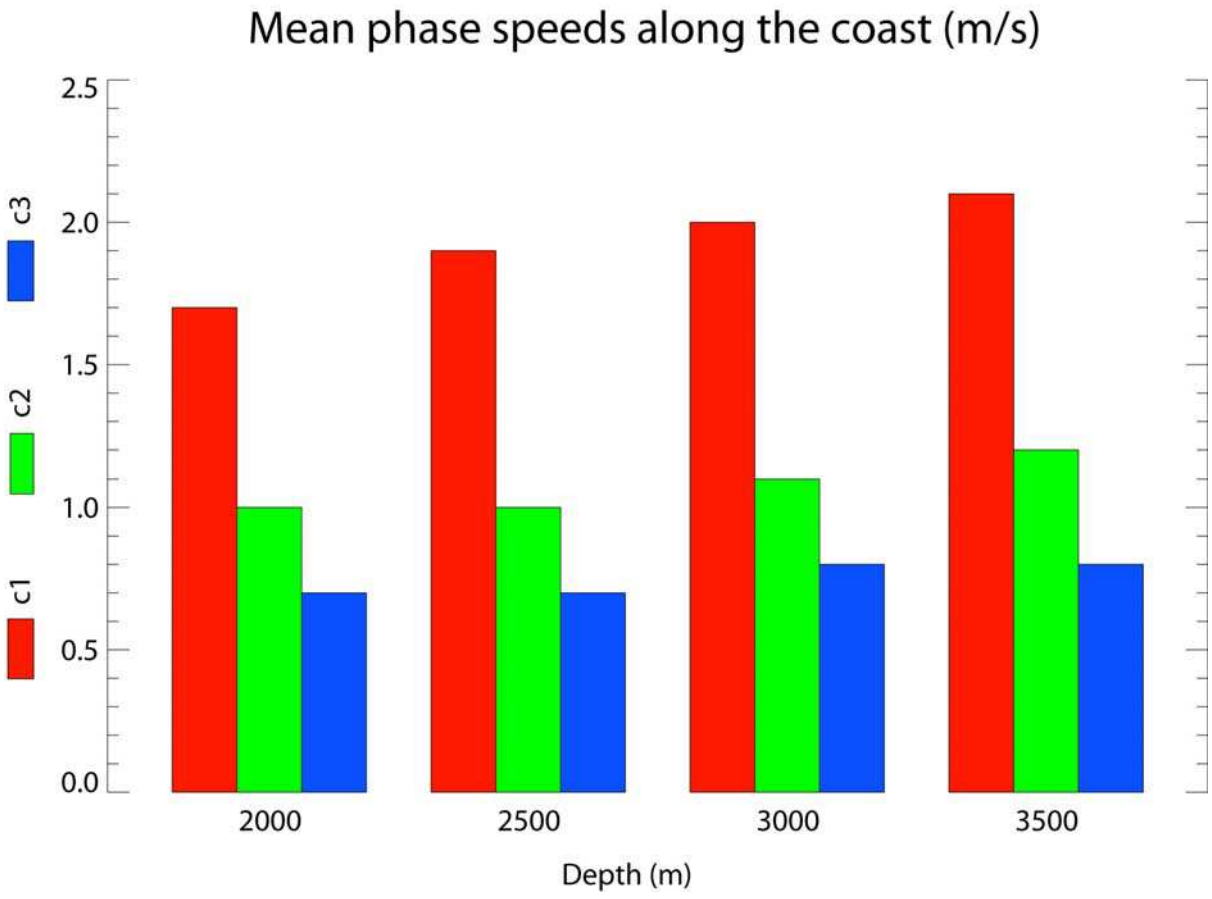

Fig. 3.15. Meridionally-averaged first to third baroclinic mode phase speeds c_n (m/s) in the 2° coastal band along different isobaths for the ROMS model.

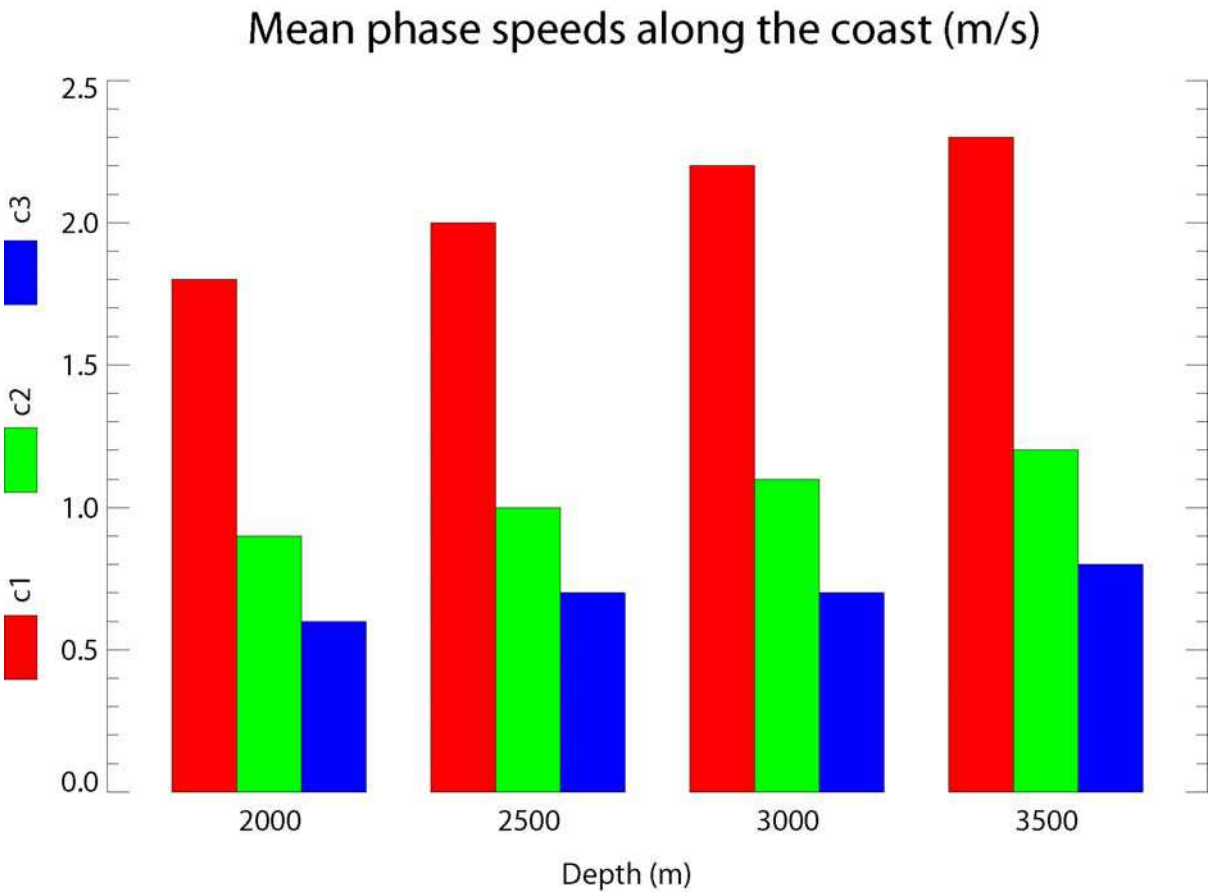

Fig. 3.16. same as fig. 3.15 except for the ORCA model.

Phase speeds c_n were estimated from the modal decomposition in the two-degree coastal band. In order to reduce the uncertainty related to the WKB approximation in this area, estimates of meridionally-averaged phase speeds were computed along four different isobaths located along the slope at 2000m, 2500m, 3000m and 3500m depths (figures 3.15 and 3.16). Consistently with Killworth and Blundell (1999), phase speeds experience little variation with latitude (not shown) but are strongly influenced by bottom topography. Estimates of phase speeds along the 3000m and 3500m isobaths compare rather well with those from Chelton et al. (1998), though they are slightly underestimated in the ROMS model: 2.0-2.1 m/s vs. 2.2-2.3 m/s for ORCA and for Chelton et al. (1998). Note however that the latter values were based on temperature and salinity profiles from the World Ocean Atlas 1994 (Levitus et al., 1994; Levitus and Boyer, 1994) interpolated onto a 1° x 1° horizontal grid: such estimates are subject to significant uncertainty because of the scarcity of the data in the region and the coarse horizontal resolution of the gridded product which may hide important differences between the density structure near the coast and farther offshore.

Estimates of the critical latitude with phase speeds computed along the 3000m and 3500m isobath are in good agreement with those from CS91, particularly for the ORCA

model, as illustrated on figure 3.26 (dashed and dotted lines). For ROMS, model-derived critical latitudes are slightly closer to the equator (fig. 3.8). These results confirm the relevance of CS91's critical latitude estimates for the simulated mean stratification (within the linear approximation), and hence the relevance of the higher meridional sampling north of 20°S for the latitudes chosen to diagnose ETRW propagation in both models (see section 2.3).

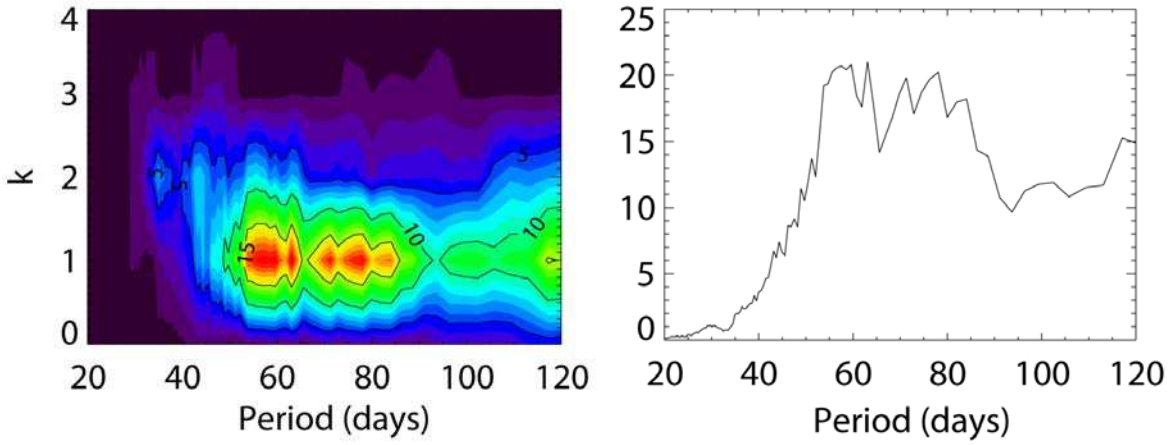

Fig. 3.17. Frequency-wavelength decomposition of high-pass filtered SLA (f_c = 150 days) simulated by ORCA at the equator between 120°E and 80°W (k=1 ~ 18000km). Eastward propagations for different wavenumbers k (left panel) and for a basin-wide wavelength (right panel) are represented. k=0 refers to standing oscillations, and is characterized by equal amplitudes for both directions of propagation. Spectrum units are cm². Contour interval is 5 cm².

The propagation characteristics of the long IEKW present in the boundary forcing are assessed by applying space-time analysis to intraseasonal SLA from ORCA over the equatorial Pacific at basin scale (fig. 3.17). The analysis clearly indicates the signature of the EKW, with an eastward sea level propagation of basin-scale wavelength, and typical frequencies around ω = (50-60 days)$^{-1}$, (70-80 days)$^{-1}$ and (120 days)$^{-1}$, consistently with earlier works (Mc Phaden and Taft, 1988; Cravatte et al., 2003; Dewitte et al., 2008b). In addition, the energy is displaced towards shorter wavelengths (k=2, k=3) for frequencies higher than (40 days)$^{-1}$, consistently with the dispersion relation (see also figure 4 from Dewitte et al. (2008b)):

$$\left(\frac{\omega}{c_n}\right)^2 - k^2 - \frac{\beta k}{\omega} = \frac{(2n+1)\beta}{c_n} \qquad (7),$$

where n is the order of the considered baroclinic mode.

Results from the vertical mode decomposition are then used to characterize IEKW propagation inside the regional model. Space-time analysis applied to baroclinic mode

contributions to sea level anomalies allows describing equatorial Kelvin wave and planetary wave motion in the regional domain and their variations with latitude (figures 3.18 and 3.19).

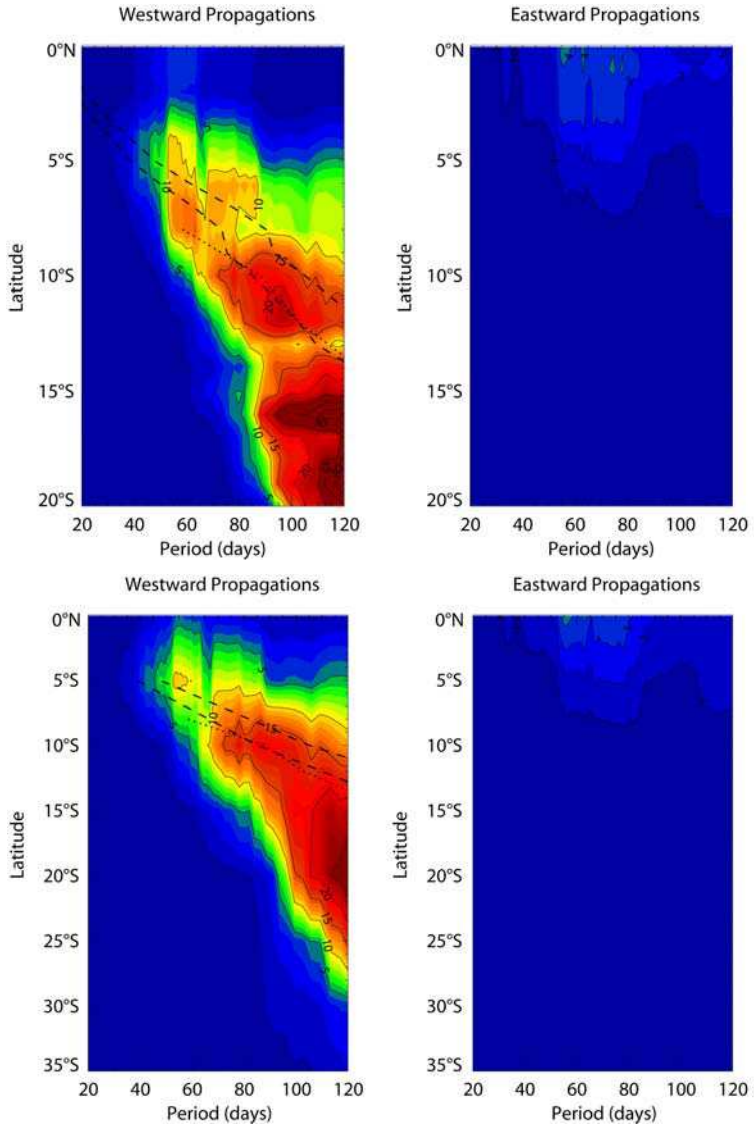

Fig. 3.18. Plots of frequency-wavelength spectra of the high-pass filtered first baroclinic mode contribution to SLA (f_c = 150 days) simulated by ROMS, sampled on a 1° meridional grid between 0°N and 20°S (top) and on a 5° meridional grid between 0°N and 35°S (bottom), and integrated over the wavelength space (from k=1 to k=4) as a function of latitude. The left (resp. right) panel is for westward (resp. eastward) propagations. Units are cm². Contour interval is 5cm² (resp. 1cm²) for westward (resp. eastward) propagations. The upper (resp. lower) dashed line is for the critical latitude derived from estimates of the first baroclinic mode phase speed computed along the 2000m (resp. 3500m) isobath (fig. 3.15). The dotted line is for the critical latitude from Clarke and Shi (1991).

Consistently with results from ORCA and previous studies (Mc Phaden and Taft, 1988; Cravatte et al., 2003; Dewitte et al., 2008b), IEKW are observed inside the regional domain between about 0°N and 5°S, with frequencies around 60 days, 80 days and 120 days for the first baroclinic mode, around 100 days and 120 days for the second baroclinic mode, and around 120 days for the third baroclinic mode (see eastward propagations on figures 3.18

and 3.19). Note that the first baroclinic mode is associated to wave energy ~40% (resp. ~130%) larger than for the second (resp. third) baroclinic mode.

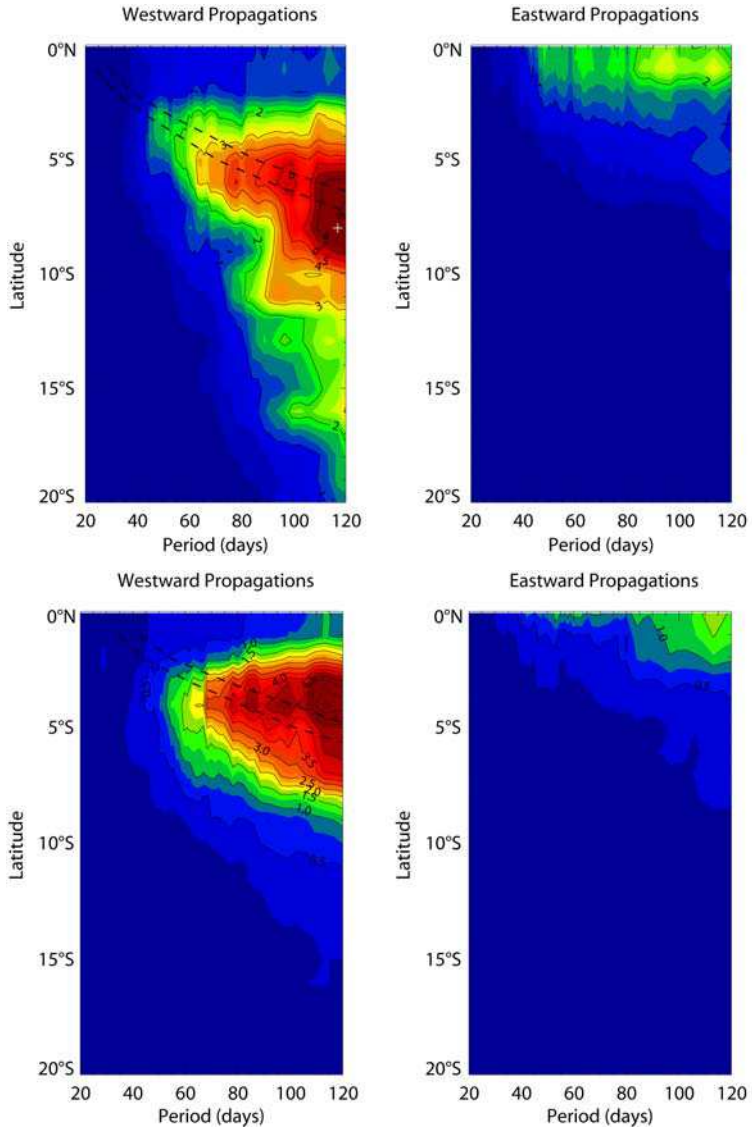

Fig. 3.19. Same as fig.3.18 (top panel), but for the second (top) and third (bottom) baroclinic modes. Contour interval is 1cm² (resp. 0.5 cm²) for the top (resp. bottom) panel. The upper (resp. lower) dashed line is for the critical latitude derived from estimates of the respective baroclinic mode phase speed computed along the 2000m (resp. 3500m) isobath (fig.3.15). The white cross on top panel is for the second baroclinic mode critical latitude at 116.9 days from Clarke and Shi (1991).

ERW propagation is also present inside the equatorial band for all three modes. Westward propagating features become more energetic than eastward propagating IEKW South of ~3-4°S, 3°S and 2°S for the first, second, and third baroclinic modes, respectively, where IEKW eventually vanish. As expected from linear theory, for frequencies and latitudes low enough, offshore westward propagation is observed, suggesting the presence of ETRW, whereas for frequencies and latitudes high enough, there is no significant wave propagation in

the zonal direction, suggesting the presence of CTW. However, the associated critical latitudes/frequencies depart significantly from estimates derived from linear theory for all three baroclinic modes, especially for the lower frequencies, no matter which estimates are considered (those from CS91 or those from model-derived parameters). Indeed, whereas linear theory does not expect any Rossby wave propagation South of 14°S, highly energetic westward motion with 120-day periodicity is observed down to about 25°S to 30°S for the first baroclinic mode. Similarly, westward propagations are diagnosed as far South as 15°S to 20°S instead of 8°S for the second baroclinic mode, and down to about 10°S instead of 5-6°S for the third baroclinic mode.

These results are confirmed by the spatial distribution of baroclinic mode contributions to intraseasonal sea level variability (figures 3.20 and 3.21), which can be used as a first approximation to monitor the variability of the westward propagating signal, since eastward propagations are negligible outside the equatorial region (figures 3.18 and 3.19) and so are standing oscillations (not shown): the variability is trapped near the coast South of respectively 13°S and 25-30°S for 60-day and 120-day oscillations for the first baroclinic mode (fig. 3.20), 5°S and 10°S for 60-day and 120-day oscillations for the second baroclinic mode (fig. 3.21), and 8°S and 10°S for 60-day and 120-day oscillations for the third baroclinic mode (not shown).

Note that most offshore variability is connected to coastal variability, which confirms that the westward propagating features diagnosed from space-time analysis are related to westward motion originating from the coast and not to forced motion locally generated by the wind within the inner basin. Maximum variability associated to each baroclinic mode at a given frequency is generally located near the coast or directly connected to it.

Interestingly, little of the energy around 120 days is of equatorial origin for the first two modes, although these frequencies are associated to maximum energy amplitudes in the intraseasonal band and are significant contributors to westward propagation south of the CS91 critical latitude (figures 3.18 and 3.19). Unlike other frequency bands, the westward propagating 120-day oscillations seem to be strongly amplified South of a given latitude, which can be higher (fig. 3.18) or lower (fig. 3.19, top panel) than the critical latitude expected from linear theory, before it is damped again at a distance sufficiently large from the equator.

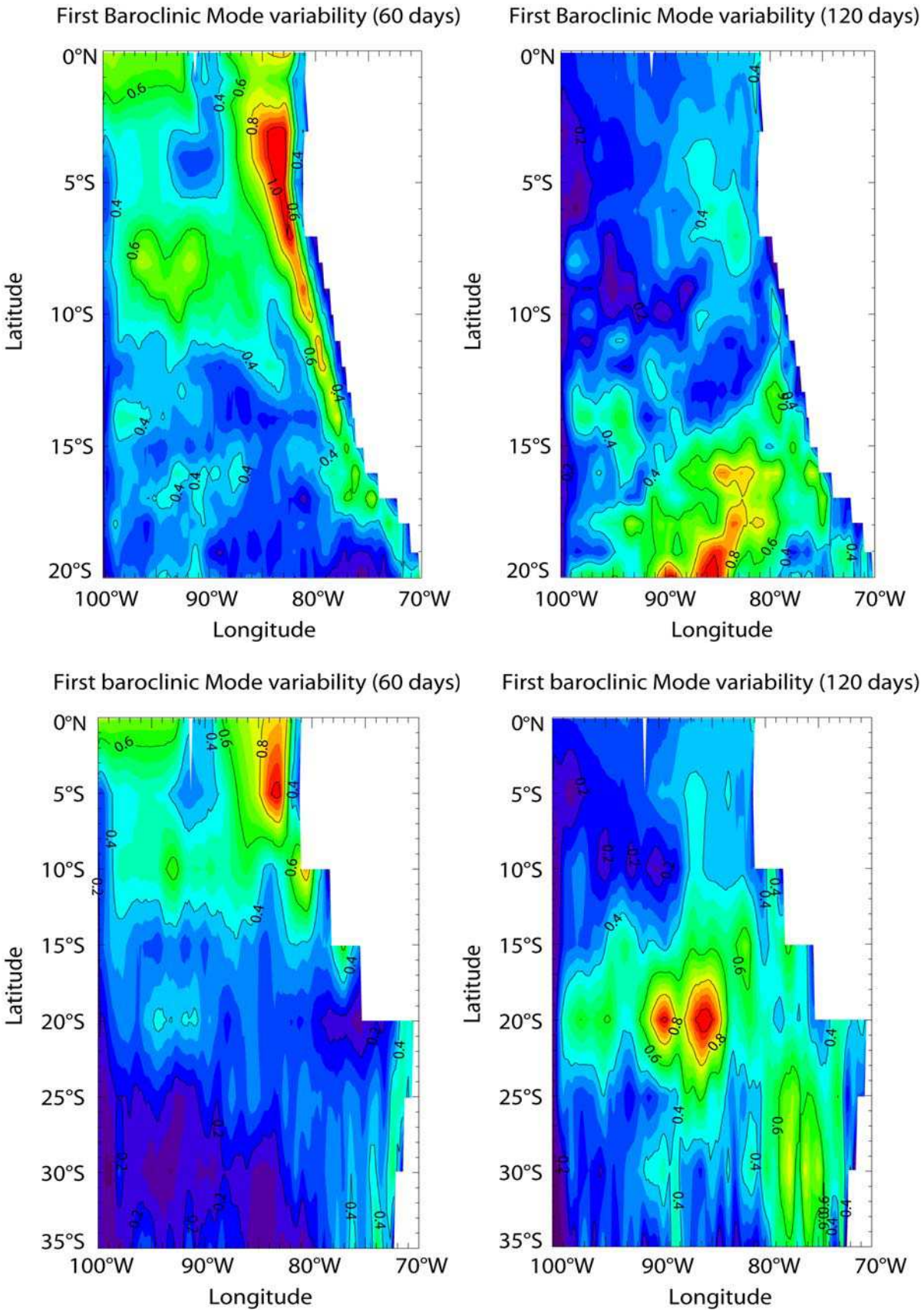

Fig. 3.20. Band-pass filtered (left: 60 days; right: 120 days) first baroclinic mode contribution to SLA variability (RMS) simulated by ROMS, sampled on a 1/6° x 1° grid between 0°N and 20°S (top) and on a 1/6° x 5° grid between 0°N and 35°S (bottom). Units are cm. Contour interval is 0.2cm.

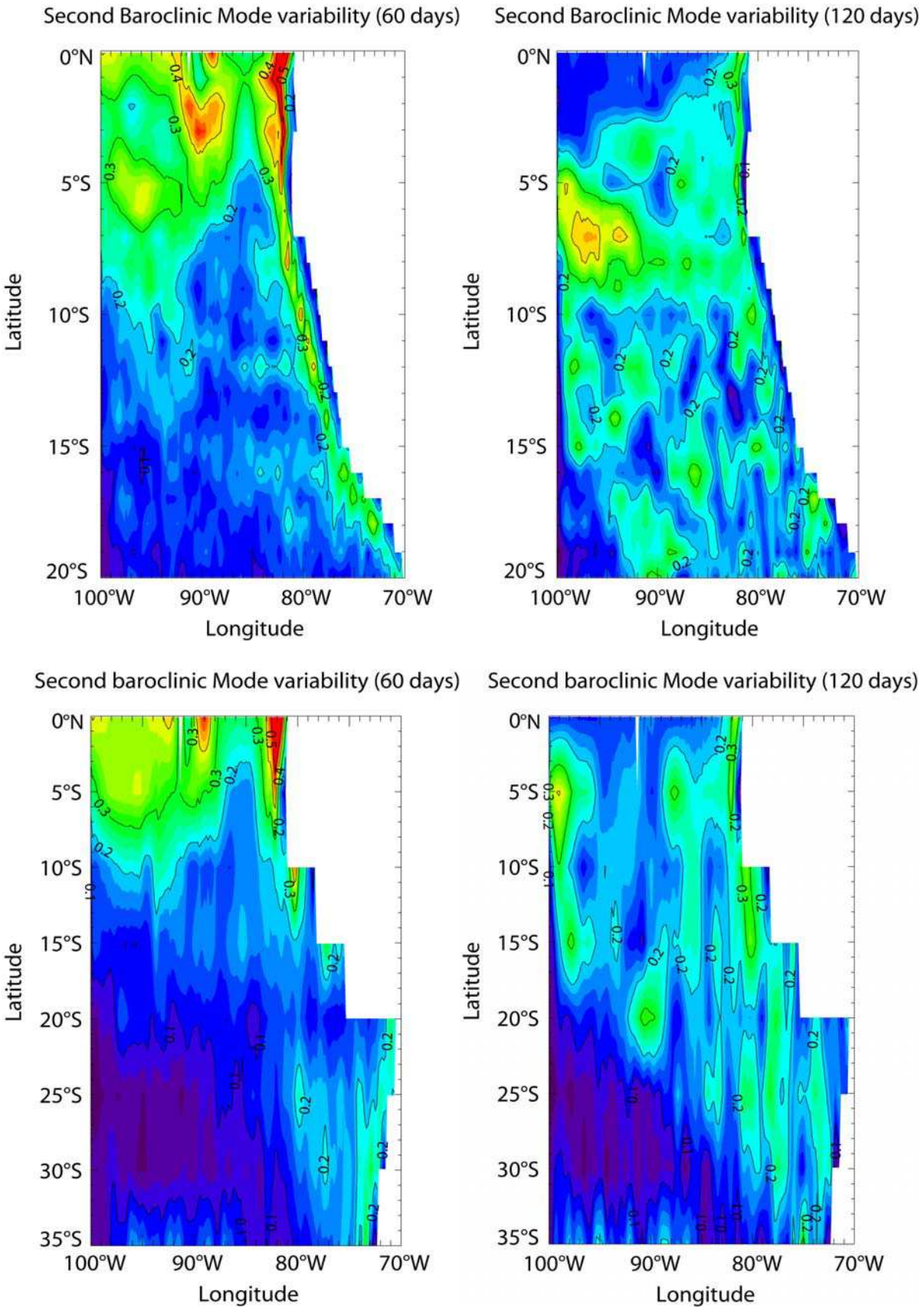

Fig. 3.21. Same as fig. 3.20, but for the second baroclinic mode.Contour interval is 0.1cm.

3.2.3.3 CTW: cross-shore and alongshore structure

Latitude (°S)	Mode 1	Mode 2	Mode 3
5	47	19	9
10	55	23	8
15	51	23	8
20	59	23	5
25	64	23	5
30	46	33	8
35	43	38	9

Table 3.1. Fractions of the [50-70 days] band-pass filtered alongshore current variance (%) explained by the first three principal components from the EOF analyses peformed at 5°S, 10°S, 15°S, 20°S, 25°S, 30°S, and 35°S (see text).

As explained in section 2., EOFs of band-pass filtered alongshore velocities are used to describe the cross-shore and alongshore structure of CTW. Rossby radii of deformation were computed for the ROMS model in order to determine the length of the cross-shore sections used for the EOF calculation. According to Chelton et al. (1998), the first Rossby radius of deformation computed from observations ranges from more than 150km near the equator to less than 30 km at the southern boundary, in other words inside the 2-degree coastal band. Just like for phase speeds, estimates of model-derived Rossby radii (fig. 3.8) were computed along the 2000m, 2500m, 3000m and 3500m isobaths. Values along the 3000m and 3500m isobaths are in good agreement with those from Chelton et al. (1998). Results from the EOF analysis presented here are for deformation radii determined from phase speeds meridionally-averaged along the 3000m isobath. It was verified that EOFs of the intraseasonal alongshore current anomalies did not exhibit significant sensitivity to the width of the cross-shore section, *i.e.* to the estimated value of the first Rossby radius of deformation (not shown).

From 5°S to 25°S, the statistically dominant first mode for [50-70 days] frequencies - which explains between 47% and 64% of the variance (table 3.1) - exhibits significant alongshore current variability trapped near the coast (at 5°S, 20°S and 25°S) or over the slope (at 10°S and 15°S) and oscillating with a periodicity around 50 to 60 days (fig. 3.22). At 5°S, 20°S and 25°S where the continental shelf is reduced or non-existant, the velocity structure is baroclinic – more precisely, it is similar to a vertical first baroclinic mode - and decays seaward with a length scale of the order of the deformation radius, similarly to the expected behaviour of idealized CKW propagating along a vertical wall over a flat bottom.

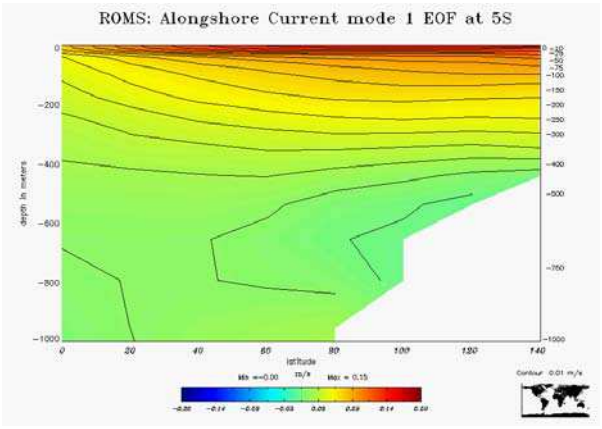
ROMS: Alongshore Current mode 1 EOF at 5S
depth in meters
latitude

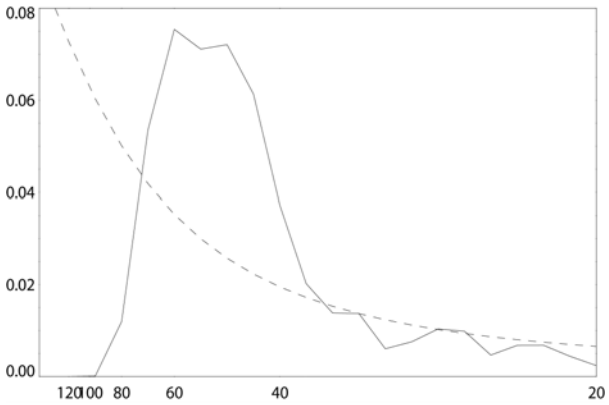
0.08
0.06
0.04
0.02
0.00
120 100 80 60 40 20

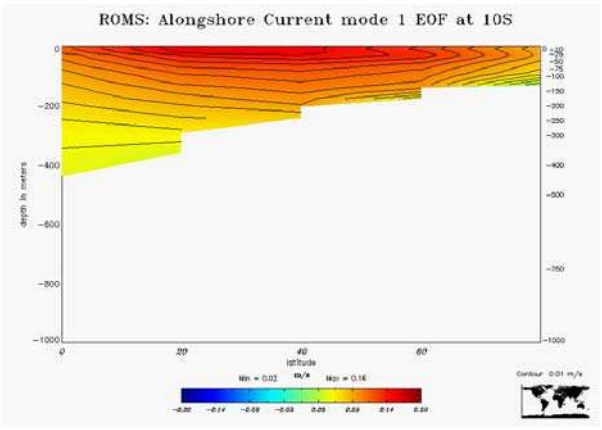
ROMS: Alongshore Current mode 1 EOF at 10S
depth in meters
latitude

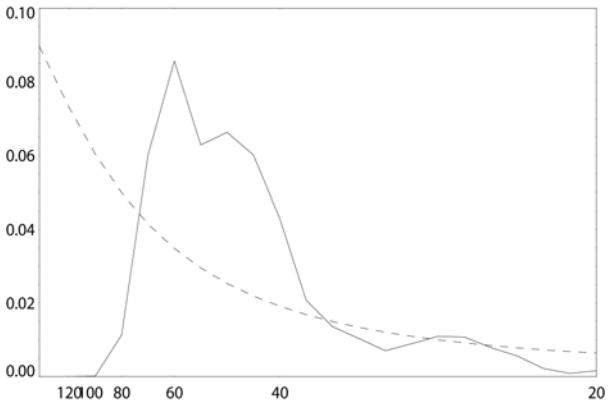
0.10
0.08
0.06
0.04
0.02
0.00
120 100 80 60 40 20

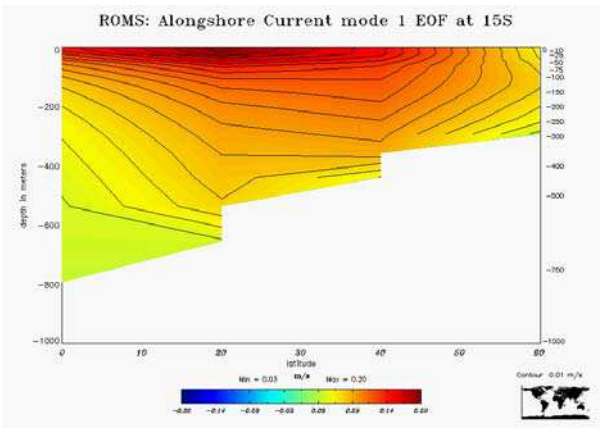
ROMS: Alongshore Current mode 1 EOF at 15S
depth in meters
latitude

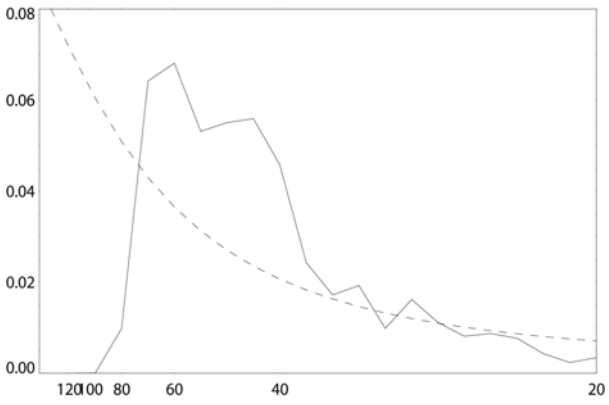
0.08
0.06
0.04
0.02
0.00
120 100 80 60 40 20

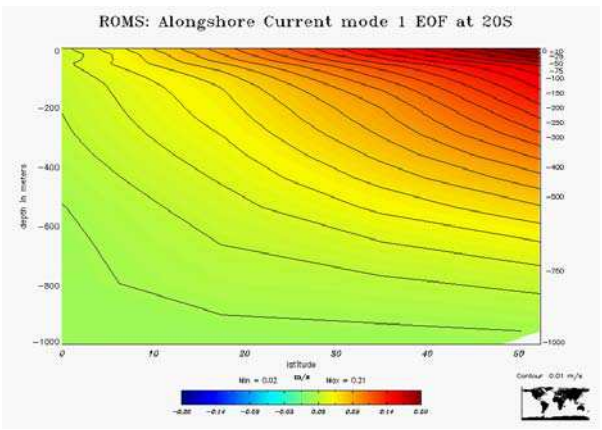
ROMS: Alongshore Current mode 1 EOF at 20S
depth in meters
latitude

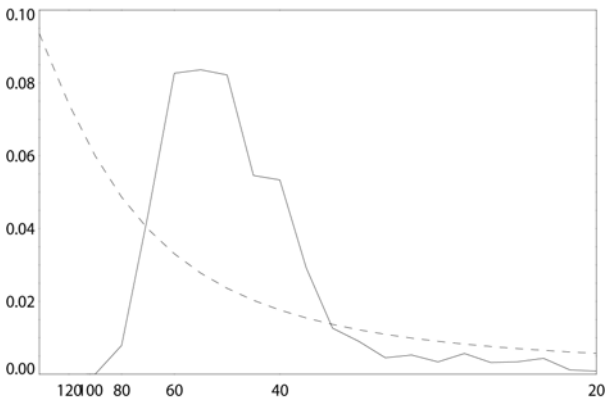
0.10
0.08
0.06
0.04
0.02
0.00
120 100 80 60 40 20

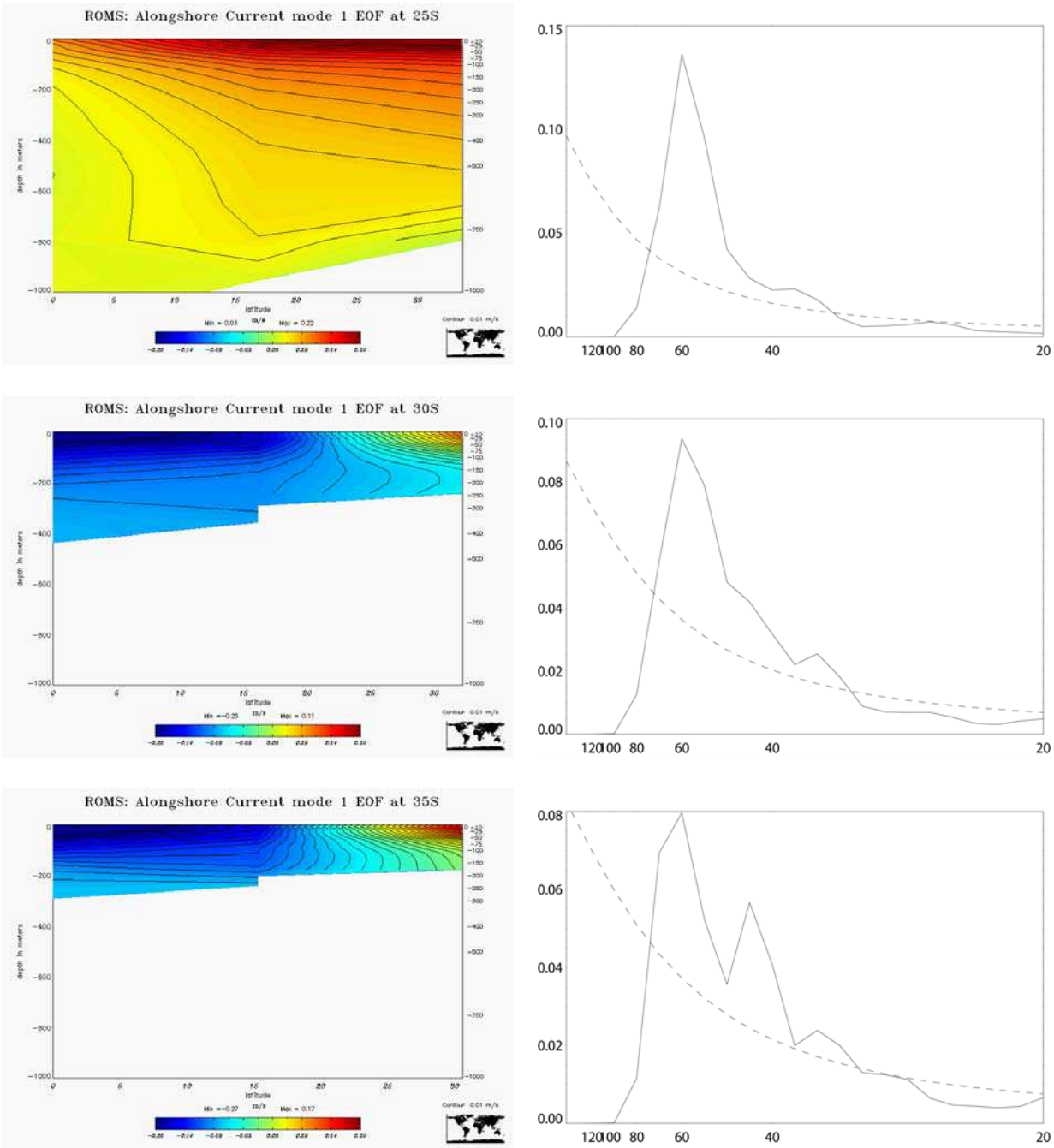

Fig. 3.22. First EOF mode of [50-70 days] band-pass filtered alongshore current anomalies performed from the surface to the bottom over cross-shore sections of lengths close to the first Rossby radius of deformation at (from top to bottom): 5°S, 10°S, 15°S, 20°S (previous page), 25°S, 30°S, 35°S (this page). For each latitude: 1st EOF mode spatial pattern (left), and frequency spectrum of the 1st EOF PC time serie (right). Spatial patterns are plotted as a function of landward cross-shore distance (km) and depth (m). Units are m/s and contour interval is 0.01 m/s. Spectra are plotted as a function of frequency, and equivalent periods (days) are indicated. Full line is for PC, and dashed line is for red noise spectrum with the same lag-1 autocorrelation.

Note that bottom topography seems to have an influence on both the cross-shore scale and the vertical scale of variability. The shallower and flatter the bottom (*e.g.* at 5°S compared to 20°S), the shorter the vertical scale. At 10°S and 15°S where the shelf is much shallower and with a reduced slope, alongshore current variability is vertically confined over

a few hundred meters between the surface and the bottom. In addition, it extends seaward beyond the radius of deformation (which is not the case at 5°S, 20°S and 25°S where the shelf is deeper and/or the slope is steeper). Maximum variability at these latitudes occurs at the surface ~20-40 km from the coast, whereas closer to the boundary, variability is weaker and tends to have a barotropic structure with more vertical isolines. This may be due to greater bottom friction near the coast: farther offshore, baroclinic motion starts to take over and maximum velocities are reached over the slope before they start to decay again in the seaward direction.

The magnitude of maximum variability ranges from 15 cm/s at 5°S to 22 cm/s at 25°S, about 2 to 3 times higher than the mean PCUC and of the order of the mean CPCC at 10°S (fig. 3.13), so that perturbations of the alongshore velocity field related to CTW motion are likely to have a large impact on the dynamics of these currents. The second EOF mode exhibits a similar structure for latitudes between 5°S and 25°S (not shown), with significant offshore and nearshore baroclinic variabilities of opposite signs oscillating at periods around 50 to 60 days, suggesting the presence of Rossby waves and/or mesoscale eddies.

Lag-correlation plots between PCs of the first EOF mode taken at different latitudes show a very clear poleward propagation, at least between 5°S and 25°S where the signals are strongly related to each other (fig. 3.23) and with a constant phase speed of about 1°/day, which is about 1.5 m/s taking coastline curvature into account. This estimate is of the order of the first baroclinic mode phase speed over the continental slope between about 1000m and 2000 m depth (fig. 3.15). Together with the first baroclinic mode-like vertical structure of the EOFs and results from the vertical mode decomposition near the coast (figures 3.20 and 3.21), it suggests that the first baroclinic mode dominates 60-day CTW propagation in this region. More generally, these results demonstrate the presence between 5°S and 25°S of poleward propagating CTW with a 60-day periodicity in the ROMS simulation, consistently with what was expected from linear theory and from the results of westward propagation analysis.

On the other hand, EOF analysis did not succeed in characterizing CTW propagation with frequencies around 120 days. Instead, these frequencies were associated to strong offshore variability (not shown), consistently with the analysis of westward propagation, which shows that ETRW/eddies can radiate along the coast as far south as 25°S to 30°S for these frequencies (fig. 3.18). The superimposition in the coastal region of westward propagating and poleward propagating motion does not always allow separating clearly these processes with statistical analysis, which seems to be the case for 120-day oscillations.

Overall, 120-day oscillations in the ESP are dominated by Rossby wave/eddy propagation rather than CTW propagation.

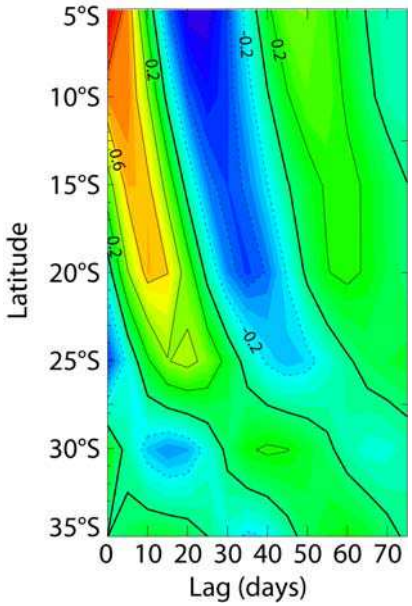

Fig. 3.23. Lag-correlation as a function of phase lag (days) and latitude (°) between the first EOF mode time series (see fig. 3.22) at 5°S and the first EOF mode time series at higher latitudes. Values are graphically interpolated from a 5° meridional grid. Values at 5°S are for the autocorrelation function. Contour interval is 0.2, and dashed lines are for negative correlations. Only positive lags are plotted.

3.2.3.4 The influence of CTW on coastal current variability

As previously shown by Shaffer et al. (1997), 50-day CTW propagating along the coast are able to trigger strong variability in the velocities of the PCUC at 30°S. In the light of these findings and results from the previous section, we apply frequency-wavelength decompositions to the velocities in the core of the PCUC. To do so, cross-shore sections of the mean alongshore currents were drawn every degree of the latitudes extending from 4°S to 40°S (see figure 3.13 for the section at 10°S). This information was used to identify the ranges of depth and distance from the coast exhibited by the PCUC over the length of the Peru-Chile coast, which allowed building an algorithm that identifies at each time step the position of the core of the PCUC, defined by maximum poleward velocities within the previously defined depth and cross-shore distance ranges. These maximum velocities were then used to define a time serie of the velocities in the core of the PCUC for each latitude.

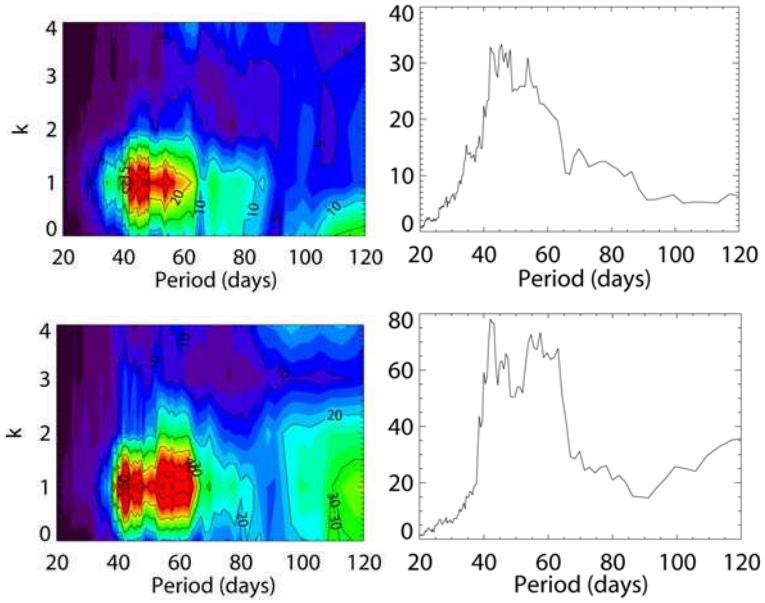

Fig. 3.24. Same as fig. 3.17, but for velocities in the core of the PCUC (top) and CPCC (bottom) simulated by ROMS between 4°S and 40°S. Spectrum units are (cm/s)².

Results from the space-time analysis are presented in figure 3.24. Strikingly, the PCUC exhibits strong fluctuations in its velocity field - that propagate southward with long wavelengths (k=1) - and frequencies around 40 to 60 days, consistently with the results from Shaffer et al. (1997). Some lower frequencies are present as well around 70-80 days but they are much weaker. The energy at 120 days characterizes both equatorward and poleward propagations (not shown), and also standing oscillations (k=0), so propagating features at these frequencies are not statistically significant (Hayashi, 1979).

The 40- to 60-day poleward propagating anomalies have a magnitude of the order of 5 cm/s, which is of the order of mean velocities in the PCUC (fig. 3.13), consistently with results from the EOF analysis. This makes such oscillations likely to dramatically impact poleward flow along the coast. These results demonstrate the impact of 40- to 60-day CTW on the variability of the PCUC over a wide range of latitude. Noteworthy, the CPCC undergoes very similar 50-day poleward propagations of higher amplitude (around 8 cm/s), which cannot be neglected either compared to mean equatorward flow (fig. 3.13).

3.2.4. On the differences between CTW and CKW

In this section, IEKW, ETRW and CTW propagations are studied in the ORCA model, in order to document differences between the CTW in ROMS and the CKW in ORCA

and their influence on the critical latitude. Such topic is of importance for nearshore current variability, as a lower (resp. higher) critical latitude should allow less (resp. more) wave energy originating from the equator to be radiated offshore as Rossby waves, and thus more (resp. less) energy to be trapped along the coast and have a higher (resp. lower) impact on the coastal currents over a longer (resp. shorter) meridional extension. The nearshore topography of the ORCA model featuring a narrower shelf and a sharper slope, it is likely to enhance the effect of stratification vs. topography on CTW and thereby favour baroclinic vs. barotropic wave structures.

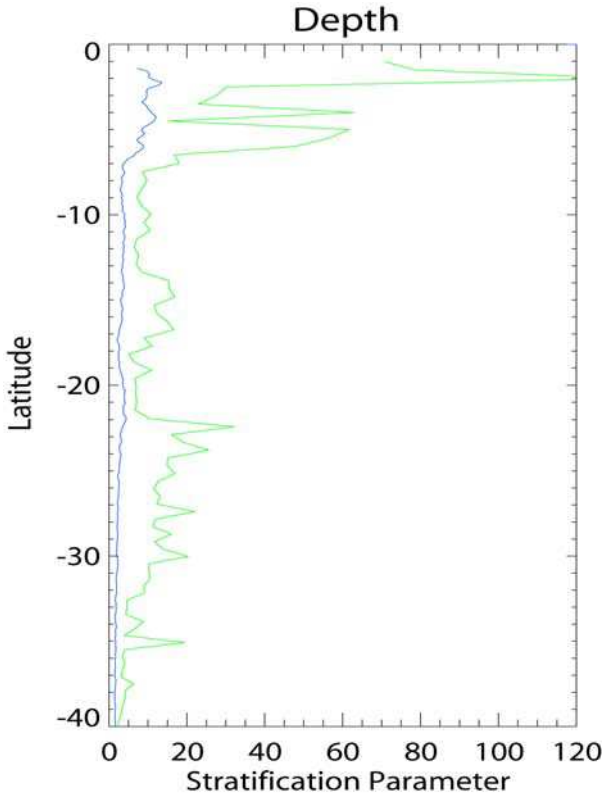

Fig. 3.25. Stratification parameter as a function of latitude (°S) for ROMS (blue curve) and ORCA (green curve).

In order to quantify such differences between the ORCA model and the ROMS model, the parameter of stratification S is computed for both models. Their respective meridional variations are shown on figure 3.25. Whereas for ROMS, S values are of the order of 1 over most of the coastline (except North of 7°S where they are higher), which indicates a mixed baroclinic-barotropic structure for CTW (consistently with results from section 3.3), for ORCA, S is always high, revealing a baroclinic structure which is more directly comparable to the idealized case considered by CS91. Note that for both models S is increasingly high towards the equator because of its inverse dependance on the Coriolis parameter f. Note also that both models exhibit small scale variations that are mainly related

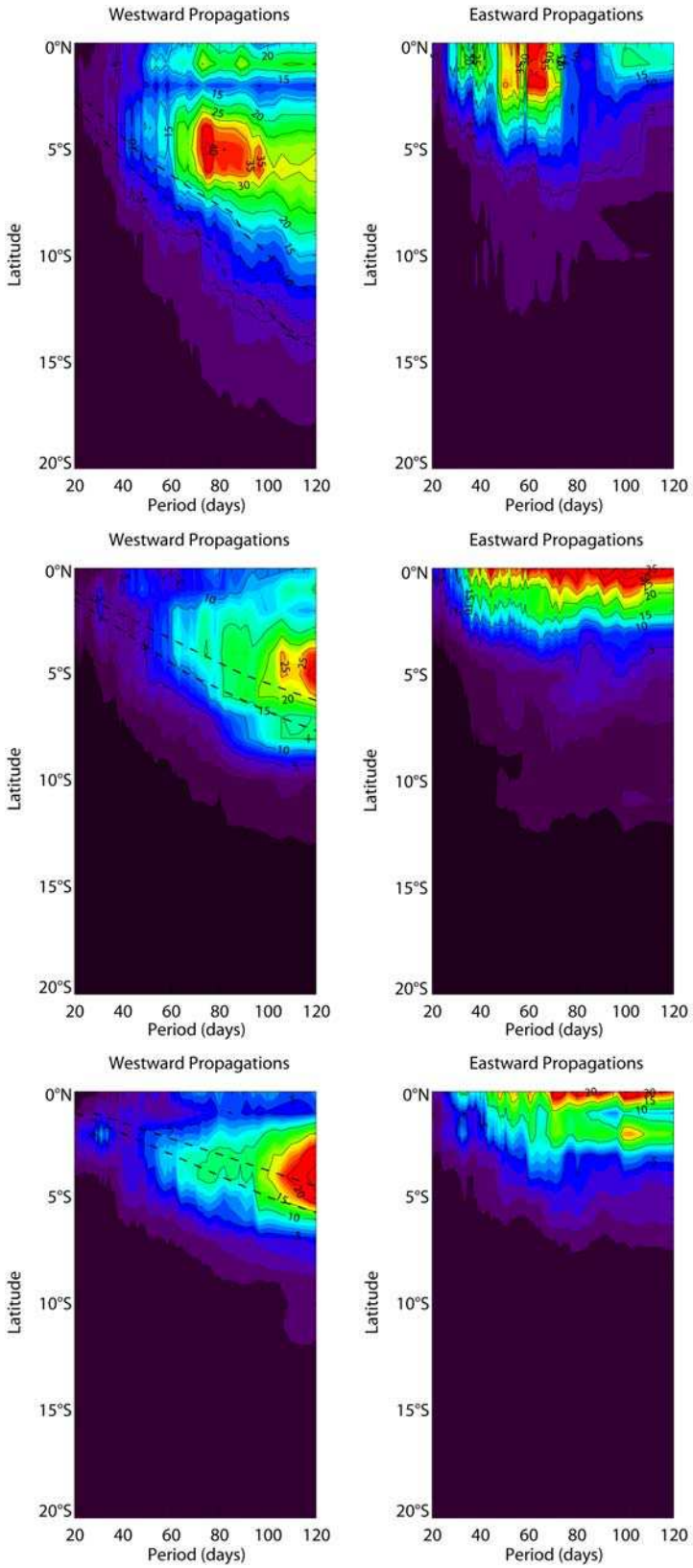

Fig. 3.26. Same as fig. 3.18 (top panel), except for ORCA and for the first (top), second (middle) and third (bottom) baroclinic modes. The upper (resp. lower) dashed lines are for the critical latitudes derived from estimates of the respective baroclinic mode phase speeds computed along the 2000m (resp. 3500m) isobath (fig. 3.16). The dotted line (top) and the black cross (middle) are for the critical latitudes from Clarke and Shi (1991).

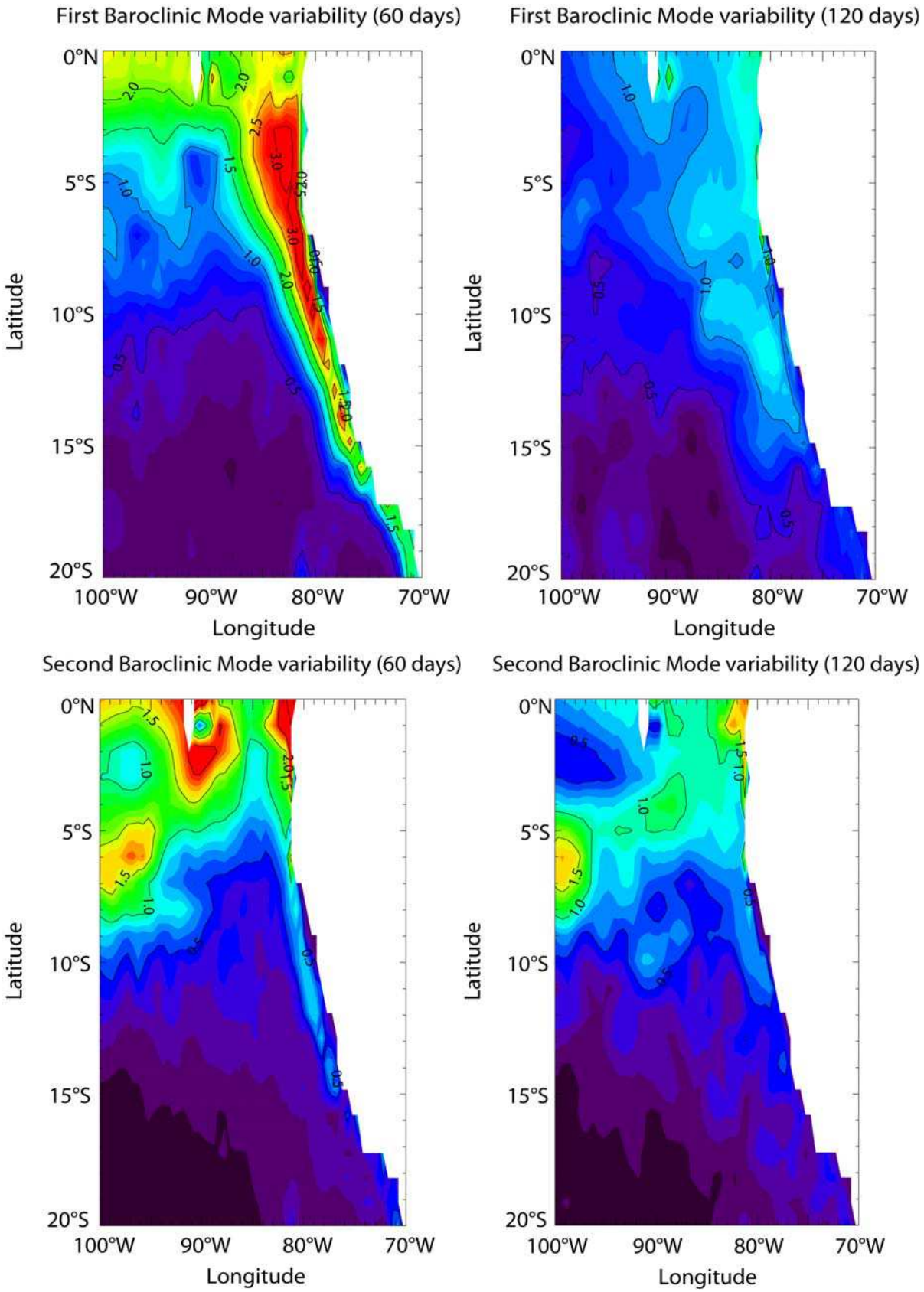

Fig. 3.27. Same as top panel of fig. 3.20, except for the ORCA model for the first (top) and second (bottom) baroclinic modes. The grid is 1/2° x 1° between 0°N and 20°S. Contour interval is 0.5cm.

to changes in the local topography rather than stratification which does not experience sharp changes along the coastline (not shown). For instance, the local increase of *S* in the ROMS model South of 20°S or even North of 7°S is due to the reduced continental shelf and slope over these areas. These small scale variations do not occur at the same latitudes in the two models because of the large differences in model topographies.

The same diagnostics used to characterize nearshore and offshore wave propagation in ROMS are repeated for ORCA. The model exhibits a very different behaviour in that Rossby wave energy agrees remarkably well with Clarke and Shi's critical latitude theory for all three baroclinic modes (fig. 3.26). Maps of baroclinic mode variability confirm that no ETRW radiation occurs South of about 10°S to 15°S (fig. 3.27).

Latitude (°S)	Mode 1	Mode 2	Mode 3
5	57	17	9
10	55	33	4
15	73	18	3
20	85	8	2
25	67	19	6
30	39	27	8
35	60	14	7

Table 3.2. Same as table 3.1 except for the ORCA model.

One may have noted that energy and variability levels are much higher than for the ROMS model: this may be due to the fact that ROMS resolves a larger number of baroclinic modes than ORCA (due to its higher resolution) so that a larger number of modes is required to account for the total sea level anomay in ROMS compared to ORCA. However, the reconstructed sea levels from ROMS and ORCA display similar levels of variability, especially in the equatorial region (not shown – see also fig.3.12 for intraseasonal sea level variability). As a consequence, results from the vertical mode decomposition for ORCA cannot be compared directly to those from ROMS in the quantitative sense; however, baroclinic modes can be used to compare model behaviour from ROMS and ORCA in the qualitative sense. Similarly to ROMS, 60-day CTW are observed along the coast at least as far South as 25°S, with slightly higher maximum variabilities ranging from 17 cm/s at 15°S to 32 cm/s at 25°S (fig. 3.28), and higher fractions of explained variance ranging from 39% to 85% (table 3.2), which is consistent with a deeper and flatter shelf and reduced bottom friction. Off central Chile at 30°S and 35°S, patterns and spectra are noisier but still display some coastal-trapped variability in the [40-60 day] band, conversely to ROMS. Lag-correlation plots (fig. 3.29) confirm the coherency between the patterns of coastal-trapped variability simulated at

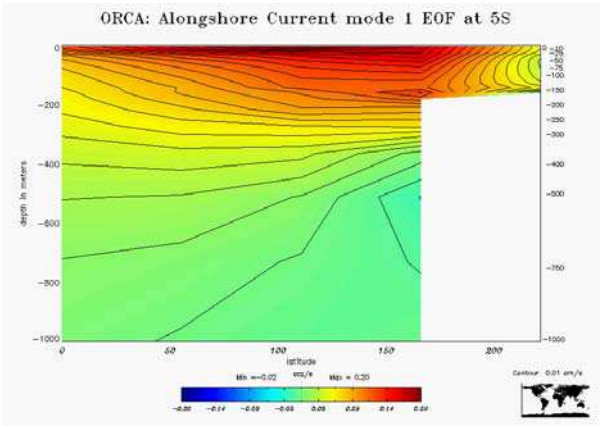
ORCA: Alongshore Current mode 1 EOF at 5S
depth in meters
latitude

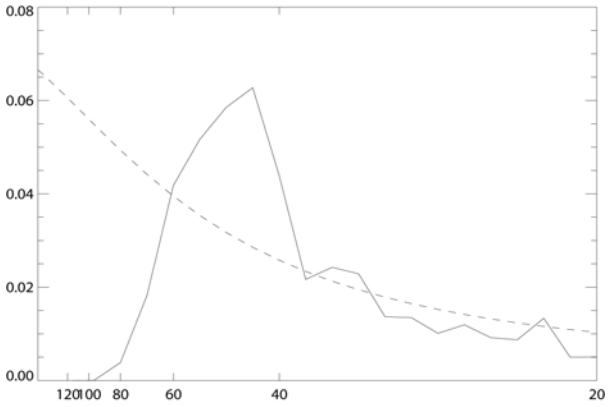
0.08
0.06
0.04
0.02
0.00
120 100 80 60 40 20

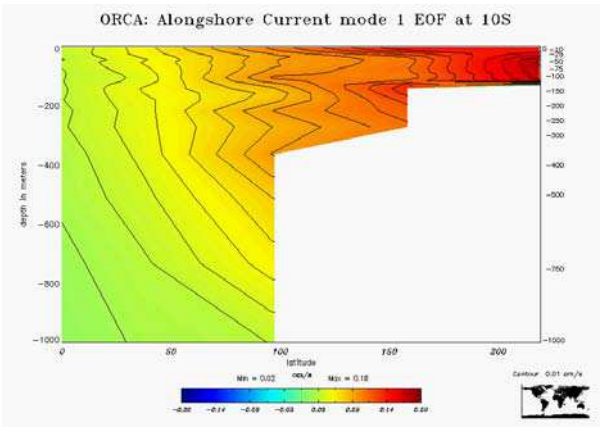
ORCA: Alongshore Current mode 1 EOF at 10S
depth in meters
latitude

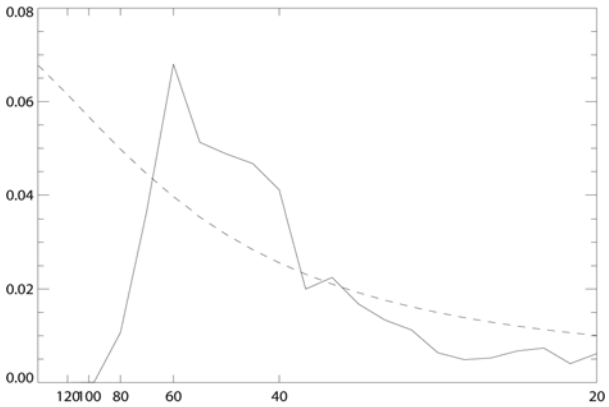
0.08
0.06
0.04
0.02
0.00
120 100 80 60 40 20

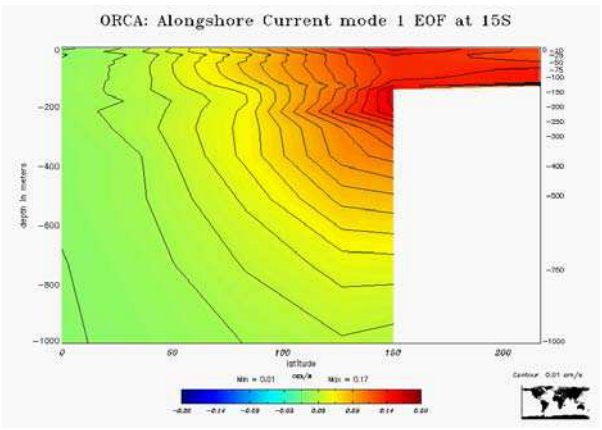
ORCA: Alongshore Current mode 1 EOF at 15S
depth in meters
latitude

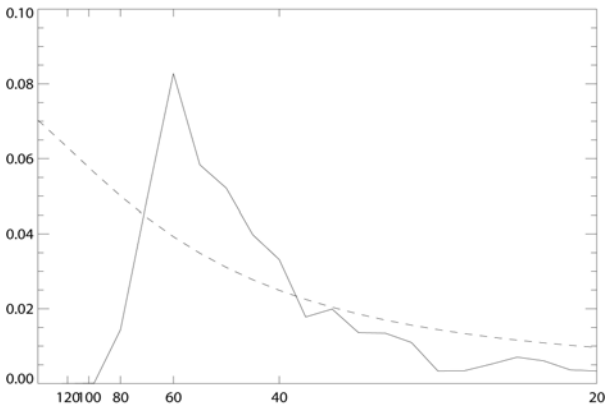
0.10
0.08
0.06
0.04
0.02
0.00
120 100 80 60 40 20

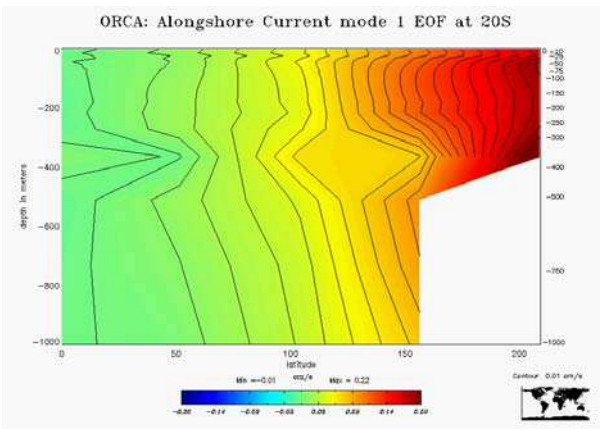
ORCA: Alongshore Current mode 1 EOF at 20S
depth in meters
latitude

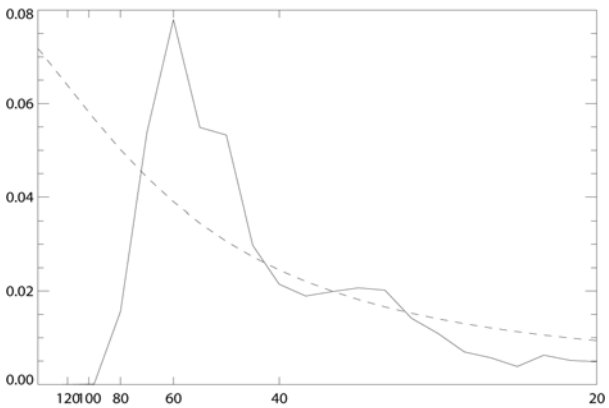
0.08
0.06
0.04
0.02
0.00
120 100 80 60 40 20

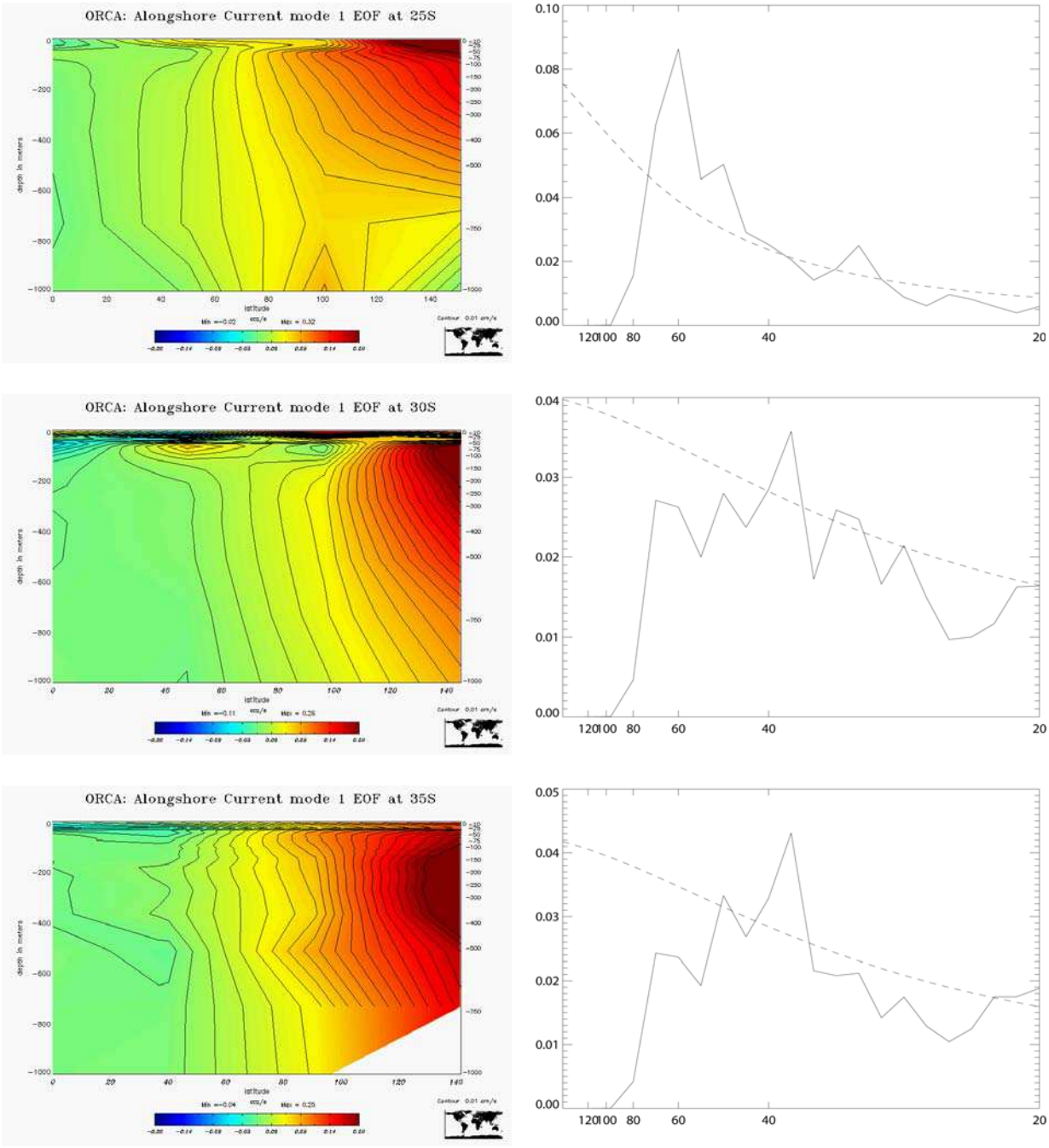

Fig. 3.28. Same as fig. 3.22, except for ORCA. EOFs were performed over 2° cross-shore sections.

different latitudes from 5°S down to 35°S, and phase speeds estimates are consistent with those from ROMS, though they are higher South of 20°S where the shelf is particularly narrow. Cross-shelf topography is sharper as expected, and has a direct influence on the cross-shore gradient of the vertical structure (fig. 3.28), as already observed for ROMS: between 5°S and 20°S, a narrow shelf ~50-100 km wide concentrates maximum current variability close to the shore in a barotropic-like structure, whereas offshore the variability has a first baroclinic mode-like structure which decays seaward at the scale of the first deformation

radius, especially at 5°S where the latter is relatively large compared to model resolution and shelf width. At 10°S and 20°S the cross-shelf scale is close to the deformation radius so that the variability is mostly barotropic and decays rapidly after the shelf break. At 25°S the cross-shelf scale of trapped variability is close to that from ROMS as the bottom is deeper there for both models. These results indicate that in the ORCA model CTW have a structure that is closer to idealized CKW than in the ROMS model, especially North of 10°S where the deformation radius is highest and South of 25°S where there is virtually no shelf, which could explain the better agreement with linear theory. On the other hand, it was previously proposed that coastline curvature could also play a role in the differences observed between ETRW propagation in ROMS and from linear theory. Though coastline angle variations in the ORCA grid agree to a large extent with those from ROMS (fig. 3.14), the coarser model resolution implies that for frequencies high enough, alongshore water particle displacements are small enough for the coastline angle to experience little change, allowing the linear approximation to remain valid to some extent. It would be interesting to test the sensitivity of the modelled critical latitude to the resolution of the grid, especially in the case of frequencies lower than intraseasonal in order to check the validity of this assumption.

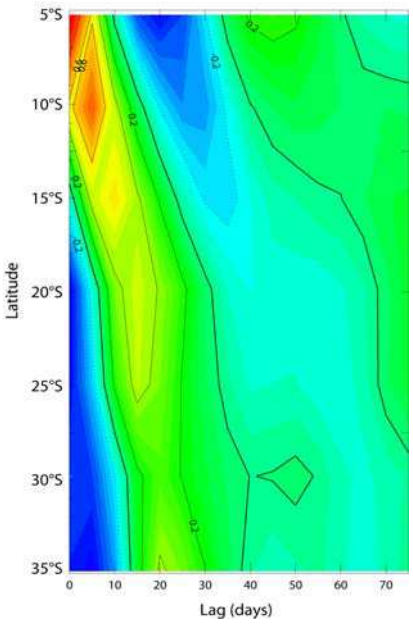

Fig. 3.29. Same as fig. 3.23, but for ORCA.

3.2.5. Discussion and conclusion

3.2.5.1. Discussion

As seen in 3.2, ROMS features westward propagation well south of the critical latitude estimated by linear theory. This behaviour might have several explanations. One is that as underlined before, the flat-bottom vertical-wall assumption behind the linear theory and used to apply the WKB approximation is rather inaccurate. This implies uncertainty on phase speeds near the coast, and thus on the critical latitude calculation, which might explain why ETRW/eddies are found South of the theoretical critical latitude, at least partly.

More generally, it means that nearshore variability cannot be accounted for by a "classical" vertical mode decomposition, because the varying topography in the cross-shore direction does not allow considering the water column at each grid point to be independent from the neighbouring points. In other words, nearshore current and pressure fields should not be projected on purely vertical modes $F_n(z)$, but on coastal-trapped modes depending on both the vertical and the cross-shore direction $F_n(x,z)$, as in Shaffer et al. (1997) or Jordi et al. (2005) for the northwestern Mediterranean who used CTW theory from the works by Chapman (1987) and Brink (1989). Unlike CKW considered in the linear theory which only differ from equatorial baroclinic waves by a no-flow condition perpendicular to the boundary, CTW have a mixed barotropic-baroclinic structure that tends towards baroclinic waves near the deep sea boundary and towards barotropic continental shelf waves near the coast.

Changes in stratification due to both the slope and coastal upwelling are likely to induce a cross-shelf gradient of baroclinic mode phase speeds c_n, which may influence the cross-shelf gradient of vortex stretching $-\frac{f}{c_n^2}p$ at a given latitude. In addition, bottom friction over the shelf and slope might modify the cross-shore gradient of alongshore velocities $\frac{\partial v}{\partial n}$ - *i.e.* relative vorticity – compared to the flat-bottom case, as suggested by figure 3.22 (compare spatial patterns at 15°S and 20°S for instance). On the other hand, bottom topography should have less effect on planetary vorticity (Killworth and Blundell, 1999). As a consequence, compared to the idealized flat-bottom vertical-wall case considered by CS91, both the relative vorticity and vortex stretching terms of the vorticity equation are likely to be modified whereas the planetary vorticity term should not, implying that for a given frequency, the critical latitude where relative vorticity starts to overtake planetary vorticity could be displaced.

Another criticable assumption made by linear theory is that the coastline be smooth enough to neglect potential effects of locally large curvature, *i.e.*

$\Delta\theta << 1$ (8), where $\Delta\theta$ is for local variation of the coastline angle.

Indeed, theories by CS91 and Grimshaw and Allen (1988) are for a nonmeridional boundary with a smoothly-varying coastline angle. Whereas such assumption remains valid for large-curvature, small-scale sectors of the coastline (such as small capes and bays or rivermouths for instance) which can be easily smoothed without diverging significantly from the real coastline, they break down in the case of larger-scale changes of the coastline direction: meridional displacements of water particles that control the planetary vorticity term are no longer associated to a unique angle θ but to several values that vary significantly over the alongshore displacements of the particles. Hence the linear relation between meridional and alongshore displacements of the particles does not hold (*i.e.* $\Delta y(t) = \Delta s(t) \sin\theta$ with a single value for θ is not verified) and the formulation (3) cannot be used. As mentioned by CS91, in such case nonlinear advection is enhanced, which modifies the vorticity equation by introducing nonlinear terms that might locally enhance or damp planetary vorticity and the associated ETRW propagation. As a consequence, the frequency-latitude threshold for planetary vs. relative vorticities is modified.

In their quantification of critical frequencies along the main ocean boundaries, CS91 identified several areas where coastline curvature is large enough to make their theory invalid, but none of them is found along the South American west coast. However, it should be noted that they used for their calculation relatively large segments compared to the Rossby radii of deformation (300km) that approximated an already highly smoothed coastline, which sometimes greatly differs from the real coastline: for instance, the northern to central Chile coast from 20°S to 40°S that they consider tends to be meridional or even to have a northwest-southeast direction on average (see their fig. 2d), whereas it is oriented in the northeast-southwest direction in the real world (fig.3.7). The Pisco-San Juan area characterized by the cape of Paracas located around 14°S followed by a rapid change of coastline angle is also quite smoothed in their study, just like the region near the territorial boundary between Peru and Chile (at 18°S).

Yet, as seen from figure 3.14, coastline curvature is large between 4°S and 8°S (Cabo Blanco area) and between 13°S and 20°S. The angle variation in these regions is of the order of 0.7 rad (40°) for the 4°S-8°S region, 0.6 rad (35°) for the 13°S-17°S region and 1.0 rad (55°) for the 17°S-20°S region, so (8) is not valid there. The 13°S-20°S region actually corresponds to the area where 120-day westward propagating oscillations of the first baroclinic mode are enhanced (figures 3.18 and 3.20), and the 4°S-8°S roughly corresponds to the corresponding area for the second baroclinic mode (figures 3.19 and 3.21). The reason why only the lower frequencies seem to be impacted by such mechanism may be that

alongshore particle displacements are higher for lower frequencies (see 1.2), making the angle variation experienced by these particles in areas of large curvature higher. However, the reason why large curvature at 4°S to 8°S affects the second mode and that at 13°S to 20°S affects the first mode is not very clear. In order to address such question, a quantification of the different terms of the vorticity equation and of their variations with latitude is needed for each of the different frequency bands of interest. Such quantification should also allow testing the hypothesis that large curvature modifies the balance between the different terms of the equation. This remains beyond the scope of the present study, but will be tested in the future.

3.2.5.2. Summary and concluding remarks

A regional eddy-permitting ocean model with boundary conditions and atmospheric forcing from the recent 1992-2000 period was used to study the influence of intraseasonal equatorial Kelvin waves with frequencies higher than $(120\ \text{days})^{-1}$ on sea level and coastal current variability off the western coast of South America. The focus is on 50- to 80-day Kelvin waves forced in the far western tropical Pacific by Westerly Wind Bursts associated to the Madden-Julian Oscillation and other atmospheric intraseasonal oscillations.

-The model is able to reproduce most observed characteristics of sea level variability, including (i) the transmission of signals of equatorial origin along the coastal wave guide, (ii) strong offshore variability off the coasts of Peru and Chile at the intraseasonal time scale as well as (iii) the cross-shore and alongshore structure of the two main coastal currents of the Humboldt Current System: the poleward Peru-Chile Under-Current and the equatorward Chile-Peru Coastal Current.

-Within the intraseasonal frequency band (T<120 days), only the 60-day CTW are efficiently trapped along the coast. The associated alongshore current variability near the coast induces strong poleward propagating 60-day frequency perturbations of the PCUC and the CPCC. These perturbations are of the order of the mean flow, which implies that the Madden-Julian Oscillation is able to modulate strongly the strength of coastal currents off Peru and Chile.

-The analysis of nearshore and offshore wave propagation reveals significant differences with linear critical latitude theory from CS91: though the meridional extension of free Extra-Tropical Rossby Wave/eddy propagation was shown to be an inverse function of wave frequency as in the linear theory, the critical latitude/frequency did not match estimates provided by CS91 for the study region. In particular, an amplification of Rossby wave propagation is observed for most intraseasonal frequencies and especially for the 120-day

harmonics South of the theoretical critical latitude, particularly for the first and second baroclinic modes. As a result, the modelled critical latitude is about 15, 10 and 5 degrees poleward from the linear estimate, which predicts the critical latitude around 15°S, 8°S and 5°S for the first, second, and third baroclinic modes, respectively.

-Two explanations were provided: first, the continental shelf and slope characterized by a cross-shore extent of the order of the first Rossby radius of deformation have a significant impact on wave propagation. Indeed, in such case CTW exhibit a mixed barotropic-baroclinic structure, conversely to the purely baroclinic CKW considered by linear theory. Bottom friction over the shelf reduces relative vorticity and thereby modifies the balance between relative and planetary vorticities, which determines the limit in the frequency-latitude space between coastal-trapped and planetary wave regimes. Whereas such mechanism should apply to most frequencies in the intraseasonal band including the 60-day oscillations, an additional mechanism is proposed for the lower frequencies of periodicity about 120 days: for these frequencies, locally large coastline curvature between 4°S and 8°S and between 13°S and 20°S are likely to introduce nonlinear advection terms in the vorticity equation, which might also participate to the local enhancement of Rossby wave propagation at these latitudes where respectively the second and first baroclinic modes would be expected to be trapped along the coast, according to linear theory.

-Such divergence from Clarke and Shi's formalism accounts for the patterns of intraseasonal sea level variability observed with altimetry in the offshore region, which is not the case for the parent coarser-resolution global model (fig. 3.12): indeed, bottom friction and nonlinear advection are damped in the former model because of a reduced continental shelf and a low resolution that limits the effect of large curvature.

These results point out the limits of using the linear theory to interprete high-resolution model solutions, at least in the case of intraseasonal wave propagation in the eastern South Pacific region. They may also provide background material for the intercomparison of different regions sharing some characteristics with HCS: for instance, most coastlines of the world ocean have a continental shelf width of the same order as the deformation radii or even higher. As a consequence, critical latitudes estimated with linear theory neglect nonlinearities that might have a significant effect on CTW and ETRW propagation as in the HCS. Such nonlinearities may thus have to be taken into account in order to describe free wave motion along other ocean boundaries. Moreover, effects due to

large curvature should be investigated as well because the approximations made by CS91 on coastline angle variations might hide other regions where curvature cannot be neglected.

Chapter 4: Conclusion and perspectives

In the following, we first present the obtained results of direct interest for downscaling experiments of climate projections over the ocean off Peru and Chile, before we focus on the scientifical advances brought by the present PhD thesis. We also summarize a few additional results obtained in collaboration with other colleagues in the framework of the PCCC (Peru-Chile Climate Change) program. Last, we review the main limitations of the present work, and provide a few perspectives for future research.

4.1. Main findings in relation to PCCC

The main idea behind both this work and the PCCC program is to use projections of future global warming provided by CGCMs of the Intergovernmental Panel on Climate Change Fourth Assessment Report (IPCC-AR4) to investigate the response of the eastern South Pacific (ESP) circulation simulated by ROMS (Regional Ocean Modelling System), an eddy-resolving regional ocean model. The present thesis brought two major contributions to the PCCC program: a methodology for the selection of the « best » climate models in the study region (chapter two), and the analysis of a regional interannual simulation of the HCS, with a focus on the role of the remote forcing by equatorial Kelvin waves on intraseasonal time scales (chapter three). The analysis of this control run is a reference to benchmark climate change downscaling studies.

Instead of studying the response of the HCS to global warming as expected from 'realistic' projections of greenhouse gas (GHG) emissions in the atmosphere for the XXIth century (the so-called SRES scenarios), we prefered choosing idealized experiments with a stronger than expected increase in atmospheric GHG concentrations. The motivation for such choice was threefold: 1) considering systematic biases of CGCMs of the current generation in the eastern tropical and South Pacific, the diversity of their responses to global warming, and large uncertainties in the SRES scenarios that depend on many assumptions and approximations in regard to future adaptation of human societies to global warming, it was decided to give up the idea of attempting to provide a 'realistic' prediction for future regional climate change that could become null and void in the next few years with the advent of improved CGCMs and climate scenarios; 2) such idealized scenarios with strong global warming allow maximizing the signal-to-noise ratio; and 3) focusing on the physical mechanisms at stake from different test cases addressing some of the theories currently proposed by the scientific community.

Two criteria were chosen to select the best models among the ensemble: 1) the representation of large-scale ENSO dynamics and properties, and 2) the simulated temperature and momentum fields at the boundaries of the domain chosen for the downscaling. An additional criterion of importance for the HCS would be the atmospheric forcing. However, most CGCMs poorly represent low-level winds and air/sea fluxes in this region and especially near the coast, which introduces strong biases in the ocean circulation. A parallel work on statistical downscaling of the wind forcing from the CGCMs was carried

out by Dr. Katerina Goubanova in the framework of the PCCC program to address this issue (see 4.3). A simple procedure of flux correction was also applied (see chapter one). As a consequence, and because few CGCMs were shown to reproduce both ENSO dynamics and mean oceanic state at the boundaries of the regional domain, the atmospheric forcing was not retained as a criterion of selection. However, it has still been assessed for information purposes.

Basin-scale ENSO mechanisms:

A study of the physical mechanisms that control ENSO-like variability in pre-industrial simulations performed with 23 CGCMs (see chapter two) allowed identifying the most reliable models in terms of basin-scale interannual equatorial variability: the « hybrid » models, with a combination of zonal advective and thermocline feedbacks like in SODA (Simple Ocean Data Assimilation), an ocean reanalysis spanning the period 1958-2001 and taken as a reference. The 6 models identified as « hybrid », which have an ENSO time scale closer to the observed on average and best represent the main coupled processes that control SST variability, should provide the most reliable predictions of ENSO evolution under global warming, assuming that a good reproduction of ENSO feedbacks ensures a better constrained sensitivity of ENSO to climate change than for the other models. In order to further diagnose large-scale ENSO variability in these models, spatial and temporal characteristics of ENSO were compared to SODA: four models clearly stand out as more 'realistic', whereas the remaining two feature several biases, including a biennial ENSO (CSIRO-MK3.0) and a peak of SST variability displaced towards the western Pacific (INM-CM3.0). These two CGCMs were therefore excluded from the rest of the study and only the four 'best' hybrid CGCMs were analyzed at the boundaries of the domain that was considered for the downscaling experiments.

Analysis of the eastern Pacific mean state and variability:

The western boundary of the regional model domain was shown to concentrate 80-90% of the exchanges between the ESP and the South Pacific basin for the coupled models as well as for reanalyzed data from SODA and for an interannual simulation performed with ORCA, an Ocean General Circulation Model (OGCM). The equatorial band at 100°W between 10°S and 10°N actually concentrates most of the variability, which motivated us to restrict the analysis to the first few hundred meters of this vertical section. To our knowledge, so far no study has been dedicated to the sensitivity of the regional ocean circulation to the

eastern equatorial Pacific mean state and variability: for this reason, the modelled temperature and velocity fields were compared to reanalyzed and observed data (when available) for different frequency bands, and the selection process was based on CGCM skill assessment. Results point out heterogeneous behaviour among the models: warm or cold biases, over- or under-estimated seasonal cycles, presence or absence of some equatorial currents like the South Equatorial Current (SEC), the Southern Sub-Surface Counter-Current (SSSCC), and the North Equatorial Counter-Current (NECC). On the other hand, some errors are systematic within the model ensemble: too weak Equatorial Under-Current (EUC) and SEC, the absence of westward flow below 150 to 200m depth, a too shallow thermocline at the equator, an excessive stratification in the cold tongue region, an excessive low-frequency modulation of the seasonal cycle, and under-estimated interannual variability. UKMO-HadGEM1 best represents the equatorial current system, but features a strongly biased temperature field. Conversely, IPSL-CM4 and INGV-ECHAM4 have quite 'realistic' equatorial surface and subsurface temperature, and fairly 'realistic' currents. In addition, some of the required data for the downscaling were not available for UKMO-HadGEM1, whereas they are easily accessible for the latter two models. For these reasons, the IPSL-CM4 and INGV-ECHAM4 models were the two models finally retained for the regional downscaling experiments.

In spite of the demonstrated skills of these two models in the tropical Pacific and ESP, there is *a priori* no garantee that the regional circulation simulated by ROMS with IPSL-CM4 and/or INGV-ECHAM4 forcing under preindustrial climate will resemble the observed. For this reason, a regional control simulation with realistic boundary and surface forcings over the 1992-2000 period was performed and appeared to agree rather well with the available observations: in particular, the simulated equatorial sea level variability is both transmitted along the coastal wave guide and reflected offshore. The simulation is also able to represent the poleward Peru-Chile Under-Current (PCUC) and the equatorward Chile-Peru Coastal Current (CPCC). The simulation was then used to investigate the remote forcing of coastal sea level and currents by coastal-trapped waves of equatorial origin (see chapter three).

4.2. Scientific outreaches

ENSO mechanisms:

To assess the impact of ENSO on the HCS under a warmer climate, it was decided to investigate the physical mechanisms of ENSO as represented by CMIP3 models under

preindustrial climate: indeed, such mechanisms can help to interprete the biases in ENSO variability exhibited by coupled climate models, and their evolution with global warming. The study of the physical mechanisms of ENSO makes use of LODCA (Linear Ocean Dynamically Coupled with the Atmosphere), an intermediate coupled model of the tropical Pacific with prescribed mean stratification and wind forcing so as to derive explicitly the tendency terms of the mixed layer heat budget in the climate models. Whereas in agreement with previous studies, the dominant terms of the heat budget are the advection of mean temperature by the zonal current anomalies ($u'\frac{\partial \overline{T}}{\partial x}$) and the advection of temperature anomalies by the mean upwelling ($\overline{w}\frac{\partial T'}{\partial z}$) for most models, the terms that most account for biases in total zonal (resp. vertical) advection were found to be the advection of temperature anomalies by the mean zonal (resp. vertical) currents, *i.e.* $\overline{u}\frac{\partial T'}{\partial x}$ (resp. $\overline{w}\frac{\partial T'}{\partial z}$), underlining the influence of mean circulation characteristics on the dynamics of ENSO. These results also extend the classical vision of the zonal advective feedback and the thermocline feedback that generally refer to $u'\frac{\partial \overline{T}}{\partial x}$ and $\overline{w}\frac{\partial T'}{\partial z}$ alone, and raise the question of the importance of $\overline{u}\frac{\partial T'}{\partial x}$ that may have to be taken into account together with $\overline{w}\frac{\partial T'}{\partial z}$ in order to understand the simulated characteristics of ENSO. The mean surface zonal currents $\overline{u}$ in the western equatorial Pacific and the mean upwelling at the base of the mixed layer $\overline{w}$ in the eastern equatorial Pacific were used as proxies for the strength of respectively the zonal advective feedback and the thermocline feedback, which lead to the definition of a model classification according to the dominant ENSO process: models with a dominant zonal advective feedback, models with a dominant thermocline feedback, and « hybrid » models with a combination of both. Consistently with theory, models with a dominant zonal advective feedback (resp. thermocline feedback) were found to be characterized by a shorter (resp. longer) ENSO cycle on average. This study (Belmadani et al., 2010) was accepted by the *Journal of Climate* on 28th January 2010 (chapter 2, section 1.) and is currently in press. A note focusing on the main results and completed by a review of the existing literature on ENSO feedbacks has also been accepted for publication in the proceedings of the French-Russian seminar entitled *« Climate variability in the tropical Pacific: mechanisms, modelling and observations »* and held in

Moscow (Russia) from 13th to 15th April 2009 (Belmadani and Dewitte, 2010). It is in press at the time of impressing the present manuscript.

Near-Annual Mode/ENSO interactions:

In addition, a near-annual mode (NAM), a coupled mode of tropical Pacific variability associated to the ocean basin mode involving equatorial Kelvin and Rossby wave propagation, was also diagnosed in the model ensemble. Its role on the ENSO feedbacks was documented: results show that the NAM is enhanced for models with a dominant zonal advective feedback and damped for models with a dominant thermocline feedback. It is suggested that the NAM, which is associated to anomalous surface zonal flow in the western equatorial Pacific, is able to interact with ENSO through nonlinear zonal advection. These nonlinearities contribute to the cold bias exhibited by most models over the western Pacific warm pool.

Propagation of intraseasonal equatorial variability into the HCS:

High-frequency processes in the equatorial Pacific also have an impact on the mean ocean circulation in the HCS: equatorial Kelvin waves (EKW) at intraseasonal frequencies are the most efficiently trapped along the west coast of South America, according to linear theory. Hence the simulated large-scale characteristics of intraseasonal EKW and their changes under global warming are likely to influence coastal upwelling and regional circulation in the ESP. In addition, the intraseasonal variability associated to such long baroclinic waves is strongest during El Niño events, which means that the impact of ENSO on the HCS (such as that described by Colas et al. (2008)) is partly related to that of the intraseasonal EKW. It is also worth noting that the latter were shown to be modulated at decadal time scales, and that such modulation is not directly related to the dominant coupled modes of tropical Pacific climate variability (Dewitte et al., 2008b). As a consequence, long-term trends observed along the Peru-Chile coast might be related to those of intraseasonal equatorial variability, and its evolution with global climate change.

These statements motivated us to analyze the remote forcing of nearshore variability off Peru and Chile in the regional control simulation by coastal-trapped waves of equatorial origin. It was found that the critical latitude, which separates the region of planetary Rossby wave propagation to the North from the region of coastal-trapped wave propagation to the South, is 5 to 15 degrees higher in the model than that predicted by linear theory for all baroclinic modes, especially for 120-day oscillations. We suggested two distinct mechanisms

that may modify the vorticity equation and combine to explain such behaviour: the effect of bottom friction over the continental shelf and slope, which is likely to have a direct influence on relative vorticity and planetary vorticity, and the nonlinear advection introduced by locally large curvature off northern Peru (4°S to 8°S) and off southern Peru to northern Chile (13°S to 20°S). Results from the coarser resolution parent ORCA model featuring a narrower shelf with reduced bottom friction and limited effect of large curvature are in better agreement with the linear theory. Whereas ROMS exhibits significant offshore variability south of the theoretical critical latitude like in altimetric data, it is absent from ORCA: we suggest that nonlinear effects related to bottom topography and coastline curvature have to be taken into account in order to understand such variability, highlighting the limits of linear theory in the ESP. The regional model also confirms the strong impact of 50- to 80-day coastal-trapped waves on the PCUC along the coasts of northern Peru down to central Chile, which has previously been observed in the latter region. Moreover, it is shown that such waves also have a strong influence on the CPCC, which suggests potential impacts on nearshore mesoscale eddy activity.

Overall, these advances in the understanding of the large-scale equatorial processes that influence the Peru-Chile upwelling system are complementary to the downscaling methodology addressed by the PCCC program. In particular, they raise the question of the importance of high frequency processes and their changes for the future behaviour of the HCS. Such processes may be only partially taken into account by PCCC, since only monthly CGCM outputs are currently available for the downscaling experiments (see below).

4.3. Additional results in the framework of the PCCC program

Future changes in the alongshore winds:

A statistical downscaling methodology was proposed by Goubanova et al. (2010) in order to correct biases in the coarse-resolution surface wind fields simulated by CGCMs over the ESP, and applied to the IPSL-CM4 model. According to their results, a strengthening of the large-scale meridional pressure gradient over the eastern subtropical Pacific is associated to an increase of surface along-shore winds by ~10-20% off central Chile during austral winter in the $4xCO_2$ simulation relatively to the Pre-industrial simulation, in agreement with results from Garreaud and Falvey (2008). However, further north off central Peru, they found that surface along-shore winds decrease by ~10% during austral summer, in contrast to those

of Bakun (1990) and Bakun and Weeks (2008) suggesting an observed increase off Peru in recent years. Importantly, such simulated trends were shown to be coherent with those exhibited by the ensemble mean across CMIP3 models (eleven CGCMs providing the data needed to perform downscaling exercices). The authors argue that the trend inferred by Bakun (1990) may be related to decadal variability rather than anthropogenic climate change, as a wind regime shift is clearly visible in the early 1970s in the data analyzed by Bakun (1990), and since coastal winds off northern Peru do not exhibit any significant trend over the 1949-1972 period (Wyrtki, 1975). On the other hand, Falvey and Garreaud (2009) found a slight warming trend in the surface ocean off northern Peru for the recent period from ERSST analyzed data (Smith and Reynolds, 2004), suggesting a possible decrease in upwelling-favorable winds, which is consistent with the predicted weakening of the tropical Pacific easterly trade winds (Vecchi et al., 2006; Vecchi and Soden, 2007).

Goubanova et al. (2010) also found an average 15-25% decrease in annual mean wind intra-seasonal variability all along the coast, and strongest in the coastal jet area off central Chile. Such changes are interpreted as the result of a weakening and poleward displacement of the Hadley circulation cell in the Southern hemisphere (Bengtsson et al., 2006; Gastineau et al., 2008), which act together with the reduction of the mean Walker circulation (Vecchi et al., 2006; Vecchi and Soden, 2007) to weaken and displace the subtropical High southwards, and to decrease the occurrence of extreme wind events over the tropics (Gastineau and Soden, 2009). Simply put, an extension to the South of warmer tropical climate is likely to shift the wind regime off central Chile to a trade wind regime characterized by stronger and steadier alongshore winds. Conversely, off Peru the reduced Walker and Hadley circulations in a warmer climate would lead to a decrease in both wind strength and variability.

Impact on coastal upwelling and mesoscale dynamics:

Based on these results, Echevin et al. (*in prep.*) studied the influence of such changes in the alongshore winds on the seasonal cycle of coastal upwelling and of the associated currents and mesoscale activity off Peru and Chile. They found that the strong 5-6°C warming of the surface ocean off central Peru in the $4xCO_2$ simulation increases the stratification near the coast, which enhances the equatorward CPCC. In addition, the intensification of the EUC in the IPSL-CM4 model (Marti et al., 2009) drives a wider and thicker poleward PCUC in the regional simulation. This induces an enhanced vertical shear stress between the CPCC and the PCUC, which results in a strong increase in eddy kinetic energy (EKE) near the coast in the northern part of the HCS. On the other hand, coastal

upwelling is found to decrease off Peru and northern Chile and to increase off central Chile, consistently with changes in the surface winds (Goubanova et al., 2010). In order to test the sensitivity of these results to future wind changes, Echevin et al. (*in prep.*) increased 4xCO_2 alongshore winds by 50%, thereby reproducing wind conditions closer to those predicted by Bakun's hypothesis off Peru (Bakun, 1990 – see chapter one): according to their results, the increase in coastal upwelling induced by stronger winds will increase the cross-shore density gradient and hence the strength of the surface and subsurface coastal currents. Compared to the standard 4xCO_2 simulation, a significant increase in EKE off both northern Peru and central Chile is observed, suggesting that the increase in coastal winds cannot compensate the dynamical effects of the strong surface warming induced by a 300% increase in GHG emissions (*i.e.* by CO_2 quadrupling).

Overall, despite the numerous limitations of the studies by Goubanova et al. (2010) and Echevin et al. (*in prep.*) (such as the use of downscaled fields from a single CGCM, or the choice of the idealized 4xCO_2 scenario for instance), predicted changes in alongshore winds and coastal upwelling agree rather well with tendencies inferred from historical wind, SST and surface chlorophyll measurements from the recent period: the response of the HCS to global warming seems to be sensitive to latitude, with stronger winds and coastal upwelling off Chile, and slightly weaker winds and upwelling off central to northern Peru. The increase in upwelling-favorable winds off Chile is also consistent with previous modelling studies, and with evidence from past and modern climate change inferred from paleo-proxies. Off Peru, changes in both surface winds and SST are in contradiction with Bakun's hypothesis. Bakun and Weeks (2008), though recognizing the proximity of Peru to the equator as a unique factor compared to other eastern boundary upwelling systems (EBUS'es), discard the potential effect of a large-scale weakening of Walker and Hadley circulations: they argue that the disconnection of coastal winds from the Pacific trade winds during El Niño events is likely to become permanent under global warming, which is expected in their study to result in a 'permanent' El Niño-like mean state in the equatorial Pacific, *i.e.* in a collapse of the zonal gradients of SST and thermocline depth, conditions which have been suggested to prevail during the Pliocene, about 3-5 million years ago (Fedorov et al., 2006). However, the relationship between alongshore winds and large-scale atmospheric circulation remains poorly understood so far, which raises doubt on the interpretation proposed by Bakun and Weeks (2008). In addition, results from high-resolution ocean modelling show that with a moderate 50% wind change off Peru, in the case of a strong global increase in surface temperatures,

warming of the surface ocean will enhance turbulence in the nearshore region, with potential negative impacts on small pelagic fish recruitment (Echevin et al., *in prep.*).

4.4. Limitations and perspectives

There are of course many limitations to the study reported in the present dissertation:

- **Model resolution**: due to limited computer resources, the chosen 1/6° horizontal resolution (~18.5km at the equator, ~14km at 40°S) is a compromise between the resolution of mesoscale eddies (the first Rossby radius of deformation ranging from ~210km at the equator to ~20km at 40°S) and computational costs. However, as a significant fraction of mesoscale activity can be found off central Chile down to ~35-40°S, ideally the resolution needed to correctly represent such features would be around 5-10km, as in the 1/15° configuration of ROMS (~7.5km at the equator, ~5.5km at 40°S) used by Colas et al. (2008). In addition, according to Capet et al. (2009), increasing resolution in regional eddy-resolving models should improve the representation of submesoscale processes such as fronts, meanders and filaments associated to coastal upwelling, which was confirmed off the Peru coast by McWilliams et al. (2009). These small-scale processes are all the more important that they can have a rectifying effect on larger-scale variability (Capet et al., 2008) and biogeochemical processes (Lévy et al., 2001). Besides, increased model resolution should allow accounting for the fine-scale spatial structure of the alongshore winds very close to the coast, and thus representing more accurately the contribution of Ekman pumping to coastal upwelling (see below). A cost-efficient method to achieve this is multiple grid nesting (fig. 4.1), though it presents the inconvenient of being limited to reduced geographic areas. It could however provide interesting results for impact studies in specific sub-regions of the HCS, through coupling with biogeochemical and individual-based models (*e.g.* Brochier et al., 2008) for instance (see below).

- **Wind forcing**: the 9-year period covered by ERS satellite measurements (Bentamy et al., 1996) presents the advantage of spanning contrasted background states of the tropical Pacific, including the strong 1997-98 El Niño. In contrast, QuickSCAT satellite measurements (CERSAT, 2002) are only available from July 1999: at the time of starting the PhD thesis, only 7 years of data were available, versus 10 years at the time of writing. ERS winds were thus chosen to force ROMS in the regional control run (CR), though QuickSCAT winds were shown to be more accurate in the ESP, especially between 17°S and 26°S (Croquette et al., 2007). In addition, for the purpose of comparing the climate change

downscaling experiments performed by Echevin et al. (*in prep.*) to the CR, the use of QuickSCAT winds to force the latter would yield better consistency, as the statistical atmospheric model built by Goubanova et al. (2010) is based on QuickSCAT data.

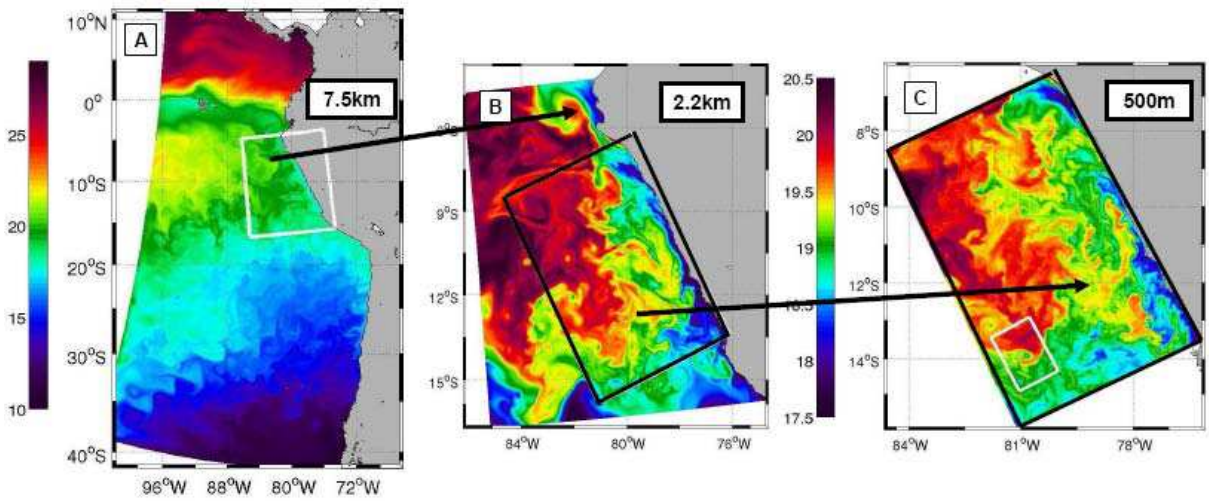

Fig. 4.1: Schematic of a multiple offline nesting strategy for the HCS, from large-scale to sub-mesoscale processes: (**A**) 1/15° configuration of the ROMS model for the ESP used by Colas et al. (2008); (**B**) nested grid (2.2km resolution) of the northern and central Peru coastal ocean; (**C**) 500m-resolution grid nested in (B) for the central Peru coast. Maps are for simulated SST (°C). Color scale for (A) (resp. for (B) and (C)) is indicated on the left (resp. right) side of the figure. *F. Colas, personal communication*.

Another issue related to the wind forcing is its cross-shore structure in the very nearshore region, which presents a drop-off zone in the first 30-50 kilometers from the coast (Capet et al., 2004; Renault, 2008), a distance of the order of the grid cell for both ERS and QuickSCAT wind data (0.5°). Hence the ROMS simulations forced by observed or downscaled winds cannot take this process into account, despite its significant influence on coastal upwelling through the associated wind stress curl and Ekman pumping (Bakun and Nelson, 1991; Halpern, 2002): for instance, Capet et al. (2004) used an atmospheric model to extrapolate QuickSCAT winds near the coast, which significantly improved the representation of coastal upwelling and associated currents in a ROMS simulation of the California Current System. An alternative is proposed by Colas et al. (2008b, 2009), who apply the empirical relations between SST and surface winds developed by Chelton et al. (2001) and Chelton et al. (2007) to the SST simulated by ROMS for the HCS (same configuration as in Colas et al., 2008) with QuickSCAT wind forcing. The surface winds obtained in the drop-off zone are used to correct QuickSCAT data, which eventually provides the wind forcing for ROMS: results show a clear improvement in the simulated nearshore SST, CPCC, PCUC and offshore EKE. QuickSCAT winds corrected with such procedure could be used in the future for the

wind forcing of the CR, and to downscale CGCM winds with the method of Goubanova et al. (2010) and test the potential effect on the simulated surface ocean warming.

- **Open boundary conditions**: in this study, the selection of CGCMs at the western boundary of the regional model was based on systematic comparison of simulated upper ocean equatorial temperature and velocity fields with reanalyzed and observed data. For practical reasons of CGCM data availability, the 'realism' of the simulated temperatures was prefered to that of the equatorial currents. However, in order to gain confidence in the relevance of such choice, the sensitivity of the regional dynamics of the HCS to the boundary forcing should be tested: in particular, how do biases in the EUC and Tsuchiya Jets or in the equatorial temperature influence coastal upwelling processes ?

Echevin et al. (*in prep.*) used a 1/9° ROMS configuration for the Peru coast (Penven et al., 2005) forced by three different OGCMs and by climatological data to investigate this question. They found that the PCUC was poorly correlated to EUC flow, consistently with recent studies, which point out that the source of PCUC waters comes mainly from the SSSCC and only minorily from the EUC (Croquette, 2007; Montes et al., 2009). However, the model configurations of Echevin et al. (*in prep.*) and Montes et al. (2009) have their western boundary at 90°W, just east of the Galapagos islands, conversely to the configuration used here. The splitting of the SEC and of the EUC around the islands in the parent models influence the boundary conditions, which is not the case in our configuration: the fact that the PCUC is more related to the SSSCC than to the EUC in their configuration does not exclude that part of SSSCC flow at 90°W could come from the EUC more to the west, *i.e.* maybe west of 100°W. In this case, the role of the EUC at 100°W on the nearshore currents and upwelling could still be significant. On the other hand, the low-frequency modulation of water mass characteristics in the HCS was recently shown to originate mainly from extra-equatorial zonal jets in the offshore region (Montes et al., 2009). Because such fluctuations are likely to induce changes in the slowly-varying mean stratification and hence in the mean circulation of the HCS, the analysis of the dynamics of these jets and their connection with large-scale circulation of the South Pacific Ocean might help understanding the low-frequency response of the HCS to global warming. Clearly, more work is needed in order to understand the influence of large-scale currents and water mass properties on the simulated dynamics of the HCS.

An unexpected result of the present work is the factor two between equatorial flow from SODA or TAO data and that from the coupled models or ORCA at the western boundary. Indeed, according to Echevin et al. (*in prep.*), SODA overestimates mean velocities

in the cores of the EUC and of the SEC by a factor two relatively to TAO data, whereas ORCA displays more realistic values. The choice of ORCA for the boundary forcing of the CR was partly motivated by the results inferred by Echevin et al. (*in prep.*) at 90°W, but it is shown here that SODA is more appropriate for the forcing of the ROMS model at 100°W. In the framework of the ANR-funded Peru Ecosystem Projection Scenarios (PEPS) program (see below), an interannual simulation over the period 1992-2000 has recently been performed by G. Cambon with SODA forcing and is currently being analyzed and compared to that with ORCA forcing. Forcing from Drakkar (Barnier et al., 2006; Molines et al., 2006), a long ocean reanalysis spanning the last fifty years will also be tested.

- **Simulation length and warming scenarios**: as underlined before, we deliberately chose to perform 10-year simulations (Echevin et al., *in prep.*) under stabilized Pre-industrial and 4xCO_2 climate rather than longer (*e.g.* 50 years) model runs under the more realistic 20th century climate and SRES scenarios, because of biases in state-of-the-art CGCMs and computational costs. As a consequence, the simulations analyzed by Echevin et al. (*in prep.*) bear a very strong warming (5°C or more for the surface ocean) that will probably take a century or more to occur in the real world (IPCC, 2007). It was shown that this warming is too strong to be compensated by a possible increase in alongshore surface winds. However, a transient response of the ocean to global warming with, say, an increase in upwelling-favorable winds seems like a possible hypothesis. This would induce a cooling of the ocean, which would be slowly compensated by the increasing radiative forcing until the latter takes over, leading to the situation described by Echevin et al. (*in prep.*). For a sustainable management of the fisheries of Peru and Chile (see the introduction of this dissertation), adaptative measures need to be taken in the near future in regard to the ongoing global climate change: in this context, a study of the long-term response of the HCS to the transient phase of IPCC scenarios with continuously increasing GHG emissions is necessary. It could be carried out with the CO_2 quadrupling scenario to garantee a good consistency with results inferred from the stabilized phase, or with SRES scenarios, with the hope of being able to simulate trends in surface winds and SST similar to those recently observed off the coasts of Peru and Chile. In any case, such trends can only be inferred from model runs of the order of 50 years (or more), which are computationally expensive. Nevertheless, a long historical control run is being prepared by V. Echevin and B. Dewitte in the framework of PEPS, over the 1958-2007 period spanned by SODA 2.0.2-4 (Carton and Giese, 2008) and by downscaled ERA-40 winds (Uppala et al., 2005), and will be used as a baseline for downscaling experiments performed under 20th century climate and SRES climate. In the long run, CMIP5 CGCMs and

climate scenarios prepared for IPCC-AR5 will start to be made available in 2010, and should be used in the future for hopefully more reliable downscaling experiments. There are numerous near-term and long-term AR5 scenarios, such as the RCP (Representative Concentration Pathways) experiments in which future GHG emissions are designed to reach a given level of radiative forcing by 2100 (Moss et al., 2008), so a specific work of scenario selection will need to be carried out.

- **Coupled climate models**: due to a lack of time, so far only the IPSL-CM4 model, identified in this thesis as the most reliable CGCM for our region, was downscaled in the framework of the PCCC program. In order to increase our confidence in the projected changes of the regional ocean circulation, other climate models will need to be downscaled in a similar way, with a priority for INGV-ECHAM4 which was also identified here as more reliable than the other IPCC models. Moreover, with the next generation of climate models, other candidates might also provide appropriate boundary conditions for ROMS. For instance, the INM-CM4.0 model developed by the Institute of Numerical Mathematics (INM) of the Russian Academy of Science, with increased atmospheric and oceanic resolutions and improved climate feedbacks (*e.g.* cloud feedback in the western tropical Pacific) was shown to correct most biases of the former INM-CM3.0 in the tropical Pacific (Volodin and Diansky, 2004), including the displaced SST variability over the warm pool (E. M. Volodin, *personal communication*). It could be interesting to test the behaviour of this model in regard to ENSO feedbacks and eastern equatorial Pacific dynamics, since the previous generation INM-CM3.0 was shown here to belong to the hybrid model category: a collaboration between IRD (Institut de Recherche pour le Développement) and INM is currently under construction to test the impact of climate change simulated by this model on the HCS.

- **Monthly CGCM outputs**: the comparison of intraseasonal variability of ORCA at the western boundary of ROMS for 5-daily outputs and for monthly means revealed that the latter damp high-frequency variability by a factor two (see chapter two). Indeed, long intraseasonal equatorial Kelvin waves (IEKW) are absent for frequencies higher than (60 days)$^{-1}$ in the monthly averages, and the associated sea level anomalies are reduced by a factor 1.5-2 for frequencies between (60 days)$^{-1}$ and (120 days)$^{-1}$ (fig. 4.2). Monthly CGCM outputs are thus likely to miss a significant fraction of changes in IEKW activity and in its possible impacts on the dynamics of the HCS: indeed, the MJO, which is responsible – together with other modes of intraseasonal atmospheric variability over the western tropical Pacific – for the triggering of IEKW over the warm pool region, is modulated at decadal time scales and is more active since the 1970s climate shift due to increased warming of the Indo-Pacific region

(Slingo et al., 1999). Predicted changes in the mean climate of the tropical Pacific, which include a stronger warming of equatorial SSTs than off the equator and a weakening of the Walker circulation and of the associated trade winds (Fedorov et al., 2006; Hansen et al., 2006; Vecchi et al., 2006, 2008) are thus likely to set favourable conditions for the development of WWB through the extension of the western Pacific warm pool, and may thereby increase IEKW and CTW activity in the eastern South Pacific. A recent study by Dewitte et al. (2008) is in agreement with this hypothesis: a positive trend for IEKW activity is observed over the period 1961-1998.

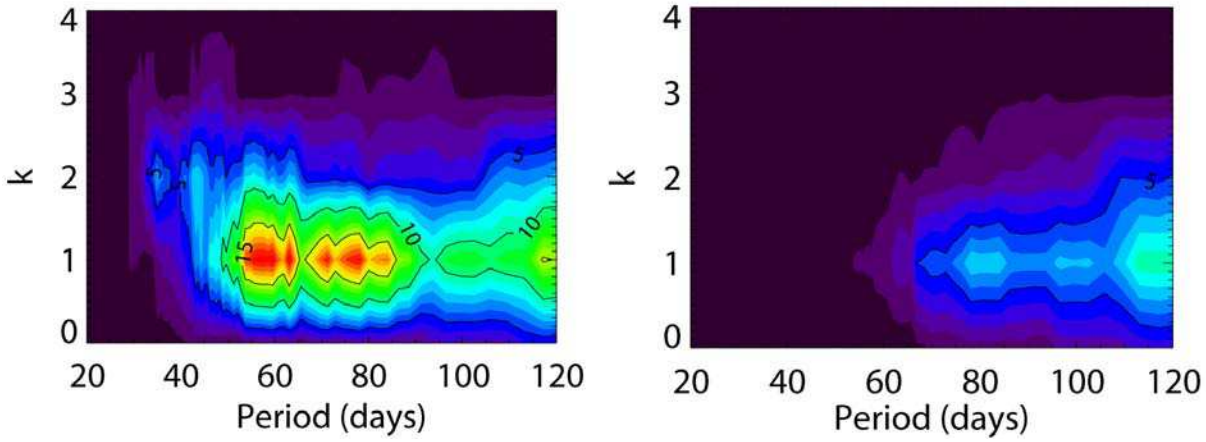

Fig. 4.2: Frequency-wavelength decompositions of ORCA SLA anomalies at the equator between 120°E and 80°W (k=1 ~ 18000km) filtered from frequencies lower than $(150\ days)^{-1}$ for 5-daily outputs (left) and monthly means (right). For both sampling frequencies, only eastward propagations are represented. Spectrum units are cm^2. Interval for coloured contours is 1 cm^2.

CMIP5 simulation requirements include the availability of daily outputs for the ocean, which might address this issue. However, the tridimensional daily outputs will be limited in space and/or time due to the extensive disk space required to archive this data. In order to ensure the availability of the ocean data needed to force the ROMS model, specific agreements with IPCC modelling groups are required: in the framework of the PEPS program, collaborations with IPSL and INM modelling groups in particular will allow obtaining such data for the targeted time periods and climate scenarios.

However, a deeper thermocline and a weaker upwelling near the equator induced by global warming cause significant changes in the intraseasonal equatorial variability simulated by the CGCMs, even in the monthly means. The intraseasonal temperature and current variabilities simulated by the IPSL-CM4 and INGV-ECHAM4 models at 100°W under preindustrial and $4xCO_2$ climate suggest a model-dependent response of IEKW to global warming (figures 4.3 and 4.4):

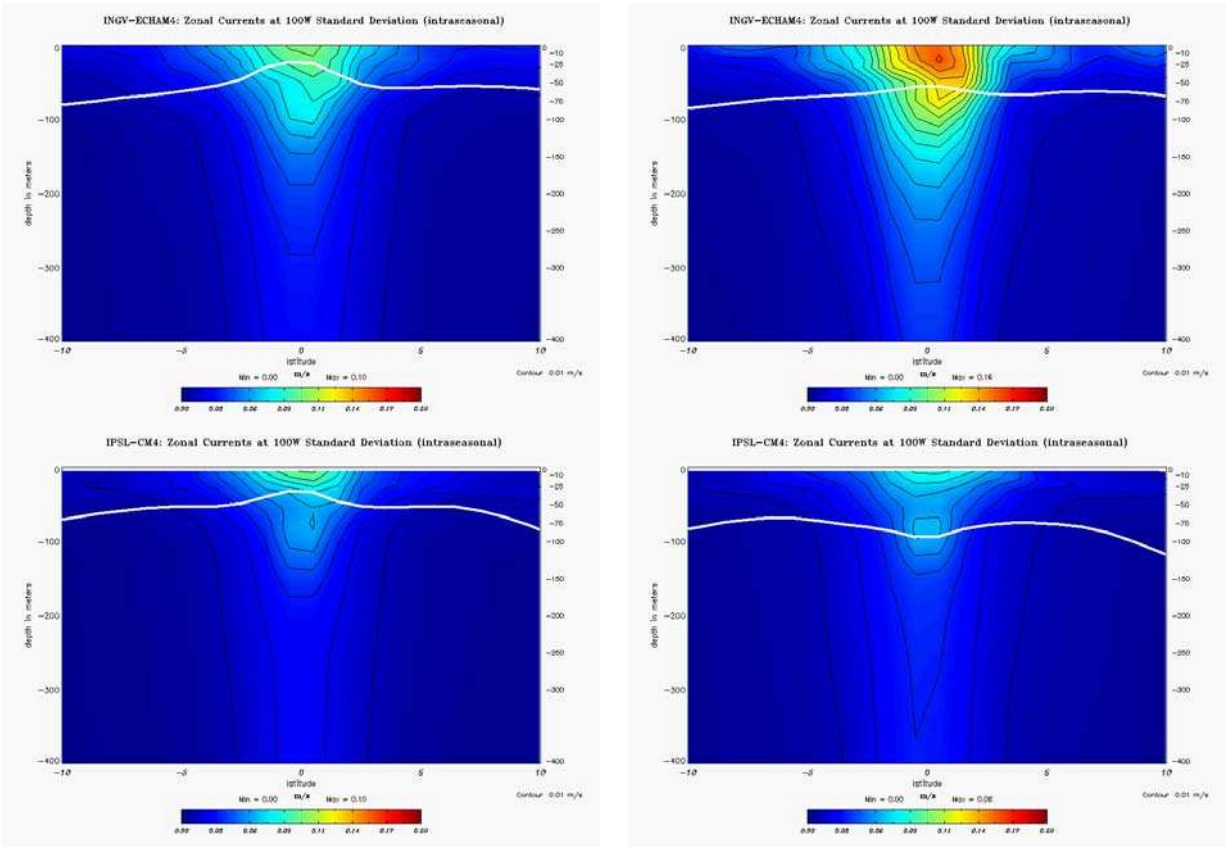

Fig. 4.3: intraseasonal zonal current variability (RMS, m/s) at 100°W (10°S-10°N, 0m-400m) for INGV-ECHAM4 (top) and IPSL-CM4 (bottom) under preindustrial (left) and 4xCO_2 climate (right). Mean 20°C isotherm depth is also indicated (white bold line). Contour interval is 1cm/s. Colour scale is blue-red: 0 cm/s –20 cm/s.

- surface zonal current variability increases by ~60% with a spatial reorganization of temperature variability for INGV-ECHAM4;

- temperature variability increases by ~50% with hardly any change in current variability for IPSL-CM4.

Such changes will have a direct impact on intraseasonal variability in the HCS: for instance, with IPSL-CM4 forcing, the sea level variability simulated by ROMS increases off both Peru and Chile (fig. 4.5). Since surface wind stress variability was shown to decrease at intraseasonal time scales over this region (Goubanova et al., 2010), the increase in sea level variability has to be related to the increase in equatorial ocean variability, highlighting the role of the remote forcing of equatorial origin on the regional ocean dynamics.

- **Mesoscale activity**: it was not considered in the analysis performed on the CR, in spite of the important contribution of mesoscale eddies to the heat budget of the upper ocean in the HCS, and their potential impacts on fish recruitment and surface chlorophyll concentrations. However, results from chapter three suggest a potential modulation of nearshore EKE by equatorial variability through the impact of coastal-trapped waves (CTW) on the coastal current system. 50- to 80-day oscillations were actually diagnosed in the time

series of the number of mesoscale eddies simulated by ROMS near the coast of central Peru (fig. 4.6), which were identified with the algorithm developed by Chaigneau et al. (2008). Moreover, it was found that the low-frequency variations of such oscillations are correlated with those of IEKW (for the first baroclinic mode in particular) with values around 60-70% and a lag of 10 days (fig. 4.7a), which is of the order of the time spent by CTW to propagate along the coast from the equator to ~15°S. On the other hand, when considering the whole intraseasonal frequency band (T<120 days), such low-frequency variations where found to be correlated with those of the local alongshore winds with values around 50-65% and a negligible lag (fig. 4.7c), suggesting that both remote and local forcings contribute to the intraseasonal variability of mesoscale activity in this area of intense eddy generation (fig. 4.7b). Yet, so far no clear relation was found for the central Chile coast (fig. 4.7a and 4.7c), in spite of the significant intraseasonal wind variability associated to the coastal jets and the intense generation of mesoscale eddies in this area (fig. 4.7b). This topic should be investigated in future studies in order to quantify the relative contributions of remote and local forcings to mesoscale activity in the HCS.

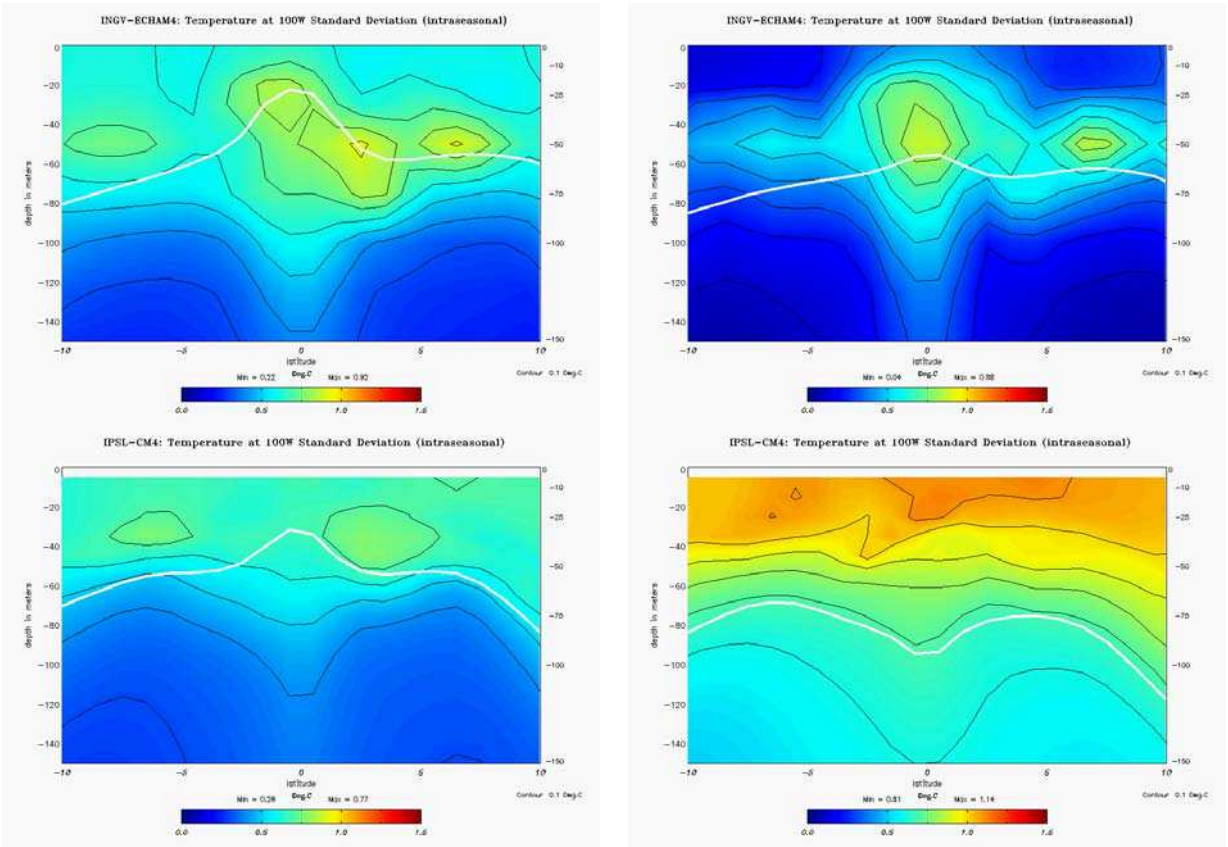

Fig. 4.4: same as fig. 4.3, but for intraseasonal temperature variability (RMS, °C) at 100°W (10°S-10°N, 0m-150m). Contour interval is 0.1°C. Colour scale is blue-red: 0–1.5°C.

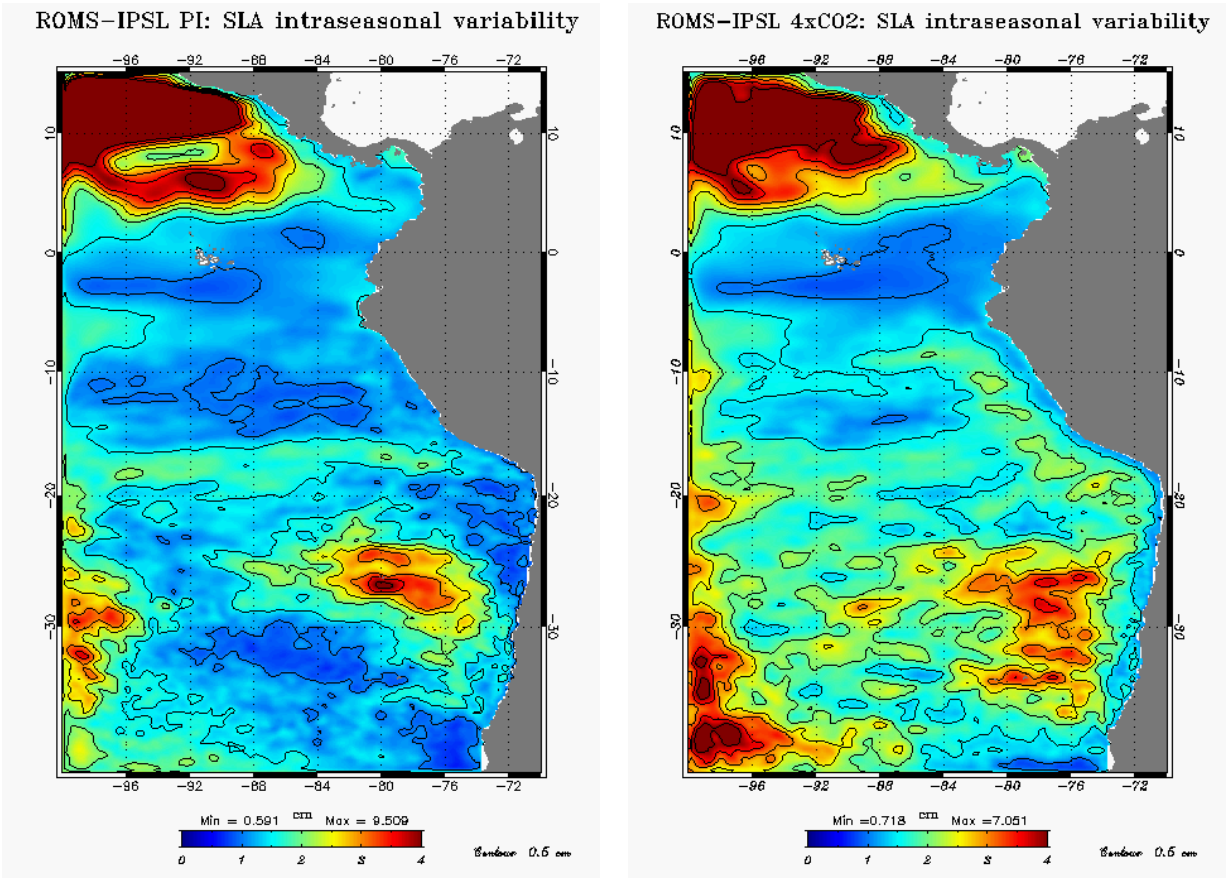

Fig. 4.5: high-pass filtered (f_c = 150 days) SLA variability (RMS) in the ESP simulated by ROMS with IPSL-CM4 forcing under pre-industrial (left) and 4xCO_2 climate (right).Unit is cm. Contour interval is 0.2 cm.

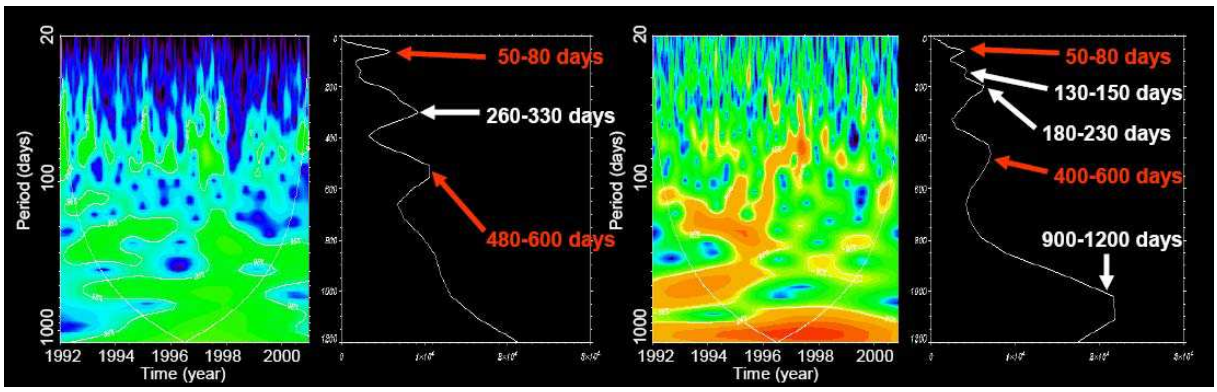

Fig. 4.6: wavelet energy spectrum and total wavelet spectrum for the anomalous amplitude of the first baroclinic mode EKW in ORCA at 100°W (left) and for the anomalous number of eddies simulated by ROMS in the first two degrees from the coast at 15°S (right). Common frequencies between the two time series are indicated in red.

- **<u>Bottom friction and coastline curvature</u>**: we suggested in chapter three that they have a significant effect on the critical latitude through the introduction of nonlinear terms in the vorticity equation. However, these terms were not quantified: the examination of the behaviour of the different terms of the vorticity equation along the coast provides a promising topic for future research. It would allow testing the validity of the hypotheses formulated to explain the divergence of the ROMS solution from linear wave theory.

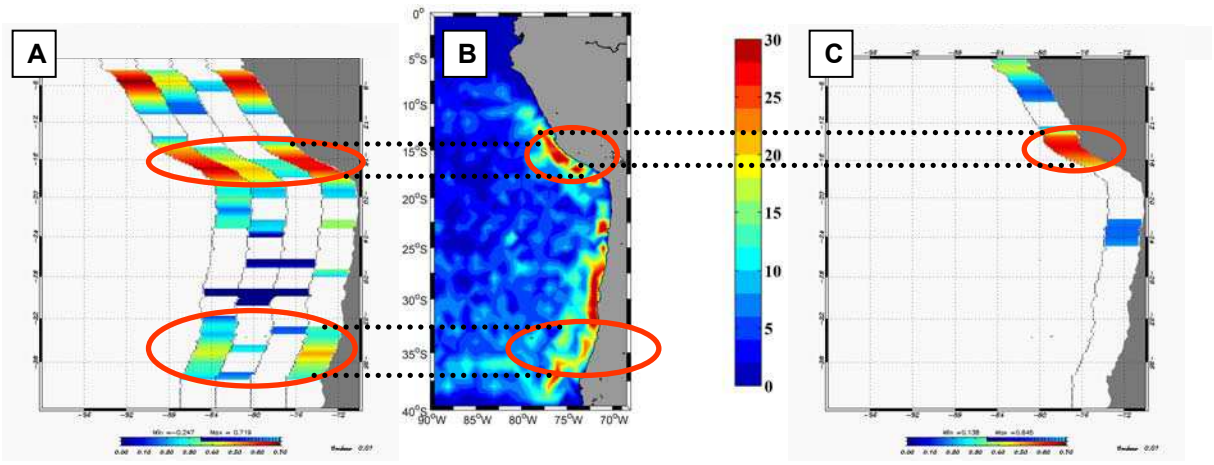

Fig. 4.7: (**A**) Maximum lag-correlation (%) between the low-frequency variations of the wavelet energy in the (50-80 days)$^{-1}$ band for respectively the first 3 baroclinic modes EKW and the number of nearshore eddies as a function of latitude; (**B**) map of eddy generation; (**C**) same as (A) but for meridional wind stress along the coast and the number of nearshore eddies for the (10-120 days)$^{-1}$ frequency band. The four bands in (A) correspond to (resp. from left to right) the sum of the first three, the third, the second, and the first baroclinic mode EKW. Only significant correlations are plotted on (A) and (C).

4.5. Long-term perspectives

In addition to the perspectives listed above, other mid- to long-term perspectives to this work can be anticipated. The study conducted on the ENSO feedbacks in IPCC-class CGCMs (Belmadani et al., 2010) opens the way for studies of the low-frequency modulation of ENSO feedbacks and its possible relation with the decadal modulation of ENSO. Also, the impact of climate change on ENSO could be investigated through changes in the related feedback processes. For instance, a central Pacific El Niño, also called El Niño « Modoki » (Ashok et al., 2007; Kao and Yu, 2009; Kug et al., 2009), has emerged since the 1990s (Larkin and Harrisson, 2005a; Ashok et al., 2007; Yeh et al., 2009), and has been shown to be mainly driven by the zonal advective feedback (Kug et al., 2009), in contrast to the eastern Pacific El Niño which is controled by a combination of the zonal advective and thermocline feedbacks. This increasing occurrence of El Niño Modoki might be related to a change in ENSO feedbacks in response to the predicted weakening of the Walker circulation and subsequent warming of the equatorial Pacific. Besides, results from chapter two suggest a significant role of the NAM in the dynamics of the ENSO cycle through its rectifying effect on the background climate. Such hypothesis will have to be confirmed by future research.

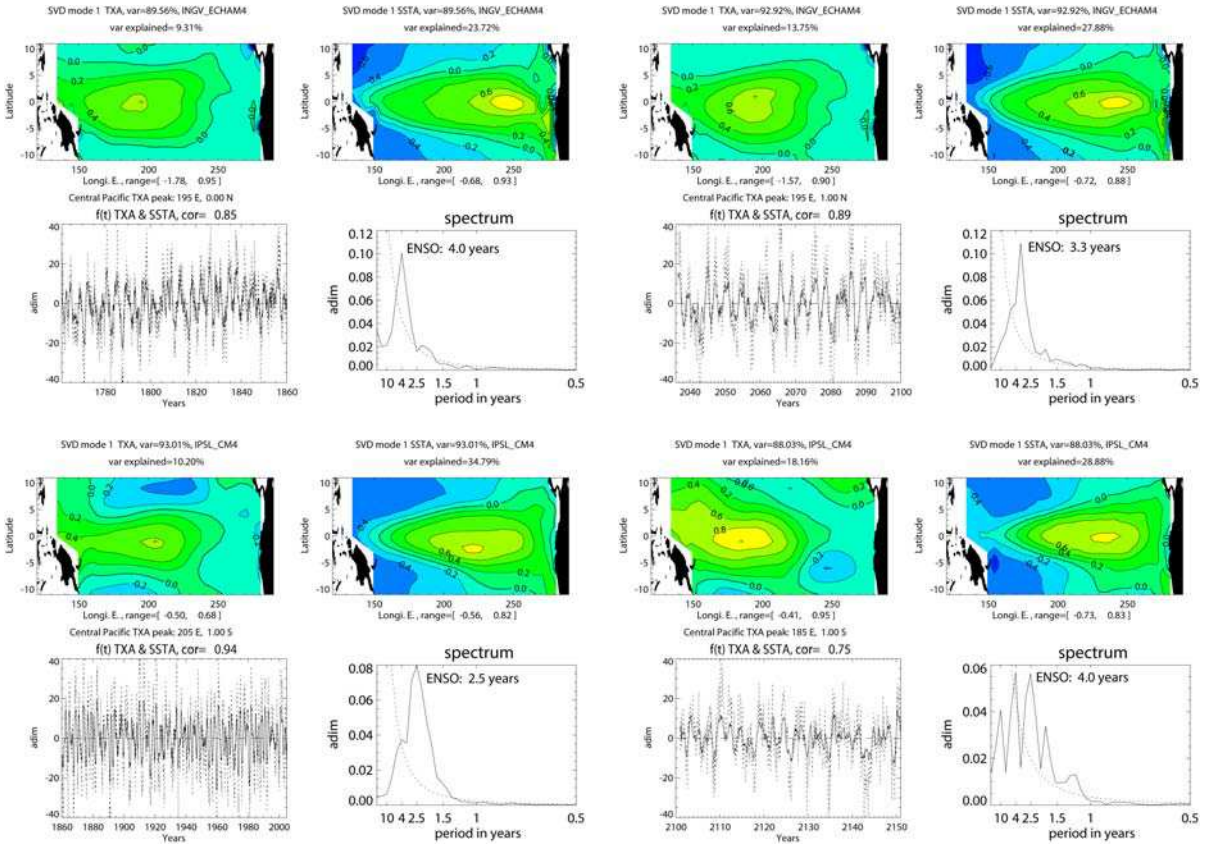

Fig. 4.8: First SVD mode between wind stress and SST anomalies (11°S-11°N, 134°E-81°W) for INGV-ECHAM4 (top) and IPSL-CM4 (bottom) under preindustrial (left) and 4xCO_2 climate (right). For each model simulation, from left to right and top to bottom: spatial patterns for zonal wind stress and SST anomalies, associated adimensionalized time series (full line for SST, dashed line for wind stress anomalies), and the corresponding frequency spectra adimensionalized by the energy integrated over the whole frequency domain (full line for SST anomalies, dashed line for red noise). CI = 0.2 units. Spatial patterns are adimensionalized by their respective variance over the domain and multiplied by 10. The location of maximum variance in wind stress anomalies is indicated by a cross on the map of the associated SVD mode. Percentage of explained variance for SST and zonal wind stress are indicated above the corresponding panels. Percentage of explained covariance is also provided. Correlation value between time series is indicated above the corresponding panel and the dominant ENSO period is mentioned on the spectrum plot.

In addition, studying the impact of climate change on ENSO should also provide material for the understanding of the impact of climate change on the HCS. Whereas Echevin et al. (*in prep.*) focused on changes in the mean state and seasonal cycle, future work will concentrate on changes in interannual variability at the regional scale, in relation to potential changes in basin-scale ENSO activity. For instance, the time scale of ENSO in the IPSL-CM4 4xCO_2 simulation is longer than in the preindustrial simulation (4.0 years vs. 2.5 years), whereas it is shorter for the INGV-ECHAM4 model (3.3 years vs. 4.0 years), as seen in figure 4.8. Such changes might have different impacts on the regional circulation and the dynamics of coastal upwelling, which are likely to produce different effects on the marine ecosystem dynamics: indeed, as proposed by Bakun and Weeks (2008), the remarkable pelagic fish productivity of the northern HCS compared to the southern HCS and other EBUS'es might be

the result of a « cyclic 're-setting' of the system by ENSO perturbations that may tend to interrupt malignant growth of adverse self-amplifying feedback loops [such as longer-lived non-productive predator species] within the nonlinear biological dynamics of the ecosystem ». It could be interesting to test the physical response of the HCS to such changes in the time scale of ENSO, particularly in terms of factors that are likely to directly influence primary productivity and the dynamics of small pelagic fish, such as upwelling, seaward Ekman transport, residence times over the continental shelf, and nearshore turbulence.

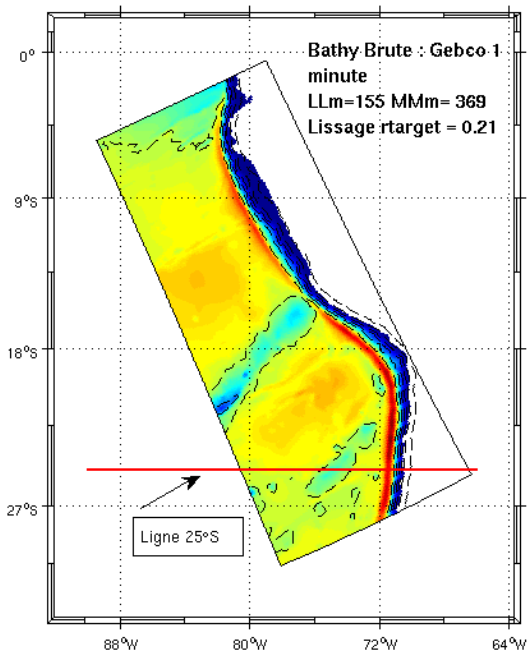

Fig. 4.9: the nested 1/12° curvilinear grid for the ROMS model configuration used in the PEPS program. The background image is for bathymetry (m). *G. Cambon, personal communication*.

The ANR-PCCC program covering the period 2006-2008 was followed by the ANR-PEPS program (P.I. Dr. V. Echevin) which started early 2009 and will last until late 2011. It is the continuation of the PCCC program in that it investigates the impact of climate change on the northern HCS ecosystems and builds on physical modelling results from PCCC. In PEPS, the ROMS climate change simulations are coupled with PISCES, a biogeochemical model (Aumont et al., 2003), in order to study the impact of global warming on nutrients and surface chlorophyll. In addition, outputs from the physical model are also used to force Ichtyop (Lett et al., 2008), an Individual-Based Model (a lagrangian particle transport model with parameterizations for enrichment, concentration and retention processes), in order to study the spatio-temporal behaviour of small pelagic fish early life stages near the Peru coast, and related changes with global warming. Last, a model of

population dynamics (Seapodym – Lehodey et al., 2003) uses the physical parameters calculated by ROMS to infer future dynamics of the Peruvian sardine and anchovy. The physical modelling effort which started with PCCC is sustained in PEPS, with atmospheric downscaling (statistical and also dynamical with the use of a regional model) and oceanic downscaling of several IPCC simulations, following the strategy described above. The 1/6° ROMS configuration presented here is retained in PEPS, but will be completed by a nesting to a 1/12° curvilinear grid covering the coasts of Peru and northern Chile (fig. 4.9) in order to meet requirements on model resolution from Seapodym.

Last but not least, the methodology developed in the framework of PCCC, PEPS and the present PhD thesis could be applied to study the impact of climate change on other EBUS'es, namely the California Current, the Benguela Current and the Canary Current. Of course some adaptations will have to be made in order to take the specificities of each system into account. For instance, ENSO and coastal-trapped waves of equatorial origin are known to have a significant impact on the eastern North Pacific and the California Current. On the other hand, ENSO has a weaker signature in the variability of Atlantic Ocean EBUS'es, though coastal-trapped waves are also present along the west coast of Africa. In addition, the Benguela Current is influenced by a specific mode of interannual-to-decadal climate variability called « Benguela-Niño » characterized by anomalous atmospheric conditions over the western tropical Atlantic and by intrusions of warm and salty waters along the coast of Namibia (Shannon et al., 1986; Boyer et al., 2000; Rouault et al., 2007). The Canary Current is probably less influenced by equatorial Atlantic variability, as intraseasonal coastal-trapped waves were not observed North of about 12°N (Polo et al., 2008). However, the Azores Current is known to have a large impact on the simulated circulation off western North Africa (E. Machu, personal communication), which implies that the dynamics of this large-scale current should be investigated in IPCC models for the purpose of studying the impact of global warming on the Canary Current System. Other regional features such as the African Monsoon and the intrusion of salty mediterranean waters through Gibraltar Strait also have an impact on coastal upwelling dynamics and should be examined carefully. Such regional modelling studies of future climate change in EBUS'es are of great interest to IRD, whose mission is to help developing countries to improve their research capacities, in order to deal with increasing environmental and societal problems, especially in the context of anthropogenic global warming. Initiatives such as the PEPS program for Peru are a first step towards a sustainable management of fisheries in EBUS'es, the regions with the most productive marine ecosystems of the world ocean.

Chapitre 4: Conclusions et perspectives

Dans ce qui suit, nous présentons en premier lieu les résultats obtenus d'un intérêt direct pour des expériences de downscaling de projections climatiques sur l'océan au large du Pérou et du Chili, avant de nous focaliser sur les avancées scientifiques apportées par la présente thèse de doctorat. Nous résumons aussi quelques résultats additionnels obtenus en collaboration avec des collègues dans le cadre du programme PCCC (Pérou-Chili Changement Climatique). Enfin, nous faisons le point sur les principales limitations de ce travail, et proposons quelques perspectives de recherches futures.

4.1. Principales découvertes en lien avec PCCC

L'idée principale derrière ce travail et le programme PCCC était d'utiliser les projections du futur réchauffement global fournies par les CGCMs du quatrième rapport d'évaluation du Groupe Intergouvernemental d'Experts sur l'évolution du Climat (GIEC, *IPCC* en anglais), afin d'étudier la réponse de la circulation du Pacifique Sud-Est (ESP) simulée par ROMS (Regional Ocean Modelling System), un modèle régional océanique de type *eddy-resolving* (*cad* dont la resolution horizontale est suffisante pour représenter les tourbillons méso-échelle). La présente thèse a apporté deux contributions majeures au programme PCCC: une méthodologie de sélection des « meilleurs » modèles climatiques pour notre région d'étude (chapitre deux), et l'analyse d'une simulation régionale interannuelle du HCS, avec un intérêt particulier pour le rôle du forçage distant par les EKW aux échelles de temps intrasaisonnières (chapitre trois). Cette analyse de la simulation de contrôle constitue une référence pour les études de downscaling du changement climatique.

Plutôt que d'étudier la réponse du HCS au réchauffement global tel qu'il est prévu pour des projections "réalistes" d'émissions de gaz à effet de serre (GES) dans l'atmosphère pour le XXI^{e} siècle (scénarios dits *SRES*), nous avons préféré choisir des expériences idealisées avec une augmentation des concentrations atmosphériques en GES plus forte que celle qui est prevue par les scenarios SRES. La motivation pour ce choix est triple: 1) considérant les biais systématiques des CGCMs de la génération actuelle dans l'Est du Pacifique tropical et du Pacifique Sud, la diversité de leurs réponses au réchauffement global, et les fortes incertitudes liées aux scénarios SRES qui dépendent de nombreuses hypothèses et approximations concernant l'adaptation future des sociétés humaines au réchauffement global, on a décidé d'abandonner l'idée d'essayer de fournir une prédiction « réaliste » du futur changement climatique regional, qui pourrait devenir caduque dans les prochaines années avec l'avènement de CGCMs et de scénarios climatiques améliorés; 2) de tels scénarios idealisés avec un fort réchauffement global permettent de maximiser le ratio signal/bruit; et 3) focaliser sur les mécanismes physiques mis en jeu à partir de différents cas tests permettant d'étudier la validité de certaines des théories actuellement proposées par la communauté scientifique.

Deux critères ont été retenus pour sélectionner les meilleurs modèles parmi l'ensemble: 1) la representation à grande échelle de la dynamique et des propriétés d'ENSO, et 2) les champs de temperature et de moment simulés aux frontières du domaine choisi pour

le downscaling. Un critère additionnel d'importance pour le HCS serait le forçage atmosphérique. Cependant, la plupart des CGCMs représentent mal les vents à basse altitude et les flux air/mer dans cette region, en particulier près de la côte, ce qui introduit des biais importants dans la circulation océanique. Un travail parallèle de downscaling statistique du forçage de vent issu des CGCMs a été réalisé par Dr. Katerina Goubanova dans le cadre du programme PCCC pour répondre à cette question (voir 4.3). Une procédure simple de correction des flux a également été appliquée (voir chapitre un). Par conséquent, et parce que peu de CGCMs reproduisent à la fois la dynamique d'ENSO et l'état moyen océanique aux frontières du domaine régional, le forçage atmosphérique n'a pas été retenu comme critère de sélection. Cependant, il a tout de même été évalué à titre d'information.

Mécanismes d'ENSO à échelle du bassin:

Une étude des mécanismes physiques qui contrôlent la variabilité de type ENSO dans les simulations pré-industrielles réalisées avec 23 CGCMs (voir chapitre deux) a permis d'identifier les modèles les plus fiables en termes de variabilité interannuelle équatoriale à l'échelle du bassin: ce sont les modèles dits « hybrides », avec une combinaison du *zonal advective feedback* et du *thermocline feedback* comme c'est le cas pour SODA (Simple Ocean Data Assimilation), une réanalyse océanique couvrant la période 1958-2001 et prise ici comme référence. Les 6 modèles identifiés comme « hybrides », dont la période d'ENSO est en moyenne plus proche des observations et qui représentent le mieux les principaux processus couplés contrôlant la variabilité de la TSM, devraient fournir les prédictions les plus fiables en ce qui concerne l'évolution d'ENSO avec le réchauffement global, en faisant l'hypothèse qu'une bonne représentation des rétroactions d'ENSO garantit une sensibilité d'ENSO au changement climatique mieux contrainte que pour les autres modèles. Afin de diagnostiquer encore d'avantage la variabilité d'ENSO à grande échelle dans ces modèles, les caractéristiques spatiales et temporelles d'ENSO sont comparées à SODA: quatre modèles apparaissent clairement comme plus 'réalistes', tandis que les deux modèles restants comportent plusieurs biais, dont un ENSO biennal (CSIRO-MK3.0) et un pic de variabilité de la TSM déplacé vers l'Ouest du Pacifique (INM-CM3.0). Ces deux CGCMs ont donc été exclus du reste de l'étude et seulement les quatre 'meilleurs' CGCMs hybrides sont analysés aux frontières du domaine considéré pour les expériences de downscaling.

Analyse de l'état moyen et de la variabilité dans l'Est du Pacifique:

Nous avons montré que la frontière Ouest du domaine régional concentre 80-90% des échanges entre l'ESP et le Pacifique Sud, à la fois pour les modèles couples, pour les données de la réanalyse SODA, et pour une simulation interannuelle réalisée avec ORCA, un Modèle Océanique de Circulation Générale (OGCM). La bande équatoriale à 100°W entre 10°S et 10°N concentre en réalité la majeure partie de la variabilité, ce qui nous a motivé à restreindre l'analyse aux premières centaines de mètres de cette section verticale. A notre connaissance, jusqu'à présent aucune étude n'a encore été dédiée à la sensibilité de la circulation océanique régionale à l'état moyen et à la variabilité dans l'Est du Pacifique équatorial: pour cette raison, les champs simulés de température et de vitesse ont été comparés à des données réanalysées et observées (lorsqu'elles étaient disponibles) pour différentes bandes de fréquence, avec un processus de sélection basé sur l'évaluation des performances des CGCMs. Les résultats révèlent des comportements hétérogènes parmi les modèles: biais chauds ou froids, cycles saisonniers sur- ou sous-estimés, présence ou absence de certains courants équatoriaux comme le Courant Sud Equatorial (SEC), le Contre-Courant Sud de SubSurface (SSSCC), et le Contre-Courant Nord Équatorial (NECC). D'autre part, certaines erreurs sont systématiques pour l'ensemble des modèles: un Sous-Courant Équatorial (EUC) et un SEC trop faibles, l'absence de flux d'est en-dessous de 150 à 200m de profondeur, une thermocline trop peu profonde à l'équateur, une stratification excessive dans la *cold tongue*, une modulation basse-fréquence excessive pour le cycle saisonnier, et une variabilité interannuelle sous-estimée. UKMO-HadGEM1 représente le mieux le système de courant équatorial, mais présente en revanche un champ de température fortement biaisé. Inversement, IPSL-CM4 et INGV-ECHAM4 ont des températures équatoriales plutôt 'réalistes' en surface comme en subsurface, ainsi que des courants relativement 'réalistes'. De plus, certaines des données requises pour le downscaling n'étaient pas disponibles pour UKMO-HadGEM1, alors qu'elles sont facilement accessibles pour ces deux derniers modèles. Pour ces raisons, les modèles IPSL-CM4 et INGV-ECHAM4 sont les deux modèles finalement retenus pour les expériences de downscaling régional.

Malgré les performances avérées de ces deux modèles dans le Pacifique tropical et dans l'ESP, il n'y a *a priori* aucune garantie que la circulation régionale simulée par ROMS avec un forçage issu d'IPSL-CM4 et/ou d'INGV-ECHAM4 pour un climat pré-industriel ressemble à celle observée. Pour cette raison, une simulation régionale de contrôle avec des forçages réalistes aux frontières et en surface sur la période 1992-2000 a été réalisée et est en bon accord avec les observations disponibles: en particulier, la variabilité simulée du niveau

de la mer équatorial est à la fois transmise le long du guide d'ondes côtier et réfléchie en direction du large. La simulation est également capable de représenter le Sous-Courant du Pérou-Chili (PCUC) dirigé vers le Sud ainsi que le Courant Côtier du Chili-Pérou (CPCC) dirigé vers l'équateur. La simulation est ensuite utilisée pour étudier le forçage à distance du niveau de la mer et des courants côtiers par des ondes piégées à la côte (CTW) d'origine équatoriale (voir chapitre trois).

4.2. Avancées scientifiques

Mécanismes d'ENSO:

Afin d'évaluer l'impact d'ENSO dans le HCS pour un climat plus chaud, nous avons décidé d'investiguer les mécanismes physiques d'ENSO tels qu'ils sont représentés par les modèles du CMIP3 pour un climat pré-industriel: en effet, l'étude de tels mécanismes peut aider à interpréter les biais dans la variabilité d'ENSO représentée par les modèles couplés, ainsi que leur évolution avec le réchauffement global. L'étude des mécanismes physiques d'ENSO est basée sur l'utilisation de LODCA (*Linear Ocean Dynamically Coupled with the Atmosphere*), un modèle couplé intermédiaire du Pacifique tropical avec une stratification moyenne et un forçage de vent prescripts, afin de pouvoir dériver explicitement les termes d'advection du bilan de chaleur de la couche de mélange dans les modèles climatiques. Tandis qu'en accord avec la littérature, les termes dominants du bilan de chaleur sont l'advection de la température moyenne par les anomalies de courants zonaux ($u'\frac{\partial \overline{T}}{\partial x}$) ainsi que l'advection des anomalies de température par l'upwelling moyen ($\overline{w}\frac{\partial T'}{\partial z}$) pour la plupart des modèles, nous avons montré que les termes qui tiennent le plus compte des biais dans l'advection zonale (resp. verticale) sont l'advection des anomalies de température par les courants moyens zonaux (resp. verticaux), *cad* $\overline{u}\frac{\partial T'}{\partial x}$ (resp. $\overline{w}\frac{\partial T'}{\partial z}$), soulignant l'influence des caractéristiques de la circulation moyenne sur la dynamique d'ENSO. Ces résultats étendent aussi la vision classique du *zonal advective feedback* et du *thermocline feedback* qui font généralement référence à $u'\frac{\partial \overline{T}}{\partial x}$ et $\overline{w}\frac{\partial T'}{\partial z}$, et posent la question de l'importance de $\overline{u}\frac{\partial T'}{\partial x}$, qui pourrait devoir être pris en compte avec $\overline{w}\frac{\partial T'}{\partial z}$ pour comprendre les caractéristiques simulées

d'ENSO. Les courants de surface zonaux moyens $\overline{u}$ dans l'Ouest du Pacifique équatorial et l'upwelling moyen à la base de la couche de mélange $\overline{w}$ dans l'Est du Pacifique équatorial ont été utilisés comme proxys de l'intensité respectivement du zonal advective feedback et du thermocline feedback, ce qui nous a conduit à la définition d'une classification des modèles en fonction du processus dominant d'ENSO: les modèles avec un zonal advective feedback dominant, les modèles avec un thermocline feedback dominant, et les modèles « hybrides » avec une combinaison des deux. En accord avec la théorie, nous avons trouvé que les modèles avec un zonal advective feedback (resp. thermocline feedback) dominant sont caracterisés par un cycle ENSO plus court (resp. plus long) en moyenne. Cette étude (Belmadani et al., 2010) a été acceptée par le *Journal of Climate* le 28 janvier 2010 (chapitre 2, section 1) et est actuellement sous presse. Une note focalisant sur les principaux résultats et complétée par une synthèse de la littérature existante sur les *feedbacks* d' ENSO a également été acceptée pour publication dans les proceedings du séminaire franco-russe *« Climate variability in the tropical Pacifique: mechanisms, modelling et observations »* tenu à Moscou (Russie) du 13 au 15 Avril 2009 (Belmadani et Dewitte, 2010). Elle est sous presse au moment de l'impression du présent manuscrit.

Intéractions Mode Quasi-Annuel/ENSO:

De plus, un mode quasi-annuel (NAM) - qui est un mode couplé du Pacifique tropical associé au mode de bassin océanique impliquant la propagation d'ondes de Kelvin et de Rossby equatorials - a aussi été diagnostiqué dans l'ensemble de modèles. Son rôle pour les feedbacks d'ENSO a été documenté: les résultats montrent que le NAM est amplifié pour les modèles avec un zonal advective feedback dominant et inhibé pour les modèles avec un thermocline feedback dominant. Nous suggérons que le NAM, qui est associé à un flux de surface zonal anormal dans l'Ouest du Pacifique équatorial, est capable d'interagir avec ENSO via l'advection zonale non-linéaire. Ces non-linéarités contribuent au biais froid représenté par la plupart des modèles dans la *warm pool* du Pacifique occidental.

Propagation de la variabilité équatoriale intrasaisonnière vers le HCS:

Les processus haute fréquence dans le Pacifique équatorial ont aussi un impact sur la circulation océanique moyenne dans le HCS: d'après la théorie linéaire, les EKW aux fréquences intrasaisonnières sont les plus efficacement piégées le long de la côte Ouest d'Amérique du Sud. Les caractéristiques à grande échelle des EKW intrasaisonnières et leurs

changements avec le réchauffement global sont donc susceptibles d'influencer l'upwelling côtier et la circulation régionale dans l'ESP. De plus, la variabilité intrasaisonnière associée à de telles ondes longues baroclines est maximale pendant les événements El Niño, ce qui signifie que l'impact d'ENSO sur le HCS (tel qu'il est décrit par Colas et al. (2008)) est partiellement lié à celui des EKW intrasaisonnières. Il a été démontré que ces dernières sont modulées à l'échelle décennale, et qu'une telle modulation n'est pas directement liée aux modes couplés dominants de la variabilité climatique du Pacifique tropical (Dewitte et al., 2008b). Par conséquent, les tendances à long terme observées le long de la côte du Pérou-Chili pourraient être liées à celles de la variabilité équatoriale intrasaisonnière dans un contexte de changement climatique global.

Ce constat nous a amené à analyser le forçage à distance de la variabilité côtière au large du Pérou et du Chili dans la simulation régionale de contrôle par les ondes piégées à la côte d'origine équatoriale. Nous avons montré que la latitude critique, qui sépare la région de propagation des ondes de Rossby (au Nord) de la région de propagation des ondes piégées à la côte (au Sud), est 5 à 15 degrés plus haute dans le modèle que celle prédite par la théorie linéaire, et ce pour l'ensemble des modes baroclines, en particulier pour les oscillations à 120 jours. Nous avons suggéré deux mécanismes distincts susceptibles de modifier l'équation de vorticité et de se combiner pour expliquer un tel comportement: l'effet de la friction de fond au-dessus du plateau continental et de la pente associée, qui est susceptible d'avoir une influence directe sur la vorticité relative et sur la vorticité planétaire, et l'advection non-linéaire introduite par la courbure localement élevée au large du Nord du Pérou (4°S à 8°S) et au large de la zone allant du Sud du Pérou au Nord du Chili (13°S à 20°S). Les résultats du modèle parent ORCA à plus basse résolution comprenant un plateau plus étroit avec une friction réduite au fond ainsi qu'un effet limité des courbures élevées sont en meilleur accord avec la théorie linéaire. Tandis que ROMS présente une variabilité du large significative au sud de la latitude critique théorique, comme c'est le cas pour les données altimétriques, cette variabilité est absente d'ORCA: nous suggérons que des effets non-linéaires liés à la bathymétrie et à la courbure du trait de côte doivent être pris en compte afin de pouvoir interpreter cette variabilité, et soulignons ainsi les limites de la théorie linéaire dans l'ESP. Le modèle régional confirme également le fort impact des ondes piégées à la côte de période 50 à 80 jours sur le Sous-Courant du Pérou-Chili (PCUC) le long des côtes Nord du Pérou jusqu'au centre du Chili, ce qui avait été observé précédemment dans cette dernière région. De plus, nous montrons que de telles ondes ont aussi une forte influence sur le Courant Côtier

du Chili-Pérou (CPCC), ce qui suggère des impacts potentiels sur l'activité tourbillonnaire mésoéchelle près de la côte.

Dans l'ensemble, ces avancées dans la compréhension des processus équatoriaux à grande échelle qui influencent le système d'upwelling du Pérou-Chili sont complémentaires de la méthodologie de downscaling mise en place par le programme PCCC. En particulier, les resultants obtenus mettent le doigt sur l'importance des processus haute fréquence et des changements associés pour le comportement futur du HCS. De tels processus pourraient n'être que partiellement pris en compte par PCCC, puisque seules les sorties mensuelles des CGCMs sont actuellement disponibles pour les expériences de downscaling (voir ci-dessous).

4.3. Résultats additionnels dans le cadre du programme PCCC

Changements futurs dans les vents parallèles à la côte:

Une méthodologie de downscaling statistique a été proposée par Goubanova et al. (2010) afin de corriger les biais dans les champs de vent de surface à basse résolution simulés par les CGCMs dans l'ESP, et appliquée au modèle IPSL-CM4. D'après leurs résultats, un renforcement du gradient méridional de pression à grande échelle dans l'Est du Pacifique subtropical est associé à une augmentation de ~10-20% des vents de surface parallèles à la côte au large du Chili central pendant l'hiver austral dans la simulation $4xCO_2$ relativement à la simulation Pré-industrielle, en accord avec les résultats de Garreaud et Falvey (2008). Cependant, plus au nord au large du Pérou central, les auteurs trouvent une diminution de ~10% des vents de surface parallèles à la côte pendant l'été austral, en désaccord avec les résultats de Bakun (1990) et de Bakun et Weeks (2008) qui suggéraient une augmentation observée au large du Pérou au cours des années récentes. Un point important: il a été montré que de telles tendances simulées sont cohérentes avec celles présentées par la moyenne d'ensemble des modèles du CMIP3 (onze CGCMs fournissant les données nécessaires pour réaliser des exercices de downscaling). Goubanova et al. (2010) argumentent que la tendance déduite par Bakun (1990) pourrait être liée à la variabilité décennale plutôt qu'au changement climatique anthropogénique, puisqu'un changement dans le régime de vent est clairement visible au début des années 70 dans les données analysées par Bakun (1990), et parce que les vents côtiers au large du Nord Pérou ne présentent aucune tendance significative sur la période 1949-1972 (Wyrtki, 1975). D'autre part, Falvey et Garreaud (2009) ont trouvé une légère tendance au réchauffement dans l'océan superficiel au large du Nord Pérou pour la

période récente à partir des données analysées ERSST (Smith et Reynolds, 2004), suggérant une possible réduction des vents favorables à l'upwelling, ce qui serait cohérent avec l'affaiblissement prévu des alizés au-dessus du Pacifique tropical (Vecchi et al., 2006; Vecchi et Soden, 2007).

Goubanova et al. (2010) ont également trouvé une diminution de 15-25% dans la moyenne annuelle de la variabilité intra-saisonnière du vent tout au long de la côte, et maximale dans la zone de jets côtiers au large du Chili central. De tels changements sont interprétés comme le résultat d'un affaiblissement et d'un déplacement vers le pôle de la cellule de circulation de Hadley dans l'hémisphère Sud (Bengtsson et al., 2006; Gastineau et al., 2008), qui participent avec la réduction de la circulation de Walker (Vecchi et al., 2006; Vecchi et Soden, 2007) à affaiblir et à déplacer l'anticyclone subtropical vers le sud, ainsi qu'à réduire l'occurrence des événements extrêmes de vent sur les tropiques (Gastineau et Soden, 2009). Formulé plus simplement, une extension vers le sud d'un climat tropical plus chaud est susceptible de transformer le régime de vent au large du Chili central en un régime d'alizés caracterisé par des vents parallèles à la côte plus forts et plus réguliers. Inversement, au large du Pérou les circulations plus faibles de Walker et de Hadley pour un climat plus chaud conduiraient à une diminution à la fois de la force et de la variabilité du vent.

Impact sur l'upwelling côtier et la dynamique mésoéchelle:

En se basant sur ces résultats, Echevin et al. (*en préparation*) ont étudié l'influence de tels changements dans les vents parallèles à la côte sur l'état moyen et sur le cycle saisonnier de l'upwelling côtier, ainsi que sur ceux des courants et de l'activité mésoéchelle associée au large du Pérou et du Chili. Nous avons trouvé que l'intense réchauffement de 5-6°C de l'océan superficiel au large du Pérou central dans la simulation $4xCO_2$ augmente la stratification près de la côte, amplifiant alors le CPCC dirigé vers l'équateur. De plus, l'intensification de l'EUC dans le modèle IPSL-CM4 (Marti et al., 2009) entraîne un PCUC plus large et plus épais dans la simulation régionale. Ceci conduit à une augmentation de la contrainte de cisaillement vertical entre le CPCC et le PCUC, et donc à une forte augmentation de l'énergie cinétique turbulente (EKE) près de la côte dans la partie Nord du HCS. D'autre part, on a trouvé que l'upwelling côtier diminue au large du Pérou et du Nord du Chili mais augmente au large du Chili central, en accord avec les changements des vents de surface (Goubanova et al., 2010). Afin de tester la sensibilité de ces résultats à de futurs changements du vent, Echevin et al. (*en preparation*) ont augmenté artificiellement les vents parallèles à la côte du scénario $4xCO_2$ de 50%, reproduisant ainsi des conditions de vent plus

proches de celles prédites par l'hypothèse de Bakun au large du Pérou (Bakun, 1990 – voir chapitre un): d'après leurs résultats, l'augmentation de l'upwelling côtier induit par des vents plus forts va augmenter le gradient de densité dans la direction perpendiculaire à la côte et donc la force des courants côtiers de surface et de subsurface. En comparaison avec la simulation $4xCO_2$ standard, une augmentation significative de l'EKE à la fois au large du Nord Pérou et du Chili central est observée, suggérant que l'augmentation des vents côtiers ne peut pas compenser les effets dynamiques de l'intense réchauffement de surface induit par une augmentation de 300% des emissions de GES (*cad* par un quadruplement du CO_2).

De manière générale, malgré les nombreuses limitations des études de Goubanova et al. (2010) et d'Echevin et al. (*en preparation*) (telles que l'utilisation de champs downscalés à partir d'un seul CGCM, ou le choix du scénario idéalisé $4xCO_2$ par exemple), les changements prédits des vents parallèles à la côte et de l'upwelling côtier sont plutôt en bon accord avec les tendances déduites des mesures historiques de vent, de TSM et de chlorophylle de surface issues de la période récente: la réponse du HCS au réchauffement global semble être sensible à la latitude, avec des vents et un upwelling côtier plus intenses au large du Chili, et des vents et un upwelling légèrement plus faibles au large de la zone allant du centre au Nord du Pérou. L'augmentation des vents favorables à l'upwelling au large du Chili est également en accord avec les etudes de modélisation antérieures, ainsi qu'avec certaines indications des changements climatiques passés et présents déduits de proxys paléoclimatiques. Au large du Pérou, les changements des vents de surface et de la TSM sont en contradiction avec l'hypothèse de Bakun. Bien que reconnaissant la proximité du Pérou par rapport à l'équateur comme un élément unique comparé aux autres systèmes d'upwelling de bord Est (EBUS), Bakun et Weeks (2008) réfutent l'effet potentiel d'un ralentissement à grande échelle des circulations de Walker et de Hadley: ils argumentent que la déconnexion entre les vents côtiers et les alizés du Pacifique pendant les événements El Niño est susceptible de devenir permanente avec le réchauffement global, dont les auteurs s'attendent à ce qu'il provoque un état moyen dans le Pacifique équatorial type 'El Niño permanent', *cad* une disparation des gradients zonaux de TSM et de profondeur de la thermocline, des conditions qui prévalaient pendant le Pliocène, il y a environ 3 à 5 million d'années d'après Fedorov et al. (2006). Cependant, la relation entre les vents parallèles à la côte et la circulation atmosphérique à grande échelle est encore mal comprise, ce qui sème le doute sur l'interprétation proposée par Bakun et Weeks (2008). De plus, les résultats de la modélisation océanique à haute résolution montrent que dans le cas d'une forte augmentation des

temperatures de surface à l'échelle globale et d'un changement de vent modéré (50%) au large du Pérou, le réchauffement de l'océan superficiel risque d'amplifier la turbulence dans la région côtière, ce qui pourrait avoir un impact négatif sur le recrutement des petits poissons pélagiques (Echevin et al., *en préparation*).

4.4. Limitations et perspectives

Il y a bien sûr de nombreuses limitations à l'étude rapportée par le présent manuscrit:

- **La résolution du modèle**: pour cause de ressources informatiques limitées, la résolution horizontale choisie de 1/6° (~18.5km à l'équateur, ~14km à 40°S) est un compromis entre la résolution des tourbillons mésoéchelle (le premier rayon de déformation de Rossby variant de ~210km à l'équateur à ~20km à 40°S) et les coûts informatiques. Cependant, comme une fraction significative de l'activité mésoéchelle est située au large du Chili central et s'étend jusqu'à ~35-40°S, idéalement la résolution nécessaire pour représenter correctement de telles structures serait autour de 5-10km, comme dans la configuration de ROMS au 1/15° (~7.5km à l'équateur, ~5.5km à 40°S) utilisée par Colas et al. (2008). De plus, d'après Capet et al. (2009), une résolution accrue dans les modèles régionaux de type *eddy-resolving* devrait améliorer la représentation de processus submésoéchelle tels que fronts, méandres et filaments associés à l'upwelling côtier, ce qui a été confirmé au large de la côte du Pérou par McWilliams et al. (2009). Ces processus de petite échelle sont d'autant plus importants qu'ils peuvent avoir un effet rectifiant sur la variabilité à plus grande échelle (Capet et al., 2008), ainsi que sur certains processus biogéochimiques (Lévy et al., 2001). De plus, une résolution du modèle augmentée devrait permettre de prendre en compte les structures spatiales à fine échelle des vents parallèles à la côte très près du littoral, et de représenter ainsi de manière plus précise la contribution du pompage d'Ekman à l'upwelling côtier (voir ci-dessous). Une méthode peu coûteuse pour y arriver est l'emboîtement multiple de grilles (fig. 4.1), bien qu'elle présente l'inconvénient d'être limitée à des zones géographiques réduites. Elle pourrait cependant fournir des résultats intéressants pour des études d'impact dans des sous-régions spécifiques du HCS, grace au couplage avec des modèles biogéochimiques et individu-centrés (*ex:* Brochier et al., 2008) par exemple (voir ci-dessous).

- **Forçage de vent**: la période de 9 ans couverte par les mesures du satellite ERS (Bentamy et al., 1996) présente l'avantage de balayer des états moyens du Pacifique tropical

contrastés, comme l'intense El Niño de 1997-98 par exemple. A l'inverse, les mesures du satellite QuickSCAT (CERSAT, 2002) sont seulement disponibles depuis juillet 1999: au moment du démarrage de cette thèse de doctorat, seuls 7 ans de données étaient disponibles, contre 10 ans au moment de l'écriture de ces lignes. Les vents ERS ont donc été choisis pour forcer ROMS dans la simulation régionale de contrôle (CR), bien qu'il ait été montré que les vents QuickSCAT sont plus précis dans l'ESP, en particulier entre 17°S et 26°S (Croquette et al., 2007). De plus, dans le but de comparer les expériences de downscaling du changement climatique réalisées par Echevin et al. (*en préparation*) au CR, l'utilisation des vents QuickSCAT pour forcer ce dernier apporterait une meilleure cohérence, puisque le modèle atmosphérique statistique construit par Goubanova et al. (2010) est basé sur des données QuickSCAT.

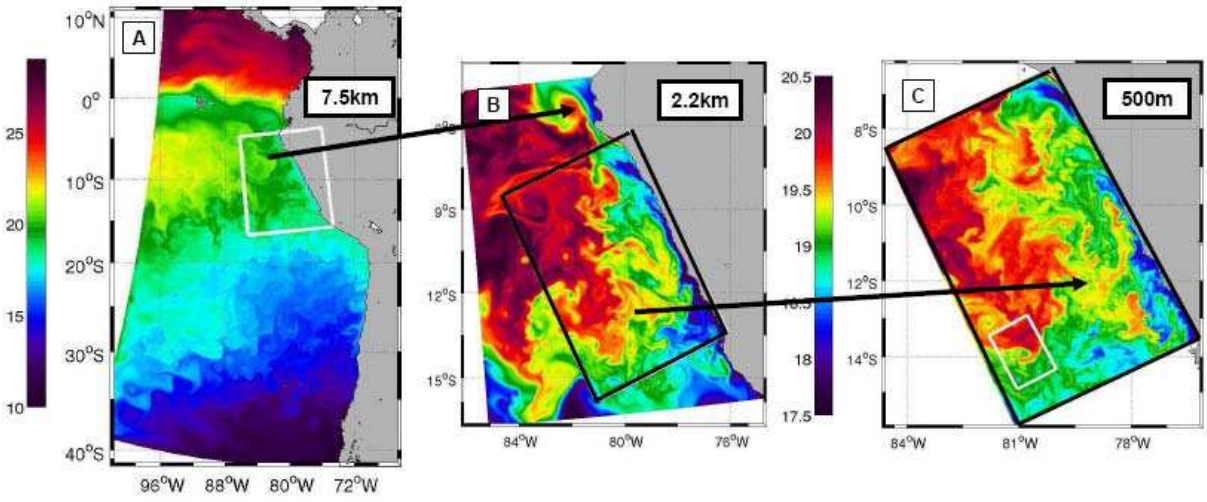

Fig. 4.1: Schéma d'une stratégie d'emboîtement multiple de grilles pour le HCS, allant des processus grande échelle aux processus sub-mésoéchelle: **(A)** configuration au 1/15° du modèle ROMS pour l'ESP utilisée par Colas et al. (2008); **(B)** grille emboîtée (résolution 2.2km) de l'océan côtier au Nord et au centre du Pérou; **(C)** grille de résolution 500m emboîtée dans (B) pour la côte centrale du Pérou. Les cartes représentent la TSM simulée (°C). L'échelle de couleurs pour (A) (resp. pour (B) et (C)) est indiquée sur le côté gauche (resp. droit) de la figure. *F. Colas, communication personnelle*.

Un autre problème lié au forçage de vent tient à sa structure dans la direction perpendiculaire à la côte dans la region située au plus près de la côte, qui présente une zone de drop-off dans les 30-50 premiers kilomètres (Capet et al., 2004; Renault, 2008), une distance de l'ordre de la maille pour la grille sur laquelle sont fournies les données de vent d'ERS comme celles de QuickSCAT (0.5°). Les simulations ROMS forcées par des vents observés ou downscalés ne peuvent donc prendre en compte ce processus, malgré son influence non négligeable sur l'upwelling côtier via le rotationnel du vent ainsi que le pompage d'Ekman associé (Bakun et Nelson, 1991; Halpern, 2002): par exemple, Capet et al. (2004) ont utilisé

un modèle atmosphérique pour extrapoler les vents QuickSCAT près de la côte, ce qui a amélioré de façon significative la représentation de l'upwelling côtier et des courants associés dans une simulation ROMS du Système de Courant de Californie. Une alternative est proposée par Colas et al. (2008b, 2009), qui appliquent les relations empiriques entre la TSM et les vents de surface développées par Chelton et al. (2001) et Chelton et al. (2007) à la TSM simulée par ROMS pour le HCS (même configuration que dans Colas et al., 2008) avec un forçage de vent QuickSCAT. Les vents de surface obtenus dans la zone de drop-off sont utilisés pour corriger les données QuickSCAT, qui fournissent finalement le forçage de vent pour ROMS: les résultats montrent une nette amélioration de la TSM simulée près de la côte, du CPCC, du PCUC et de l'EKE du large. Les vents QuickSCAT corrigés avec une telle procédure pourraient être utilisés dans le futur pour le forçage de vent du CR, ainsi que pour downscaler les vents des CGCMs avec la méthode de Goubanova et al. (2010), et tester ainsi l'effet potentiel sur le réchauffement de l'océan simulé en surface.

- **Conditions aux frontières ouvertes**: dans cette étude, la sélection des CGCMs à la frontière Ouest du modèle régional était basée sur la comparaison systématique avec des données réanalysées et observées des champs de température et de vitesse simulés pour l'océan équatorial superficiel. Pour des raisons pratiques de disponibilité des données des CGCMs, le 'réalisme' des températures simulées a été préféré à celui des courants équatoriaux. Cependant, dans le but d'obtenir plus de confiance dans la pertinence d'un tel choix, la sensibilité de la dynamique régionale du HCS au forçage aux frontières devrait être testée: en particulier, comment les biais dans l'EUC et dans les Jets Tsuchiya ou dans les températures équatoriales influencent-ils les processus d'upwelling côtier?

Echevin et al. (*en preparation*) ont utilisé une configuration de ROMS au 1/9° pour la côte du Pérou (Penven et al., 2005) forcée par trois OGCMs différents et par des données climatologiques pour étudier cette question. Ils ont trouvé que le PCUC était peu corrélé au flux de l'EUC, en accord avec des études récentes, qui indiquent que la source des eaux du PCUC proviennent principalement du SSSCC et seulement minoritairement de l'EUC (Croquette, 2007; Montes et al., 2009). Cependant, les configurations modèle d'Echevin et al. (*en preparation*) et de Montes et al. (2009) ont leur frontière Ouest située à 90°W, juste à l'Est des îles Galapagos, contrairement à la configuration utilisée ici. La division du SEC et de l'EUC autour des îles dans les modèles parents influence les conditions aux frontières, ce qui n'est pas le cas dans notre configuration: le fait que le PCUC soit d'avantage lié au SSSCC qu'à l'EUC dans leur configuration n'exclut pas qu'une partie du flux du SSSCC à 90°W puisse provenir de l'EUC plus à l'Ouest, *cad* peut être à l'Ouest de 100°W. Dans ce

cas, le rôle de l'EUC à 100°W sur les courants côtiers et sur l'upwelling pourrait malgré tout être significatif. D'autre part, on a montré récemment que la modulation basse fréquence des caractéristiques des masses d'eau dans le HCS trouve son origine principalement au niveau des jets zonaux extra-équatoriaux de la region hauturière (Montes et al., 2009). Puisque de telles fluctuations sont susceptibles d'introduire des changements dans la stratification moyenne et donc dans la circulation moyenne du HCS, l'analyse de la dynamique de ces jets et de leur connexion avec la circulation de l'Océan Pacifique Sud à grande échelle pourrait nous aider à comprendre la réponse à basse fréquence du HCS au réchauffement global. Clairement, plus de travaux sont nécessaires pour comprendre l'influence des courants et des propriétés des masses d'eau à grande échelle sur la dynamique du HCS.

Un résultat inattendu de ce travail est le facteur deux entre les flux équatoriaux déduits des données SODA ou TAO et ceux déduits des modèles couplés ou d'ORCA à la frontière Ouest. En effet, d'après Echevin et al. (*en préparation*), SODA surestime les vitesses moyennes au coeur de l'EUC et du SEC d'un facteur deux relativement aux données TAO, tandis qu'ORCA présente des valeurs plus réalistes. Le choix d'ORCA pour le forçage aux frontières du CR était partiellement motivé par les résultats obtenus par Echevin et al. (*en préparation*) à 90°W, mais on a montré ici que SODA est plus approprié pour le forçage du modèle ROMS à 100°W. Dans le cadre du programme PEPS (pour *Peru Ecosystem Projection Scenarios*) financé par l'ANR (voir ci-dessous), une simulation interannuelle sur la période 1992-2000 a récemment été réalisée par G. Cambon avec un forçage issu de SODA et est actuellement analysée et comparée à la simulation forcée par ORCA. Un forçage par Drakkar (Barnier et al., 2006; Molines et al., 2006), une réanalyse océanique longue couvrant les cinquante dernières années sera également testé.

- **<u>Longueur de simulation et scénarios de réchauffement</u>**: comme nous l'avons souligné précédemment, nous avons délibérément choisi de réaliser des simulations de 10 ans (Echevin et al., *en préparation*) avec des climats Pré-industriel et $4xCO_2$ (stabilisé) plutôt que des simulations plus longues (*ex:* 50 ans) avec les scénarios *climat du 20^e siècle* et *SRES*, plus réalistes, à cause des biais des CGCMs de la génération actuelle ainsi que des coûts informatiques. En conséquence, les simulations analysées par Echevin et al. (*en préparation*) présentent un réchauffement très fort (5°C ou plus pour l'océan de surface) qui prendront probablement un siècle ou plus avant de se réaliser dans le monde réel (IPCC, 2007). Nous avons montré que ce réchauffement est trop fort pour pouvoir être compensé par une éventuelle augmentation des vents de surface parallèles à la côte. Cependant, une réponse transitoire de l'océan au réchauffement global avec, disons, une augmentation des vents

favorables à l'upwelling semble être une hypothèse plausible. Ceci induirait un refroidissement de l'océan, qui serait progressivement compensé par un forçage radiatif croissant jusqu'à ce que ce dernier prenne le dessus, entraînant alors la situation décrite par Echevin et al. (*en préparation*). Pour une gestion durable des pêcheries au Pérou et au Chili (voir le préambule de ce manuscrit), des mesures adaptatives devront être prises dans le futur proche en relation avec le changement climatique global déjà en cours: dans ce contexte, une étude de la réponse à long terme du HCS au changement climatique au cours de la phase transitoire des scénarios IPCC avec des émissions de GES en augmentation continue est nécessaire. Celle-ci pourrait être réalisée avec un scénario de quadruplement du CO_2 afin de garantir une bonne cohérence avec les résultats déduits de la phase stabilisée, ou bien avec les scénarios SRES, avec l'espoir de pouvoir simuler des tendances dans les vents de surface et dans la TSM qui soient similaires à celles récemment observées au large des côtes du Pérou et du Chili. Dans tous les cas, de telles tendances peuvent uniquement être déduites de simulations de l'ordre de 50 ans (ou plus), qui ont un coût informatique élevé. Une simulation de contrôle historique longue est actuellement préparée par V. Echevin et B. Dewitte dans le cadre de PEPS, sur la période 1958-2007 couverte par SODA 2.0.2-4 (Carton et Giese, 2008) et par les vents ERA-40 (Uppala et al., 2005) downscalés, et sera utilisée comme reference pour les expériences de downscaling réalisées pour un climat du 20^{e} siècle et un climat SRES. CGCMs et scénarios climatiques du CMIP5 préparés pour l'IPCC-AR5 commenceront à être disponibles dès 2010, et devraient être utilisés dans le futur pour des expériences de downscaling plus fiables. De nombreux scénarios AR5 à court- et long-terme seront disponibles, tels que les expériences RCP (*Representative Concentration Pathways*) dans lesquelles les futures émissions de GES sont conçues afin d'atteindre un niveau donné de forçage radiatif à l'horizon 2100 (Moss et al., 2008), ce qui implique qu'un travail spécifique de sélection de scénario devra être réalisé.

- **Modèles climatiques couplés**: à cause du manque de temps disponible, pour l'instant seul le modèle IPSL-CM4, identifié dans cette thèse comme le CGCM le plus fiable pour notre région, a été downscalé dans le cadre du programme PCCC. Afin d'accroître notre confiance dans les changements projetés de la circulation océanique régionale, d'autres modèles de climat devront être downscalés de façon analogue, avec une priorité pour INGV-ECHAM4 qui a également été identifié ici comme plus fiable que les autres modèles IPCC. De plus, avec la prochaine génération de modèles climatiques, d'autres candidats pourraient aussi fournir des conditions aux frontières appropriées pour ROMS. Par exemple, il a été démontré que le modèle INM-CM4.0 développé par l'Institut de Mathématiques Numériques

(INM) de l'Académie des Sciences Russe, qui présente des résolutions atmosphérique et océanique augmentées ainsi que des rétroactions climatiques améliorées (*ex:* le *cloud feedback* dans l'Ouest du Pacifique tropical), a permis de corriger la plupart des biais qui caractérisaient le précédent INM-CM3.0 dans le Pacifique tropical (Volodin et Diansky, 2004), y compris la variabilité déplacée de la TSM sur la *warm pool* (E. M. Volodin, *communication personnelle*). Il pourrait être intéressant de tester le comportement de ce modèle en regard des feedbacks d'ENSO et de la dynamique de l'Est du Pacifique équatorial, puisqu'on a montré ici que le modèle INM-CM3.0 de la précédente géneration appartient à la catégorie des modèles hybrides: une collaboration entre l'IRD (Institut de Recherche pour le Développement) et l'INM est actuellement en cours de définition dans le but de tester l'impact du changement climatique simulé par ce modèle sur le HCS.

- **Sorties mensuelles des CGCMs**: la comparaison de la variabilité intrasaisonnière d'ORCA à la frontière Ouest de ROMS pour des sorties tous les 5 jours et pour des moyennes mensuelles a révélé que ces dernières atténuent la variabilité haute fréquence par un facteur deux (voir chapitre deux). En effet, les ondes de Kelvin équatoriales intrasaisonnières (IEKW) de grande longueur d'onde sont absentes des moyennes mensuelles pour des fréquences supérieures à $(60 \text{ jours})^{-1}$, et les anomalies de niveau de la mer associées sont réduites d'un facteur 1.5-2 pour des fréquences allant de $(60 \text{ jours})^{-1}$ à $(120 \text{ jours})^{-1}$ (fig. 4.2). Les sorties mensuelles des CGCMs sont donc susceptibles de manquer une fraction significative des changements de l'activité des IEKW et de leurs impacts potentiels sur la dynamique du HCS: en effet, la MJO, qui est responsable – avec d'autres modes de variabilité atmosphérique intrasaisonnière du Pacifique tropical occidental – du déclenchement des IEKW dans la region de la *warm pool*, est modulée aux échelles de temps décennales et s'est montrée plus active depuis le changement de régime climatique des années 70, à cause d'un réchauffement accru de la région Indo-Pacifique (Slingo et al., 1999). Les changements prédits du climat moyen du Pacifique tropical, qui incluent un réchauffement plus fort des TSMs équatoriales qu'hors équateur ainsi qu'un affaiblisssement de la circulation de Walker et des alizés associés (Fedorov et al., 2006; Hansen et al., 2006; Vecchi et al., 2006, 2008), sont donc susceptibles de mettre en place des conditions favorables au développement de WWB via l'extension vers l'est de la *warm pool* du Pacifique Ouest, et pourraient ainsi augmenter l'activité des IEKW et des CTW dans le Pacifique Sud-Est. Une étude récente de Dewitte et al. (2008) est en accord avec cette hypothèse: une tendance positive est observée pour l'activité des IEKW sur la période 1961-1998.

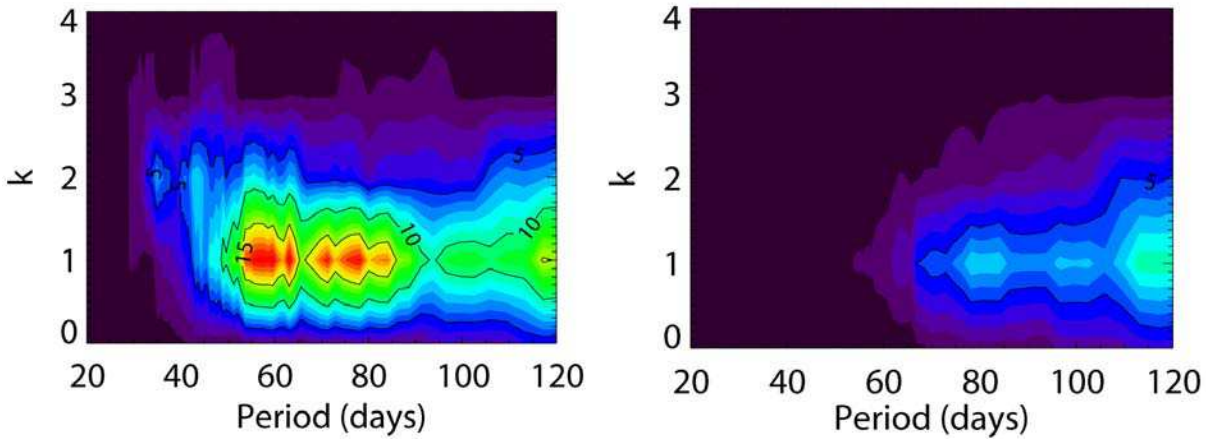

Fig. 4.2: Décompositions fréquence-longueur d'onde des anomalies de SLA du modèle ORCA à l'équateur entre 120°E et 80°W (k=1 ~ 18000km), filtrées des fréquences inférieures à (150 jours)$^{-1}$ pour des sorties tous les 5 jours (à gauche) et pour des moyennes mensuelles (à droite). Pour chacune des deux fréquences d'échantillonnage, seules les propagations vers l'est sont représentées. L'unité du spectre est le cm². L'intervalle pour les contours colorés est de 1 cm².

Les spécifications des simulations du CMIP5 incluent la disponibilité de sorties journalières pour l'océan, qui pourraient aider à résoudre ce problème. Cependant, les sorties journalières tridimensionnelles seront limitées dans l'espace et/ou dans le temps du fait de l'étendue de l'espace disque requis pour archiver ces données. Afin de s'assurer de la disponibilité des données océaniques nécessaires au forçage du modèle ROMS, des accords spécifiques avec les groupes de modélisation de l'IPCC sont requis: dans le cadre du programme PEPS, des collaborations avec les groupes de modélisation de l'IPSL et de l'INM en particulier permettront d'obtenir de telles données pour les périodes temporelles et les scénarios climatiques visés.

Cependant, une thermocline plus profonde et un upwelling plus faible près de l'équateur induits par le réchauffement global provoquent des changements significatifs de la variabilité équatoriale intrasaisonnière simulée par les CGCMs, y compris pour les moyennes mensuelles. Les variabilités intrasaisonnières de la température et des courants simulées par les modèles IPSL-CM4 et INGV-ECHAM4 à 100°W pour un climat pré-industriel et 4xCO_2 suggèrent une réponse des IEKW au réchauffement global dépendente de chaque modèle (figures 4.3 et 4.4):

- la variabilité des courants zonaux augmente de ~60% en surface avec une réorganization spatiale de la variabilité en temperature pour INGV-ECHAM4;

- la variabilité de la temperature augmente de ~50% avec quasiment pas de changement de la variabilité des courants pour IPSL-CM4.

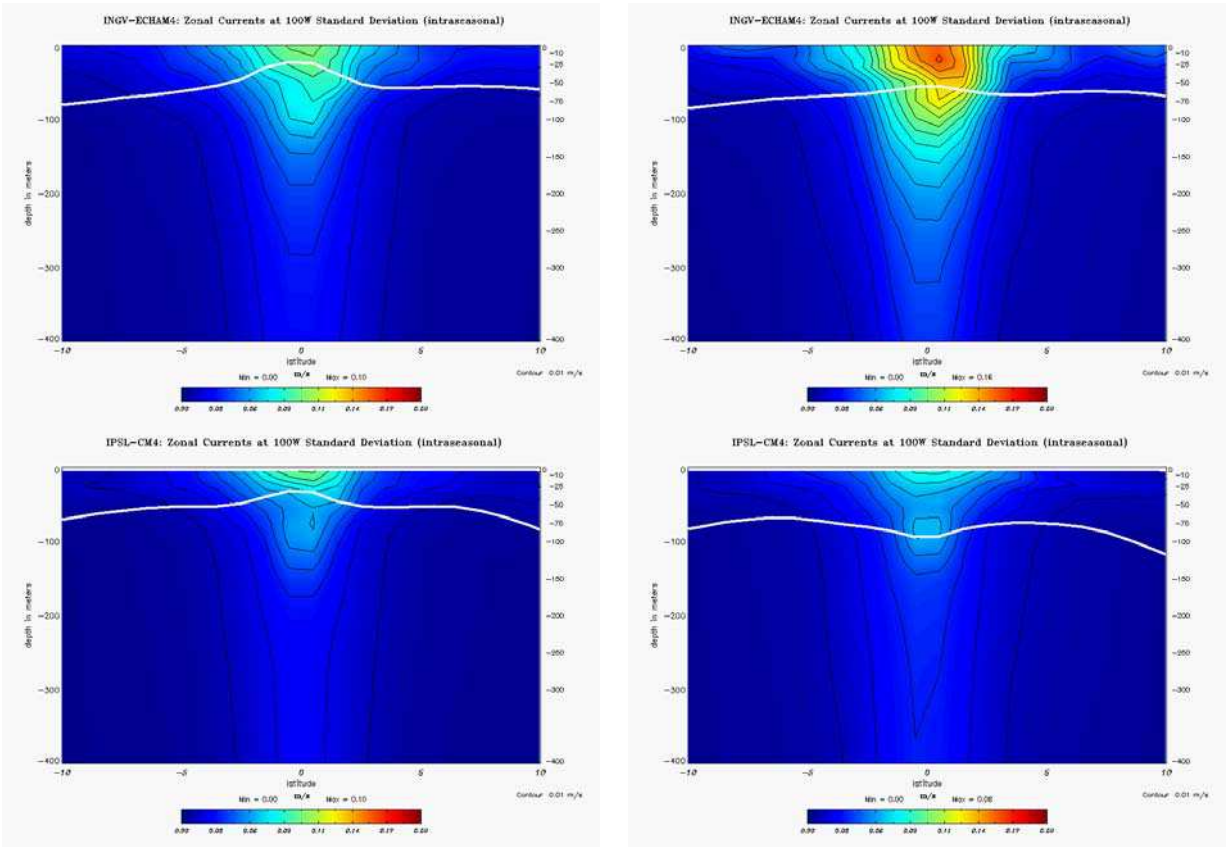

Fig. 4.3: variabilité intrasaisonnière des courants zonaux (RMS, m/s) à 100°W (10°S-10°N, 0m-400m) pour INGV-ECHAM4 (en haut) et IPSL-CM4 (en bas), pour un climat pré-industriel (à gauche) et 4xCO_2 (à droite). La profondeur moyenne de l'isotherme 20°C est également indiquée (courbe blanche). L'intervalle de contour est de 1cm/s. L'échelle de couleur est bleu-rouge: 0 cm/s –20 cm/s.

De tels changements auront un impact direct sur la variabilité intrasaisonnière dans le HCS: par exemple, avec un forçage IPSL-CM4, la variabilité du niveau de la mer simulée par ROMS augmente au large à la fois du Pérou et du Chili (fig. 4.5). Puisqu'il a été montré que la variabilité de la tension de vent de surface diminue aux échelles de temps intrasaisonnières dans cette région (Goubanova et al., 2010), l'augmentation de la variabilité du niveau de la mer doit être liée à l'augmentation de la variabilité océanique dans la région équatoriale, ce qui souligne le rôle du forçage distant d'origine équatoriale dans la dynamique océanique régionale.

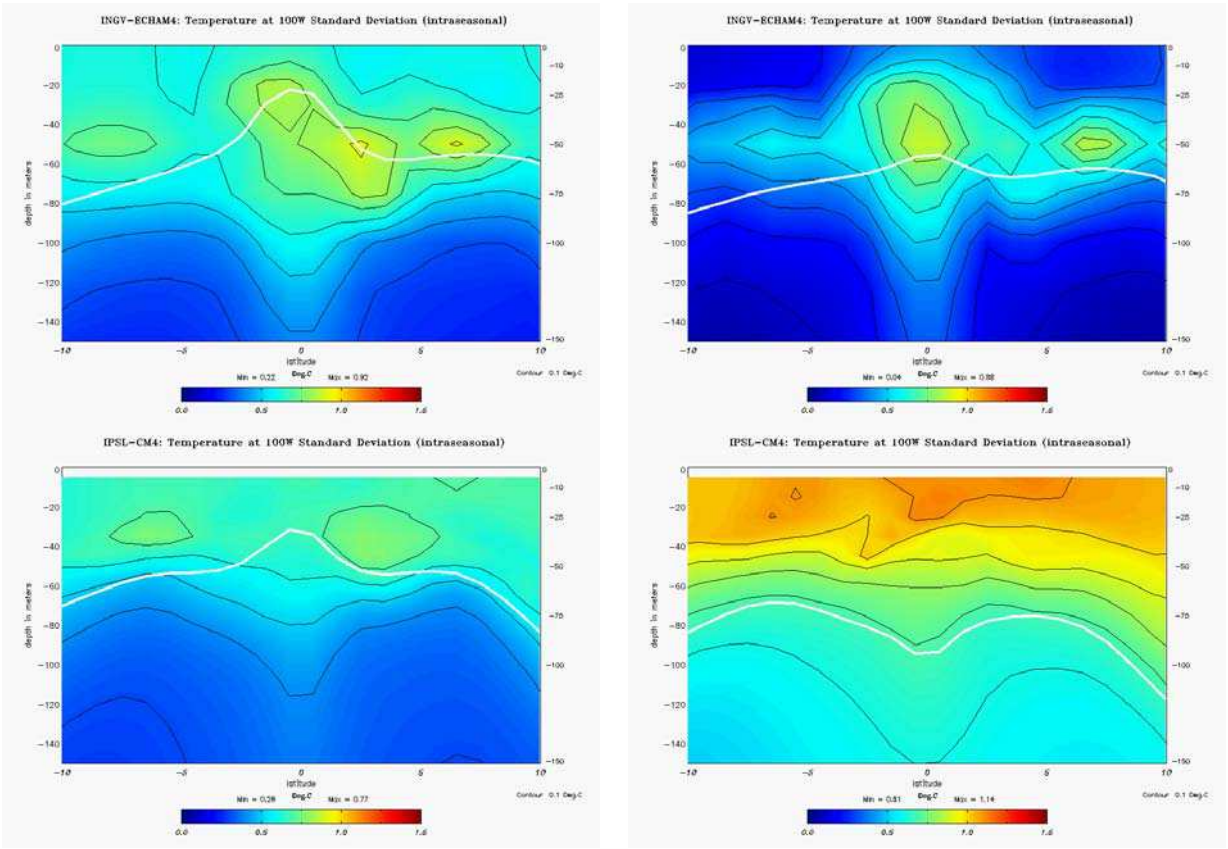

Fig. 4.4: Idem fig. 4.3, mais pour la variabilité intrasaisonnière de la température (RMS, °C) à 100°W (10°S-10°N, 0m-150m). L'intervalle de contour est de 0.1°C. L'échelle de couleur est bleu-rouge: 0–1.5°C.

- **<u>Activité mésoéchelle</u>**: elle n'a pas été considérée explicitement dans l'analyse réalisée sur le CR, malgré la contribution importante des tourbillons mésoéchelle au bilan de chaleur de l'océan superficiel dans le HCS, et malgré les impacts potentiels de ces derniers sur le recrutement des poissons et sur les concentrations de chlorophylle en surface. Cependant, les résultats du chapitre trois suggèrent une possible modulation de l'EKE près de la côte par la variabilité équatoriale, via l'impact des CTW sur le système de courant côtier. Des oscillations de période 50 à 80 jours ont en effet été diagnostiquées dans les séries temporelles du nombre de tourbillons mésoéchelle simulés par ROMS près de la côte centrale du Pérou (fig. 4.6), identifiés au moyen de l'algorithme développé par Chaigneau et al. (2008). De plus, nous avons découvert que les variations à basse fréquence de telles oscillations sont corrélées avec celles des IEKW (pour le premier mode barocline en particulier) avec des valeurs autour de 60-70% et un retard de 10 jours (fig. 4.7a), qui est de l'ordre de la durée prise par les CTW pour se propager le long de la côte de l'équateur à ~15°S. D'autre part, si l'on considère la totalité de la bande de fréquence intrasaisonnière (T<120 jours), on a découvert que de telles variations à basse fréquence sont corrélées avec celles des vents locaux parallèles à la côte, avec des valeurs autour de 50-65% et un retard

négligeable (fig. 4.7c), ce qui suggére qu'à la fois le forçage distant et le forçage local contribuent à la variabilité intrasaisonnière de l'activité mésoéchelle dans cette région caractérisée par une génération intense de tourbillons (fig. 4.7b). Cependant, jusqu'à présent aucune relation claire de ce type n'a pu être trouvée pour la côte centrale du Chili (fig. 4.7a et 4.7c), et ce malgré la variabilité intrasaisonnière significative du vent associée aux jets côtiers et malgré la génération intense de tourbillons mésoéchelle dans cette zone (fig. 4.7b). Cette question devra être investiguée par des études futures afin de quantifier les contributions relatives du forçage distant et du forçage local à l'activité mésoéchelle dans le HCS.

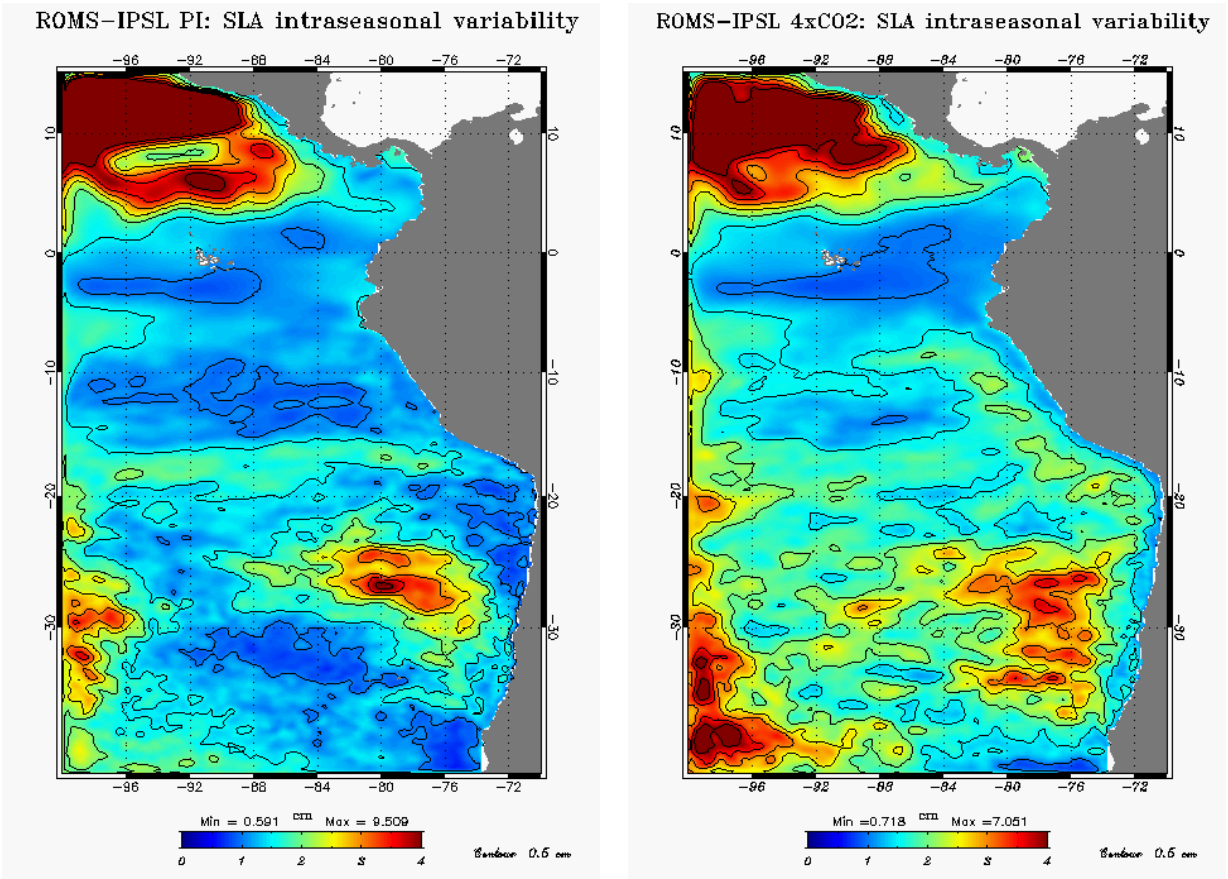

Fig. 4.5: variabilité (RMS) de la SLA filtrée des basses fréquences (f_c = 150 jours) dans l'ESP simulée par ROMS avec un forçage issu du modèle IPSL-CM4 pour un climat pré-industriel (à gauche) et 4xCO_2 (à droite).L'unité est le cm. L'intervalle de contour est de 0.2 cm.

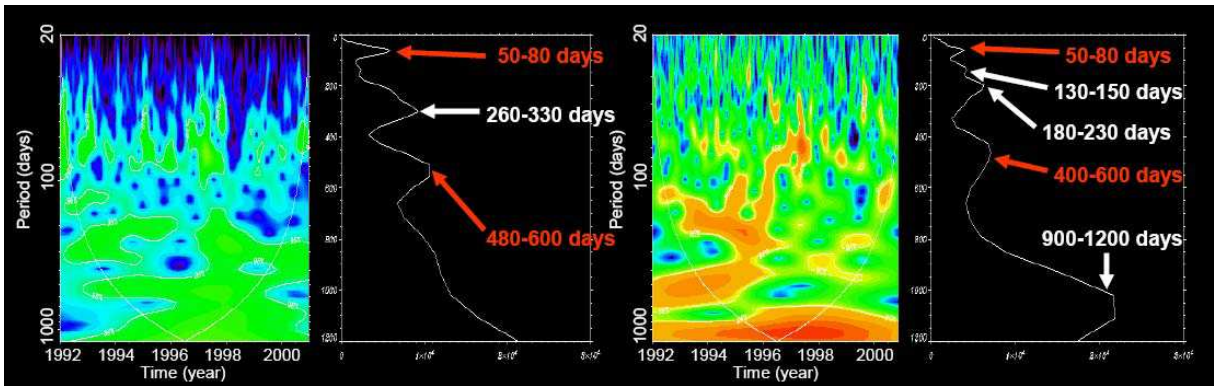

Fig. 4.6: spectre en ondelettes et spectre total en ondelettes pour l'amplitude anormale du premier mode barocline associé à l'EKW simulée par ORCA à 100°W (à gauche) et pour le nombre anormal de tourbillons simulés par ROMS dans les deux premiers degrés depuis la côte à 15°S (à droite). Les fréquences communes entre les deux séries temporelles sont indiquées en rouge.

- **<u>Friction de fond et courbure du trait de côte</u>**: nous suggérons au chapitre trois qu'ils ont un effet significatif sur la latitude critique via l'introduction de termes non-linéaires dans l'équation de vorticité (chapitre trois). Cependant, ces termes n'ont pas été quantifiés: l'examen du comportement des différents termes de l'équation de vorticité le long de la côte constitue une piste prometteuse pour de futures recherches. Elle pourrait permettre de tester ainsi la validité des hypothèses formulées afin d'expliquer la divergence de la solution ROMS de la théorie linéaire des ondes.

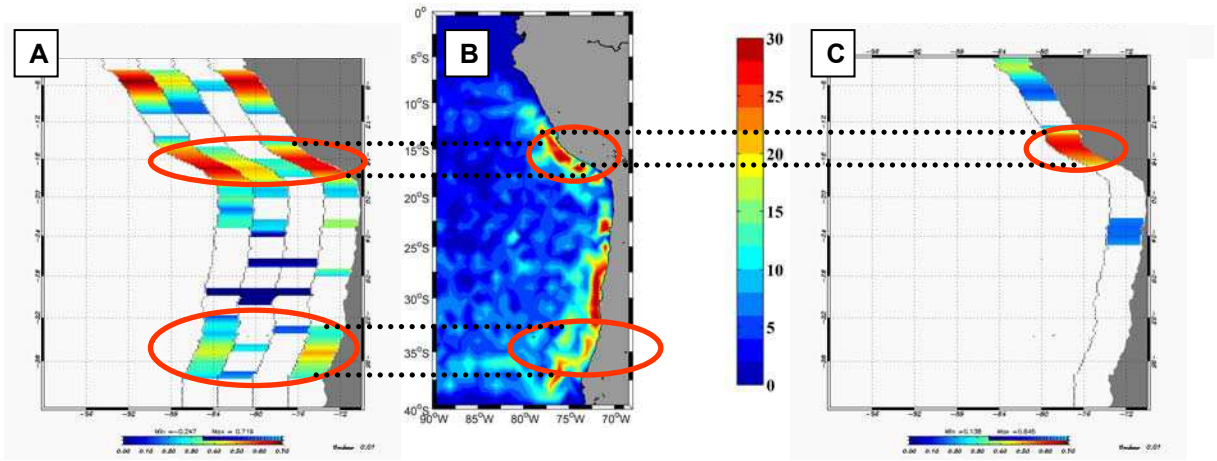

Fig. 4.7: **(A)** Maximum de la corrélation retardée (%) entre les variations à basse fréquence de l'énergie de l'ondelette dans la bande (50-80 jours)$^{-1}$ pour respectivement les 3 premiers modes baroclines de l'EKW et le nombre de tourbillons côtiers, en fonction de la latitude; **(B)** carte de génération de tourbillons; **(C)** idem (A) mais pour la tension de vent méridional le long de la côte et le nombre de tourbillons côtiers pour la bande de frequence (10-120 jours)$^{-1}$. Les 4 bandes en (A) correspondent à (resp. de gauche à droite) la somme des trois premiers, le troisième, le second, et le premier mode barocline de l'EKW. Seules les corrélations significatives sont tracées en (A) et (C).

4.5. Perspectives à long terme

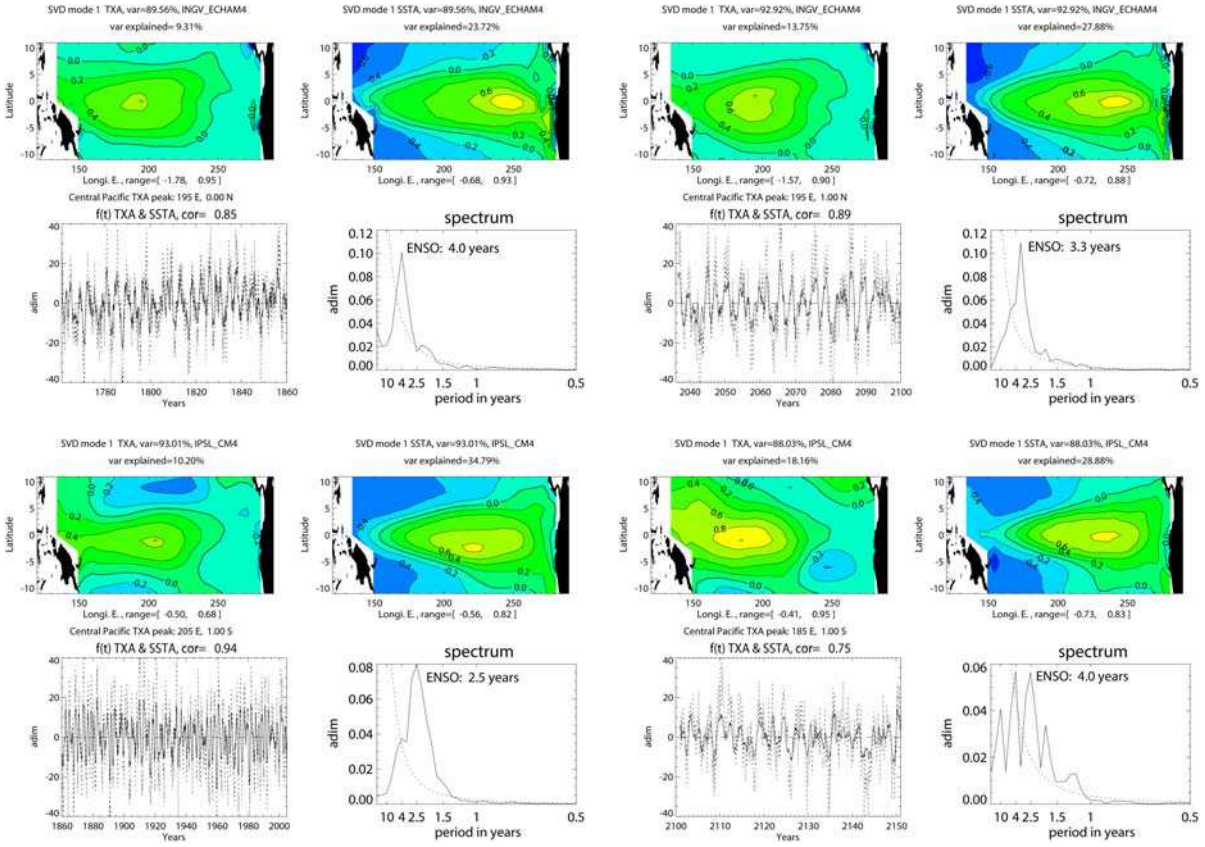

Fig. 4.8: Premier mode SVD entre les anomalies de tension de vent et celles de TSM (11°S-11°N, 134°E-81°W) pour INGV-ECHAM4 (en haut) et IPSL-CM4 (en bas), pour un climat pré-industriel (à gauche) et 4xCO_2 (à droite). Pour chaque simulation, de gauche à droite et de haut en bas: distributions spatiales des anomalies de tension de vent zonal ainsi que de TSM, séries temporelles associées adimensionnalisées (trait plein pour les anomalies de TSM, trait en pointillés pour les anomalies de tension de vent), et spectres en fréquence correspondants adimensionnalisés par l'énergie intégrée sur la totalité du domaine fréquentiel (trait plein pour les anomalies de TSM, trait en pointillés pour le bruit rouge). IC = 0.2 unités. Les structures spatiales sont adimensionnalisées par leurs variances respectives sur le domaine et multipliées par 10. La position du maximum de variance des anomalies de tension de vent est indiquée par une croix sur la carte du mode SVD associé. Les pourcentages de variance expliquée pour la TSM et pour la tension de vent zonal sont indiqués au-dessus des panneaux correspondants. Le pourcentage de covariance expliquée est également fourni. La valeur de corrélation entre les deux séries temporelles est indiquée au-dessus du panneau correspondant et la période dominante d'ENSO est mentionnée sur le spectre.

En plus des perspectives listées ci-dessus, d'autres perspectives à moyen terme et à long terme peuvent être anticipées pour ce travail. L'étude conduite sur les feedbacks d'ENSO dans les CGCMs de l'IPCC (Belmadani et al., 2010) ouvre la voie aux études de la modulation basse fréquence des feedbacks d'ENSO et de son éventuelle relation avec la modulation décennale d'ENSO. De plus, l'impact du changement climatique sur ENSO pourrait être étudié via les changements des processus de retroaction associés. Par exemple, un El Niño du Pacifique central, également appelé El Niño « Modoki » (Ashok et al., 2007; Kao et Yu, 2009; Kug et al., 2009), est apparu depuis les années 90 (Larkin and Harrisson, 2005a; Ashok et al., 2007; Yeh et al., 2009), et il a été montré qu'il est principalement

contrôlé par le *zonal advective feedback* (Kug et al., 2009), contrairement à l'El Niño du Pacifique oriental qui lui est contrôlé par une combinaison du *zonal advective feedback* et du *thermocline feedback*. Cette occurrence croissante d'El Niño Modoki pourrait être liée à un changement dans les feedbacks d'ENSO en réponse à l'affaiblissement attendu de la circulation de Walker et au réchauffement conséquent du Pacifique équatorial. Par ailleurs, les résultats du chapitre deux suggèrent que le NAM joue un rôle important dans la dynamique du cycle ENSO via son effet rectifiant sur le climat moyen. Cette hypothèse devra être confirmée par des recherches futures.

De plus, étudier l'impact du changement climatique sur ENSO devrait aussi fournir des éléments pour la comprehension de l'impact du changement climatique sur le HCS. Alors qu'Echevin et al. (*en préparation*) ont focalisé leur etude sur les changements de l'état moyen et du cycle saisonnier, les travaux futurs se concentreront sur les changements de la variabilité interannuelle à l'échelle régionale, en relation avec les changements potentiels de l'activité ENSO à échelle du bassin. Par exemple, l'échelle de temps d'ENSO dans la simulation $4xCO_2$ d'IPSL-CM4 est plus longue que dans la simulation pré-industrielle (4.0 ans contre 2.5 ans), tandis qu'elle est plus courte pour le modèle INGV-ECHAM4 (3.3 ans contre 4.0 ans), comme on peut le voir sur la figure 4.8. De tels changements pourraient avoir différents impacts sur la circulation régionale et sur la dynamique de l'upwelling côtier, qui sont susceptibles de produire différents effets sur la dynamique de l'écosystème marin: en effet, comme l'ont proposé Bakun et Weeks (2008), la productivité en poisson exceptionnelle du Nord HCS comparé au Sud HCS et aux autres EBUS pourrait être le résultat d'un « 're-démarrage' cyclique du système par les perturbations liées à ENSO qui pourrait tendre à interrompre la croissance maligne de boucles de rétroactions adverses auto-entretenues [telles que des prédateurs non-productifs à la plus grande espérance de vie] au sein de la dynamique biologique non-linéaire de l'écosystème ». Il pourrait être intéressant de tester la réponse physique du HCS à de tels changements de l'échelle de temps associée à ENSO, particulièrement en termes de facteurs susceptibles d'influencer directement la productivité primaire et la dynamique des petits poissons pélagiques, tels que l'upwelling, le transport d'Ekman vers le large, les temps de résidence au-dessus du plateau continental, et la turbulence près de la côte.

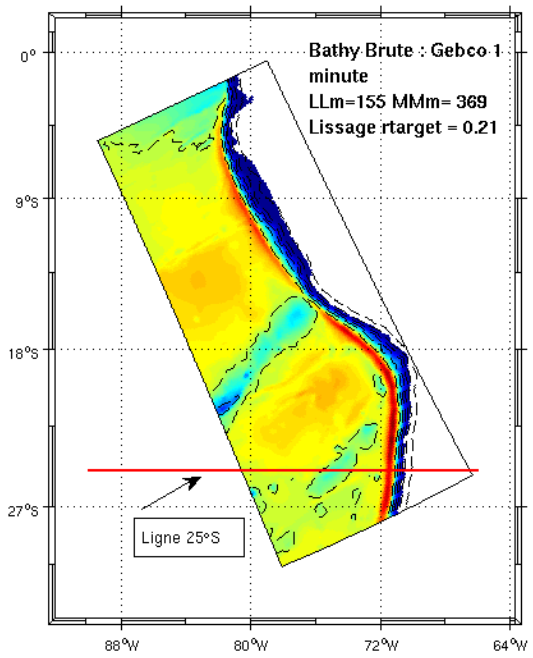

Fig. 4.9: grille curvilinéaire au 1/12° emboîtée pour la configuration du modèle ROMS utilisée dans le programme PEPS. L'image d'arrière-plan représente la bathymétrie (m). *G. Cambon, communication personnelle*.

Le programme ANR-PCCC qui couvrait la période 2006-2008 a été suivi du programme ANR-PEPS (P.I. Dr. V. Echevin), qui a démarré au début de l'année 2009 et durera jusqu'à la fin de l'année 2011. Il s'agit de la continuation du programme PCCC dans la mesure où PEPS étudie l'impact du changement climatique sur les ecosystèmes du Nord HCS et repose sur les résultats de modélisation physique issus de PCCC. Dans PEPS, les simulations ROMS du changement climatique sont couplées avec PISCES, un modèle biogéochimique (Aumont et al., 2003), afin d'étudier l'impact du réchauffement global sur les nutriments et sur la chlorophylle de surface. De plus, les sorties du modèle physique sont également utilisées pour forcer Ichtyop (Lett et al., 2008), un modèle individu-centré (un modèle lagrangien de transport particulaire avec des paramétrisations pour les processus d'enrichement, de concentration et de rétention), afin d'étudier le comportement spatio-temporel des oeufs et larves de petits poissons pélagiques près de la côte du Pérou, ainsi que les changements associés dus au réchauffement global. Enfin, un modèle de dynamique des populations (Seapodym – Lehodey et al., 2003) utilise les paramètres physiques calculés par ROMS pour en déduire la dynamique future de la sardine et de l'anchois péruviens. L'effort de modélisation physique qui a démarré avec PCCC est maintenu avec PEPS, et inclut le downscaling atmosphérique (statistique mais aussi dynamique avec l'utilisation d'un modèle

régional) et océanique de plusieurs simulations IPCC, en suivant la stratégie décrite plus haut. La configuration ROMS au 1/6° présentée ici est retenue dans PEPS, mais sera complétée par un *nesting* (emboîtement) vers une grille curvilinéaire au 1/12° couvrant les côtes du Pérou et du Nord Chili (fig. 4.9) afin de remplir les pré-requis en résolution modèle formulés par nos collègues utilisateurs de Seapodym.

Enfin, la méthodologie développée dans le cadre de PCCC, PEPS et de la présente thèse de doctorat pourrait être appliquée à l'étude de l'impact du changement climatique dans d'autres EBUS, *cad* dans le Courant de Californie, le Courant du Benguela et le Courant des Canaries. Bien entendu certaines adaptations seront nécessaires afin de prendre en compte les spécificités de chaque système. Par exemple, ENSO et les ondes piégées à la côte d'origine équatoriale sont connus pour leur impact significatif sur le Pacifique Nord-Est et le Courant de Californie. D'autre part, ENSO a une signature plus faible dans la variabilité des EBUS de l'Océan Atlantique, bien que des ondes piégées à la côte soient également présentes le long de la côte Ouest de l'Afrique. De plus, le Courant du Benguela est influencé par un mode spécifique de variabilité climatique interannuelle à décennale appelé « Benguela-Niño » et caractérisé par des conditions atmosphériques anormales sur l'Ouest de l'Atlantique tropical ainsi que par des intrusions d'eaux chaudes et salées le long de la côte de Namibie (Shannon et al., 1986; Boyer et al., 2000; Rouault et al., 2007). Le Courant des Canaries est probablement moins influencé par la variabilité de l'Atlantique équatorial, car des ondes intrasaisonnières piégées à la côte n'ont pas été observées au Nord d'environ 12°N (Polo et al., 2008). Cependant, le Courant des Açores est connu pour son fort impact sur la circulation simulée au large de l'Ouest de l'Afrique du Nord (E. Machu, *communication personnelle*), ce qui implique que la dynamique de ce courant à grande échelle devra être investiguée dans les modèles IPCC afin d'étudier l'impact du réchauffement global sur le Système de Courant des Canaries. D'autres structures régionales telles que la Mousson Africaine et l'intrusion d'eaux mediterrannéennes salées via le Détroit de Gibraltar ont aussi un impact sur la dynamique de l'upwelling côtier et devraient être examinées avec attention. De telles études de modélisation régionale du changement climatique futur dans les EBUS sont d'un grand intérêt pour l'IRD, dont la mission est d'aider les pays en développement à améliorer leurs capacités de recherche, afin de pouvoir faire face à des problèmes croissants d'ordre environnemental et sociétal, en particulier dans un contexte de réchauffement global anthropogène. Des initiatives telles que le programme PEPS pour le Pérou constituent un premier pas vers une gestion durable des pêcheries dans les EBUS, ces régions dont les écosystèmes marins sont les plus productifs de l'océan mondial.

A. Global climate change: past, present and future

A.1. The observed post-1850 global warming

In this section, we draw a synthetic portrait of global warming observed since the pre-industrial era (~1850 AD) and of its main contributors: anthropogenic greenhouse gases (GHGs). Most results presented here are taken from the Summary for Policymakers made by Working Group I to the Fourth Assessment Report of the Intergovernmental Panel on Climate Change (IPCC, 2007).

What is global warming ?

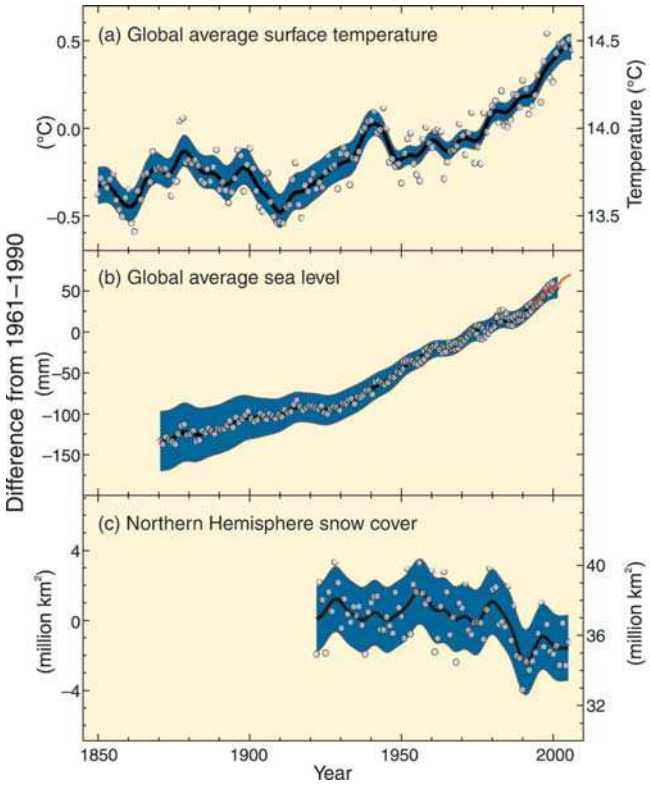

Fig. A.1: Observed changes in **(a)** global average surface temperature (°C) between 1850 and 2005, **(b)** global average sea level (mm) from altimetric data (red) and tide gauge measurements (blue) between 1870 and 2005, and **(c)** Northern Hemisphere snow cover (10^6 km^2) for March-April between 1920 and 2005. All changes are relative to corresponding averages for the period 1961–1990. Smoothed black curves are for decadal average values whereas grey circles are for yearly values. The shaded areas are the uncertainty intervals estimated from a comprehensive analysis of known uncertainties (a and b) and from the time series (c). *Adapted from IPCC (2007)*.

Global warming is the increase in the average temperature of the Earth, both over land and ocean, observed since the mid-19th century, and its projected continuation. Global

surface temperatures increased about 0.6°C to 0.9°C during the XXth century (fig. A.1a) (IPCC, 2007). The Intergovermental Panel on Climate Change (IPCC) concluded in its Fourth Assessment Report (AR4) that increasing atmospheric concentrations of GHGs resulting from human activity (*e.g.* fossil fuel burning and deforestation) caused most of the observed warming since 1950. In addition, the IPCC concludes that variations in natural phenomena (*e.g.* solar radiation and volcanoes) caused most of the warming between 1850 and 1950 but had a slight cooling effect after 1950 (Ammann et al., 2007; Hegerl et al., 2007). Indeed, global climate responds to different types of forcings external to the climate system, such as those mentioned above. Variations in the Earth's orbit around the Sun also constitute an external forcing to the Earth's climate, but they are too slow to explain the observed global temperature change.

Radiative forcing and greenhouse gases

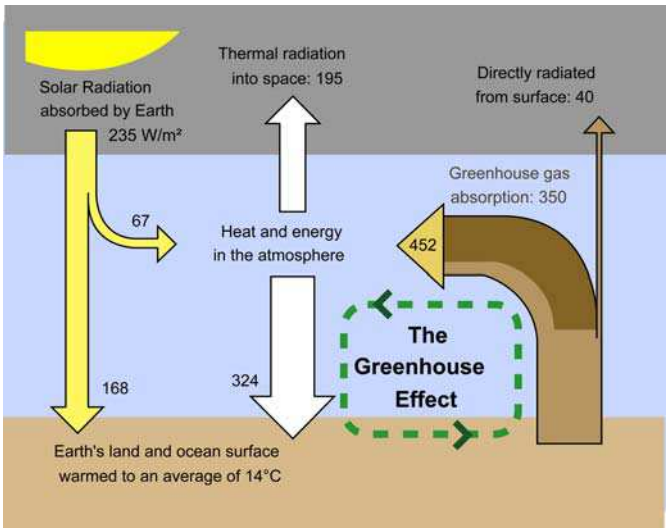

Fig. A.2: Schematic of greenhouse effect showing energy flows (W/m^2) between the atmosphere (blue band), space (grey band), and the Earth's surface (light brown band). *Adapted from Kiehl and Trenberth (1997).*

Changes in the energy balance of the global climate system are expressed in terms of **radiative forcing**: it is a measure (in W/m^2) of the influence that a factor has in altering the balance of incoming and outgoing energy in the Earth-atmosphere system and an index of the importance of that factor as a potential climate change process. Positive forcing tends to warm the surface while negative forcing tends to cool it. Main sources of radiative forcing include:

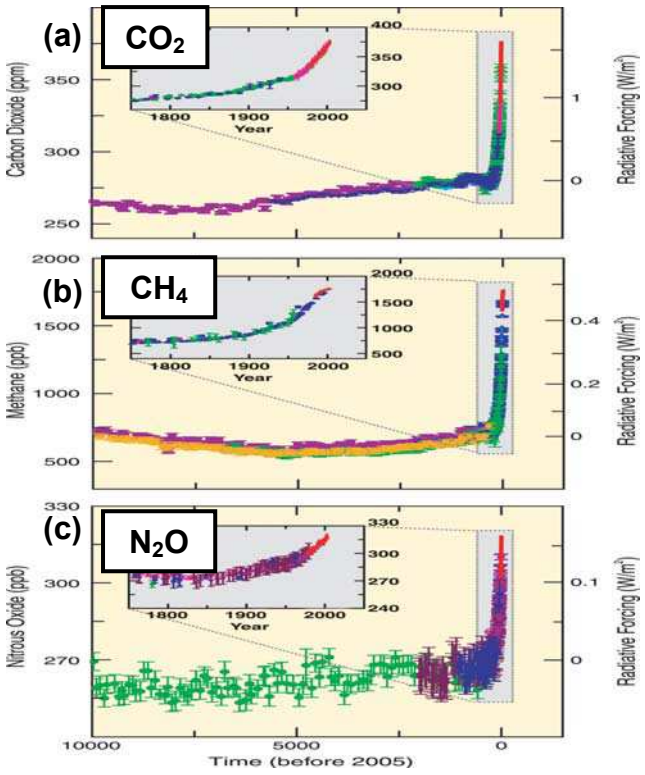

Fig. A.3: Atmospheric concentrations of **(a)** CO_2 (ppm), **(b)** CH_4 (ppb) and **(c)** N_2O (ppb) over the last 10,000 years (large panels) and since 1750 (inset panels). Data are from ice cores (dots and error bars with different colours for different studies) and atmospheric measurements (red lines). The corresponding radiative forcings (W/m^2) are shown on the right hand axes of the large panels. *Adapted from IPCC (2007)*.

- **Greenhouse gases**: the so-called greenhouse effect (fig. A.2) is a positive radiative forcing and is the mechanism by which absorption and emission of infrared radiation by atmospheric gases warm the Earth's surface and lower atmosphere (Fourier, 1824; Arrhenius, 1896). According to estimates calculated by Kiehl and Trenberth (1997), sunlight at the top of the atmosphere brings an energy flow to the Earth of 1366 W/m^2. Due to the atmosphere's geometry and related reflection, only 235W/m^2 eventually reach the lower atmosphere (fig. A.2). In addition, the atmosphere recycles heat from the surface and provides an additional 324 W/m^2, whereas 195W/m^2 are radiated back to space. Over 75% of surface heat recycling by the atmosphere is due to the effect of GHGs present in the atmosphere (*ie* the greenhouse effect) that absorb thermal radiation emitted by the surface. The greenhouse effect is a natural process of the Earth's climate and is essential to maintain surface temperature conditions suitable for the development and sustainability of life. Under stable conditions, the amount of energy received by the global climate system from solar radiation is in balance with the amount of heat radiated back into space, and the Earth's average surface temperature is kept constant. However, recent observations indicate that the Earth absorbs 0.70 to 1.00 W/m2 more than it radiates it into space (Hansen et al., 2005). Most scientists now consider that this

increase in radiative forcing is due to the increase in the atmospheric concentration of GHGs and is the main responsible for global warming. 36-70% of the greenhouse effect is due to water vapor; the rest comes from carbon dioxide CO_2 (9-26%), methane CH_4 (4-9%), ozone O_3 (3-7%) and other gases such as nitrous oxide N_2O or CFCs (chlorofluorocarbons) (Kiehl and Trenberth, 1997). Since the industrial revolution, which started around 1750 and experienced a second impulse around 1850, the atmospheric concentrations of GHGs such as CO_2, CH_4 and N_2O have increased dramatically (fig. A.3) due to fossil fuel burning (75%) and land-use change (25%) including deforestation (IPCC, 2001). Today's levels are higher than at any time during the last 650000 years (Neftel et al., 1985), and have probably not been that high since about 20 million years ago (Pearson and Palmer, 2000). In addition, the modern rate of concentration increase is also unprecedented (fig.A.3).

- **Aerosols**: they act as a negative radiative forcing by increasing the reflection of sunlight (IPCC, 2001) and consist of small solid or liquid particles produced by volcanoes and pollutants and gathering in the atmosphere in the form of clouds. However, it is known that they also produce nonlinear positive or negative forcings to the radiation budget: some of the human-induced aerosols can absorb a fraction of the incoming solar radiation, heating the atmosphere and cooling the surface (Ramanathan et al., 2005). In addition, some aerosols can deposit and increase albedo, which directly heats the surface (Ramanathan et al., 2008).

- **Solar variation**: solar radiations follow a 11-year cycle caused by the magnetic activity of the sun with a nearly-constant amplitude over the last 30 years, for which reliable satellite data have been available (Wilson and Mordvinov, 2003), which raises doubt on the potential responsibility of solar variation in global warming. However, 400 years of sunspot observations reveal significant low-frequency modulation of solar activity on multi-decadal to centenial time scales, with an observed maximum since ~1950. These slow changes have been a primary cause for past climate change (NRC, 1994), and are responsible for 16 to 36% of recent global warming, according to a recent study (Stott et al., 2003).

In addition, the effect of radiative forcing on climate can introduce additional positive/negative feedbacks that amplify/damp the global warming trend. At the global scale, the main positive feedback is the water vapor feedback, by which warming increases the amount of water vapor in the atmosphere, which induces further warming through the greenhouse effect. Conversely, the main negative feedback is the effect of temperature on the emission of infrared radiation, by which warming increases radiation emitted by a given body to space, resulting in a cooling effect that opposes the warming trend. There exist a number of other feedbacks to radiative forcing: these include cloud feedback (Cess et al., 1990; Soden

and Held, 2005), lapse rate (NRC, 2004), ice-albedo feedback (Deser et al., 2000), arctic methane release (Zimov et al., 2006), reduced CO_2 absorption by the oceans (Buesseler et al., 2007), and gas release of biological origin (Simo, 2002; Repo, 2009).

In addition to these global feedbacks, many smaller-scale feedbacks act to regionally or locally modulate global warming. Of particular interest for the study of climate change in EBUS'es, the faster warming of land versus sea (Sutton et al., 2007) is thought to intensify subtropical highs and thereby upwelling-favorable winds, leading to a cooling effect that feedbacks negatively on the warming trend, according to Bakun's hypothesis (Bakun, 1990; Bakun and Weeks, 2008) (see chapter 1, section 2.).

Observed temperature change

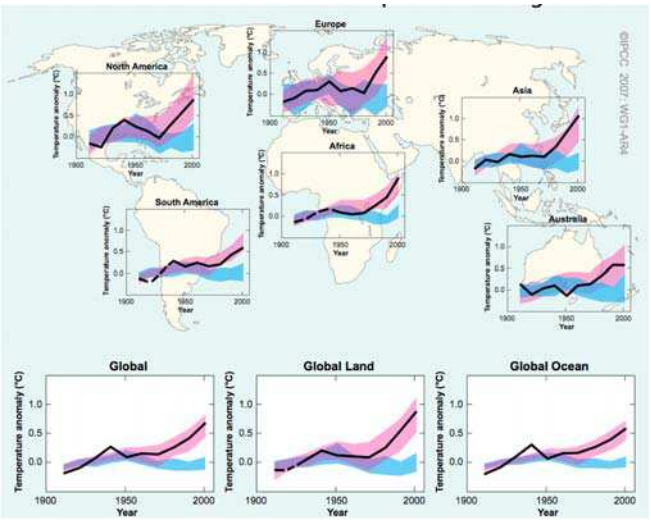

Fig. A.4: Comparison of observed continental- and global-scale changes in surface temperature with results simulated by climate models using natural and anthropogenic forcings. Decadal averages of observations are shown for the period 1906–2005 (black line) plotted against the centre of the decade and relative to the corresponding average for 1901–1950. Lines are dashed where spatial coverage is less than 50%. Blue shaded bands show the 5–95% range for 19 simulations from 5 climate models using only the natural forcings due to solar activity and volcanoes. Red shaded bands show the 5–95% range for 58 simulations from 14 climate models using both natural and anthropogenic forcings. *Adapted from IPCC (2007).*

The most obvious expressions of modern climate change are the increase in globally averaged surface air temperature (0.6°C to 0.9°C for the XXth century) and sea level (~15cm for the same period) and the decrease in northern hemisphere snow cover (~2 million km^2 since 1920), as seen on figure A.1. Whereas surface air temperature rise and ice melting are the result of the direct effect of radiative anthropogenic GHG forcing, sea level rise is almost equally due to the thermosteric expansion effect of temperature increase in the ocean and to

the melting of continental snow and ice (mainly from Greenland and Antarctica) that feeds river input into the oceans (Lombard et al., 2006).

Yet, these global averages hide important geographical differences (fig.A.4). Land heats up more quickly than the ocean (0.25°C/decade vs. 0.13°C/decade) (IPCC, 2007) because of the difference in heat capacity for solid soil and liquid water and because the ocean loses more heat through evaporation (Sutton et al., 2007). The northern hemisphere has thereby heaten up more quickly during the last century than the southern hemisphere because more continental mass is located North from the equator, but also because it features large areas of seasonal snow and sea-ice cover subject to the ice-albedo feedback, conversely to the southern hemisphere where the ice cover suffers less seasonal variations: less ice in summer in the northern hemisphere induces weaker albedo and thus stronger warming. However, the fact that more industrialized countries can be found in the northern hemisphere does not contribute to this meridional asymmetry because GHGs have a residence time in the atmosphere long enough to mix between the two hemispheres (IPCC, 2001). At continental, ocean-basin and regional scales, long-term changes include changes in artic temperatures and ice cover, large-scale changes in precipitation, wind distibution, ocean salinity, and extreme weather events including drought, flooding, heat waves and the intensity of tropical cyclones (IPCC, 2007).

As mentioned above, local climate feedbacks account for most observed geographical variability of climate change, highlighting the need for regional-to-local scale studies of climate change and of its impacts on the environment and the associated ecosystems. Such studies, though focusing on small-scale climate dynamics, receive input from larger-scale observations and future climate change projections. In the next sub-section, we overview the global warming scenarios constructed by the IPCC and the climate models that simulate future XXIst century warming.

A.2. IPCC scenarios and climate models

As explained in the previous sub-section, global warming is the result of increasing GHG concentrations in the atmosphere. Though there still lacks a clear and complete view of the long-term effects of climate change and related complex feedback mechanisms, the fact that climate will keep warming in the next decades to centuries is unequivocal: first, because the thermal inertia of the climate system, in particular that associated to thermal expansion of

the ocean, would sustain future warming for at least a century, even if GHG release in the atmosphere stopped tomorrow (fig. A.8) (IPCC, 2007). Second, because the residence time of GHGs in the atmosphere is long enough to sustain additional warming for centuries (IPCC, 2007). And third, because in spite of climate change mitigation initiatives and political decisions, human societies will definitely continue to rely on activities that release GHGs in the atmosphere for at least a few decades. However, how human activity will evolve in the next century and how the related radiative forcing will change in the future is highly dependent on many factors such as changes in demography, energy use and sources, or technological advances, among others. In order to deal with the uncertainty related to the future evolution of GHG atmospheric concentrations and other forcing agents (*e.g.* aerosols), the IPCC has elaborated a set of emission scenarios for the next century and beyond, in the framework of its Fourth Assessment Report (fig. A.5). These scenarios are used to run simulations with a multi-model ensemble under the framework of the World Climate Research Programme's (WCRP's) Coupled Model Intercomparison Project, phase 3 (CMIP3). Here we briefly review the main groups of scenarios:

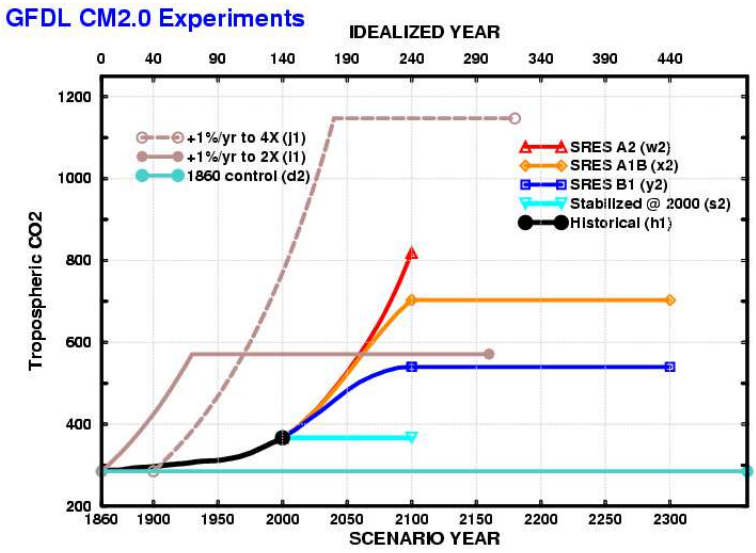

Fig. A.5: Past, present and future tropospheric CO_2 concentration under different IPCC scenarios. *Image courtesy of Geophyscial Fluid Dynamics Laboratory (GFDL).*

- **SRES** scenarios, for Special Report on Emission Scenarios (Nakicenovic and Swart, 2000). A wide range of 40 emission scenarios was defined using a modelling approach based on different possible societal choices in response to global warming, from the more optimistic environmentally-oriented and regionalized B2 scenarios to the more pessimistic economically-driven globalized A1 scenarios (fig. A.6). Each scenario family itself include a

range of scenarios driven by different alternatives of human adaptation and/or mitigation. Most studies of future climate change based on SRES scenarios have focused on three contrasted scenarios, called A2 (pessimistic), B1 (optimistic), and A1B (median). GHG concentration in such scenarios are prolungations of historical levels and start from year 2000. In some SRES scenarios, GHG concentrations stabilize after 2100 (at 550ppm for B1 and 720ppm for A1B), but their main purpose is to study the transient climate response during the XXIst century. After 2100, the uncertainty in societal choices and development and in climate change-induced feedbacks is too large to make any reliable predictions. Model responses to these scenarios are compared to their corresponding responses to historical GHG levels within the so-called « Climate of the 20th Century » experiment (20c3m, *aka* h1 in fig.A.5). The SRES scenarios provide meaningful information for the scientific community and for decision-makers. However, there is still significant uncertainty in the predicted scenarios. In addition, the realism of state-of-the-art global climate models is currently limited by many biases that induce a great diversity of responses to climate change among the models and reduce our confidence in modelled climate projections. For these reasons, and before more realistic scenarios and climate models are made available, we chose to focus in the PCCC program on a second family of scenarios, the 1% year^{-1} CO_2 increase experiments.

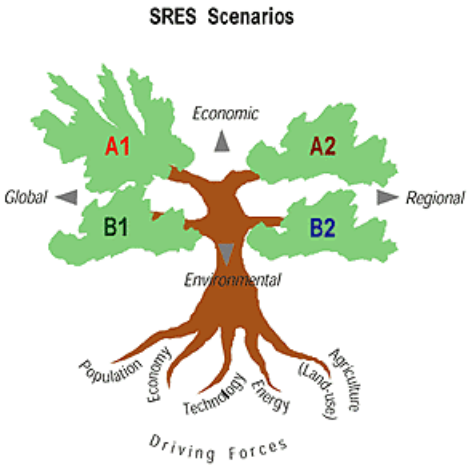

Fig. A.6: Schematic of the SRES A1, A2, B1 and B2 scenario families. Main factors contributing to the definition of these scenarios include changes in population, economy, technology, energy, land-use and agriculture. The four different families differ in choices of global vs. regional economy and energy use, and in favouring economical choices vs. environmental choices. *Adapted from IPCC (2007)*.

- **1% year^{-1} CO_2 increase** scenarios: in these academical experiments, which had already been defined for the Third Assessment Report (TAR) of the IPCC, GHG concentrations increase by 1% every year, starting from pre-industrial levels estimated for 1860 (fig. A.5). In the « 1% per Year to Doubling » experiment (also called 2xCO_2), levels

are stabilized after doubling of the initial concentrations, which occurs after 70 years. The « 1% per Year to Quadrupling » experiment (also called $4xCO_2$) is basically the same experiment, except that stabilization occurs after quadrupling of the initial levels, which takes 140 years. Though these scenarios also allow studying the transient response of the climate system, their main interest is that climate models are integrated for several centuries, and at least 150 years of simulation are available for the period following GHG stabilization. Taking into account approximately 100 years for global surface temperatures to stabilize after the stabilization of emissions (IPCC, 2007), long model integrations are a pre-requisite for the study of the impact of a stable modified climate. Model responses to these scenarios are compared to their corresponding responses to GHG levels kept constant at their pre-industrial levels, within the so-called « Pre-Industrial Control » experiment (PIcntrl, *aka* d2 in fig.A.5). The PCCC program is based on the comparison of the PIcntrl and $4xCO_2$ climate scenarios, which highlights the impact of climate change in an extreme and idealized framework, and allows focusing on the key mechanisms at stake. For this reason, results from the regional climate change experiments presented in chapter 4 do not necessarily pretend to be used as realistic predictions of climate change in the HCS region. Instead, they aim at understanding regional climate feedbacks, quantifying their effect in terms of regional ocean circulation and coastal upwelling dynamics, and testing the validity of theories of regional climate change such as the so-called Bakun's hypothesis (Bakun and Weeks, 2008) for instance (see chapter 1, section 2.). In addition, the PCCC program proposes a methodology of climate change studies which will be possible to apply on future generations of climate models with improved realism and more reliable climate scenarios. Note that the Fifth Assessment Report of the IPCC (IPCC-AR5) is currently in preparation, and simulations from a new generation of climate models will start to become available in 2010. It was decided here to drop off the transition period and focus on the stabilized regime only: indeed, studying the transient response of the HCS to CO_2 increase would require the integration of the regional ocean model for several decades (50 years or so), because of the presence of climate regime shifts in the region at decadal to multi-decadal time scales. Considering the number of simulations to be performed with different CGCMs over different periods for both $4xCO_2$ and preindustrial control experiments, the computational cost would have been tremendous and would have required a work of pre- and post-processing as well as of model output analysis that is too heavy to be carried out in the framework of a PhD thesis. Thus, the chosen approach was to select sub-periods of ten years within both the stabilized period of the $4xCO_2$ experiment and the pre-industrial experiment (see chapter four).

- Other scenarios developed for the IPCC-AR4 include the « 20th Century Climate Change Commitment » experiment (s2 in fig.A.5), in which GHG concentrations are kept constant at year 2000 values for a hundred years integration, the « 2xCO_2 Equilibrium » experiment with a slab ocean (simplified ocean model) and instantaneous CO_2 doubling until stabilization (~100 years), the Atmospheric Model Intercomparison Project (AMIP) simulation, the atmosphere-only counterpart of CMIP in which ocean surface and sea ice boundary conditions are prescribed to match observations over the late 20th century (1979-2000), and some control experiments (« Present-Day Control » and « Slab Ocean Control »).

Climate projections for the next century published by the IPCC (IPCC, 2007) are based on the results of a group of climate models from the WCRP CMIP3. At the time of writing, there are 25 Coupled General Circulation Models (CGCMs) developed by 16 different laboratories and institutions from 13 countries: Australia, Canada, China, Corea, Denmark, France, Germany, Italy, Japan, Norway, Russia, UK, and USA. The reader is invited to refer to chapter 2 for a more complete description of these models. CGCMs, sometimes called AOGCMs (for Atmospheric-Oceanic General Circulation Models), are complex mathematical models of the general circulation of the atmosphere and the ocean coupled together within a unified framework: they are run simultaneously, and the atmospheric model outputs feedback on the ocean model, whereas the oceanic model outputs feedback on the atmospheric model. They are based on the Navier-Stokes equations applied to a rotating Earth with thermodynamic terms for various energy sources (*e.g.* radiation, latent heat). Atmospheric and Oceanic General Circulation Models (AGCMs and OGCMs) are key components of CGCMs, together with sea-ice and land-surface components. These computationally intensive numerical models are based on the integration of a variety of fluid dynamical, chemical, and sometimes biological equations. Such equations are resolved at each point of the tridimensional model grid, which consists of a superposition of spheric layers that cover the globe and account for the different geophysical spheres present on top of the surface of our planet: ocean, land, sea-ice, atmosphere, biosphere (fig. A.7)… CGCMs of the current generation have horizontal spatial resolutions of the order of 2°x1° for the ocean and 3°x2.5° for the atmosphere. These rather coarse resolutions compensate the simulation lengths for which they are designed (~100-500 years) in terms of computer costs. Indeed, monthly to hourly outputs are required for these long global climate simulations, and this already has a cost of the order of 50 tera flops per simulation, which requires the use of supercomputers such as the NEC Earth Simulator (Japan) or IBM Blue Gene (USA). Technological progress in supercomputing progressively allows running CGCMs of

increasing complexity and spatial resolution. Together with scientific progress in the understanding of climate, it will provide the scientific community with more realistic models and hopefully more reliable climate projections. For the time being, one can only rely on global climate projections provided by the current model generation. A review of the main characteristics of these future projections is presented in the next section.

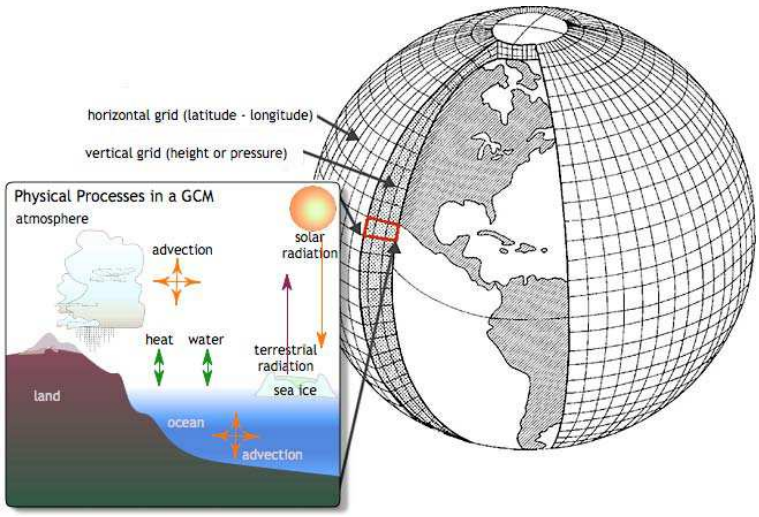

Fig. A.7: Schematic of a CGCM. The insert image represents some of the main coupled land-ocean-atmosphere physical processes resolved by the CGCM for each point of the global grid represented on the right.

A.3. Future XXIst century climate change

Since IPCC's First Assessment Report (FAR) in 1990 (IPCC, 1990), assessed projections have suggested a global average temperature increase between 0.15°C and 0.3°C per decade for the 1990-2005 period. These values can now be compared with observed values of roughly 0.2°C per decade, strengthening our confidence in short-term projections. According to CMIP3 multi-model averages under SRES A2, A1B and B1 scenarios, global average surface temperature will increase by 1.8°C (B1) to 3.6°C (A2) in the XXIst century, though with estimated uncertainty ranging from about 1.8°C (B1) to 3.5°C (A2) (fig. A.8). This is much more than the observed warming during the XXth century (0.6-0.9°C). Likewise, according to IPCC (2007), expected changes in the global climate system are very likely to be larger than those observed during the last century. These projected changes show a large-scale geographical distribution similar to that observed since 1900 (fig. A.9): for all three scenarios, warming is more pronounced over land than water, and over the northern hemisphere than over the southern hemisphere. Arctic regions are expected to undergo the strongest warming, with values reaching 8°C in some areas for the last decade of the XXIst century under the

most pessimistic scenario (A2). In some projections, arctic late-summer sea ice disappears almost entirely (IPCC, 2007). Other expected impacts of future global warming include further reduction of ice and snow cover, further sea level rise, increasing frequence of extreme weather events (heat waves, heavy rainfall, tropical cyclones…), changes in large-scale precipitation, wind and temperature patterns, and weakening of the Meridional Overturning Circulation (MOC) (IPCC, 2007) and of the Walker circulation (Vecchi et al., 2006, 2008), among others. One should note that both past and future anthropogenic CO_2 emissions will continue to contribute to warming and sea level rise for more than a millenium, because of the time scales required for the removal of this gas from the atmosphere (IPCC, 2007).

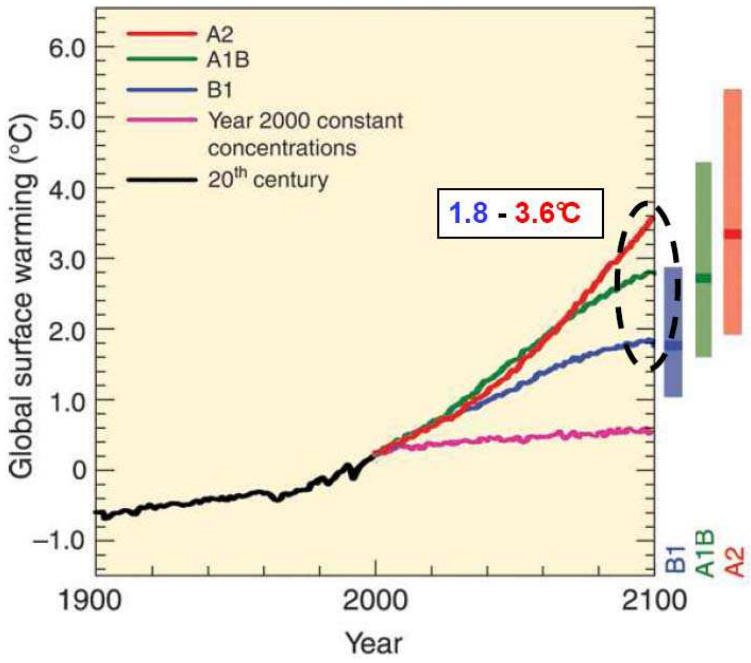

Fig. A.8: Multi-model averages for modern (1900-2000) and future (2000-2100) surface warming (°C). Solid lines are multi-model global averages of surface warming (relative to 1980–1999) for the scenarios A2 (red), A1B (green) and B1 (blue), shown as continuations of the 20th century simulations (black). The pink line is for the experiment where concentrations were held constant at year 2000 values. The coloured bars on the right indicate the best estimate (solid line within each bar) and the likely range assessed for the three SRES scenarios. The assessment of the best estimate and likely ranges in the coloured bars includes the CGCMs in the left part of the figure, as well as results from a hierarchy of independent models and observational constraints. *Adapted from IPCC (2007)*.

To summarize this section, we now know that global warming is real, and that it is very likely that global warming is caused by anthropogenic emissions of GHGs in the atmosphere. We also know that because of the long residence time of GHGs in the atmosphere and the strong inertia of the climate system (in particular that associated to the oceans), global warming is here to stay. The intensity of such warming and of its impacts on the world climate will depend on choices made by societies in regard to their emissions.

However, there are still many things that we do not know. There are large uncertainties in climate projections for the next century because global climate models suffer from numerous biases in the representation of past and present climate, and because they exhibit widespread behaviour in response to climate change. Recent trends are also subject to questioning in some parts of the world were observations for the XXth century have been rather scarce. This is the case for western South America, a region for which the IPCC-AR4 did not provide any clear conclusion, neither in terms of observed climate change, nor in terms of future warming. However, there exist a few studies on this subject, based on theory, paleoclimate records, historical measurements and climate modelling. The object of section 2. from chapter 1 is to provide a review of these studies, with additional input from a few studies conducted on other EBUS'es.

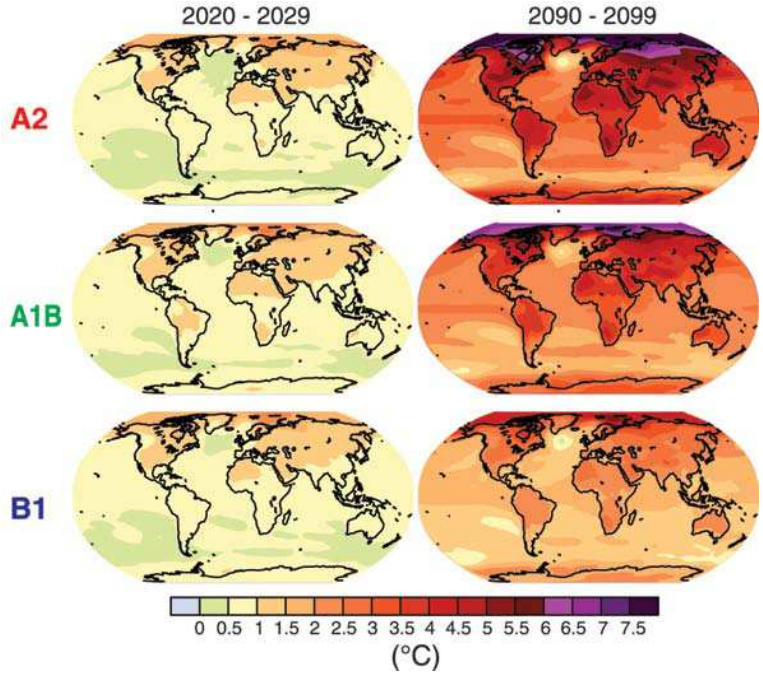

Fig. A.9: Multi-model average projections of surface temperature changes (°C) relative to the period 1980–1999 for the B1 (top), A1B (middle) and A2 (bottom) SRES scenarios averaged over the decades 2020–2029 (left) and 2090– 2099 (right). *Adapted from IPCC (2007)*.

References

AchutaRao, K., and K. Sperber, 2002: Simulation of the El Niño-Southern Oscillation: Results from the Coupled Model Intercomparison Project (CMIP). *Clim. Dyn.*, **19**, 191-209.

---, and ---, 2006: ENSO simulation in coupled ocean-atmosphere models: Are the current models better ? *Clim. Dyn.*, **27**, 1-15.

Amante, C., and B. W. Eakins, 2009: ETOPO1 1 arc-minute global relief model: Procedures, data sources and analysis. *NOAA Technical Memorandum NESDIS NGDC-24*, 19 pp.

Ammann, C. M., F. Joos, D. S. Schimel, B. L. Otto-Bliesner, and R. A. Tomas, 2007: Solar influence on climate during the past millennium: Results from transient simulations with the NCAR Climate System Model. *Proc. Natl. Acad. Sci. U.S.A.*, **104**, 10, 3713–3718.

An, S.-I., and B. Wang, 2000: Interdecadal change of the structure of the ENSO mode and its impact on the ENSO frequency. *J. Clim.*, **13**, 2044-2055.

---, and F.-F. Jin, 2001: Collective role of thermocline and zonal advective feedbacks in the ENSO mode. *J. Clim.*, **14**, 3421-3432.

Anderson, J. J., A. Okubo, A. Robbins, and A. Richards, 1982: A model for nitrite and nitrate distributions in oceanic oxygen minimum zones. *Deep-Sea Res.*, **29**, 1113– 1140.

Antonov, J. I., R. A. Locarnini, T. P. Boyer, A. V. Mishonov, and H. E. Garcia, 2006: World Ocean Atlas 2005, Volume 2: Salinity. S. Levitus, Ed. *NOAA Atlas NESDIS* **62**, U.S. Government Printing Office, Washington, D.C., 182 pp.

Arrhenius, S., 1896: On the influence of carbonic acid in the air upon the temperature of the ground. *London, Edinburgh, and Dublin Philosophical Magazine and Journal of Science (5th series)*, **41**, 237–275.

Ashok, K., S. Behera, A.S. Rao, H.Y. Weng, and T. Yamagata, 2007: El Niño Modoki and its teleconnection. *J. Geophys. Res.*, **112**:C11007. doi: 10.1029/2006JC003798.

---, S. Iizuka, S. A. Rao, N. H. Saji, and W.-J. Lee, 2009a: Processes and boreal summer impacts of the 2004 El Niño Modoki: An AGCM study. *Geophys. Res. Lett.*, **36**, L04703, doi:10.1029/2008GL036313.

---, C.-Y. Tam, and W.-J. Lee, 2009b: ENSO Modoki impact on the Southern Hemisphere storm track activity during extended austral winter. *Geophys. Res. Lett.*, **36**, L12705, doi:10.1029/2009GL038847.

Auad, G., A. Miller, and E. Di Lorenzo, 2006: Long-term forecast of oceanic conditions off California and their biological implications. *J. Geophys. Res.*, **111**, C09008, doi:10.1029/2005JC003219.

Aumont, O., E. Maier-Reimer, S. Blain, and P. Monfray, 2003: An ecosystem model of the global ocean including Fe, Si, P colimitations. *Global Biogeochem. Cycles*, **17**, 2, 1060, doi:10.1029/2001GB001745.

Bakun, A., 1990: Global climate change and intensification of coastal upwelling. *Science*, **247**, 198-201.

---, and C. S. Nelson, 1991: The seasonal cycle of wind stress curl in subtropical eastern boundary current regions. *J. Phys. Oceanogr.*, **21**, 1815-1834.

---, and S. J. Weeks, 2008: The marine ecosystem off Peru: What are the secrets of its fishery productivity and what might its future hold? *Progr. Oceanogr.*, **79**, 290-299.

Barber, R., and F. Chavez, 1983: Biological consequences of El Niño. *Science*, **222**, 203–210.

Barnier, B., G. Madec, T. Penduff, J.-M. Molines, A.-M. Treguier, J. Le Sommer, A. Beckmann, A. Biastoch, C. Böning, J. Dengg, C. Derval, E. Durand, S. Gulev, E. Rémy, C. Talandier, S. Theetten, M. Maltrud, J. McClean, and B. De Cuevas, 2006: Impact of partial steps and momentum advection schemes in a global ocean circulation model at eddy-permitting resolution. *Ocean Dyn.*, DOI: 10.1007/s10236-006-0082-1.

Barton, E. D., and C. Roy, 2009: Canary Current upwelling: More or less? *In preparation.*

Battisti, D. S., and A. C. Hirst, 1989: Interannual variability in the tropical atmosphere/ocean system: Influence of the basic state and ocean geometry. *J. Atmos. Sci.*, **46**, 1687-1712.

Belmadani, A., and B. Dewitte, 2010: ENSO feedbacks in the IPCC-AR4 models. *Climate variability in the tropical Pacific: Mechanisms, modelling and observations,* Y. duPenhoat and A. Kislov [Eds.], MAKS-press, Moscow, Russia, 170pp., in press.

---, ---, and S.-I. An, 2010: ENSO feedbacks and associated time scales of variability in a multi-model ensemble. *J. Clim.*, in press.

---, V. Echevin, and B. Dewitte: The influence of intraseasonal equatorial Kelvin waves on nearshore variability off Peru and Chile: A modelling study. *J. Geophys. Res.*, to be submitted.

Bengtsson, L., K. I. Hodges, and E. Roeckner, 2006: Storm tracks and climate change. *J. Clim.*, **19**, 3518–3543.

Bentamy, A., Y. Quilfen, F. Gohin, N. Grima, M. Lenaour, and J. Servain, 1996: Determination and validation of average wind fields from ERS-1 scatterometer measurements. *The Global Atmosphere and Ocean System*, **4**, 1–29.

Bernal, P. A., F. L. Robles, and O. Rojas, 1982: Variabilidad fisica y biologica en la region meridional del sistema de corrientes Chile-Peru. *Monogr. Biol.*, **2**, 75-102.

Bertrand, S., B. Dewitte, J. Tam, A. Bertrand, and E. Diaz, 2008: Impact of Kelvin wave forcing in the Peru Humboldt Current system: Scenarios of spatial reorganization from physics to fishers. *Progr. Oceanogr.*, **79**, 278–289.

Bjerknes, J., 1966: A possible response of the atmospheric Hadley circulation to equatorial anomalies of ocean temperature. *Tellus*, **18**, 820–829.

---, 1969: Atmospheric teleconnections from the equatorial Pacific. *Mon. Wea. Rev.,* **97,** 163–172.

Blanco, J. L., A. C. Thomas, M. E. Carr, and P. T. Strub, 2001: Seasonal climatology of hydrographic conditions in the upwelling region off northern Chile. *J. Geophys. Res.*, **106**, 11451-11467.

---, M.-E. Carr, A. C. Thomas, and P. T. Strub, 2002: Hydrographic conditions off Northern Chile during the 1996-1998 La Niña and El Niño events. *J. Geophys. Res.*, **107**, C3, 3017, doi:10.1029/2001JC001002.

Blanke, B., and R. Raynaud, 1997: Kinematics of the Pacific equatorial undercurrent: An eulerian and lagrangian approach from GCM results. *J. Phys. Oceanogr.*, **27**, 1038–1053.

Bony, S., and J.-L. Dufresnes, 2005: Marine boundary layer clouds at the heart of tropical cloud feedback uncertainties in climate models. *Geophys. Res. Lett.*, **32**, L20806, doi:10.1029/2005GL023851.

Boyer, D., J. Cole, and C. Bartholome, 2000: Southwestern Africa: Northern Benguela Current region. *Marine Pollution Bulletin*, **41**, 123-140.

Brandhorst, W., 1971: Condiciones oceanograficas estivales frente a la costa de Chile. *Rev. Biol. Mar.* (Valparaiso), **14**, 3, 45-84.

Brink, K. H., 1982: A comparison of long coastal trapped wave theory with observations off Peru. *J. Phys. Oceanogr.*, **12**, 897-913.

---, 1989: Energy conservation in coastal-trapped wave calculations. *J. Phys. Oceanogr.*, **19**, 1011-1016.

---, and D. C. Chapman, 1987: Programs for computing properties of coastal-trapped waves and wind-driven motions over the continental shelf and slope. *Woods Hole Oceanogr. Inst. Tech. Rep.* WHOI-87-24, 122 pp.

---, D. Halpern, A. Huyer, and R. L. Smith, 1983: The physical environment of the Peruvian upwelling system. *Progr. Oceanogr.*, **12**, 185–305.

Brochier, T., C. Lett, J. Tam, P. Fréon, F. Colas, and P. Ayon, 2008: An individual-based model study of anchovy early life history in the northern Humboldt current system. *Progr. Oceanogr.*, **79**, 313-325.

Buesseler, K. O., C. H. Lamborg, P. W. Boyd, P. J. Lam, T. W. Trull, R. R. Bidigare, J. K. B. Bishop, K. L. Casciotti, F. Dehairs, M. Elskens, M. Honda, D. M. Karl, D. A. Siegel, M. W. Silver, D. K. Steinberg, J. Valdes, B. Van Mooy, and S. Wilson, 2007: Revisiting carbon flux through the ocean's twilight zone. *Science*, **316**, 5824, 567–570.

Burgers, G., M. A. Balmaseda, F. C. Vossepoel, G. J. van Oldenborgh, and P. J. van Leeuwen, 2002: Balanced ocean-data assimilation near the equator. *J. Phys. Oceanogr.*, **32**, 2509-2529.

Cai, W., and T. Cowan, 2006: SAM and regional rainfall in IPCC AR4 models: Can anthropogenic forcing account for southwest Western Australian winter rainfall reduction? *Geophys. Res. Lett.*, **33**, L24708, doi:10.1029/2006GL028037.

---, and ---, 2009: La Niña Modoki impacts Australia autumn rainfall variability. *Geophys. Res. Lett.*, **36**, L12805, doi:10.1029/2009GL037885.

Camayo, R., and E. J. D. Campos, 2006: Application of wavelet transform in the study of coastal trapped waves off the west coast of South America. *Geophys. Res. Lett.*, **33**, 22601, doi:10.1029/2006GL026395.

Cane, M. A., 2005: The evolution of El Niño, past and future. *Earth Planet. Sci. Lett.*, **230**, 227-240.

---, and D. W. Moore, 1981: A note on low-frequency equatorial basin modes. *J. Phys. Oceanogr.*, **11**, 1578-1584.

Capet, X., P. Marchesiello, and J. C. McWilliams, 2004: Upwelling response to coastal wind profiles. *Geophys. Res. Lett*., **13**, L13311, doi:10.1029/2004GL020123.

---, E. J. Campos, and A. M. Paiva, 2008: Submesoscale activity over the Argentinian shelf. *Geophys. Res. Lett*., **35**, L15605, doi:10.1029/2008GL034736.

---, F. Colas, P. Penven, P. Marchesiello, and J. C. McWilliams, 2009: Eddies in eastern-boundary subtropical upwelling systems. Ocean modeling in an eddying regime. *Geophys. Monogr. Series*, **177**, M. W. Hecht and H. H. Hasumi [Eds.], AGU, Washington D.C., 350pp.

Capotondi, A., A. Wittenberg, and S. Masina, 2006: Spatial and temporal structure of tropical Pacific interannual variability in 20th century coupled simulations. *Ocean Mod.*, **15**, 274-298.

Carr, M.-E., P. T. Strub, A. C. Thomas, and J. L. Blanco, 2002: Evolution of 1996-1999 La Niña and El Niño conditions off the western coast of South America: A remote sensing perspective. *J. Geophys. Res.*, **107**, C12, 3236, doi:10.1029/2001JC001183.

Carton, J. A., and B. S. Giese, 2008: A reanalysis of ocean climate using Simple Ocean Data Assimilation (SODA). *Mon. Wea. Rev.*, **136**, 2999-3017.

---, and ---: SODA: A reanalysis of ocean climate. *Personal communication.*

CERSAT, 2002: Mean wind fields (MWF product)-User Manual-Volume1: QuikSCAT. *C2-MUT-W-04-IF,*

CERSAT- IFREMER. http://www.ifremer/cersat.fr.
Cess, R. D., G. L. Potter, J. P. Blanchet, G. J. Boer, A. D. Del Genio, M. Déqué, V. Dymnikov, V. Galin, W. L. Gates, S. J. Ghan, J. T. Kiehl, A. A. Lacis, H. Le Treut, Z.-X. Li, X.-Z. Liang, B. J. McAvaney, V. P. Meleshko, J. F. B. Mitchell, J.-J. Morcrette, D. A. Randall, L. Rikus, E. Roeckner, J. F. Royer, U. Schlese, D. A. Sheinin, A. Slingo, A. P. Sokolov, K. E. Taylor, W. M. Washington, R. T. Wetherald, I. Yagai, and M.-H. Zhang, 1990: Intercomparison and interpretation of climate feedback processes in 19 atmospheric general circulation models. *J. Geophys. Res.*, **95**, D10, 16601–16615.
Chaigneau, A., and O. Pizarro, 2005a: Surface circulation and fronts of the South Pacific Ocean, east of 120°W. *Geophys. Res. Lett.*, **32**, L08605, doi:10.1029/2004GL02207.
---, and ---, 2005b: Eddy characteristics in the eastern South Pacific. *J. Geophys. Res.*, **110**, C06005, doi:10.1029/2004JC002815.
---, A. Gizolme, and C. Grados, 2008: Mesoscale eddies off Peru in altimeter records: Identification algorithms and eddy spatio-temporal patterns. *Progr. Oceanogr.*, **79**, 106-119.
---, G. Eldin, and B. Dewitte, 2009: Eddy activity in the four major upwelling systems from altimetry (1992-2007). *Progr. Oceanogr.*, **83**, 117-123.
Chapman, D. C., 1987: Application of wind-forced, long, coastal-trapped wave theory along the California coast. *J. Geophys. Res.*, **92**, 1789–1816.
Chavez, F. P., 1995: A comparison of ship and satellite chlorophyll from California and Peru. *J. Geophys. Res.*, **100**, 24855–24862.
---, J. Ryan, S. E. Lluch-Cota, and M. Niquen, 2003: From anchovies to sardines and back: Multidecadal change in the Pacific ocean. *Nature*, **299**, 217-221.
---, A. Bertrand, R. Guevara-Carrasco, P. Soler and J. Csirke, 2008: The northern Humboldt Current System: Brief history, present status and a view towards the future. *Progr. Oceanogr.*, **79**, 95–105.
Chelton, D. B., M. G. Schlax, and R. Samelson, 2007: Summertime coupling between sea surface temperature and wind stress in the California Current System. *J. Phys. Oceanogr.*, **37**, 3, 495-517.
---, M. G. Schlax, J. M. Lyman, and G. C. Johnson, 2003: Equatorially-trapped Rossby waves in the presence of meridionally-sheared baroclinic flow in the Pacific. *Progr. Oceanogr.*, **56**, 323–380.
---, S. K. Esbensen, M. G. Schlax, N. Thum, M. H. Freilich, F. J. Wentz, C. L. Gentemann, M. J. McPhaden, and P. S. Schopf, 2001: Observations of coupling between surface wind stress and sea surface temperature in the eastern tropical Pacific. *J. Clim.*, **14**, 1479–1498.
---, R. A. deSzoeke, M. G. Schlax, K. El Naggar, and N. Siwertz, 1998: Geographical variability of the first baroclinic Rossby radius of deformation. *J. Phys. Oceanogr.*, **28**, 433-460.
Cibot, C., E. Maisonnave, L. Terray, and B. Dewitte, 2005: Mechanisms of tropical Pacific interannual-to-decadal variability in the ARPEGE/ORCA global coupled model. *Clim. Dyn.*, **24**, 823-842.
Clarke, A. J., 1983: The reflection of equatorial waves from oceanic boundaries. *J. Phys. Oceanogr.*, **13**, 1193-1207.
---, 1989: Theoretical understanding of eastern ocean boundary poleward undercurrents. *Coastal Estuarine Studies*, **34**, 26–39, S. Neshyba, C. N. K. Mooers, R. L. Smith, and R. T. Barber (Eds.), Springer, New York.
---, and C. Shi, 1991: Critical frequencies at ocean boundaries. *J. Geophys. Res.*, **96**, 10731-10738.
---, and S. Van Gorder, 1994: On ENSO coastal currents and sea level. *J. Phys. Oceanogr.,* **24,** 661–680.
Colas, F., X. Capet, J. C. McWilliams, and A. Shchepetkin, 2008a: 1997-98 El Niño off Peru: A numerical study. *Progr. Oceanogr.*, **79**, 138-155.
---, ---, X. Jin, J. Molemaker, D. B. Chelton, and J. C. McWilliams, 2008b: Wind stress and sea surface temperature coupling in eastern boundary upwelling systems. *"Eastern Boundary Upwelling Systems" symposium, 2-6 June 2008, Las Palmas (Spain)*.
---, ---, and J. C. McWilliams, 2009: Dynamics of the Peru/Chile current system. *In preparation*.
Combes, V., E. Di Lorenzo, F. Gomez, S. Hormazabal, P. T. Strub, and D. Putrasahan, 2009: Modelling interannual and decadal variability in the Humboldt Current upwelling system. *J. Phys. Oceanogr.*, in preparation.
Cravatte, S., J. Picaut, and G. Eldin, 2003: First and second baroclinic Kelvin modes in the equatorial Pacific at intraseasonal timescales. *J. Geophys. Res.,* **108,** 3266, doi:10.1029/2002JC001511.
Cromwell, T., R. B. Montgomery, and E. D. Stroup, 1954: Equatorial undercurrent revealed by new methods. *Science*, **119**, 648–649.
Cronin, T., G. Dwyer, T. Kamiya, S. Schwede, and D. Willard, 2003: Medieval Warm Period, Littel Ice Age and 20th century temperature variability from Chesapeake Bay. *Global Planet. Change*, **36**, 17-29.
Croquette, M., 2007: Contribution à l'étude de l'upwelling du Pérou-Chili. *Thèse de l'Université de Paul Sabatier*, 186 pp.

---, G. Eldin, C. Grados, and M. Tamayo, 2007: On differences in satellite wind products and their effects in estimating coastal upwelling processes in the south-east Pacific. *Geophys. Res. Lett.*, **34**, L11608, doi:10.1029/2006GL027538.

Cucalon, E., 1987: Oceanic variability off Ecuador associated with an El Niño event in 1982– 1983. *J. Geophys. Res.*, **92**, 14309–14322.

Da Silva, A. M., C. C. Young, and S. Levitus, 1994: Atlas of surface marine data 1994, vol. 1. *Algorithms and procedures, technical report*, Natl. Oceanogr. and Atmos. Admin., Silver, Spring, Md.

Demarcq, H., 2009: Trends in primary production, sea surface temperature and winds in upwelling systems (1998-2007). *Progr. Oceanogr.*, in press, doi:10.1016/j.pocean.2009.07.022.

Déqué, M., C. Dreveton, A. Braun, and D.Cariolle, 1994: The ARPEGE/IFS atmosphere model: A contribution to the French community climate modelling. *Clim. Dyn.*, **10**, 249-266.

Deser, C., J. E. Walsh, and M. S. Timlin, 2000: Arctic sea ice variability in the context of recent atmospheric circulation trends. *J. Clim.*, **13**, 617–633.

Dewitte, B., 2000: Sensitivity of an intermediate coupled ocean-atmosphere model of the tropical Pacific to its oceanic vertical structure. *J. Clim.*, **13**, 2363-2388.

---, C. Cibot, C. Périgaud, S.-I. An, and L. Terray, 2007: Interaction between Near-Annual and ENSO modes in a CGCM simulation: Role of the equatorial background mean state. *J. Clim.*, **20**, 1035-1052.

---, M. Ramos, V. Echevin, O. Pizarro, and Y. duPenhoat, 2008a: Vertical structure variability in a seasonal simulation of a medium-resolution regional model of the Eastern South Pacific. *Progr. Oceanogr.*, **79**, 120-137.

---, S. Purca, S. Illig, L. Renault, and B. S. Giese, 2008b: Low-frequency modulation of intraseasonal equatorial kelvin wave activity in the Pacific from SODA: 1958-2001. *J. Clim.*, **21**, 6060-6069.

Diffenbaugh, N. S., 2005: Response of large-scale eastern boundary current forcing in the 21st century. *Geophys. Res. Lett.*, **32**, L19718, doi:10.1029/2005GL023905.

Di Lorenzo, E., A. J. Miller, N. Schneider, and J. C. McWilliams, 2005: The warming of the California current system: Dynamics and ecosystem implications. *J. Phys. Oceanogr.*, **35**, 336–362.

Durand, M.-H., P. Cury, R. Mendelssohn, C. Roy, A. Bakun, and D. Pauly, 1998: *Global versus local changes in upwelling systems*. 558 pp, Editions ORSTOM, Paris.

Echevin, V., O. Aumont, J. Ledesma, and G. Flores, 2008: The seasonal cycle of surface chlorophyll in the Peruvian upwelling system: A modelling study. *Progr. Oceanogr.*, **79**, 167-176.

---, K. Goubanova, A. Belmadani, and B. Dewitte, 2010: Change in seasonal cycle of the upwelling of the Humboldt system associated to global warming: A downscaling experiment with the IPSL-CM4 model. *J. Geophys. Res.*, submitted.

---, F. Colas, P. Penven, and A. Chaigneau: Sensitivity of regional model simulations of the North Humboldt Current System to their equatorial boundary conditions. *In preparation*.

Eden, C., and A. Timmermann, 2004: The influence of the Galapagos Islands on tropical temperatures, currents and the generation of tropical instability waves. *Geophys. Res. Lett.*, **31**, L15308, doi:10.1029/2004GL020060.

Ekman, V. W., 1905: On the influence of the earth's rotation on ocean currents. *Ark. Mat. Astron. Fys.*, **11**, 1-52.

Enfield, D. B., 1976: Oceanography of the region north of the equatorial front, physical aspects. *F.A.O. Fish. Rep.*, **185**, 299–334.

---, 1981: Thermally-driven wind variability in the planetary boundary layer above Lima, Peru. *J. Geophys. Res.*, **86**, 2005–2016.

---, 1986: Zonal and seasonal variability of the equatorial Pacific heat balance. *J. Phys. Oceanogr.*, **16**, 1038–1054.

---, 1987: The intraseasonal oscillation in eastern Pacific sea levels: How is it forced? *J. Phys. Oceanogr.,* **17,** 1860–1876.

Escobar, D., 1993: Evaluacion climatologica y sinoptica del fenomeno de vientos Paracas. *Tesis para optar el titulo de Ingeniero Meteorologico*, Universidad Nacional Agraria La Molina, 62pp.

Falvey, M., and R. Garreaud, 2009: Regional cooling in a warming world: Recent temperature trends in the southeast Pacific and along the west coast of subtropical South America (1979-2006). *J. Geophys. Res.*, **114**, D04102, doi:10.1029/2008JD010519.

F.A.O., 2009: The state of world fisheries and aquaculture 2008. *FAO Fisheries and Aquaculture Department*, Rome, Italy.

Fedorov, A. V., and S. G. Philander, 2000: Is El Niño changing ? *Science,* **288**, 1997. doi:10.1126/science.288.5473.1997

---, and ---, 2001: A stability analysis of tropical ocean-atmosphere interactions: bridging measurements and theory for El Niño. *J. Clim.,* **14**, 3086-3101.

---, P. S. Dekens, M. McCarthy, A. C. Ravelo, P. B. deMenocal, and M. Barreiro, 2006: The Pliocene paradox (mechanisms for a permanent El Niño). *Science,* **312,** 1485–1489.

Fiedler, P. C., 1994: Seasonal and interannual variability of coastal zone color scanner phytoplankton pigments and winds in the eastern Pacific. *J. Geophys. Res.*, **99**, 18371–18384.

Fonseca, T. R., 1989: An overview of the poleward undercurrent and upwelling along the Chilean coast. *Poleward Flows Along Eastern Ocean Boundaries*, **34**, S. J. Neshyba, C. N. K. Mooers, R. L. Smith, and R. T. Barber (Eds.), 203–218, Springer, New York.

Fourier, J., 1824: Remarques générales sur les temperatures du globe terrestre et des espaces planétaires. *Annales de Chimie et de Physique*, **27**, 136–167.

Fuenzalida, R., W. Schneider, J. Garcès-Vargas, and L. Bravo, 2009: Satellite altimetry data reveals jet-like dynamics of the Humboldt Current. *J. Geophys. Res.*, **113**, C07043, doi:10.1029/2007JC004684.

Garcia-Herrera, R., H. F. Diaz, R. R. Garcia, M. R. Prieto, D. Barriopedro, R. Moyano, and E. Hernandez, 2008: A chronology of El Niño events from primary documentary sources in northern Peru. *J. Clim.*, **21**, 1948-1962.

Garreaud, R., and R. Muñoz, 2005: The low-level jet off the west coast of subtropical South America: Structure and variability. *Mon. Wea. Rev.*, **133**, 8, 2246-2261.

---, and M. Falvey, 2009: The coastal winds off western subtropical South America in future climate scenarios. *International Journal of Climatology*, **29**, 4, 543-554.

Gastineau, G., and B. J. Soden, 2009: Model projected changes of extreme wind events in response to global warming. *Geophys. Res. Lett.*, **36**, L10810, doi:10.1029/2009GL037500.

---, H. Le Treut, and L. Li, 2008: Hadley circulation changes under global warming conditions indicated by coupled climate models. *Tellus A*, **60**, 863–884.

Gordon, C., C. Cooper, C.A. Senior, H.T. Banks, J.M. Gregory, T.C. Johns, J.F.B. Mitchell and R.A. Wood, 2000: The simulation of SST, sea ice extents and ocean heat transports in a aroundion of the Hadley Cbetween coupled model without flux adjustments. *Clim. Dyn.*, **16**, 147-168.

Goubanova, K., V. Echevin, B. Dewitte, F. Codron, K. Takahashi, P. Terray, and M. Vrac, 2010: Statistical downscaling of sea-surface wind over the Peru-Chile upwelling region: Diagnosing the impact of climate change from the IPSL-CM4 model. *Clim. Dyn.*, revised.

Graham, N., M. Hughes, C. Ammann, K. Cobb, M. Hoerling, D. Kennett, J. Kennett, B. Rein, L. Stott, P. Wigand, and T.Y. Xu, 2007: Tropical Pacific – mid-latitude teleconnections in medieval times. *Clim. Change*, **83**, 241-285.

Grimshaw, R., and J. S. Allen, 1988: Low-frequency baroclinic waves off coastal boundaries. *J. Phys. Oceanogr.*, **18**, 1124-1143.

Guilyardi, E., 2006: El Niño-mean state-seasonal cycle interactions in a multi-model ensemble. *Clim. Dyn.*, **26**, 329-348.

---, A. Wittenberg, A. Fedorov, M. Collins, C. Wang, A. Capotondi, G. J. van Oldenborgh, and T. Stockdale, 2009: Understanding El Niño in ocean-atmosphere general circulation models: Progress and challenges. *Bull. Amer. Meteor. Soc.*, doi:10.1175/2008BAMS2387.1, 325-340.

---, S. Gualdi, J. M. Slingo, A. Navarra, P. Delecluse, J. Cole, G. Madec, M. Roberts, M. Latif, and L. Terray, 2004: Representing El Niño in coupled ocean-atmosphere GCMs: The dominant role of the atmospheric component. *J. Clim.*, **17**, 4623-4629.

Gunther, E. R., 1936a: A report on oceanographical investigation in the Peru coastal current. *Discovery Rep.*, **13**, 107-276.

---, 1936b: Variations in behaviour of the Peru coastal current: With a historical introduction. *Geogr. J.*, **88**, 1, 37-61, doi:10.2307/17868600.

Gutierrez, D., A. Sifeddine, D. Field, L. Ortlieb, G. Vargas, F. Chavez, F. Velazco, V. Ferreira, P. Tapia, R. Salvatteci, H. Boucher, M. Morales, J. Valdes, J.-L. Reiss, A. Campusano, M. Boussafir, M. Mandeng Yogo, M. Garcia, and T. Baumgartner, 2009: Rapid reorganization in ocean biogeochemistry off Peru towards the end of the Little Ice Age. *Biogeosciences*, **6**, 835-848.

Halpern, D., 2002: Offshore Ekman transport and Ekman pumping off Peru during the 1997-98 El Niño. *Geophys. Res. Lett.*, **29**, 5, 1075, doi:10.1029/2001GL014097.

Hansen, J., L. Nazarenko, R. Ruedy, M. Sato, J. Willis, A. Del Genio, D. Koch, A. Lacis, K. Lo, S. Menon, T. Novakov, J. Perlwitz, G. Russell, G. A. Schmidt, and N. Tausnev, 2005: Earth's energy imbalance: confirmation and implications. *Science*, **308**, 5727, 1431-1435.

---, M. Sato, R. Ruedy, K. Lo, D. W. Lea, and M. M. Elizade, 2006: Global temperature change. *Proc. Natl. Acad. Sci.*, **103**, 14288.

Hayashi, Y., 1979: A generalized method of resolving transient disturbances into standing and traveling waves by space-time spectral analysis. *J. Atmos. Sci.*, **36**, 1017-1029.

---, 1982: Space-time spectral analysis and its applications to atmospheric waves. *J. Meteor. Soc. Japan,* **60,** 156–171.

Hegerl, G. C., F. W. Zwiers, P. Braconnot, N. P. Gillett, Y. Luo, J. A. Marengo Orsini, N. Nicholls, J. E. Penner, and P. A. Stott, 2007: Understanding and attributing climate change. In: *Climate Change 2007: The*

Physical Science Basis. Contribution of Working Group I to the Fourth Assessment Report of the Intergovernmental Panel on Climate Change, S. Solomon, D. Qin, M. Manning, Z. Chen, M. Marquis, K. B. Averyt, M. Tignor, and H. L. Miller (Eds.). Cambridge University Press, Cambridge, UK, and New York, NY, USA, pp 84.

Helly, J. J., and L. A. Levin, 2004: Global distribution of naturally occurring marine hypoxia on continental margins. *Deep-Sea Res.*, I, **51**, 1159–1168.

Hormazabal, S., G. Shaffer, and O. Pizarro, 2002: Tropical Pacific control of intraseasonal oscillations off Chile by way of oceanic and atmospheric pathways. *Geophys. Res. Lett.*, **29**, 6, 10.1029/2001GL013481.

---, ---, N. Silva and E. Navarro, 2006: The Peru Chile undercurrent and the oxygen minimum zone variability off central Chile. *Suplemento Gayana*, **70**, ISSN 0717-652X.

Hourdin, F., I. Musat, S. Bonv, P. Braconnot, F. Codron, J.-L. Dufresne, L. Fairhead, M.-A. Filiberti, P. Friedlingstein, J.-Y. Grandpeix, G. Krinner, P. LeVan, Z.-X. Li, and F. Lott, 2006: The LMDZ4 general circulation model: Climate performance and sensitivity to parametrized physics with emphasis on tropical convection. *Clim. Dyn.*, **27**, 7-8, 787-813.

Hill, A. E., B. M. Hickey, F. A. Shillington, P. T. Strub, K. H. Brink, E. D. Barton, and A. C. Thomas, 1998: Eastern Ocean boundaries. *The Sea*, **11**, A. R. Robinson and K. H. Brink (Eds.), 29–67, John Wiley, Hoboken, N. J.

Hirst, A. C., 1986: Unstable and damped equatorial modes in simple coupled ocean-atmosphere models. *J. Atmos. Sci.*, **43**, 606-630.

Huyer, A., 1980: The offshore structure and subsurface expression of sea level variations off Peru, 1976 – 1977. *J. Phys. Oceanogr.*, **10**, 1755–1768.

---, R. L. Smith, and T. Paluszkiewicz, 1987: Coastal upwelling off Peru during normal and El Niño times, 1981-1984. *J. Geophys. Res.,* **92**, C13, 14297-14307.

---, M. Knoll, T. Paluzkiewicz, and R. L. Smith, 1991: The Peru Undercurrent: A study in variability. *Deep-Sea Res.*, **39**, 247– 279.

IPCC, 2007: Climate change 2007: The physical science basis. *Contribution of Working Group I to the Fourth Assessment Report of the Intergovernmental Panel on Climate Change*, S. Solomon, D. Qin, M. Manning, Z. Chen, M. Marquis, K. B. Averyt, M. Tignor, and H. L. Miller (Eds.). Cambridge University Press, Cambridge, UK, and New York, NY, USA, pp 18.

---, 2001: Climate change 2001: The scientific basis. *Contribution of Working Group I to the Third Assessment Report of the Intergovernmental Panel on Climate Change*, J. T. Houghton, Y. Ding, D. J. Griggs, M. Noguer, P. J. van der Linden, X. Dai, K. Maskell, and C. A. Johnson (Eds.). Cambridge University Press, Cambridge, UK, and New York, NY, USA, pp 881.

---, 1990: Scientific Assessment of Climate Change. *Contribution of Working Group I to the First Assessment Report of the Intergovernmental Panel on Climate Change*, WMO, UNEP. J. T. Houghton, G. J. Jenkins and J. J. Ephraums (Eds.). Cambridge University Press, 365 pp.

Izumo, T., 2005: The equatorial undercurrent, meridional overturning circulation, and their roles in mass and heat exchanges during El Niño events in the tropical Pacific ocean. *Ocean Model.*, **55**, 2, 110-123.

Jahncke, J., D. Checkley, and G. L. Hunt, 2004: Trends in carbon flux to seabirds in the Peruvian upwelling system: Effects of wind and fisheries on population regulation. *Fisheries Oceanogr.*, **13**, 208-223.

Jiang, C., L. Thompson, K. A. Kelly, and M. F. Cronin, 2009: The roles of intraseasonal Kelvin waves and tropical instability waves in SST variability along the equatorial Pacific in an isopycnal ocean model. *J. Clim.*, **22**, 3470-3487.

Jin, F.-F., 1996: Tropical ocean-atmosphere interaction, the Pacific cold tongue, and the El Niño-Southern Oscillation. *Science*, **274**, 76-78.

---, 1997a: An equatorial ocean recharge paradigm for ENSO. Part I: Conceptual model. *J. Atmos. Sci.*, **54**, 811-829.

---, 1997b: An equatorial ocean recharge paradigm for ENSO. Part II: A stripped-down coupled model. *J. Atmos. Sci.*, **54**, 811-829.

---, and S.-I. An, 1999: Thermocline and zonal advective feedbacks within the equatorial ocean recharge oscillator model for ENSO. *Geophys. Res. Lett.*, **26** (19), 2989-2992.

---, J.-S. Kug, S.-I. An, and I.-S. Kang, 2003: A near-annual coupled ocean-atmosphere mode in the equatorial Pacific Ocean. *Geophys. Res. Lett.*, **30**, 1080, doi:10.1029/2002GL015983.

Johns, T. C., J. M. Gregory, W. J. Ingram, C. E. Johnson, A. Jones, J. A. Lowe, J. F. B. Mitchell, D. L. Roberts, D. M. H. Sexton, D. S. Stevenson, S. F. B. Tett, and M. J. Woodage, 2003: Anthropogenic climate change for 1860 to 2100 simulated with the HadCM3 model under updated emissions scenarios. *Clim. Dyn.*, **20**, 583-612.

---, C. F. Durman, H. T. Banks, M. J. Roberts, A. J. McLaren, J. K. Ridley, C. A. Senior, K. D. Williams, A. Jones, G. J. Rickard, S. Cusack, W. J. Ingram, M. Crucifix, D. M. H. Sexton, M. M. Joshi, B.-W. Dong, H. Spencer, R. S. R. Hill, J. M. Gregory, A. B. Keen, A. K. Pardaens, J. A. Lowe, A. Bodas-Salcedo, S.

Stark, and Y. Searl, 2006: The new Hadley Cbetween climate model HadGEM1: Evaluation of coupled simulations. *J. Clim.*, **19**, 7, 1327-1353.
Johnson, E. R., 1991: The scattering at low frequencies of coastally trapped waves. *J. Phys. Oceanogr.*, **21**, 913–932.
Johnson, G. C., M. J. McPhaden, and E. Firing, 2001: Equatorial Pacific Ocean horizontal velocity, divergence, and upwelling. *J. Phys. Oceanogr.*, **31**, 839-849.
---, B. M. Sloyan, W. S. Kessler, and K. E. McTaggart, 2002: Direct measurements of upper ocean current and water properties across the tropical Pacific during the 1990s. *Progr. Oceanogr.*, **52**, 31–61.
Jordi, A., A. Orfila, G. Basterretxea, and J. Tintoré, 2005: Coastal trapped waves in the northwestern Mediterranean. *Cont. Shelf Res.*, **25**, 185-196.
Joseph, R., and S. Nigam, 2006: ENSO evolution and teleconnections in IPCC's twentieth-century climate simulations: Realistic representation? *J. Clim.,* **19,** 4360–4377.
Kalnay, E., M. Kanamitsu, R. Kistler, W. Collins, D. Deaven, L. Gandin, M. Iredell, S. Saha, G. White, J. Woollen, Y. Zhu, A. Leetmaa, R. Reynolds, M. Chelliah, W. Ebisuzaki, W. Higgins, J. Janowiak, K. C. Mo, C. Ropelewski, J. Wang, R. Jenne, and D. Joseph, 1996: The NCEP/NCAR 40-year reanalysis project. *Bull. Am. Meteorol. Soc.*, **74**, 789–799.
Kang, I.-S., J.-S. Kug, S.-I. An, and F.-F. Jin, 2004: A near-annual Pacific Ocean basin mode. *J. Clim.*, **17**, 2478-2488.
Kao, H.-Y., and J.-Y. Yu, 2009: Contrasting Eastern-Pacific and Central-Pacific types of ENSO. *J. Clim.*, **22**, 615-632.
Karnauskas, K. B., R. Murtugudde, and A. J. Busalacchi, 2007: The effect of the Galapagos islands on the equatorial Pacific cold tongue. *J. Phys. Oceanogr.*, **37**, 1266-1281.
Keen, R. A., 1982: The role of cross-equatorial cyclone pairs in the Southern Oscillation. *Mon. Wea. Rev.*, **110**, 1405-1416.
Kessler, W. S., 2006: The circulation of the eastern tropical Pacific: A review. *Prog. Oceanogr.*, **69**, 181-217.
---, and M. J. McPhaden, 1995: Oceanic equatorial waves and the 1991–1993 El Niño. *J. Clim.,* **8,** 1757–1774.
---, ---, and K. M. Weickmann, 1995: Forcing of intraseasonal Kelvin waves in the equatorial Pacific. *J. Geophys. Res.,* **100,** 10613–10632.
---, L. M. Rothstein, and D. Chen, 1998: The annual cycle of SST in the eastern tropical Pacific, as diagnosed in an ocean GCM. *J. Clim.*, **11**, 777–799.
Kiehl, J. T., and K. E. Trenberth, 1997: Earth's annual global mean energy budget. *Bull. Am. Met. Assoc.*, **78**, 197–208.
Killworth, P. D., and J. R. Blundell, 1999: The effect of bottom topography on the speed of long extratropical planetary waves. *J. Phys. Oceanogr.*, **29**, 2689–2710.
Kirtman, B. P., 1997: Oceanic Rossby wave dynamics and the ENSO period in a coupled model. *J. Clim.*, **10**, 1690–1704.
Klein, S., and D. Hartmann, 1993: The seasonal cycle of low stratiform clouds. *J. Clim.*, **6**, 1587-1606.
Knauss, J. A., 1960: Measurements of the Cromwell Current. *Deep-Sea Res.*, **6**, 265–286.
Koutavas, A., and J. Lynch-Stieglitz, 2004: Variability of the marine ITCZ over the eastern Pacific during the past 30000 years: Regional perspective and global context. *The Hadley Circulation: Present, Past and Future*, R. S. Bradley and H. F. Diaz (eds.), Kluwer Academic Publishers, 347-369.
Kug, J.-S., F.-F. Jin, and S.-I. An, 2009: Two types of El Niño events: Cold tongue El Niño and warm pool El Niño. *J. Clim.*, **22**, 1499-1515.
Large, W. G., and G. Danabasoglu, 2006: Attribution and impacts of upper-ocean biases in CCSM3. *J. Clim.*, **19**, 2325–2346.
---, J. McWilliams, and S. Doney, 1994: Oceanic vertical mixing: A review and a model with a nonlocal boundary layer parameterization. *Review of Geophysics*, **32**, 363–403.
Larkin, N. K., and D.E. Harrison, 2005a: On the definition of El Niño and associated seasonal average U.S. weather anomalies. *Geophys. Res. Lett.*, **32**, L13705, doi:10.1029/2005GL022738.
--- and ---, 2005b: Global seasonal temperature and precipitation anomalies during El Niño autumn and winter. *Geophys. Res. Lett.*, **32**, L16705, doi:10.1029/2005GL022860.
Lehodey, P., F. Chai, and J. Hampton, 2003: Modelling climate-related variability of tuna populations from a coupled ocean-biogeochemical-populations dynamics model. *Fisheries Oceanogr.*, **12**, 4, 483-494.
Leloup, J., and A. Clement, 2009: Why is there a minimum in projected warming in the tropical North Atlantic Ocean? *Geophys. Res. Lett.*, **36**, L14802, doi:10.1029/2009GL038609.
Lengaigne, M., J.-P. Boulanger, C. Menkes, S. Masson, P. Delecluse, G. Madec, 2002: Ocean response to the March 1997 westerly wind event. *J. Geophys. Res.*, **107**, 8015, doi:10.1029/2001 JC000841.
Leth, O., and G. Shaffer, 2001: A numerical study of the seasonal variability in the circulation off central Chile. *J. Geophys. Res.*, **106**, C10, 22, 229-22, 248.

---, and J. F. Middleton, 2004: A mechanism for enhanced upwelling off central Chile: eddy advection. *J. Geophys. Res.*, **109**, C12020, doi:10.1029/2003JC002129.
Le Traon, P. Y., F. Nadal, and N. Ducet, 1998: An improved mapping method of multisatellite altimeter data. *J. Atmos. Ocean. Technol.*, **15**, 522–534.
Lett, C., P. Penven, P. Ayon, and P. Fréon, 2007: Enrichment, concentration and retention processes in relation to anchovy (Engraulis ringens) eggs and larvae distributions in the northern Humboldt upwelling ecosystem. *J. Mar. Res.*, **64**, 189-200.
---, P. Verley, C. Mullon, C. Parada, T. Brochier, P. Penven, and B. Blanke, 2008: A lagrangian tool for modeling ichthyoplankton dynamics. *Environmental Modelling and Software*, **28**, 1210-1214.
Levitus, S., and T. P. Boyer, 1994: World Ocean Atlas 1994*,* Volume 4: Temperature*. NOAA Atlas NESDIS* **4**, U.S. Department of Commerce, 117 pp.
---, R. Burgett, and T. P. Boyer, 1994: World Ocean Atlas 1994*,* Volume 3: Salinity. *NOAA Atlas NESDIS* **3**, U.S. Department of Commerce, 99 pp.
Lévy, M., P. Klein, and A.-M. Tréguier, 2001: Impacts of sub-mesoscale physics on phytoplankton production and subduction. *J. Mar. Res.*, **59**, 535-565.
Lin, J.-L., 2007: Interdecadal variability of ENSO in 21 IPCC AR4 coupled GCMs. *Geophys. Res. Lett.*, **34**, L12702, doi:10.1029/2006GL028937.
Locarnini, R. A., A. V. Mishonov, J. I. Antonov, T. P. Boyer, and H. E. Garcia, 2006: World Ocean Atlas 2005, Volume 1: Temperature. S. Levitus, Ed. *NOAA Atlas NESDIS* **61**, U.S. Government Printing Office, Washington, D.C., 182 pp.
Logerwell, E. A., B. Lavaniegos, and P. E. Smith, 2001: Spatially-explicit bioenergetics of Pacific sardine in the Southern California Bight: are mesoscale eddies areas of exceptional prerecruit production? *Prog. Oceanogr.*, **49**, 391-406.
Lombard, A., A. Cazenave, P.-Y. Le Traon, S. Guinehut, and C. Cabanes, 2006: Perspectives on present-day sea level change: A tribute to Christian le Provost. *Ocean Dyn.*, doi10.1007/s10236-005-0046-x.
Lukas, R., 1986: The termination of the equatorial undercurrent in the eastern Pacific. *Prog. Oceanogr.*, **16**, 63-90.
Madden, R. A., and P. R. Julian, 1971: Detection of a 40–50 day oscillation in the zonal wind field of the tropical Pacific. *J. Atmos. Sci.,* **28,** 702–708.
---, and ---, 1972: Description of global-scale circulation cells in the tropics with a 40–50 day period. *J. Atmos. Sci.,* **29,** 1109–1123.
Madec, G., P. Delecluse, M. Imbard, and C. Lévy, 1998: OPA 8.1 ocean general circulation model reference manual. *Notes du Pôle de Modélisation*, Laboratoire d'Océanographie Dynamics et de Climatologie, Institut Pierre Simon Laplace des sciences de l'environnement global, **11** (December 1998).
Mantua, N. J., and D. S. Battisti, 1995: Aperiodic variability in the Zebiak-Cane coupled ocean-atmosphere model: Air-sea interactions in the western equatorial Pacific. *J. Clim.*, **8**, 2897-2927.
Marchesiello, P., J. C. McWilliams, and A. Shchepetkin, 2001: Open boundary conditions for long-term integration of regional oceanic models. *Ocean Modelling*, **3**, 1–20.
---, ---, and ---, 2003: Equilibrium structure and dynamics of the California Current System. *J. Phys. Oceanogr.*, **33**, 753–783.
---, S. Herbette, L. Nykjaer, and C. Roy, 2004: Eddy-driven dispersion processes in the Canary Current upwelling system: Comparison with the California system. *Globec Int. Newsl.*, **10**, 5–7.
Marti, O., P. Braconnot, J.-L. Dufresne, J. Bellier, R. Benshila, S. Bony, P. Brockmann, P. Cadule, A. Caubel, F. Codron, N. de Noblet, S. Denvil, L. Fairhead, T. Fichefet, M.-A. Foujols, P. Friedlingstein, H. Goosse, J.-Y. Grandpeix, E. Guilyardi, F. Hourdin, A. Idelkadi, M. Kageyama, G. Krinner, C. Lévy, G. Madec, J. Mignot, I. Musat, D. Swingedouw, and C. Talandier, 2009: Key features of the IPSL ocean atmosphere model and its sensitivity to atmospheric resolution. *Clim. Dyn.*, doi:10.1007/s0038200906406.
Martin, G. M., M. A. Ringer, V. D. Pope, A. Jones, C. Dearden and T. J. Hinton, 2006: The physical properties of the atmosphere in the new Hadley Cbetween Global Environment Model, HadGEM1. Part1: Model description and global climatology. *J. Clim.*, **19**, 7, 1274-1301.
McCreary, J., 1981: A linear stratified ocean model of the coastal undercurrent. *Phil. Trans. R. Soc. Lond. A.,* **302**, 385–413.
---, and S. Chao, 1985: Three-dimensional shelf circulation along an eastern ocean boundary. *J. Mar. Res.,* **43**, 1, 13–36.
McGregor, H. V., M. Dima, H. W. Fischer, and S. Mulitza, 2007: Rapid 20th-century increase in coastal upwelling off northwest Africa. *Science*, **315**, 637-639.
McPhaden, M. J., 1993: TOGA-TAO and the 1991–93 El Niño-Southern Oscillation event. *Oceanography,* **6,** 36–44.

---, and B. A. Taft, 1988: Dynamics of seasonal and interannual variability in the eastern equatorial Pacific. *J. Phys. Oceanogr.*, **18**, 1713–1782.
---, A. J. Busalacchi, R. Cheney, J.-R. Donguy, K. S. Gage, D. Halpern, M. Ji, P. Julian, G. Meyers, G. T. Mitchum, P. P. Niiler, J. Picaut, R. W. Reynolds, N. Smith, and K. Takeuchi, 1998: The Tropical Ocean-Global Atmosphere observing system: A decade of progress. *J. Geophys. Res.*, **103**, C7, 14169–14240.
---, S. E. Zebiak, and M. H. Glantz, 2006: ENSO as an integrating concept in Earth science. *Science*, **314**, 1740–1745.
McTaggart, K. E., and Johnson, G. C., 1999: CTD measurements during 1997 and 1998 as part of the Global Ocean–Atmosphere–Land System (GOALS)/Pan American Climate Studies (PACS). *NOAA Data Report ERL PMEL*, **66**, 770 pp.
McWilliams, J. C., F. Colas, and M. J. Molemaker, 2009: Cold filamentary intensification and oceanic surface convergence lines. *Geophys. Res. Lett.*, **36**, L18602, doi:10.1029/2009GL039402.
Meehl, G. A., 1987: The annual cycle and interannual variability in the tropical Indian and Pacific Ocean regions. *Mon. Wea. Rev.*, **115**, 27-50.
---, C. Covey, T. Delworth, M. Latif, B. McAvaney, J. F. B. Mitchell, R. J. Stouffer, and K. E. Taylor, 2007: The WCRP CMIP3 multimodel dataset: A new era in climate change research. *Bull. Amer. Meteor. Soc.,* **88,** 1383–1394.
Merryfield, W. J., 2006: Changes to ENSO under CO_2 doubling in a multimodel ensemble. *J. Clim.*, **19**, 4009-4027.
Mitchell, T. P., and J. M. Wallace, 1992: The annual cycle in equatorial convection and sea surface temperature. *J. Clim.*, **5**, 1140–1156.
Molines, J.-M., B. Barnier, T. Penduff, L. Brodeau, A.-M. Treguier, S. Theetten, and G. Madec, 2006: Definition of the global ½° experiment with CORE interannual forcing, ORCA05-G50. *LEGI report*, LEGI-DRA-1-11-2006 (November 2006).
Montecinos, A., O. Leth, and O. Pizarro, 2007: Wind-driven interdecadal variability in the eastern tropical and South Pacific. *J. Geophys. Res.*, **112**, C04019, doi:10.1029/2006JC003571.
Montes, I., F. Colas, X. Capet, and W. Schneider, 2009: On the pathways of the equatorial subsurface currents in the eastern equatorial Pacific and their contribution to the Peru-Chile undercurrent. *Submitted*.
Moore, D. W., 1968: Planetary-gravity waves in an equatorial ocean. *PhD thesis, Harvard Univ.*, Cambridge, Massachussets, USA.
Moss, R., M. Babiker, S. Brinkman, E. Calvo, T. Carter, J. Edmonds, I. Elgizouli, S. Emori, L. Erda, K. Hibbard, R. Jones, M. Kainuma, J. Kelleher, J.-F. Lamarque, M. Manning, B. Matthews, J. Meehl, L. Meyer, J. Mitchell, N. Nakicenovic, B. O'Neill, R. Pichs, K. Riahi, S. Rose, P. Runci, R. Stouffer, D. van Vuuren, J. Weyant, T. Wilbanks, J.-P. van Ypersele, and M. Zurek, 2008: Towards new scenarios for analysis of emissions, climate change, impacts, and response strategies. *Intergovernmental Panel on Climate Change*, Geneva, 132pp.
Muñoz, R., and R. Garreaud, 2005: Dynamics of the low-level jet off the subtropical west coast of South America. *Mon. Wea. Rev.*, **133**, 3661-3677.
Nakicenovic, N., and R. Swart (Eds), 2000: Special report on emissions scenarios. *Cambridge Univ. Press, New York*.
Neelin, J. D., and F.-F. Jin, 1993: Modes of interannual tropical ocean-atmosphere interaction – A unified view. Part II: Analytical results in the weak-coupling limit. *J. Atmos. Sci.*, **50**, 3504-3522.
---, D. S. Battisti, A. C. Hirst, F.-F. Jin, Y. Wakata, T. Yamagata, and S. E. Zebiak, 1998: ENSO theory. *J. Geophys. Res.*, **103**, C7, 14261-14290.
Neftel, A., E. Moor, H. Oeschger, and B. Stauffer, 1985: Evidence from polar ice cores for the increase in atmospheric CO_2 in the past two centuries. *Nature*, **315**, 45-47.
NRC (National Research Council), 1994: Solar influences on global change. *Washington, D.C., National Academy Press*, pp.36, ISBN 0-309-05148-7.
---, 2004: Understanding climate change feedbacks. *Panel on Climate Change Feedbacks, Climate Research Committee, National Academy Press*, ISBN 0-309-09072-5.
Neshyba, S. J., C. N. K. Mooers, R. L. Smith, and R. T. Barber, 1989: Poleward flows along eastern ocean boundaries. *Coastal and Estuarine Studies*, **34**, 374pp. Springer-Verlag New York, Inc. ISBN 0-387-97175-O.
Parker, D. E., 1973: Equatorial Kelvin waves at 100 millibars. *Quart. J. Roy. Meteor. Soc.,* **99,** 116–129.
Pearson, P. N., and M. R. Palmer, 2000: Atmospheric carbon dioxide concentrations over the past 60 million years. *Nature*, **406**, 6797, 695-699.
Pedlosky, J., 1987: *Geophysical Fluid Dynamics*. 710 pp., Springer-Verlag, New York.
Penven, P., C. Roy, J. R. E. Lutjeharms, A. Colin de Verdière, A. Johnson, F. Shillington, P. Fréon, and G. Brundrit, 2001: A regional hydrodynamic model of the Southern Benguela. *S. Afr. J. Sci.,* **97**, 472– 476.

---, V. Echevin, J. Pasapera, F. Colas, and J. Tam, 2005: Average circulation, seasonal cycle, and mesoscale dynamics of the Peru Current System: A modelling approach. *J. Geophys. Res.*, **110**, C10021, doi:10.1029/2005JC002945.

---, P. Marchesiello, L. Debreu, and J. Lefevre, 2008: Software tools for pre- and post-processing of oceanic regional simulations. *Environ. Modell. Softw.*, **23**, 660-662.

Philander, S. G. H., 1978: Instabilities of zonal equatorial currents, 2. *J. Geophys. Res.*, **83**, 3679–3682.

---, and P. Delecluse, 1983: Coastal currents in low latitudes (with application to the Somali and El Niño currents). *Deep-Sea Res.*, **30**, 887–902.

Picaut, J., F. Masia, and Y. du Penhoat, 1997: An advective-reflective conceptual model for the oscillatory nature of the ENSO. *Science*, **277**, 663-666.

Pizarro, O., A. J. Clarke, and S. Van Gorder, 2001: El Niño sea level and currents along the South American coast: Comparison of observations with theory. *J. Phys. Oceanogr.*, **31**, 1891-1903.

---, G. Shaffer, B. Dewitte, and M. Ramos, 2002: Dynamics of seasonal and interannual variability of the Peru-Chile Undercurrent. *Geophys. Res. Lett.*, **29**, 12, 1581, 10.1029/2002GL014790.

Polo, I., A. Lazar, B. Rodriguez-Fonseca, and S. Arnault, 2008: Oceanic Kelvin waves and tropical Atlantic intraseasonal variability: 1. Kelvin wave characterization. *J. Geophys. Res.*, **113**, C07009, doi:10.1029/2007JC004495.

Pope, V., M. L. Gallani, P. R. Rowntree, and R. A. Stratton, 2000: The impact of new physical parameterizations in the Hadley Cbetween climate model: HadAM3. *Clim. Dyn.*, **16**, 123-146.

Ramanathan, V., C. Chung, D. Kim, T. Bettge, L. Buja, J. T. Kiehl, W. M. Washington, Q. Fu, D. R. Sikka, and M. Wild, 2005: Atmospheric brown clouds: Impacts on South Asian climate and hydrological cycle. *Proc. Natl. Acad. Sci. U.S.A.*, **102**, 5326–5333.

---, M. Agrawal, H. Akimoto, M. Aufhammer, S. Devotta, L. Emberson, S. I. Hasnain, M. Iyngararasan, A. Jayaraman, M. Lawrance, T. Nakajima, T. Oki, H. Rodhe, M. Ruchiwarat, S. K. Tan, J. Vincent, J. Y. Wang, D. Yang, Y. H. Zhang, H. Autrup, L. Barregard, P. Bonasoni, M. Brauer, B. Brunekreef, G. Carmichael, C. E. Chung, J. Dahe, Y. Feng, S. Fuzzi, T. Gordon, A. K. Gosain, N. Htun, J. Kim, S. Mourato, L. Naeher, P. Navasumrit, B. Ostro, T. Panwar, M. R. Rahman, M. V. Ramana, M. Rupakheti, D. Settachan, A. K. Singh, G. St. Helen, P. V. Tan, P. H. Viet, J. Yinlong, S. C. Yoon, W.-C. Chang, X. Wang, J. Zelikoff, and A. Zhu, 2008: Atmospheric brown clouds: Regional assessment report with focus on Asia. *United Nations Environment Programme*.

Ramos, M., B. Dewitte, O. Pizarro, and G. Garric, 2008: Vertical propagation of extratropical Rossby waves during the 1997-1998 El Niño off the west coast of South America in a medium-resolution OGCM simulation. *J. Geophys. Res.*, **113**, C08041, doi:10.1029/2007JC004681.

Rasmusson, E. M., and T. H. Carpenter, 1982: Variations in tropical sea surface temperature and surface wind fields associated with the Southern Oscillation/El Niño. *Mon. Wea. Rev.,* **110,** 354–384.

Rein, B., A. Lückge, and F. Sirocko, 2004: A major Holocene ENSO anomaly during the Medieval period. *Geophys. Res. Lett.*, **31**, L17211, doi:10.1029/2004GL020161.

Renault, L., 2008: Impact des jets côtiers atmosphériques sur l'upwelling du Système de Courants de Humboldt. *Thèse de l'Université de Paul Sabatier*, 245 pp.

---, B. Dewitte, M. Falvey, R. Garreaud, V. Echevin, and F. Bonjean, 2009: Impact of atmospheric coastal jet off central Chile on sea surface temperature from satellite observations (2000–2007). *J. Geophys. Res.*, **114**, C08006, doi:10.1029/2008JC005083.

Repo, M. E., 2009: Large N_2O emissions from cryoturbated peat soil in tundra. *Nature Geoscience*, **2**, 189, doi:10.1038/ngeo434.

Reverdin, G., C. Frankignoul, E. Kestenare, and M. J. McPhaden, 1994: Seasonal variability in the surface currents of the equatorial Pacific. *J. Geophys. Res.*, **99**, 20323-20344.

Ringer, M. A., G. M. Martin, C. Z. Greeves, T. J. Hinton, P. M. James, V. D. Pope, A. A. Scaife, R. A. Stratton, P. M. Inness, J. M. Slingo, and G.-Y. Yang, 2006: The physical properties of the atmosphere in the new Hadley Cbetween Global Environment Model, HadGEM1. Part2: Aspects of variability and regional climate. *J. Clim.*, **19**, 7, 1302-1326.

Robles, F., 1979: Water masses and circulation in the SE Pacific and the El Niño event. *PhD thesis*, University of Wales, United Kingdom.

Roeckner, E., K. Arpe, L. Bengtsson, M. Christoph, M. Claussen, L. Dümenil, M. Esch, M. Giorgetta, U. Schlese, and U. Schulzweida, 1996: The atmospheric general circulation model ECHAM-4: Model description and simulation of present-day climate. *Reports of the Max Planck Institute*, Hamburg, No. 218, 90 pp.

Ropelewski, C. F., M. S. Halpert, and X. Wang, 1992: Observed tropospheric biennial variability and its relationship to the Southern Oscillation. *J. Clim.,* **5,** 594–614.

Rouault, M., S. Illig, C. Bartholomae, C. J. C. Reason, and A. Bentamy, 2007: Propagation and origin of warm anomalies in the Angola Benguela upwelling system in 2001. *J. Mar. Sys.*, **68**, 3-4, 473-488.

Rowe, G. D., E. Firing, and G. C. Johnson, 2000: Pacific equatorial subsurface countercurrent velocity, transport, and potential vorticity. *J. Phys. Oceanogr.*, **30**, 1172–1187.

Royer, J.-F., D. Cariolle, F. Chauvin, M. Déqué, H. Douville, R. M. Hu, S. Planton, A. Rascol, J.-L. Ricard, D. Salas-Mélia, F. Sevault, P. Simon, S. Somot, S. Tytéca, L. Terray, and S. Valcke, 2002: Simulation des changements climatiques au cours du 21-ième siècle incluant l'ozone stratosphérique. *C. R. Geophys.*, **334**, 147-154.

Schopf, P. S., and M. J. Suarez, 1988: Vacillations in a coupled ocean-atmosphere model. *J. Atmos. Sci.*, **45**, 549-566.

Seo, H., A. J. Miller, and J. O. Roads, 2007: The Scripps Coupled Ocean-Atmosphere Regional (SCOAR) model, with applications in the eastern Pacific sector. *J. Clim.*, **20**, 381-402.

Sepulchre, P., L. C. Sloan, M. Snyder, and J. Fiechter, 2009: Impacts of Andean uplift on the Humboldt Current system: A climate model sensitivity study. *Paleoceanogr.*, **24**, PA4215, doi:10.1029/2008PA001668.

Shaffer, G., O. Pizarro, L. Djurfeldt, S. Salinas, and J. Rutllant, 1997: Circulation and low-frequency variability near the Chilean coast: Remotely forced fluctuations during the 1991-1992 El Niño. *J. Phys. Oceanogr.*, **27**, 217-235.

---, S. Hormazabal, O. Pizarro, and S. Salinas, 1999: Seasonal and interannual variability of currents and temperature off central Chile. *J. Geophys. Res.*, **104**, C12, 29951-29962.

Shannon, L. V., A. J. Boyd, G. B. Brundrit, and J. Taunton-Clark, 1986: On the existence of an El Niño-type phenomenon in the Benguela system. *Journal of Marine Research*, **44**, 495-520.

Shchepetkin, A. F., and J. C. McWilliams, 1998: Quasi-monotone advection schemes based on explicit locally adaptive dissipation. *Mon. Weather Rev.*, **126**, 1541–1580.

---, and ---, 2005: The Regional Oceanic Modeling System: A split-explicit, free-surface, topography-following-coordinate ocean model. *Ocean Modelling*, **9**, 347-404.

Sifeddine, A., D. Gutierrez, L. Ortlieb, H. Boucher, F. Velazco, D. Field, G. Vargas, M. Boussafir, R. Salvatteci, V. Ferreira, M. Garcia, J. Valdes, S. Caquineau, M. Mandeng Yogo, F. Cetin, J. Solis, P. Soler, and T. Baumgartner, 2008: Laminated sediments from the central Peruvian continental slope: A 500 year record of upwelling system productivity, terrestrial runoff and redox conditions. *Progr. Oceanogr.*, **79**, 190-197.

---, ---, M. Gurgel, M. Garcia, L. Ortlieb, M. Boussafir, F. Velazco, H. Boucher, S. Caquineau, and J. Valdes: Interdecadal to centennial variability of paleoproductivity and redox conditions in the Peruvian continental margin during the last two millenia. *In preparation*.

Silva, N., and S. Neshyba, 1979: On the southernmost extension of the Peru-Chile Undercurrent. *Deep-Sea Res*., **26**, A, 1387-1393.

---, and T. R. Fonseca, 1983: Geostrophic component of the oceanic flow off northern Chile. *Conferencia Internacional sobre Recursos Marinos del Pacifico*, P. Arana (Ed.), 59-70.

Simo, R., 2002: Global ocean emission of dimethylsulfide predicted from biogeophysical data. *Global Biogeochemical Cycles*, **16**, 1018, doi:10.1029/2001GB001829.

Skogen, M. D., 2005: Clupeoid larval growth and plankton production in the Benguela upwelling system. *Fish. Oceanogr.*, **14**, 1, 64-70.

Slingo, J. M., D. P. Rowell, K. R. Sperber, and F. Nortley, 1999: On the predictability of the interannual behaviour of the Madden-Julian oscillation and its relationship with El Niño. *Q. J. R. Meteorol. Soc.*, **125**, 554, 583-609.

Sloyan, B. S., G. C. Johnson, and W. S. Kessler, 2003: The Pacific cold tongue: an indicator of hemispheric exchange. *J. Phys. Oceanogr.*, **33**, 1027–1043.

Smith, R. L., 1983: Peru coastal currents during El Niño: 1976 and 1982. *Science*, **221**, 1397-1399.

Smith, T. M., and R. W. Reynolds, 2004: Improved extended reconstruction of SST (1854–1997). *J. Clim.*, **17**, 2466–2477.

---, ---, T. C. Peterson, and J. Lawrimore, 2008: Improvements to NOAA's historical merged land-ocean surface temperature analysis (1880–2006). *J. Clim.*, **21**, 2283–2296.

Smith, W. H. F., and D. T. Sandwell, 1997: Global seafloor topography from satellite altimetry and ship depth soundings. *Science*, **277**, 1957-1962.

Snyder, M. A., L. C. Sloan, N. S. Diffenbaugh, and J. L. Bell, 2003: Future climate change and upwelling in the California Current. *Geophys. Res. Lett.*, **30**, doi:10.1029/2003GL017647.

Soden, B. J., and I. M. Held, 2005: An assessment of climate feedbacks in coupled ocean-atmosphere models. *J. Clim.*, **19**, 14, 3354-3360.

Spillane, M. C., D. B. Enfield, and J. S. Allen, 1987: Intraseasonal oscillations in sea level along the west coast of the Americas. *J. Phys. Oceanogr.*, **17**, 313-325.

Steger, J. M., C. A. Collins, and P. C. Chu, 1998: Circulation in the Archipielago de Colon (Galapagos Islands), November 1993. *Deep-Sea Res.* II, **45**, 1093–1114.

Stott, P. A., G. S. Jones, and J. F. B. Mitchell, 2003: Do models underestimate the solar contribution to recent climate change? *J. Clim.*, **16**, 4079-4093.
Strub, P. T., and C. James, 2002: The 1997-1998 oceanic El Niño signal along the southeast and northeast Pacific boundaries - an altimetric view. *Progr. Oceanogr*, **54**, 439–458.
---, J. M. Mesias, and C. James, 1995: Altimeter observations of the Peru-Chile countercurrent. *Geophys. Res. Lett.*, **22**, 211– 214.
---, ---, V. Montecino, J. Rutllant, and S. Salinas, 1998: Coastal ocean circulation off western South America. *The Sea*, **11**, A. R. Robinson and K. H. Brink (Eds.), 273-314, John Wiley, Hoboken, N. J.
Strong, A. E., 1986: Monitoring El Niño using satellite based sea surface temperatures. *Ocean-Air Interact.*, **1**, 11-28.
Suarez, M. J., and P. S. Schopf, 1988: A delayed oscillator for ENSO. *J. Atmos. Sci.*, **45**, 3283-3287.
Sutor, M. M., T. J. Cowles, W. T. Peterson, and S. D. Pierce, 2005: Acoustic observations of finescale zooplankton distributions in the Oregon upwelling region. *Deep-Sea Res.*, II, **52**, 109-121.
Sutton, R. T., B. Dong, and J. M. Gregory, 2007: Land/sea warming ratio in response to climate change: IPCC AR4 model results and comparison with observations. *Geophys. Res. Lett.*, **34**, L02701, doi:10.1029/2006GL028164.
Sverdrup, H. U., 1947: Wind-driven currents in a baroclinic ocean; with application to the equatorial currents of the eastern Pacific. *Proc. Natl. Acad. Sci. U.S.A.*, **33**, 318– 326.
Swenson, M. S., and D. V. Hansen, 1999: Tropical Pacific Ocean mixed layer heat budget: The Pacific cold tongue. *J. Phys. Oceanogr.*, **29**, 69–81.
Takahashi, K., 2005: The annual cycle of heat content in the Peru Current region. *J. Clim.*, **18**, 23, 4937-4954.
Taschetto, A. S., and M. H. England, 2009: El Niño Modoki impacts on Australian rainfall. *J. Clim.*, **22**, 3167–3174.
Timmermann, A., F.-F. Jin, and J. Abshagen, 2003: A nonlinear theory for El Niño bursting. *J. Atmos. Sci.*, **60**, 152-165.
Toggweiler, J. R., K. Dixon, and W. S. Broecker, 1991: The Peru upwelling and the ventilation of the South Pacific thermocline. *J. Geophys. Res.*, **96**, 20467–20497.
Tourre, Y. M., Y. Kushnir, and W. B. White, 1999: Evolution of interdecadal variability in sea level pressure, sea surface temperature, and upper ocean temperature over the Pacific Ocean. *J. Phys. Oceanogr.,* **29,** 1528–1541.
Tsuchiya, M., 1975: Subsurface countercurrents in the eastern equatorial Pacific. *J. Mar. Res.*, **33**, 145-175.
---, 1985: The subthermocline phosphate distribution and circulation in the far eastern equatorial Pacific Ocean. *Deep-Sea Res.*, **32**, 299–313.
UNESCO, 1981: Tenth Report of the Joint Panel on Oceanographic Tables and Standards. *UNESCO Tech. Pap. Mar. Sci.*, **37**, 144 pp.
Uppala, S. M., P. W. Kalberg, A. J. Simmons, U. Andrae, V. da Costa Bechtold, M. Fiorino, J. K. Gibson, J. Haseler, A. Hernandez, G. Kelly, X. Li, K. Onogi, S. Saarinen, N. Sokka, R. P. Allan, E. Anderson, K. Arpe, M. A. Balmaseda, A. C. M. Beljaars, L. van den Berg, J. Bidlot, N. Borman, S. Caires, A. Dethof, M. Dragosavac, M. Fisher, M. Fuentes, S. Hagemann, E. Holm, B. J. Hoskins, L. Isaksen, P. A. E. M. Janssen, R. Jenne, A. McNally, J.-F. Mahfouf, J.-J. Mocrette, N. A. Rayner, R. W. Saunders, P. Simon, A. Sterl, K. E. Trenberth, A. Untch, D. Vasiljevic, P. Viterbo, and J. Woollen, 2005: The ERA-40 reanalysis, *Quart. J. Roy.Meteor. Soc.*, **131**, 2961-3012.
van Oldenborgh, G. J., S. Y. Philip, and M. Collins, 2005: El Niño in a changing climate: A multi-model study. *Ocean Science*, **1**, 81-95.
Vargas, G., S. Pantoja, J. A. Rutllant, C. B. Lange, and L. Ortlieb, 2007: Enhancement of coastal upwelling and interdecadal ENSO-like variability in the Peru-Chile current since late 19th century. *Geophys. Res. Lett.*, **34**, L13607, doi:10.1029/2006GL028812.
Vazquez, J., A. Tran, R. Sumagaysay, E. A. Smith, and M. Hamilton, 1995: NOAA/NASA AVHRR oceans pathfinder sea surface temperature data set user's guide version 12. *JPL Technical Report*, pp. 55.
Vecchi, G. A., B. J. Soden, A. T. Wittenberg, I. M. Held, A. Leetmaa, and M. J. Harrison, 2006: Weakening of tropical Pacific atmospheric circulation due to anthropogenic forcing. *Nature,* **327,** 216–219.
---, and ---, 2007: Global warming and the weakening of the tropical Pacific circulation. *J. Clim.,* **20,** 4316–4340.
---, A. Clement, and B. J. Soden, 2008: Examining the tropical Pacific's response to global warming. *Eos, Trans. Amer. Geophys. Union,* **89,** 81–83.
Vega, A., Y. duPenhoat, B. Dewitte, and O. Pizarro, 2003: Equatorial forcing of interannual Rossby waves in the South eastern Pacific. *Geophys. Res. Lett.*, **30**, 1197–1200.
Vélez, J. A., W. Watson, W. Arntz, M. Wolff, and S. B. Schnack-Schiel, 2005: Larval fish assemblages in Independencia Bay, Pisco, Peru: temporal and spatial relationships. *Mar. Biol.*, **147**, 77-91.

Vialard, J., C. Menkes, J.-P. Boulanger, P. Delecluse, E. Guilyardi, M. J. McPhaden, and G. Madec, 2001: A model study of oceanic mechanisms affecting equatorial Pacific sea surface temperature during the 1997-98 El Niño. *J. Phys. Oceanogr.*, **31**, 7, 1649–1675.

Volodin, E. M., and N. A. Diansky, 2004: El-Niño reproduction in coupled general circulation model of atmosphere and ocean. *Russian meteorology and hydrology*, **12**, 5-14.

Wang, B., and S.-I. An, 2001: Why the properties of El Niño changed during the late 1970s. *Geophys. Res. Lett.,* **28,** 3709–3712.

Wang, G., and H. H. Hendon, 2007: Sensitivity of Australian rainfall to Inter–El Niño variations. *J. Clim.*, **20**, 4211– 4226.

Weare, B., P. T. Strub, and M. D. Samuels, 1976: Marine climate atlas of the tropical Pacific Ocean. *Contributions in Atmospheric Science*, **20**. University of California-Davis, Davis, California.

Webb, D. J., and B. A. de Cuevas, 2003: The region of large sea surface height variability in the Southeast Pacific Ocean. *J. Phys. Oceanogr.*, **33**, 5, 1044–1056.

Weisberg, R. H., and C. Wang, 1997: A western Pacific oscillator paradigm for the El Niño-Southern Oscillation. *Geophys. Res. Lett.,* **24,** 779–782.

Weng, H., K. Ashok, S. K. Behera, S. A. Rao, and T. Yamagata, 2007: Impacts of recent El Niño Modoki on dry/wet conditions in the Pacific rim during boreal summer. *Clim. Dyn*. **29**, 113-129.

---, S. K. Behera, and T. Yamagata, 2009: Anomalous winter climate conditions in the Pacific rim during recent El Niño Modoki and El Niño events. *Clim. Dyn.*, **32**, 663-674.

Willett, C.S., R. Leben, and M. F. Lavin, 2006: Eddies and mesoscale processes in the eastern tropical Pacific: A review. *Progr. Oceanogr.*, **69**, 2–4, 218–238.

Wilson, R. C., and A. V. Mordvinov, 2003: Secular total solar irradiance trend during solar cycles 21-23. *Geophys. Res. Lett.*, **30**, 5, 1199.

Wittenberg, A. T., 2009: Are historical records sufficient to constrain ENSO simulations? *Geophys. Res. Lett.,* **36,** L12702, doi:10.1029/2009GL038710.

Wu, R., and B. P. Kirtman B. P., 2005: Near-annual SST variability in the equatorial Pacific in a Coupled General Circulation Model. *J. Clim.*, **18**, 4454–4473.

Wyrtki, K., 1963: The horizontal and vertical field of motion in the Peru Current. *Bull. Scripps Inst. Oceanogr.*, **8**, 313–344.

---, 1966: Oceanography of the eastern equatorial Pacific Ocean. *Oceanography and Marine Biology Annual Review*, **4**, 33–68.

---, 1967: Circulation and water masses in the eastern equatorial Pacific Ocean. *J. Oceanol. Limnol.*, **1**, 117–147.

---, 1975: El Niño-the dynamic response of the equatorial Pacific Ocean to atmospheric forcing. *J. Phys. Oceanogr.*, **5**, 4, 572-584.

---, 1981: An estimate of equatorial upwelling in the Pacific. *J. Phys. Oceanogr.*, **11**, 1205–1214.

Xie, P., and P. A. Arkin, 1996: Analysis of global monthly precipitation using gauge observations, satellite estimates, and numerical model predictions. *J. Climate*, **9**, 840–858.

Xie, S.-P., T. Miyama, Y. Wang, H. Xu, S. P. De Szoeke, R. J. O. Small, K. J. Richards, T. Mochizuki, and T. Awaji, 2007: A regional ocean-atmosphere model for eastern Pacific climate: Toward reducing tropical biases. *J. Clim.*, **20**, 1504-1522.

Xu, H., Y. Wang, and S.-P. Xie, 2004: Effects of the Andes on eastern Pacific climate: A regional atmospheric model study. *J. Clim.*, **17**, 589-602.

Xue, Y., T. M. Smith, and R. W. Reynolds, 2003: Interdecadal changes of 30-yr SST normals during 1871-2000. *J. Clim.*, **16**, 1601-1612.

Yeh, S.-W., J.-S. Kug, B. Dewitte, M.-H. Kwon, B. P. Kirtman, and F.-F. Jin, 2009: El Niño in a changing climate. *Nature*, **461**, 511-514.

Yu, J.-Y., and C. R. Mechoso, 1999: Links between annual variations of peruvian stratocumulus clouds and of SST in the eastern equatorial Pacific. *J. Clim.*, **12**, 11, 3305-3318.

Yu, X. R., and M. J. McPhaden, 1999a: Dynamical analysis of seasonal and interannual variability in the equatorial Pacific. *J. Phys. Oceanogr.*, **29**, 2350–2369.

---, and ---, 1999b: Seasonal variability in the equatorial Pacific. *J. Phys. Oceanogr.*, **29**, 925–947.

Yu, Z. J., J. P. McCreary, and J. A. Proehl, 1995: Meridional asymmetry and energetics of tropical instability waves. *J. Phys. Oceanogr.*, **25**, 2997–3007.

Zebiak, S. E., and M. A. Cane, 1987: A model El Niño-Southern Oscillation. *Mon. Wea. Rev.,* **115,** 2262–2278.

Zelle, H., G. J. van Oldenborgh, G. Burgers, and H. A. Dijkstra, 2005: El Niño and global change: Results from ensemble simulations with the NCAR CCSM. *J. Clim.*, **18**, 4669–4683.

Zhang, R.-H., L. M. Rothstein, and A. J. Busalacchi, 1999: Interannual and decadal variability of the subsurface thermal structure in the Pacific Ocean. *Clim. Dyn.,* **15,** 703–717.

Zimov, S. A., E. A. G. Schuur, and F. S. Chapin III, 2006: Climate change: Permafrost and the global carbon budget. *Science*, **312**, 5780, 1612-1613.